Novel magnetisation transfer catalysts and their applications in hyperpolarised magnetic resonance

Ben. J. Tickner

Doctor of Philosophy

University of York

Chemistry

April 2020

Abstract

Signal Amplification By Reversible Exchange (SABRE) is a hyperpolarisation technique that uses iridium catalysts to transfer magnetisation from *para*hydrogen (p-H$_2$) to target substrates. Relayed polarisation *via* ^{1}H exchange involving [Ir(H)$_2$(IMes)(NH$_3$)$_3$]Cl achieves 1400-fold ^{13}C and 700-fold ^{1}H NMR signal enhancements at 9.4 T for non-ligating alcohols such as 3-methyl-1-butanol. This is extended to natural products, lactate esters and pyruvate.

Sodium pyruvate ^{13}C NMR signal enhancements of just 65-fold are only visible <15 minutes after pyruvate addition to [Ir(H)$_2$(IMes)(NH$_2$R)$_3$]Cl due to formation of [Ir(H)$_2$(κ^2-OOCC(CH$_3$)NR)(IMes)(NH$_2$R)]. Hyperpolarised ^{13}C sites of these bound imine ligands exist as singlet states with NMR signal enhancements and lifetimes of 750-fold and 20 s respectively. The chemical shift of the hydride ligands vary by 15.5 ppm allowing ligand sensing applications.

The hyperpolarisation of α-keto acids *via* [Ir(H)$_2$(IMes)(κ^2-O-substrate)(sulfoxide)] achieves ^{13}C NMR signal enhancements of 2135-fold for sodium pyruvate-1,2-[^{13}C$_2$] and 985-fold for sodium ketoisokaproate-[1-^{13}C] in methanol-d_4 at 9.4 T. EXSY and DFT studies reveal that [IrCl(H)$_2$(IMes)(sulfoxide)$_2$] plays an important role by refreshing p-H$_2$.

SABRE hyperpolarised ^{13}C NMR was used to monitor the reaction between pyruvate and H$_2$O$_2$. Kinetic fitting at 298 K yields a rate constant (0.056 ± 0.003 dm^3 mol^{-1} s^{-1}) consistent with values obtained from thermal ^{1}H NMR and UV spectroscopy. Interestingly, a short lived 2-hydroxy-2-propanoate intermediate can be detected in a single scan ^{13}C NMR spectrum at 273 K.

The polarisation transfer catalysts presented expand the scope of SABRE and allow MR applications such as chemosensing, reaction monitoring, and intermediate detection. Hyperpolarisation of molecules such as pyruvate is now achieved using a readily accessible and simple approach that does not involve chemical modification.

Table of Contents

List of Figures

Figure 6.3: a) Photograph of the apparatus used to insert three 10 mm NMR tubes into the imaging coil of the 9.4 T magnet. This consists of three NMR tubes inside a larger 50 mL Falcon tube filled with water. A 3D printed holder was inserted into the Falcon tube to hold the three NMR tubes in place. Paper tissue was used to adjust the NMR tubes to the appropriate height b) i) Overlaid ^{1}H FLASH (greyscale) and ^{13}C CSI image (coloured scale) of SABRE hyperpolarised **22-1,2-[$^{13}C_2$]** with regions ii), iii) and iv) corresponding to hyperpolarised pyruvate, thermally polarised pyruvate and glacial ethanoic acid reference respectively. The ^{13}C CSI image (16 × 16) was recorded using 5° flip angles and a 20 mm slice thickness. TE = 1.2ms, TR = 100ms, 1200 spectral points, 20 kHz sweep width, 17.4 kHz offset. The coloured scale denotes the area of the

List of Tables

Acknowledgements

Author's Declaration

I declare that this thesis is a presentation of original work and I am the sole author. This work has not previously been presented for an award at this, or any other, University. All sources are acknowledged as references. Any DFT calculations were performed by Dr. Richard O. John. X ray diffraction data were collected and solved by Dr Sam. J. Hart, Dr. Rachel R. Parker, or Dr. Adrian C. Whitwood. The iridium precatalysts used in this work were synthesised by Dr. Victoria Annis, Hannah Kettle, or Dr. Peter J. Rayner. Some of the work detailed in this thesis has been presented in the publications listed below (given in the Appendix).

- P. J. Rayner, B. J. Tickner, W. Iali, M. Fekete, A. D. Robinson and S. B. Duckett, Relayed Hyperpolarisation from *Para*hydrogen Improves the NMR Detectability of Alcohols, *Chem. Sci.*, 2019, **10**, 7709-7717.

- B. J. Tickner, W. Iali, S. S. Roy, A. C. Whitwood and S. B. Duckett, Iridium α-Carboxyimine Complexes Hyperpolarized with *Para*hydrogen Exist in Nuclear Singlet States before Conversion into Iridium Carbonates, *ChemPhysChem*, 2019, **20**, 241-245.

- B. J. Tickner, R. O. John, S. S. Roy, S. J. Hart, A. C. Whitwood and S. B. Duckett, Using Coligands to gain Mechanistic Insight into Iridium Complexes Hyperpolarized with *Para*hydrogen, *Chem. Sci.*, 2019, **10,** 5235-5245**.**

- W. Iali, S. S. Roy, B. J. Tickner, F. Ahwal, A. J. Kennerley and S. B. Duckett, Hyperpolarising Pyruvate through Signal Amplification by Reversible Exchange (SABRE), *Angew. Chem.*, 2019**, 131**, 10377-10381.

- B. J. Tickner, J. S. Lewis, R. O. John, A. C. Whitwood and S. B. Duckett, Mechanistic Insight into Novel Sulfoxide Containing SABRE Polarisation Transfer Catalysts, *Dalton Trans.*, 2019**, 48**, 15198-15206.

- B. J. Tickner, R. R. Parker, A. C. Whitwood and S. B. Duckett, Probing the Hydrogenation of Vinyl Sulfoxide using *Para*hydrogen, *Organomet.*, 2019**, 38**, 4377-4382*.*

- B. J. Tickner, O. Semenova, W. Iali, P. J. Rayner, A. C. Whitwood and S. B. Duckett, Optimising the Hyperpolarisation of Pyruvate using SABRE by Tuning the Active Magnetisation Transfer Catalyst, *Cat. Sci. Technol.,* 2020, **10**, 1343-1355.

- B. J. Tickner, P. J. Rayner and S. B. Duckett, Using SABRE hyperpolarized ^{13}C NMR to interrogate organic transformations of pyruvate, *Anal. Chem.*, In Press.

Chapter 1: Introduction

Magnetic Resonance (MR) techniques use magnetic fields and radiofrequency (*r.f.*) pulses to excite nuclear spins within molecules and are some of the most versatile tools available for the structural characterisation of molecules.[1-3] Nuclear Magnetic Resonance (NMR) is commonly used in the routine detection and structural elucidation of a wide range of molecules including organic compounds, inorganic complexes, proteins and many others. The related Magnetic Resonance Imaging (MRI) can produce anatomically detailed 3D images for clinical disease diagnosis. MRI is able to investigate soft tissue structure and is most commonly used to detect abnormalities in tissue morphology.[4] The use of non-ionising and non-invasive radiation (compared to PET, CT or X rays) is an additional advantage and as a result, MRI is routinely used in clinical medicine. The fundamentals of MR are discussed in section 1.1.

Many approaches have been developed to improve disease diagnosis by MRI including administration of paramagnetic contrast agents which are discussed in section 1.2. While these agents can improve MR contrast, they do not change intrinsic MR sensitivity. The cause of MR insensitivity on the molecular level, and the different hyperpolarisation techniques used to address this problem, are discussed in section 1.3. It is an aim of scientists working in this area to use hyperpolarised biomolecules as *in vivo* reporters to study human metabolomics and provide imaging methodologies that give information about tissue function in addition to static tissue structure.[5] The types of molecules commonly used as hyperpolarised contrast agents are discussed in section 1.5.

1.1 Theory of Magnetic Resonance (MR)

1.1.1 Fundamentals of Nuclear Magnetic Resonance (NMR)

Spectroscopic techniques generally rely on the excitation of a ground state energy level to form a higher energy excited state. As energy levels are quantised, specific frequencies of radiation are required to excite transitions between them. These energies can be calculated according to Equation 1.1, where ΔE is the energy difference between two energy levels, h is Planck's constant, and v is the radiation frequency.[1]

$$\Delta E = hv \qquad (1.1)$$

Unlike electronic or vibrational spectroscopy which use ultraviolet (UV) or infrared (IR) frequencies to excite electronic or vibrational transitions respectively, NMR uses radiowaves to excite transitions between nuclear spin energy levels.[1] As nuclear spin energy levels are very closely spaced in energy, only low frequency (and low energy) radiation is needed to match the resonance condition described in Equation 1.1.

The phenomenon of MR is based upon the property of nuclear spin, $(\hat{I})$, which is a vector containing contributions from each of the Cartesian directions, $(\hat{I}_x, \hat{I}_y, \hat{I}_z)$.[2] Nuclear spin is described using the nuclear spin quantum number, I, which takes integer or half integer values. Those nuclei for which $I = 0$, such as ^{12}C or ^{16}O, have no nuclear spin and do not exhibit MR properties.[1] Nuclear spins in which $I > 0$ will contain both nuclear spin, $(\hat{I})$, and magnetic moment, $(\hat{\mu})$, which is also a vector. The nuclear spin, $(\hat{I})$, and magnetic moment, $(\hat{\mu})$, are related through a proportionality constant called the gyromagnetic ratio, γ, as shown in Equation 1.2.[2]

$$\hat{I} = \gamma\hat{\mu} \qquad (1.2)$$

The magnetic moment $(\hat{\mu})$ of a collection of nuclei are each randomly aligned, or isotropic, in the absence of a magnetic field.[3] They become aligned in the presence of a magnetic field (B_0), as depicted in Figure 1.1a-b. In the simplest case where nuclei contain $I = 1/2$, two possible nuclear spin energy levels arise from alignment of $\hat{\mu}$ with the direction of the field to give a lower energy state, α, or against the direction of the field to give a higher energy state, β (Figure 1.1b).[3]
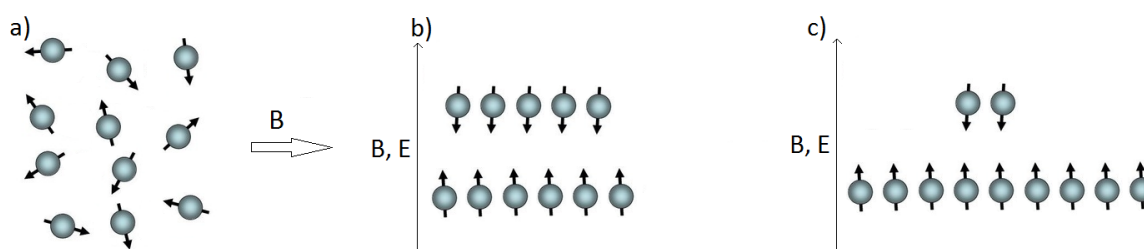
Figure 1.1: a) Nuclear spins have magnetic moment (μ) which are randomly aligned (isotropic) in the absence of a magnetic field. b) When a magnetic field (B_0) is applied these magnetic moments become aligned either parallel or antiparallel to the direction of the applied field. The energy difference between the two alignments is small, but there is a slight preference for parallel alignment. c) Hyperpolarised systems, which are discussed in section 1.3, have a much greater population difference between nuclear spin energy levels.

1.1.2 Vector model of NMR

MR is able to study the nuclear spin properties of molecules *via* their interactions with external magnetic fields and *r.f.* pulses.[3] The alignment of magnetic moments in the direction of an applied magnetic field creates net nuclear magnetisation, $\hat{M}$. This is a vector that contains contributions from M_z, M_x, and M_y.[2] The net magnetisation of nuclei along the direction of the applied magnetic field is labelled M_z and will depend on how many nuclei are present in the sample and the energy spacings between nuclear spin states. Under thermal conditions net magnetisation is orientated along the direction of B_0 while contributions from M_x and M_y are 0 as nuclear spins are randomly orientated in the transverse (xy) plane.[3] This is depicted in Figure 1.2a in which the vectors $\hat{M}$ and B_0 are parallel. Upon the application of an *r.f.* pulse, $\hat{M}$ is rotated away from the direction of B_0 and the two are no longer parallel.[3] The magnetisation vector experiences a

twisting force resulting in the precession of $\widehat{M}$ around B_0 as shown in Figure 1.2b. This precession will occur at the Larmor Frequency, ω, described in Equation 1.3.[3]

$$\omega = -\gamma\, B_0 \qquad (1.3)$$

As the magnetisation precesses around the magnetic field it maps out a circle on the transverse plane which is largest when $\widehat{M}$ is perpendicular to B_0. At this point M_x and M_y make a contribution to $\widehat{M}$ while the longitudinal magnetisation, M_z is 0.[3] NMR signals are detected in the transverse plane from precessing xy magnetisation. The resulting MR signals are most intense when $\widehat{M}$ is rotated 90º from M_z to M_{xy}. It is therefore important to choose *r.f.* pulses of appropriate duration such that $\widehat{M}$ is rotated into the transverse plane. A rotating frame of reference can be used to simplify these descriptions which rotates in the transverse plane at the Larmor frequency such that M_{xy} rotating at this frequency appears static, as shown in Figure 1.2c.[1, 3]
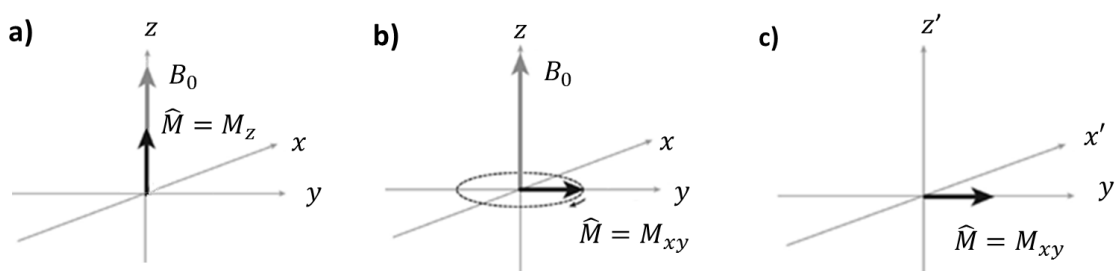
Figure 1.2: a) At thermal equilibrium the net magnetisation, M_z is oriented along the direction of the magnetic field, B_0 b) Upon application of a 90º *r.f.* pulse $\widehat{M}$ is rotated away from the direction of B_0 and into the transverse plane where precession around B_0 at the Larmor frequency can be detected. c) In a frame rotating at the Larmor frequency in the opposite sense, $\widehat{M}$ appears stationary.

When a magnetic field is applied to an ensemble of nuclear spins, the magnetisation does not appear instantaneously. Instead, nuclear spins must come into thermal equilibrium with the applied magnetic field which involves the exchange of energy between the spin system and the environment.[6] The time taken for the magnetisation to reach equilibrium is characterised by a time constant, T_1, often called the longitudinal or spin lattice relaxation time.[6] This time constant also describe the relaxation of $\widehat{M}$ from the transverse to the longitudinal plane and is given in Equation 1.4 where t is time.

$$M_z(t) = \widehat{M}\left(1 - e^{\frac{-t}{T_1}}\right) \qquad (1.4)$$

The decay of magnetisation in the transverse plane is due to random dephasing of magnetic moments interacting with other spins and is also characterised by a time constant, T_2, as described by Equation 1.5. This is termed the transverse or spin spin relaxation time and is typically shorter than T_1.[6]

$$M_{xy}(t) = \hat{M}\left(e^{\frac{-t}{T_2}}\right) \qquad (1.5)$$

1.1.3 Insensitivity of NMR

The interaction between nuclear spin and magnetic field is very weak and causes only a small energy difference between the two possible alignments.[1] The energies of these nuclear spin levels can be predicted by finding the eigenvalues of the Schrödinger equation using a nuclear spin Hamiltonian.[2] As the energy differences between these states are very small there is only a slight preference for nuclei to align in the direction of the applied magnetic field. Therefore, a small population difference across nuclear spin energy levels results from very small energy differences between the two (aligned or not aligned) situations.[7] These population differences can be described by the Boltzmann law, given in Equation 1.6 where N_α and N_β are the populations of α and β states, k is the Boltzmann constant, and T is temperature.

$$\frac{N_\alpha}{N_\beta} = e^{\frac{\gamma h B_0}{4\pi kT}} \qquad (1.6)$$

Under thermal conditions there is an excess of only 1 in 32,000 ^{1}H nuclear spins in the α state at 9.4 T.[5] This leads to a molecular insensitivity which is even greater for low γ nuclei such as ^{13}C for which there is an excess of only 1 in 800,000 spins in the α state at 1.5 T. The application of *r.f.* pulses drive transitions between α and β levels; only those excesses of spins are visible to NMR.[3] Therefore, MR is an insensitive technique on the molecular level as its signal intensity is proportional to small population differences across nuclear spin energy levels.[7] This often necessitates the use of concentrated samples ($>$ mM) to generate sufficient signal, which is not the case for other spectroscopic techniques such as mass spectrometry ($<$ pM), or X ray diffraction (a single crystal).

Polarisation (P) is a term used to describe the extent to which nuclei align with, or against, the applied magnetic field and is given in Equation 1.7.[7] Polarisation can be increased either by reducing the temperature or increasing the strength of the magnetic field, according to Equation 1.4, although in reality there are both low temperature restrictions for living samples and limitations on the strengths of magnets that can be made (up to 24 T).

$$P = \frac{N_\alpha - N_\beta}{N_\alpha + N_\beta} = \tanh\left(\frac{\gamma h B_0}{4\pi kT}\right) \qquad (1.7)$$

Hyperpolarisation is a term used to describe any technique that can produce non Boltzmann population distributions across nuclear spin energy levels (Fig 1.1c).[5,7] Hyperpolarisation has been used to generate MR signals enhanced by many orders of magnitude and has gone some way to address the insensitivities of NMR.[7] These techniques are discussed further in Section 1.3.

1.2 MRI contrast agents

For MRI, the molecular insensitivity of MR usually necessitates imaging the large abundance of water protons in the body to achieve sufficient signal strength. MRI therefore detects water molecules in the body and can produce images of exquisite contrast that distinguish tissues based on the different longitudinal relaxation times (T_1) of their water protons.[4] MR sensitivity describes how many nuclear spins are observable and can be improved using the hyperpolarisation techniques described later (section 1.3). MR contrast is related to distinction of nuclear spins in one area of tissues from others and can be important when diagnosing differences in tissue structure.[4, 6] Improving the contrast or sensitivity of magnetic resonance (MR) techniques is the focus of much attention.[6, 7]

Contrast can be artificially created in tissues by injecting paramagnetic gadolinium-based T_1 contrast agents,[6, 8] or Chemical Exchange Saturation Transfer (CEST) agents.[9-12] T_1 contrast agents artificially reduce T_1 of surrounding water molecules by a dipolar coupling mechanism between the unpaired Gd f^7 electrons and coordinated water molecules.[6] Three key parameters determine how effective such Gd centres relax surrounding water molecules, as summarised in Figure 1.3a.

1. The number of water molecules in the coordination sphere (q) of the Gd centre
2. The rate at which the water molecules exchange at the free Gd coordination site (ι_M)
3. The rate at which the molecule tumbles through solution (ι_R)

For maximum relaxivity the molecule must have a high rate of water exchange and a low rate of molecular tumbling. Relaxivity is also dependant on magnetic field strength and therefore contrast agents are likely to work optimally at a selected field. Free paramagnetic centres often tumble too fast in solution to give great increases in relaxivity, and free Gd is toxic in the body causing side effects such as nephrogenic system fibrosis (NSF).[13] Other concerns over the long term health implications of injecting gadolinium complexes, such as metal deposition in the brain, have recently emerged.[13, 14] The coordination of Gd by chelating ligands reduces both q and toxicity and has yielded clinically approved contrast agents, the structures of some of these are shown in Figure 1.3b.

Agents of this type have been used to detect disorders of the blood brain barrier,[15] and to image blood vessels[16] which has improved the diagnosis of cardiovascular diseases or angiogenesis by cancer cells.[17] There have been attempts to direct contrast agents to particular tissues by conjugation with antibodies[18] or incorporation into pH sensitive gels that are released only at sites of cancer.[19] Alternatively, Chemical Exchange Saturation Transfer (CEST) agents are a type of *r.f.* selective contrast agent that avoids the health implications of injecting Gd. CEST agents contain exchangeable protons (usually amide, carboxylic acid, or hydroxyl groups) and generate contrast *via* magnetism transfer to bulk water following selective presaturation of the agent

followed by proton exchange.[9-12] In CEST, the exchanging pools of spins are distinguished not because of their relaxation times, but because some are selectively excited.[11]
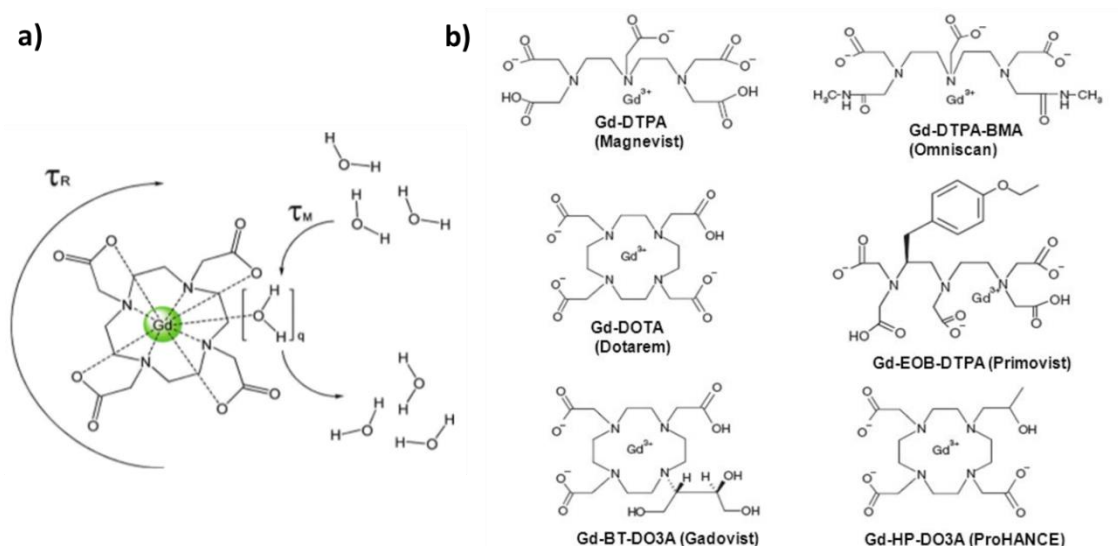
Figure 1.3: a) Water relaxivity is mediated by the hydration number (q), water exchange rate (t_M), and molecular tumbling rate (t_R) of gadolinium-based MRI contrast agents b) Structures of some clinically approved Gd-based contrast agents.

Over the last 30 years, new approaches have been developed to create functional MRI (fMRI) in which MR signals of bulk water are dependant on biological events or external stimuli. The most common of these relies on the change in MR signal upon oxygenation or deoxygenation of blood.[20] These Blood Oxygen Level Dependant (BOLD) signals are a consequence of the different magnetic properties of oxyhemoglobin and deoxyhemoglobin.[20] These BOLD signals have been related to neuronal activity and many studies have linked BOLD signals to changes in brain function.[20] Despite this, the link between brain activity and BOLD signals are not yet fully understood.[21] Other, less developed approaches, use MRI contrast agents responsive to biological targets such as metal ions,[22] neurotransmitters[23] and proteins.[24] This provides advantages compared to the BOLD signal as the release of transition metal ions or neurotransmitters are important in neuronal signalling or other biochemical pathways.[25] Therefore, the synthesis of contrast agents whose MR signal can respond to changes in these biological stimuli has received significant attention.[26]

While contrast enhanced MRI can give great information on the structure and morphology of living tissues (allowing diagnosis of physical differences in morphology) it provides little detail about the biological function or disease state of tissues. While these approaches have moved towards functional MR, the molecular insensitivity of MR has not been addressed. A more direct and reliable way to investigate tissue function by magnetic resonance is to image low concentration biomolecules *in vivo*.[5] Imaging individual biomolecules, rather than bulk water molecules, provides a route to studying the biochemical function of tissues in the body in real time. In order to image individual biomolecules in the body, substantial signal gains are needed

to observe and image low concentration biomolecules, drugs, or metabolites. Hyperpolarisation is now therefore being used to create naturally occurring non-toxic agents with greatly enhanced MR signals with advantages compared to injecting other contrast agents such as those based on toxic paramagnetic heavy metals.

1.3 Hyperpolarisation techniques

Over the last few decades, many hyperpolarisation techniques have been developed to create MR signals enhanced by up to five orders of magnitude.[5] This section describes the techniques commonly used to create hyperpolarised molecules in the liquid state, although Spin Optical Exchange Pumping (SOEP) can produce hyperpolarised ^{3}He[27] and ^{129}Xe[28] gases suitable for lung imaging. The hyperpolarisation approaches focussed on here include dissolution Dynamic Nuclear Polarisation (d-DNP) and *Para*-Hydrogen Induced Polarisation (PHIP). All hyperpolarisation techniques involve polarisation transfer from an external source which is usually either an unpaired electron in the case of DNP [29, 30] (section 1.3.1) or *para*-hydrogen in the case of PHIP (section 1.3.2).[31-34]

1.3.1 Dynamic Nuclear Polarisation (DNP)

DNP was first theoretically suggested by Albert Overhauser in 1953[35] and experimentally observed by Carver and Slichter in the same year.[36, 37] The technique exploits the greater polarisation of an electron by transferring it to nuclei through microwave irradiation at the resonance frequency of the electron in a magnetic field. This commonly occurs when the to-be-polarised nuclei and an organic free radical are frozen together in a glass matrix at low temperature (<10 K).[29, 38] Electrons contain electron spin which can align with, or against, an applied magnetic field. This creates two non degenerate electron spin energy levels, in an analogous way to that of proton nuclear spin shown in Figure 1.1b; this principle is the basis of Electron Paramagnetic Resonance (EPR) spectroscopy.[39] The energy difference between these two states can also be determined using equations 1.1 and 1.3 and is proportional to the gyromagnetic ratio of the electron (γ_e). As γ_e is 660 times larger than that of the proton (γ_H), the electron Zeeman levels are further spaced and therefore contain a greater population difference across them.[39] Overhauser suggested that this greater electron polarisation could be transferred to a proton to give NMR signals enhanced by a maximum theoretical factor of 660,[35] as shown in Equation 1.8 in which ε' is the NMR signal enhancement, ρ is the coupling between the electron and nuclei, f is a leakage factor between 0 and 1 that describes how nuclear spin is relaxed by electron spin, and s is a saturation factor that describes how well EPR transitions are saturated.[40]

$$\varepsilon' = \rho f s \frac{\gamma_e}{\gamma_n} \qquad (1.8)$$

Polarisation transfer from electrons to nuclei is complex and the DNP effect is commonly explained using three models:

1. Solid effect which considers a single coupled proton and electron

2. Cross effect which considers a single nuclei coupled to two electrons and is commonly applied to polarisation using biradicals

3. Thermal mixing which considers the coupling of multiple nuclei to multiple electrons

The solid effect most commonly applies to cases in which the homogenous EPR linewidth of the electron, δ, and the inhomogenous EPR spectral breadth, Δ, are both smaller than the nuclear Larmor frequency.[41] Trityl radicals (such as *tris*[8-carboxyl-2,2,6,6-benzo(1,2-d:4,5-d)-bis(1,3)dithiole-4-yl]methyl sodium salt, commonly referred to as OX063) are commonly employed in DNP and have narrow EPR linewidths. Therefore, their use as polarising agents is often described using the solid effect.[40] A coupled proton-electron system is depicted in Figure 1.4a containing four different energy levels. EPR allowed transitions in which $\Delta m_e \pm 1$ and $\Delta m_n = 0$ can be saturated as can NMR allowed transitions in which $\Delta m_n \pm 1$ and $\Delta m_e = 0$.[40] The solid effect relies on saturation of one of the EPR forbidden transitions in which $\Delta m_e \pm 1$ and $\Delta m_n \pm 1$ to yield enhanced population differences across NMR allowed transitions, shown in Figure 1.4b. The model relies on saturation of EPR forbidden transitions as excitation of both EPR allowed transitions would result in no net polarisation increase across nuclear spin energy levels. A similar cancellation effect results from saturation of both EPR forbidden transitions. It is therefore important to use radicals with narrow line widths that can efficiently saturate only one forbidden EPR transition leading to a high value of s (1) and a closer to theoretical maximum enhancement value.[40]
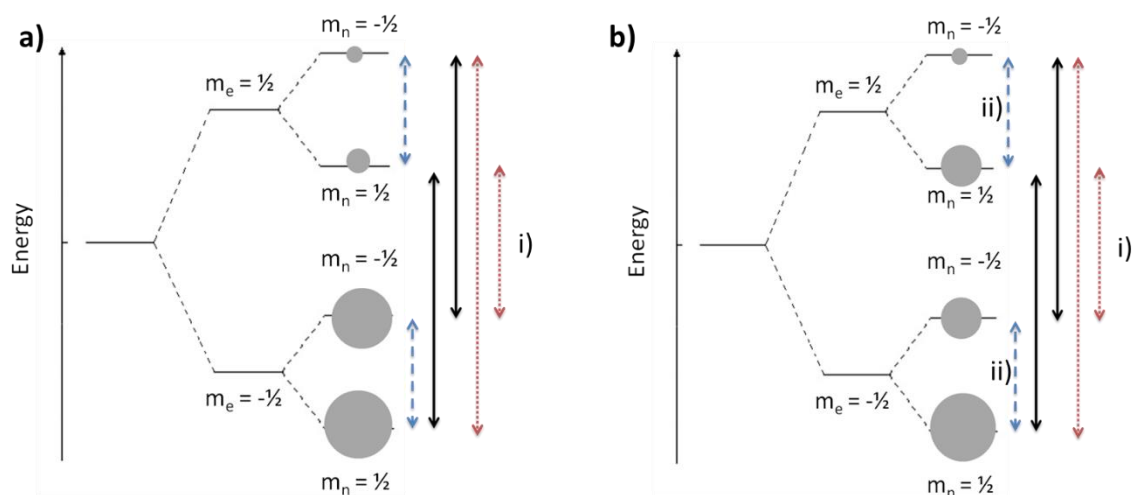
Figure 1.4: a) Energy levels for a weakly coupled nuclei (I = 1/2) and single unpaired electron with allowed EPR transitions shown in solid black lines, allowed NMR transitions in dashed blue, and forbidden transitions in dotted red. Circles represent the populations of each of the four energy levels under thermal conditions.[40] b) Saturation of one of the EPR forbidden transitions (i) leads to a population redistribution that increases polarisation across NMR allowed transitions (ii).[40] Saturation of the second EPR allowed transition is not shown but would yield equal signal enhancement of the opposite sign. Saturation of both allowed or forbidden transitions simultaneously would lead to a cancelling out of NMR signal enhancement.

In those cases where the EPR spectral line width is greater than the Larmor frequency, the cross effect and thermal mixing models are more appropriate.[42] The cross effect considers coupling between one nuclei and two electrons, a condition that is commonly met when biradicals (such as dinitroxides) are used as polarising agents. In this case, a similar energy level diagram to those shown in Figure 1.4 can be constructed between a coupled three spin system (two electrons and a nuclei). Now, saturation of allowed EPR resonances of either electron yields polarised NMR transitions with enhancements of opposite sign depending on which electron is saturated.[43]

In reality, a hyperpolarised sample will contain multiple nuclei and electrons all interacting together. Thermal mixing therefore considers cases where more than two electrons are coupled to nuclei and is more commonly applied to conditions in which the radical is present in high concentrations.[42] As spin spin interactions are very strong and interactions with the surrounding lattice are weak the system can be thought of as isolated from its surroundings and a thermodynamic model using the concept of spin temperatures is often used.[43] Three energy reservoirs are considered: the electron Zeeman interaction (EZI), the nuclear Zeeman interaction (NZI), and the electron spin spin coupling interaction (ESSI). Excitation close to the EPR resonance condition effectively cools the EZI, as shown in Figure 1.5, which in turn heats both ESSI and NZI giving rise to greater nuclear polarisations.[42]
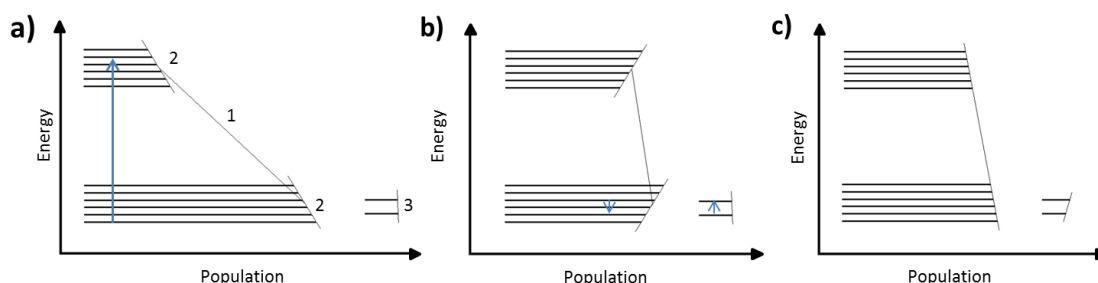
Figure 1.5: a) EZI (1), ESSI (2), and NZI (3) have the relative energies and population differences under thermal conditions shown here, each reservoir has a distinct spin temperature displayed by the solid black lines.[42] b) Upon irradiation close to the EPR frequency the EZI is heated c) Subsequent cooling of the ESSI leads to cooling of the NZI and consequently hyperpolarised NMR signals for nuclei. The three reservoirs attain a common spin temperature.[43]

It is common for multiple polarisation mechanisms to occur, particularly in cases where EPR line widths contain both homogenous and inhomogeneous line broadening. Theoretical treatment of DNP polarisation mechanisms, and the relative contributions of each is an active area of research. Generally, higher NMR signal enhancements are achieved when DNP is performed at low (0-5 K) temperatures under which conditions solid samples are used and the electron polarisation is greater. The formation of hyperpolarised solids is of limited use for *in vivo* applications and liquid state DNP typically suffers from lower NMR signal enhancements.[44] A significant advancement came in 2003 with the development of dissolution DNP (d-DNP). This involves the polarisation of solids at ~1.2 K followed by injection of superheated solvent to rapidly melt the hyperpolarised solids before they are ejected into an NMR or MRI instrument.[29] The ability to convert the agent from the solid state to the liquid state in a matter of seconds without significant loss of hyperpolarisation has enabled the generation of hyperpolarised ^{13}C labelled molecules for use in *in vivo* metabolic studies which is discussed later (section 1.5). d-DNP has found the most success in clinical applications and can produce ^{1}H and ^{13}C NMR signals in the liquid state that have polarisation levels of 92% and 70% in times as low as 150 seconds and 20 minutes respectively.[30]

38

1.3.2 *Para*-Hydrogen Induced Polarisation (PHIP)

Para-Hydrogen Induced Polarisation (PHIP) could provide a lower cost and faster route to hyperpolarising molecules compared to d-DNP which is usually a more time consuming, expensive, and technologically demanding technique.[45] PHIP uses *para*-hydrogen (*p*-H$_2$) as the hyperpolarisation source and its magnetisation is typically incorporated into molecules by hydrogenation reactions, such as the hydrogenation of alkenes into alkanes, or oxidative addition of hydrogen to a metal centre.[34, 46]

Molecular hydrogen is formed of two coupled spin-1/2 ^{1}H nuclei and can exist as two spin isomers: *para*-hydrogen (*p*-H$_2$) and *ortho*-hydrogen (*o*-H$_2$).[47] *p*-H$_2$ is a lower energy singlet state with nuclear spin of 0 while *o*-H$_2$ is a triplet state consisting of three degenerate energy levels with a nuclear spin of 1, as shown in Figure 1.6a. At room temperature and pressure hydrogen

exists in a 25:75 p-H_2:o-H_2 ratio,[47] but if cooled (to 28 K) in the presence of a spin exchange catalyst such as Fe_2O_3 or activated charcoal then spin disallowed transitions from o-H_2 to p-H_2 occur and up to 98% enriched p-H_2 can be produced.[48] When the catalyst is removed and the temperature increased, enriched p-H_2 survives.

When hydrogen is placed in a magnetic field the energy levels of triplet o-H_2 lose their degeneracy and have the energy ordering shown in Figure 1.6b.[31, 32] In a case where enriched p-H_2 $\left(\frac{1}{\sqrt{2}}\alpha\beta - \beta\alpha\right)$ is used, only the $\alpha\beta$ and $\beta\alpha$ levels are populated.[32] p-H_2 is an NMR silent singlet state and is antisymmetric with respect to spin exchange. In other words, if the sign of one of the α or β states is changed then the sign of $|S_0\rangle$ is also inverted.[2] Singlet magnetisation does not commute with common MR relaxation mechanisms such as dipolar coupling which is symmetric with respect to spin exchange.[49, 50] Therefore, the enriched p-H_2 state can have lifetimes as long as many hours.[48]
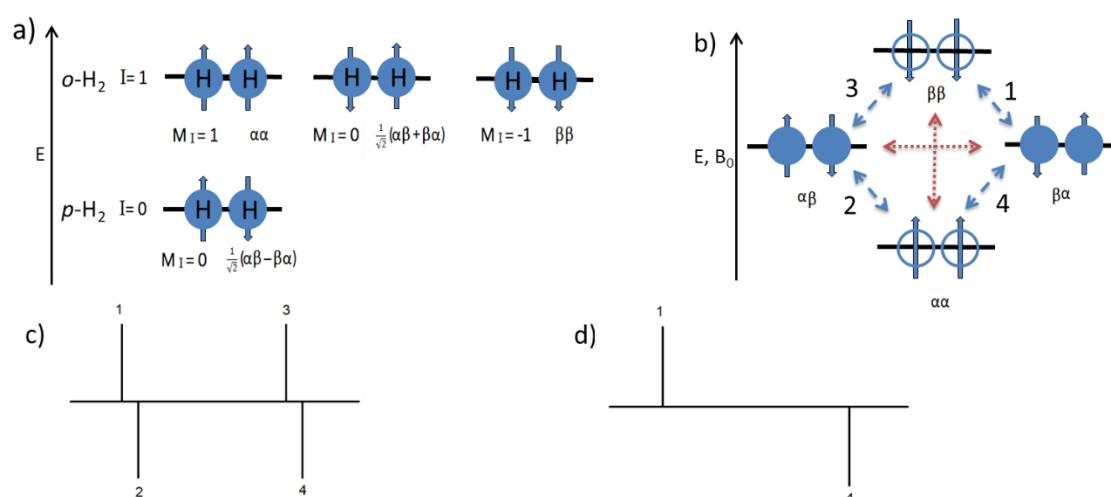
Figure 1.6: a) Diatomic hydrogen exists as two different spin isomers: o-H_2 (a triply degenerate state with I=1) and p-H_2 (a singlet state with I=0).[47] b) The approximate energy levels of diatomic hydrogen in a magnetic field are shown. In cases where room temperature and pressure equilibrated hydrogen (25:75 p-H_2:o-H_2) is used there will be almost equal populations in all energy levels. When enriched p-H_2 is used only the $\alpha\beta$ and $\beta\alpha$ levels of the hydrogenation product are populated, as shown by the filled blue circles, resulting in greater population differences across the NMR allowed transitions shown with a blue dashed line.[31, 32] NMR disallowed transitions are shown with a red dotted line. c) A representative PASADENA spectrum resulting from population of both $\alpha\beta$ and/or $\beta\alpha$ levels. d) A representative ALTADENA spectrum resulting from population of one of the $\alpha\beta$ or $\beta\alpha$ levels.

Singlet magnetisation is of interest due to its long lifetimes which can extend beyond T_1.[50] The preservation of hyperpolarised signals for a longer time period can have exciting applications in allowing chemical processes to be monitored over a longer time period.[51] Detecting true long lived singlet states can be challenging because the symmetry of the two coupled spins must be broken to allow for their detection by NMR.[2] Despite these challenges, Carravetta et al. were able to create pseudo singlet eigenstates in molecules with coupled spin ½ pairs *via r.f.* excitation in 2004.[50, 52] These states can be created in molecules with not only coupled ^1H-^1H spin pairs but

also ^{13}C-$^{13}C^{53,\,54}$ or ^{15}N-$^{15}N^{51,\,55,\,56}$ spin pairs with examples reported for alkynes,[53, 54] N_2O,[51] diazirines,[55] and diazines.[56] A ^{13}C-^{13}C nuclear pseudo singlet state in a naphthalene derivative with a lifetime greater than 1 hour has been reported.[57] Interestingly, singlet magnetisation in a mixed ^{15}N-^{13}C spin pair (acetonitrile) strongly coupled at low field has been reported.[58]

It has been shown that singlet order can be transferred from p-H_2 to target substrates *via* PHIP. In 1986, Bowers and Weitekamp showed that if p-H_2 can be incorporated into a molecule *via* hydrogenation, the populations of nuclear spin energy levels of the hydrogenated product will be linked to those of the starting dihydrogen molecule.[31, 33] As the nuclear spin of p-H_2 is 0 it is 'NMR silent' and can only be made visible to an NMR experiment if its symmetry is broken. PHIP provides a route to the hyperpolarisation of unsaturated molecules in the liquid state by breaking the symmetry of p-H_2 *via* chemical hydrogenation. PHIP is a general term that encompasses techniques such as *Para*-hydrogen And Synthesis Allow Dynamic Nuclear Alignment (PASADENA) in which hydrogenation occurs in a high magnetic field and results in population of both $\alpha\beta$ and $\beta\alpha$ states and Adiabatic Longitudinal Transport After Dissociation Engenders Net Alignment (ALTADENA) which describes hydrogenation at low fields and results in the selective population of only one of the $\alpha\beta$ or $\beta\alpha$ levels.[59] Since its introduction in the late 1980s, the enhanced MR signals produced by PHIP have been used to detect low concentration analytes and intermediates which has largely been applied to elucidation of mechanisms in catalysis.[46 60] PHIP has also been used to study hydrogenation reactions catalysed by homogenous catalysts,[46, 61] metal clusters,[62, 63] frustrated Lewis pairs[64, 65] or solid surfaces,[66, 67] often by making shot lived or low concentration intermediates in these processes visible to NMR. Nevertheless, the hydrogenation of some unsaturated clinical agents with p-H_2 has been used to produce hyperpolarised agents suitable for *in vivo* detection.[68-70] For example, diethyl succinate-[1-^{13}C]-d_2 has been hyperpolarised using PHIP, injected, and imaged *in vivo*.[71]
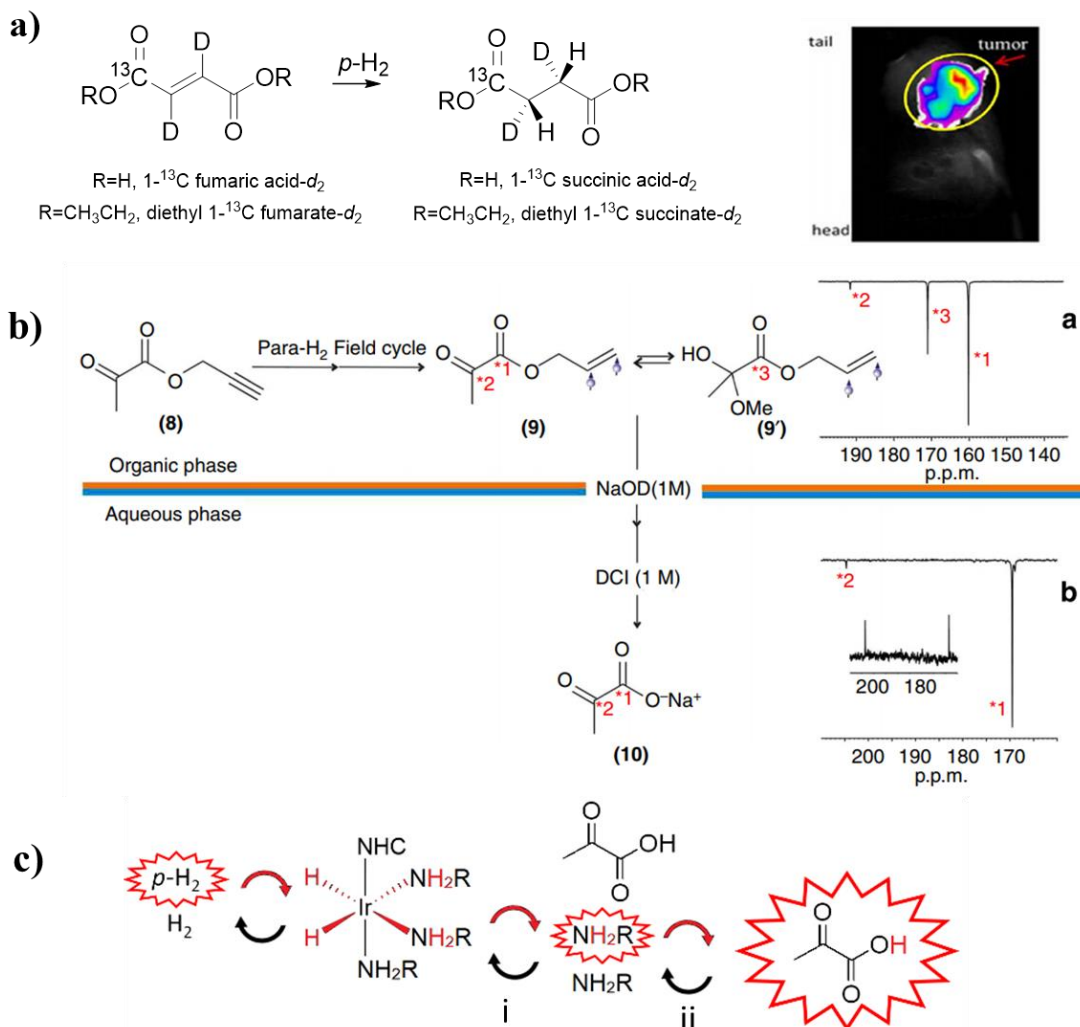
Figure 1.7: a) Polarisation of succinic acid-[1-^{13}C]-d_2 and diethyl succinate-[1-^{13}C]-d_2 using PHIP and a false colour *in vivo* ^{13}C MRI image of hyperpolarised diethyl succinate-[1-^{13}C]-d_2 injected into a mouse with a RENCA tumour taken from Zacharias et al.[71] b) PHIP-SAH functionalises pyruvate as an ester with an unsaturated side arm. Upon *p*-H$_2$ hydrogenation and field cycling the side arm is cleaved in a simultaneous hydrolysis and phase separation step. Reprinted by permission from Springer [Nature communications, *Para*Hydrogen Induced Polarization of ^{13}C carboxylate resonance in acetate and pyruvate, F. Reineri, T. Boi and S. Aime, copyright 2015].[70]

A limitation of PHIP is that target molecules must contain a readily available unsaturated precursor that can undergo a hydrogenation reaction with *p*-H$_2$. A variation of PHIP called *Para*-Hydrogen Induced Polarisation by Side Arm Hydrogenation (PHIP-SAH) has been used to address this weakness.[70, 72-75] PHIP-SAH involves functionalisation of a target as an ester with an unsaturated side arm. Upon side arm hydrogenation with *p*-H$_2$ in chloroform-*d* and a field cycling step to transfer polarisation from the side arm to a ^{13}C labelled site, the side arm is rapidly cleaved in an aqueous hydrolysis step, as summarised in Figure 1.7b.[73] A significant advantage of PHIP-SAH is that rapid (1 s) hydrolysis and phase separation occur simultaneously which removes the toxic Rh hydrogenation catalyst and chloroform-*d* solvent and allows production of hyperpolarised agents in aqueous solutions.[70, 72-75] PHIP-SAH has been applied to molecules like pyruvate and acetate which do not have readily available unsaturated precursors and are not traditionally amenable to hyperpolarisation using PHIP.[70, 72-75] While pyruvate polarisation levels of 5%[73] have been achieved, these are significantly lower than those that can be achieved using

DNP (up to 70%[38]). Nevertheless, PHIP-SAH can provide NMR signal enhancements sufficient for real time monitoring of pyruvate metabolism *in vivo*.[72, 74, 75]

1.3.3 Signal Amplification By Reversible Exchange (SABRE)

A limitation of PHIP is that substrates must be chemically altered *via* a hydrogenation reaction. A further restriction is that the technique is one shot in nature as once the p-H_2 hydrogenation has been performed the PHIP effect will no longer be observed. Signal Amplification By Reversible Exchange (SABRE) is an ALTADENA-like technique first demonstrated in 2009 that allows the hyperpolarisation of substrates without the direct chemical incorporation of p-H_2.[76] SABRE is a technique belonging to the PHIP family that also uses p-H_2 to hyperpolarise multiple nuclei in a fast, cheap, and reproducible fashion without chemically altering the substrate. Polarisation transfer occurs in a low (0-10 mT) field when both substrate and p-H_2 are in reversible exchange with an iridium catalyst, as shown in Figure 1.8. A SABRE active catalyst typically of the form $[Ir(H)_2(NHC)(substrate)_3]Cl$ (where NHC is an *N*-heterocyclic carbene) is formed from hydrogenation of a stable $[IrCl(COD)(NHC)]$ precursor (where COD is *cis,cis*-1,5-cyclooctadiene).[76, 77] p-H_2 is incorporated into the active $[Ir(H)_2(NHC)(substrate)_3]Cl$ catalyst *via* oxidative addition and polarisation transfer occurs from these metal hydrides to *trans*-bound substrates *via* a temporary scalar *J*-coupled network. As both p-H_2 and substrate are in reversible exchange with the active catalyst, magnetisation of the ligand free in solution is built up catalytically. Polarisation transfer from p-H_2 derived hydrides to *trans*-bound substrates occurs when the chemical shift difference between the hydrides and the substrate ($\Delta\delta_{HH'}$) is equal to the hydride-hydride coupling ($^2J_{HH}$).[78] The rate of this magnetisation transfer has been reported to be proportional to $1/2J$ where *J* is the ^3J or ^4J coupling between hydride and substrate ($J_{HH'}$).[79] At high magnetic fields (*i.e.* 9.4 T) the chemical shift differences and *J* coupling constants between the hydride and substrate spins are different. They can be made equal by moving to lower field regimes (mT) as the chemical shift differences, which are dependent on the magnetic field, will collapse to equal the *J* coupling constant. For transfer from hydrides to proton this resonance condition is usually around 6.5 mT which is often met when performing a 'shake and drop' experiment in which the substrate, catalyst, and p-H_2 are shaken in an NMR tube in the stray field of a 9.4 T magnet and dropped into the spectrometer for analysis.[76] Handheld magnetic shakers have been developed to control the polarisation transfer field (PTF) more precisely[80] while flow systems and p-H_2 bubbling reactors have also been developed to reproducibly control the PTF, although these usually give less efficient p-H_2 mixing in solution than manual shaking and typically the NMR signal enhancements that result are lower.[81, 82]
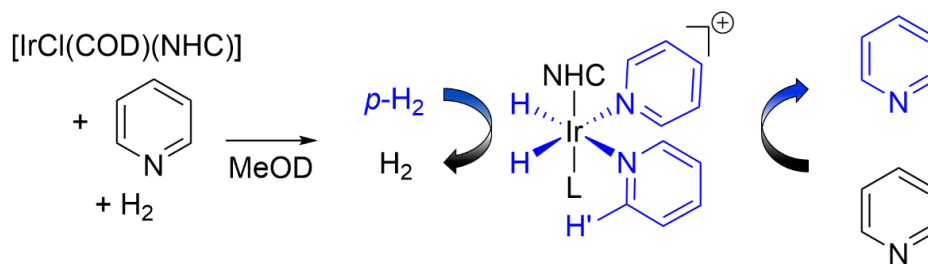
Figure 1.8: a) SABRE catalytically transfers magnetisation from *p*-H$_2$ derived hydride ligands to a ligated substrate (in this example it is pyridine) when both are in reversible exchange with an iridium catalyst (where NHC is an *N*-heterocyclic carbene) at low (0-10 mT) magnetic field.

Polarisation transfer from *p*-H$_2$ derived hydrides can also occur directly to heteronuclei (such as ^{15}N or ^{13}C sites) in a target molecule at much lower microtesla fields. These fields can be lower than the Earth's magnetic field and a metal shielded solenoid is often used to provide the specific fields necessary for such polarisation transfer conditions. This has given rise to a variation of SABRE which is essentially the same, but has nonetheless been rebranded as an alternative approach termed SABRE-SHield Enabled Alignment Through Heteronuclei (SABRE-SHEATH). This has been demonstrated on a range of ^{15}N containing functionalities including *N*-heterocycles,[83, 84] nitriles,[84] Schiff bases,[85] and diazirines.[86] Signal gains for less well studied nuclei such as ^{13}C,[87, 88] ^{19}F,[89, 90] ^{31}P,[91] ^{119}Sn and ^{31}Si[92] have also been reported. Singlet magnetisation can also be prepared from *p*-H$_2$ using SABRE. Theis et al. have created ^{15}N$_2$-diazirine analogues with singlet state lifetimes of 23 minutes[55] and similar results have been published for ^{13}C-based molecular tracers, albeit with lower efficiency.[93] While the polarisation transfer conditions between metal hydrides and the substrate are matched at low field (μT), *r.f.* driven transfer at high-field (T) is also possible.[94, 95]

The most common molecules hyperpolarised using SABRE are those that can coordinate to iridium. *N*-heterocycles such as pyridine,[76, 96-99] nicotinamides,[76, 83, 100] pyrazines,[97, 98] pyrazoles[99] and nitriles[101] are common with the highest reported polarisation levels of 65% for ^{1}H of methyl-4,6-*d*$_2$-nicotinate[102] which approaches typical levels that can be obtained using DNP (91%).[30] A wide range of biomolecules and drugs have been polarised using SABRE, some examples are shown in Figure 1.9. A comprehensive list of all the different classes of molecules hyperpolarised using SABRE is given in the recent review by Barskiy et al.[79] SABRE is heteronuclear in scope and significant 72,000-fold ^{15}N NMR signal enhancement of metronidazole,[84] 3,588-fold ^{31}P NMR signal enhancements of a partially deuterated pyridyl phosphonate ester,[91] 1,300-fold ^{19}F signal gains of 3-fluoropyridine[89] and 823-fold ^{13}C NMR signal enhancements for the *meta* resonance of pyridine have all been reported.[103] SABRE is typically limited to substrate that are able to ligate to iridium and there is also a steric limit to coordination, as suggested by low NMR signal enhancements of sterically large pyrazoles.[99] While many different metabolites and drug

molecules contain *N*-heterocycles, SABRE is yet to demonstrate significant signal gains for biomolecules commonly used in biomolecular imaging studies using d-DNP. Most of these metabolites (such as carboxylic acids, amino acids, peptides, discussed in section 1.5) do not contain the *N*-heterocyclic motifs typically required for SABRE.
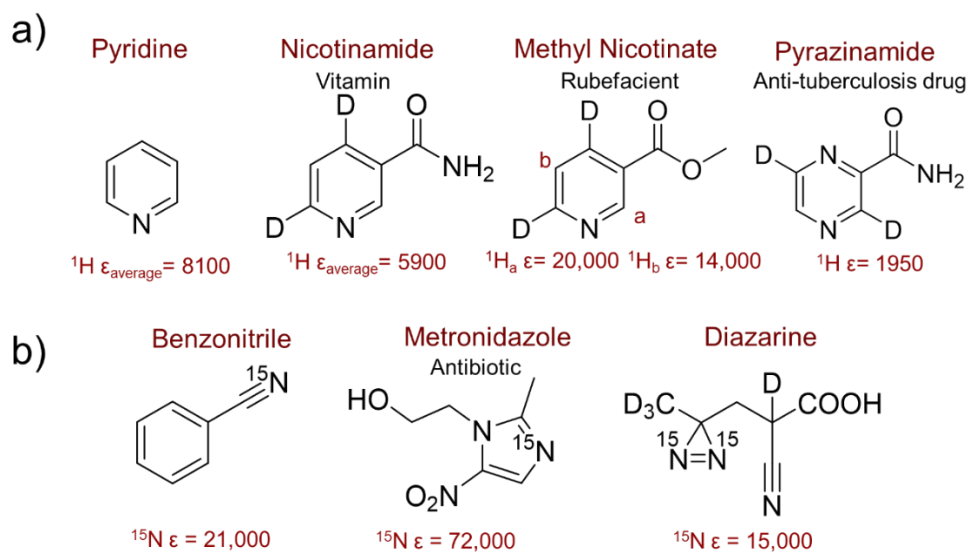
Figure 1.9: A summary of some of the highest a) ^{1}H[60, 66, 82,] and b) ^{15}N[86] NMR signal gains achieved using SABRE. These NMR signal gains are recorded at 8-10 T in methanol-d_4 and quoted in per fold.

A recent development, termed SABRE-Relay, has allowed hyperpolarisation to be relayed from one molecule to another by means of proton exchange.[104] Small NMR signal enhancements for solvent molecules in cases where both solvent and hyperpolarised substrates contain labile protons have been reported and it has been suggested that exchange of hyperpolarised protons is responsible for these observations.[105] These ideas have been extended and improved to allow the relay of hyperpolarisation from functional groups such as amines (carrier molecules) to functionalities including alcohols, carboxylic acids, and amides (substrates/targets) *via* exchange of a hyperpolarised proton.[48, 104, 106-108] The carrier molecule must bind reversibly to the SABRE catalyst to receive hyperpolarisation from *para*-hydrogen and contain an exchangeable proton to relay this magnetisation onto a target substrate, as summarised in Figure 1.10. Molecules can now be polarised without direct interaction with the iridium catalyst which rapidly expands the potential scope of the technique. Reported examples include hyperpolarisation of alcohols,[48, 108] carboxylic acids,[104] amides,[104] sugars[107] and silanols[109] which could not be achieved using traditional SABRE (some examples are given in Figure 1.10). SABRE-Relay therefore offers huge potential to hyperpolarise a much wider range of biologically relevant substrates that contain exchangeable protons, rather than *N*-heterocycles.
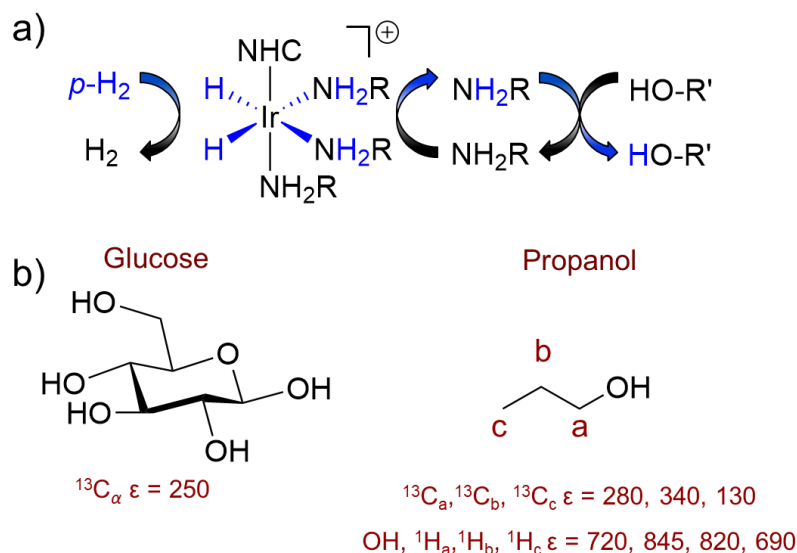
Figure 1.10: a) In SABRE-Relay a hyperpolarised carrier molecule (typically an amine) is able to ligate to the iridium catalyst and receive polarisation from p-H$_2$. The carrier is able to relay this polarisation to non-ligated molecules *via* exchange of hyperpolarised proton. b) Examples of molecules hyperpolarised using SABRE-Relay.[107, 108] NMR signal gains are recorded at 9.4 T and quoted per fold.

The hyperpolarised magnetisation created using SABRE (and other hyperpolarisation techniques) is short lived and will decay back to its Boltzmann derived state according to T_1. Any hyperpolarised agent must have a suitably long T_1 time that the agent can be injected and imaged before the signal has decayed. A number of methods have been used to extend relaxation times of SABRE hyperpolarised agents such as deuterium labelling of proton sites[97, 102, 110, 111] or magnetisation storage in a singlet state.[112-115] By deuterium labelling, proton polarisation is concentrated on fewer sites and T_1 relaxation of the remaining ^{1}H sites is usually slower as a consequence of the lower gyromagnetic ratio of deuterium compared to a proton. In the case of *in vivo* metabolomic studies using DNP, organic radicals are filtered prior to injection to reduce relaxation and toxicity. If a hyperpolarised agent for *in vivo* detection is to be produced using SABRE then the iridium catalyst must be removed prior to injection. Various methods have been reported to remove the SABRE catalyst from solution which usually involves addition of a chelating ligand attached to a silica support which can then easily be filtered out of solution.[116] Other approaches have involved a biphasic system in which the hyperpolarisation occurs in an organic layer containing the catalyst while the hyperpolarised agent remains in an aqueous layer that can be extracted and injected.[117] This approach is only available to a limited range of molecules with appropriate solubility in both organic and aqueous phases.

SABRE hyperpolarisation using solid supported heterogeneous catalysts generally yields NMR signal enhancements smaller by roughly an order of magnitude than can be achieved using homogenous catalysts.[118, 119] Poor solubility of the highest performing SABRE catalysts and p-H$_2$ yield low NMR signal enhancements in pure D$_2$O.[120] While water soluble precatalysts for hyperpolarisation in D$_2$O have been synthesised they continue to yield low NMR signal enhancements.[100, 121] Despite the limitations in its substrate scope and biocompatability, SABRE

provides advantages to other hyperpolarisation techniques as it allows for the fast and comparatively cheap hyperpolarisation of substrates without chemical alteration. While SABRE has not delivered the high NMR signal gains in biocompatible solvents necessary for biomolecular imaging studies, high sensitivity analytical applications have been demonstrated including reaction monitoring and detecting low concentration analytes in mixtures.[122-124]

1.4 Quantifying hyperpolarisation levels

When comparing hyperpolarisation levels for different agents, or of similar agents hyperpolarised using different techniques, it is important that standardised measurements of polarisation or signal gains are used to allow for meaningful comparison. One approach is to quote the percentage of nuclei that are observed in the hyperpolarised measurement. The equation for polarisation (Equation 1.7) is given in Section 1.1.3. For ^1H at 9.4 T and 298 K, the polarisation value is calculated from these equations as 3.2×10^{-5} which can simply be multiplied by 100 to give a polarisation % of 0.0032%. In other words, only 1 in 32, 000 ^1H nuclei contribute to the MR signal at 298 K and 9.4 T. If only one nuclear spin state is populated, leaving the other empty, then a polarisation of 1 results and the polarisation percentage is 100%. Under these conditions every nuclear spin would contribute to the MR signal. A polarisation of 0 describes a situation in which nuclear spin energy levels are equally populated and no MR signals are produced. In reality, thermally polarised samples will contain polarisation levels somewhere between these two extremes, while hyperpolarised samples will contain greater polarisation. These can be derived by multiplying thermal polarisation by a NMR signal enhancement factor (ε) as summarised in Equation 1.9.

$$P \% = \varepsilon \times 100 \times \frac{\gamma h B_0}{4\pi k T} \qquad (1.9)$$

A NMR signal enhancement factor (ε) is often quoted (usually per fold) and describes the factor by which the hyperpolarised response is larger than its thermal counterpart. It is most commonly calculated by dividing the hyperpolarised signal integral (S_{Hyp}) by its thermal counterpart (S_{The}) as shown in Equation 1.10. For this comparison to be meaningful it is essential that hyperpolarised and thermal spectra have been recorded and processed with the same spectral and acquisition parameters. It is also important that reference spectra are recorded at the same magnetic field as polarisation, and NMR signal enhancements depend on the magnetic field strength.

$$\varepsilon = \frac{S_{Hyp}}{S_{The}} \qquad (1.10)$$

In many cases there is not sufficient thermal polarisation to observe signal in a single scan MR spectrum. In these cases, it is common that a more concentrated sample of the same agent is used to provide sufficient signal. The ratio between hyperpolarised signal per atom and the thermal

signal per atom is used to account for these concentration differences and to provide a NMR signal enhancement, as given in Equation 1.11 where Mr_{sub} and M_{sub} are the molecular mass and mass of hyperpolarised substrate used and S_{Ref}, M_{ref} and Mr_{ref} are the reference compound thermal signal intensity, mass and molecular mass respectively.[125]

$$\varepsilon = \frac{S_{Hyp} Mr_{sub} M_{ref}}{S_{Ref} Mr_{ref} M_{sub}} \qquad (1.11)$$

Instead of using a more concentrated thermal sample, an alternative approach is to record a thermal spectrum with a higher number of scans such that a reference signal can be discerned. It is important that all other spectral and processing parameters are constant and that the sample has sufficient time to fully relax between scans. The increased number of scans (NS_{The}) must then be considered when determining the NMR signal enhancement, as given in Equation 1.12. A similar approach can be used based on signal to noise ratios (*SINO*) rather than integral intensities, as given in Equation 1.13.

$$\varepsilon = \frac{S_{Hyp} NS_{The}}{S_{The}} \qquad (1.12)$$

$$\varepsilon = \frac{SINO_{Hyp}\sqrt{NS_{The}}}{SINO_{The}} \qquad (1.13)$$

NMR signal enhancements will decrease as the time after the initial hyperpolarisation step is increased. It is therefore not uncommon for predicted maximum NMR signal enhancements, ε_0, to be calculated according to Equation 1.14 where *t* is the time between hyperpolarisation step and measurement.[126] While ε_0 values are often quoted they are not meaningful as the magnetic field, and subsequently the T_1, often changes dramatically during transfer between the site of polarisation and the site of measurement. It is also not realistic to achieve delivery times of 0 seconds, therefore while quoting them gives a measure of the performance of a hyperpolarisation technique, maximum NMR signal enhancements based on such assumptions are rarely achieved experimentally.[127]

$$\varepsilon_0 = \frac{\varepsilon}{e^{\left(-\frac{t}{T_1}\right)}} \qquad (1.14)$$

In Section 1.3.1 it was discussed that in DNP the gyromagnetic ratio of the electron is 660 times greater than that of the proton resulting in a maximum NMR signal enhancement, ε', of 660 as shown in Equation 1.8. These NMR signal enhancements are recorded in the solid state and are distinguished from those NMR signal enhancements, ε, recorded at room temperature (T_{obs}) that account for the temperature difference and greater thermal polarisation at elevated temperatures, as given in Equation 1.15 where T_{irr} is the irradiation temperature.[40]

$$\varepsilon = \varepsilon' \left(\frac{T_{obs}}{T_{irr}} \right) \tag{1.15}$$

1.5 Hyperpolarised agents for studying metabolism *in vivo*

Hyperpolarisation techniques (discussed in section 1.3) can produce non toxic contrast agents with sufficient MR signal gains to allow their real time imaging *in vivo*.[5, 45] This can involve imaging the spatial distribution of injected agents which has advantages for angiography and blood flow, or tracking the metabolism of injected agents to reveal information about the disease state of certain tissues in the body. This section focusses on the use of hyperpolarised agents to track metabolism, rather than uptake or bio-distribution. Both DNP and PHIP have been used to produce hyperpolarised contrast agents for both purposes.[128-131] Metabolomic studies have used hyperpolarised contrast agents to track the metabolism of biomolecules enabling the diagnosis and detection of certain diseases through metabolic differences or irregulatories.[72, 75, 132-137] The agents used in such studies are typically those involved in the major metabolic pathways in the body. A major pathway in which biomolecules are metabolized by living cells is the Krebs cycle, (also called the citric acid cycle or tricarboxylic acid cycle).[138] This cycle uses an energy source usually in the form of sugars such as glucose and breaks them down into pyruvate in a process called glycolysis. Pyruvate is metabolized further into a range of products described in the citric acid cycle shown in Figure 1.11.[138]
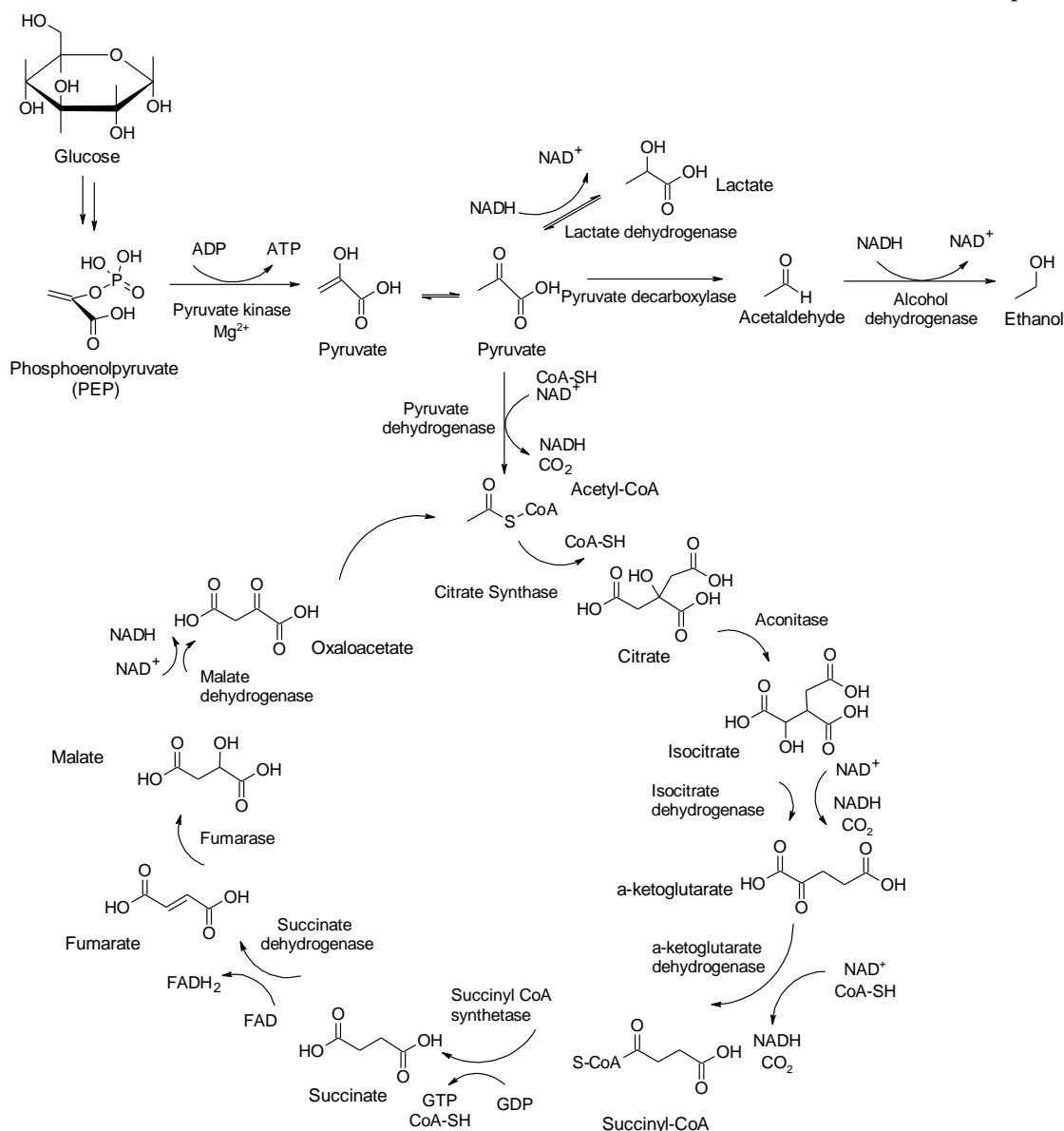
Figure 1.11: Some of the main metabolic pathways of glucose metabolism in living tissues.

While many ^{13}C labelled metabolites hyperpolarised using dissolution Dynamic Nuclear Polarisation (d-DNP) have been reported as metabolic tracers (a review of reported examples is given in Keshari et al.[41]), [^{13}C]-pyruvate is the most widely reported example[132-136, 139-141] and is the only hyperpolarised contrast agent used for *in vivo* human studies to date.[132, 137] There are several reasons for this use. For example, pyruvate can be hyperpolarised with high NMR signal enhancements sufficient for biomolecular imaging *in vivo*. The most common method used to hyperpolarise pyruvate is d-DNP[132-136, 139-141] as pyruvic acid exists as a glass forming liquid at room temperature and can therefore be hyperpolarised with ^{13}C polarisation levels up to 70%.[38] Pyruvate also sits at the metabolic junction of many processes: it is synthesised from the glycolysis of sugars such as glucose and can serve as an energy source to cells either aerobically, *via* the tricarboxylic acid cycle, or it can be converted anaerobically into lactate.[138] The anaerobic conversion of pyruvate to lactate can be exploited by measuring the ratios of hyperpolarised pyruvate to lactate and correlating areas with high ratios to regions of anaerobic respiration and

therefore likely sites of cancer or inflammation.[132-136, 139-141] This enables information on the disease states of tissues to be extracted from hyperpolarised imaging data in a way that cannot be achieved using other imaging agents, angiography tracers, or traditional T_1-based contrast agents. In addition, pyruvate is metabolised on a timescale faster than its hyperpolarised signal decay. It is essential that hyperpolarised signals last long enough that the agent can be injected and imaged, and long enough that the hyperpolarised label remains when the agent is metabolically converted into other products. Pyruvate has a reported T_1 time of 40 ± 6 s at 14.1 T,[70] which can be extended to 57 ± 6 s at 9.4 T when a D_2O buffer is used.[133] These relaxation times are generally long enough to allow chemical transformations to occur and still have enhanced signals for the metabolic product(s). These factors have resulted in a versatile agent that is currently under clinical trials for routine human use. The first studies have already been performed (2013) using d-DNP hyperpolarised pyruvate to successfully localise areas of prostate cancer in humans.[132] Since then further studies have used pyruvate hyperpolarised using d-DNP to track metabolism in the human heart[142] and brain,[137] a summary of some of these studies are shown in Figure 1.12.
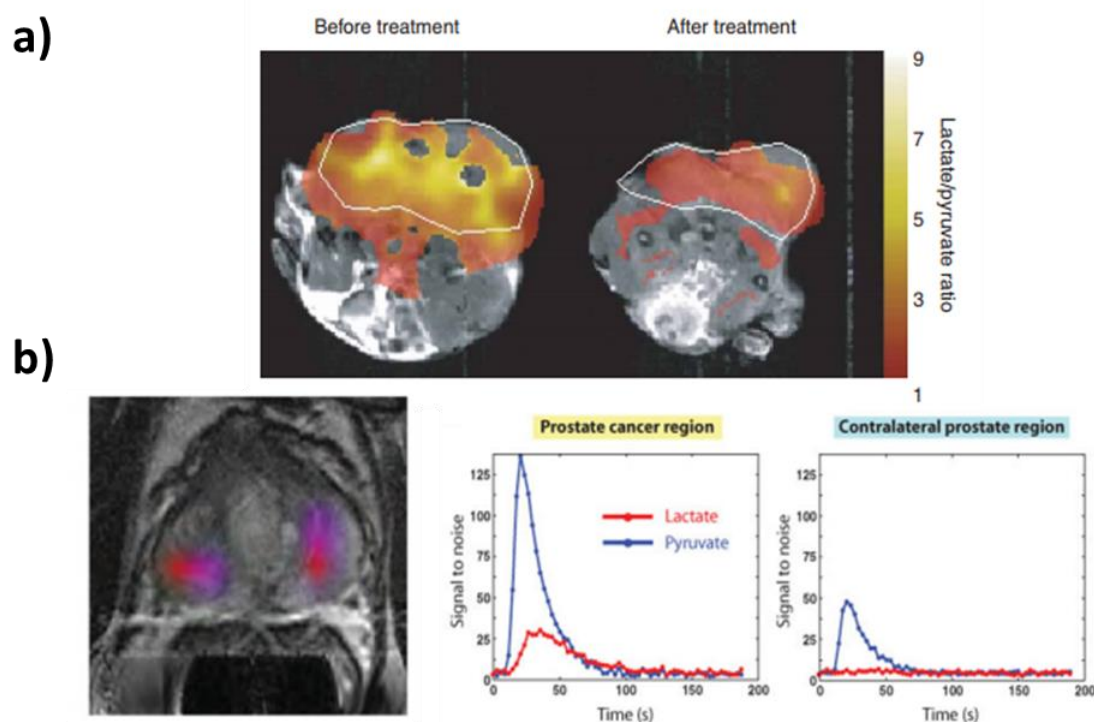
Figure 1.12: a) The hyperpolarised lactate/pyruvate ratio determined in cancerous tissue can be used as a biomarker for treatment response. Upon treatment of breast cancer in mice with etoposide, a reduction of the lactate/pyruvate ratio is observed 20 hours after treatment, whereas it would typically take several weeks for the tumour to shrink in size. Taken from Day *et* al[143] b) High levels of hyperpolarised pyruvate uptake and high lactate/pyruvate ratios have been correlated to areas of prostate cancer in humans. Reprinted from Nelson et al. *Sci Transl Med.*, 2013, 5, 198ra108-198ra108.[132] Reprinted with permission from AAAS.

As hyperpolarised pyruvate has found success as a clinical imaging agent, effort has been directed into optimising its hyperpolarised NMR signal enhancement using d-DNP including varying the identity and concentrations of the radical polarising agent and dopants used.[144] Approaches have used the *in situ* UV generation of radicals from pyruvate as a source of unpaired electrons in

DNP.[145] When the sample is melted the pyruvate radicals annihilate which proves an advantage compared to other organic free radicals which must be filtered out before a biocompatible bolus can be injected. Other Krebs cycle metabolites such as fumarate have been hyperpolarised using d-DNP[113] and their metabolism into other products followed *in vivo*.[134, 146]

1.6 Perspectives on hyperpolarised MR

d-DNP has found the most success in producing hyperpolarised tracers suitable for metabolic imaging. Despite, this the technique uses expensive equipment that is not readily accessible to a wide range of institutions. PHIP and its derivative PHIP-SAH have also been used for this purpose.[70, 73] PHIP-SAH provides many advantages over DNP as it is fast, cheap and does not need the technologically demanding equipment necessary for DNP experiments. However, the hyperpolarised agent is still produced in a batch synthesis and there are chemical alteration steps that must occur. Despite these advantages, the maximum reported polarisation levels for pyruvate-1-[^{13}C] achieved using PHIP-SAH are much lower (5%)[73] than can be achieved with DNP (70%).[38] SABRE contains several advances compared to both PHIP and DNP. It is, like PHIP, also able to hyperpolarise molecules rapidly in a low cost method that is simple to implement. SABRE provides additional advantages as it produces hyperpolarised molecules in a continuous catalytic process. Polarisation can be refreshed simply by addition of fresh p-H$_2$ and therefore SABRE can be used for the continual polarisation of molecules (unlike PHIP or DNP).[82] Currently, SABRE has some major limitations which include its inability to produce significant NMR signal gains in the aqueous solvents necessary for *in vivo* study. To date, no reports of imaging SABRE hyperpolarised contrast agents in living animals have been reported. Nevertheless, exciting applications in a growing range of areas including mixture analysis[122-124, 147-149] and reaction monitoring[109, 150] have been reported.

Advances in DNP hyperpolarisation are progressing at an astonishing rate with major developments in this area occurring in only the last few years. These include the use of non-persistent radicals as hyperpolarising agents and the development of cryogen free polarisers[145] which are being made to operate at higher temperatures and at reduced cost.[38] While SABRE is a technique in its infancy (it is only 10 years old) significant breakthroughs are required to realise *in vivo* biomolecular imaging applications. These feats will require significant developments to create SABRE polarisation transfer catalysts that work efficiently in D$_2$O. This will be hampered by the low solubility of p-H$_2$ in such solvents.[151] Engineering solutions are also required to design equipment that can rapidly transfer SABRE hyperpolarised agents into animals in a rapid, reproducible and safe way.

1.7 Thesis aims

This work is primarily focused at developing new polarisation transfer catalysts that are able to catalyse magnetisation transfer from p-H$_2$ derived hydride ligands to substrates of interest. Current polarisation transfer catalysts of the form [Ir(H)$_2$(NHC)(substrate)$_3$]Cl are limited to the polarisation of N-donor substrates. This thesis will utilise relayed polarisation transfer effects involving [Ir(H)$_2$(NHC)(amine)$_3$]Cl catalysts to polarise non ligating substrates and synthesise novel polarisation transfer catalysts that can result in the ligation and polarisation of O-donor substrates such as pyruvate. The magnetisation transfer catalysts investigated in this thesis will allow polarisation of a much wider range of substrates. Expansion of the substrate scope of SABRE will allow novel applications in the areas of biomolecular imaging, chemosensing, and reaction monitoring.

The recent technique SABRE-Relay utilises [Ir(H)$_2$(NHC)(amine)$_3$]Cl catalysts and relayed proton exchange between amines and targets with labile protons is investigated further. SABRE-Relay is applied to the hyperpolarisation of OH-containing molecules beginning with simple alcohols before expansion to more complex OH-containing structures. This begins by discussing the development of SABRE-Relay as a novel technique and investigating how it can be used to relay polarisation from carrier amine molecules to alcohols *via* exchange of hyperpolarised protons. This is investigated and optimised for some simple alcohols including 3-methyl-1-butanol (summarised in Figure 1.13), a common additive in many foods and drinks. Several factors are explored to achieve the highest possible alcohol NMR signal enhancements including the identity of the carrier amine, concentrations, role of contaminant water and polarisation transfer field. This is then extended to different classes of alcohols such as the secondary and tertiary alcohols 3-pentanol and 2-methyl-2-butanol to investigate the effect of CH branching on the propagation of polarisation from the exchanging OH to other sites within the alcohol. Potential applications of SABRE-Relay including detection of low concentrations of alcohols in mixtures are presented and discussed before the SABRE-Relay technique is extended further by hyperpolarising more complex OH-containing agents including lactate esters and pyruvate in Chapter 3.
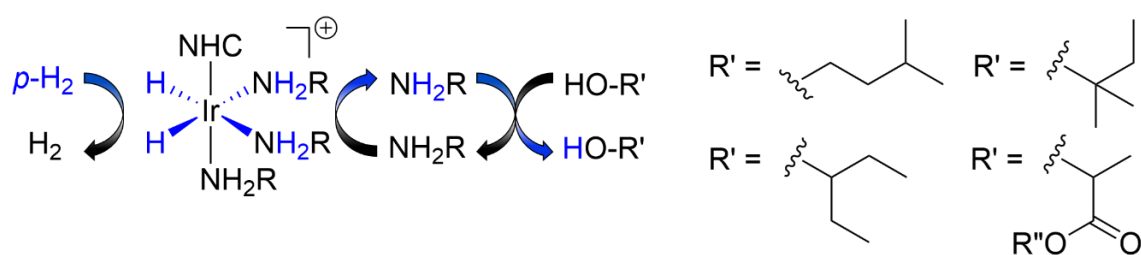
Figure 1.13: Application of SABRE-Relay to the simple alcohols 3-methyl-1-butanol, 3-pentanol and 2-methyl-2-butanol and more complex molecules including lactate esters.

The hyperpolarisation of agents such as pyruvate is also investigated using SABRE-Relay in addition to the creation of novel pyruvate containing polarisation transfer catalysts in which pyruvate is able to coordinate directly to the SABRE catalyst. This begins by overcoming weak pyruvate ligation by investigating the potential of several different classes of coligands to form SABRE active polarisation transfer catalysts in Chapter 5, as summarised in Figure 1.14.
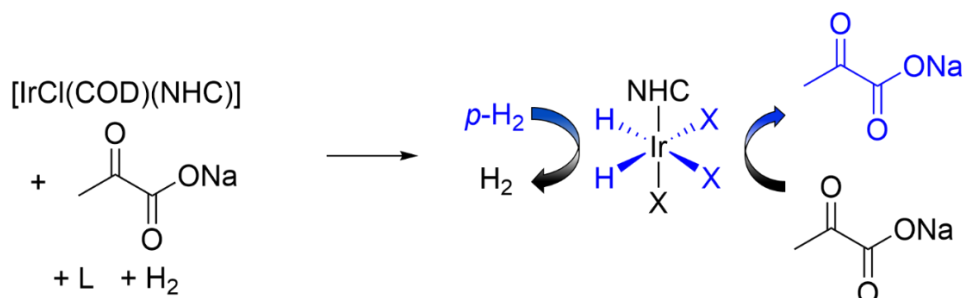
Figure 1.14: Formation of SABRE active magnetisation transfer catalysts that contain ligated pyruvate (X is L or pyruvate).

The formation of active SABRE catalysts containing bound pyruvate is explored and optimised by varying factors including the catalyst, coligand, concentrations and temperature. The ligand exchange processes within these active catalysts are also investigated and discussed. Potential applications of SABRE hyperpolarisation for biomedical imaging and reaction monitoring are discussed in Chapter 6.

Chapter 2: Investigation and optimisation of SABRE-Relay using alcohols

2.1 Introduction

Hyperpolarisation methods using p-H_2 have been used since the 1990s[31-34] and since then, the types of molecules that can be polarised using this technique has increased rapidly.[45] *Para*Hydrogen Induced Polarisation (PHIP) is typically used to polarise unsaturated molecules, typically alkenes or alkynes, using a p-H_2 hydrogenation reaction.[31, 32] This reaction breaks the symmetry of p-H_2 and creates non Boltzmann population distributions in the nuclear spin energy levels of the hydrogenated product. This allows for the detection of hydrogenated products with NMR signal intensities several orders of magnitude higher that those derived from thermal Boltzmann conditions.[68, 69, 131] PHIP has been used to polarise many unsaturated precursors, with some examples shown in Figure 2.1. A major limitation of hyperpolarisation using PHIP is that molecules must be chemically altered (hydrogenated) during the hyperpolarisation process, which limits the types of amenable substrates to those that contain unsaturated functionality. This weakness has been addressed by a variation of PHIP called PHIP-SAH which involves the functionalisation of molecules which have no unsaturated precursors with side arms which can be easily hydrogenated.[70] Transfer of polarisation from the side arm to the substrate and subsequent hydrolysis of the hydrogenated side arm has yielded aqueous solutions of hyperpolarised biomolecules which are suitable for *in vivo* imaging.[135]

The types of molecules amenable to PHIP was expanded in 2009 with the development of the Signal Amplification By Reversible Exchange (SABRE) technique which allows for substrate hyperpolarisation without direct incorporation of p-H_2 into the target molecule. Here, the symmetry of p-H_2 is broken by reversible addition to a metal centre. Polarisation can then be transferred to ligated substrates through the formation of a temporary J-coupled network within an organometallic iridium SABRE catalyst. This non hydrogenative approach allows for the hyperpolarisation of molecules without their chemical alteration and has been extended to a much wider range of functional groups that typically include iridium ligating N-donor motifs such as pyridines,[76, 96, 97, 99] nicotinamides,[76, 83, 100] pyrazines[96, 97] and even nitriles[103] with some examples given in Figure 2.1.
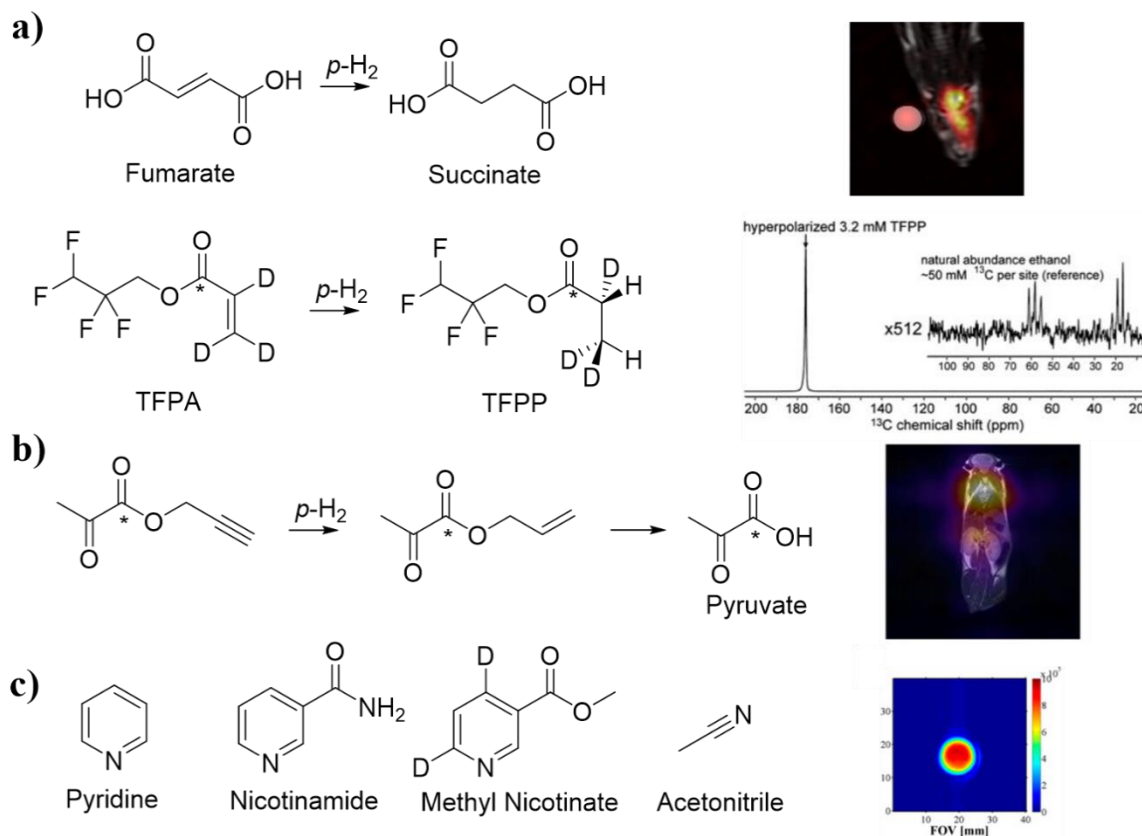
Figure 2.1: Some of the molecules hyperpolarised using a) PHIP[68, 152] b) PHIP-SAH[72, 73] and c) SABRE.[76, 101, 102] PHIP hyperpolarised succinate has been used to image brain cancer (a) while PHIP-SAH hyperpolarised pyruvate has also been imaged for *in vivo* cancer detection (b). SABRE has been used to image *N*-heterocyclic substrates like methyl nicotinate *in vitro* (c). a) is reprinted from 'Towards hyperpolarised ^{13}C-succinate imaging of brain cancer' 186, 1, 150-155, Copyright (2007) with permission from Elsevier.[8] b) Taken from Cavallari *et al*[72] c) Taken from Rayner *et al*[102]

In 2017, SABRE-Relay was developed which allows the hyperpolarisation of molecules without the need for direct interaction with the SABRE catalyst.[104, 106] In this variation of SABRE, a target substrate can become hyperpolarised by proton exchange with a hyperpolarised carrier molecule, rather than by traditional reversible exchange with the SABRE catalyst. As early as 2015, small NMR signal enhancements (up to 40-fold) of methanol solvent signals were observed in SABRE when pyridine was used as a substrate.[105] This was explained by a relayed proton exchange effect which is summarised in Figure 2.2. Similar proton exchange effects have also been used previously to relay polarisation from H_2O hyperpolarised using DNP to amino acids.[153, 154] Since then, these effects have been exploited to relay polarisation to new target molecules. Significant improvements in the relayed NMR signal enhancements (to signal gains of up to 4 orders of magnitude) were made when amines were employed as hyperpolarisation carriers.[106] Here, the carrier amine molecule binds reversibly to the SABRE catalyst to receive hyperpolarisation from *p*-H_2 whilst also containing exchangeable protons that can transfer onto a target substrate, such as an alcohol, as shown in Figure 2.2.[104] By removing the need for direct interaction with the iridium catalyst, SABRE-Relay offers the potential to hyperpolarise a much wider range of biologically relevant substrates that contain exchangeable protons, rather than *N*-heterocycles.
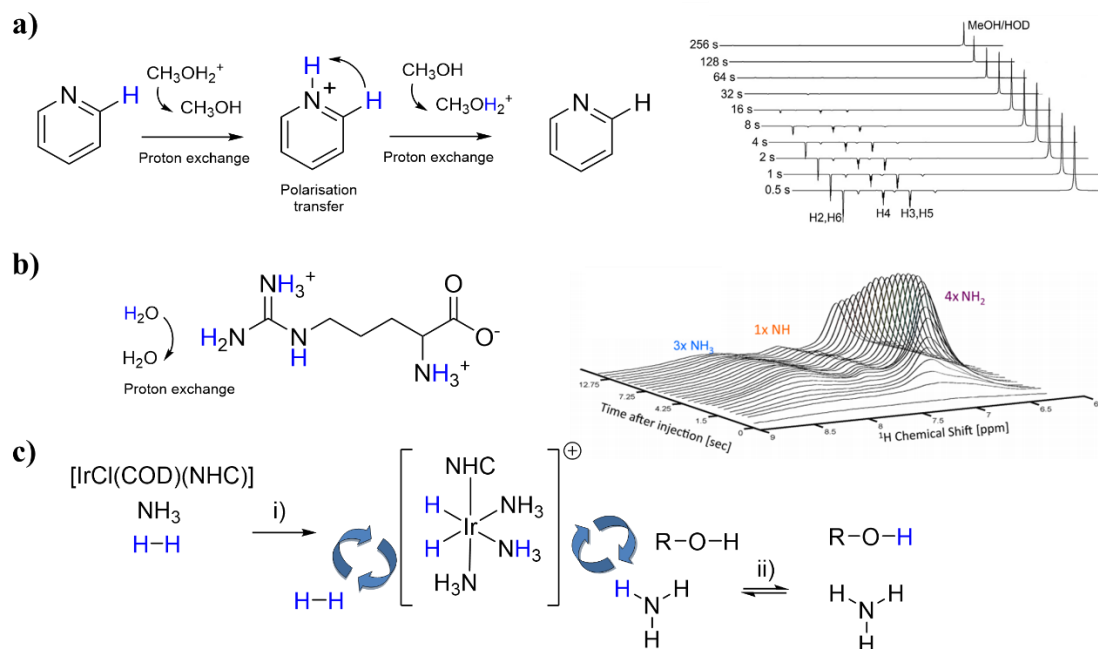
Figure 2.2: a) Proposed proton exchange effects have resulted in the relay of polarisation from SABRE hyperpolarised pyridine to solvent methanol.[105] Reprinted from 'Nuclear spin hypeprolalrisation of the solvent using signal amplification by reversibe exchange (SABRE)' 257, 15-23, Copyright (2015) with permission from Elsevier. b) Proton exchange effects from d-DNP polarised H_2O have resulted in hyperpolarised arginine resonances.[153] Reprinted (adapted) with permission from T. Harris, O. Szekely and L. Frydman, *J. Phys. Chem. B*, 2014, 118, 3281-3290 copyright (2014) American Chemical Society. c) In traditional SABRE, a precatalyst, *p*-H_2, and a carrier molecule (here ammonia), react together to form an active SABRE complex (step i). Subsequent exchange of hyperpolarised carrier protons with those of a target substrate (here an alcohol) allow relayed hyperpolarisation effects (step ii).

In traditional SABRE, NMR signal enhancements are usually optimised by changing a variety of factors that include substrate and catalyst concentrations, identity of the catalyst, solvent, polarisation transfer field (PTF), hydrogen pressure, and temperature.[155] Some of the most important factors in determining the NMR signal enhancements that can be achieved using SABRE include the efficiency of polarisation transfer from *p*-H_2 derived hydride ligands to ligated substrates within the active polarisation transfer catalyst and the T_1 relaxation rate which describes how quickly this enhanced magnetisation decays. The lifetime of the active SABRE catalyst is therefore very important: if this is too short then there is not sufficient time for magnetisation transfer to occur before the ligand dissociates.[155-157] Alternatively, if the ligand residence time is too long then relaxation induced by the paramagnetic iridium centre can limit signal gains. The exchange rate of substrate and *p*-H_2 on and off the active catalyst are therefore important parameters that ultimately determine the catalyst lifetime. It has been suggested that a substrate exchange rate of 4.5 s^{-1} would give the optimum SABRE performance.[157] It has been shown that variations of the substrate, catalyst, solvent, and temperature all have an effect on the catalyst lifetime which in turn influences the NMR signal enhancements of a substrate of interest.[87, 91, 96-98, 110, 121, 158, 159] Deuteration of substrate, solvent and catalyst is also often used to increase NMR signal enhancements using SABRE. This is due to a combination of reducing the

number of available ^{1}H sites that can receive polarisation and reduced T_1 relaxation within the active complex.[102]

The efficiency of polarisation transfer will not only depend on the lifetime of the catalyst, but the magnetic field at which polarisation transfer occurs. The most efficient polarisation transfer from p-H$_2$ derived hydrides to ^{1}H sites within the *trans*-bound carrier molecule within the active catalyst occurs at magnetic fields around 6.5 mT.[76] Theoretical treatments of this effect have shown that for polarisation transfer to occur the coupling between the two hydrides (J_{HH}) must be the same as the difference in chemical shift (δ_{HS}) between the hydride and substrate proton within the active complex.[78] J_{HH} in these types of complexes is typically 7-8 Hz and is independent of the magnetic field strength. At high field (*i.e.* 9.4 T) $\Delta\delta_{HS}$ is typically around 30 ppm (~12,000 Hz) but at a polarisation transfer field (PTF) of around 6.5 mT the chemical shift difference is of the order of a few Hz. Descriptions involving Level Anti-Crossings (LACs) have also been used to help explain these polarisation transfer effects.[94, 160] The PTF is often altered, in addition to the factors described previously, to achieve the optimum polarisation transfer and obtain the highest substrate NMR signal enhancements.

It is expected that all of these factors will be important in SABRE-Relay as they will determine the finite amount of polarisation on the carrier molecule available for relay to other substrates (step i of Figure 2.3). Therefore, those carrier molecules which receive the most polarisation from catalysts of the form [Ir(H)$_2$(NHC)(carrier)$_3$]Cl are likely to yield the highest relayed polarisation transfer. The efficiency of these catalysts for hyperpolarisation of various different amines has been previously reported.[106] In SABRE-Relay, there are two additional processes occurring which are summarised in Figure 2.3. The first is the relay of polarisation from carrier to an alcohol substrate *via* proton exchange (step ii of Figure 2.3). Secondly, in order to pass polarisation into the aliphatic groups of the alcohol, transfer must occur from the exchanging alcohol OH into the CH framework of the substrate (step iii of Figure 2.3). This is expected to occur through effects that include thermal mixing at low field,[161] J coupling, or Nuclear Overhauser Enhancement (NOE).[153] The rate of proton exchange between carrier and substrate is also expected to depend on factors such as temperature, solvent, and the identity of the carrier and substrate. Additionally, polarisation transfer within the alcohol CH framework is also expected to be magnetic field dependant.
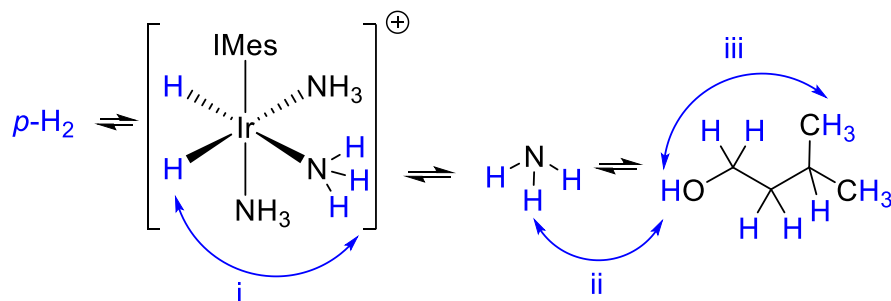
Figure 2.3: Polarisation transfer to an alcohol *via* SABRE-Relay occurs in three steps: i) polarisation transfer from *p*-H₂ derived hydrides to the bound carrier molecule which is expected to be optimal at around 6.5 mT ii) relay of polarisation from carrier to alcohol *via* proton exchange which is expected to be field independent iii) propagation of polarisation from the exchanging OH to other CH sites within the alcohol, which in this example is 3-methyl-1-butanol, 1.

This chapter focusses on optimising the recently discovered SABRE-Relay process. The chosen substrate is the primary alcohol 3-methyl-1-butanol (**1**), which is a commonly used food and drink additive.[162-164] It contains four different ^{13}C environments and four ^{1}H environments in addition to the alcohol proton which is not usually discerned by NMR due to fast proton exchange. The structure of **1** and its ^{1}H and ^{13}C NMR spectra recorded under Boltzmann conditions are shown in Figure 2.4. An optimisation approach similar to those used in traditional SABRE[102, 155] is used here in which factors such as the identity of carrier, amount of carrier and substrate, and polarisation transfer field are varied. These factors are likely to play an important role in each of the three key steps shown in Figure 2.3. Therefore, the effect of each of these factors on SABRE-Relay efficiency is examined and discussed in the following sections.
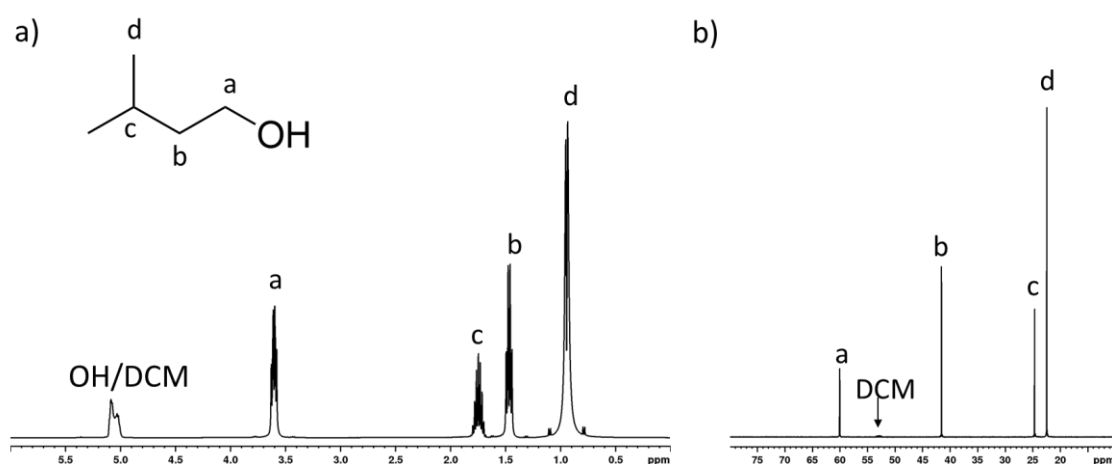
Figure 2.4: a) 16 scan ^{1}H and b) 128 scan ^{13}C NMR spectra of 1 (0.5 mL) in dichloromethane-*d₂* (0.1 mL) recorded under Boltzmann derived conditions at 298 K and 9.4 T.

2.2 Effect of carrier molecule on hyperpolarisation of 3-methyl-1-butanol (1)

3-methyl-1-butanol (**1**) was chosen as a test substrate as it was expected to yield high ^1H and ^{13}C NMR signal enhancements. This was tested by recording single scan ^1H and ^{13}C hyperpolarised NMR spectra under SABRE-Relay conditions. A sample was prepared containing the iridium precatalyst [IrCl(COD)(IMes)] (**2**) (5 mM) (where IMes = 1,3-bis(2,4,6-trimethyl-phenyl)imidazol-2-ylidene and COD = *cis,cis*-1,5-cyclooctadiene), **1** (5 eq. relative to iridium) and carrier NH_3 (**3**) (7 eq.) in dichloromethane-d_2 (0.6 mL). This sample was shaken for 10 seconds at 6.5 mT with 3 bar p-H_2 before being dropped into the spectrometer for collection of single scan ^1H or ^{13}C NMR spectra at 9.4 T (p-H_2 was refreshed and the sample re-shaken between different measurements). Example spectra are shown in Figure 2.5 and exhibit enhanced ^1H and ^{13}C NMR resonances corresponding to **1**. The ^1H and ^{13}C NMR signals for **1** (average of all sites) are enhanced by 565-fold and 1275-fold compared to their Boltzmann derived signal strengths. The formation of a *tris* NH_3 substituted active catalyst of the form [Ir(H)$_2$(IMes)(Nsub)]Cl is evident from its characteristic hydride peak at δ −23.8.[106] The structure of this complex is shown in Figure 2.2c and its chemical shifts match with those previously reported.[106] Therefore, **1** is amenable to hyperpolarisation by SABRE-Relay and is an appropriate substrate to use for subsequent optimisation and to gain greater understanding of the SABRE-Relay process.
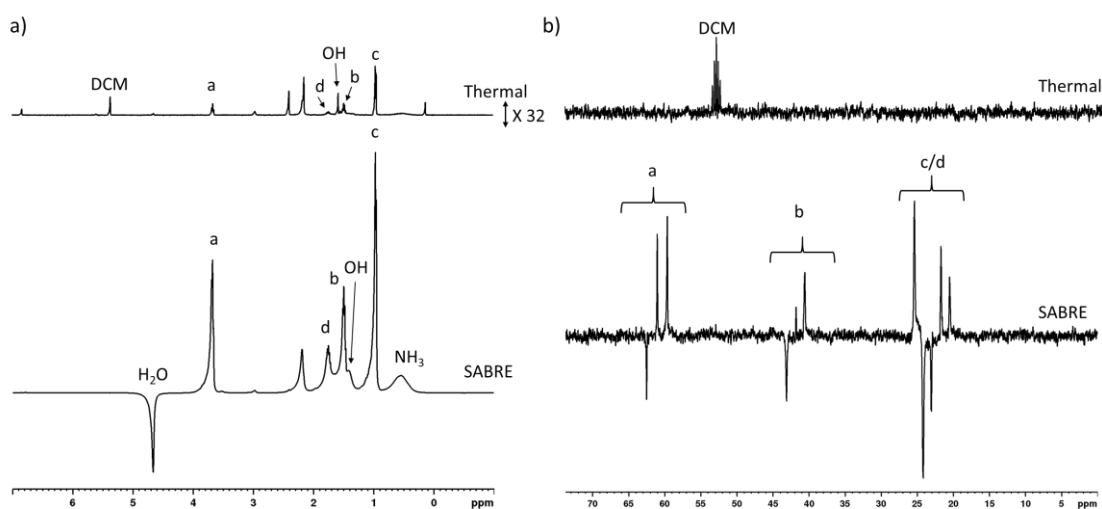
Figure 2.5: Hyperpolarised a) ^1H and b) ^{13}C NMR spectra of a solution containing 2 (5 mM), 3 (7 eq.) and 1 (5 eq.) in dichloromethane-d_2 (0.6 mL) shaken with 3 bar p-H_2 at 298 K and 6.5 mT for 10 seconds. Enhanced resonances of 1 are labelled according to the positions denoted in Figure 2.4. The thermally polarised reference NMR spectrum is shown above. All acquisition and processing parameters were the same for thermal and hyperpolarised NMR spectra (NS=1).

While the most common hyperpolarisation carrier used in initial reports of alcohol hyperpolarisation using SABRE-Relay was **3**, the use of primary amines such as benzylamine-d_7 (**4-d_7**) or phenethylamine (**5**) have been reported.[104, 106] The identity of the carrier amine is

expected to play an important role in determining the relayed alcohol NMR signal enhancements. The pK_a of the carrier amine is likely to play a role in determining the efficiency of NH $\leftrightarrow$ OH exchange which is expected to occur through RNH_3^+ and RO^- intermediates.[165, 166] Therefore, the hyperpolarisation of **1** using the carrier amines **4-d_7** ($pK_a = 9.34$[167]) and **5** ($pK_a = 9.83$[167]) was investigated and compared to that achieved using **3** ($pK_a = 9.21$[167]). When carriers **4-d_7** and **5** were used, the ^1H NMR signal enhancements for **1** were lower by a factor of *c.a.* 7 and 60 respectively (as summarised in Table 2.1) compared to those achieved using carrier **3** and now no observable ^{13}C NMR signal enhancements were observed. At this stage, only total NMR signal enhancements of **1** (per proton, averaged across all sites) are discussed to compare the efficiency of SABRE-Relay with each carrier molecule. A more detailed breakdown of polarisation on each site within the alcohol framework is discussed in section 2.5. The poor SABRE-Relay performance of **1** when **4-d_7** and **5** are used is attributed to the much lower reported hyperpolarisation levels of these carriers compared to **3** when each is hyperpolarised using traditional $[Ir(H)_2(NHC)(carrier)_3]Cl$ catalysts.[106] Therefore, when **4-d_7** and **5** are used there is much less polarisation available for relay into **1**. Despite this, **4-d_7** and **5** yield comparable NMR signal enhancements for their NH protons, yet the polarisation of **1** is 7 times lower when **5** is used compared to **4-d_7**. This suggests that while the initial polarisation of the amine carrier is very important in determining ultimate SABRE-Relay efficiency, other factors such as the efficiency of proton exchange will play an important role. This suggests that hyperpolarised NH $\leftrightarrow$ OH exchange appears more efficient in the **4-d_7** system and allows more optimal polarisation relay when compared to NH $\leftrightarrow$ OH exchange in the **5** system. However, the origin of this effect is challenging to rationalise considering that proton exchange rates, pK_a, and relaxation times of the NH protons are all likely to be different. In this case the higher performance of **4-d_7** compared to **5** is expected to be most closely related to a longer relaxation time of its NH proton.[104, 106] The use of **3** as a carrier is necessary to achieve high alcohol polarisation and future work will predominantly focus on the use of **3** as a carrier to derive alcohol polarisation using SABRE-Relay.

Table 2.1: Total hyperpolarised ^1H and ^{13}C NMR signal enhancements (averaged per site) of 1 (5 eq.) and the indicated carrier (5-10 eq.) when they are shaken in a sample containing 2 (5 mM) and 3 bar *p*-H_2 in anhydrous dichloromethane-d_2 (0.6 mL) at 298 K and 6.5 mT for 10 seconds.

Carrier	Total 3-methyl-1-butanol (**1**) NMR signal enhancements /fold		^1H enhancement of carrier NH /fold
	^1H	^{13}C	
NH$_3$ (**3**)	565 ± 10	1275 ± 70	295 ± 55
Benzylamine-d_7 (**4-d_7**)	75 ± 5	N/A	50 ± 5
Phenethylamine (**5**)	10 ± 1	N/A	40 ± 5

2.3 Effect of alcohol and amine concentration on the hyperpolarisation of 3-methyl-1-butanol (1)

A common approach to optimising NMR signal enhancements using SABRE is to vary the concentration of substrate relative to the iridium precatalyst.[92, 102, 155] It is expected that varying the amount of carrier molecule relative to the catalyst will have a large effect on the intrinsic carrier polarisation levels. Optimisation of the carrier polarisation will result in a greater finite amount of magnetisation available for relay on to the alcohol which is likely to result in higher alcohol signal gains. Once an optimum catalyst/carrier ratio is identified to achieve maximum carrier polarisation, the carrier/alcohol ratio can be varied in a similar way to find the optimal conditions for polarisation relay. The effect of carrier and alcohol concentration on the resulting NMR signal enhancements was therefore measured by using samples containing a fixed amount of carrier (**3**) and a variable amount of alcohol (**1**) (from 2.5-20 equivalents relative to metal (**2**)). The NMR signal enhancements of **1** were measured as a function of its concentration and measurements were repeated at three different fixed concentrations of **3**. The resultant NMR signal enhancements of **1**, which are presented in Figure 2.6, appear to be most dependent on the concentration of **3** as this factor determines the maximum finite amount of polarisation available for relayed transfer to **1**. For example, ^{1}H and ^{13}C NMR signal enhancements of **1** (5 eq.) decrease from 660 to 60-fold and 1260 to 50-fold respectively when the amount of **3** is increased from 7 to 18 eq. These large changes in NMR signal gains (up to a factor of 11 and 25 for ^{1}H and ^{13}C respectively) upon variation of carrier concentration are much greater than those caused by variation of the alcohol concentration. For example, when the amount of **3** is fixed (7 eq.) the ^{1}H and ^{13}C NMR signal enhancements of **1** only decrease from 660 to 200-fold and 1260 to 250-fold respectively when the amount of **1** is increased from 5 to 20 eq. These changes of just a factor of three and five for ^{1}H and ^{13}C NMR signal gains respectively suggest that the carrier polarisation is the dominant factor in determining substrate polarisation.

The SABRE performance of the carrier is therefore highly important, and an optimal amount of between 5 and 10 equivalents of **3** should be used to achieve the highest NMR signal enhancements of **1**. These amounts of carrier relative to catalyst are commonly reported to give the highest NMR signal gains for many types of substrates in SABRE.[48, 92, 98, 103, 155, 158] Further variation of alcohol concentration could yield increases of its NMR signal enhancements. When low concentrations of **1** are used, regardless of the concentration of **3**, NMR signal enhancements of **1** remain low. This is related to an decreased likelihood of NH ↔ OH exchange when **1** is present in small amounts. This is supported by high NH polarisation at low **1** concentration. As the amount of **1** is increased the NH polarisation decreases, as shown in Figure 2.6, and polarisation of **1** increases as the likelihood of NH ↔ OH exchange increases. For example, when 7 equivalents of **3** relative to the catalyst is used, increasing the concentration of **1** from 2.5 to 10 equivalents is accompanied by a decrease in the NH polarisation from 500 to 200-fold. This

trend is true regardless of the concentration of **3**, although when higher amounts of **3** are used (18 eq.) slightly higher amounts of **1** (10 eq.) are needed to give the optimal alcohol NMR signal enhancement. This suggests that **1** and **3** should be in roughly a 1:1 ratio to achieve the optimum relayed transfer effect. Optimum NMR signal enhancements of **1** are derived from using 5-10 equivalents of **3** to maximise the amount of finite carrier polarisation (step i of Figure 2.3), and a 1:1 carrier to substrate ratio to optimise subsequent polarisation relay (step ii of Figure 2.3). These same trends were observed when considering both ^{1}H and ^{13}C NMR signal enhancements of **1**.
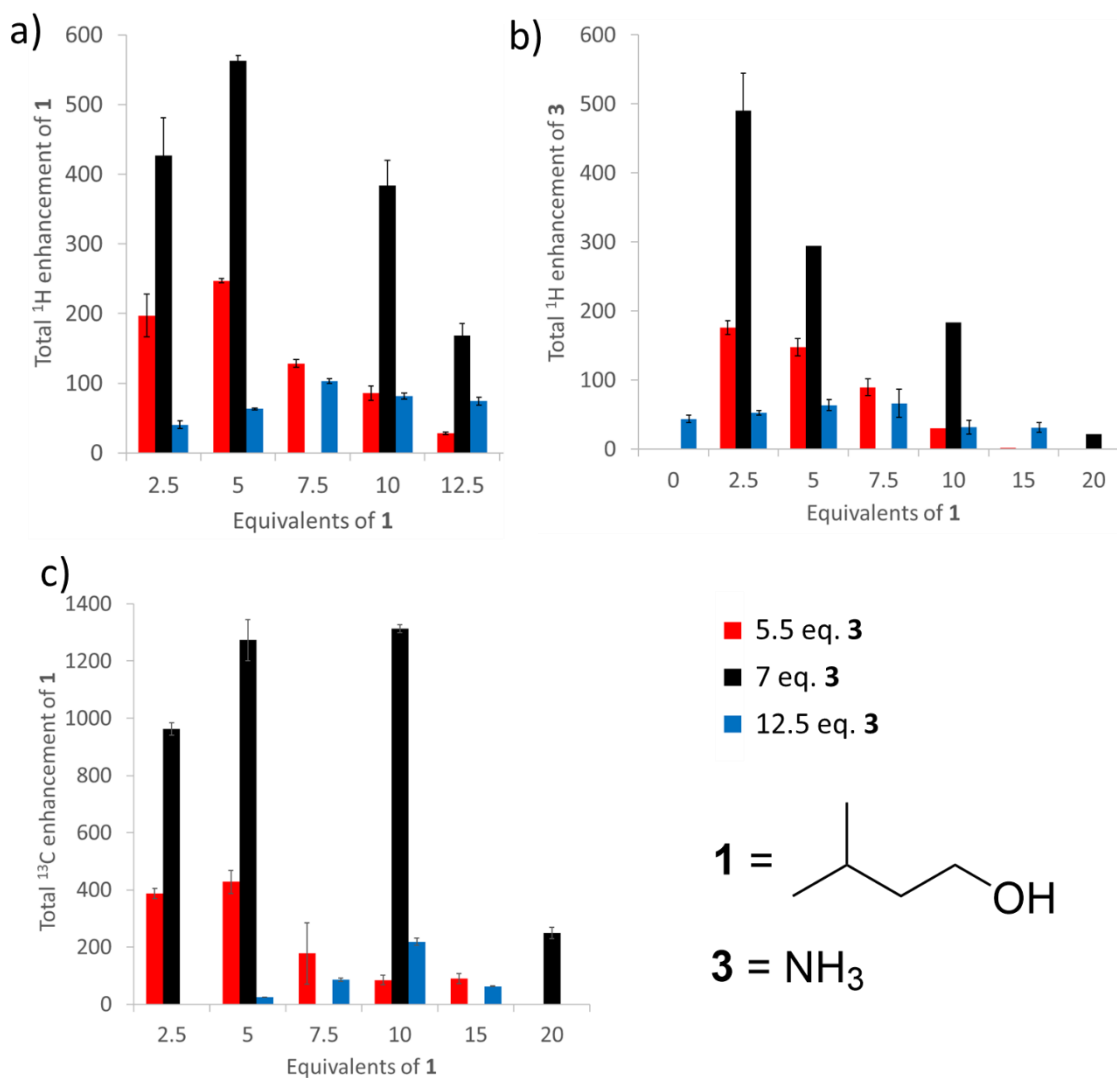
Figure 2.6: Total ^{1}H NMR signal enhancements (per proton in fold) of a) 1 and b) 3 and c) ^{13}C NMR signal enhancement of 1 when the amount of 1 or 3 relative to 2 is varied. All other factors such as the amount of 2 (5 mM), solvent (0.6 mL anhydrous dichloromethane-d_2), p-H$_2$ pressure (3 bar), shaking time (10 seconds), and temperature (298 K), were kept constant.

While the NMR signal enhancements of **1** are much lower when **4-d_7** and **5** carriers are used (compared to **3**), as discussed earlier, the same trends between alcohol concentration and alcohol NMR signal enhancements are revealed for **4-d_7** and **5**, as shown in Figure 2.7. While only total NMR signal enhancements per proton for the alcohol have been presented to allow comparisons to be made between different conditions and their effect on relayed polarisation efficiency to the

alcohol, NMR signal enhancements per proton for individual ^{1}H sites within the alcohol also follow the same trends when the amount of alcohol, carrier, or the carrier identity is changed. Therefore, these qualitative relationships are features of the SABRE-Relay mechanism and are independent of the carrier identity. This is supported by similar results on related substrates (including alcohols) that report NH_3 as a more efficient carrier compared to aliphatic amines and similar concentration effects (see Appendix 1).[48, 104, 107, 108]
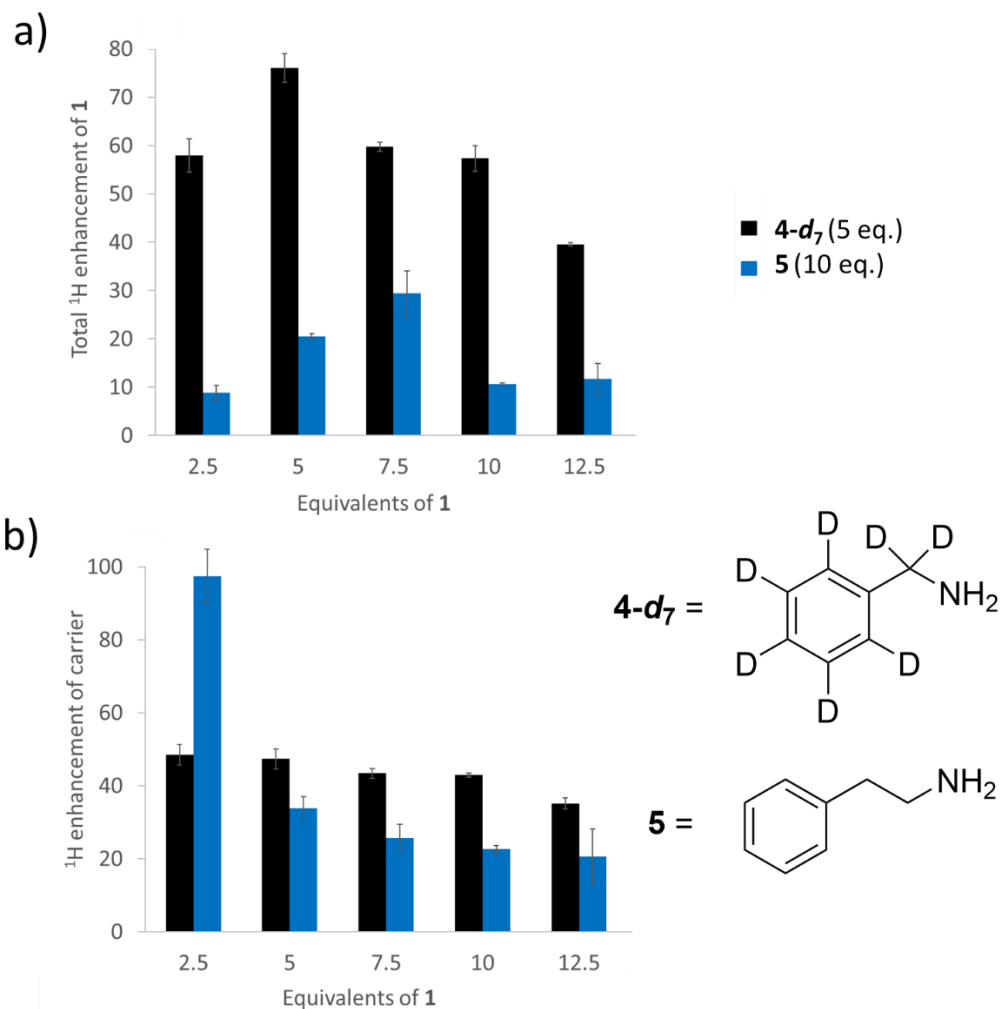
Figure 2.7: Total ^{1}H (per proton in fold) of a) 1 (5 eq.) and b) the carrier when the amount of 1 relative to 2 was varied. All other factors such as the amount of 2 (5 mM), solvent (0.6 mL anhydrous dichloromethane-d_2), p-H$_2$ pressure (3 bar), shaking time (10 seconds), and temperature (298 K) were kept constant. Note that when considering the carrier polarisation in the case of 5, the integrals of the phenyl resonances, which overlap with those of [Ir(H)$_2$(IMes)(phenethylamine)$_3$]Cl, were excluded from NMR signal enhancement calculations.

2.4 Effect of contaminant water on SABRE-Relay performance of alcohols

SABRE-Relay relies on proton exchange and therefore, the NMR signal enhancements relayed to an alcohol substrate could be optimised by improving the efficiency of proton exchange. Similarly, they could be hampered by the presence of other molecules that interfere with the NH ↔ OH exchange pathway. Contaminant water molecules contain exchangeable protons which may facilitate proton exchange between carrier and alcohol. Water could therefore act as a secondary carrier through which polarisation is passed, as shown in Figure 2.8. Alternatively, the presence of water may have a detrimental effect if proton exchange between water and carrier is more efficient than between water and substrate or carrier and substrate. Diluting the polarisation of the carrier to other exchangeable groups may result in a reduction of polarisation transfer to the target alcohol by spin dilution effects. Therefore, the effect of adding increasing amounts of H_2O or D_2O on the ^1H NMR signal enhancements of **1** was determined. These measurements, presented in Figure 2.8, were recorded by normalising the initial ^1H NMR signal enhancement prior to water addition before calculating NMR signal enhancements after H_2O or D_2O addition.
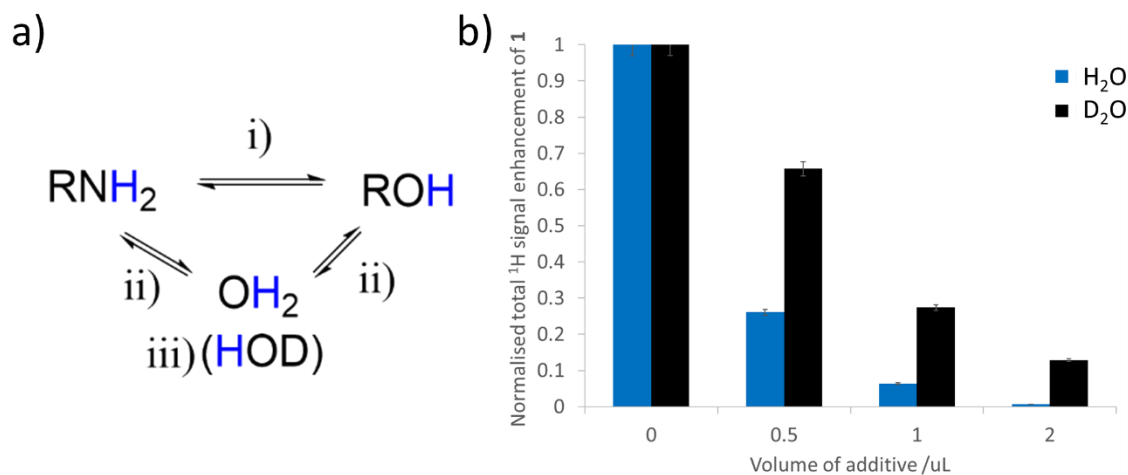
Figure 2.8: a) Proton exchange can occur directly between carrier and substrate (step i) or proton exchange from carrier to the substrate can occur *via* water (step ii). In the presence of mixtures of H_2O and D_2O, transfer can occur *via* HOD (step iii). b) Normalised total ^1H NMR signal enhancements of 1 recorded after addition of increasing amounts of H_2O and D_2O to a sample of 2 (5 mM), 1 (5 eq.) and 3 (4.5 eq.) in anhydrous dichloromethane-d_2 (0.6 mL) and shaking with 3 bar p-H_2 for 10 seconds at 6.5 mT.

Upon the addition of H_2O (0.5 μL) to a solution containing preactivated **2** (5 mM), **3** (4.5 eq.) and **1** (5 eq.), in dichloromethane-d_2 (0.6 mL) and shaking with 3 bar p-H_2 for 10 seconds at 6.5 mT the ^1H NMR signal enhancements of **1** decreased by a factor of four, which suggests that proton exchange between carrier and water is efficient and results in less polarisation relay onto the target alcohol. As the concentration of water is increased this trend continues with a decrease in NMR signal enhancements of **1** as more hyperpolarisation is diluted into water rather than the target alcohol. The binding of water to polarisation transfer catalysts of the form [Ir(H)$_2$(NHC)(substrate)$_3$]Cl where substrate is an *N*-heterocycle has been reported.[121, 168] It is

71

therefore possible that reduced SABRE performance could also be related to the increased formation of water adducts at higher water concentrations which changes the identity of the active [Ir(H)$_2$(NHC)(NH$_3$)$_3$]Cl catalyst.

Adding D$_2$O similarly decreases the NMR signal enhancements of **1**, but to a lesser extent than its *protio* counterpart. It is likely that this difference is due to relaxation effects, rather than exchange effects. It is expected that addition of D$_2$O is accompanied by the formation of HOD in solution (from small amounts of H$_2$O in wet reagents and solvent). HOD will relax more slowly than H$_2$O and, subsequently, polarisation relay *via* HOD is more likely to survive until it is exchanged onto **1** resulting in a less significant drop in efficiency. Commercial alcohols and solvents used, if not rigorously dried, will contain trace amounts of water which may have a large influence on SABRE-Relay efficiency. This may provide a huge challenge for substrates that require dissolution in water to overcome solubility issues. These results suggest that drying solvents and removing all water will give higher NMR signal enhancements of **1**. This was confirmed by performing these experiments with **1** (5 eq.) and **3** (5 eq.) in dichloromethane-d_2 (0.6 mL) taken from a stock bottle which yielded total ^{1}H NMR signal enhancements for **1** of only 95-fold. When dichloromethane-d_2 was used from a freshly opened ampule these NMR signal enhancements increased to 250-fold which could be improved further to 275-fold when dichloromethane-d_2 dried using molecular sieves was used. Therefore, anhydrous dichloromethane-d_2 dried in this way is used and care is taken to exclude water from these systems where possible.

2.5 SABRE-Relay performance as a function of alcohol class

The primary alcohol **1** exists as other geometric isomers such as 3-pentanol (**6**) and 2-methyl-2-butanol (**7**). These contain secondary and tertiary alcohol groups and are all cheap and readily available materials. Branching in the alcohol substrate is likely to have an effect on both the efficiency of proton exchange and the spread of polarisation from the exchanging OH to the CH framework of the alcohol. Therefore, ^{1}H and ^{13}C NMR signal enhancements of **6** and **7** were measured using the optimal conditions for SABRE-Relay of **1** (5 equivalents alcohol and ~7 equivalents of **3**). The structures of these alcohols in addition to their ^{1}H and ^{13}C NMR signal enhancements and ^{1}H T_1 times, including a comparison to those of **1** are shown in Figure 2.9.

When comparing these alcohol classes, the primary alcohol **1** gives the highest NMR signal enhancements, followed by the secondary alcohol **6**, while the tertiary alcohol **7** gave the lowest. Interestingly, the OH NMR signal enhancement of **6** and **7** are comparable (200-300-fold) which suggests that differences in polarisation level of the CH framework is not related to polarisation of the carrier, or even the efficiency of proton exchange, but rather the propagation of polarisation within the alcohol. This will depend on the coupling efficiency between spins in the alcohol, and on relaxation times. T_1 is the time taken to establish equilibrium magnetisation in the direction of

the magnetic field (B_o). Any hyperpolarised signal will decay in intensity over time and should last as long as possible. It is therefore important to have both high NMR signal enhancement but also a long T_1. Small NMR signal enhancements may not correspond to inefficient polarisation transfer; it may indicate that polarisation is lost quickly due to relaxation effects.
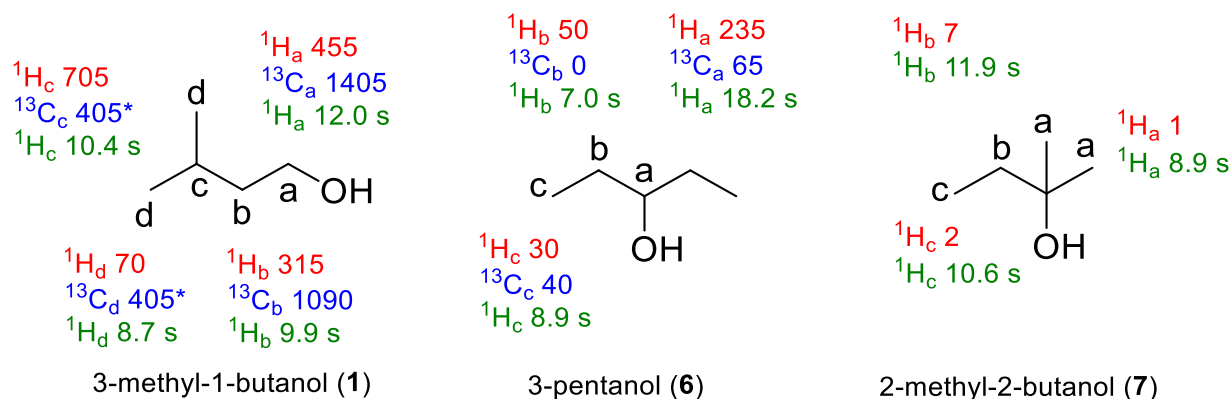
Figure 2.9: ^1H and ^{13}C NMR signal enhancements (per ^1H (red) or ^{13}C (blue)) of different alcohols (5 eq.) when shaken for 10 seconds with 3 bar p-H_2 at 6.5 mT with 2 (5 mM) and 3 (6-8 eq.) in anhydrous dichloromethane-d_2 (0.6 mL). Note that no hyperpolarised ^{13}C NMR signals of 7 were discerned. *The total NMR signal enhancement for these three carbon signals, per carbon atom, is 405-fold due to overlap of the CH and CH_3 carbon signals. ^1H T_1 times were measured using an inversion recovery pulse sequence and are shown in green.

In the case of **1**, polarisation spreads from the OH proton to the adjacent CH framework *via* two ^3J coupling interactions. In **6**, polarisation is transferred from OH to CH *via* one ^3J coupling interaction. To transfer polarisation from OH to CH_2 in **7** involves a weaker ^4J coupling which could explain why NMR signal enhancements for **7** are much lower. ^1H and ^{13}C sites closest to the OH group are typically the most enhanced as they are closest to the exchanging OH, while those sites remote from the exchanging OH group are enhanced very weakly. Generally, there is a correlation between ^1H T_1 values and ^1H NMR signal enhancements. For example, in the secondary and tertiary alcohol those sites closest to the OH group have the longest T_1 times (18.2 s and 11.9 s respectively) and consequently the highest NMR signal enhancements (235-fold and 7-fold respectively). When considering the primary alcohol **1**, the site with the highest ^1H NMR signal enhancement (705-fold) is the CH proton (c of Figure 2.3), followed by those of the CH_2 group adjacent to the OH group (a, 455-fold) and the CH_2 group (b, 315-fold). The lowest NMR signal gain is for the methyl groups (d, 70-fold). In this example the efficiency of polarisation propagation from OH to the CH group must be efficient to yield such a high signal gain for this site (705-fold) which is likely sustained by a long T_1 (10.4 s). As both ^1H and ^{13}C polarisation are achieved by shaking these samples at the same 6.5 mT field it is also possible that polarisation is passing between proton sites *via* the enhanced naturally abundant ^{13}C sites they are directly bound to. This makes rationalising these effects, and determining the dominant coupling responsible for efficient polarisation propagation, challenging.

2.6 Effect of polarisation transfer field on SABRE-Relay performance of alcohols

In SABRE, polarisation transfer from the p-H_2 derived hydrides to the *trans*-bound carrier molecule within the active catalyst occurs most optimally at magnetic fields around 6.5 mT[76] (step i of Figure 2.3) as discussed in section 2.1. It has already been shown in section 2.3 how the starting amine polarisation is important in determining the relayed alcohol NMR signal enhancement. Therefore, it is important that a polarisation transfer field (PTF) is used that yields the highest possible polarisation on the carrier molecule. However, in SABRE-Relay subsequent propagation of polarisation from the exchanging OH into the aliphatic CH groups of the alcohol will occur most optimally at a particular magnetic field. The current success in polarising substrates using SABRE-Relay[48, 104, 106-109] may be due to the fact that the fields to transfer polarisation from hydrides to carrier (step i of Figure 2.3) and to transfer polarisation from substrate OH into the substrate framework (step iii of Figure 2.3) are both optimal at around 6.5 mT. Studying the field dependence of alcohol polarisation using SABRE-Relay is therefore important to achieve optimal substrate NMR signal enhancements. The approach taken here firstly optimises the field required for transfer from hydrides to carrier (step i of Figure 2.3) before examining if alcohol NMR signal enhancements can be further increased by shaking at a variable second field.

The highest performing carriers **3** and **4-d_7** were shaken (without alcohol) with 3 bar p-H_2 for 10 seconds at different fields and the resulting NMR signal enhancements are shown in Figure 2.10. These fields are achieved experimentally using a range of handheld shakers which can achieve fields between 40 and 140 G.[80] The sample is simply placed inside them and shaken before being quickly removed and manually transferred to a 9.4 T spectrometer for recording hypeprolarised NMR spectra. In the case of **3**, replacement of p-H_2 between different shakes removes small amounts of **3** from solution. This can have a dramatic effect on NMR signal enhancements which are very sensitive to the amounts of carrier present as previously discussed. This effect can be large when performing a large number of experiments. Therefore, when **3** is used as a carrier the NMR sample is frozen with liquid nitrogen during p-H_2 replacement and shaken only once at each field. This results in only a slight loss of **3** (2-3 eq. over eight shakes). Full PTF profiles are collected by shaking a sample once at each of the eight different polarisation transfer fields. This is repeated two additional times with fresh samples containing slightly different amounts of **3** (differences of 2-3 equivalents relative to iridium). When these results are normalised the same PTF dependency is observed in each case. An average measurement is shown in Figure 2.10. While **4-d_7** generally yields lower NMR signal enhancements it provides easier experimental handling as it is a liquid at room temperature and known amounts can easily be measured into an NMR tube. This is not the case for **3** which is added to the samples as a gas using a Schlenk line (see section 7.2.1). As a result, the amount of **4-d_7** remains constant

throughout multiple repeat experiment which allows p-H_2 to be refreshed a large number of times without altering the ratio of **4-d_7** in solution. Therefore, three repeats for each of the eight PTF fields can be collected using the same sample. The optimum polarisation transfer fields for **3** and **4-d_7** was found to be 8 and 6 mT respectively which is consistent with those reported in the literature for similar substrates.[106]
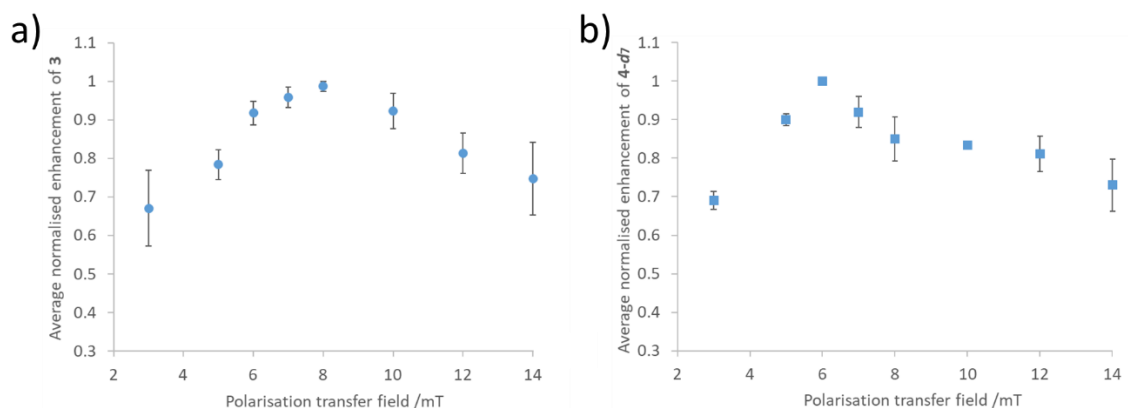
Figure 2.10: Average normalised ^1H signal enhancements for the carriers a) 3 and b) 4-d_7 when 5-10 eq. were shaken for 10 seconds with 2 (5 mM) and 3 bar p-H_2 in anhydrous dichloromethane-d_2 (0.6 mL) at varying polarisation transfer fields.

Now that the optimum PTF for **3** and **4-d_7** carriers have been confirmed the next step is to shake samples of alcohol and carrier with p-H_2 at two different fields. The first, at 8 mT, will optimally transfer polarisation to the carrier and the second, variable field, will optimise transfer within the alcohol. Therefore, a sample containing **2** (5 mM) with **3** (7 eq.) and **1** (5 eq.) was shaken with 3 bar p-H_2 for 7 seconds at 8 mT before shaking for 7 seconds at a different field. The NMR signal enhancements of the carrier (**3**) and the alcohol (**1**), which are shown in Figure 2.11a-b, are largest when shaken at 8 mT followed by 7-10 mT. Similarly, when these measurements are repeated shaking firstly at 6 mT followed by a second variable field the optimum alcohol NMR signal enhancements are obtained when the second field is 8 mT. This is indicative of the fact that 8 mT is the optimum field for polarisation of **3**. These results confirm that the NMR signal enhancement and transfer efficiency from p-H_2 to the carrier is most important as this determines the finite amount of polarisation available for transfer to the alcohol.
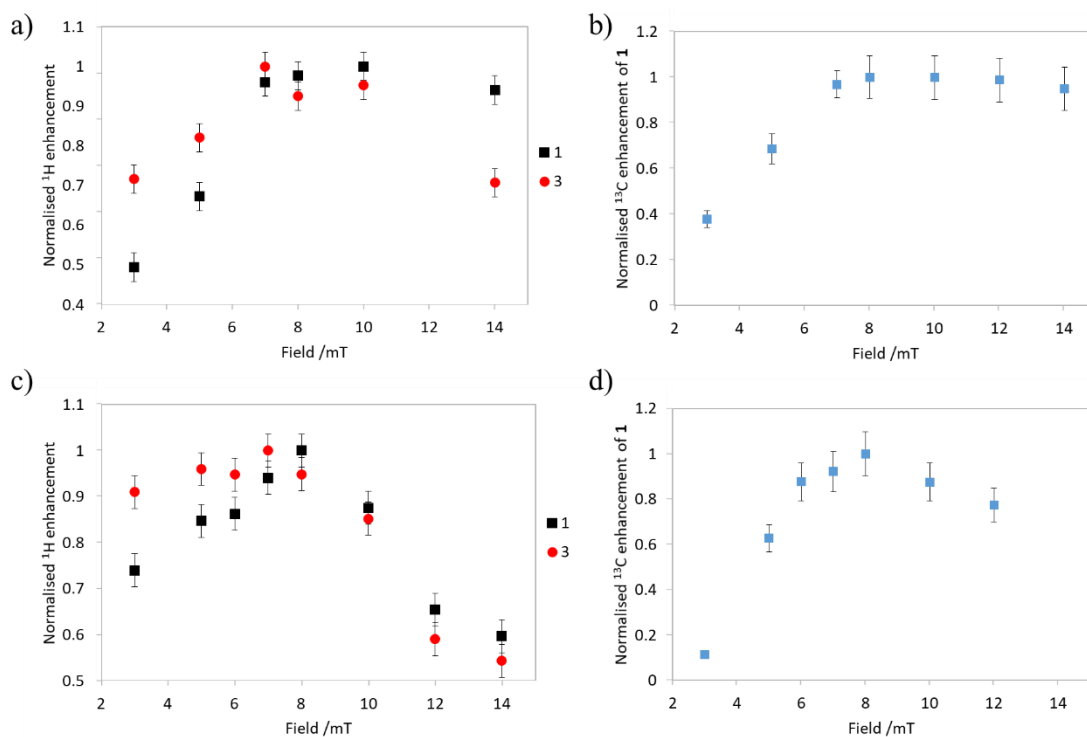
Figure 2.11: Normalised ^{1}H and ^{13}C NMR signal enhancements for 1 (5 eq.) with 3 (7 eq.) shaken for 7 seconds with *p*-H$_2$ at a)-b) 8 mT or c)-d) 6 mT before shaking for 7 seconds at a different field. The total NMR signal enhancements of 1 and 3 are each normalised to their maximum value. Each data point represents one *p*-H$_2$ shake. Errors have been calculated based on three measurements recorded using 4-*d$_7$* as a carrier (data in Figure 2.9).

It is difficult to tease out differences between the optimal field for transfer between hydrides and carrier (step i of Figure 2.3) and the optimum field for transfer within the alcohol (step iii of Figure 2.3) because the system will relax and depolarise at any period of the shaking time that the system is not at the 6-8 mT optimum field for transfer to the carrier. This limits the polarisation available for subsequent transfer to alcohol and consequently, there appears to be little benefit in shaking at a second field. Therefore, the most optimum field for polarisation of alcohols using SABRE-Relay is the optimum field for carrier polarisation, which is around 6-8 mT depending on the carrier used. There may be other fields at which polarisation transfer within the alcohol may be more efficient, but these will be challenging to implement experimentally given that alcohol polarisation is derived from carrier polarisation which is optimum at 6-8 mT. Creation of handheld shakers that are able to rapidly switch between different magnetic fields on a millisecond timescale may address this challenge.

Hyperpolarised ^{13}C NMR signals of **1** when shaken at 6-8 mT are visible and can be up to four orders of magnitude higher than those recorded under Boltzmann conditions which suggests that these 6-8 mT fields are also appropriate for transfer to ^{13}C from the exchanging OH. This may not be true for other heteronuclei and transfer might be improved using sophisticated pulse sequences such as ^{1}H-^{13}C INEPT or high field radiofrequency excitation to move OH polarisation

to heteronuclear sites in a target substrate.[95, 156, 169, 170] In SABRE-SHEATH, direct transfer from p-H$_2$ to heteronuclei of bound substrates is achieved by shaking at μT fields.[83, 171] Approaches such as SABRE-SHEATH cannot be used in conjunction with SABRE-Relay because polarisation must be relayed through the protons of a carrier molecule in a first step that will always be optimal at 6-8 mT. Direct heteronuclear polarisation using SABRE-Relay is not possible as the technique fundamentally relies on relayed proton exchange effects. This may prove to be a limitation of SABRE-Relay and may become more obvious for hyperpolarising sites that require vastly different PTF matching conditions than required for target ^{1}H sites using SABRE-Relay.

2.7 Using SABRE-Relay to detect alcohols in mixtures

SABRE can make low concentration molecules visible to NMR and has found applications in the detection of analytes in solution.[122-124, 147, 148, 172] In order to make SABRE a quantitative detection method, the intensity of hyperpolarised responses of an analyte of interest must show a linear relationship with its concentration in solution. This can be a challenge to achieve as NMR signal enhancements typically change as the ratio between substrate and catalyst are altered. Eshuis et al. have developed an elegant solution to this problem.[122, 124] They have shown that for dilute substrates/analytes in the presence of a second substrate, termed a coligand (L), a linear relationship between concentration and NMR signal enhancement of the analyte can be achieved. Under these dilute substrate concentration regimes the most abundant metal species formed in solution is [Ir(H)$_2$(NHC)(L)$_3$]Cl, where L is the coligand 1-methyl-1,2,3-triazole. As there is only a very low amount of analyte present in solution only small amounts of [Ir(H)$_2$(NHC)(L)$_2$(analyte)]Cl form and the likelihood of forming [Ir(H)$_2$(NHC)(L)(analyte)$_2$]Cl or [Ir(H)$_2$(NHC)(analyte)$_3$]Cl complexes is low. This approach cannot only detect nanomolar concentrations of analytes but their amount can be quantified using a standard addition method.[122] This involves making many additions of known concentrations of the analyte and measuring the linear increase in hyperpolarised analyte signal after each addition. The linear line of best fit produced can be used to calculate the concentration of target analyte that was originally in the mixture prior to spiking with known additions. Some examples of this approach are shown in Figure 2.12.[122-124, 147, 148, 172]
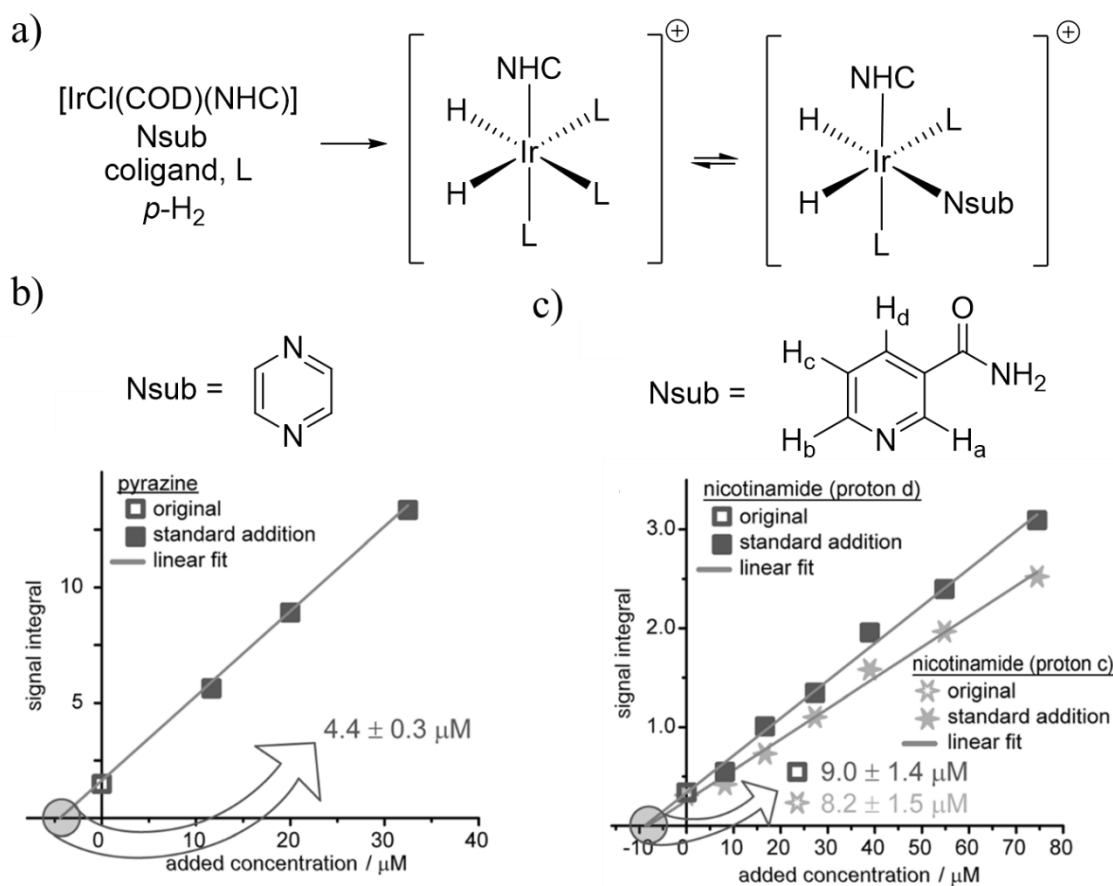
Figure 2.12: Eshuis et al. have shown that SABRE can be used to quantitatively determine the concentration of an analyte (b-c).[122] This can be done when the analyte is dilute in comparison to the metal complex and a coligand (a). Taken from Eshuis et al.[122]

This low concentration quantification approach could be extended to the detection of dilute concentrations of alcohols in mixtures using SABRE-Relay. In fact, the primary alcohol **1** is an additive often present in a wide range of food and drinks. Its concentration in a range of alcoholic drinks is often used as an indication of quality control.[162, 163] For example, tequila is made from the *agave* plant, which is native to Mexico, and can be classified into many different types: two of these are *agave* and *mixed*. *Agave* describes tequilas made exclusively from *agave* juices (100%) and water while *mixed* describes those which contains *agave* juices (as low as 50%) mixed with other sugars.[162, 163] According to Mexican law all 100% *agave* tequila must be bottled in Mexico: distinguishing between authentic 100% *agave* tequila and *mixed* tequilas is therefore very important. This is commonly done by GC-MS analysis of low concentration alcohols including **1**, which is found at higher concentrations in authentic *agave* tequila.[162, 163] Similar approaches are taken to distinguish different types of whiskey.[164] SABRE-Relay could provide a route to determining the concentration of **1** in mixtures and therefore the authenticity of alcoholic drinks such as tequila.

Initially, an equimolar mixture of the primary and secondary alcohols **1** and **6** (28 mM) were hyperpolarised using SABRE-Relay to demonstrate that signals for both alcohols could be observed and clearly distinguished, as shown in Figure 2.13a. In these experiments a ^{1}H-^{13}C

INEPT pulse sequence was used to transfer polarisation from the exchanging OH to the ^{13}C resonances *via* a *r.f.* pulse. This presents much simpler spectra with only one peak per carbon resonance and no overlap of carbon multiplet peaks. This is advantageous as it creates carbon signals that have a larger signal to noise ratio and are easier to interpret. SABRE-Relay can also be used to detect **1** in a mixture containing a range of eight different alcohols of similar concentration, as shown in Figure 2.13b. Here, responses for **1** (60 mM) and **6** (46 mM) could be distinguished in just one scan. Detection of these hyperpolarised signals using ^{13}C NMR spectroscopy is much more advantageous than using ^{1}H NMR spectroscopy which suffers from severe peak overlap. The ^{13}C NMR signal enhancements for the sites containing directly bound OH groups are 290 and 345-fold for **1** and **6** respectively. When this is extended to a mixture of eight different alcohols ^{13}C NMR signal enhancements for **1** and **6** are again observed but these are now just 85 and 40-fold due to spin dilution across the multitude of different alcohols. NMR signal enhancements of **6** in these mixtures can be higher than those of **1** despite the data in Figure 2.9 showing that in isolation secondary alcohols do not hyperpolarise as well as primary alcohols. This suggests that when mixtures of different alcohols are used each alcohol can act as a hyperpolarisation carrier by exchanging with every other alcohol in addition to the carrier. In these mixtures, the presence of other alcohols alters proton exchange efficiencies such that relay of polarisation to **6** appears more efficient. This could also be the effect of differing INEPT transfer efficiencies for different alcohols. Therefore, it is clear that interpreting the magnitude of NMR signal enhancements is much more challenging when mixtures of alcohols are used due to multiple competing exchange processes. Nevertheless, responses for **1** and **6** at concentrations of 28 mM are clearly visible to ^{13}C NMR spectroscopy in only one scan and can be distinguished from a wide range of alcohols of similar concentrations.
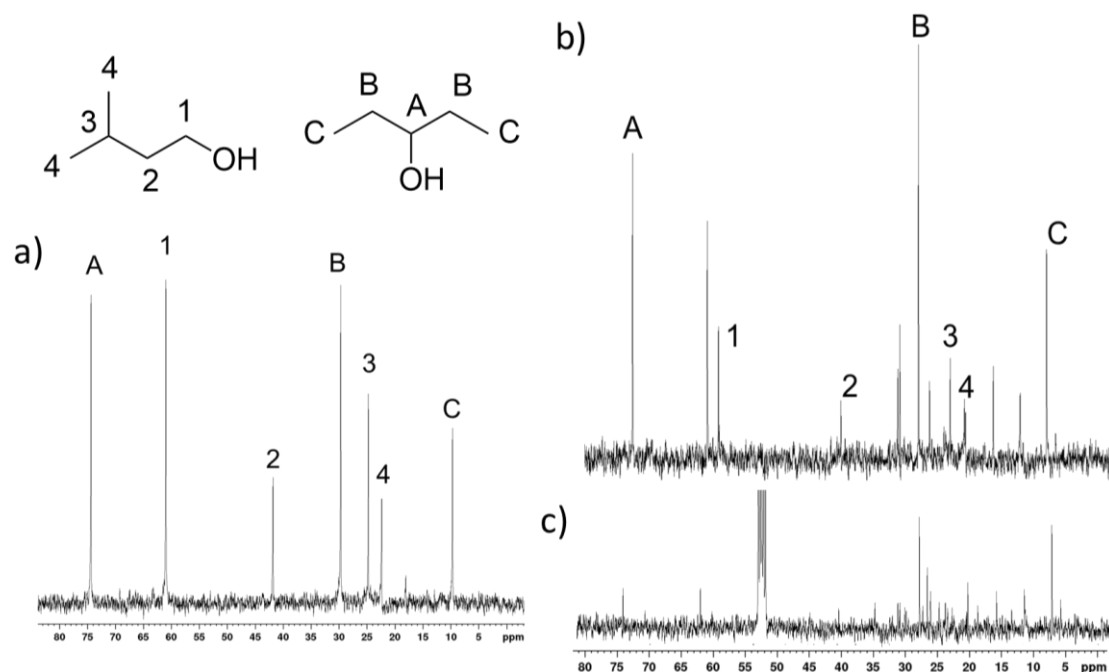
Figure 2.13: Hyperpolarised ^{1}H-^{13}C INEPT NMR spectra for a mixture of a) equimolar 1 and 6 (5 eq. relative to 5 mM 2) and b) 50 μL of a solution containing 1 (4 μL), 7 (5 μL), 2-pentanol (3 μL), 1-pentanol (4.5 μL), 1-heptanol (3.5 μL), 1-octanol (1.5 μL), geraniol (1 μL) and citronellol (2.5 μL) hyperpolarised by shaking with an anhydrous dichloromethane-d_2 (0.6 mL) solution of 2 (5 mM), 3 (14-15 eq.) and 3 bar p-H$_2$ for 10 seconds at 6.5 mT. Note a) and b) are recorded with a delay time, τ, of 2 ms c) ^{13}C NMR spectrum of the same mixture used in b) after 676 thermal scans.

These results show that hyperpolarisation using SABRE-Relay can allow ^{13}C NMR detection of **1** in mixtures of other similarly concentrated alcohols. In order to make SABRE-Relay a quantitative detection method its hyperpolarised signal intensity should scale linearly with its concentration. This can be achieved under the typically dilute conditions reported by Eshuis et al. and coworkers.[122, 124, 147] In order to apply this to SABRE-Relay a similar standard addition approach, discussed previously, was investigated. Under such dilute conditions the use of ^{1}H NMR spectroscopy, which has a greater NMR receptivity than a ^{13}C NMR measurement, is necessary. Here, a solution of **2** (2 mM) in dichloromethane-d_2 (0.6 mL) and 3 bar H$_2$ was used with **4-d_7** (5 eq.). **3** was not used due to the difficulty in controlling its precise amount in solution. Dilute additions of ethanol (with each 5 μL addition corresponding to an increase in total ethanol concentration of 50 μM) were added and shaken for 10 seconds at 6.5 mT to detect a hyperpolarised ^{1}H ethanol response. Ethanol concentrations as low as 50 μM could be detected with a signal to noise ratio of 33. Upon further addition of ethanol the hyperpolarised signal for the CH$_2$ group, which was free from spectral overlap, was found to increase in a linear fashion, as shown in Figure 2.14a. While this may suggest that SABRE-Relay could be used to determine ethanol concentrations in mixtures, calculation of the initial ethanol concentration using the line of best fit (as depicted in Figure 2.12) yields a value of 103 ± 9 μM which is significantly different to the known value of 50 μM. This discrepancy suggests that while there is a linear relationship between signal intensity and concentration this cannot be used in the same way to quantitatively calculate unknown substrate concentrations using SABRE-Relay. This can be

indicative of much more complex relationships between substrate concentration and proton exchange efficiencies.

In order to reduce the detection limit of this technique these experiments were repeated using the coligand approach used by Eshuis et al.[122, 124, 147] In these experiments the coligand imidazole (**8**) (5 eq.) was used as it is expected to bind to the catalyst with a similar affinity to **4-d_7**. In contrast to the experiments described above, here, the alcohol:carrier ratio was kept constant (1:1) by making additions of a dilute solution of equimolar **4-d_7** and **1** to a solution of [IrCl(COD)(SIMes)] (**9**) (3 mM) and **8** (5 eq.) in dichloromethane-d_2 (0.6 mL) preactivated with 3 bar H_2. It is expected that as more **4-d_7** is added its NMR signal gains should scale linearly with its concentration in accordance with literature reports.[122, 124, 147] Similarly, the NMR signal enhancements of **1** should also scale linearly as the proton exchange process should not be altered by the constant 1:1 carrier:alcohol ratio. When such experiments are performed a ^{1}H NMR signal for hyperpolarised **1** could be distinguished at concentrations as low as 100 μM in a single scan which indeed increase linearly with subsequent additions, as shown in Figure 2.14b. This approach involving a coligand did not appear to reduce the detection limit with 50 μM alcohol now being below the detection limit. This increased detection limit is likely related to polarisation leakage into **8**, which could be prevented by further optimisation of coligands to include those that lack ^{1}H sites. The calculated initial concentration of **1** from the line of best fit was 147 ± 8 μM which is, again, inconsistent with the known starting value of 92 μM. Therefore, in this case, there appears little additional benefit of using a coligand. Therefore, the previous approach using a significant carrier excess rather than a 1:1 carrier to substrate ratio is continued.
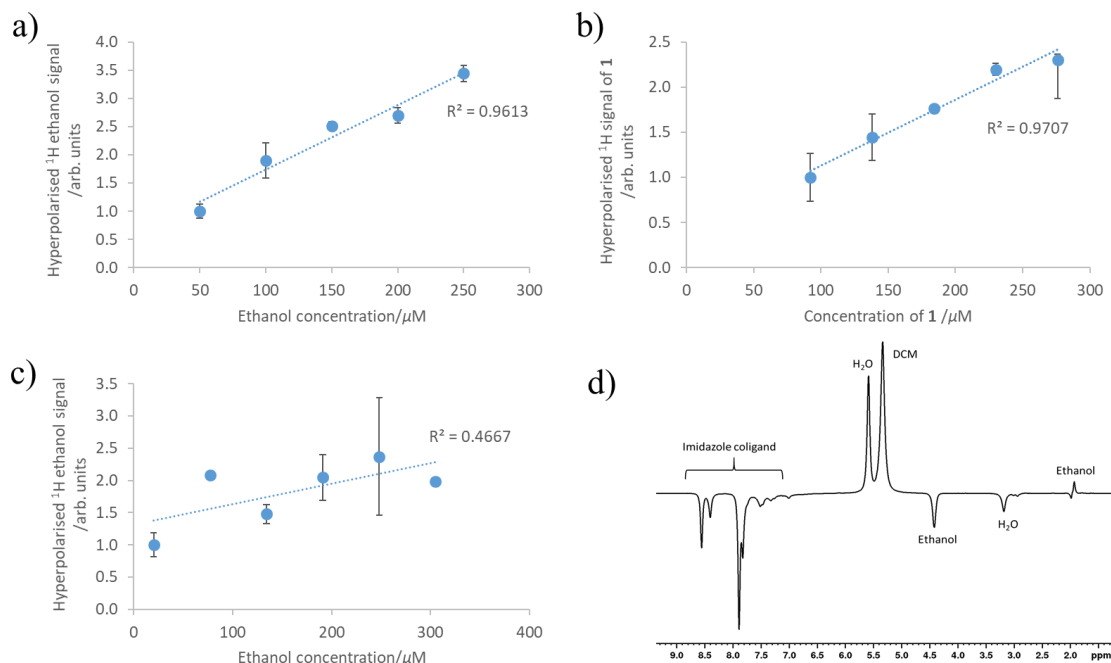
Figure 2.14: a) Hyperpolarised ethanol ^{1}H CH$_2$ NMR signal intensity increases linearly when $5\,\mu$L additions of ethanol ($1\,\mu$L in dichloromethane-d_2 (1.4 mL)) are made to preactivated 2 (5 mM) and 4-d_7 (5 eq.) with 3 bar H$_2$ in anhydrous dichloromethane-d_2 (0.6 mL). b) When an alternative approach is used, hyperpolarised signals of 1 again increase linearly when $5\,\mu$L additions of an equimolar 1:4-d_7 solution ($0.6\,\mu$L of each in 1 mL anhydrous dichloromethane-d_2) are made to preactivated 9 (3 mM) and 8 (5 eq.) with 3 bar H$_2$ in anhydrous dichloromethane-d_2 (0.6 mL). c) Repeating a) using an initial $5\,\mu$L addition of diluted 40% ethanol:H$_2$O ($0.4\,\mu$L Ethanol, $0.6\,\mu$L H$_2$O in dichloromethane-d_2 (1.4 mL)) followed by standard additions ($5\,\mu$L) of dilute ethanol ($1\,\mu$L in dichloromethane-d_2 (1.4 mL)) does not yield a linear relationship. d) Hyperpolarised ^{1}H NMR spectra after shaking 0.1 mL Jose Cuervo tequila with a solution of preactivated 9 (3 mM), 8 (5 eq.) and 4-d_7 ($0.5\,\mu$L) with 3 bar H$_2$ in dichloromethane-d_2 (0.6 mL) at 6.5 mT for 10 seconds.

Potential applications such as determining ethanol concentration in alcoholic drinks, blood, or urine will be further complicated by the presence of large quantities of H$_2$O in these mixtures. This is exemplified when the experiment above was repeated by using known mixtures of 40% Ethanol:H$_2$O to mimic an alcoholic drink. This mixture was added to a solution of **2** (2 mM) with **4-d_7** (5 eq.) in dichloromethane-d_2 (0.6 mL) and 3 bar H$_2$ followed by standard additions of 100% ethanol. Here, the hyperpolarised ethanol ^{1}H NMR signal no longer increases linearly with subsequent ethanol additions, as shown in Figure 2.14c. This indicates significant changes in the substrate:H$_2$O ratio upon subsequent ethanol additions which appears to have a dramatic effect on proton exchange efficiency and the subsequent NMR signal enhancements. The presence of competing exchange processes may hamper quantitative substrate determination using SABRE-Relay. For example, when dilute amounts of the alcoholic drinks whiskey (40% ABV) or peach schnapps (15% ABV) were added to a solution of **2** (2 mM) in dichloromethane-d_2 (0.6 mL) with **4-d_7** (5 eq.) and 3 bar p-H$_2$, the hyperpolarised ^{1}H ethanol signal in whiskey was higher than that in the peach schnapps sample, but was not comparable to that in a known 40% ethanol:H$_2$O mixture despite containing similar amounts of ethanol. This further confirms that quantitative analysis is challenging and prevents the use of a calibration curve to allow determination of alcohol concentrations. The presence of other OH-containing molecules in such alcoholic drinks,

or small variations in carrier/substrate/catalyst/water ratios between different samples, may be responsible for such effects in these dilute systems.

While the SABRE-Relay technique does yield a linear response for hyperpolarised alcohol signal as a function of its concentration under dilute conditions, this relationship cannot currently be used to give accurate alcohol concentrations. Nevertheless, alcohol concentrations as low as 28 μM can be detected in a single scan SABRE-Relay hyperpolarised ^{13}C NMR spectrum, and signals can be detected in the presence of a large number of similarly concentrated alcohols. However, alcohol hyperpolarisation levels are affected by the presence of other molecules with exchanging protons. For example, hyperpolarised signals for **1** are not observed in these alcoholic drinks despite a 32 scan thermal ^{1}H spectrum confirming its presence. This is likely related to large excesses of other molecules with labile protons such as ethanol and water whose exchange processes dominate. Indeed, when alcohol water mixtures are used there is no longer a linear relationship between alcohol NMR signal enhancements and alcohol concentration. Nevertheless, these results show that low (μM) concentration alcohols can be detected using SABRE-Relay and further work will be needed to create an approach in which alcohol concentration can be determined quantitatively by SABRE-Relay, even in mixtures that contain multiple species with exchangeable protons.

2.8 Conclusions

In this chapter the SABRE-Relay mechanism has been investigated using the simple alcohol **1** as a test substrate. It is clear that each of the three steps of the SABRE-Relay mechanism i) polarisation transfer from p-H$_2$ to carrier ii) polarisation relay from carrier to substrate *via* proton exchange and iii) propagation of polarisation within the substrate framework all play an important role in determining substrate NMR signal enhancements. Under particular conditions each of these steps can become rate limiting and variation of certain factors can improve the efficiency of each step. For example, the finite amount of polarisation on the carrier molecule available for relayed transfer is often important and can be optimised by variation of the carrier identity and the carrier to catalyst ratio. Carrier **3** relays the highest alcohol polarisation compared to use of **4-d_7** or **5**. The alcohol NMR signal enhancement is most dependant on the efficiency of carrier polarisation which is optimum when 5-10 equivalents of carrier are used. Further refinement of alcohol NMR signal enhancements can result from variation of the carrier to alcohol ratio. This effectively tunes OH ↔ NH exchange which is most efficient when the alcohol and carrier are in a 1:1 ratio. Destructive competing proton exchange processes with contaminant water can reduce alcohol NMR signal enhancements. Therefore, anhydrous conditions should be used where possible to achieve optimal SABRE-Relay performance. This may be a serious limitation of the technique.

The class of alcohol can influence polarisation propagation from the exchanging OH into the substrate aliphatic framework. When comparing the primary, secondary and tertiary alcohols **1**, **6** and **7**, the former polarise more strongly. The reduced performance of secondary and tertiary alcohols **6** and **7**, which contain similar levels of OH polarisation, is more likely related to inefficient transfer through the *J*-coupling network within the alcohol CH framework. This highlights the tension between the multiple factors that determine SABRE-Relay performance: initial carrier polarisation, proton exchange efficiency, and transfer within the alcohol framework. Separation of the field dependencies of each of these steps is challenging and an optimum polarisation transfer field of 6-8 mT, which corresponds to the optimal PTF for polarisation of the carrier, is required. Polarisation transfer into certain heteronuclei may be limited by this matching condition which may be a fundamental limitation of the ^{1}H derived polarisation relay. Despite this, 1400-fold ^{13}C NMR signal enhancements and 700-fold ^{1}H NMR signal enhancements for **1** can be achieved at these PTF fields which is a significant development for SABRE as polarisation of these types of non hydrogenatable, non ligating substrates with such high signal gains can not be achieved using traditional SABRE or PHIP.

SABRE-Relay can be used to detect alcohols like **1** which are present in mixtures. Concentrations as low as 28 μM can be detected in a single scan ^{13}C NMR spectrum and this detection limit could be reduced through further optimisation of the carrier molecule, catalyst or coligand. While **1** can be detected in a mixture of several different alcohols of similar concentrations its polarisation levels are affected by the presence of other alcohols, which all contain exchangeable groups. This precludes the detection of small quantities of **1** in the presence of much higher concentrated alcohols, such as ethanol, whose exchange processes dominate. When these alcohols are used alone under dilute anhydrous conditions a linear relationship between hyperpolarised signal intensity and concentration results which may allow for qualitative comparisons of alcohol concentrations to be made. This relationship, however, does not allow for the quantitative determination of substrate concentration and breaks down when extended to alcohol water mixtures. Despite these limitations, SABRE-Relay could become a useful tool for the detection and quantification of substrates in solution.

SABRE-Relay contains many of the features of the traditional SABRE mechanism but additional proton exchange and polarisation propagation steps necessitate consideration of additional effects which make the SABRE-Relay approach much more complex to optimise. Despite this, general features are present and the technique can be used to polarise alcohols with high signal gains which is a class of substrate that has previously eluded hyperpolarisation using *p*-H$_2$-based methods.

Chapter 3. SABRE-Relay of more complex OH-containing molecules

3.1 Introduction

Traditional Magnetic Resonance Imaging (MRI) can produce anatomically detailed 3D pictures of living tissues in a non-invasive manner.[4] These achievements have resulted in its routine use for the diagnosis of disease. Despite these successes, MRI is insensitive on the molecular level and must therefore take advantage of the large ^1H MR signal from bulk water protons in different tissues of the body.[4] MRI is able to differentiate these water molecules based on their T_1 or T_2 relaxation times, which allows images of high contrast to be produced.[6] MRI can therefore provide useful information on tissue structure in a non-invasive way and is commonly used to diagnose structural abnormalities or differences in morphology (*i.e.* tumours).[4] Despite widespread use, MRI typically provides little information as to the function or disease state of tissues.[4]

The production of hyperpolarised contrast agents has been the focus of much interest as this allows metabolic pathways and biochemical processes of tissues to be interrogated.[5] For example, pyruvate is respired aerobically in healthy cells but anaerobic pathways, such as conversion into lactate, are upregulated in areas of cancer.[138] HP-MRI using pyruvate therefore provides a route to distinguishing areas of cancer based on enhanced pyruvate to lactate conversion and was first applied to human studies of prostate cancer in 2013.[132] Since then, further in human studies of various target organs have been performed.[142, 173] While there are several hyperpolarisation techniques (described in Chapter 1), d-DNP is the only one currently used to produce hyperpolarised agents for in human studies with ^{13}C polarisation levels as high as 70% achieved in 20 minutes.[38] However, d-DNP uses complex experimental apparatus to transfer polarisation from electrons to nuclei (see section 1.3.1). The high cost and limited availability of d-DNP polarisers mirror the complexity of the experimental setup.

Much attention has been directed at hyperpolarisation of molecules using p-H_2-based methods to provide a faster, cheaper and refreshable alternative to DNP.[68, 69, 71] Many potential agents suitable for *in vivo* study have been reported. One of these, succinate, has received significant attention for hyperpolarisation using PHIP because it can be made easily from its unsaturated precursor, fumarate.[68, 69, 71] Studies have shown that ^{13}C-succinic acid-d_2 and other derivatives such as diethyl ^{13}C-succinate-d_2 can be polarised using PHIP with polarisation levels as high as 8% and 2% respectively.[71] When injected into mice these agents accumulate in certain cancer cell lines and *in vivo* metabolism can be tracked.[71]

Signal Amplification By Reversible Exchange (SABRE) is an alternative method that transfers polarisation from p-H_2 to a substrate when both are in reversible exchange with an iridium catalyst.[76] Catalytic magnetisation transfer occurs *via* the formation of temporary J-coupled networks within an organometallic complex.[78] Therefore, substrates can be polarised without their chemical modification as direct p-H_2 incorporation is no longer necessary. SABRE has traditionally been used to polarise iridium ligating structures which typically contain *N*-donor sites.[79] However, SABRE-Relay has removed this restriction by relaying polarisation from ligands such as amines to non-ligating ligands such as alcohols,[108] sugars,[107] silanols[109] and many others,[104] *via* the exchange of hyperpolarised protons, as summarised in Figure 3.1. It is expected that SABRE-Relay can provide a useful tool for hyperpolarising a much wider range of naturally occurring biomolecules which do not contain unsaturated or iridium ligating motifs and are therefore unsuitable for hyperpolarisation by traditional PHIP or SABRE.
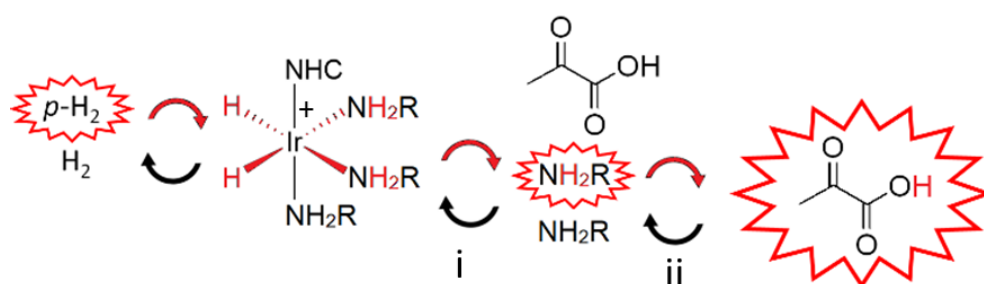
Figure 3.1: SABRE-Relay uses p-H_2 to hyperpolarise carrier molecules like amines when both the carrier and p-H_2 are in reversible exchange with an iridium catalyst (step i). Polarisation can then be relayed to non-ligating substrates (the potential target shown in this example is pyruvate) *via* proton exchange (step ii).

In Chapter 2, the mechanism of relayed polarisation transfer in SABRE-Relay was investigated using the simple alcohol 3-methyl-1-butanol as a test substrate. The carrier NH_3 (**3**) was found to give higher alcohol polarisation compared to the use of benzylamine-d_7 (**4-d_7**) or phenethylamine (**5**). Alcohol NMR signal enhancements were dependant on the efficiency of polarisation transfer to the carrier which is optimum when 5-10 equivalents of carrier are used. Further refinement of alcohol NMR signal enhancement was possible by variation of the carrier to alcohol ratio. This effectively tunes OH $\leftrightarrow$ NH exchange which is most efficient when the alcohol and carrier are in a 1:1 ratio. Alcohol NMR signal enhancements were found to be highest when polarisation transfer fields of 6-8 mT were used in order to maximise the finite amount of carrier polarisation available for relayed transfer to a substrate. While SABRE-Relay was extended to include the secondary and tertiary alcohols 2-pentanol and 2-methyl-2-butanol, these are simple alcohols containing only aliphatic CH frameworks. In this chapter, optimised SABRE-Relay conditions will be extended to more complex molecules that contain OH groups such as natural products, neurotransmitters, and metabolites. This may present greater potential applications for biomedical imaging than the simple alcohols explored in Chapter 2.

3.2 Extending SABRE-Relay to more complex OH-containing molecules

A range of target substrates, **10-17**, with OH-containing functionality have been selected and their structures are shown in Figure 3.2. Choline chloride, **10** has been hyperpolarised using DNP and used to monitor the action of choline kinase enzymes, which is often altered in various types of cancer.[174, 175] β-hydroxybutyric acid, **11**, is a ketone body that is produced from metabolism of acetoacetate and can be used as a redox state marker of mitochondria.[176] Similarly, glycogenolytic and gluconeogenic liver tissue can be distinguished by monitoring metabolism of dihydroxyacetone, **12**.[177] Norepinephrine, **13**, and ascorbic acid, **14**, are neurotransmitters and vitamins respectively of biological significance which may provide useful information on the disease state of tissues in the body. The terpene derived products nerol, **15**, geraniol, **16**, and linalool, **17**, are all biologically occurring molecules present in natural oils and used commonly in perfumes.
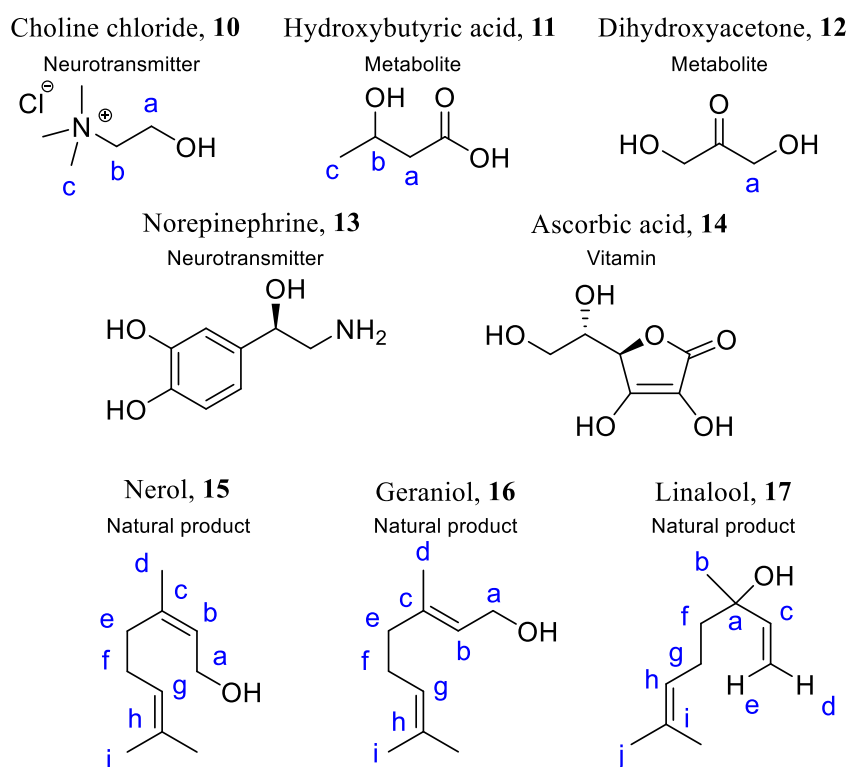
Figure 3.2: Substrates 10-17 investigated as more complex OH-containing SABRE-Relay targets.

The hyperpolarisation of **10-17** using SABRE-Relay was investigated by shaking each of **10-17** (5 eq. relative to iridium) with 3 bar p-H$_2$ for 10 seconds at 6.5 mT in a solution of [IrCl(COD)(IMes)] (**2**) (5 mM) pre-activated with NH$_3$ (5-10 eq.) in dichloromethane-d_2 (0.6 mL). SABRE is most commonly performed in organic solvents (methanol-d_4, ethanol-d_6, dichloromethane-d_2 and chloroform-d) which is necessary due to the limited solubility of both SABRE precatalysts and p-H$_2$ in aqueous solvents (D$_2$O).[155] SABRE hyperpolarisation in D$_2$O has been reported, but this is typically achieved using specialised catalysts in which the carbene ligand has been functionalised with water solubilising groups and typically yields much lower

substrate polarisation (^{1}H ε < 100-fold).[100, 120, 121] In the case of SABRE-Relay, solvents with exchangeable protons (methanol-d_4, ethanol-d_6) are not used to prevent competing proton exchange processes. Conversely, dichloromethane-d_2 is a SABRE-Relay compatible solvent and is used in this work.[48, 104, 108, 109] Despite this, **10**-**14** are insoluble in dichloromethane-d_2 and therefore, they are solubilised in 10 μL H$_2$O before addition to a solution of [IrCl(COD)(IMes)] (**2**) (5 mM) pre-activated with NH$_3$ (**3**) (5-10 eq.) in dichloromethane-d_2 (0.6 mL). When hyperpolarising alcohols using SABRE-Relay, destructive competing proton exchange processes with contaminant water were found to reduce alcohol NMR signal enhancements.[107-109] Therefore, use of the anhydrous conditions necessary for optimal SABRE-Relay performance is difficult to achieve for **10**-**14** which exist as solids at room temperature and are not soluble in SABRE-compatible organic solvents. For example, when **10**-**12** are solubilised in H$_2$O (10 μL) and shaken with 3 bar p-H$_2$ for 10 seconds at 6.5 mT in a solution of **2** (5 mM) pre-activated with NH$_3$ (5-10 eq.) in dichloromethane-d_2 (0.6 mL) only low ^{1}H NMR signal enhancements are obtained (<11-fold), as summarised in Table 3.1.

The use of dimethylformamide as a co-solvent for hyperpolarisation of target molecules such as glucose using SABRE-Relay has been reported.[107] This can help solubilise target agents in a dichloromethane-d_2/dimethylformamide mixture without adding solvent (like H$_2$O) that contain exchangeable protons. Much larger volumes of dimethylformamide are required to solubilise **10** (0.1 mL) compared to H$_2$O (10 μL). ^{1}H NMR signal enhancements of **10** were found to double from 5-fold to 10-fold when **10** was solubilised in dimethylformamide (0.1 mL) and shaken with 3 bar p-H$_2$ for 10 seconds at 6.5 mT in a solution of **2** (5 mM) pre-activated with NH$_3$ (5-10 eq.) in dichloromethane-d_2 (0.5 mL). However, overall ^{1}H NMR signal enhancement remained low and no ^{13}C NMR signals were observed in single scan NMR spectra. Observation and quantification of ^{1}H NMR signal enhancements was hampered by overlap of ^{1}H resonances of **10** with dimethylformamide. Substrates **12**-**14** showed no ^{1}H or ^{13}C NMR signal enhancements when analogous samples were prepared in dimethylformamide (0.1 mL) and dichloromethane-d_2 (0.5 mL) mixtures, as summarised in Table 3.1.

Table 3.1: ^{1}**H and** ^{13}**C NMR signal enhancements for 10-17 when each is shaken with 3 bar** *p*-**H**$_2$ **for 10 seconds at 6.5 mT in a solution of 2 (5 mM) pre-activated with NH**$_3$ **(5-10 eq.) in dichloromethane-***d*$_2$**. Substrates are either used neat, dissolved in H**$_2$**O (10** *μ***L) or dimethylformamide (0.1 mL) as indicated. Anhydrous solvents are used and the total solvent volume is 0.6 mL.** ^{13}**C NMR signal gains are measured using a** ^{1}**H-**^{13}**C INEPT pulse sequence. Sites are labelled according to Figure 3.2.**

Substrate	Solubilising agent	^{1}H signal gains /fold	^{13}C signal gains /fold
10	10 μL H$_2$O	a-c: 5 ± 1	N/A
10	0.1 mL dimethylformamide	a: 5 ± 1; b: 11 ± 1; c: N/A$^+$	N/A
11	10 μL H$_2$O	a: 0; b: 8 ± 1; c: 5 ± 1	N/A
12	10 μL H$_2$O	a: 6 ± 1	N/A
13	0.1 mL dimethylformamide	N/A	N/A
14	0.1 mL dimethylformamide	N/A	N/A
15	N/A	a: 170 ± 15; b: 45 ± 5	a: 500 ± 25; b: 235 ± 25
16	N/A	a: 270 ± 15; b: 115 ± 5; d/e/f: 355 ± 20; g: 30 ± 5	a: 160 ± 10; b: 120 ± 10; c: 30 ± 5
17	N/A	b: 60 ± 5; c: 7 ± 1; d: 3 ± 1; e: 1 ± 1; f/g: 60 ± 15; h: 4 ± 1	a: 120 ± 1; f: 35 ± 5

$^+$Overlap with dimethylformamide, N/A = no signal gains observed, missing resonance labels corresponds to no observed signal gains.

In contrast, **15-17** exist as liquids at room temperature and pressure and do not require solubilisation in H$_2$O or dimethylformamide. When these substrates (5 eq.) are added to a solution of **2** (5 mM) pre-activated with NH$_3$ (5-10 eq.) in anhydrous dichloromethane-*d*$_2$ (0.6 mL) and shaken with 3 bar *p*-H$_2$ for 10 seconds at 6.5 mT much higher ^{1}H (up to 355-fold for **16**) and ^{13}C NMR signal gains (500-fold for **15**) are observed. Signal gains for **15** are localised to sites close to the exchanging OH group, while those of **16**, which contains an *E* arrangement around the alkene bond, are spread more evenly within the coupled CH framework of the substrate. Tertiary alcohol **17** has lower NMR signal enhancements (up to ~60-fold for ^{1}H sites and ~120-fold for ^{13}C sites) which is related to less efficient coupling within the substrate and supports previous observations in section 2.5 that tertiary alcohols generally display less efficient SABRE-Relay performance than primary alcohols.

Low SABRE-Relay performance for agents **10-14** is attributed to low solubility in SABRE compatible solvents such as dichloromethane-*d*$_2$, which necessitates solubilisation in either H$_2$O or dimethylformamide. In the case of H$_2$O, the introduction of a large pool of exchangeable protons can interfere with the relayed proton exchange from carrier to substrate. While the relayed polarisation of amino acids from DNP hyperpolarised H$_2$O has been used to produce significant signal gains for the amino acids,[153, 178] in this work relayed polarisation transfer *via* H$_2$O did not yield significant substrate signal gains. This is likely related to efficient proton exchange between the carrier molecule and H$_2$O and inefficient proton exchange between H$_2$O and the substrate of interest at the concentrations used in these SABRE-Relay studies. Co-solvents were not required for **15-17** which yielded appreciable ^{1}H and ^{13}C NMR signal gains using SABRE-Relay (up to 355-fold and 500-fold respectively, as shown in Table 3.1).

3.3 Hyperpolarising lactate and lactate esters using SABRE-Relay

To date, sodium pyruvate-1-[^{13}C] is the most commonly reported agent used for HP imaging studies.[72, 75, 132-137, 139-141] The reasons for this are given in more detail in section 1.5. To summarise, upregulated conversion of pyruvate into products such as lactate by the enzyme lactate dehydrogenase (LDH) is often used as a hallmark of cancer[72, 75, 132-135, 137, 140, 141] or inflammation.[136, 139] In the first in-human study, doses of HP pyruvate were typically *c.a.* 1.5 mM[132] which is significantly higher than the pyruvate concentration in blood plasma (*c.a.* 0.06 mM).[179] In similar studies with mice, the injected doses are higher than physiological concentrations (*c.a.* 8 mM compared to 0.2 mM).[179] As the endogenous lactate pool is larger than the pyruvate pool (*c.a.* 4 mM lactate compared to 0.2 mM pyruvate in mouse plasma)[179] these large HP pyruvate doses are necessary to observe metabolism *in vivo*. It has been suggested that metabolic imaging using HP ^{13}C labelled lactate may be more beneficial as doses of physiological concentrations can then be administered.[179] This approach will allow the reverse metabolic conversion from lactate to pyruvate to be monitored, although the size of hyperpolarised ^{13}C label on the pyruvate product will be limited by the small size of the pyruvate pool. The hyperpolarisation of lactate-1-[^{13}C] and its use for *in vivo* metabolic studies in mice[179, 180] and rats[181] has been reported with polarisation transfer from ^{13}C to ^{1}H[180] and deuterium labelled lactate-1-[^{13}C][179] used to aid observation of metabolic conversion to pyruvate and other products.

Lactate, and pyruvate, both contain exchangeable OH groups in the form of an alcohol and carboxylic acid group respectively. Therefore, they may be amenable to hyperpolarisation using SABRE-Relay which could provide time and cost advantages to hyperpolarisation using DNP. The hyperpolarisation of lactates using SABRE-Relay is discussed in this section, while its application to pyruvate is discussed in section 3.4-3.5.

3.3.1 Hyperpolarisation of sodium lactate using SABRE-Relay

The application of SABRE-Relay to more complex OH-containing structures was discussed in section 3.2. A key factor limiting SABRE-Relay performance is the presence of contaminant water,[107] which in the case of some substrates is necessary to allow solubilisation in SABRE-Relay compatible solvents. Sodium lactate (**18**) is not soluble in dichloromethane-d_2 or chloroform-*d*. Therefore, **18** (5 eq.) in H$_2$O (10 μL) was added to a solution of **2** (5 mM) and **3** (5-10 eq.) preactivated with 3 bar H$_2$. Shaking for 10 seconds with 3 bar *p*-H$_2$ at 6.5 mT followed by insertion into the 9.4 T spectrometer yielded no discernible ^{1}H or ^{13}C NMR signal enhancements. This is consistent with the results presented for **10-14** in section 3.2.

3.3.2 Hyperpolarisation of lactate esters using SABRE-Relay

In recent years, PHIP-SAH has emerged as a route to hyperpolarise molecules using p-H$_2$ that do not contain unsaturated functionality.[70] This approach is discussed in Chapter 1 and has also been applied to lactate.[74] Lactate, which does not contain an unsaturated double bond that can be readily hydrogenated using p-H$_2$, can be functionalised as an ester that does contain such functionality. Upon hydrogenation of the modified lactate ester with p-H$_2$, lactate can be regenerated in a rapid hydrolysis step.[74] An approach of this type could be applied to produce lactate hyperpolarised using SABRE-Relay. For example, the lactate esters methyl lactate (**19**), ethyl lactate (**20**) and butyl lactate (**21**) all exist as liquids at room temperature and pressure. Therefore, they do not require solubilisation in H$_2$O and are expected to yield high NMR signal enhancements using SABRE-Relay. These lactate esters, the structures of which are shown in Figure 3.3, are in fact used in a wide range of applications. **19** and **20** are non toxic biodegradeable solvents and **20** has uses as a degreaser and as a food additive. **20** is also used in skin products to treat acne as hydrolysis into lactic acid and ethanol can alter skin pH.[182] Hydrolysis of SABRE-Relay hyperpolarised **19-21** could produce hyperpolarised **18** in a process similar in design to PHIP-SAH. In this case, a 'side arm' is added to change physical properties and enhance solubility, rather than to introduce a p-H$_2$ acceptor.
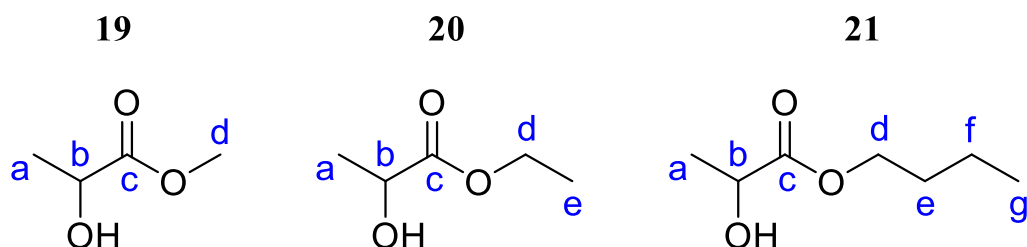
Figure 3.3: Substrates 19-21 investigated as SABRE-Relay hyperpolarisation targets.

Samples containing **2** (5 mM) and the highest performing carriers **3** (8-9 eq.) or **4-d_7** (5 eq.) in dichloromethane-d_2 (0.6 mL) were activated with 3 bar H$_2$ overnight before **19**, **20** or **21** (5 eq.) were added under an N$_2$ atmosphere before being shaken with 3 bar p-H$_2$ for 10 seconds at 6.5 mT. These conditions were chosen as they were found to give high NMR signal enhancements for simple alcohols (see Chapter 2) and similar conditions have been reported for related substrates.[104, 106-109] The ^{1}H and ^{13}C NMR signal enhancements for **19-21** achieved using these SABRE-Relay conditions are shown in Table 3.2.

Table 3.2: ^{1}H and ^{13}C NMR signal enhancements for 19-21 when each (5 eq.) is shaken with 3 bar p-H$_2$ for 10 seconds at 6.5 mT in a solution of 2 (5 mM) pre-activated with 3 (8-9 eq.) or 4-d_7 (5 eq.) in dichloromethane-d_2 (0.6 mL). Sites are labelled according to Figure 3.3. ^{1}H T_1 were measured thermally at 9.4 T using an inversion recovery sequence.

Substrate	Site	^{1}H T_1 /s	^{1}H NMR signal enhancement /fold		^{13}C NMR signal enhancement /fold	
		Carrier 3	Carrier 3	Carrier 4-d_7	Carrier 3	Carrier 4-d_7
19	a	5.9	30 ± 5	110 ± 10	1015 ± 30	530 ± 55
	b	24.4	55 ± 5	115 ± 10	445 ± 20	250 ± 20
	c	-	-	-	65 ± 10	30 ± 5
	d	11.4	15 ± 5	40 ± 5	0	0
20	a	5.0	15 ± 5	135 ± 5	575 ± 5	240 ± 5
	b	13.5*	15 ± 5*	90 ± 5*	380 ± 40	310 ± 20
	c	-	-	-	75 ± 10	45 ± 5
	d	13.5*	15 ± 5*	90 ± 5*	0	0
	e	8.1	2 ± 1	20 ± 5	0	0
21	a	4.1$^£$	25 ± 5	30 ± 5$^&$	195 ± 40	150 ± 5
	b	5.6$^%$	30 ± 5	35 ± 5	210 ± 50	330 ± 25
	c	-	-	-	40 ± 5	50 ± 5
	d	5.6$^%$	0	30 ± 5	0	0
	e	5.8	0	30 ± 5$^&$	0	0
	f	4.1$^£$	0	4 ± 1$^$$	0	0
	g	6.4	0	4 ± 1$^$$	0	0

* $^£$ $^%$ $^&$ $^$$ Values are averaged across the two sites due to signal overlap

The ^{13}C NMR signal enhancements for **19**-**21**, shown in Table 3.2, are generally higher when **3** is used as a carrier compared to **4-d_7**, however, when ^{1}H signal gains are compared, the maximum values are achieved using **4-d_7**. This suggests that polarisation transfer efficiency from the exchanging OH group to ^{13}C sites in the substrate is more efficient when **3** is used. This could be a result of more optimal OH-NH exchange or relaxation effects and is consistent with the results presented for simple alcohols in Chapter 2 in which **3** was the highest performing carrier, although for simple alcohols both ^{1}H and ^{13}C NMR signal gains were highest using **3**. This suggests that one set of optimal SABRE-Relay conditions may not exist for every substrate or nuclei of interest and that several 'good' conditions should be tested for each new substrate and used as a starting point for further optimisation of NMR signal gains. The sites with the highest ^{1}H or ^{13}C NMR signal enhancements were the CH$_3$ or CH groups of the lactate and little polarisation transfer across the ester group into the side arm was observed. Generally, the efficiency of relayed polarisation transfer to ^{1}H and ^{13}C sites using both **3** and **4-d_7** as carriers increases as the length of the side arm is decreased (**19**>**20**>**21**).

For utilisation of these enhanced MR signals it is important that the carbonyl group receives the largest amount of polarisation. This is because it is more isolated from other NMR active spins within the molecule and therefore it generally has the longest T_1 time which is of use in preserving magnetisation for *in vivo* injection or chemical transformation. Estimates of hyperpolarised ^{13}C magnetisation lifetimes of **19**-**21** measured at 9.4 T by leaving the hyperpolarised sample in the magnet for a varying time interval before recording a single scan ^{13}C NMR spectra are *c.a.* <5 s, ~20 s and ~50 s for the CH$_3$, CH and CO sites respectively. These compare well with values reported in the literature.[74] The SABRE NMR signal enhancements presented in Table 3.2 show that the majority of the attained ^{13}C polarisation resides on the more rapidly relaxing CH$_3$ and CH

groups and only modest (<100-fold) NMR signal enhancements can be achieved for the slowly relaxing CO site.

In PHIP-SAH, field cycling[70] or *r.f.* excitation[183, 184] are typically used to transfer polarisation from ^{1}H sites on the side arm to a ^{13}C labelled carbonyl resonance. These pulse sequences are usually based on INEPT (Insensitive Nuclei Enhanced by Polarisation Transfer)[1, 2] and similar approaches can be taken here to transfer SABRE-Relay derived ^{1}H polarisation to the ^{13}C carbonyl site. When simple alcohols are polarised (Chapter 2) use of a ^{1}H decoupled ^{1}H-^{13}C INEPT sequence did not yield improved levels of ^{13}C polarisation from exchanging OH groups to directly bound ^{13}C sites. However, in the case of **19-21**, the OH group and target CO site are now separated by three bonds and therefore the use of INEPT pulse sequences may be advantageous. The effect of a ^{1}H-^{13}C INEPT sequence following hyperpolarisation of **19**-**21** using SABRE-Relay was examined using the samples containing **4-d_7** discussed earlier. These sequences contain a variable delay time (τ) which is related to the ^{1}H-^{13}C J coupling constant ($\tau = 1/4J$).[2] The J coupling value between OH and CO sites in **19**-**21** is unknown and delay times of 2 ms and 25 ms are used to optimise magnetisation transfer from ^{1}H to ^{13}C through both short range (10 Hz) and long range (125 Hz) scalar couplings. These sequences were unable to improve signal gain on the carbonyl site of **19**, although CO polarisation of **20** and **21** could be increased from 45 ± 5-fold to 300 ± 45-fold and from 50 ± 5-fold to 370 ± 40-fold when INEPT transfer using a delay time of 2 ms was employed. In contrast, no improvements in ^{13}C NMR signal enhancements were achieved when INEPT transfer was performed using a delay time of 25 ms. However, an improvement in relative signal to noise was observed, as shown in Figure 3.4. These results suggest that polarisation transfer from OH to CO sites can occur through a short range coupling, despite the two sites not being closely located. This indicates that polarisation transfer between them is likely occurring *via* the ^{1}H CH site (route i of Figure 3.4a) or the directly bound carbon site (route ii of Figure 3.4a) rather than directly between the two (route iii of Figure 3.4a). This could be investigated further by using a wider range of delay times. Some example hyperpolarised ^{13}C and ^{1}H-^{13}C INEPT NMR spectra are shown in Figure 3.4.
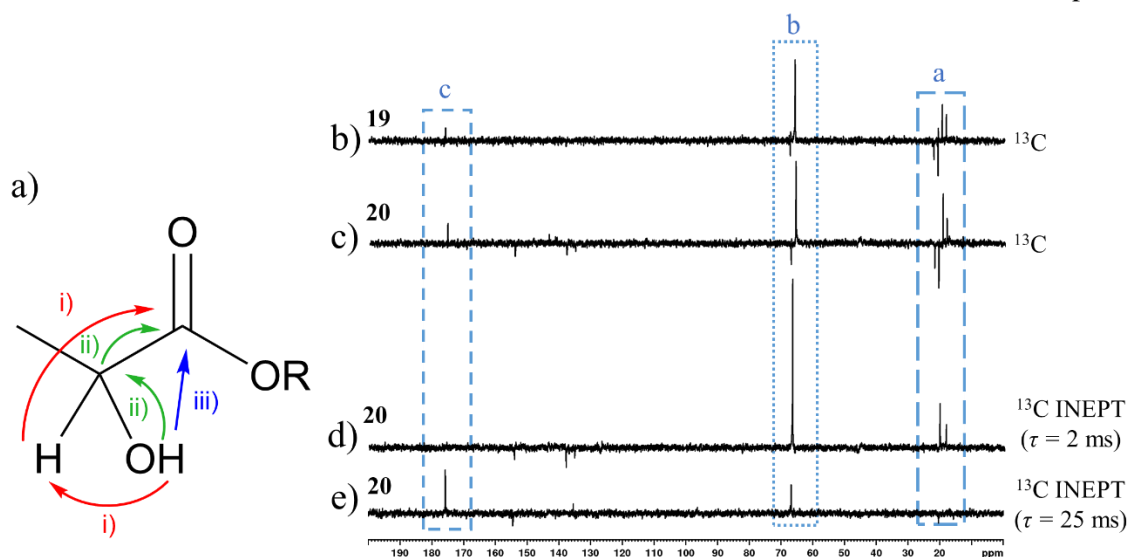
Figure 3.4: a) Possible polarisation transfer routes from OH to the carbonyl carbon involving i) indirect transfer *via* the ^{1}H CH site ii) indirect transfer *via* the directly bound ^{13}C site or iii) direct transfer *via* low field mixing. Hyperpolarised single scan b)-c) ^{13}C and d)-e) ^{13}C INEPT NMR spectra recorded with delay times (τ) of d) 2 ms and e) 25 ms when solutions of b) 19 or c)-e) 20 (5 eq.) are shaken with 3 bar p-H$_2$ for 10 seconds at 6.5 mT in a solution of 2 (5 mM) pre-activated with b) 3 (8-9 eq.) or c)-e) 4-d_7 (5 eq.) in dichloromethane-d_2 (0.6 mL) Resonances are labelled according to those shown in Figure 3.3.

The efficiency of INEPT transfer depends on many factors including the rate of proton exchange, relaxation rates and scalar coupling within the aliphatic framework of the substrate. For example, rapid OH exchange is likely to scramble the *J* coupling value between OH and other sites within the substrate which is likely to limit the efficiency of INEPT transfer. A range of different INEPT sequences with optimised delay times to transfer polarisation from ^{1}H sites to ^{13}C sites (or other X nuclei) have been developed[185] which could be used to achieve more significant levels of relayed heteronuclear polarisation. Further investigation of the mechanism of polarisation transfer and identification of which *J* coupling values are most important will benefit further development of this technique.

3.3.3 Feasibility of producing hyperpolarised lactate from hydrolysis of lactate esters

The production of lactate from lactate esters can be achieved by rapid hydrolysis with NaOH (1 M) followed by HCl (1 M) in D$_2$O at 363 K.[70, 73] As sodium lactate, **18**, could not be hyperpolarised using SABRE-Relay, hydrolysis of the lactate esters **19-21** hyperpolarised using SABRE-Relay could be a route to producing hyperpolarised **18**. Experiments were performed that involved the addition of NaOH (1 M) followed by HCl (1 M) in D$_2$O at 363 K to solutions of **19-21** hyperpolarised using SABRE-Relay. This was achieved by shaking the solutions described earlier with p-H$_2$ for 10 seconds at 6.5 mT at room temperature before placing the NMR tube into a thermostatically controlled water bath at 363 K at Earth's field, removing the lid, and injecting NaOH followed by HCl in D$_2$O (0.6 mL, final concentrations of 1 M). The sample was then shaken for ~2 seconds to ensure mixing before being placed back into the water bath to

allow phase separation. The aqueous layer was removed *via* plastic syringe and injected into a separate NMR tube for interrogation by a single scan ^{13}C NMR spectrum. These experiments revealed no hyperpolarised ^{13}C NMR signals for any species. This is attributed to the long times (~90 s) required to perform these manual hydrolysis and separation steps. This is compounded by the fact that the starting polarisation levels here are much lower than those achieved using techniques such as PHIP-SAH that use a similar procedure (~1% initial SABRE-Relay ^{13}C polarisation compared to 5% PHIP-SAH polarisation after hydrolysis and separation).[73] Additionally, the majority of ^{13}C polarisation in **19-21** resides on aliphatic ^{13}C sites which contain T_1 values significantly shorter than the time required for the hydrolysis step. This suggests that to produce SABRE-Relay hyperpolarised lactate *via* hydrolysis of **19-21** will firstly require further optimisation of their ^{13}C NMR signal gains with emphasis on optimising polarisation transfer from OH to the CO group. This can be achieved by modification of the delay time in [1]H-^{13}C INEPT sequences to achieve both optimal NMR signal enhancement, and maximum signal to noise. Other approaches such as field cycling[70] or high field *r.f.* transfer[156] could also be used. Once significant polarisation levels for the CO groups of **19-21** can be achieved, optimised hydrolysis conditions with shorter transfer times may yield SABRE-Relay hyperpolarised **18** in the future.

3.4 Hyperpolarising pyruvate using SABRE-Relay

Sodium pyruvate (**22**) contains exchangeable protons and may also become hyperpolarised *via* relayed proton exchange effects. Pyruvic acid is an α-ketoacid that contains both ketone and carboxylic acid functionalities; its carboxylic acid proton (pK$_a$ of 2.5) is readily lost at physiological pH to form the pyruvate anion in which the negative charge is delocalised around both oxygen's of the carboxylate group.[186, 187] Enol pyruvate can also form as a result of keto-enol tautomerisation and is stabilised by conjugation between adjacent enol and carboxyl groups.[187] This tautomerisation is important in biology as the enolisation of glycerate-2-phosphate to form phosphoenolpyruvate is a key step in the formation of pyruvate in glycolysis,[138] although no enol forms of pyruvate have been assigned throughout this thesis. The C_2 core of pyruvate is electron deficient due to bonding of both carbon atoms to electronegative oxygen's and therefore these carbons can be the site of nucleophilic attack. The keto carbon, often labelled as position 2, of pyruvate is the most susceptible to reaction with nucleophiles as it is the most electron deficient.[186, 187] The carboxylate carbon is less susceptible to reaction with nucleophiles due to the presence of the delocalised negative charge. Water in solution can act as a nucleophile and can form pyruvate hydrate following reaction at the more electron deficient keto carbon, as shown in Figure 3.5a.[186, 187] These effects are illustrated when a ^{13}C NMR spectrum of a solution of **22-1,2-[[13]C$_2$]** (150 mM) dissolved in dichloromethane-d_2 (0.6 mL) and 40 μL H$_2$O is collected (shown in Figure 3.5b). ^{13}C NMR resonances are observed at δ 169.7 and 205.2 ($^1J_{CC}$ = 62 Hz) and δ 94.1 and 178.8 ($^1J_{CC}$ = 64 Hz) which arise from pyruvate and pyruvate hydrate (**23**) respectively.
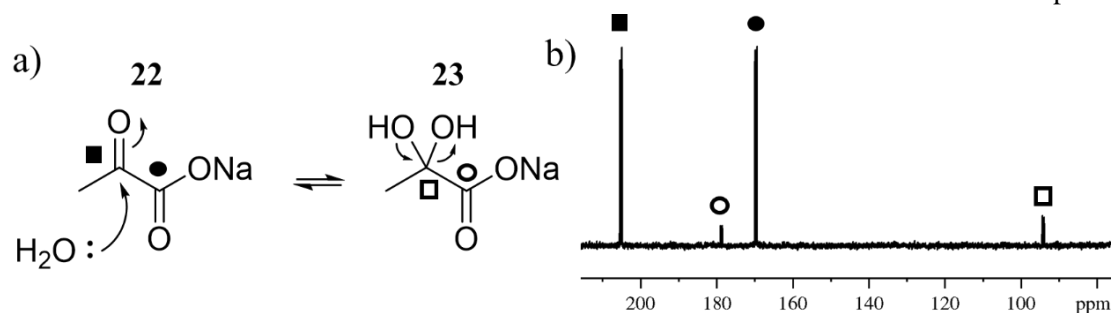
Figure 3.5: a) In aqueous media an equilibrium exists between pyruvate and its hydrated form b) A ^{13}C NMR spectrum of 22-1,2-[^{13}C$_2$] (150 mM) dissolved in dichloromethane-d_2 (0.6 mL) and H$_2$O (40 μL) shows resonances of pyruvate and its hydrated counterpart.

3.4.1 Reaction between pyruvate and amines

α-Keto acids such as pyruvate exhibit interesting chemical reactivity as they can react with a range of nucleophiles at the 2 position (in addition to water). α-Keto acids can also be functionalised as esters and can become decarboxylated by reaction with reagents such as H$_2$O$_2$[188] (this is explored in more detail in Chapter 6). Amines are commonly employed as polarisation carriers in SABRE-Relay and they are also known to act as nucleophiles.[104, 106, 107, 109] As nitrogen atoms hold their electron lone pairs more distantly from the nucleus, they are more readily donated to electrophiles than oxygen-based nucleophiles such as water. Therefore, reaction of pyruvate with amines is possible and is well known to occur in biological systems.[189, 190] These effects are confirmed by recording a ^{13}C NMR spectrum after the addition of benzylamine (**4**) to an aqueous solution of **22-1,2-[^{13}C$_2$]**. ^{13}C NMR resonances for **22** and **23** are observed in addition to signals at δ 73.7 and 182.4 ($^1J_{CC}$ = 55 Hz) and δ 169.0 and 203.4 ($^1J_{CC}$ = 62 Hz) (as shown in Figure 3.6) for the hemiaminal intermediate (**24**) and imine product (**25**) respectively.
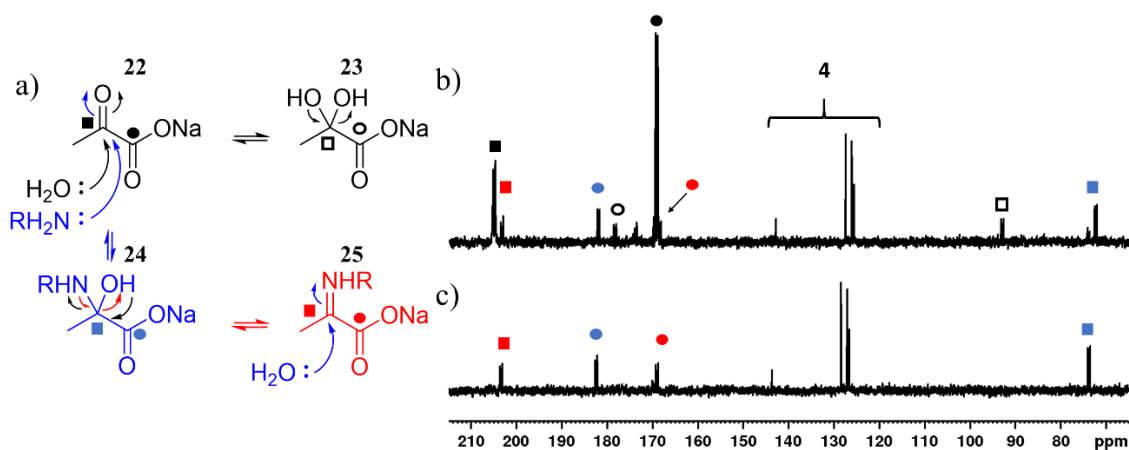
Figure 3.6: a) Summarised scheme to show the reaction between pyruvate and amine to form an equilibrium mixture containing pyruvate, pyruvate hydrate, hemiaminal, and imine. Note that proton transfer steps are not shown. b)-c) ^{13}C NMR spectrum b) 15 minutes and c) 6 hours after the addition of equimolar 4 to 22-1,2-[^{13}C$_2$] (150 mM) in dichloromethane-d_2 (0.6 mL) and H$_2$O (40 μL).

3.4.2 Reaction of pyruvate with [Ir(H)$_2$(IMes)(amine)$_3$]Cl

The activation of **2** (5 mM) with the amines benzylamine (**4**) or phenethylamine (**5**) (5-20 eq.) and H$_2$ gas (3 bar) in dichloromethane-d_2 (0.6 mL) overnight yields a single hydride resonance at δ −23.7 or −24.1 respectively for the complexes [Ir(H)$_2$(IMes)(benzylamine)$_3$]Cl (**26**) or [Ir(H)$_2$(IMes)(phenethylamine)$_3$]Cl (**27**) respectively. These complexes have been previously reported in the literature and have been used as SABRE polarisation transfer catalysts to produce strongly enhanced NMR signals for **4** or **5** free in solution.[104, 106] At this point, **22-1-[^{13}C$_2$]** (5 eq.) in H$_2$O (40 μL) is added to these solutions under a flow of N$_2$ gas and p-H$_2$ (3 bar) is added. When shaken with fresh p-H$_2$ for 10 seconds at 6.5 mT, hyperpolarised ^{13}C NMR signals at δ 169.5, 170.2, and 178.7 are observed which correlate to the organic species **24**, **22** and **25** respectively, as shown in Figure 3.7. At this time point the pyruvate ^{13}C NMR signal is enhanced by a factor of <10-fold. Upon shaking with fresh p-H$_2$, these hyperpolarised ^{13}C NMR signals are still visible, although they decrease in intensity upon successive p-H$_2$ shaking, as shown in Figure 3.7a. Eventually, these hyperpolarised signals are no longer visible upon fresh p-H$_2$ shaking and are eventually replaced by a new hyperpolarised ^{13}C resonance at δ 174.6 over a timescale of several minutes.
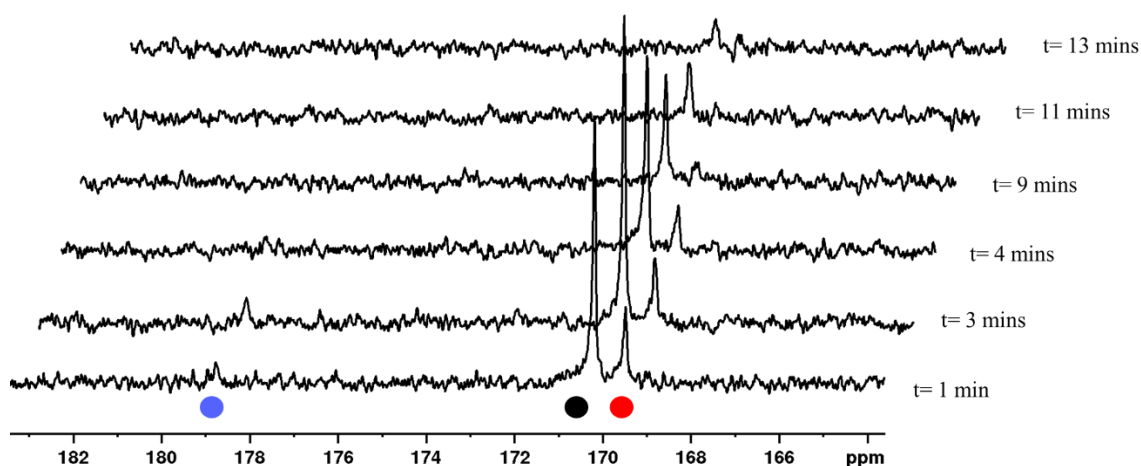
Figure 3.7: An example series of partial single scan hyperpolarised ^{13}C NMR spectra recorded when 22-1-[^{13}C] (5 eq.) in H$_2$O (40 μL) is shaken with 3 bar p-H$_2$ for 10 seconds at 6.5 mT at the indicated time intervals after addition to a solution of 2 (5 mM) and 4 (10 eq.) in dichloromethane-d_2 (0.6 mL) activated with 3 bar H$_2$ overnight.

When the reaction between **26** or **27** and **22-1-[^{13}C]** is monitored using ^{1}H NMR spectroscopy, the intensity of the hydride signal of **26** or **27** decreases upon the addition of **22-1-[^{13}C$_2$]**. Two sets of new hydride resonances appear at δ −21.9 and −27.6 ($^2J_{HH}$ = 9.5 Hz) and δ −24.0 and −27.4 ($^2J_{HH}$ = 8.0 Hz) following addition of **22-1-[^{13}C]** to **26**. Similarly, signals at δ −21.6, −28.0 and δ −23.9, −27.8 form when **22-1-[^{13}C]** is added to **27**. The identity of these species was confirmed by using 2D NMR characterisation at 245 K. They were found to be of the form [Ir(H)$_2$(κ^2-OOCC(CH$_3$)NR)(IMes)(NH$_2$R)] where R = CH$_2$Ph (**28**) and R = (CH$_2$)$_2$Ph (**29**) and are formed following addition of **22** to **26** or **27** respectively, as summarised in Figure 3.8. Two

isomers of **28** or **29** are formed depending on the geometry of the coordinated imine which can be in the same plane as the hydride ligands (denoted **28A** and **29A**) or in a plane perpendicular to the hydride ligands (to give **28B** and **29B**). Structural confirmation by 2D NMR was aided by using **22-1,2-[^{13}C$_2$]** and **4-[^{15}N]**. For example, a connection was observed in a ^{15}N-^{1}H HMQC experiment between the hydride signal of **28A** at δ −21.9 and a ^{15}N signal at δ 276.9 due to a *trans* ^{1}H-^{15}N coupling of 20.7 Hz between the hydride and the bound imine. An additional ^{15}N signal for bound amine was recorded at δ −2.7 which is located *trans* to the carbene ligand from NOE measurements. Identification of the imine ligand in the same plane as the hydrides was confirmed from NOE interactions between the CH$_3$ groups of the carbene ligand and imine. NMR resonances for **28** and **29** are given in the experimental section 7.4.1-2 (Tables 7.1-7.2 and 7.3-7.4 respectively).

Complexes **28** and **29** are formed from the coordination of the *a*-carboxyimine that forms from the *in situ* reaction of pyruvate and amine. It is likely that **28** and **29** are formed from condensation between pyruvate and the excess of free amine, followed by displacement of amine by the formed imine resulting in **28** and **29**. This process could also be facilitated by the presence of the transition metal catalyst as it has been reported to be catalysed by a cobalt (III) centre containing coordinated pyruvate and amine ligand.v[191] In this reported example, ligation of both pyruvate and amine to the metal centre promotes nucleophilic attack of the amine to ligated pyruvate as the latter is made more electron deficient by coordination to the metal. The carboxyimine complexes **28** and **29** would result from an analogous process in this system. While it is possible that **28** and **29** are formed directly from a metal catalysed reaction of **26** or **27** with **22**, intermediates containing ligated pyruvate are not observed in thermal or hyperpolarised NMR measurements and the reaction between pyruvate and amine occurs in the absence of metal catalyst (section 3.4.1).
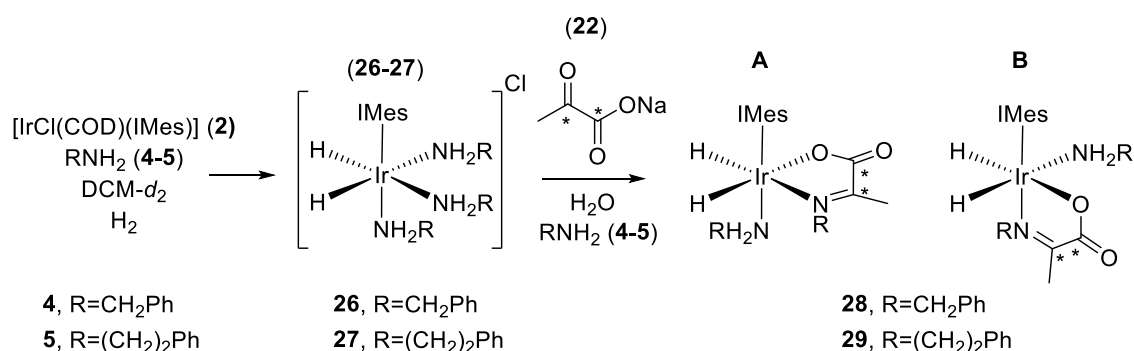
Figure 3.8: 2 (5 mM) reacts with the amines 4 or 5 (5-20 eq.) and H$_2$ (3 bar) in dichlromethane-d_2 (0.6 mL) to produce 26 or 27 respectively. Upon the addition of 22-1-[^{13}C] in H$_2$O (40 μL), iridium *a*-carboxyimine complexes 28 and 29 are formed from the *in situ* condensation of pyrvuate and amine.

Complexes **28A** and **28B** were found to exist in a 30:1 ratio one hour after addition of **22** to **26** at 298 K, although after 7 hours at 298 K an equilibrium ratio of 2:1 confirms that **28A** is the thermodynamically more stable product. In contrast, **29A** and **29B** form in an 11:1 ratio one hour after addition of **22** to **27** at 298 K which changes to a 1:2 ratio after the solution is left for 7 hours

at 298 K. This suggests that **29B** is now the thermodynamically favoured product. The formation of similar ruthenium, cobalt, nickel, copper and zinc β-ketoimine complexes has been reported[192-194] and a similar ruthenium α-carboxyimine chelate has also been reported.[191] The formation of **28** and **29** effectively deactivates **26** and **27** such that pyruvate polarisation cannot be observed at longer reaction times. The hyperpolarised ^{13}C NMR signal at δ 174.6 observed at longer reaction times correlates with **28B** and **29B** and is discussed further in Chapter 4. The *in situ* condensation reaction that occurs between pyruvate and the amine carriers used in SABRE-Relay to form **28** and **29** may limit the NMR signal enhancements that can be attained due to catalyst deactivation. Nevertheless, the behaviour and hyperpolarisation of **28** and **29** is explored further in Chapter 4.

3.4.3 Formation of iridium carbonate complexes from 28 and 29.

Further reaction products following addition of **22** to **26** and **27** can be observed when the H_2 atmosphere of solutions containing **26** or **27** is replaced by N_2 or air. In these cases the slow precipitation of single crystals occurs which were analysed by Dr. Adrian C. Whitwood using single crystal X ray diffraction.[195] This revealed these crystals are $[Ir(IMes)(\eta^2\text{-}CO_3)(\kappa^2\text{-}OOCC(CH_3)NR)(NH_2R)]$ which contain a bound carbonate ligand where R = CH_2Ph (**30**) and R = $(CH_2)_2Ph$ (**31**), the structures of which are shown in Figure 3.9. Only one isomer of **30** and **31** is observed in the crystalline state, despite **28** and **29** existing as two regioisomers. IR spectroscopy of **31** shows vibrational bands for $\nu_{(OCO)}$ at 1584 and 1486 cm^{-1} which are consistent with other iridium and osmium $\eta^2\text{-}CO_3^{2-}$ complexes (with reported $\nu_{(OCO)}$ values at 1580, 1482 cm^{-1} and 1575, 1496 cm^{-1} respectively).[196, 197] When **28** is synthesized from **22-1-[^{13}C]**, and the resulting crystals of **31** analysed using ^{13}C NMR spectroscopy, a signal for the bound $^{13}CO_3^{2-}$ ligand at δ 172 was observed. This suggests that the η^2-bound carbonate ligands of **30** and **31** are derived from pyruvate. This transformation is perhaps unsurprising considering that metal pyruvate complexes have been reported to thermally degrade to give metal carbonates at high temperatures.[198] Other iridium complexes containing η^2-bound carbonate ligands have been reported.[199] The formation of **30** and **31** is expected to occur over long timescale (>weeks) as solutions of **28** and **29** are stable under H_2 over this timescale. Therefore, **30** and **31** are likely to constitute minor decomposition products that crystalize out of solution.
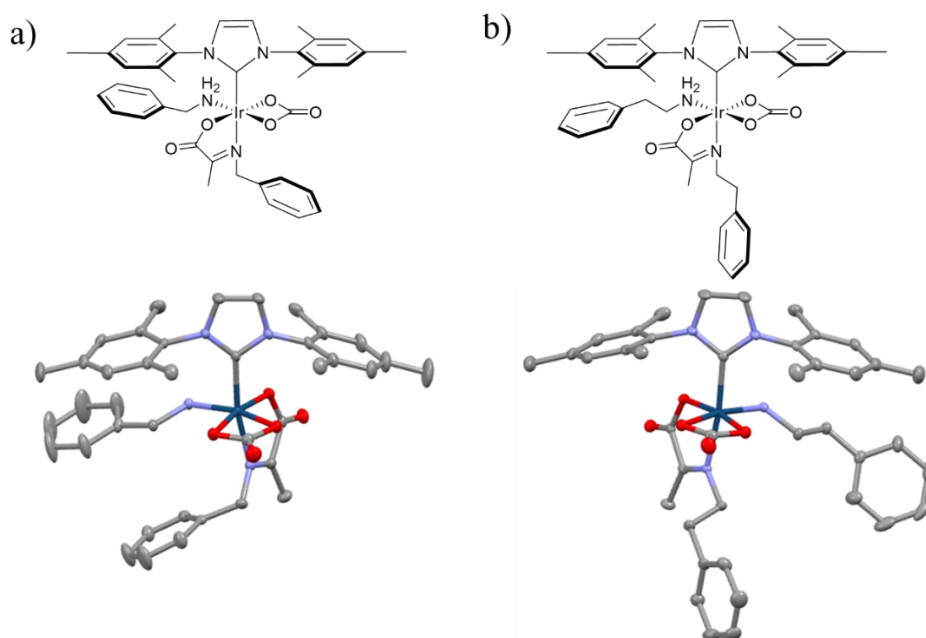
Figure 3.9: Structures of 30 and 31 determined from X ray crystallography. Note that any solvent of crystallisation and all hydrogen atoms have been omitted for clarity. X ray diffraction data were collected and solved by Dr. Adrian C. Whitwood.[195]

3.5 Optimisation of pyruvate hyperpolarisation using SABRE-Relay

The pyruvate ^{13}C NMR signal enhancements achieved using SABRE-Relay (ε_{max}) should be as high as possible. The *in situ* condensation reaction that occurs between pyruvate and the amine carriers used in SABRE-Relay may limit the NMR signal enhancements that can be attained. Despite this, SABRE-Relay might be an appropriate method to hyperpolarise pyruvate if ε_{max} can be increased and the rate of catalyst deactivation slowed to occur on timescales longer than those required for hyperpolarisation. The parameter ι_{80} is introduced to describe the % drop in hyperpolarised pyruvate ^{13}C NMR signal enhancement after fresh p-H_2 shaking 80 seconds after addition of pyruvate. ι_{80} will depend on the rate of reaction between pyruvate and amine, and the rate of formation of the iridium carboxyimine product. ι_{80} can therefore be used to compare different conditions and should be as low as possible to allow refreshable hyperpolarisation of pyruvate using SABRE-Relay. Several factors such as the identity and concentration of the carrier amine, water quantity, and iridium precatalyst are changed to optimise both ε_{max} and reduce catalyst deactivation.

3.5.1 Optimisation of pyruvate ^{13}C NMR signal enhancement by variation of water content

The presence of water is essential to solubilise pyruvate in the SABRE-Relay compatible solvent of dichloromethane-d_2 (0.6 mL). Water quantity is expected to influence SABRE-relay performance, and from previous experiments involving alcohol substrates (section 2.4) and more complex molecules (section 3.2) it might be expected that the maximum pyruvate ^{13}C NMR

signal enhancement (ε_{max}) will decrease at high water concentrations. Water is also expected to influence the % drop in hyperpolarised pyruvate ^{13}C NMR signal after fresh p-H$_2$ shaking 80 seconds after addition of pyruvate (ι_{80}) as the mechanism of imine formation, shown in Figure 3.6a, predicts that high water concentrations favour formation of pyruvate. This was tested by addition of **22-1-[^{13}C]** (5 eq.) in a variable amount of H$_2$O to preactivated solutions of **27** in dichloromethane-d_2 (0.6 mL) followed by p-H$_2$ shaking at 6.5 mT for 10 seconds. Values of ε_{max} and ι_{80} at different H$_2$O concentrations are shown in Table 3.3.

Table 3.3: Values of ε_{max}, and ι_{80} when 22-1-[^{13}C] (5 eq.) dissolved in the indicated amount of H$_2$O is added to preactivated 27 in dichloromethane-d_2 (0.6 mL) and shaken with 3 bar p-H$_2$ for 10 seconds at 6.5 mT. These are one shot experiments with errors taken from typical values using alcohol substrates (Chapter 2) for which repeat measurements with consistent ε_{max} values could be achieved.

H$_2$O volume/ μL	ε_{max} /fold	ι_{80} /%
5	12 ± 2	36
10	9 ± 2	25
20	17 ± 3	30
40	7 ± 2	16

When pyruvate is solubilised in 5 μL H$_2$O, the ι_{80} value is 36% which decreases to 16% as the volume of water is increased to 40 μL. This change suggests that at higher water concentrations the equilibrium position between pyruvate and imine is pushed towards pyruvate. This leads to slower rates of catalyst deactivation and smaller hyperpolarised signals of the imine product. Despite these changes, ε_{max} appears comparable at different water concentrations and therefore, 40 μL volumes of H$_2$O are used to maximise the time window over which hyperpolarised pyruvate signals are visible.

3.5.2 Optimisation of pyruvate ^{13}C NMR signal enhancement by variation of amine identity and concentration

The identity of the carrier amine is expected to have a large effect on ε_{max}. It has been shown in Chapter 2 how the efficiency of polarisation transfer from p-H$_2$ to the carrier amine *via* polarisation transfer catalysts of the form [Ir(H)$_2$(IMes)(amine)$_3$]Cl can be the most important step in determining the efficiency of relayed polarisation transfer to alcohols. Additionally, the identity and concentration of amine is expected to influence the equilibrium position between pyruvate and imine and the rate of catalyst deactivation. Therefore, a range of different amines were tested by activating them (5-20 eq.) with **2** (5 mM) and 3 bar H$_2$ in dichloromethane-d_2 (0.6 mL) overnight to form [Ir(H)$_2$(IMes)(amine)$_3$]Cl.[104, 106] Subsequently, **22-1-[^{13}C]** (5 eq.) in H$_2$O (40 μL) was added and shaken with 3 bar p-H$_2$ for 10 seconds at 6.5 mT and values of ε_{max} and ι_{80} were determined. These values using the carrier amines phenylethylamine (**4**), benzylamine (**5**), phenylpropylamine (**32**), phenoxyethylamine (**33**) and aniline (**34**) are shown in Table 3.4.

Table 3.4: Values of ε_{max} and ι_{80} when 22-1-[^{13}C] (5 eq.) dissolved in H$_2$O (40 μL) is added to preactivated solutions of 2 (5 mM) and the indicated amine in dichloromethane-d_2 (0.6 mL) and shaken with 3 bar p-H$_2$ for 10 seconds at 6.5 mT. These are one shot experiments with errors taken from typical values using alcohol substrates (Chapter 2) for which repeat measurements with consistent ε_{max} values could be achieved.

Entry	Amine	Amount (eq. relative to Ir)	ε_{max} /fold	ι_{80} /%
1	Benzylamine (**4**)	5.0	5 ± 1	2
2	Benzylamine (**4**)	10.0	5 ± 1	10
3	Benzylamine (**4**)	20.0	5 ± 1	25
4	Benzylamine-d_7 (**4-d_7**)	5.0	22 ± 5	3
5	Benzylamine-d_7 (**4-d_7**)	10.0	48 ± 5	7
6	Benzylamine-d_7 (**4-d_7**)	20.0	36 ± 5	43
7	Phenethylamine (**5**)	3.5	14 ± 2	3
8	Phenethylamine (**5**)	5.0	7 ± 2	4
9	Phenethylamine (**5**)	7.5	13 ± 2	10
10	Phenethylamine (**5**)	10.0	7 ± 2	16
11	Phenethylamine (**5**)	12.5	11 ± 2	10
12	Phenethylamine (**5**)	20.0	3 ± 1	45
13	Phenylpropylamine (**32**)	10.0	9 ± 1	24
14	Phenoxyethylamine (**33**)	5.0	13 ± 2	2
15	Phenoxyethylamine (**33**)	10.0	14 ± 2	4
16	Aniline (**34**)	10.0	4 ± 1	1
17	Aniline-d_5 (**34-d_5**)	10.0	7 ± 1	3

The data shown in Table 3.4 suggests that the decay of hyperpolarised pyruvate signal is generally slower when lower concentrations of amine are used. For example, as the concentration of the carrier amine **5** is increased from 3.5-20 equivalents relative to the iridium catalyst, ι_{80} increases from 3% to 45% (entry 7 compared to entry 12 of Table 3.4). Similar increases in ι_{80} are observed upon increases in the concentrations of carriers **4**, **4-d_7**, and **33** which likely indicates that as amine concentration is increased deactivation of the system to form products analogous to **28** and **29** is more rapid. Trends in ε_{max} are more challenging to rationalise as additional factors such as amine polarisation, relaxation of the active catalyst, and efficiency of proton exchange will all influence SABRE-Relay performance.

When comparing ε_{max} and ι_{80} values for samples containing the same amounts (10 eq.) of the amines **4**, **5**, and **32**, an increase of ι_{80} from 10%, to 16% and 24% for **4**, **5** and **32** respectively (entries 2, 10 and 13 of Table 3.4) is observed as the length of the aliphatic chain between the amine and phenyl groups of the carrier are increased. This change is indicative of a faster rate of condensation reaction as the nucleophilicity of the amine group increases as the nitrogen lone pair becomes more localised. The faster rate of catalyst deactivation is confirmed from appearance of hyperpolarised ^{13}C NMR signals of the deactivated imine complex at shorter reaction times when more reactive amines are used, as shown in Figure 3.10. For example, when comparing the amines **4**, **5**, and **32**, hyperpolarised ^{13}C NMR signals of the imine complex formed using the more nucleophilic **5** and **32** are observed 10 minutes after pyruvate addition compared to 100 minutes using **4**.

This is supported by a low ι_{80} of just 1% when the less nucleophilic **34** is used (entry 16 of Table 3.4) in which the nitrogen lone pair is delocalised around the aromatic ring. In this case a reduced donor power of the amine reduces the ability to form magnetisation transfer catalysts of the form [Ir(H)$_2$(IMes)(Aniline)$_3$]Cl.[106] Therefore, in cases where aniline is used as a carrier an

acetonitrile coligand is also added to form stable SABRE active catalysts.[101, 106] This is a common strategy in SABRE[155] and further work could optimise the identity and amount of coligand used. The disadvantage of this approach is that the finite amount of p-H$_2$ derived polarisation can be wasted by unwanted transfer into the coligand. This is supported by the slightly lower ε_{max} value achieved using **34** compared to using **4**, **5**, and **32** (4-fold compared to 5, 7, and 9-fold respectively).
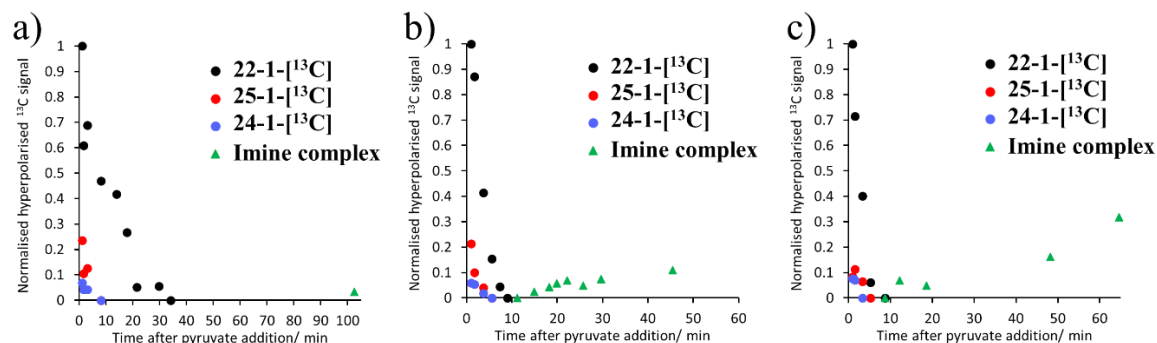
Figure 3.10: Time courses of the change in hyperpolarised ^{13}C NMR signals that occur following addition of 22-1-[^{13}C] (5 eq.) in H$_2$O (40 μL) to preactivated solutions containing 2 (5 mM) and a) 4 b) 5 and c) 32 (10 eq.) in dichloromethane-d_2 (0.6 mL). Each data point is a separate measurement involving shaking with fresh p-H$_2$ (3 bar) for 10 seconds at 6.5 mT.

For most efficient SABRE-Relay transfer to pyruvate, polarisation should be concentrated exclusively on the NH$_2$ group of the carrier. Any transfer to other sites in the carrier molecule could be a significant source of wasted polarisation. This can be prevented by deuterating ^{1}H sites of the carrier. Labelling approaches of this type have been used to optimise NMR signal gains of target molecules using SABRE as it reduces the number of ^{1}H receptor sites that polarisation can be transferred to and it increases the lifetime (T_1) of hyperpolarised signals.[97, 102, 110, 111] It is expected that deuteration of proton sites or physically separating the amine from the CH carrier framework *via* a spacer atom/group could localise polarisation on the exchanging NH$_2$. Two amines were employed to illustrate these effects: phenethyoxyamine (**33**), which is analogous to **5** but contains an oxygen spacer between the phenyl ring and ethylamine group, and **4-d_7**. The presence of the oxygen spacer in **33** increases ε_{max} by roughly a factor of two (from 7-fold to 14-fold, entries 10 and 15 of Table 3.4 respectively). Deuteration of the carrier amine is able to increase ε_{max} by up to a factor of ten (from 5-fold to 48-fold when 10 eq. carrier is used, entries 2 and 5 of Table 3.4 respectively). Therefore, deuteration of the carrier appears the most appropriate approach to localise polarisation on the carrier NH site and optimise pyruvate NMR signal enhancements. While **33** prevents polarisation leakage into the phenyl ring, magnetisation can still spread from the amine into the CH resonances of the ethyl group explaining the smaller increase in ε_{max} when **33** is used compared to **4-d_7**. The carrier **4-d_7** (5 eq.) is used for future studies as this yielded the highest ε_{max} with the lower amounts giving a slower rate of catalyst decomposition (ι_{80}). Therefore, conditions are selected to balance the need for a high ε_{max} with a low ι_{80}

3.5.3 Optimisation of pyruvate ^{13}C NMR signal enhancement by variation of iridium precatalyst

The identity of the magnetisation transfer catalyst plays a crucial role in facilitating polarisation transfer from p-H$_2$ derived hydride ligands to the carrier molecule,[48, 104, 106, 107, 109] which will determine the finite amount of polarisation available for relayed transfer to pyruvate. The identity of the carbene ligand is highly important and its modification has been used to tune the exchange rate and consequently the NMR signal enhancement of a particular substrate.[96, 97, 200] Alteration of this ligand can also influence relaxation of the ligated substrate and catalyst solubility.[100] Similar effects may play a role when optimising pyruvate ^{13}C NMR signal enhancements using SABRE-Relay. Therefore, a series of different iridium precursors synthesised by Dr. Victoria Annis and Dr. Peter J. Rayner, the structures of which are shown in Figure 3.11, were used to hyperpolarise pyruvate by SABRE-Relay,
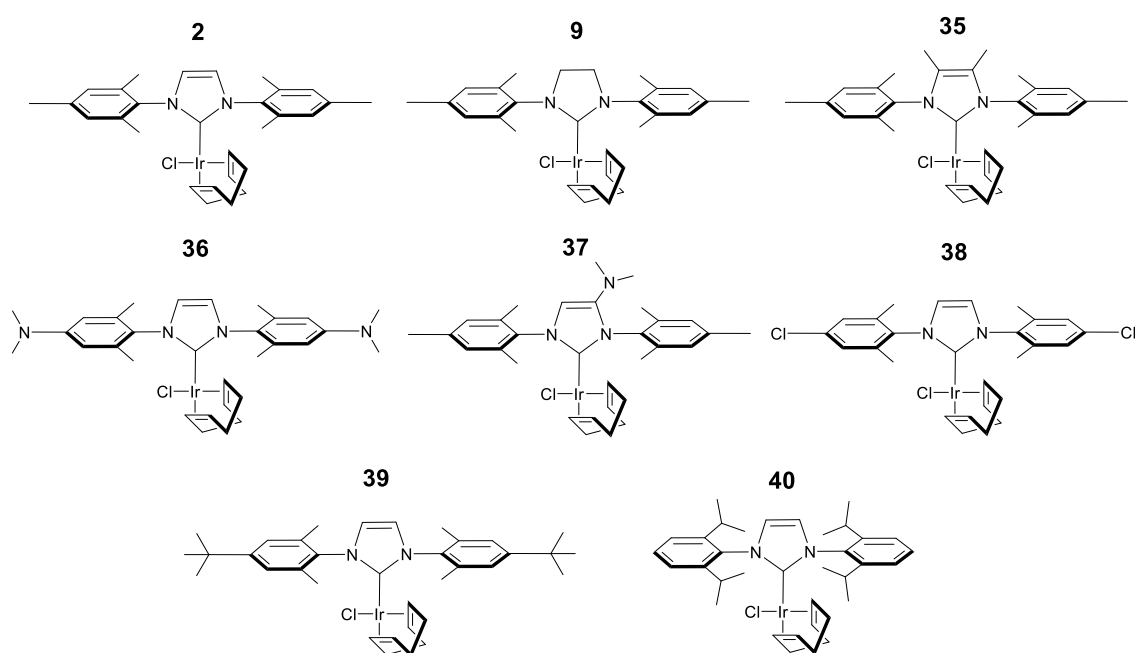
Figure 3.11: Structures of the precatalysts, synthesised by Dr. Victoria Annis and Dr. Peter J. Rayner, used in this work.

These precatalysts were tested by activating each (5 mM) with **4-d_7** (5 eq.) and 3 bar H$_2$ in dichloromethane-d_2 (0.6 mL) before addition of **22-1-[^{13}C]** (5 eq.) in H$_2$O (40 μL) and 10 second p-H$_2$ shaking at 6.5 mT. Values of ε_{max} and ι_{80} for these precatalysts are shown in Table 3.5.

Table 3.5: Values of ε_{max} and ι_{80} when 22-1-[^{13}C] (5 eq.) dissolved in H_2O (40 μL) is added to preactivated solutions of the indicated precatalyst (5 mM) and 4-d_7 (5 eq.) in dichloromethane-d_2 (0.6 mL) and shaken with 3 bar p-H_2 for 10 seconds at 6.5 mT. These are one shot experiments with errors taken from typical values using alcohol substrates (Chapter 2) for which repeat measurements with consistent ε_{max} values could be achieved. Values of buried volume[159, 200, 201] and Tolman electronic parameter[200] are taken from the literature.

Precatalyst	ε_{max} /fold	ι_{80} /%	Buried volume /%	Tolman electronic parameter /cm^{-1}
2	5 ± 1	2	31.6	2049.5
9	33 ± 4	7	32.7	2051.5*
35	55 ± 5	9	31.4	2047.2
36	55 ± 5	9	31.6	2047.6
37	50 ± 5	5	32.6	2048.8
38	20 ± 3	8	31.7	2051.7
39	65 ± 7	5	31.7	2049.6
40	27 ± 4	10	32.6	2050.1

*Value taken from Kelly et al.[202] and may not be comparable to those taken from Rayner et al.[200]

The identity of the carbene ligand has an effect on ε_{max} and ι_{80}, as shown in Table 3.5. Differences in ι_{80} as a function of precatalyst may be indicative of a metal catalysed condensation reaction. Alternatively, these variations could also simply relate to different rates of catalyst deactivation which is expected to be a bimolecular process involving metal catalyst and imine free in solution. The largest ε_{max} is achieved using **39** (65-fold) which contains sterically bulky tertiary butyl groups on the carbene ligand. Despite this, other sterically large precatalysts with large % buried volumes (such as **37** and **40**) are not able to achieve such high ε_{max}. It is therefore expected that ε_{max} is dependent not only on steric factors but also electronic effects of the carbene ligand. However, no clear trend between either ε_{max} or ι_{80} and the steric or electronic properties of the precatalyst (Table 3.5) are discernible. Additional factors such as relaxation within the active catalyst, and the rate of catalyst deactivation will also play a role. Therefore, developing a rational to achieve high ε_{max} through synthetic catalyst design is challenging. This is consistent with other literature reports which show that selection of an optimal catalyst based only on a steric or electronic parameter is extremely challenging.[200] Nevertheless, it has been shown that variation of the catalyst can increase ε_{max} by more than a factor of ten (from 5-fold for **2** to 65-fold for **39**).

3.6 Conclusions

This chapter has extended SABRE-Relay from the hyperpolarisation of simple alcohols (as presented in Chapter 2) to a wider range of more complex OH-containing molecules. SABRE-Relay can achieve ^{1}H and ^{13}C NMR signal enhancements of up to 355-fold and 500-fold respectively for natural products such as nerol, geraniol and linalool. Lactate esters such as methyl lactate can also be hyperpolarised with ^{1}H and ^{13}C NMR signal gains as high as 110-fold and 1015-fold respectively. This shows that SABRE-Relay can be a useful approach in the hyperpolarisation of small molecules of potential biological relevance. The hyperpolarisation of these examples cannot be achieved using alternative techniques such as PHIP or SABRE because these targets do not have the unsaturated or iridium ligating functionalities essential for these approaches. Instead, polarisation transfer catalysts of the form [Ir(H)$_2$(NHC)(amine)$_3$]Cl are able to hyperpolarise carrier amines with significant signal gains, with subsequent proton exchange

effects allowing relayed transfer of hyperpolarisation to the target molecules discussed. This approach does not involve chemical alteration of the target molecule which presents advantages compared to PHIP and PHIP-SAH and it uses much simpler technology than DNP.

While SABRE-Relay is able to enhance NMR signals of selected examples, it has not expanded the substrate scope of SABRE as significantly as might have been expected. Although the technique relies on proton exchange, it has not been used to hyperpolarise all molecules containing exchangeable protons tested here. One of the reasons for this is due to the physical properties of the target molecule which must either be a liquid at room temperature or pressure, or it must be soluble in a SABRE-Relay compatible solvent. These solvents must not contain exchangeable protons, which could serve as a hyperpolarisation sink, and should be compatible with solubilisation of both iridium catalyst and p-H_2. This usually necessitates using organic solvents such as dichloromethane-d_2 or chloroform-d which are often unable to solubilise target molecules, particularly those of biological interest. The presence of large amounts of contaminant water (which in some cases may be necessary to aid substrate solubilisation) limits SABRE-Relay efficiency by creating unwanted proton exchange pathways. These findings are consistent with previous reports of SABRE-Relay hyperpolarisation.[48, 104, 107]

Application of SABRE-Relay to a larger range of molecules may be possible by solvent optimisation or by introduction of solubilising molecular tags. The former approach has already been used to hyperpolarise sugars including glucose using SABRE-Relay by solubilisation in mixtures of dimethylformamide and dichloromethane.[107] The hydrolysis of lactate esters hyperpolarised using SABRE-Relay could be used as a route to produce hyperpolarised lactate. Currently, NMR signal gains are too low to observe hyperpolarised lactate although future improvements in catalyst design, carrier hyperpolarisation levels and utilisation of more efficient pulse sequences to transfer ^1H derived magnetisation to longer lived ^{13}C sites may allow such an application in the future.

SABRE-Relay can yield pyruvate ^{13}C NMR signal enhancements of up to 65-fold, although there are significant challenges associated with this approach. The main limitation is the *in situ* condensation between pyruvate and amine upon pyruvate addition to $[Ir(H)_2(NHC)(amine)_3]Cl$ which results in the formation of iridium carboxyimine complexes. At this point the system is effectively deactivated to further pyruvate hyperpolarisation. The behaviour and hyperpolarisation of these complexes is explored in much more detail in Chapter 4. This decomposition process can be reduced by using larger volumes of solubilising water, low amine concentrations, and less nucleophilic amine carriers. The resulting pyruvate ^{13}C NMR signal enhancement can also be improved by deuteration of the carrier amine or variation of the carbene ligand. Under optimised conditions a pyruvate ^{13}C NMR signal enhanced by 65-fold can be observed at 9.4 T and this signal is still discernible in a single scan ^{13}C NMR spectra 15 minutes after pyruvate addition to **26** or **27**. This timescale may be compatible with preparation times

required for utilisation in applications such as biomedical imaging studies. However, the ^{13}C polarisation levels (0.05%) are significantly lower than those that can be achieved for pyruvate using DNP (70%),[38] or even those of simple alcohols using SABRE-Relay (1%) [48, 104, 107, 108] (see Chapter 2). These limitations could be addressed by redesigning SABRE-Relay to include new classes of carrier molecules that can relay polarisation from the iridium catalyst to pyruvate without reacting to form decomposition products. Alternatively, a more fruitful approach may be to design novel polarisation transfer catalysts in which pyruvate can become hyperpolarised *via* direct coordination to the iridium catalyst. This is explored in more detail in Chapter 5.

SABRE-Relay has the potential to hyperpolarise molecules in a fashion that is inaccessible to alternative techniques such as SABRE or PHIP. However, it is currently only applicable to niche molecules and cannot deliver NMR signal enhancements comparable to other hyperpolarisation techniques such as d-DNP. This may limit the widespread use of the technique in hyperpolarised MR, particularly for applications in which hyperpolarisation in aqueous solvents is essential.

Chapter 4. Hyperpolarisation of iridium carboxyimine complexes

4.1 Introduction

Transition metal complexes have wide applications in catalysis and materials science.[203] Organometallic complexes were some of the first species to be hyperpolarised using *para*hydrogen (*p*-H_2) in the late 1980s.[32, 34] The *Para*Hydrogen Induced Polarisation (PHIP) effect was first observed through enhanced metal hydride signals of rhodium and iridium complexes,[31, 32] with some examples given in Figure 4.1. Since then, many more examples of PHIP hyperpolarised metal dihydride complexes have emerged.[204] Other hyperpolarisation techniques such as Dynamic Nuclear Polarisation (DNP) have hyperpolarised ^{89}Y heteronuclei in a range of inorganic complexes.[205, 206] Metal complexes are now rarely used as hyperpolarisation targets and are more commonly exploited to catalytically facilitate the hyperpolarisation of smaller organic molecules either by acting as direct hydrogenation catalysts (in PHIP)[45, 68, 73, 126] or catalytically transferring *p*-H_2 spin order to ligated molecules through temporary *J*-coupled networks in an organometallic complex (in SABRE).[76, 78] The types of materials typically hyperpolarised by PHIP and DNP nowadays are usually small organic molecules. These are typically organic reaction products for low concentration detection[122-124] or naturally occurring biomolecules for *in vivo* imaging[68-70, 73, 132-137, 139-141] and are discussed in section 1.5.
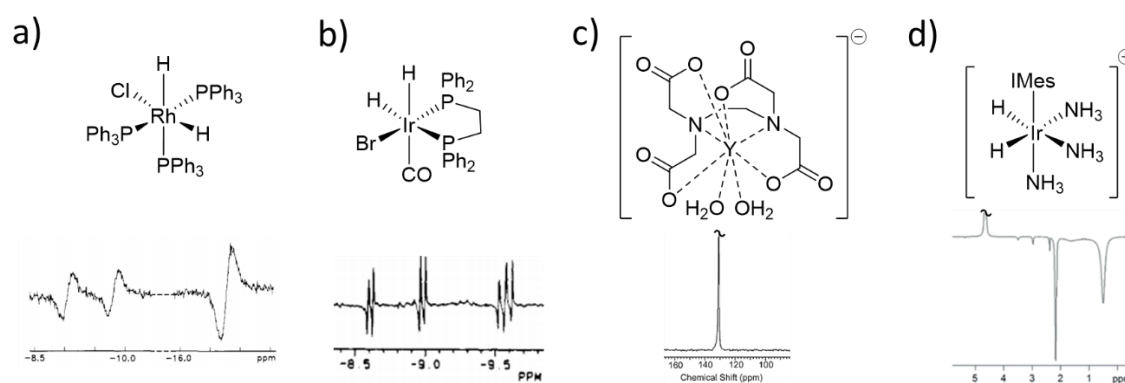
Figure 4.1: Examples of hyperpolarised metal complexes a) PHIP hyperpolarised hydride resonances of [RhCl(H)$_2$(PPh$_3$)$_3$][31] Reprinted (adapted) with permission from C. R. Bowers and D. P. Weitekamp, *J. Am. Chem. Soc.*, 1987, 109, 5541-5542 Copyright (1987) American Chemical Society b) PHIP hyperpolarised hydride resonances of [IrBr(H)$_2$(dppe)] where dppe is 1,2-bis(diphenylphosphino)ethane.[32] Reprinted (adapted) with permission from T. C. Eisenschmid, R. U. Kirss, P. P. Deutsch, S. I. Hommeltoft, R. Eisenberg, J. Bargon, R. G. Lawler and A. L. Balch, *J. Am. Chem. Soc.*, 1987, 109, 8089-8091. Copyright (1987) American Chemical Society c) DNP hyperpolarised ^{89}Y NMR signal of [Y(EDTA)(H$_2$O)]$^-$ where EDTA is ethylenediaminetetraacetic acid[206] d) SABRE hyperpolarised ^{1}H NMR resonances of [Ir(H)$_2$(IMes)(NH$_3$)$_3$]$^+$ (where IMes = 1,3-bis(2,4,6-trimethyl-phenyl)imidazole-2-ylidene) with resonances for free NH$_3$ and NH$_3$ bound *trans* to hydrides at δ 0.5 and 2.1 respectively.[106]

In SABRE, iridium complexes undergo reversible oxidative addition of p-H$_2$ to form metal dihydride species.[76] The PHIP enhanced magnetisation of these p-H$_2$ derived hydrides can be transferred to nuclei of other ligands within the organometallic complex through a temporary J-coupled network.[76, 78] Polarisation transfer from p-H$_2$ derived hydrides can occur at mT or μT fields for transfer to ^{1}H or X nuclei sites in ligated substrates respectively.[78, 83] This transfer can also be radiofrequency driven at high fields (*i.e.* 9.4 T).[95, 169, 170] While SABRE often uses these effects to achieve the polarisation of a target organic ligand in solution, hyperpolarised resonances for these ligands bound in an iridium SABRE catalyst can also be visible.[102, 106] The hyperpolarisation of short lived metal complexes can allow their low concentration detection in solution which is of great benefit in elucidating reaction mechanisms.[61] *Para*-hydrogen based hyperpolarisation methods can therefore be used as a unique tool to help detect species that would otherwise be extremely challenging to observe by NMR.[46]

In this chapter the hyperpolarisation of neutral complexes of the type [Ir(H)$_2$(κ^2-OOCC(CH$_3$)NR)(IMes)(NH$_2$R)] is investigated where R = CH$_2$Ph (**28**) and R = (CH$_2$)$_2$Ph (**29**). **28** and **29** are synthesized *in situ* by reaction of [IrCl(COD)(IMes)] (**2**) (where IMes = 1,3-bis(2,4,6-trimethyl-phenyl)imidazol-2-ylidene and COD = *cis,cis*-1,5-cyclooctadiene) with the amines benzylamine (**4**) or phenethylamine (**5**) (5 eq.) respectively in dichloromethane-d_2 (0.6 mL) in an NMR tube under a 3 bar H$_2$ atmosphere. The reaction was left overnight at room temperature to allow the formation of [IrH$_2$(IMes)(NH$_2$R)$_3$]Cl (**26**; R = CH$_2$Ph and **27**; R = (CH$_2$)$_2$Ph). The formation of **26** and **27** was confirmed by the presence of its characteristic hydride resonances at δ –24.1 or –23.7 respectively in a ^{1}H NMR spectrum.[106] At this point a solution of sodium pyruvate-1,2-[^{13}C$_2$] (**22**) (5 eq. relative to **2**) in H$_2$O (40 μL) was added to these solutions of **26** or **27** under a flow of N$_2$ gas. The 3 bar H$_2$ atmosphere was replaced and the solution left overnight to allow for the formation of an equilibrium mixture of **28** or **29**. The formation and characterisation of **28** and **29** is described in more detail in Chapter 3 and is summarised in Figure 4.2.
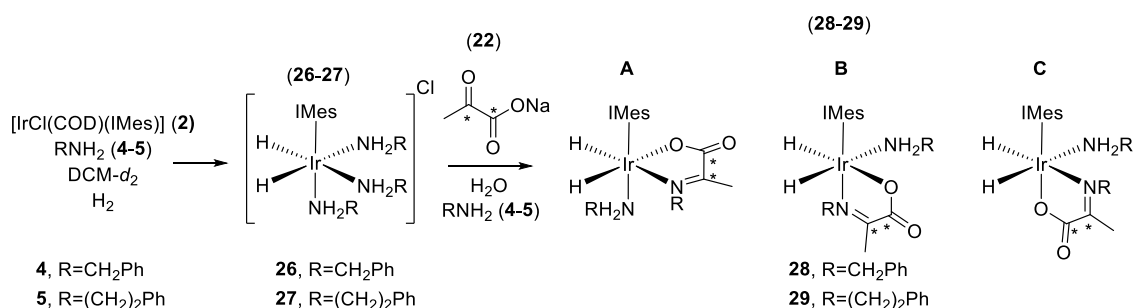
Figure 4.2: Formation of the iridium *a*-carboxyimine complexes 28 and 29 investigated in this chapter where IMes = 1,3-bis(2,4,6-trimethyl-phenyl)imidazole-2-ylidene. An asterisk (*) denotes a ^{13}C labelled position. The formation of these complexes is discussed in Chapter 3. Isomer C is not detected in solution.

In solution, **28** and **29** exist as two isomers that are distinguished by the coordination geometry of the imine, as shown in Figure 4.2. Those isomers containing coordinated imine in the same

plane as the hydride ligands are denoted **A** while those isomers containing ligated imine in the plane perpendicular to that of the hydrides are labelled **B**. There is a third isomer, **C**, which can arise from interchange of the imine binding sites, although this isomer was not observed during the course of this work. In the case of **28**, isomers **28A** and **28B** were found to exist in a 30:1 ratio one hour after addition of **22** to **26** at 298 K. After 7 hours at 298 K an equilibrium ratio of 2:1 confirms that **28A** is the thermodynamically more stable product. In contrast, species **29A** and **29B** formed in a 11:1 ratio one hour after addition of **22** to **27** at 298 K, although this changes to a 1:2 ratio after the solution is left for 7 hours at 298 K. This suggests that for **29**, isomer **B** is the thermodynamically favored product.

In Chapter 3, **28B** and **29B** were found to exhibit enhanced NMR resonances for their hydride ligands and enhanced ^{13}C NMR signals for their bound imine when equilibrium mixtures of **28** or **29** were shaken with p-H$_2$. These catalysts present an excellent opportunity to study magnetisation transfer within metal complexes which is explored further in this chapter. The NMR signal gains of these metal complexes is quantified and optimized and the ligand exchange processes governing their hyperpolarisation efficiencies are also investigated to produce a rational for achieving high SABRE performance in these metal complexes. These studies can have applications in a range of areas including intermediate detection and mechanistic elucidation of catalytic processes.

4.2 Creating heteronuclear ^{13}C$_2$ singlet order within 28B and 29B

[Ir(H)$_2$(κ^2-OOCC(CH$_3$)NR)(IMes)(NH$_2$R)] where R = CH$_2$Ph (**28**) and R = (CH$_2$)$_2$Ph (**29**) can be synthesized from **2** (5 mM), **22** (5 eq.) and the amines **4** or **5** (5-20 eq.) respectively in a 3 bar H$_2$ atmosphere, as detailed in section 4.1. When solutions of **28** and **29** in dichloromethane-d_2 (0.6 mL) are shaken for 10 seconds with 3 bar p-H$_2$ at 6.5 mT and immediately placed into a 9.4 T NMR spectrometer for collection of a single scan ^{1}H NMR spectrum the hydride resonances of **28B** and **29B** become strongly enhanced while those of **28A** and **29A** appear unaffected, as shown in Figure 4.3a. The hyperpolarised hydride signals of **28B** and **29B** both appear as antiphase peaks due to p-H$_2$ hydrogenation at both high field and low field producing a combination of ALTADENA and PASADENA effects.[32, 34] This means populations of $\alpha\beta$ and $\beta\alpha$ levels within the dihydride products are derived from p-H$_2$ spin order, as depicted in Figure 4.3b. These hydride NMR signal enhancements could not be easily quantified due to internal cancellation effects caused by overlap of broadened antiphase peaks.
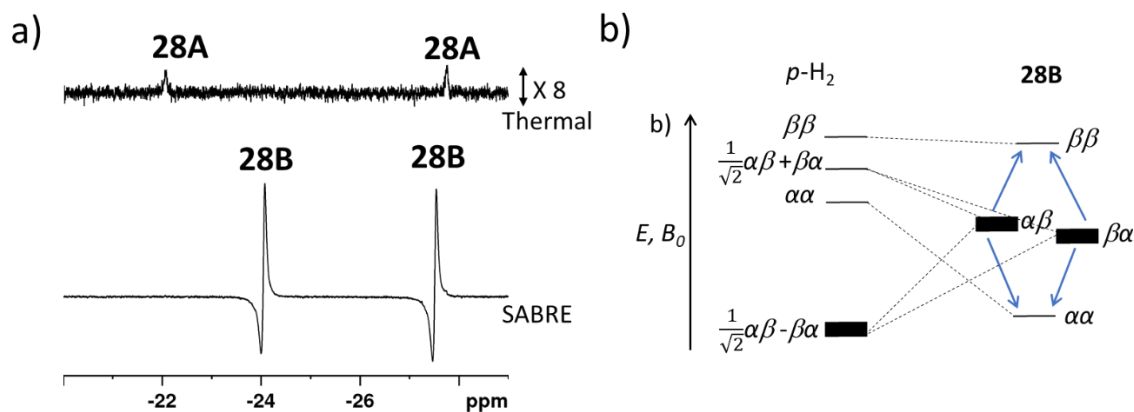
Figure 4.3: a) Example hyperpolarised ^{1}H NMR spectrum of 28 recorded using a 45° r.f. pulse with the analogous thermal spectrum (expanded vertically by a factor of 8) shown above. b) This line shape results from population (denoted by line thickness) of $\alpha\beta$ and $\beta\alpha$ nuclear spin energy levels of 28B (right) which are derived from the populated $\frac{1}{\sqrt{2}}\alpha\beta$-$\beta\alpha$ level in p-H$_2$ (left).[207]

When samples of **28** and **29** are shaken with fresh p-H$_2$ at 6.5 mT NMR signals for both the ^{13}C$_2$ sites of the imine ligand within **28B** or **29B** are strongly enhanced when observed with a 90° r.f. excitation pulse. A hyperpolarised ^{13}C NMR signal for free imine is not observed suggesting that the imine ligand does not exchange freely in solution over the timescale of this measurement. Interestingly, the two hyperpolarised ^{13}C NMR signals of the bound imine appear in an unusual 'up up down down' pattern which are indicative of singlet magnetisation,[57, 86, 112-114] as shown in Figure 4.4. These coupled ^{13}C-^{13}C spin pairs in **28B** and **29B** contain chemical shift differences of 4.8 and 6.1 ppm respectively ($^2J_{CC}$ = 66 Hz) at 9.4 T. At the mT polarisation transfer fields these spins are strongly coupled to the hydride ligands allowing the initial singlet state of p-H$_2$ to be transferred to the ^{13}C$_2$ pair which results in these unusual patterns.[55, 208] ^{13}C NMR signal enhancements could not be calculated by reference to a single scan thermal measurement as the ^{13}C NMR resonances of **28B** and **29B** recorded under Boltzmann derived conditions are too weak to be observed in a single scan. Therefore, the ^{13}C NMR signal enhancements of **28B** and **29B** were calculated as 420-fold and 280-fold respectively by reference to a more concentrated reference signal of **22** (as described in section 1.4, equation 1.11). As singlet magnetisation is shared equally between the coupled ^{13}C spin pair, these NMR signal enhancements effectively describe the average magnetisation on each ^{13}C site.
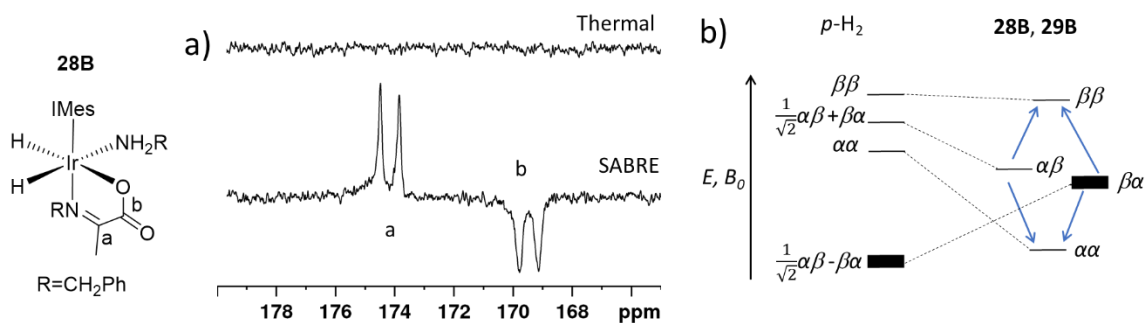
Figure 4.4: a) An example hyperpolarised ^{13}C NMR spectrum of 28 recorded using a 90° r.f. pulse with the analogous thermal spectrum shown above. b) This line shape results from population (denoted by line thickness) of $\beta\alpha$ nuclear spin energy levels of $^{13}C_2$ sites within 28B (right) which is derived from the populated $\frac{1}{\sqrt{2}}\alpha\beta$-$\beta\alpha$ level in p-H_2 (left).

The creation of singlet magnetisation using r.f. pulses was first reported in 2004.[50, 52] This type of magnetisation is typically immune to dipolar relaxation and can therefore contain lifetimes longer than T_1 values.[51, 54, 57] Singlet magnetisation in ^1H-^1H,[209, 210] ^{13}C-^{13}C,[53, 87] ^{15}N-^{15}N[55, 56, 86, 208] or even ^{13}C-^{15}N[58] spin pairs has also been derived from p-H_2 using SABRE but these approaches often involve the use of complex pulse sequences. Such singlet order is typically created in small organic molecules,[51, 54, 57, 58, 112, 208, 211, 212] although singlet magnetisation in ^1H-^1H spin pairs of metal dihydride complexes, arising from oxidative addition of p-H_2, has been reported.[168, 208, 210] In the case of **28B** and **29B**, heteronuclear singlet order is transferred spontaneously from p-H_2 at low field (~6 mT) without complex instrumentation or r.f. excitation. Interestingly, **28B** and **29B** are an unusual example of a heteronuclear (non ^1H) singlet state observed within a transition metal complex. This is unusual as the iridium centre might be expected to promote singlet relaxation.[213, 214] To investigate further, the lifetime of this $^{13}C_2$ singlet magnetisation was measured to determine if long-lived magnetisation could be created using SABRE.

The methods commonly used to measure the lifetimes of singlet states in pairs of coupled spins at either high field (T_{HF}) or low field (T_{LF}) are summarised in Figure 4.5.[56, 93, 114, 210] These usually involve shaking the sample with 3 bar p-H_2 for 10 seconds at 6.5 mT. The sample can then be immediately transferred to a 9.4 T spectrometer before ^{13}C NMR spectra are recorded with a 90° r.f. pulse. The sample can be left at 9.4 T for a variable storage time, τ_{HF}, before the acquisition sequence is applied. Alternatively, the sample can be stored in a mu-metal shield (~ 1 μT) for a variable time interval, τ_{LF}, before returning the sample to the 9.4 T NMR spectrometer and immediately recording a ^{13}C NMR spectrum. These experimental approaches are summarised in Figure 4.5. As the storage time (τ) is increased the hyperpolarised signal, S_t, will relax. A decay curve is produced by plotting this signal decay as a function of storage time which can then be fitted to an exponential decay to extract a lifetime, T_{HF} or T_{LF}.[112, 114]
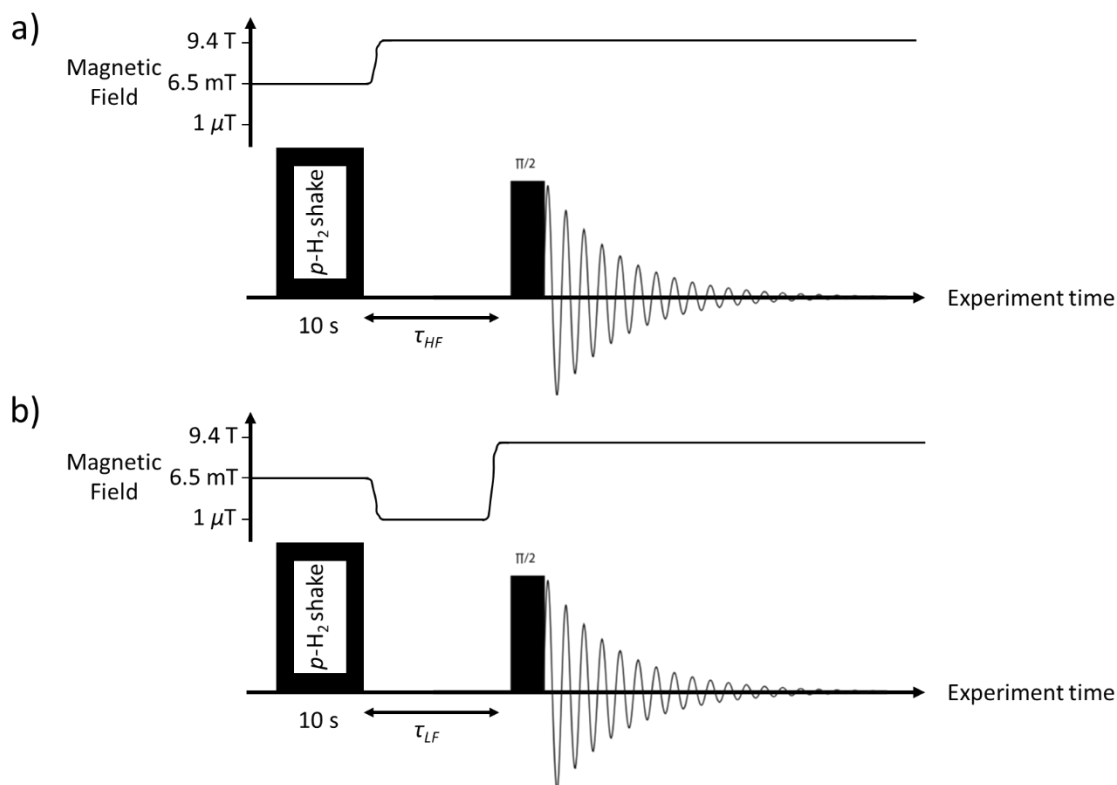
Figure 4.5: Depiction of the experimental procedure used for determination of a) high field lifetime (T_{HF}) and b) low field lifetime (T_{LF}) of $^{13}C_2$ singlet order within 28B and 29B.

When such methods are applied here (method a of Figure 4.5), the high field (9.4 T) lifetime, T_{HF}, of the hyperpolarised $^{13}C_2$ magnetic states within **28B** and **29B** are too short to allow for an appropriate decay profile to be obtained. When these experiments are repeated by storing the sample at low magnetic field in a mu-metal shield (~1 μT) (method b of Figure 4.5) hyperpolarised $^{13}C_2$ signal decay of **28B** and **29B** is produced which show a dependence on p-H_2 pressure, an example is given in Figure 4.6a. This is likely related to replenishment of $^{13}C_2$ singlet order as p-H_2 exchange continues during the storage time. Therefore, these decay curves contain contributions from both the low-field singlet state lifetime (T_{LF}) and the rate of p-H_2 refreshment (p_H). This was confirmed by recording a similar signal decay plot in which the sample was shaken at low field (~6 μT) for the last 5 seconds of the storage time to dissolve fresh p-H_2 for alternating data points. The hyperpolarised ^{13}C NMR signal intensity for these data points were significantly higher than samples which were not shaken for a portion of the storage time, as shown in Figure 4.6b. This suggests that continuous repolarisation is occurring during the storage time. Therefore, the hyperpolarised $^{13}C_2$ NMR signal decay profile of **28B** and **29B** was fit to a bi-exponential function that contains contributions from both the singlet state lifetime (T_{LF}) and p-H_2 repolarisation (p_H). This function is described in Equation 4.1 where S_0 is the hyperpolarised $^{13}C_2$ NMR signal intensity at $t = 0$ and A and B are constants.

$$S_t = S_0 + Ae^{-\frac{\tau_{LF}}{T_{LF}}} + Be^{-\frac{\tau_{LF}}{p_H}} \qquad (4.1)$$

The effects of singlet relaxation and p-H_2 refreshment can be deconvoluted by recording measurements at different p-H_2 pressures as T_{LF} will be independent of p-H_2 pressure while p_H will vary as a function of p-H_2 pressure. Recording these measurements at p-H_2 pressures of 1, 2 and 3 bar followed by bi-exponential fitting of these $^{13}C_2$ NMR signal decay curves according to Equation 4.1 yields singlet state lifetimes (T_s) of 10.9 ± 1.1 s and 8.8 ± 1.4 s for **28B** and **29B** respectively.
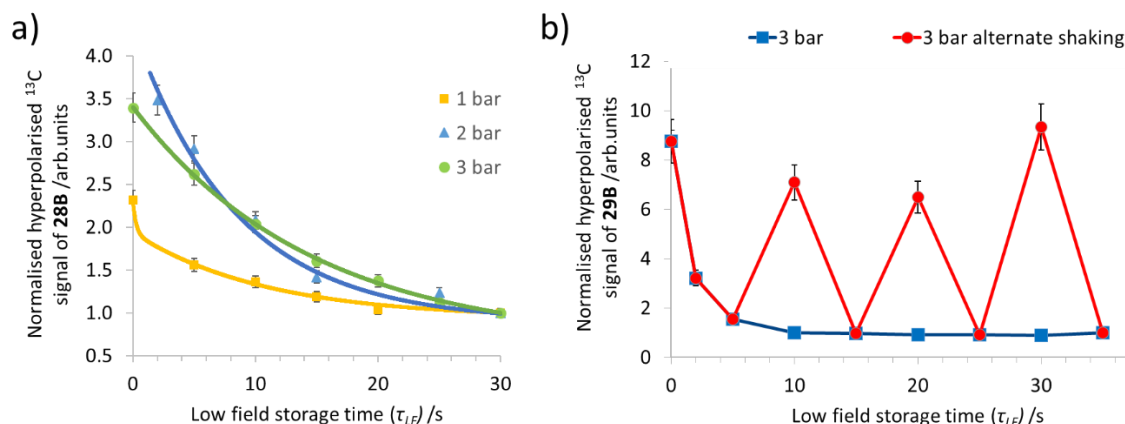
Figure 4.6: a) Example decay of hyperpolarised $^{13}C_2$ NMR signal of 28B measured at different p-H_2 pressures. Experimental data points are shown with markers while fitted values according to a biexponential decay are shown with solid lines. b) Decay of hyperpolarised NMR $^{13}C_2$ NMR signal of 29B measured at 3 bar p-H_2 by hyperpolarising in the stray field of the 9.4 T magnet and storing in a mu-metal shield for differing time periods (blue) and repeated when the samples stored for 10, 20 and 30 seconds were shaken in the mu-metal shield for the last 5 seconds of the storage time (red). Solid lines in b) are included for visual aid only.

Currently, some of the longest reported singlet lifetimes are 26 minutes at low field for the coupled $^{15}N_2$ spins in $^{15}N_2O^{212}$ and over an hour for a $^{13}C_2$ spin pair in a naphthalene derivative.[57] In these examples singlet magnetisation is created using complex instrumentation and *r.f.* excitation to populate the singlet $|S_0\rangle$ state. Here, SABRE can create singlet magnetisation naturally which provides many cost and time advantages. Theis et al. have exploited SABRE-SHEATH to create singlet $^{15}N_2$ magnetisation in $^{15}N_2$-diazirine which has a lifetime of 23 ± 3 minutes.[55] The singlet lifetimes of **28B** and **29B** are significantly shorter than these examples suggesting that singlet order within them cannot be described as 'long-lived' as there are still significant relaxation pathways. This is perhaps unsurprising considering that the magnetisation exists within a metal complex which may provide a source of relaxation. Nevertheless, this work provides a rare example of heteronuclear singlet order surviving within a metal complex which may be of future use in the detection of low concentration catalytic intermediates.

4.3 Investigating hydrogen exchange processes of 28B and 29B

The source of singlet order within **28B** and **29B** is p-H_2, which can be refreshed upon p-H_2 exchange. Therefore, the mechanism of hydrogen exchange within **28B** and **29B** was investigated

to determine its role in achieving high $^{13}C_2$ NMR signal enhancements within **28B** and **29B**. These are neutral 18 electron complexes that could exchange hydrogen in a number of ways, as depicted in Figure 4.7. Hydrogen could coordinate to these complexes in an associative process (path a of Figure 4.7) to form 20 electron species of the form $[Ir(H_2)(H)_2(\kappa^2\text{-}OOCC(CH_3)NR)(IMes)(NH_2R)]$. This is an unlikely process as it breaks the 18 electron rule and transition metal complexes with 20 valence electrons are rare.[215, 216] It is much more likely that hydrogen exchange will proceed through a pathway that involves 16 or 18 electron intermediates.[217, 218] This could occur through reductive elimination of H_2 (path b of Figure 4.7) to initially form a 16 electron square planar product which subsequently binds fresh H_2. This cycle of H_2 reductive elimination and oxidative addition will be accompanied by changes in metal oxidation state and geometry. There may therefore be a large barrier to these processes if large orbital reorganization energies are involved.[219] On the basis of H_2 exchange processes in similar Ir(III) complexes, it is more likely that H_2 oxidative addition and subsequent exchange is preceded by dissociative amine loss (path c of Figure 4.7) from 18 electron **28** or **29** to form 16 electron $[Ir(H)_2(\kappa^2\text{-}OOCC(CH_3)NR)(IMes)]$.[97]

28B; R=CH$_2$Ph   **29B**; R=(CH$_2$)$_2$Ph
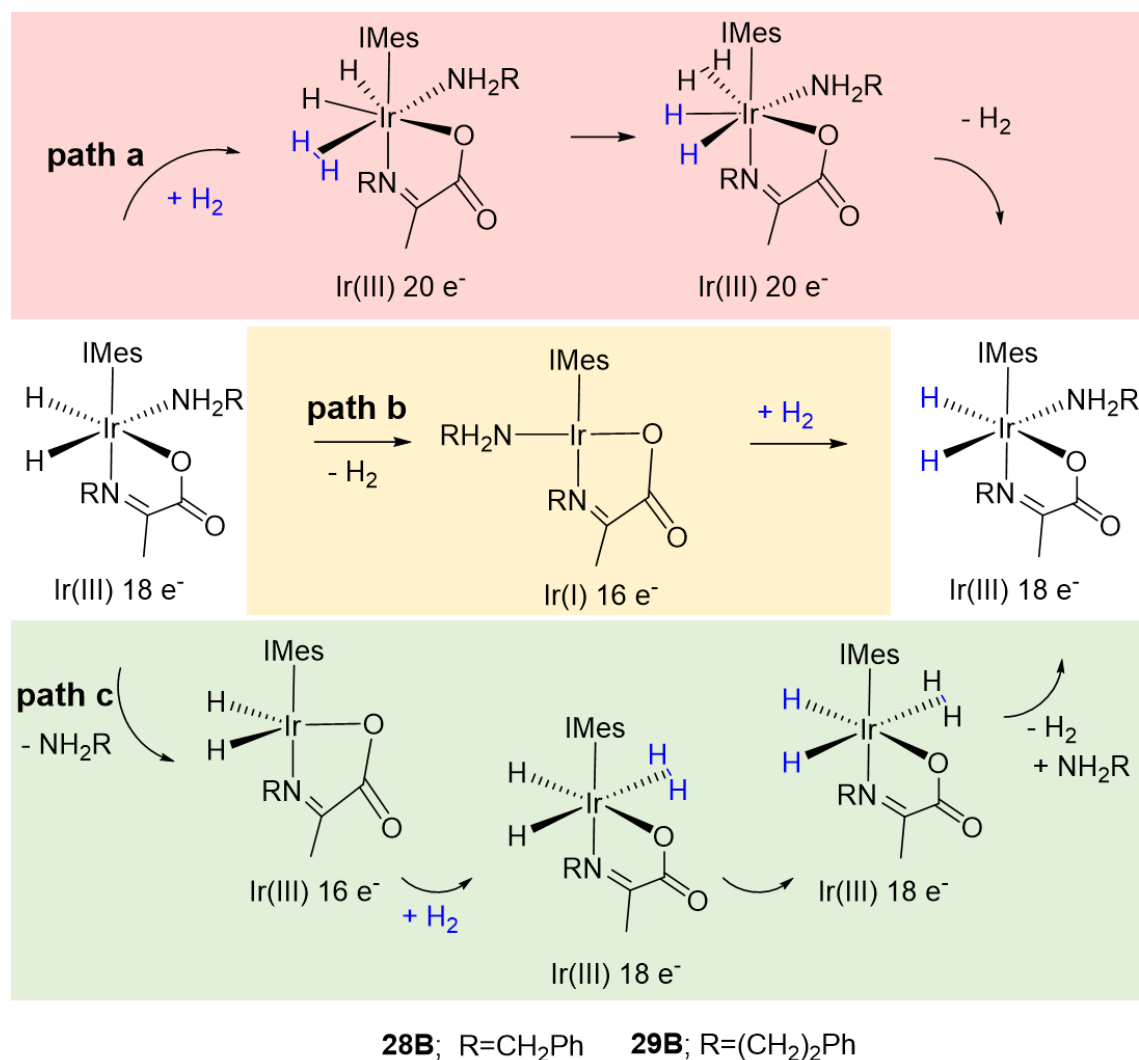
Figure 4.7: Potential hydrogen exchange pathways in 28B and 29B.

A combination of exchange spectroscopy (EXSY)[220] and Density Functional Theory (DFT)[221] were used to investigate hydrogen exchange pathways within **28B** and **29B**. EXSY experiments were performed to measure the exchange rate between the hydride ligands and free H_2. In this experiment, the hydride resonance *trans* to amine is selectively excited before recording a ^1H NMR spectrum after a time delay, as summarised in Figure 4.8a. Upon the selective excitation of either hydride signals of **28B** or **29B**, evolution into free H_2 and the inequivalent hydride site is observed, an example is shown in Figure 4.8b. In contrast, excitation of the hydride ligands of **28A** or **29A** does not show chemical exchange into other products suggesting that they are inert on this timescale. These measurements also do not reveal any exchange between **A** and **B** isomers on this timescale suggesting that interconversion between the two forms is slow. These results show there is a reaction pathway in **28B** and **29B** that allows for both H_2 exchange and interchange of the hydride ligand sites.
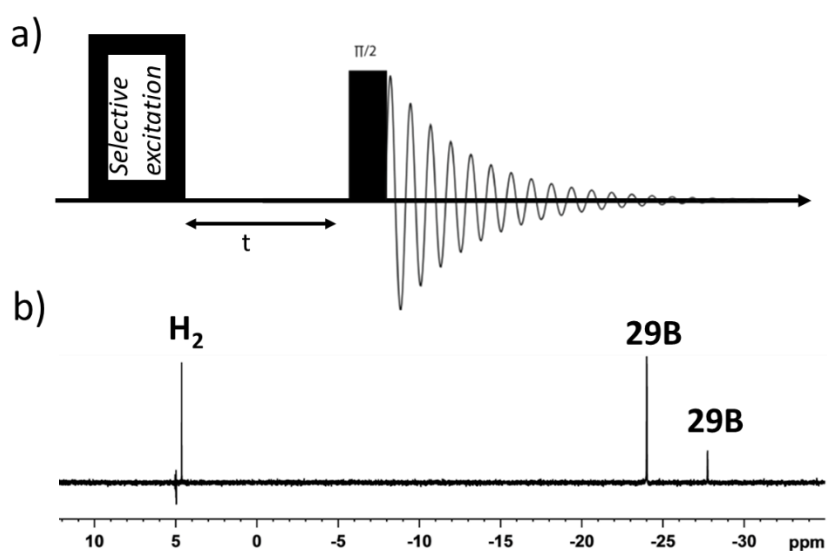
Figure 4.8: a) Depiction of the EXSY measurement process b) A typical EXSY spectrum of 29B at 283 K recorded 0.05 s after selective excitation of the hydride ligand *trans* to amine.

Hydrogen exchange is expected to follow path c of Figure 4.7 in which the key step is dissociative amine loss to form an important five coordinate intermediate [Ir(H)$_2$(κ^2-OOCC(CH$_3$)NR)(IMes)]. This intermediate can then react with H_2 to reform the starting complex in which its excited hydride ligands have been replaced with unexcited hydride ligand *via* hydrogen exchange. In contrast, the five coordinate intermediate [Ir(H)$_2$(κ^2-OOCC(CH$_3$)NR)(IMes)] can also be ligated by an amine; rebinding of the amine is able to reform the starting complex. In this case the excited label of **28B** or **29B** will remain unchanged if the amine rebinds in the same orientation. However, coordination of the amine on a different face of this intermediate will reform **28B** or **29B** with interchanged hydride ligands. This effect results from the asymmetry of the imine bound within the 16-electron intermediate [Ir(H)$_2$(κ^2-OOCC(CH$_3$)NR)(IMes)]. These pathways are summarised in Figure 4.9.
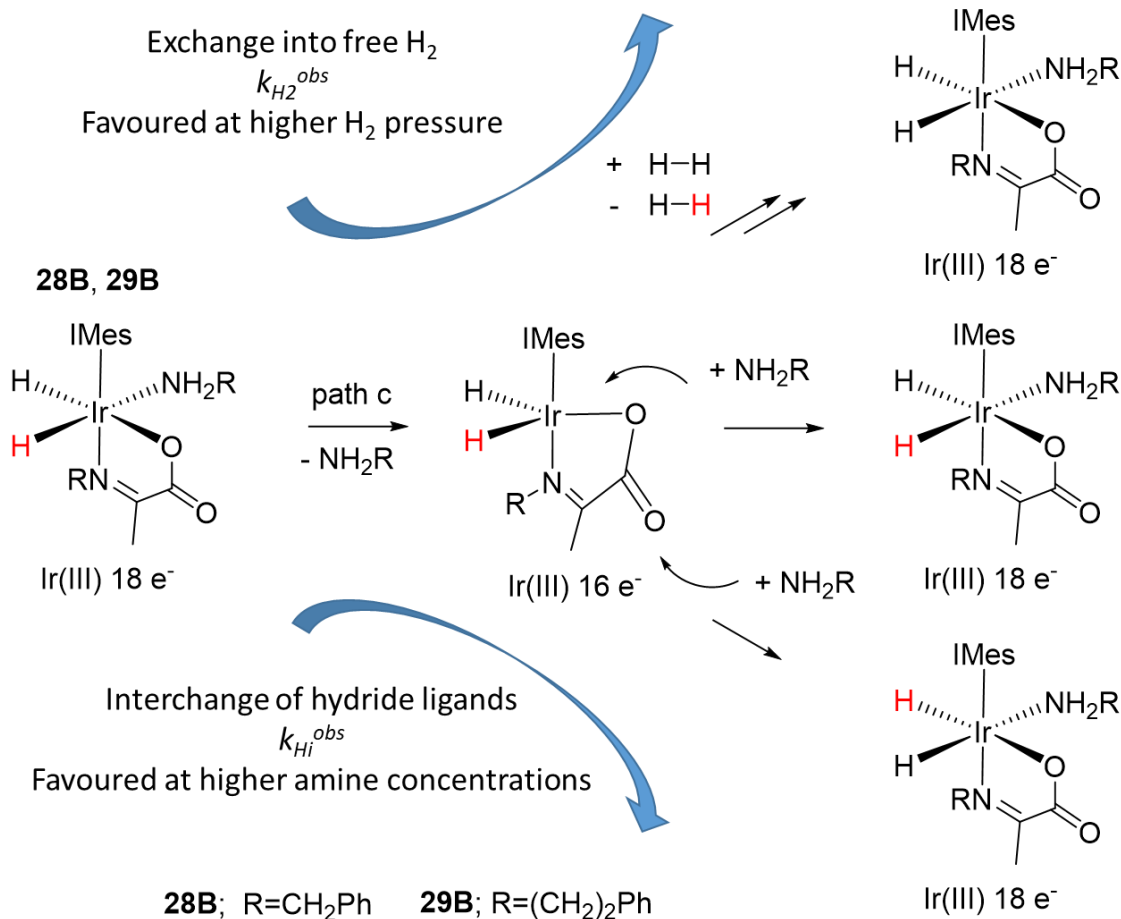
Figure 4.9: Exchange processes of **28B** and **29B** that can lead to exchange of hydrogen or interchange of hydride ligands.

The rate of these two exchange processes: H_2 exchange (k_{H2}^{obs}) and interchange of the hydride ligand sites (k_{Hi}^{obs}) can be measured by recording a series of EXSY spectra in which the delay between selective excitation of hydride *trans* to amine and spectral acquisition is increased. A series of integral intensities of the excited resonance and evolved resonances are collected and plotted as a function of the delay time, an example is given in Figure 4.10a. These integral intensities can be interpreted as a percentage abundance and can be fit to a three site exchange model described by equations 4.2-4.4. Expected percentage abundances of these species (starting **28B** or **29B**, free hydrogen $(H - H)$, and the hydride interchanged products (**28Bi** or **29Bi**)) at varying time delays were calculated at time t where ∂t is an incremental time difference and k_{-H2}^{obs} and k_{-Hi}^{obs} are the reverse observed rates of hydrogen exchange and hydride interchange.

$$[28B]_{t+\partial t} = [28B]_t + \left(k_{-H2}^{obs}[H-H] - k_{H2}^{obs}[28B] - k_{Hi}^{obs}[28B] + k_{-Hi}^{obs}[28Bi]\right)\partial t \quad (4.2)$$

$$[28Bi]_{t+\partial t} = [28Bi]_t + \left(k_{-H2}^{obs}[H-H] - k_{H2}^{obs}[28Bi] - k_{-Hi}^{obs}[28Bi] + k_{Hi}^{obs}[28B]\right)\partial t \quad (4.3)$$

$$[H-H]_{t+\partial t} = [H-H]_t + \left(k_{H2}^{obs}[28B] - 2k_{-H2}^{obs}[H-H] + k_{H2}^{obs}[28Bi]\right)\partial t \quad (4.4)$$

The observed rate of hydrogen production (k_{H2}^{obs}) and hydride site interchange (k_{Hi}^{obs}) are determined from fitting the lowest sum of the least squared fit between the EXSY determined abundances and those predicted by the kinetic model described in equations 4.2-4.4. An example is shown in Figure 4.10a. Transition state barriers for these processes can be calculated by recording measurements at a range of different temperatures (see Figure 4.10b). The activation enthalpy ($\Delta H^{\ddagger}$) and activation entropy ($\Delta S^{\ddagger}$) of hydrogen exchange or hydride interchange can be calculated from equation 4.5where T is temperature, k_B is Boltzmann's constant, h is Planck's constant, and R is the ideal gas constant. The Gibbs free energy of activation ($\Delta G^{\ddagger}$) can be calculated using Equation 4.6. Errors were calculated according to established procedures.[222]

$$\ln\left(\frac{k_{RE}}{T}\right) = \ln\left(\frac{k_B}{h}\right) + \frac{\Delta S^{\ddagger}}{R} - \frac{\Delta H^{\ddagger}}{RT} \qquad (4.5)$$

$$\Delta G^{\ddagger} = \Delta H^{\ddagger} - T\Delta S^{\ddagger} \qquad (4.6)$$
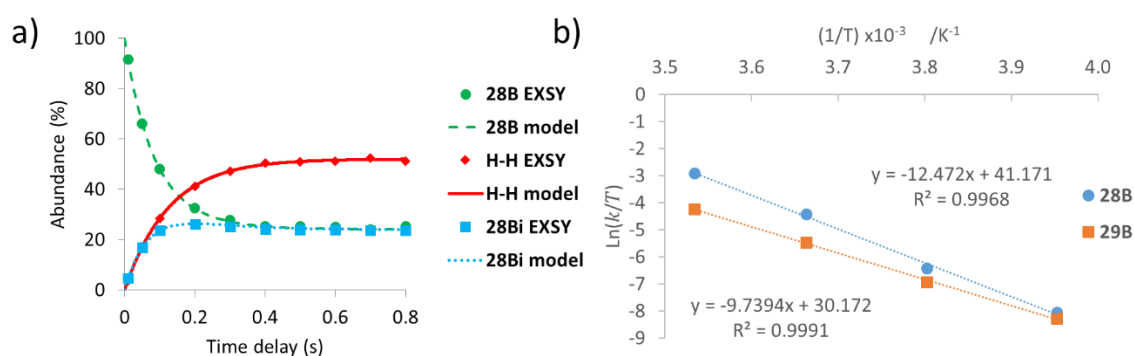
Figure 4.10: a) % Abundances calculated from EXSY data (marker points) and the model (lines) for a solution of 29B at 283 K. b) An Eyring plot of $\ln\left(\frac{k_{H2}}{T}\right)$ against $\frac{1}{T}$ yields a straight line with intercepts and gradients used to calculate thermodynamic parameters for the observed rate of hydrogen loss from 28B and 29B according to equations 4.5 and 4.6.

The EXSY data were used to estimate the rate of free H_2 production as 15.5 ± 0.6 s^{-1} for **28B** at 283 K. The transition state barriers $\Delta H^{\ddagger}$ and $\Delta S^{\ddagger}$ for free H_2 production are 103.7 ± 1.6 kJ mol^{-1} and 145 ± 6 J K^{-1} mol^{-1} respectively. The observed rate of H_2 formation from **29B** was slower than that from **28B** (4.11 ± 0.06 s^{-1}) at 283 K while transition state barriers were also lower ($\Delta H^{\ddagger}$ and $\Delta S^{\ddagger}$ for free H_2 production of 81.0 ± 2.2 kJ mol^{-1} and 53 ± 5 J K^{-1} mol^{-1} respectively). Similar octahedral iridium carbene complexes have been reported to exchange hydrogen at rates between 0.56 and 5.11 s^{-1} at the higher temperature of 295 K.[92] Therefore, hydrogen exchange processes of **28B** and **29B** are relatively rapid. It is suggested that faster H_2 exchange within **28B** accounts for the higher ^{13}C NMR signal enhancements (420-fold for **28B** versus 280-fold for **29B**) as enhanced p-H_2 exchange is able to constantly 'top up' p-H_2 derived singlet order within **28B** and **29B**. Rapid hydrogen exchange is therefore very important in both obtaining high ^{13}C$_2$ NMR signal enhancements and refreshing ^{13}C$_2$ singlet order.

On the basis of hydrogen exchange processes reported for similar Ir(III) systems it is expected that hydrogen exchange follows a pathway similar to that of path c of Figure 4.7 in which hydrogen exchange is preceded by dissociative amine loss from 18 electron **28B** or **29B** to form a 16 electron five coordinate intermediate.[97] This proposal was investigated by measuring these observed hydrogen exchange (k_{H2}^{obs}) and hydride interchange (k_{Hi}^{obs}) rates for **29B** as a function of amine concentration and hydrogen pressure. These rates are shown in Table 4.1 and Table 4.2 respectively.

Table 4.1: Rate constants for H$_2$ production (k_{H2}^{obs}) and hydride interchange (k_{Hi}^{obs}) of 29B determined by EXSY at 273 K as a function of amine concentration when H$_2$ pressure was fixed at 3 bar. Note amine concentration is relative to 2 (5 mM).

[Amine]	k_{H2}^{obs}/s^{-1}	k_{Hi}^{obs}/s^{-1}
5 eq.	1.85 ± 0.05	0.40 ± 0.02
10 eq.	1.47 ± 0.03	0.70 ± 0.01
15 eq.	1.13 ± 0.01	0.88 ± 0.01

The k_{H2}^{obs} rates of Table 4.1 decrease as the amine concentration is increased supporting the hypothesis that hydrogen exchange occurs following dissociative amine loss. This change supports the fact that the [Ir(H)$_2$(κ^2-OOCC(CH$_3$)NR)(IMes)] intermediate is more likely to undergo hydride ligand interchange at higher amine concentrations by reforming **29B** rather than reacting with H$_2$. This is indicated by a reduction in k_{H2}^{obs} and increase of k_{Hi}^{obs} when higher amine concentrations are used. In contrast, when the H$_2$ pressure is increased the five coordinate intermediate is more likely to react with H$_2$ than amine which is indicated by an increase in k_{H2}^{obs} and a decrease of k_{Hi}^{obs}.

Table 4.2: Rate constants for H$_2$ production (k_{H2}^{obs}) and hydride interchange (k_{Hi}^{obs}) of 29B determined by EXSY at 273 K as a function of H$_2$ pressure when amine concentration was fixed at 15 eq. relative to 2 (5 mM).

H$_2$ pressure	k_{H2}^{obs}/s^{-1}	k_{Hi}^{obs}/s^{-1}
1 bar	0.60 ± 0.01	1.05 ± 0.01
2 bar	0.95 ± 0.01	0.92 ± 0.01
3 bar	1.13 ± 0.01	0.88 ± 0.01

Density Functional Theory (DFT) calculations were performed by Dr. Richard O. John (details are given in the experimental section 7.5) to gain further insight on these ligand exchange processes. These calculations allow the relative energies of the closely related **28A-28C** to be determined and are given in Table 4.3. The theoretical stability ordering of **28A ≥ 28B ≫ 28C** is consistent with ^{1}H NMR observations in solution. The energies of products formed from direct H$_2$ loss to form a four coordinate Ir(I) 16-electron product are also shown and depicted graphically in Figure 4.11. As the ΔH and ΔG changes to form these products are both greater than 100 kJ mol^{-1} at 298 K direct H$_2$ loss is likely to be accompanied by a large transition state barrier.[223] This suggests that hydrogen exchange *via* path b of Figure 4.7 is unlikely to occur. In

contrast, the [Ir(H)$_2$(H$_2$)(κ^2-OOCC(CH$_3$)NR)(IMes)] intermediate formed in path c, is more stable by over 60 kJ mol^{-1}. This supports a route to H$_2$ exchange in a cycle that involves iridium complexes with constant oxidation states. The energy changes for amine loss from **28A** are larger than from **28B** which supports the experimentally observed reduced reactivity for isomers of type **A**.

Table 4.3: Relative energies of 28 and computed thermodynamic parameters related to ligand exchange processes at 298 K. All values are in kJ mol^{-1} and relative to 28B which is set as a zero point. Note these are product energies and not transition state barriers. These DFT calculations have been performed by Dr. Richard O. John.[224]

Process	Energy	28A	28B	28C
Relative energies	ΔH	−4.0	0	9.5
	ΔG	−0.9	0	20.3
H$_2$ loss	ΔH	126.2	136.7	126.2
	ΔG	99.9	104.6	99.9
Amine loss	ΔH	141.4	94.7	141.4
	ΔG	92.7	41.1	92.7
H$_2$ addition to 5	ΔH	53.1	32.8	53.1
coordinate intermediate	ΔG	35.7	11.4	35.7

ΔG_{28B} = 104.6 kJ mol^{-1}
ΔH_{28B} = 136.7 kJ mol^{-1}

ΔG_{28C} = 79.6 kJ mol^{-1}
ΔH_{28C} = 116.7 kJ mol^{-1}

ΔG_{28A} = 100.8 kJ mol^{-1}
ΔH_{28A} = 121.8 kJ mol^{-1}

ΔG_{28A} = 93.6 kJ mol^{-1}
ΔH_{28A} = 145.4 kJ mol^{-1}

ΔG_{28C} = 83.2 kJ mol^{-1}
ΔH_{28C} = 121.1 kJ mol^{-1}

ΔG_{28A} = −57.0 kJ mol^{-1}
ΔH_{28A} = −88.3 kJ mol^{-1}

ΔG_{28B} = 41.1 kJ mol^{-1}
ΔH_{28B} = 94.7 kJ mol^{-1}

ΔG_{28B} = −29.7 kJ mol^{-1}
ΔH_{28B} = −61.9 kJ mol^{-1}

Gibbs Energy/ kJ mol^{-1}

28C

28B
28A
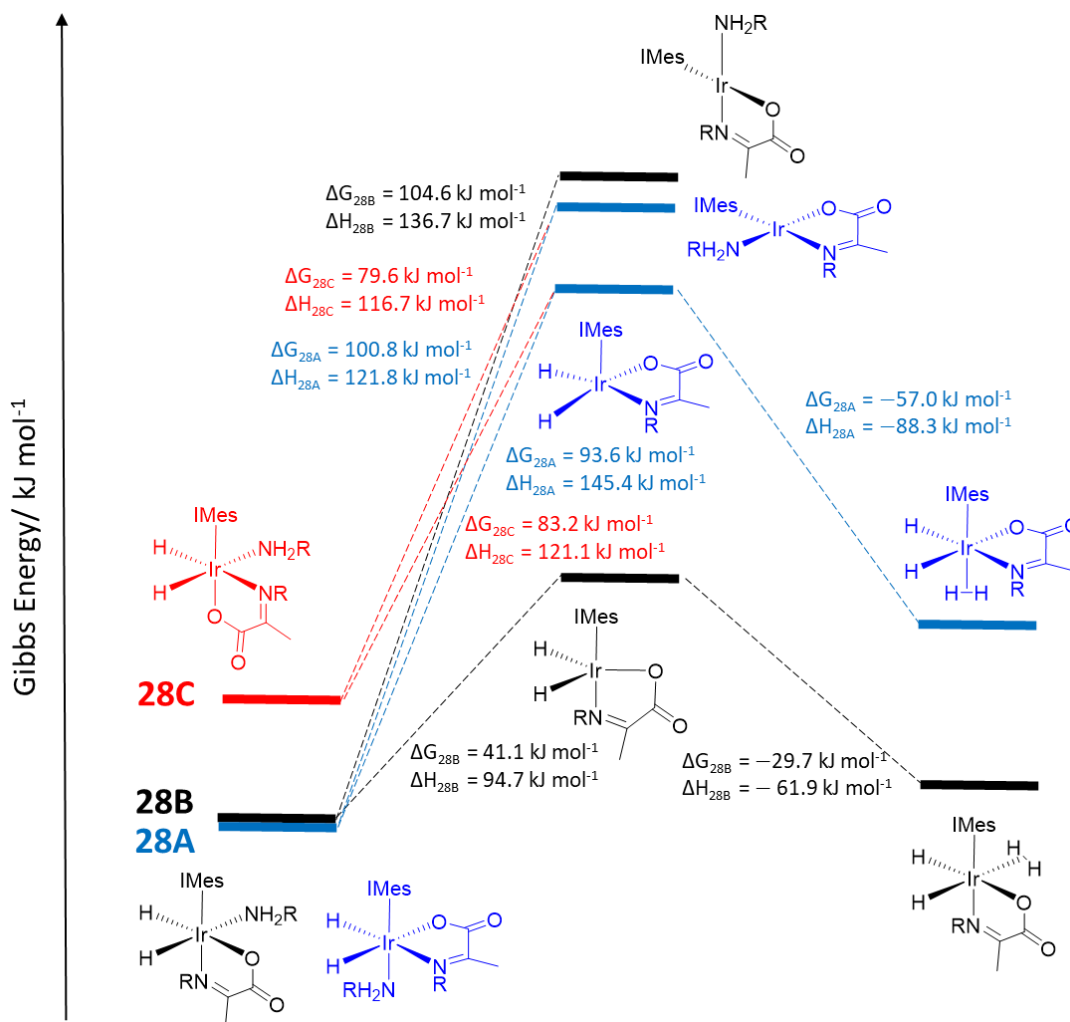
Figure 4.11: DFT energy level diagram showing the relative energies of 28A-C and the energies of species arising from H$_2$ or amine loss. These are intermediate energies and not transition state energies. These DFT calculations have been performed by Dr. Richard O. John.[224]

4.4 Formation of novel iridium carboxyimine complexes 44, 45, and 47 by variation of coligand

The investigation into the mechanism of H$_2$ loss from **28B** and **29B** described in section 4.3 support a pathway preceded by amine loss. Therefore, amine dissociation from **28B** and **29B** may be a key factor mediating p-H$_2$ exchange and determining the resultant NMR signal enhancements and singlet state lifetimes. Therefore, solutions of **29** were mixed with various different neutral two electron nitrogen, oxygen, and sulphur donors to form novel complexes in which the amine ligand of **29** is replaced by a coligand, as shown in Figures 4.12 and 4.14. When **29** is mixed with the coligands acetonitrile-d_3 (**41-d_3**) or thiophene (**42**) (5 eq. relative to starting **2**) both the broad hydride resonances of **29B** at δ −24.03 and −27.80 and the sharp hydride resonances of **29A** at δ −21.70 and −27.91 appear unchanged. Therefore, **41-d_3** and **42** are unable to compete with amine for binding to **29**. However, when pyridine (**43**) is added to solutions of **29** in dichloromethane-d_2, new hydride resonances immediately appear at δ −23.47 and −27.37 which

have a mutual $^2J_{HH}$ coupling constant (7.5 Hz). These hydride resonances result from a new species, **44B** in which pyridine has replaced the amine ligand of **29B**. When this solution is left overnight at 278 K additional resonances at δ −20.96 and −26.99 ($^2J_{HH}$ = 9 Hz) become visible which belong to **44A** in which pyridine has replaced the amine ligand of **29A**. At this time point all four complexes, **29A**, **29B**, **44A**, and **44B**, are present in solution.
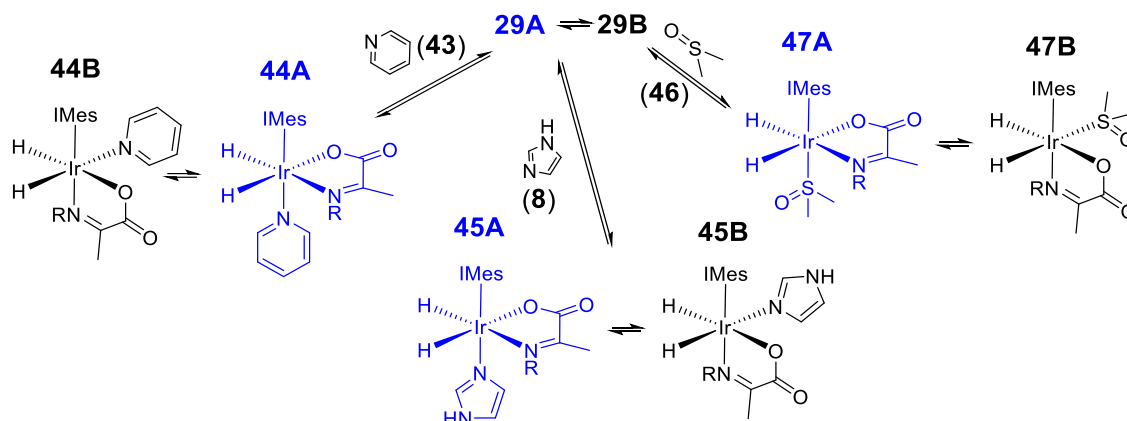
Figure 4.12: Addition of the coligands pyridine (43), imidazole (8), or dimethylsulfoxide (46) to solutions of 29 form 44, 45, and 47 in which the amine ligand is replaced with the added coligand.

Similar effects are observed when **29** is mixed with imidazole (**8**); new hydride resonances appear at δ −21.96 and −28.14 ($^2J_{HH}$ = 8 Hz) and correspond to **45B**, in which imidazole has replaced the amine ligand of **29B**. Similarly to **44B**, **45B** forms rapidly after the addition of coligand (in this case imidazole) to **29** at room temperature. A species analogous to **44A**, **45A**, with resonances at δ −21.41 and −27.59 ($^2J_{HH}$ = 9 Hz) forms after a longer time period. The time course of this reaction is shown in Figure 4.13. Similarly, the dimethylsulfoxide (**46**) complexes **47A** and **47B** can be formed with broad hydride resonances at δ −13.37 and −25.77 and sharp resonances at δ −21.14 and −25.89 ($^2J_{HH}$ = 9 Hz) respectively.

These complexes (**44**, **45**, and **47**) are characterised using a combination of mass spectrometry and 2D NMR techniques (see sections 7.4.5-7.4.6). For some equilibrium mixtures NMR characterisation is extremely challenging due to severe peak overlap caused by the presence of multiple complexes in solution. In the case of an equilibrium mixture of **29** and **45**, addition of ~3 mL degassed hexane caused the precipitation of **45A** as a bright orange solid which was isolated by filtration and drying under vacuum. This product was re-dissolved in dichloromethane-d_2 and the resultant solution used for 2D NMR characterisation at 245 K using a similar approach to those of **28** and **29** presented in Chapter 3. Full NMR characterisation data for **45A** is given in the experimental section 7.4.5.

The formation of **44**, **45** or **47** from **29** was monitored by recording a series of ^{1}H NMR spectra at 298 K over a 17 hour time period after the addition of pyridine, imidazole or dimethylsulfoxide respectively. In the case of pyridine, signals for **29B**, and then **29A**, decrease upon pyridine addition leading first to the detection of **44B** and then **44A**. The proportion of each of these four

complexes was determined using the integral intensities of the hydride resonance *trans* to nitrogen which appears in an NMR spectral region free from peak overlap. A kinetic model was created to fit this time course data that allowed exchange of all four species with the 12 rate constants described in Figure 4.13 and Equations 4.7-4.12 where $[X]_{t-\delta t}$ and $[X]_t$ are the concentration or proportion of species **X** in solution at t-δt and t where ∂t is an incremental time difference. (L is the added coligand pyridine, imidazole or dimethylsulfoxide in the case of n= **44**, **45** or **47** respectively). The model does not take into account the common $[Ir(H)_2(H_2)(\kappa^2\text{-}O OCC(CH_3)NR)(IMes)]$ intermediate that will form irrespective of the identity of the ligand that is lost.
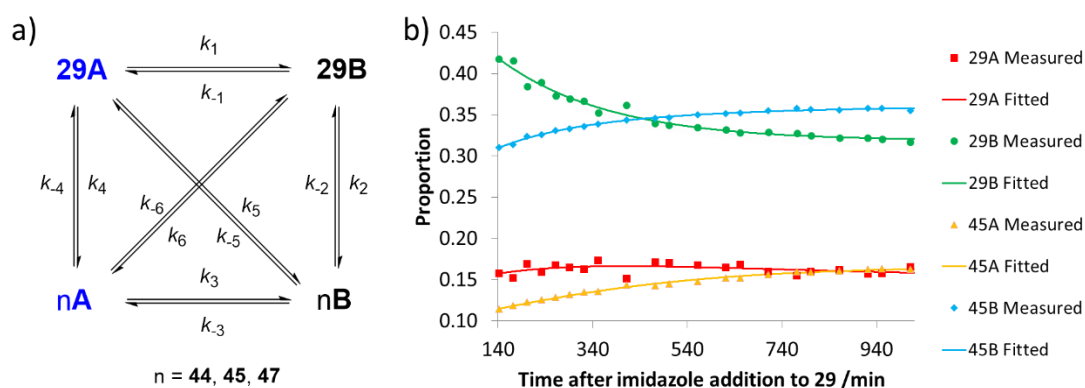
Figure 4.13: a) Exchange model used for kinetic modelling transmission rates for the interconversion between 29 and 44, 45 or 47. b) An example of the kinetic time course for conversion between 29 and 45 (data points) with the fit (solid lines) according to the model described.

$$[\mathbf{29B}]_t = [\mathbf{29B}]_{t-\delta t} + (k_1[\mathbf{29B}] - k_{-1}[\mathbf{29A}] - k_6[L][\mathbf{29B}] + k_{-6}[nA][5] - k_2[\mathbf{29B}][L] + k_{-2}[nB][5])\partial t \qquad (4.7)$$

$$[\mathbf{29A}]_t = [\mathbf{29A}]_{t-\delta t} + (k_{-1}[\mathbf{29B}] - k_1[\mathbf{29A}] - k_4[L][\mathbf{29A}] + k_{-4}[nA][5] - k_5[\mathbf{29A}][L] + k_{-5}[nB][5])\partial t \qquad (4.8)$$

$$[nB]_t = [nB]_{t-\delta t} + (-k_{-2}[nB][5] + k_2[\mathbf{29B}][L] - k_{-3}[nB] + k_3[nA] - k_{-5}[nB][5] + k_5[\mathbf{29A}][L])\partial t \qquad (4.9)$$

$$[nA]_t = [nA]_{t-\delta t} + (k_4[\mathbf{29A}][L] - k_{-4}[nA][5] - k_{-6}[nA][5] + k_6[\mathbf{29B}][L] - k_3[nA] + k_{-3}[nB])\partial t \qquad (4.10)$$

$$[L]_t = [L]_{t-\delta t} + (-k_2[\mathbf{29B}][L] + k_{-2}[nB][5] - k_4[\mathbf{29A}][L] + k_{-4}[nA][5] + k_5[nB][5] - k_{-5}[\mathbf{29A}][L] + k_{-6}[nA][5] - k_6[\mathbf{29B}][L])\partial t \qquad (4.11)$$

$$[5]_t = [5]_{t-\delta t} + (k_4[\mathbf{29A}][L] - k_{-4}[nA][5] - k_5[nB][5] + k_{-5}[\mathbf{29A}][L] + k_6[\mathbf{29B}][L] + k_2[\mathbf{29B}][L] - k_{-2}[nB][5] - k_{-6}[nA][5])\partial t \qquad (4.12)$$

Pseudo first order transmission rates for interconversion between these species were found by minimizing the sum of the squared differences between experimentally determined intensities from the NMR data and values predicted by the kinetic model in the same way as the hydrogen exchange rates described in Section 4.3. Initial data at short reaction times were excluded from the fit due to the release of large amounts of free amine in solution upon its replacement by pyridine in **29B** which in turn may influence the equilibrium position between amine and imine. This same process was repeated to determine the transmission rates for amine replacement in **29** with imidazole or dimethylsulfoxide in **45** and **47** respectively. While all the fitted transmission

rates are given in section 7.6.2 only the rate constants labelled k_2 and k_4 according to Figure 4.13 are given in Table 4.4 and discussed further as these describe interconversion rates from **29A** or **29B** to the coligand replaced products.

Table 4.4: Selected fitted rate constants describing interconversion between 29 and 44, 45, or 47 calculated by fitting the EXSY data (an example is shown in Figure 4.13b) to the model in Figure 4.13a described by Equations 4.7-4.12. A full table including all the rate constants are given in section 7.6.2.

Coligand added to 29	Process	Transmission rate /10^{-6} s^{-1}
Pyridine	**29B → 44B**	9 ± 2
	29A → 44A	7 ± 3
Imidazole	**29B → 45B**	3^{*}
	29A → 45A	2^{*}
Dimethylsulfoxide	**29B → 47B**	6 ± 1
	29A → 47A	0.0^{*}
Equimolar pyridine and imidazole	**29B → 44B**	4.8^{*}
	29A → 44A	0.6^{*}
	29B → 45B	7.8^{*}
	29A → 45A	0^{*}

*rate constants and errors less than 1×10^{-6} s^{-1} were set by this model to 0.

Collectively, these transmission rates are consistent with faster amine loss from **29B** with a higher k of $9 \pm 2 \times 10^{-6}$ s^{-1} than from **29A** where k is $7 \pm 3 \times 10^{-6}$ s^{-1} when pyridine is used as the coligand. Similarly, when imidazole is used a faster effective rate of amine replacement from **29B** to form **44B** is suggested ($k = 3 \times 10^{-6}$ s^{-1}) when compared to **29A** ($k = 2 \times 10^{-6}$ s^{-1}), although both these changes occur slower than those in the pyridine system. Therefore, the rate of imidazole binding to $[Ir(H)_2(\kappa^2\text{-}O\text{OCC}(CH_3)N\text{R})(IMes)]$ must be slower than that of pyridine.

To further confirm this observation, pyridine and imidazole (5 eq. each) were both added to **29** to create an equilibrium mixture of **29**, **44** and **45**. Transmission constants were calculated in a similar way using modified rate equations as described in section 7.6.3. These transmission constants are also presented in section 7.6.3 and support faster amine replacement in **29B** when compared to **29A.** In fact, the rate of amine replacement with pyridine is higher by a factor of four compared to replacement with imidazole.

4.5 Formation of novel iridium complexes by loss of imine

The addition of some coligands cannot only replace the amine, but over long time scales they can replace the imine to form the novel iridium complexes shown in Figure 4.14, all of which have been characterised using 2D NMR spectroscopy and Mass Spectrometry (MS). Full NMR characterisation data is given in section 7.4. For example, the addition of benzyl isocyanide (**48**) initially results in the formation of the amine replacement product, **49B**, with hydride resonances at δ −8.49 and −24.69 ($^2J_{HH}$ = 5.5 Hz). This is confirmed by NOE measurements that show the hydride resonance *trans* to benzyl isocyanide is close in space to the diastereotopic CH_2 resonances of the bound imine (δ 3.72 and 3.87) and the phenyl protons of the isocyanide (δ 6.96) while the hydride resonance *trans* to the imine is close in space to the CH_2 group of the isocyanide (δ 2.13) and the diastereotopic CH_2 resonances of the bound imine (δ 3.72 and 3.87). Over time, products formed from loss of the imine are detected. Two singlets appear at δ −10.22 and −12.34 which also are present in a 1:12 ratio when H_2 is added to a solution of **29** (5 mM), **5** (5 eq.), and **48** (5 eq.). NMR characterisation of this mixture showed the singlet at δ −12.34 resonates from $[Ir(H)_2(CNCH_2Ph)_3(IMes)]Cl$, **50**. This is confirmed from NOE measurements between the hydride and the IMes resonances (δ 7.08, 6.98, 2.28 and 2.00). The hydride resonance shows NOE cross peaks to the CH_2 groups of both *cis* and *trans* isocyanide ligands (δ 4.82 and 4.73) respectively and ~12 Hz couplings to the isocyanide NC and CH_2 carbons at δ 150.78, 113.95 and 117.93 for the *cis* and *trans* sites respectively. The *cis* and *trans* isocyanide ligands are differentiated based on the 1:2 integral intensities for their CH_2 resonances. Mass spectrometry analysis of this mixture confirms that *tris* isocyanide and *bis* isocyanide amine complexes are present. While the identity of the complex resonating at δ −10.22 could not be determined from NMR characterisation due to its low concentration, it is expected to correspond to the *bis* isocyanide amine complex $[Ir(H)_2(CNCH_2Ph)_2(IMes)(NH_2(CH_2)_2Ph)]Cl$, **51**. The formation of iridium(III) isocyanide products have been reported.[225, 226]
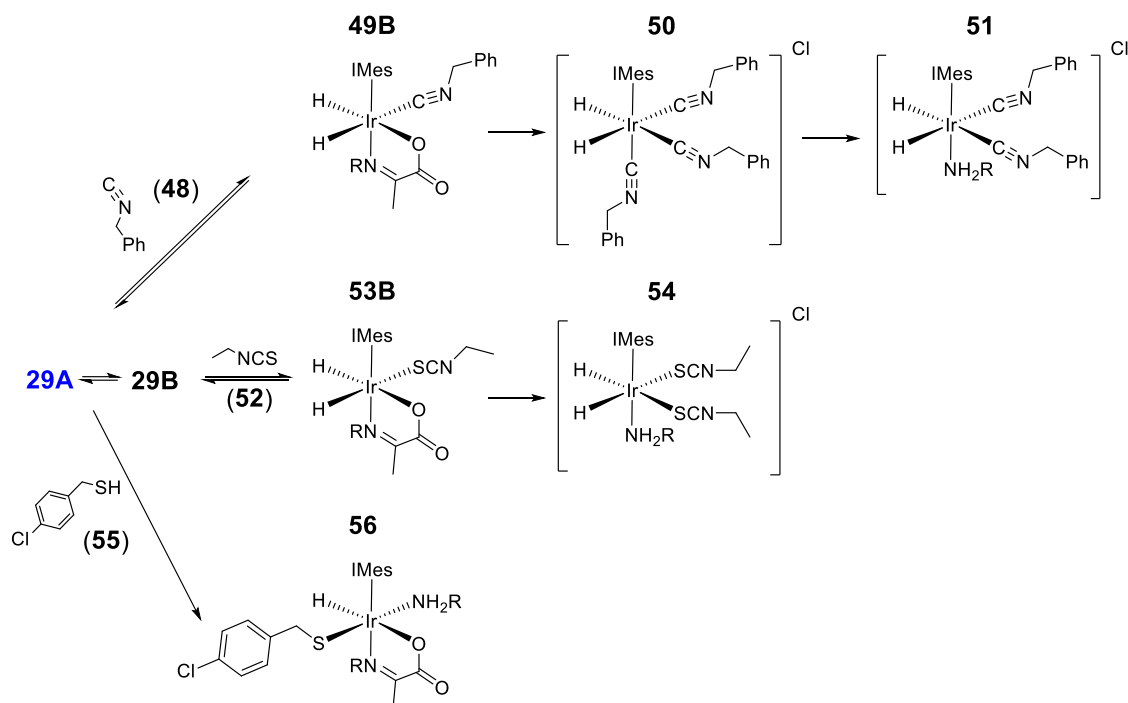
Figure 4.14: Addition of coligands 48, 52, or 55 can form novel iridium complexes with displaced imine ligand where R= (CH₂)₂Ph.

The addition of ethyl isothiocyanate (**52**) (4 eq.) to **29** initially yields resonances for **53B** at δ −17.87 and −28.27 ($^2J_{HH} = 9$ Hz), before proceeding more rapidly to the imine loss complex [Ir(H)₂(IMes)(SCNEt)₂(NH₂(CH₂)₂Ph)]Cl, **54** which yields a single hydride signal at δ −16.05. This is confirmed by NOE cross peaks between the hydride and the IMes ligand (δ 2.16) and the amine ligand (δ 6.96). The ethyl isothiocyanate ligand is located from an NOE cross peak with the amine ligand. The ratio of **29A**, **29B**, **53B** and **54** is 0:7:1:3 after 30 mins. Therefore, the binding of ethyl isothiocyanate is strong enough that it can displace the chelated imine. This is supported by the wide range of reported stable isothiocyanate complexes.[227, 228] However, **54** is not formed when **2** (5 mM), **5** (5 eq.), and ethyl isothiocyanate (5 eq.) react with H₂.

When 4-chlorobenzenemethanethiol (**55**) (5 eq.) is added to **29**, the major product that forms, **56**, gives rise to a single hydride signal at δ −21.56 due to a complex which is stable for several weeks at 278 K. Characterisation using 2D NMR spectroscopy proved it is a monohydride with retained amine and carboxyimine ligands. A 10 Hz coupling is observed between the hydride signal and the ^{13}C NMR resonances of the bound imine at δ 167.86 and 175.51. The hydride resonance shows NOE cross peaks with those of the amine (δ 1.88, 2.08, 2.22, 6.86). Therefore, **56** corresponds to the H₂ replacement product [Ir(H)(κ^2-OOCC(CH₃)NR)(SCH₂PhCl)(IMes)] that is formed by SH oxidative addition. Similar reactivity is known for metal surfaces[229] and bimetallic complexes.[230, 231] Related iridium *N*-heterocyclic carbene complexes that contain bound thiolates have been prepared from the displacement of Ir-Cl under basic conditions.[232] Here, SH activation to form **56** is more likely than a similar thiol deprotonation. Products related to **56** are expected to account for SABRE catalyst deactivation using supported thiols.[116]

4.6 Using hydride hyperpolarisation of iridium carboxyimine complexes for coligand sensing

The hydride ligand chemical shifts of the iridium carboxyimine complexes presented in section 4.4-4.5 (**28**, **29**, **44**, **45**, **47**, **49**, and **53**) are highly sensitive to the identity of the coligand. The largest chemical shift differences, which span a window of ~15.5 ppm, are observed for the hydride position *trans* to the coligand, L, as summarised in Figure 4.15. This sensitivity may allow for unique sensing applications for complexes of this type, with diagnostic hydride NMR chemical shifts indicative of the presence of a particular coligand in a mixture.
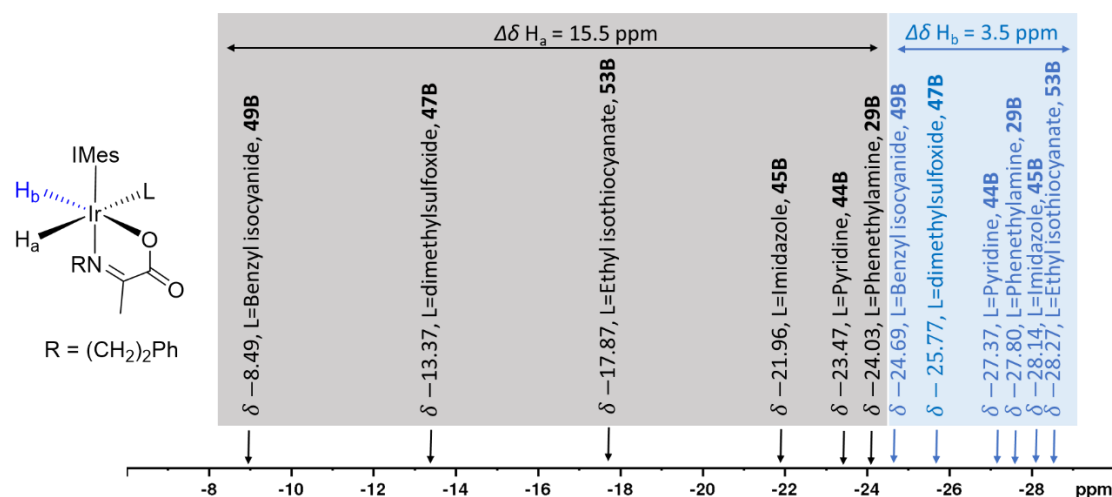
Figure 4.15: Hydride NMR chemical shifts of carboxyimine complexes (at 298 K) are highly sensitive to the identity of the coligand, L.

Hyperpolarisation of the amine replaced products **44**, **45**, **47**, **49**, and **53** is now investigated to test the hypothesis that coligand loss from **29B** is important in mediating *p*-H$_2$ exchange and determining overall NMR signal enhancements and singlet state lifetimes. When equilibrium mixtures of **29** and **44** are shaken with *p*-H$_2$ for 10 seconds at 6.5 mT before being placed into a 9.4 T NMR spectrometer, hyperpolarised hydride resonances of **29B** and **44B** are observed, as shown in Figure 4.16. The hyperpolarised hydride response for **44B** is 100 times more intense than that of **29B** which is now only 2% of its value before pyridine addition. Similar effects can be observed when equilibrium mixtures of **29** and **45** are hyperpolarised. Now, signals for **45B** are 16 times more intense than those of **29B**, which drops to 20% of its intensity prior to imidazole addition, as shown in Figure 4.16. In contrast, equilibrium mixtures of **29** and **49**-**51**, **53**-**54** or **56** do not give significant hyperpolarised ^{1}H or ^{13}C NMR responses for any species.
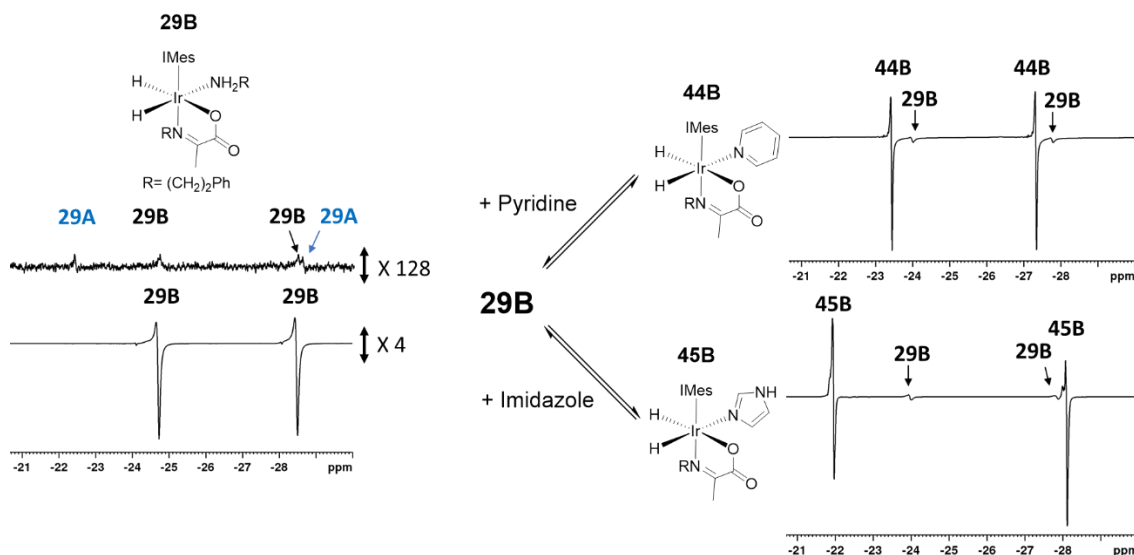
Figure 4.16: Partial thermal (upper) and hyperpolarised (lower) ^{1}H NMR spectra for 29B are shown (left). Shaking equilibrium mixtures of 29 and 44 or 29 and 45 yield hyperpolarised hydride resonances for 29B, 44B and 45B (right). These spectra are all recorded using the same parameters and are shown on a comparable vertical scale (note those of 29 (left) are scaled vertically by the indicated factor).

It might be expected that the large difference in hyperpolarisation levels between starting amine complex **29B** and the amine replacement products **44B** and **45B** is due to more rapid hydrogen exchange in the amine replaced products. In fact, when these hydrogen exchange rates were measured in the same way as those described in Section 4.3, the rate of free hydrogen production from **44B** was slow (0.17 ± 0.01 s^{-1} at 273 K compared to 1.14 ± 0.03 s^{-1} at 273 K for **29B**). No exchange of hydride ligand was noted for **45B**. Therefore, the NMR signal gains of **44B** and **45B** are not due to direct PHIP. Instead, these complexes are predominantly hyperpolarised by coligand addition to the hyperpolarised five coordinate reaction intermediate that forms upon amine loss from **29B**. Furthermore, T_1 measurements of 3.5 s, 7.7 s, and 7.0 s for the hydride ligands of **29B**, **44B** and **45B** respectively suggest that the more intense hydride signals of **44B** and **45B**, upon formation from **29B**, is aided by slower relaxation rather than direct hydrogen exchange effects.

The NMR signal enhancement of **45B** compared to **29B** in the equilibrium mixture of **29** and **45** is higher compared to **44B** and **29B**. This suggests that pyridine is more effective than imidazole at competing with the amine for the free iridium binding site. The overall higher signals of the equilibrium mixture of **29** and **45** is due to higher amounts of **29B** present in this equilibrium mixture (32%) meaning more of the hyperpolarised five coordinate intermediate [Ir(H)$_2$(κ^2-OOCC(CH$_3$)NR)(IMes)] is there to be trapped when compared to the **29/44** mixture (12%).

Interestingly, when a sample of both pyridine and imidazole (5 eq.) are added to **29** to form an equilibrium mixture of **29**, **44** and **45** this sample yielded hyperpolarised resonances for **29B**, **44B** and **45B** when shaken with p-H$_2$ for 10 seconds at 6.5 mT, as shown in Figure 4.17a. Higher levels of hydride hyperpolarisation in **45B** are observed compared to **44B** (in a ratio of 1:3:5 for **29B**, **44B** and **45B** respectively). The kinetics of these systems, which were investigated in

section 4.4, can be considered to establish links between hyperpolarised signal intensities and the rate and strength of coligand binding to the five coordinate [Ir(H)$_2$(κ^2-OOCC(CH$_3$)NR)(IMes)] intermediate. It might be expected from kinetic considerations that the hyperpolarised signals for **44B** should be four times larger than **45B** mirroring the four times faster rate of amine replacement with pyridine. The fact that this does not appear to be the case is unlikely related to different relaxation times of the hydride sites in these complexes, but rather due to different extents of polarisation transfer to other sites in these metal complexes and the possibility of direct PHIP occurring to different extents in each complex. For example, polarisation is localised on the hydride ligands of **45B** whereas in **44B** polarisation spreads into the ^{1}H sites of the pyridine coligand. This was confirmed when an addition of equimolar pyridine-d_5 and imidazole was made to **29**. Now, the hyperpolarised hydride signals are observed in a 1:6:5 intensity ratio for **29B**, **44B-d_5**, and **45B** respectively. Here, **44B-d_5** now exhibits a hydride signal higher than **45B** as the spread of hyperpolarisation into pyridine has been reduced. While these hyperpolarisation levels are now consistent with a faster rate of pyridine binding compared to imidazole, outstanding differences in H$_2$ exchange rates mean they do not completely mirror the factor of four difference in observed interconversion rate constants discussed earlier. This suggests that while these complexes are formed from the same common intermediate the rate constant ratio of the formation of each cannot be used as a measure to predict or evaluate their hyperpolarisation levels, or *vice versa*.
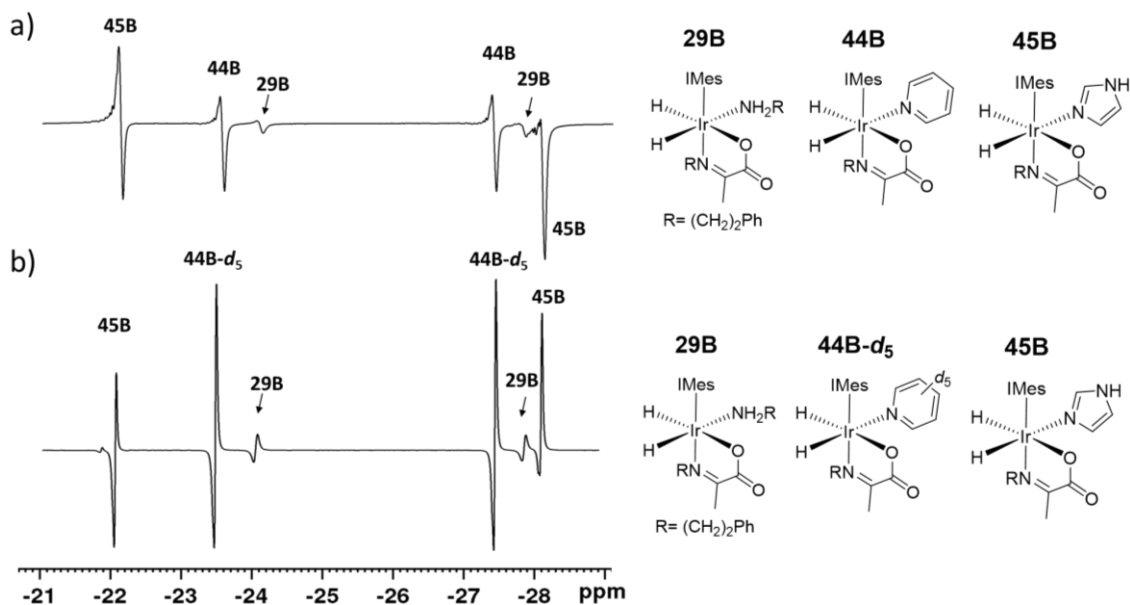
Figure 4.17: Partial hyperpolarised ^{1}H NMR spectra for an equilibrium mixture of a) 29, 44 and 45 b) 29, 44-d_5 and 45 in dichloromethane-d_2 (0.6 mL) shaken with 3 bar p-H$_2$ for 10 seconds at 6.5 mT. Spectra are shown on the same vertical scale.

While the chemical shifts of the iridium carboxyimine complexes presented are sensitive to the coligand identity their hyperpolarisation levels cannot always be used as an indication of the coligand binding strength. Despite this, these complexes have NMR chemical shifts sensitive to a range of different coligands. It is therefore expected that they could have novel sensing

applications in the future as their chemical shifts and enhanced NMR signals can provide information on the identity of coligands in solution. This may have future beneficial applications in detecting low concentration coligands in solution.

4.7 Effect of coligand, L, on $^{13}C_2$ NMR signal enhancements and singlet order of iridium carboxyimine complexes

Hydrogen exchange in iridium complexes **44**, **45**, and **47** containing pyridine, imidazole and dimethyl sulfoxide respectively is significantly reduced compared to **28** and **29**. The effect of this on the $^{13}C_2$ singlet order of the bound imine is investigated further. Upon addition of the coligands pyridine and imidazole to solutions of **29**, hyperpolarised NMR responses for the $^{13}C_2$ labelled imine cores of **44B** and **45B** at δ 174.79 and 167.71 ($^{1}J_{CC}$ = 66.5 Hz) and δ 175.63 and 166.76 ($^{1}J_{CC}$ = 66.5 Hz) respectively are observed. The $^{13}C_2$ NMR resonances of **44B** and **45B** partially overlap with those of **29B** suggesting that diagnostic coligand identification cannot be made based on 1D ^{13}C NMR spectroscopy. The hyperpolarised resonances of **44B** are of similar intensity to **29B**, while those of **45B** are 17 times smaller than **29B** in the **29/45** mixture, as shown in Figure 4.18. Interestingly, the hyperpolarised $^{13}C_2$ NMR resonances of **44B** and **45B** do not exhibit the unusual spectral patters typical of the singlet state of **29B**. This is consistent with rapid decoherence of $^{13}C_2$ singlet order leaving a dominant amount of Zeeman magnetisation. The importance of hydrogen exchange in refreshing $^{13}C_2$ singlet order within **28B** and **29B** was discussed in section 4.3, therefore it is perhaps unsurprising that any $^{13}C_2$ singlet order within **44B** and **45B**, which contain slower p-H_2 exchange, decoherers before it can be observed.
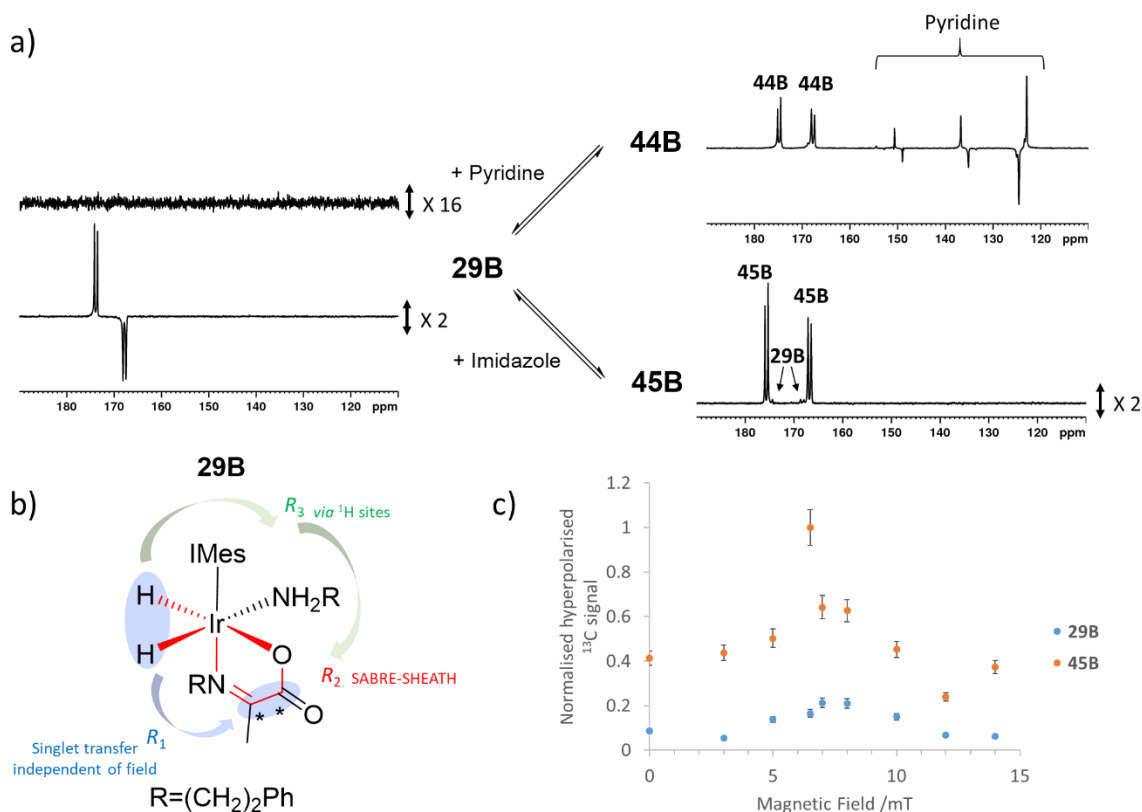
Figure 4.18: a) Partial thermal and hyperpolarised ^{13}C NMR spectra for 29B are shown. Upon addition of the coligands pyridine or imidazole, 44B and 45B form which exhibit hyperpolarised ^{13}C NMR resonances in addition to those of 29B. These spectra are all recorded using the same parameters and are shown on a comparable vertical scale (note the indicated scaling factors). b) Different routes to create hyperpolarised ^{13}C magnetisation within 29B c) Field dependence of ^{13}C hyperpolarisation when an equilibrium mixture of 29 and 44 are shaken with p-H$_2$ at varying polarisation transfer fields.

There are three mechanisms, summarised in Figure 4.18b, in which hyperpolarised ^{13}C$_2$ magnetisation can be created in these complexes. R_1 describes singlet magnetisation transfer from p-H$_2$ which is independent of magnetic field at low field.[49] R_2 concerns direct polarisation transfer to create ^{13}C$_2$ Zeeman magnetisation at ultra-low μT field (SABRE-SHEATH).[88, 233] Finally, R_3 describes Zeeman magnetisation transferred from the hydrides to ^{13}C$_2$ sites *via* non-hydride ^{1}H sites which is likely to be optimal at 6.5 mT.[125] For mixtures containing solely **28** or **29** shaken at 6.5 mT the resonance condition for R_1 is most optimally met and singlet magnetisation profiles dominate. The maintenance of the singlet state in **28B** and **29B** is prolonged due to ongoing p-H$_2$ exchange but it is reduced in **44B** and **45B** due to their much slower H$_2$ exchange rates. Singlet decoherence during the formation of **44B** and **45B** is efficient and Zeeman magnetisation is predominantly observed. When **45B** is mixed with p-H$_2$ at different polarisation transfer fields a hyperpolarised ^{13}C$_2$ NMR response for **45B** is observed at all magnetic fields, although maximum signal intensity is achieved at 6.5 mT as shown in Figure 4.18c. This suggests that some field independent singlet magnetisation (R_1) is created as well as field dependant Zeeman magnetisation (R_3) which is optimum at 6.5 mT. A signal can also be achieved under SABRE-SHEATH conditions when shaking in a mu-metal shield (~ 1 μT) (R_2).

4.8 Isotopic labelling to improve NMR signal enhancements of 28B, 29B and 44B.

In order to preserve hyperpolarised $^{13}C_2$ singlet magnetisation within **28B** and **29B** the coupled spin pair of the imine core should be isolated from other active spins in the complex which could act as relaxation sources through dipolar coupling.[214] Deuterium labelling has often been used as a method to increase the lifetime of hyperpolarised signals by reducing the number of sites to which polarisation can spread and slowing relaxation pathways.[76, 98, 102, 111] Therefore, a series of isotopically labelled analogues of **28** were synthesized, the structures of which are all shown in Figure 4.19. The isotopologues **28B-d_{14}** and **28B-d_{38}** were synthesized using deuterium labelled amine (**4-d_7**) and catalyst (**2-d_{24}**) precursors in the same process shown in Figure 4.2. When **28B-d_{14}** and **28B-d_{38}** were shaken with 3 bar p-H_2 for 10 seconds at 6.5 mT their $^{13}C_2$ NMR signal enhancements were higher than their *protio* analogues (up to 560-fold for **28B-d_{38}** compared to 420-fold for **28B**, as shown in Table 4.5). A similar increase in ^{13}C NMR signal gain upon deuterium labelling was observed when the isotopologue **29B-d_{32}** was synthesised from **5-d_4** and **2-d_{24}** (340-fold $^{13}C_2$ NMR signal enhancements for **29B-d_{32}** compared to 280-fold for **29B**).
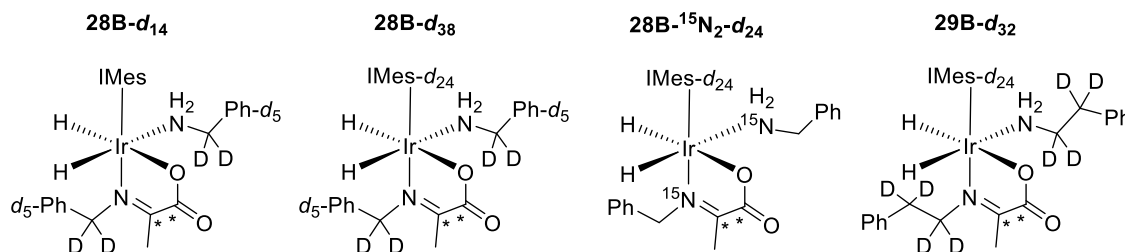
Figure 4.19: Isotopologues of 28B and 29B synthesised in this work.

The low field singlet state lifetimes (T_{LF}) of the isotopologues **28B-d_{14}**, **28B-d_{38}**, and **29B-d_{32}** were measured in the same way as those of **28B** and **29B** (described in section 4.2). Hyperpolarised $^{13}C_2$ singlet magnetisation in **28A-d_{14}**, which contains only deuterium labels in its amine and imine ligand, has a lifetime of 7.9 ± 0.9 s which is comparable to that of **28B** (10.9 ± 1.1 s). However, when **28B-d_{38}** was created by deuterating positions of its carbene, amine, and imine ligands, a T_{LF} of 19.9 ± 1.0 s was observed which is significantly longer than that of **28B**. This suggests that interactions with the carbene ligand are important in mediating singlet ^{13}C NMR relaxation within these complexes and subsequently, this relaxation pathway can be suppressed when the carbene is deuterated.

It has been reported that ^{13}C hyperpolarisation can be increased by removing quadrupolar ^{14}N nuclei in similar systems.[88] Therefore, a **28B-$^{15}N_2$-d_{24}** isotopologue was synthesized in which ^{15}N-labelled **4** and **2-d_{24}** were used as precursors. The resulting $^{13}C_2$ NMR signal enhancement of 750-fold and lifetime of 17.5 ± 3.9 s suggests that the presence of ^{15}N has not extended singlet lifetime

in this case, although a higher $^{13}C_2$ NMR signal enhancement compared to **28B-d_{38}** (560-fold) indicates that polarisation transfer to ^{13}C sites may be enhanced by transfer *via* ^{15}N.

Table 4.5: NMR signal enhancements and singlet lifetimes for isotopologues of 28B and 29B. NMR signal enhancements are an average of three measurements.

Complex	ε ^1H hydride /fold	ε $^{13}C_2$ imine /fold	$^{13}C_2$ singlet lifetime /s
28B	N/A*	420 ± 20	10.9 ± 1.1
28B-d_{14}	110 ± 10	510 ± 20	7.9 ± 0.9
28B-d_{38}	300 ± 20	560 ± 30	19.9 ± 1.0
28B-$^{15}N_2$-d_{24}	480 ± 40	750 ± 40	17.5 ± 3.9
29B	N/A*	280 ± 10	8.8 ± 1.4
29B-d_{32}	740 ± 40	340 ± 20	-

*^1H hydride signals cannot be easily quantified in these cases due to their broad linewidths with severe internal cancellation.

As deuterium labelling was able to enhance the singlet state lifetime of **28B**, the effect on **44B** was also examined by using **5-d_4**, **2-d_{22}**, and pyridine-d_5 to create an equilibrium mixture of **29B-d_{32}** and **44B-d_{33}**. The structure of these complexes are shown in Figure 4.20 and their NMR signal enhancements are given in Table 4.6. The resulting $^{13}C_2$ NMR signals of both **29B-d_{32}** and **44B-d_{33}** after polarisation transfer at 6.5 mT are stronger than their *protio*-analogues, as shown in Table 4.5. Deuterium labelling restricts the R_3 transfer route, which can now only occur through the non-labelled CH_3 group of the imine or the NH_2 group of the amine. This may favour R_1 and consequently, the singlet spin order of **44B-d_{33}** does not decohere as rapidly in this case. When repeated at 6.5 mT with a 5 second storage period in a mu-metal shield before detection the signals for **44B-d_{33}** lose much of their singlet profile due to decoherence effects at low field (~6 mT) during these 5 seconds. Synthesizing **44B** with ^{15}N-labeled pyridine to create **44B-^{15}N** gives rise to a $^{13}C_2$ NMR signal profile more typical of the singlet state, as shown in Figure 4.20c. This suggests that in this case the ^{15}N label enhances singlet state retention and supports that quadrupolar ^{14}N plays a role in singlet relaxation within **44B**.
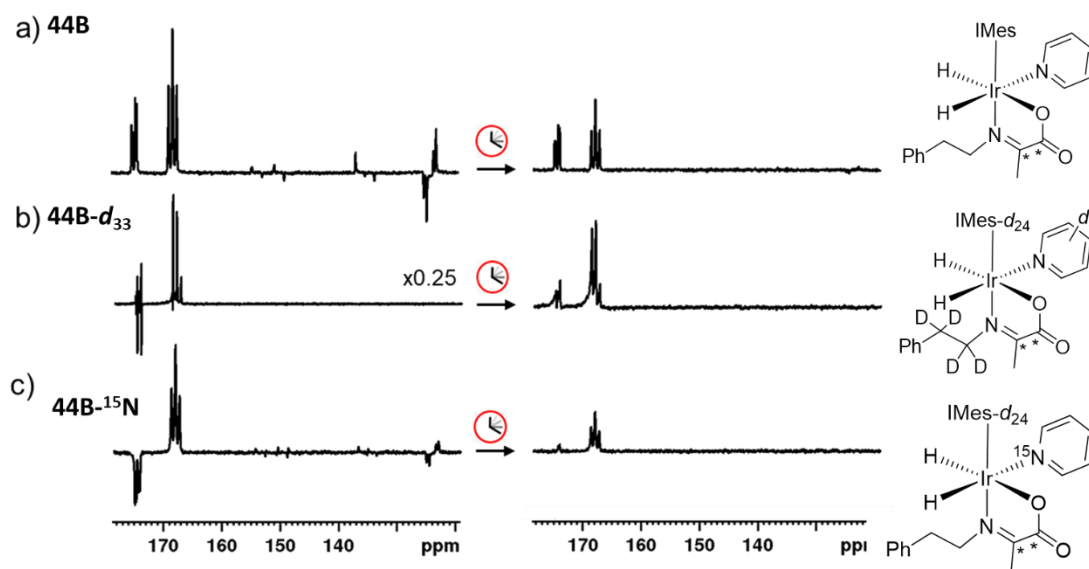
Figure 4.20: Partial hyperpolarised ^{13}C NMR spectra for equilibrium mixtures of a) 29B and 44B, b) 29B-d_{32} and 44B-d_{33}, c) 29B and 44B-^{15}N after shaking for 10 seconds at 6.5 mT (left) and after shaking for 10 seconds at 6.5 mT and then leaving in a mu-metal shield for 5 seconds (right). These spectra are all recorded using the same parameters and are shown on a comparable vertical scale (note the indicated scaling factors). Accompanying ^{13}C NMR signal enhancements are shown in Table 4.6.

Table 4.6: NMR signal enhancements for equilibrium mixtures of isotopologues of 29B and 44B. NMR signal enhancements are an average of three measurements.

Complex	ε ^{1}H hydride /fold	ε $^{13}C_2$ imine /fold	ε ^{13}C Total pyridine$^&$ /fold
29B /44B	N/A*	**29B**: 220 ± 25	-
	N/A*	**44B**: 190 ± 20	400 ± 20
29B-d_{32} /44B-d_{33}	**29B-d_{32}**: 720 ± 35	**29B-d_{32}**: 330 ± 20	0
	44B-d_{33}: 380 ± 15	**44B-d_{33}**: 260 ± 15	-
29B /44B-^{15}N	**29B**: 230 ± 15	**29B**: 230 ± 20	190 ± 15
	44B-^{15}N: 390 ± 20	**44B-^{15}N**: 260 ± 15	-

*^{1}H hydride signals cannot be easily quantified in these cases due to their broad linewidths with severe internal cancellation.
$^&$Includes hyperpolarised resonances for pyridine bound in **44** and free in solution.

Hyperpolarised ^{13}C NMR resonances of bound and free pyridine are also observed in **44B** in addition to those of the labelled $^{13}C_2$ imine as shown in Figure 4.20a. No ^{13}C NMR signals of the amine or imidazole ligands of **29B** or **44B** are visible. This suggests that the exchange rate of pyridine in **44B** is suitable to observe polarisation transfer from p-H$_2$ derived hydrides whereas in the case of **29B** and **45B** coligand exchange is too fast or slow respectively to observe appreciable polarisation build-up of the coligand. Hyperpolarised ^{13}C NMR signals for pyridine are not observed in **44B-d_{33}**, as shown in Figure 4.20. This suggests that at this 6.5 mT polarisation transfer field the main route in which ^{13}C sites of bound pyridine are hyperpolarised in SABRE complexes occurs through the pyridine proton sites and direct transfer, or nitrogen

mediated transfer, is less efficient. **44B-^{15}N** yielded hyperpolarised ^{13}C NMR responses for pyridine of lower intensity than in **44B**. Therefore, at this polarisation transfer field there is no significant polarisation transfer pathway between hydride ligands and ^{13}C sites of pyridine and carboxyimine *via* ^{15}N.

The presence of coligands in solution causes rapid decoherence of ^{13}C$_2$ singlet order which is likely related to suppression of p-H$_2$ exchange caused by coligand binding to the five coordinate [Ir(H)$_2$(κ^2-OOCC(CH$_3$)NR)(IMes)] rather than binding of fresh p-H$_2$. Despite this, ^{13}C$_2$ NMR signal enhancements can be increased and partial singlet order retained by deuterium labelling. The use of ^{15}N labelling in the coligand is able to retain singlet order within the bound imine core.

4.9 Conclusions

In this chapter the hyperpolarisation of some novel metal complexes using SABRE is investigated. The formation of [Ir(H)$_2$(κ^2-OOCC(CH$_3$)NR)(NH$_2$R)(IMes)] (where R = CH$_2$Ph (**28**) and R = (CH$_2$)$_2$Ph (**29**)) from the *in situ* condensation reaction between amine and pyruvate has been presented in Chapter 3. In solution, these complexes were found to exist as two isomers, labelled **A** or **B** of Figure 4.2, that are distinguished depending on the coordination geometry of the imine. Although a third isomer, **C**, is possible, it was not detected in this work. When solutions of **28** or **29** are shaken with p-H$_2$, strongly hyperpolarised hydride ^{1}H and ^{13}C NMR resonances of the non-exchanging coordinated imine are observed. These complexes present a unique opportunity to explore the hyperpolarisation of metal complexes further and develop novel applications for their use.

This chapter has shown that iridium carboxyimine complexes can exist as naturally occurring refreshable heteronuclear singlet states. Only those isomers denoted as **B** of Figure 4.2 exhibit rapid hydrogen exchange and consequently produce high levels of hydride NMR signal enhancements through SABRE. When the imine is 1,2-[^{13}C$_2$] labelled, polarisation transfers naturally from hydride sites to create ^{13}C$_2$ singlet order in the imine at low field (μT). The lifetimes of the ^{13}C$_2$ singlet state was determined as 10.9 ± 1.1 s in **28B** and 8.8 ± 1.4 s for **29B**. When comparing these complexes, **28B** undergoes a faster rate of H$_2$ loss (15.5 ± 0.6 s^{-1}) compared to **29B** (4.11 ± 0.06 s^{-1}) at 283 K which is expected to account for the higher ^{13}C NMR signal enhancements (420-fold for **28B** versus 280-fold for **29B**). These ^{13}C NMR signal enhancements and singlet lifetimes can be extended to 750-fold and 20 s respectively when isotopic labelling techniques are used to create **28B-^{15}N$_2$-d_{24}**. To form such heteronuclear singlet order within a metal complex is a significant observation and further investigation into the mechanism of hydrogen exchange was performed. EXSY and DFT studies support a hydrogen exchange mechanism preceded by dissociative amine loss to form a key five coordinate intermediate [Ir(H)$_2$(κ^2-OOCC(CH$_3$)NR)(IMes)L].

These ideas have been extended further by varying the identity of the coligand (L of Figure 4.2) in order to create a range of novel [Ir(H)$_2$(κ^2-OOCC(CH$_3$)NR)(IMes)L] complexes in which the coligand L is amine (**44**), pyridine (**45**), dimethylsulfoxide (**47**), benzyl isothiocyanide (**49**) or ethyl isothiocyanate (**53**). In the case of **49** and **53**, further reaction occurs to yield products that include [Ir(H)$_2$(CNCH$_2$Ph)$_3$(IMes)]Cl (**50**), [Ir(H)$_2$(CNCH$_2$Ph)$_2$(IMes)(NH$_2$(CH$_2$)$_2$Ph)]Cl (**51**) and [Ir(H)$_2$(SCNEt)$_2$(NH$_2$(CH$_2$)$_2$Ph)]Cl (**54**). Upon the addition of thiol a novel SH activated [Ir(H)(κ^2-OOCC(CH$_3$)NR)(SCH$_2$PhCl)(IMes)] product (**56**) is formed. When hyperpolarised with p-H$_2$, complexes in which L is amine, pyridine, or imidazole show significant ^{1}H hydride and ^{13}C$_2$ imine NMR signal enhancements. Dissociative coligand loss is a key step in rapid p-H$_2$ exchange and the presence of coligands can effectively trap such hyperpolarised intermediates. Despite this, interpretation of hyperpolarised signal intensities is not always indicative of the rates of coligand binding to the same intermediate. While coligand addition causes rapid decoherence of ^{13}C$_2$ singlet order this can be preserved to some extent by isotopic labelling techniques. A route is developed to produce strong ^{13}C NMR signal gains in these complexes using isotopic labelling (up to 750-fold) and NMR signal enhancements for free coligands including pyridine (400-fold) could be used to allow its quantification from a mixture of coligands.

A common strategy employed in improving substrate NMR signal enhancements in SABRE is to use coligands to block catalyst binding sites such that polarisation transfer is concentrated into only one bound substrate.[102, 155] Chelating ^{12}C-carboxyimines may provide a viable route to increasing substrate polarisation by blocking coordination sites. These complexes could be used for exciting sensing applications in the future as their hydride chemical shifts are highly sensitive to the identity of bound ligands. They could in principle be applied to detect any low concentration molecule in solution, as long as the molecule is able to coordinate iridium. Distinguishing mixtures of the coligands tested here based on their aromatic or aliphatic ^{1}H NMR chemical shifts can be challenging to due severe peak overlap in this spectrally crowded region. The indirect detection of these molecules from the hydride chemical shifts of their carboxyimine complexes could provide indicative spectral patterns in a typically uncrowded region of ^{1}H NMR. Iridium carboxyimine complexes could therefore act as unique sensors with changes in ^{1}H hydride NMR chemical shift (~15.5 ppm) and hydride hyperpolarisation levels used to give information about the identity and binding strengths of coligands in solution. These complexes provide a rare example of naturally occurring heteronuclear singlet states existing in a transition metal complex. These complexes establish a route to create a continually refreshable heteronuclear singlet state in a metal complex through a reversible interaction with p-H$_2$ and could be used for novel sensing and hyperpolarisation applications in the future.

Chapter 5. Using sulfoxide-based magnetisation transfer catalysts to hyperpolarise pyruvate

5.1 Introduction

Magnetic Resonance Imaging (MRI) can produce anatomically detailed images of living tissues and is widely used for the clinical diagnosis of disease.[4] However, the fundamental principles of MRI rely on those of Magnetic Resonance (MR) which are insensitive on a molecular level. This usually necessitates imaging the large abundance of water protons in the body to get sufficient signal.[4] MR images therefore map out water molecules in the body and can produce images of exquisite contrast by distinguishing tissues based on the different longitudinal relaxation times (T_1) of their water protons.[6] While this can give information on the structure and morphology of living tissues, it gives no detail about the metabolic function of such tissues. Imaging individual biomolecules, rather than bulk water molecules, allows real time examination of the metabolic state of tissues in the body.[5] To do this requires significant signal gains to observe and image low concentration biomolecules, drugs, or metabolites in the body.[5]

Hyperpolarisation techniques can address these sensitivity problems.[143, 234, 235] Of these, Dynamic Nuclear Polarisation (DNP) has found the most success in clinical applications and can produce ^{1}H and ^{13}C NMR signals with polarisation levels of 92% and 70% in just 150 seconds and 20 minutes respectively.[30] DNP has been applied to the hyperpolarisation of agents such as pyruvate,[132, 133, 135, 136, 139-141, 146] succinate,[68, 69] fumarate[113, 146] and the enhanced MR signals have allowed the *in vivo* detection of these biomolecules and their metabolic by-products. The most widely studied of these molecules for use as a hyperpolarised metabolic tracer is [^{13}C]-pyruvate.[132, 133, 135, 136, 139-141, 146] One reason for this is that rapid anaerobic conversion of pyruvate to lactate in cancer cells (the Warburg effect)[138] can allow differentiation between healthy and cancerous tissue from differences in pyruvate to lactate conversion, a feat not possible using traditional H_2O-based MRI. As a result, hyperpolarised [^{13}C]-pyruvate has been used as an *in vivo* contrast agent culminating in human prostate cancer studies.[132] For these purposes, pyruvate is typically hyperpolarised in a batch process using DNP which can take >20 minutes and requires a specialist DNP polariser which is only available to select institutions.[38]

In contrast, *Para*-Hydrogen Induced Polarisation (PHIP) does not require such instrumentation.[32, 34, 45] PHIP uses *p*-H_2, an isomer of hydrogen gas that exists as a nuclear spin singlet, as its source of polarisation. Since the 1990s, *p*-H_2 has typically been incorporated into a substrate *via* a hydrogenation reaction which has limited the method to molecules that contain unsaturated

functionality.[31, 32, 61, 66] A variant of PHIP termed *Para*-Hydrogen Induced Polarisation by Side Arm Hydrogenation (PHIP-SAH) has been used to alleviate this restriction.[70, 73] In this approach, substrates like pyruvate (and others) are derivatised as an ester with an unsaturated side arm. Upon hydrogenation of this side arm with p-H$_2$ and a field cycling step to transfer polarisation from the side arm to the ^{13}C labelled carboxylate, the side arm is rapidly cleaved in a hydrolysis step to yield hyperpolarised pyruvate in aqueous solutions. While this approach is considered cheaper and faster than DNP, it is still a batch process and involves chemical alternation of the target molecule. Reported ^{13}C pyruvate polarisation levels achieved using PHIP-SAH are lower than those produced using DNP (5%[73] compared to 70%[38])

Alternatively, Signal Amplification By Reversible Exchange (SABRE) is a non-hydrogenative p-H$_2$-based method that transfers polarisation from p-H$_2$ to a substrate when both are in reversible exchange with an iridium catalyst.[76] Catalytic magnetisation transfer occurs *via* the formation of temporary *J*-coupled networks within the inorganic complex.[78] SABRE is therefore not a batch process and can hyperpolarise molecules continually without their chemical alteration.[82, 170] SABRE has been most successfully applied to the hyperpolarisation of molecules with *N*-donor motifs that coordinate to iridium. *N*-heterocycles such as pyridine,[76, 96-99] nicotinamides,[76, 83, 100] pyrazines,[97, 98] and pyrazoles[99] provide common examples although other *N*-functionalities including nitriles,[101] amines[106] and diazirines[55, 86, 208] have also been used. *a*-Keto acids such as pyruvate represent structures usually thought of as being incompatible with hyperpolarisation using SABRE as they contain no *N*-donor sites required for iridium ligation.

Recently, SABRE-Relay, has allowed the hyperpolarisation of non-ligating substrates which receive hyperpolarised protons *via* exchange from a carrier.[106, 108] Amines have been reported to act as suitable hyperpolarisation carriers that both receive polarisation through reversible iridium ligation and relay this polarisation to other non-ligating substrates through proton exchange.[106] SABRE-Relay has expanded the types of molecules that are amenable to hyperpolarisation using SABRE to molecules such as alcohols[108] and sugars.[107] The application of SABRE-Relay to alcohols, natural products, lactates, and pyruvate is explored in Chapters 2 and 3. Pyruvate contains a labile carboxylic acid proton that might become hyperpolarised *via* SABRE-Relay. However, when SABRE-Relay is used to hyperpolarise pyruvate in this way, ^{13}C NMR signal enhancements of just $\sim$50-fold were achieved.[104] While this can be increased to 65-fold by tuning the catalyst and carrier, as discussed in Chapter 3, a more significant problem is the rapid *in situ* condensation of the amine carrier with pyruvate. This reaction forms products of the type [Ir(H)$_2$(κ^2-*O*OCC(CH$_3$)*N*R)(IMes)(NH$_2$R)] which deactivate the catalyst to polarisation of pyruvate. The formation of these complexes is detailed in Chapter 3 and their hyperpolarisation properties are explored further in Chapter 4. This decomposition provides a serious challenge when hyperpolarising pyruvate using SABRE-Relay as the hyperpolarised signals are weak and are rapidly destroyed by chemical transformation. SABRE-Relay can therefore only become a viable tool for hyperpolarising pyruvate if it is redesigned to involve carrier molecules with labile

protons that hyperpolarise without chemically reacting with pyruvate: this presents a huge challenge. There are also other limitations of SABRE-Relay associated with the presence of water necessary to dissolve pyruvate in SABRE-Relay compatible solvents.[107]

A more fruitful approach may be to create an active magnetisation transfer catalyst that contains ligated pyruvate, and undergoes both pyruvate and p-H_2 exchange. If such a catalyst can be formed there could be potential to hyperpolarise pyruvate *via* SABRE with more substantial signal gains as the process would not rely on relayed proton exchange effects. Instead, polarisation could be transferred directly from p-H_2 derived hydride ligands to ^{13}C sites in the coordinated pyruvate. In fact, the coordination of a-keto acids to metals has been reported in the literature and interactions between pyruvate and the metal active sites of various enzymes has been studied since the 1960s.[236, 237] Pyruvate and related structures, such as lactate and oxalate, are typically able to coordinate metals through a variety of different coordination modes which are summarised in Figure 5.1.[238] While pyruvate does not contain the typical *N*-donor functionality common to substrates hyperpolarised using SABRE,[79] it does contain two *O*-donor sites in the form of its carboxylate (COO^-) and ketone (CO) groups which give rise to two possible coordination modes (mode 1 and 2 respectively of Figure 5.1). A κ^2 bidentate binding mode involving coordination through both carboxylate and ketone groups (mode 3 of Figure 5.1) is also possible. Coordination of pyruvate to various different metals through these binding modes has been reported.[198, 236, 237, 239, 240] For example, coordination of pyruvate to manganese active sites of a pyruvate carboxylase enzyme *via* its ketone group (mode 2 of Figure 5.1) has been determined from relaxation measurements of the adjacent CH_3 group.[240] Similar binding modes to cobalt and copper have been confirmed using relaxation and electron spin resonance (ESR) measurements.[236, 237] Alternatively, X ray crystal structures of a magnesium-pyruvate complex found within bacteria have revealed κ^2 pyruvate coordination (mode 3 of Figure 5.1).[239] More recently, a series of metal pyruvate hydrazine complexes of the form [M(N$_2$H$_2$)$_n$(pyruvate)$_m$] were synthesised where M = Co, Ni, Zn or Cd. These species were characterised using a combination of IR, powder diffraction, magnetic moment calculations and thermogravimetric analysis and were found to be octahedral species containing four pyruvate ligands bound through the carboxylate moiety (mode 1 of Figure 5.1).[198] Some examples of reported metal pyruvate complexes are shown in Figure 5.1. An additional κ^2 mode in which pyruvate binds through both oxygen atoms of its carboxylate group (mode 4 of Figure 5.1) could be possible.
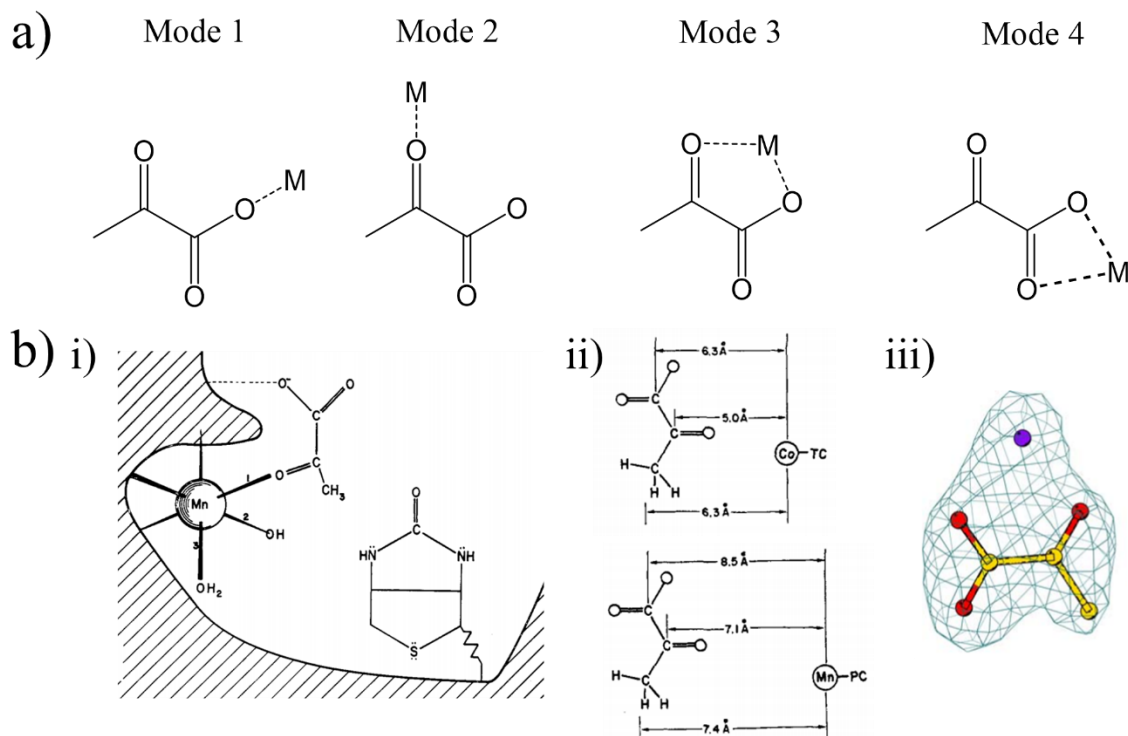
Figure 5.1: a) Coordination modes of pyruvate to a metal centre. Mode 1 involves coordination through the carboxylate oxygen while mode 2 involves the ketone oxygen. Bidentate coordination through both motifs (mode 3) or both oxygen sites of the carboxylate group (mode 4) are also possible. b) Reported examples of pyruvate coordination to a metal centre i) Proposed structure of a pyruvate carboxylase-pyruvate complex in solution. Reprinted (adapted) with permission from A. S. Mildvan and M. C. Scrutton, *Biochemistry*, 1967, 6, 2978-2994 Copyright 1967 American Chemical Society[240] ii) Comparison of the geometries of the transcarboxylaseCo(II)-pyruvate and carboxylase-Mn(II)-pyruvate determined from EPR and NMR measurements. Reprinted (adapted) with permission from C.-H. Fung, A. S. Mildvan and J. S. Leigh Jr, *Biochemistry*, 1974, 13, 1160-1169 Copyright (1974) American Chemical Society[236] iii) Electron density corresponding to pyruvic acid and Mg^{2+} in Salmonella typhimurium 2-methylisocitratelyase determined by X ray crystallography. Reprinted from D. K. Simanshu, P. S. Satheshkumar, H. S. Savithri and M. R. N. Murthy, Crystal structure of Salmonella typhimurium 2-methylisocitrate lyase (PrpB) and its complex with pyruvate and Mg^{2+}, *Biochem. Biophys. Res. Commun.*, 2003, 311, 193-201. Copyright (2003), with permission from Elsevier.[239]
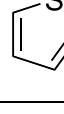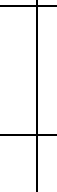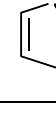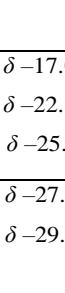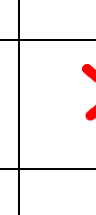
While it is clear that pyruvate ligation to metals is possible from the range of different examples reported,[198, 236, 239, 240] no examples of iridium pyruvate complexes could be found in the literature. The ability of some different coligands to coordinate to iridium and the hyperpolarisation of the novel iridium complexes that formed was explored in Chapter 4. The work presented in this chapter aims to investigate the formation of iridium pyruvate complexes by using appropriate coligands to help overcome weak iridium pyruvate ligation. The properties of these complexes will be investigated to establish whether they can transfer p-H_2 derived singlet order from hydride ligands to ligated pyruvate. It is anticipated that using such species as magnetisation transfer catalysts could hyperpolarise pyruvate in a cheap and reversible method without relying on inefficient relayed proton exchange (SABRE-Relay),[104] multiple chemical alteration steps (PHIP-SAH),[70] or technically demanding equipment (DNP).[241]

5.2 Overcoming weak pyruvate ligation using appropriate coligands

The first step in SABRE typically involves the conversion of a [IrCl(COD)(NHC)] precatalyst (where COD is *cis*,*cis*-1,5-cyclooctadiene and NHC is an *N*-heterocyclic carbene) into SABRE active [Ir(H)$_2$(NHC)(*N*sub)$_3$]Cl (where *N*sub is an *N* donor substrate) which reversibly binds both H$_2$ and *N*sub.[77, 242-244] In order to hyperpolarise pyruvate using SABRE the formation of complexes of the type [Ir(H)$_2$(NHC)(L)(pyruvate)] that exchange H$_2$ and pyruvate is essential. The presence of a coligand, L, is necessary in this case as pyruvate does not contain the *N*-donor sites typically required for iridium ligation in these systems.[79, 155] The much harder *O*-donor binding modes of pyruvate (summarised in Figure 5.1) are not compatible with the formation of stable iridium pyruvate complexes when [IrCl(COD)(IMes)] (**2**) (where IMes = 1,3-bis(2,4,6-trimethyl-phenyl)imidazole-2-ylidene) (5 mM) and sodium pyruvate (**22**) (6 eq.) in methanol-d_4 (0.6 mL) are mixed together with 3 bar H$_2$. Therefore, a range of different coligands (5 eq. relative to **2**) were added to a solution containing **2** (5 mM), **22-1,2-[^{13}C$_2$]** (6 eq.), and 3 bar *p*-H$_2$ in methanol-d_4 (0.6 mL) to identify classes of coligands that could result in the formation of stable [Ir(H)$_2$(NHC)(L)(pyruvate)] type species. This was tested by searching for additional sets of ^{13}C NMR resonances corresponding to ligated pyruvate, in addition to those for the free ligand, and 2-oxy-2-methoxypropanoate which exists in an equilibrium with pyruvate in these methanol-d_4 solvents.[186, 187] The formation of any hydride containing complexes was examined by recording ^{1}H NMR spectra. These solutions were also shaken with 3 bar *p*-H$_2$ for 10 seconds in a mu-metal shield to observe any enhanced pyruvate ^{13}C NMR signals in these solutions.

The use of coligands has been used in SABRE to enhance substrate polarisation either by blocking coordination sites[102, 122, 124] or by reducing steric crowding around the iridium centre such that more sterically demanding substrates can be polarised.[245 246, 247] Common coligands include molecules with *N*-donor sites such as acetonitrile[101, 246] or methyl triazole.[122, 124] Here, coligands were tested that contained a range of *N*, *O, S* and *P*-donor sites and they are summarised in Table 5.1.

Table 5.1: A summary of the results of testing a solution of 2 (5 mM), 22-1,2-[^{13}C$_2$] (6 eq.) and the indicated coligand (5 eq.) in methanol-d_4 (0.6 mL) with 3 bar H$_2$. These samples were left to react with H$_2$ for 1 hour at 323 K before they were shaken with 3 bar p-H$_2$ for 10 seconds in a mu-metal shield for observation of enhanced pyruvate ^{13}C NMR signals.

Coligand	Structure	Formation of hydride containing complexes?	Additional ^{13}C resonances corresponding to ligated pyruvate?	^{13}C Pyruvate polarisation upon p-H$_2$ shaking?
Imidazole (8)		✔ δ −22.3	✘	✘
Acetonitrile (41)		✔ δ −15.4	✘	✘
Thiophene (42)		✔ δ −17.0 δ −22.6 δ −25.5	✘	✘
Dimethylsulfoxide (46)		✔ δ −27.1 δ −29.1	✔	✔
Ethylisothiocyanate (52)		✔ δ −13.3 δ −14.9 δ −19.8	✘	✘
4-chlorobenzenemethanethiol (55)		✘	✘	✘
Benzylaldehyde (57)		✔ δ −22.0 δ −22.5 δ −26.7	✘	✘
Triphenylphosphine (58)		✔ δ −7.8	✘	✘

Coligands such as imidazole (8) and acetonitrile (41) have been hyperpolarised using SABRE, as previously reported.[101, 248] When 8 or 41 (5 eq.) are added to a solution containing 2 (5 mM) and 22 (6 eq.) with 3 bar p-H$_2$ in methanol-d_4 (0.6 mL) the formation of hydride containing complexes at δ −22.3 and −15.4 respectively were observed. These hydride resonances were enhanced when shaken with p-H$_2$ at 6.5 mT but in each case ^{13}C NMR spectroscopy showed no visible ^{13}C NMR signals for pyruvate bound to iridium which suggests that ligation has not occurred. When these nitrogen-based donors are used it is expected that they outcompete pyruvate for iridium binding as is typical of SABRE with such N-donor substrates.[79, 155] In these cases,

$[Ir(H)_2(IMes)(imidazole)_3]Cl$ or $[Ir(H)_2(IMes)(acetonitrile)_3]Cl$ are likely to form which could give rise to these single hydride signals.[101, 248] The chemical shift of the hydride ligands of $[Ir(H)_2(IMes)(imidazole)_3]Cl$ has been previously reported and is consistent with the signal observed at δ –22.3.[248]

The coligands thiophene (**42**), ethylisothiocyanate (**52**), and benzaldehyde (**57**) result in the formation of hydride containing products within 1 hour of H_2 addition, although no enhanced hydride NMR signals were observed for any of these species upon shaking with p-H_2 at 6.5 mT. Similarly, no additional ^{13}C NMR resonances or ^{13}C NMR hyperpolarisation is observed when these coligands are used. In contrast, the use of 4-chlorobenzenemethanethiol (**55**) as a coligand did not yield the formation of any hydride containing species in the first hour after initial H_2 addition. The growth of single crystals was observed when this solution was stored at 278 K for several months. These crystals were examined by Dr. Adrian C. Whitwood using single crystal X ray diffraction and contained $[Ir_2(H)_4(\mu\text{-}SCH_2PhCl)_2(IMes)_2]$ (**59**), the structure of which is shown in Figure 5.2a. The formation of **59** in solution is not indicated within the first 1 hour of H_2 addition as no hydride containing complexes were observed by ^1H NMR spectroscopy (Table 5.1). This further suggests that pyruvate coordination in this system does not occur and, rather, SH bond activation has taken place over a longer timescale. This reactivity is not unusual as both S-H activation[230, 231] and the formation of related thiolate bridged iridium dimers have been reported.[249-252]

The coligand triphenylphospine (**58**) was also tested as phosphines were originally used in the first generation of SABRE active magnetisation transfer catalysts, although they are often less efficient SABRE catalysts due to slow hydrogen exchange.[76, 96] Upon initial addition of 3 bar H_2 to a solution containing **2** (5 mM), **58** (5 eq.) and **22-1,2-[$^{13}C_2$]** (6 eq.) in methanol-d_4 (0.6 mL) a broad hydride resonance is observed at δ –7.8. No additional ^{13}C NMR signals were observed, even when shaking with p-H_2. The growth of single crystals was also observed when this solution was left for several months at 278 K. These were identified by Dr. Adrian C. Whitwood using single crystal X ray diffraction as fac-$[Ir(H)_3(PPh_3)_3]$ (**60**), the structure of which is shown in Figure 5.2b. **60** is likely to be present in solution, as indicated by the hydride resonance δ –7.8. This suggests that in these systems pyruvate is unable to outcompete phosphine binding, which can in this case displace the carbene ligand.
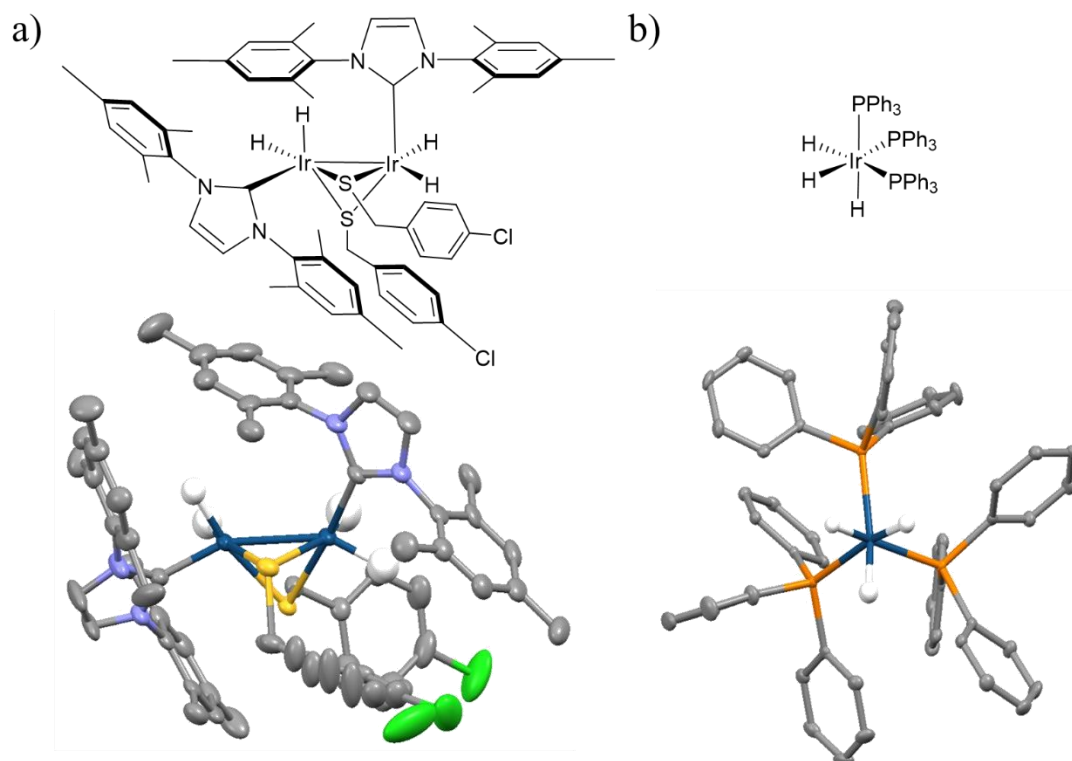
Figure 5.2: Structure of a) [Ir$_2$(H)$_4$(μ-SCH$_2$PhCl)$_2$(IMes)$_2$] (59) and b) *fac*-[Ir(H)$_3$(PPh$_3$)$_3$] (60) determined by X ray diffraction studies. Note that any solvent of crystallisation and all non-hydride hydrogen atoms have been omitted for clarity. One of the bridging μ-SCH$_2$PhCl ligands in 59 was disordered and partially occupied two sites. For refinement details, see the experimental section 7.4.10. X ray diffraction data were collected and solved by Dr. Adrian C. Whitwood.[253]

In contrast, when **22-1,2-[^{13}C$_2$]** (6 eq.) is added to **2** (5 mM) in the presence of dimethylsulfoxide (**46**) (6 eq.) and 3 bar H$_2$ in methanol-d_4 (0.6 mL), hydride complexes are formed with a major species resonating at δ –27.1 and –29.1. These resonances are strongly enhanced upon shaking with *p*-H$_2$ at 6.5 mT, as shown in Figure 5.3a. More notably, when ^{13}C NMR spectra are recorded, additional sets of ^{13}C NMR resonances are observed at δ 168 and 207. These resonances are also enhanced, in addition to those free pyruvate at δ 169 and 203, when the sample is shaken with *p*-H$_2$ in a mu-metal shield, as shown in Figure 5.3b. Interestingly, the ^{13}C NMR signal profile appears in an unusual pattern that is indicative of the formation of ^{13}C$_2$ singlet order by SABRE at low field.[54, 56] This is consistent with the formation of an active polarisation transfer catalyst that enables coherent transfer of singlet order from *p*-H$_2$ derived hydride ligands into the two coupled ^{13}C$_2$ sites. Similar effects are observed for complexes of the form [Ir(H)$_2$(κ^2-*O*OCC(CH$_3$)*N*R)(IMes)(NH$_2$R)] where R = CH$_2$Ph (**28**) and R = (CH$_2$)$_2$Ph (**29**) as detailed in Chapter 4.
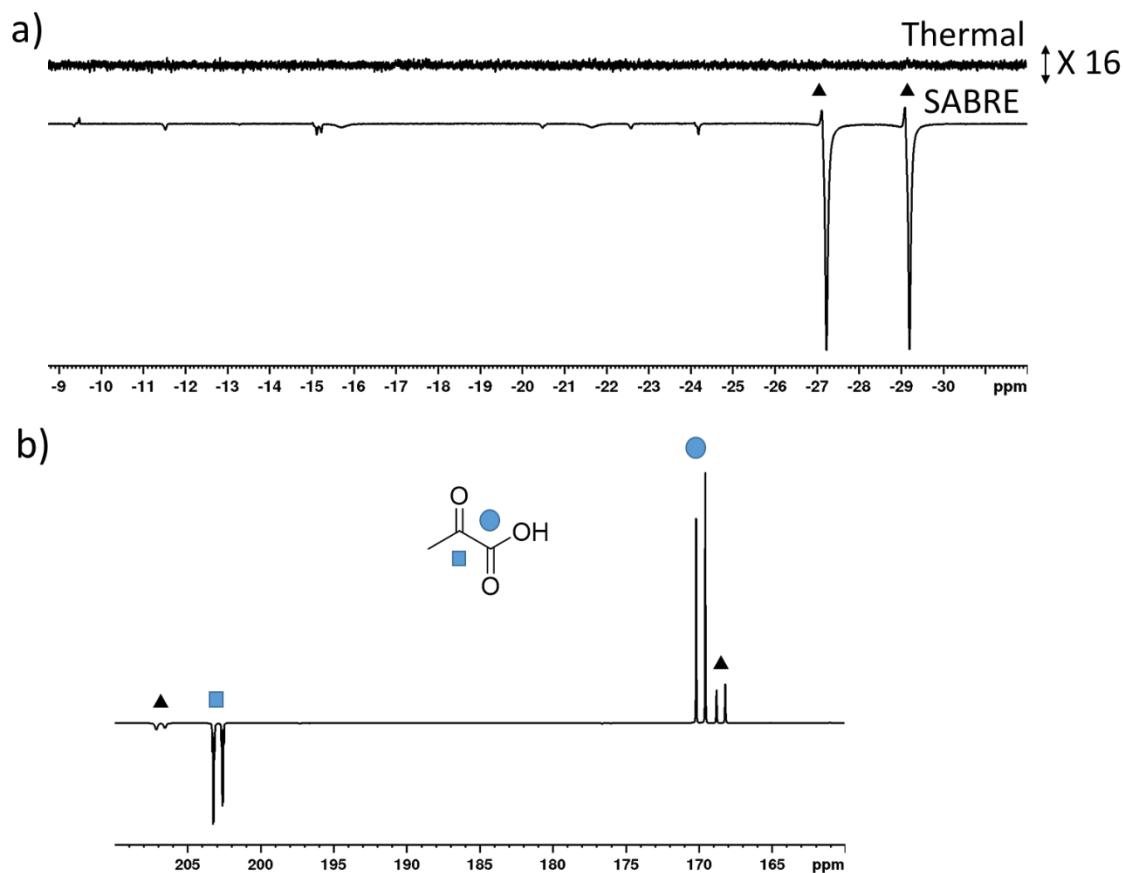
Figure 5.3: Partial hyperpolarised a) ^{1}H and b) ^{13}C NMR spectra when a mixture of 2 (5 mM), 22-1,2-[^{13}C$_2$] (6 eq.) and 46 (6 eq.) in methanol-d_4 (0.6 mL) is shaken with 3 bar p-H$_2$ for 10 seconds at a) 6.5 mT or b) ~6 μT in a mu-metal shield. In a) the thermal spectrum is shown expanded vertically by a factor of 16 relative to b). Signals marked with a black triangle are expected to correspond to an active magnetisation transfer catalyst containing ligated pyruvate.

Of the coligands tested here, the observation of hydride complexes that exhibit strongly enhanced PHIP resonances with additional ^{13}C NMR resonances corresponding to bound **22** was observed only when **46** was used as a coligand. It is clear that under these conditions active polarisation transfer catalysts form which are expected to be of the type [Ir(H)$_2$(NHC)(pyruvate)(dimethylsulfoxide)L] where L is yet unidentified. It is this active species that is likely giving rise to the enhanced hydride signals at δ –27.1 and –29.1 and strongly hyperpolarised ^{13}C NMR resonances at δ 168 and 207 (shown in Figure 5.3). It is noteworthy that sulfoxides such as **46** have been used to stabilise reactive metal species[254] and feature as ligands in a wide range metal catalysts.[255] The exact identity of the polarisation transfer catalyst responsible for these observations is explored further and the mode of pyruvate coordination identified.

5.3 Identification of [Ir(H)$_2$(κ^2-pyruvate)(dimethylsulfoxide)(IMes)] polarisation transfer catalysts

The identity of the species giving rise to the hyperpolarised hydride and ^{13}C NMR signals shown in Figure 5.3 is investigated further. The binding modes of both **22** and **46** were also examined. The coordination of **46** to metal centres has been reported through either its oxygen or sulfur donor atoms.[256] Examples of Ir(III) dimethylsulfoxide complexes generally contain an *S*-bonded motif.[256] A sample containing **2** (5 mM), **22-1,2-[^{13}C$_2$]** (6 eq.) and **46** (6 eq.) with 3 bar *p*-H$_2$ in methanol-d_4 (0.6 mL) was used for 2D NMR characterisation at 245 K to determine some of the inorganic species present in these mixtures. A 32 scan ^{1}H NMR spectrum at this temperature showed there were three main complexes present in solution with distinct sets of hydride resonances at δ –15.47, –21.53 ($^2J_{HH}$ = 6 Hz); δ –14.89, –24.01 ($^2J_{HH}$ = 7 Hz) and δ –27.15 and –29.03 ($^2J_{HH}$ = 10 Hz) which are mutually coupled in a 2D ^{1}H-^{1}H COSY NMR spectrum, as shown in Figure 5.4. Of these species, only the latter was found to exhibit strongly hyperpolarised hydride resonances when shaken with *p*-H$_2$ at 6.5 mT at 298 K. It is this species that is therefore expected to correspond to an active magnetisation transfer catalyst.
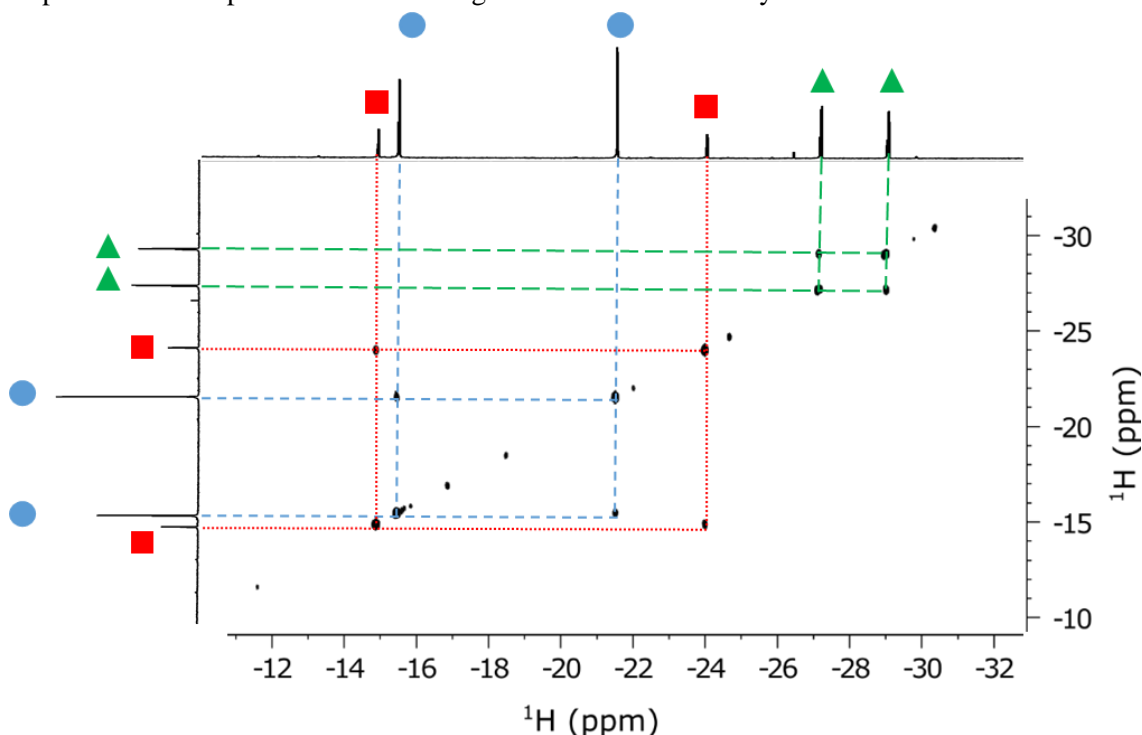
Figure 5.4: a) A partial ^{1}H-^{1}H COSY NMR spectrum at 245 K of a mixture of 2 (5 mM), 22-1,2-[^{13}C$_2$] (6 eq.) and 46 (5 eq.) in methanol-d_4 (0.6 mL) after the addition 3 bar *p*-H$_2$.

Cross peaks from the hydride resonances of these three complexes to various other aliphatic resonances *via* through space interactions were observed in a 2D ^{1}H-^{1}H NOESY spectrum at 245 K and are shown in Figure 5.5a. These cross peaks reveal that the hydride resonances at δ –15.47 and –21.53 are close in space to protons resonating at δ 2.20, 3.19 and 3.27 while the latter hydride resonance at δ –21.53 is close in space to additional resonances at δ 2.83, 3.12 and 7.02. This species also exhibits an exchange peak with H$_2$ at δ 4.61. It is expected that the resonances

at δ 2.20 and 7.02 correspond to an IMes ligand within this complex as they are consistent with previously reported values[76, 101, 106, 158, 245] while those at δ 3.19, 3.27 and δ 2.83, 3.12 likely belong to the CH$_3$ groups of bound **46**. This was confirmed by identifying their ^{13}C NMR signals through [13]C-^{1}H HMQC measurements. The mode of sulfoxide coordination is usually confirmed through X ray crystallography, IR spectroscopy, or from comparison of ^{1}H NMR chemical shifts which are generally shifted ~1 ppm downfield relative to that of the free ligand upon *S*-donor binding.[257] In contrast, coordination through the oxygen atom is accompanied by a smaller (< 0.5 ppm) downfield shift relative to the free ligand. The ^{1}H NMR signals assigned to bound **46** are consistent with those reported for an *S*-donor binding mode (between δ 3.3 and 3.8).[258] The remaining resonances for this species are found by recording ^{1}H-^{1}H COSY measurements which prove that this species is of the form [Ir(X)(H)$_2$(dimethylsulfoxide)$_2$(IMes)], **61**. The structure and characteristic resonances of **61** at 245 K are given in Figure 5.6 and Table 5.2 respectively. The arrangement of the dimethylsulfoxide ligands is confirmed from NOE measurements which are shown in Figure 5.5a. The identity of the ligand X cannot yet be confirmed from these 2D NMR measurements but it is expected to be either Cl, OH$_2$, or OD(CD$_3$).
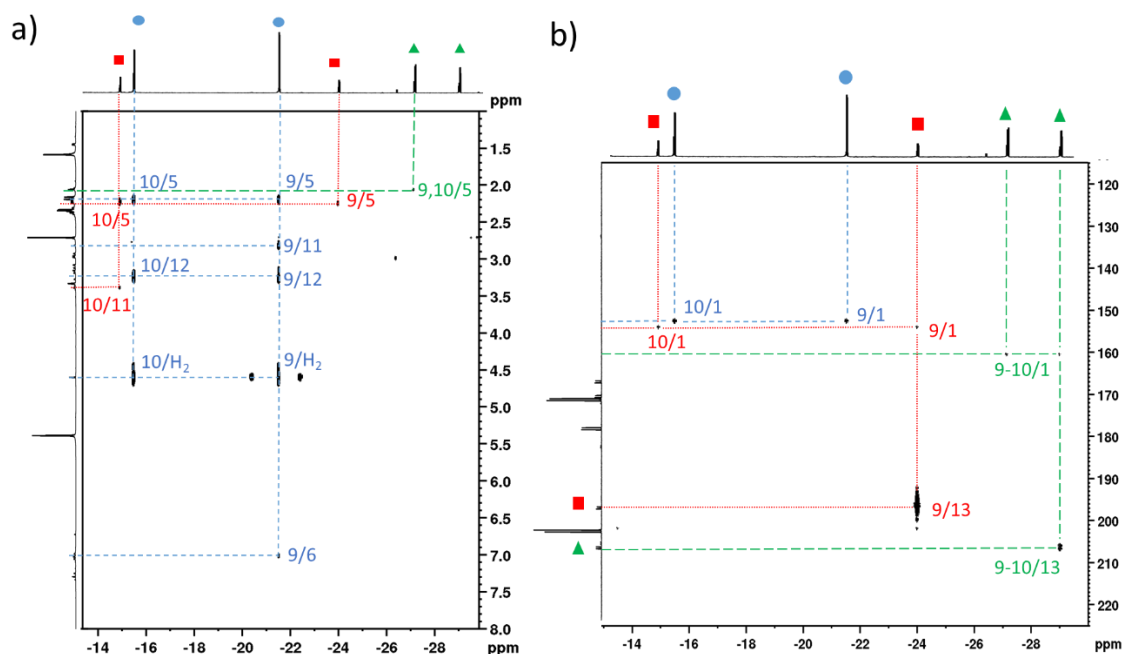
Figure 5.5: Partial a) [1]H-^{1}H NOESY 2D spectrum b) [13]C-^{1}H HMQC (τ = 25 ms) spectrum at 245 K of a mixture of 2 (5 mM), 22-1,2-[[13]C$_2$] (6 eq.) and 46 (5 eq.) in methanol-d_4 (0.6 mL) after the addition of 3 bar p-H$_2$. The resonances are labelled according the positions shown in Figure 5.6.

The remaining two major hydride containing complexes at δ –14.89, –24.01 and δ –27.15, –29.03 show similar NOE cross peaks to their IMes ligands at δ 2.24 and 2.05 respectively. Neither of these species show an exchange peak with H$_2$. When these complexes are examined by ^{13}C NMR spectroscopy, pairs of coupled ^{13}C NMR resonances are observed at δ 168.55, 206.41 ($^2J_{CC}$ = 60 Hz) and δ 166.40, 196.50 ($^1J_{CC}$ = 63 Hz) in addition to those of pyruvate and 2-oxy-2-methoxypropanoate at δ 169.38, 202.14 ($^1J_{CC}$ = 62 Hz) and δ 97.43, 176.60 ($^1J_{CC}$ = 61 Hz)

respectively. These additional sets of pyruvate resonances are expected to correspond to two different bound pyruvate ligands. In a long range ^{13}C-^{1}H HMQC measurement, the bound pyruvate resonance at δ 196.50 shows a distant coupling to the hydride signal at δ –24.01 while that at δ 206.41 shows a correlation to the species resonating at δ –29.03. Therefore, these two hydride containing species contain pyruvate bound in different orientations. Additional ^{1}H NOE measurements link the pyruvate CH_3 groups to their respective IMes and dimethylsulfoxide ligands and prove these two species are of the form [Ir(H)$_2$(κ^2-pyruvate)(dimethylsulfoxide)(IMes)], **62**. A long range ^{13}C-^{1}H HMQC measurement also shows cross peaks to the carbene carbon atoms for each of these three major complexes in solution. The structures of these complexes and their characteristic resonances are also shown in Figure 5.6 and Table 5.2 respectively. The two isomers of **62** are differentiated based on the geometry of pyruvate coordination. The species containing pyruvate and hydride ligands in the same plane is labelled **62a** while the isomer containing these ligands in perpendicular planes is labelled **62b**, as shown in Figure 5.6. The κ^2 binding mode (mode 3 of Figure 5.1) of pyruvate in this system is confirmed. As the hydride and bound pyruvate ^{13}C NMR resonances of **62a** are strongly enhanced upon shaking with p-H$_2$ (as shown in Figure 5.3) it is expected to be the active magnetisation transfer catalyst.

Figure 5.6: Structures of 61 and 62 formed when 3 bar p-H$_2$ is added to a solution containing 2 (5 mM), 22-1,2-[^{13}C$_2$] (6 eq.) and 46 (5 eq.) in methanol-d_4 (0.6 mL) as determined by 2D NMR characterisation at 245 K.
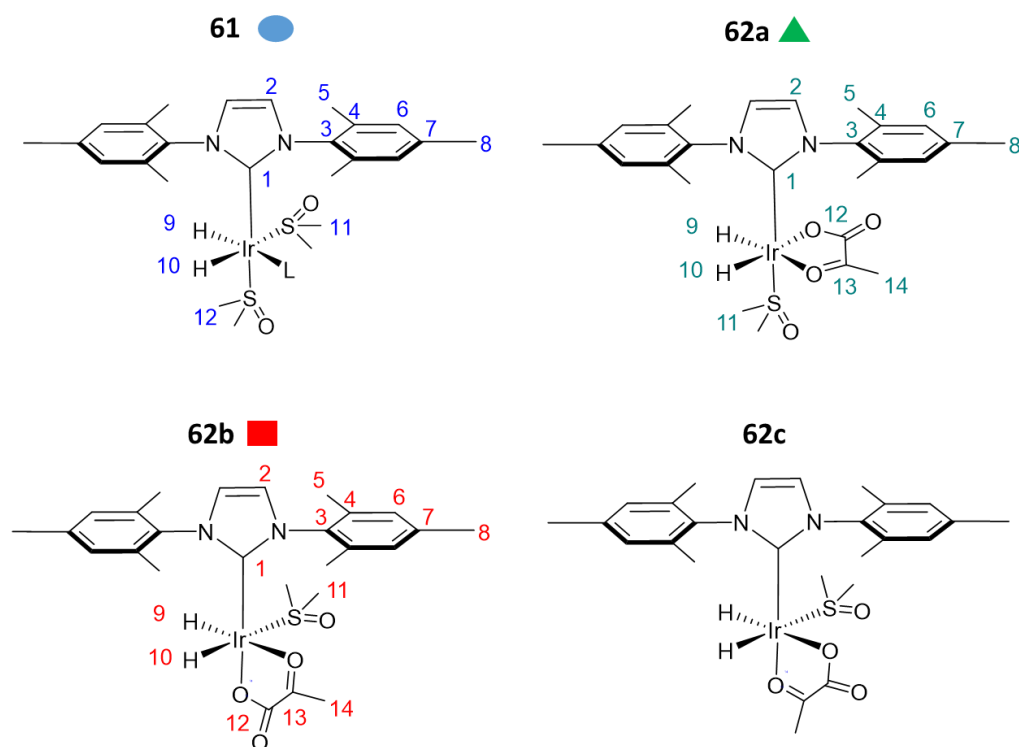
Table 5.2: ^{1}H and ^{13}C NMR resonances of the dominant species formed when 3 bar p-H$_2$ is added to a solution containing 2 (5 mM), 22-1,2-[^{13}C$_2$] (6 eq.) and 46 (5 eq.) in methanol-d_4 (0.6 mL) as determined by 2D NMR characterisation at 245 K. The resonance labels and symbols correspond to the position and structures depicted in Figure 5.6.

Resonance	61 ^{1}H	61 ^{13}C	62a ^{1}H	62a ^{13}C	62b ^{1}H	62b ^{13}C
1	-	152.49	-	160.30	-	153.89
2	7.24	123.42	7.28	122.67	~7.2 (overlap)*	~120-130 (overlap)*
3	-	135.22	-	139.80	-	~120-130 (overlap)*
4	-	136.49/137.99	-	136.90	-	~120-130 (overlap)*
5	2.20	17.55/18.34	2.05, 2.16	16.61, 16.68	2.01, 2.24	16.63, 17.13
6	7.02	128.56	6.99, 7.05	128.21, 128.77	6.88, 7.13	128.19, 129.41
7	-	138.43	-	139.65	-	~120-130 (overlap)*
8	2.37	19.95	2.35	19.73	2.35	18.12
9	−21.53	-	−27.15/−29.03	-	−24.01	-
10	−15.47	-	−27.15/−29.03	-	−14.89	-
11	2.83, 3.12	48.77, 39.85	3.09	47.25	3.38	46.49
12	3.27, 3.19	43.74	-	168.55	-	166.40
13			-	206.41	-	196.50
14			2.08	26.54	1.64	19.92

*resonances cannot be discerned due to peak overlap (it is the minor species in solution).

A further isomer of **62**, **62c**, containing pyruvate ligated in a different orientation (rotated by 180° relative to **62b**, as shown in Figure 5.6) is not visible to ^{1}H or ^{13}C NMR in solution. NOE measurements at 245 K show a cross peak between the pyruvate CH$_3$ group and the phenyl protons on the mesityl group of the carbene ligand which indicates these groups are close in space. This is also confirmed from Density Functional Theory (DFT) calculations performed by Dr. Richard O. John that show **62b** exhibits the structure shown in Figure 5.6 and that **62a** is the most stable species, as detailed in Table 5.3.

Table 5.3: Relative enthalpy (H) and Gibbs free energies (G) of the isomers of 62 determined from DFT calculations. Energies are relative to those of 62a which is set as a zero point. These DFT calculations have been performed by Dr. Richard O. John.[224]

Complex	ΔH /kJ mol^{-1}	ΔG /kJ mol^{-1}
62b	8.5	14.8
62c	22.6	28.1

The use of a sulfoxide coligand allows the formation of stable complexes containing a bound pyruvate ligand that can become hyperpolarised using SABRE. The formation and behaviour of these complexes is now investigated in more detail.

5.4 Formation of sulfoxide containing polarisation transfer catalysts

Pyruvate NMR signal gains can be achieved *via* SABRE by using a sulfoxide coligand to form a suitable polarisation transfer catalyst [Ir(H)$_2$(κ^2-pyruvate)(dimethylsulfoxide)(IMes)] (**62**), as described in Section 5.2. In these cases, [IrCl(H)$_2$(dimethylsulfoxide)$_2$(IMes)] (**61**) and **62** are expected to be important in the catalytic transfer of magnetisation from p-H$_2$ to ligated ^{13}C pyruvate sites. The formation and behaviour of these species is expected to be extremely important in understanding this novel catalytic system and optimising the pyruvate ^{13}C NMR signal enhancements that can be achieved.

5.4.1 Behaviour of [IrCl(COD)(IMes)] (2) in methanol-d_4

When the SABRE precatalyst **2** (5 mM) is dissolved in methanol-d_4 (0.6 mL) at 298 K, ^{1}H NMR signals for **2** are observed in addition to a minor species, **63**, which is only ~2% abundant compared to **2**. The abundance of **63** rises to 13% after H$_2$O (50 μL) is added, as shown in Figure 5.7a, suggesting this species contains a H$_2$O ligand that was initially present as a contaminant in methanol-d_4. When this was repeated in a solution of methanol-d_4 (0.6 mL) doped with **46** (5 μL), the abundance of **2** after the addition of H$_2$O (50 μL) was only 6%. There was no evidence for the displacement of chloride in **2** over the timescale of these measurements to form [Ir(COD)(dimethylsulfoxide)(IMes)]Cl. This is in contrast to N-donor ligands which readily displace chloride within **2**.[77, 78, 242] The presence of **63** (at 3% abundance) was also observed by ^{1}H NMR spectroscopy in a solution of **2** (5 mM) in chloroform-d (0.6 mL). Addition of H$_2$O (50 μL) to this mixture was accompanied by an increase in the abundance of **63** to 5%, although the immiscibility of H$_2$O and chloroform-d prevent the use of higher water concentrations.
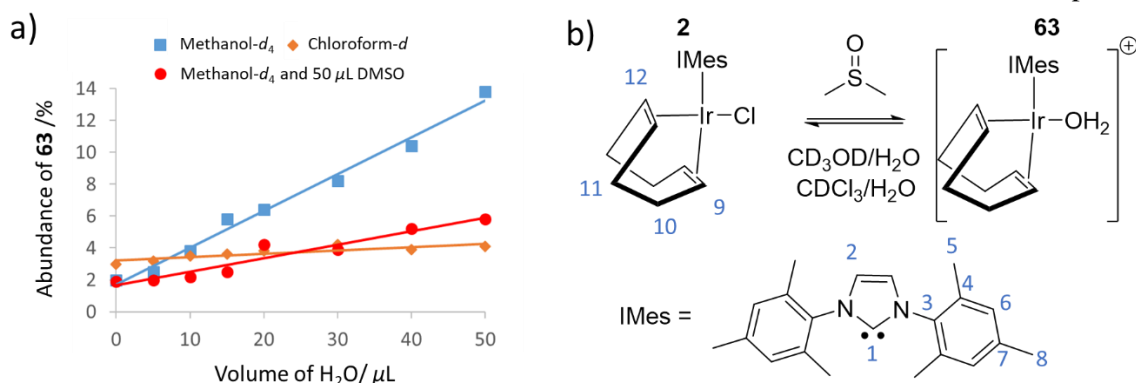
Figure 5.7: a) The proportion of 63 in solution increases as the water content of methanol-d_4 or chloroform-d is increased. b) 2D NMR characterisation confirms 63 is [Ir(COD)(IMes)(OH$_2$)]Cl. The resonance labels correspond to the chemical shift data presented in Table 5.4.

The common presence of **63** in both methanol-d_4 and chloroform-d suggests it is unlikely to contain a bound methanol ligand, but rather an aqua ligand. This is confirmed by 2D NMR data at 245 K which show a NOE connection between a resonance at δ 8.15 and signals of the IMes group at δ 2.16. ^{1}H NMR signals of bound aqua ligands in *hexa*-aqua species typically resonate between δ 8 and 11.[259] Therefore, **63** can be assigned as [Ir(COD)(IMes)(OH$_2$)]Cl with its bound aqua ligand resonating at δ 8.15. The formation of **63** is not unusual as iridium aqua complexes have been reported and the starting reagents and solvents used in this work are not rigorously dried.[168]

Table 5.4: ^{1}H and ^{13}C NMR resonances of [IrCl(COD)(IMes)] (2) (5 mM) and [Ir(COD)(IMes)(OH$_2$)]Cl (63) in methanol-d_4 (0.6 mL) at 245 K where the resonance labels correspond to those shown in Figure 5.7.

Resonance	[IrCl(COD)(IMes)] (2)		[Ir(COD)(IMes)(OH$_2$)]Cl (63)	
	^{1}H	^{13}C	^{1}H	^{13}C
1	-	N/A	-	N/A
2	7.31	123.93	6.96	122.48
3	-	139.91	-	139.77
4	-	138.67, 137.30	-	N/A
5	2.21, 2.30	17.31, 18.46	2.16, 2.17	16.64, 19.25
6	7.05, 7.08	128.89, 127.97	6.72	128.34, 128.71
7	-	136.05	-	N/A
8	2.38	19.87	2.30	17.28
9	3.10	131.87	3.01	N/A
10	1.27, 1.64	28.52/33.04	1-2 (overlap)	N/A
11	3.99	121.16	4.22	N/A
12	1.38, 1.74	28.52/33.04	1-2 (overlap)	N/A
Ir-OH_2	-	-	8.15	-

5.4.2 Hydrogen addition to [IrCl(COD)(IMes)] (2) in the presence of dimethylsulfoxide (46)

When H$_2$ (3 bar) is added to equilibrium mixtures of **2** (5 mM) and **63** containing **46** (4 eq.) in methanol-d_4 (0.6 mL) at 245 K an initial ^{1}H NMR spectrum reveals two hydride resonances at $\delta -15.49$ and -21.51 ($^2J_{HH} = 5.5$ Hz). NMR characterisation of this mixture at 245 K reveals this product is in fact [Ir(H)$_2$(IMes)(dimethylsulfoxide)$_2$(L)], **61**. This species has been observed when 3 bar H$_2$ is added to solutions containing **2** (5 mM), **46** (5 eq.), and **22-1,2-[^{13}C$_2$]** (6 eq.) and its NMR resonances have been shown previously (see Table 5.2). To confirm the identity of L in **61**, this hydrogenation reaction was repeated at 245 K in both chloroform-d and dichloromethane-d_2. In these cases, hydride NMR resonances appear at $\delta -15.50$, -21.12 and $\delta -15.67$, -21.36 respectively. The similarity in these resonances suggests the presence of **61** in both solvents. The identity of L in **61** is therefore unlikely to be methanol and is more likely to be either an aqua or chloride ligand. To confirm this, H$_2$ addition to a solution containing [IrBr(COD)(IMes)] (**64**) (5 mM) and **46** (4 eq.) in methanol-d_4 (0.6 mL) yielded different hydride signals at $\delta -15.67$ and -20.45 at 255 K. This suggests that a different product is formed which is likely [IrBr(H)$_2$(dimethylsulfoxide)$_2$(IMes)] (**65**). Furthermore, when this reaction is repeated in methanol-d_4 (0.6 mL) using [Ir(CH$_3$CN)(COD)(IMes)]PF$_6$ (**66**) (5 mM) as the precatalyst, [Ir(H)$_2$(CH$_3$CN)(dimethylsulfoxide)$_2$(IMes)]PF$_6$ (**67**) forms which yields signals at $\delta -15.76$ and -19.83 at 255 K. There was no evidence in ^{1}H NMR spectra for the displacement of CH$_3$CN by sulfoxide. Therefore, the ligand L in **61** is likely to be Cl which is indicated by large chemical shift differences (up to ~ 1.7 ppm) for the hydride ligand *trans* to this site.

When H$_2$ (3 bar) is reacted with an equilibrium mixture of **2** (5 mM) and **63** in methanol-d_4 (0.6 mL) in the presence of **46** (5 eq.) at 245 K, no evidence for the formation of H$_2$ addition products (in addition to **61**) are observed. This indicates that H$_2$ addition to **2** is slow, but hydrogenation of the COD ligand in the [IrCl(H)$_2$(COD)(IMes)] intermediate (**68**) (shown in Figure 5.10) is rapid. The kinetic time course of this reaction in both methanol-d_4 and chloroform-d at 245 K are shown in Figure 5.10. Throughout this hydrogenation reaction, the proportion of **63** remains roughly constant suggesting that formation of equilibria involving **63** is slow. Therefore, the pathway to form **61** in these systems is most likely to involve direct H$_2$ addition to **2** rather than **63**. This is supported by the observation of resonances for **68** (at $\delta -13.39$ and -18.42) in addition to those of **61** when H$_2$ addition is repeated in chloroform-d at 245 K. In this solvent **68** is now visible as hydrogenation proceeds more slowly. However, the resonances of **68** rapidly disappear upon warming this solution to 298 K leading to the rapid formation of **61** which is summarised in Figure 5.8.
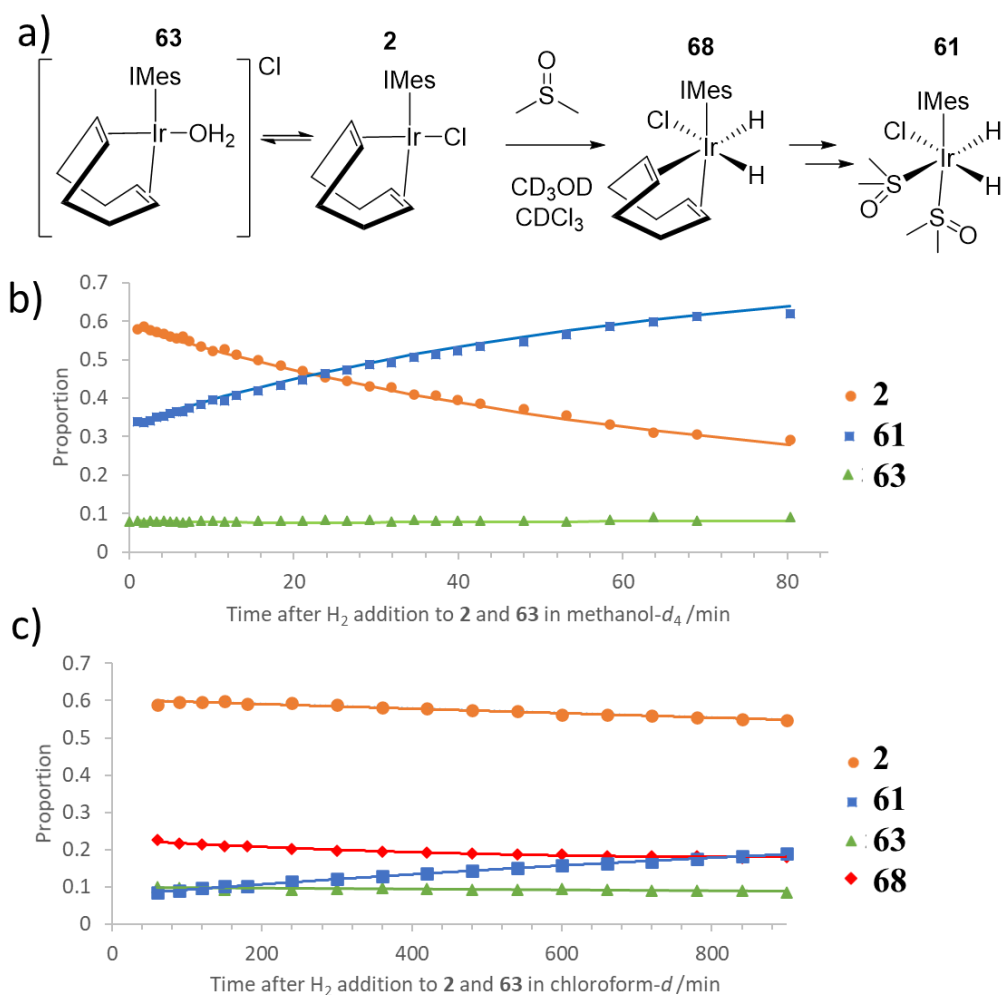
Figure 5.8: a) Summary of the reaction pathway for the hydrogenation of 2 to form 61 (*via* 68) in the presence of 46 and H$_2$, b) Time course for hydrogenation of an equilibrium mixture of 2 (5 mM) and 63 with 3 bar H$_2$ at 245 K in the presence of 46 (5 eq.) in a) methanol-*d*$_4$ (0.6 mL) or b) chloroform-*d* (0.6 mL).

5.4.3 [IrCl(H)$_2$(dimethylsulfoxide)$_2$(IMes)] (61) as a SABRE polarisation transfer catalyst

When a solution containing **61** is shaken with *p*-H$_2$ for 10 seconds at 6.5 mT, its hydride NMR signals are found to hyperpolarise very weakly and only a small NMR signal gain for free **46** (~7-fold) is observed, as shown in Figure 5.9. At 298 K the hydride resonances of **61** appear incredibly broad (line width of ~120 Hz) which is consistent with rapid hydrogen exchange in methanol-*d*$_4$. Indeed, rapid H$_2$ exchange within **61** may result in a low SABRE enhancement of free **46** due to rapid consumption of *p*-H$_2$ or a short lived nature of the active polarisation transfer catalyst.
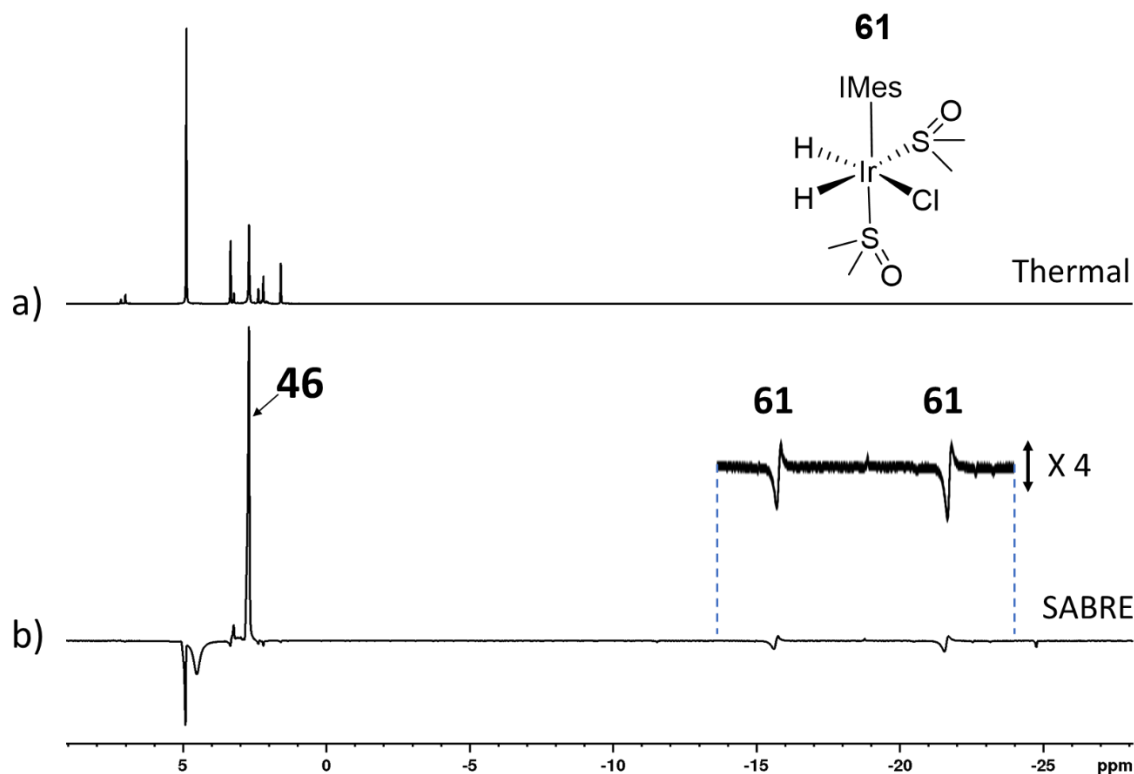
Figure 5.9: a) Thermal ^{1}**H NMR spectrum of 61 in methanol-**d_4 **(0.6 mL) at 298 K b) Hyperpolarised** ^{1}**H NMR spectrum after shaking 61 with 3 bar** p-**H**$_2$ **for 10 seconds at 6.5 mT.**

Investigations into the behaviour of **61** are restricted by its instability in methanol-d_4 over a time period of several hours at 298 K. **61** is also unstable when exposed to oxygen, as shown in Figure 5.10, which prevents the synthesis and isolation of **61** as a SABRE catalyst precursor and necessitates using **2** as a stable starting precursor.
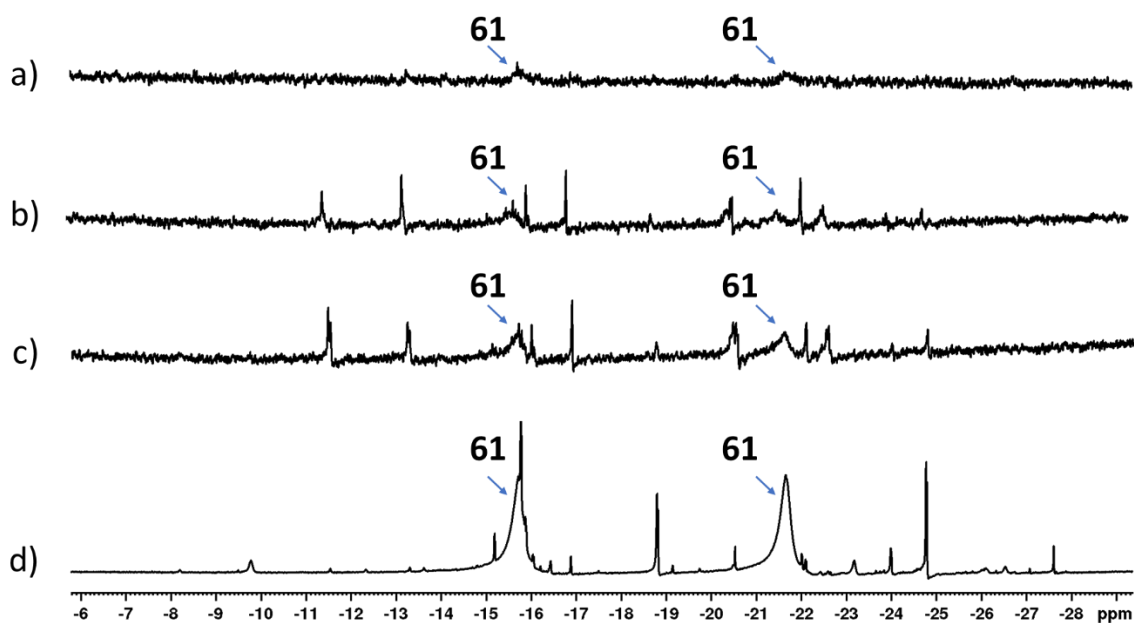
Figure 5.10: a) ^{1}**H NMR spectrum of 61 at 298 K yields broad resonances for the rapidly exchanging hydrides b)** ^{1}**H NMR spectrum of 61 after exposing to oxygen c)** ^{1}**H NMR spectrum of 61 after isolating as a solid and re-dissolving in methanol-**d_4 **(0.6 mL) d) Synthesis and isolation of a larger batch of 61 (10 mg) yielded a less pure sample. Vertical expansion of a)-c) is not the same as d).**

5.4.4 Addition of sodium pyruvate to [IrCl(H)$_2$(dimethylsulfoxide)$_2$(IMes)] (61)

When sodium pyruvate-1,2-[^{13}C$_2$] (22-1,2-[^{13}C$_2$], 6 eq.) is added to a solution of preformed 61 in methanol-d_4 (0.6 mL) at 245 K, two hydride containing products are formed. These are two isomers of [Ir(H)$_2$(κ^2-pyruvate)(dimethylsulfoxide)(IMes)], 62 as shown in Figure 5.11. The NMR resonances of 62 have been previously discussed and are detailed in Table 5.2.

When this equilibrium mixture of 61 and 62 was warmed to 298 K the main hydride containing complex observed using ^{1}H NMR spectroscopy is 62a and resonances for 61 and 62b cannot be easily discerned. 62 can also be detected shortly after H$_2$ addition to a solution of 2 (5 mM) containing both 46 (10 eq.) and 22-1,2-[^{13}C$_2$] (6 eq.) in methanol-d_4 (0.6 mL) at 298 K. Therefore, equilibrium mixtures of 61 and 62 can be formed from 2 without having to form 61 in a prior step.
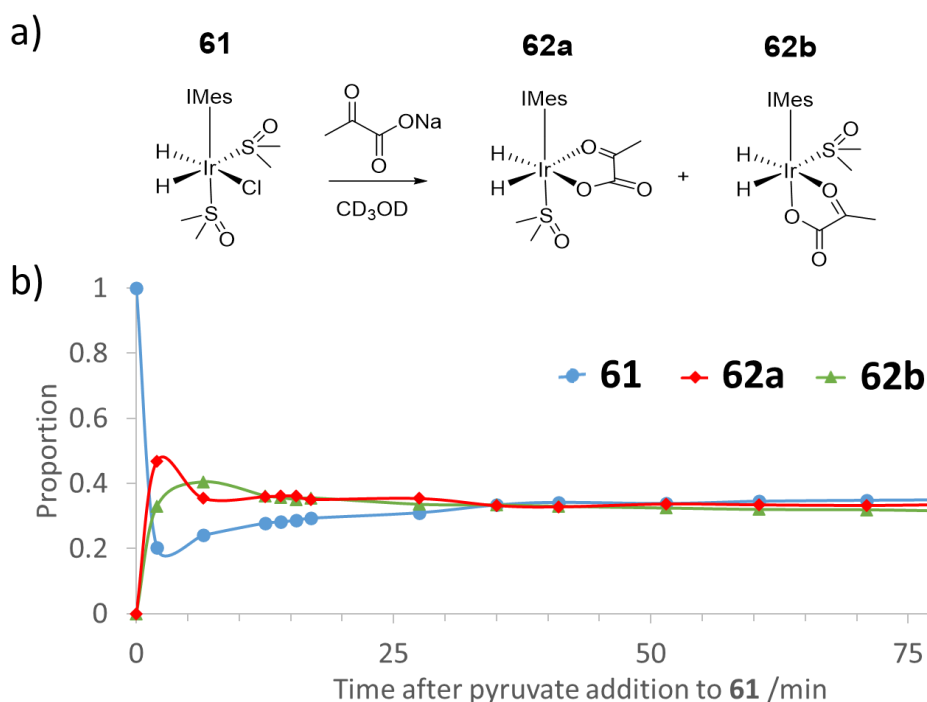
Figure 5.11: a) Reaction of 61 and 22-1,2-[^{13}C$_2$] to form 62 b) Monitoring addition of 22-1,2-[^{13}C$_2$] (6 eq.) to 61 in methanol-d_4 (0.6 mL) using ^{1}H NMR spectroscopy. 22-1,2-[^{13}C$_2$] was added at 298 K to a solution of preformed 61 at 245 K before being replaced into a 9.4 T spectrometer at 245 K. Therefore, there is a rapid temperature change at the beginning of this data set.

In traditional SABRE catalysis, a substrate typically displaces the chloride ligand of 2 to form a [Ir(COD)(IMes)(Nsub)]Cl type complex (where Nsub is an N-donor substrate) which then undergoes hydrogen addition.[77] In these sulfoxide derived systems, there are significant differences in the mechanism of active catalyst formation. Neither pyruvate nor sulfoxide displace the chloride ligand of 2 and hydrogen addition occurs directly to 2 to form 61 (*via* 68). After the H$_2$ addition reaction, pyruvate ligation can occur and the active magnetisation transfer catalyst, 62 is formed. In traditional SABRE, magnetisation transfer catalysts undergo reversible exchange

of H_2 and Nsub ligands *via* a common five coordinate intermediate.[217, 218] The mechanism of ligand exchange within **61** and **62** is therefore investigated further to provide a rationale for the high pyruvate NMR signal gains that are produced in section 5.6.

5.5 Mechanism of ligand exchange in sulfoxide containing polarisation transfer catalysts

In SABRE, ligand exchange within the active polarisation transfer catalyst is important for both refreshing p-H_2 derived singlet order within the hydride ligands of the active catalyst and allowing for the build-up of polarisation of the free substrate in solution.[79, 155] Exchange Spectroscopy (EXSY) can be used to investigate these exchange processes on the NMR timescale.[220] The behaviour of **62** can be examined in a similar approach by synthesising a sample containing an equilibrium mixture of both **61** and **62**. Upon the selective excitation of the hydride resonances of **62**, chemical exchange into H_2 is not observed on the NMR timescale. Additionally, when ^{13}C-EXSY is used to excite resonances of pyruvate bound within **62a**, no exchange into free pyruvate is observed on the timescale of the measurement. **62a** therefore appears to be relatively stable in agreement with DFT data (Table 5.3). This may be surprising considering the strong hydride polarisation observed upon shaking with p-H_2 which indicates that some ligand exchange processes must occur to allow incorporation of p-H_2. As **62a** exhibits strongly enhanced hydride signals upon p-H_2 shaking it might be expected to undergo rapid p-H_2 exchange. However, these EXSY measurements suggest that this is not the case. As **62** appears to exhibit slow ligand exchange **61**, which is also present, may be important in mediating p-H_2 exchange within equilibrium mixtures of **61** and **62**.

In order to confirm this hypothesis, the exchange processes of a solution containing only **61** were investigated further. **61** yields four distinct ^{1}H NMR signals for the CH_3 groups of its two sulfoxide ligands, as listed in Table 5.2. Upon selective excitation of bound sulfoxide resonances *cis* to carbene in **61**, chemical exchange into free sulfoxide is observed, as shown in Figure 5.12a. In contrast, exchange of the sulfoxide orientated *trans* to carbene is not observed on this timescale, although interchange of the inequivalent sulfoxide CH_3 groups is observed. This suggests that loss of the sulfoxide ligand *cis* to IMes can lead to scrambling of the inequivalent CH_3 resonances of the sulfoxide *trans* to IMes.
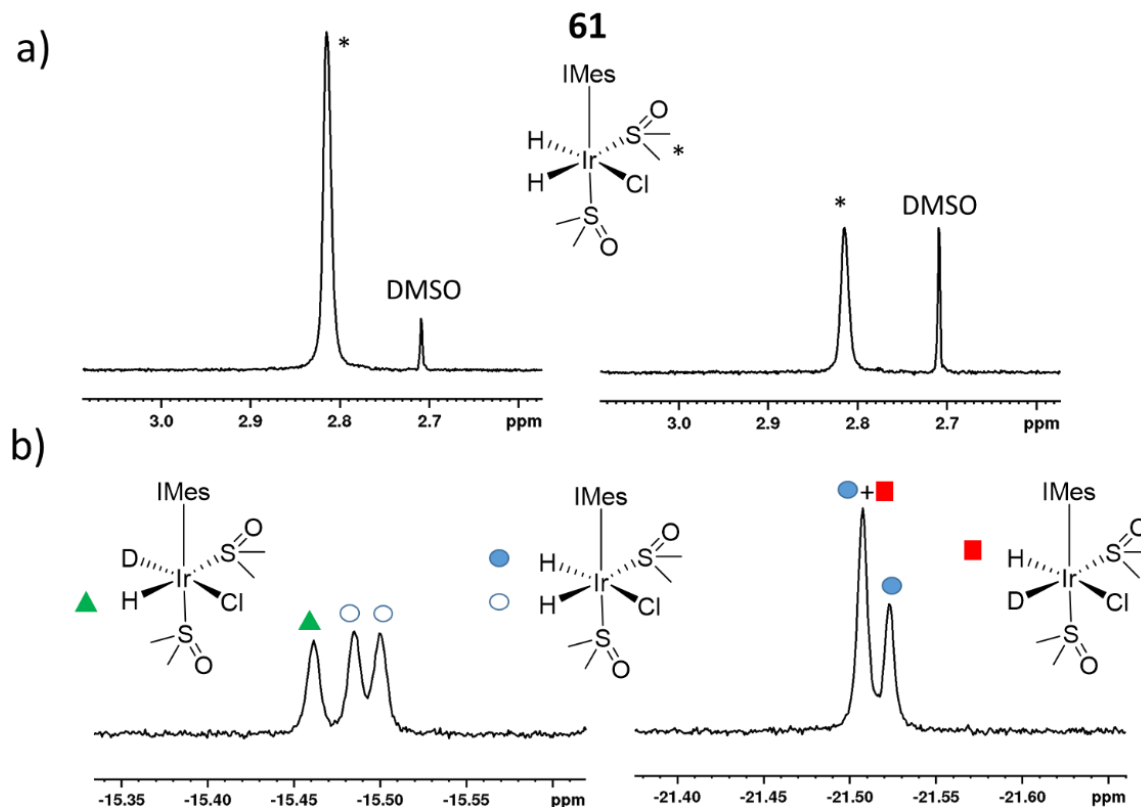
Figure 5.12: a) After selective excitation of the bound 46 resonance *trans* to hydride in 61, exchange to free 46 is observed after a mixing time of 0.1 s (left). When the mixing time is increased to 0.4 s (right) the free 46 peak increases in intensity. b) ¹H NMR spectrum of 61 at 245 K allows distinct resonances for 61 and 61-*d* to be discerned.

Density Functional Theory (DFT) calculations were performed by Dr. Richard O. John to support these observations. They revealed that the four coordinate 16 electron product formed from direct H_2 loss from **61** is high in energy, as shown in Table 5.5. Similarly, the five coordinate intermediate formed from loss of **46** *trans* to carbene is also unstable, undergoing spontaneous rearrangement to form an intermediate with a vacancy in the equatorial plane. This is consistent with the EXSY measurements which show no exchange of this ligand on this timescale. In contrast, the loss of **46** that lies *cis* to carbene appears most favourable as the ligand loss product, [IrCl(H)₂(dimethylsulfoxide)(IMes)], appears most stable. Therefore, this five coordinate intermediate is expected to be important in H_2 and sulfoxide exchange.

Table 5.5: DFT calculated relative enthalpy (H) and Gibbs free energies (G) of products formed from ligand loss from 61. These energies are relative to those of 61 which are set as a zero point and are not transition state barriers. These DFT calculations have been performed by Dr. Richard O. John.[260]

Loss of ligand from **61**	*ΔH* /kJ mol⁻¹	*ΔG* /kJ mol⁻¹
H₂	89.0	58.5
Cl	39.6	3.9
46 *cis* carbene	32.7	−10.1

In these systems H/D exchange leading to the formation of [IrCl(D)(H)(dimethylsulfoxide)₂(IMes)] (**61-*d***) (and presumably

159

[IrCl(D)$_2$(dimethylsulfoxide)$_2$(IMes)] (**61-d_2**)) was evident, even at low temperature (245-265 K), as shown in Figure 5.12b. Deuterium exchange within these systems can occur *via* binding of methanol-d_4 solvent to the five coordinate [IrCl(H)$_2$(dimethylsulfoxide)(IMes)] intermediate which can lead to the formation of **61-d** and **61-d_2** alongside HD and D$_2$ gas. While methanol bound adducts are not directly observed, they have been indirectly detected in SABRE using Chemical Exchange Saturation Transfer (CEST) experiments.[168] It has been proposed that these methanol-d_4 bound adducts account for the deuterium isotope exchange often observed in SABRE experiments.[150, 168] These EXSY measurements show no exchange between **61** and **61-d** which confirms that this isotope exchange process is slow.

In contrast to traditional SABRE active magnetisation transfer catalysts, **62** displays slow ligand exchange kinetics. However, **61** does undergo rapid H$_2$ exchange on the NMR timescale and it is through this complex that fresh p-H$_2$ is likely delivered indirectly into **62**. This suggests that the catalytic build-up of magnetisation in solution is much more complex as p-H$_2$ exchange and substrate polarisation are localised within two different catalysts (**61** and **62a** respectively). This is a significant departure from traditional SABRE catalysis in which both of these processes occur in the same [Ir(H)$_2$(IMes)(Nsub)$_3$]Cl type species (where Nsub is an N-donor species).[76, 79, 155] Optimising the pyruvate signal gains these systems can produce is a significant challenge as the effect of both H$_2$ refreshment within **61**, pyruvate polarisation within **62a**, and the exchange between **61** and **62a** must all be considered.

5.6 Optimisation of pyruvate $^{13}C_2$ NMR signal enhancement using SABRE

Optimising the gain in pyruvate ^{13}C NMR signal delivered by sulfoxide-based polarisation transfer catalysts *via* SABRE is important for a range of potential applications that are discussed in more detail in Chapter 6. Typically, SABRE efficiency can be improved by variation of factors including polarisation transfer field, carbene ligand, temperature, p-H$_2$ pressure, and solvent.[79, 98, 155-157] Therefore, the effect of these factors on the pyruvate $^{13}C_2$ NMR signal gains that can be achieved using SABRE is investigated.

5.6.1 Effect of polarisation transfer field on pyruvate $^{13}C_2$ NMR signal enhancement

Polarisation transfer catalysts of the form [Ir(H)$_2$(κ^2-pyruvate)(dimethylsulfoxide)(IMes)] (**62**) are able to catalytically transfer magnetisation from p-H$_2$ derived hydride ligands to ligated ^{13}C pyruvate spins. The efficiency of magnetisation transfer within such complexes is usually dependant on the magnetic field experienced by the sample.[99, 261, 262] This effect arises from a matching condition in which most efficient transfer occurs when the J coupling between the hydride ligands (J_{HH}) equals the chemical shift difference (δ_{HS}) between the hydride and substrate spin.[78] For polarisation transfer to ^{1}H spins, these conditions are usually achieved at fields of

around 6.5 mT. However, these fields are typically around 1 μT for transfer to heteronuclei including ^{15}N and ^{13}C.[53, 83, 171, 233] These effects have also been described using Level Anti-Crossings (LAC).[94, 160]

The effect of magnetic field was tested by activating a sample containing **2** (5 mM), dimethylsulfoxide (**46**) (4 eq.), and **22-1,2-[^{13}C$_2$]** (6 eq.) in methanol-d_4 (0.6 mL) under 3 bar H$_2$ for 1 hour at room temperature. This sample was then shaken with 3 bar p-H$_2$ for 10 seconds at magnetic fields ranging between 0.1 and 2 μT. These fields were achieved by shaking the sample inside a solenoid coil within a mu-metal shield. This device is described in Iali et al. (Appendix 4) and can produce variable magnetic fields depending on the current placed through the solenoid.[263] The ^{13}C NMR signal enhancements for free and bound pyruvate as a function of these magnetic fields are shown in Figure 5.13. They appear to be independent of magnetic field between 0.2 and 1 μT, although there is a slight decrease in polarisation transfer efficiency at 1.5 μT and 2 μT. This apparent independence of NMR signal enhancement on polarisation transfer field is perhaps unsurprising considering that hyperpolarised ^{13}C$_2$ magnetisation in **22-1,2-[^{13}C$_2$]** is created in a ^{13}C$_2$ singlet state. Unlike magnetism transfer to isolated ^{1}H or ^{13}C sites, the creation of this type of magnetism has been reported to be independent of magnetic field which is confirmed by the results shown in Figure 5.13.[49, 50, 93, 209] This is only the case for **22-1,2-[^{13}C$_2$]**; a field dependency will be observed for hyperpolarisation of **22-1-[^{13}C]** and **22-2-[^{13}C]** using SABRE as these do not contain two coupled ^{13}C spins and therefore singlet magnetisation cannot be created. The hyperpolarisation of **22-1-[^{13}C]** and **22-2-[^{13}C]** as a function of magnetic field is discussed in more detail in Iali et al. (Appendix 4).[263]
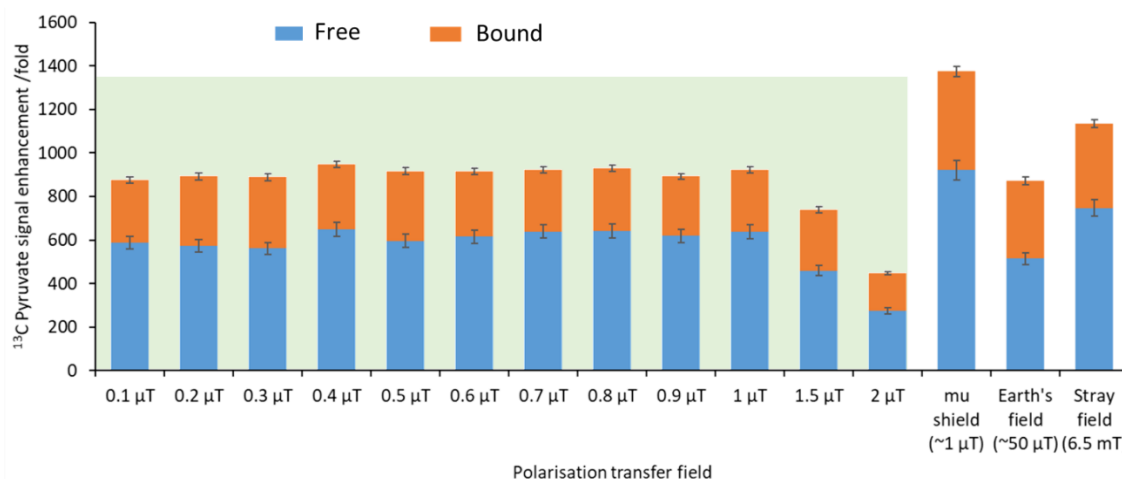
Figure 5.13: NMR signal enhancements for free (blue, lower) and bound (orange, upper) 22-1,2-[^{13}C$_2$] when a sample containing 2 (5 mM), 46 (4 eq.) and 22-1,2-[^{13}C$_2$] (6 eq.) in methanol-d_4 (0.6 mL) is shaken with 3 bar p-H$_2$ for 10 seconds at the indicated magnetic field. The region highlighted in green corresponds to magnetic fields achieved using a mu-metal shielded solenoid. These are single shot measurements as the sample degraded over time, therefore error bars are calculated from measurements using a more stable sample (see section 5.6.2).

Polarisation transfer was also performed in a mu-metal shield (without a solenoid) and at both Earth's magnetic field and in the stray field of a 9.4 T NMR spectrometer. The NMR signal enhancements in the Earth's magnetic field were comparable to those achieved between

0.1 and 1 μT ($\sim$600-fold and $\sim$300-fold for free and bound pyruvate respectively). However, those in the stray field and the mu-metal shield were higher (up to 1000-fold for free pyruvate in the mu-metal shield). These variations are likely related to different transfer times between shaking and insertion into the spectrometer. This transfer time is *c.a* 2-3 seconds longer when using the solenoid housed within a mu-metal shield due to the need to replace the NMR tube inside the spinner before insertion into the spectrometer. During this transfer time, hyperpolarised magnetisation can relax leading to a lower observed NMR signal enhancement compared to shaking in the stray field or mu-metal shield. Similarly, longer transfer times are present when shaking in the Earth's field due to the need to shake at further distances from the magnet.

A comparison of hyperpolarisation levels and hyperpolarisation lifetimes of **22-[1-^{13}C], 22-[2-^{13}C]** and **22-[1,2-^{13}C$_2$]** is given in Iali et al. (Appendix 4).[263] Briefly, polarisation transfer to **22-[1-^{13}C]** or **22-[2-^{13}C]** is optimised at polarisation transfer fields of 0.9 μT and 0.3 μT respectively. Therefore, there is a benefit in using **22-[1,2-^{13}C$_2$]** as a substrate in this work as hyperpolarised ^{13}C magnetisation can be created at any magnetic field. While the creation of hyperpolarised singlet order within **22-1,2-[^{13}C$_2$]** is independent of magnetic field, the decay of this magnetisation is not.[211] Therefore, there may be a benefit in performing the polarisation transfer step at magnetic fields at which hyperpolarised singlet order decays slowly. These effects could explain the drop in hyperpolarised signal intensity when 1.5 μT and 2 μT fields are used. For this work, hyperpolarisation will be performed in the mu-metal shield as this experimental setup has a short transfer time and resulted in the highest pyruvate NMR signal gains (Figure 5.13).

5.6.2 Effect of sulfoxide identity on pyruvate ^{13}C$_2$ NMR signal enhancement

The effect of sulfoxide identity on the formation of **61** and **62** and the subsequent pyruvate NMR signal enhancement was examined. To do this, samples containing **2** (5 mM) were activated in methanol-d_4 (0.6 mL) with 3 bar H$_2$ in the presence of **22-1,2-[^{13}C$_2$]** (6 eq.) and one of the ten sulfoxides (**46, 69-77**) (4 eq.) shown in Figure 5.14.
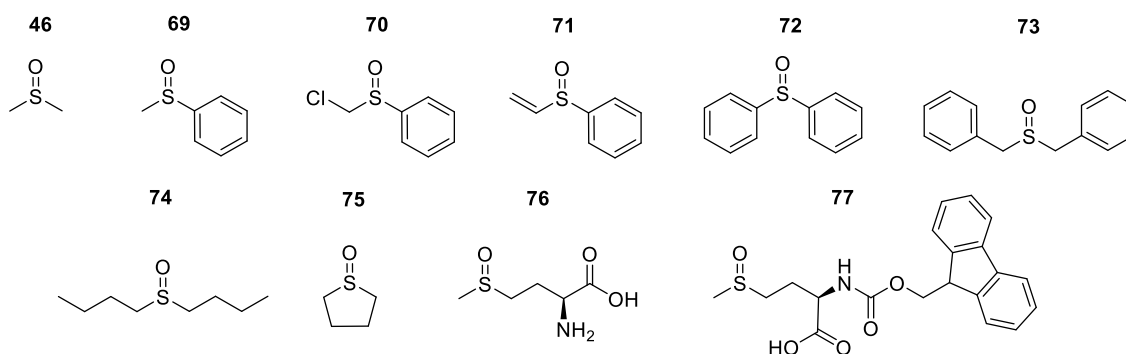
Figure 5.14: Structures of the sulfoxides 46, 69-77 used in this work.

The pyruvate ^{13}C NMR signal enhancement was measured after shaking these samples with fresh *p*-H$_2$ at several time points during the first 90 minutes following H$_2$ addition. Several key parameters are determined to compare the performance of each system. The first, ε_{max}, describes the highest recorded free pyruvate ^{13}C NMR signal enhancement for either the [1-^{13}C] or [2-^{13}C]

site. The second, τ_{60}, denotes the percentage decrease in ε_{max} over the first 60 minutes of reaction with H_2. R_{62a} is the ratio of the **62a** type product at ε_{max} relative to the sum of all hydride containing species. The relative absolute integrals of the enhanced hydride ^1H NMR signals of **62a**, S_{62a}, was also monitored during this period. These values are recorded for each of the sulfoxides tested in Table 5.6.

Table 5.6: Comparison of ε_{max}, τ_{60}, S_{62a}, and R_{62a} for solutions of 2 (5 mM), 22-1,2-[$^{13}C_2$] (6 eq.) and the specified sulfoxide of Figure 5.14 (4 eq.) in methanol-d_4 (0.6 mL) after shaking with 3 bar p-H_2 for 10 seconds in a mu-metal shield.

Sulfoxide	$^{13}C_1$ ε_{max} /fold*	$^{13}C_2$ ε_{max} /fold*	τ_{60} /%	S_{62a} / arb. units	R_{62a} /%
Dimethylsulfoxide (**46**)	1215 ± 40	910 ± 30	23	50	60
Phenylmethylsulfoxide (**69**)	1090 ± 35	1035 ± 30	6	85	90
Chlorophenylmethylsulfoxide (**70**)	1090 ± 35	1040 ± 30	32	20	93
Phenylvinylsulfoxide (**71**)	115 ± 5	105 ± 5	92	5	N/A [+]
Diphenylsulfoxide (**72**)	555 ± 15	545 ± 15	3	60	90
Dibenzylsulfoxide (**73**)	195 ± 5	180 ± 5	3	5	70
Dibutylsulfoxide (**74**)	400 ± 10	385 ± 10	9	25	45
Tetramethylenesulfoxide (**75**)	1150 ± 35	1040 ± 30	60	70	95
Methioninesulfoxide (**76**)	0	0	N/A	N/A	0
Fmoc-L-methioninesulfoxide (**77**)	130 ± 5	115 ± 5	17	N/A [&]	N/A [&]

*These are single shot measurements as there is a change in ε_{max} over time which prevents consistent repeat measurements in some cases. Therefore, errors are based on an average of three measurements for a sample containing **69** for which ε_{max} was consistent over the time needed to record three measurements.

[+] Rapid sample degradation prevented recording R_{62a} at a similar time point to ε_{max}

[&] No signals for a species of type **62a** were discernible

When sulfoxides **46**, **69-77** are used, hyperpolarised pyruvate ^{13}C NMR signals are observed immediately after shaking the sample with 3 bar p-H_2 in a mu-metal shield. These pyruvate ^{13}C NMR signal enhancements were found to gradually decrease over the next 90 minute time period. A representative example using sulfoxide **46** is shown in Figure 5.15. In most of these cases, the major complex present in solution is analogous to **62a**. The hydride signals of **62a** dominate the hyperpolarised ^1H hydride NMR region, and the intensity of these signals also decreases with increasing reaction time. Sulfoxide **76** appeared to be an exception with no NMR signals for species analogous to **62** observed. In this case there is no evidence of pyruvate coordination to iridium and consequently, this sulfoxide does not result in any hyperpolarised ^{13}C NMR signals. Poor performance of **76** is related to the formation of an insoluble white precipitate which is likely a [**22**-COO$^-$$^+NH_3$-**76**] salt. Using the protected analogue, **77**, appears to enable pyruvate coordination and subsequently, a ^{13}C NMR signal enhancement is again observed, although this is only ~100-fold. This is consistent with the absence of hydride signals for species of type **62**: therefore, these low pyruvate NMR signal enhancements are linked to a low concentration of active catalyst, **62** in solution.
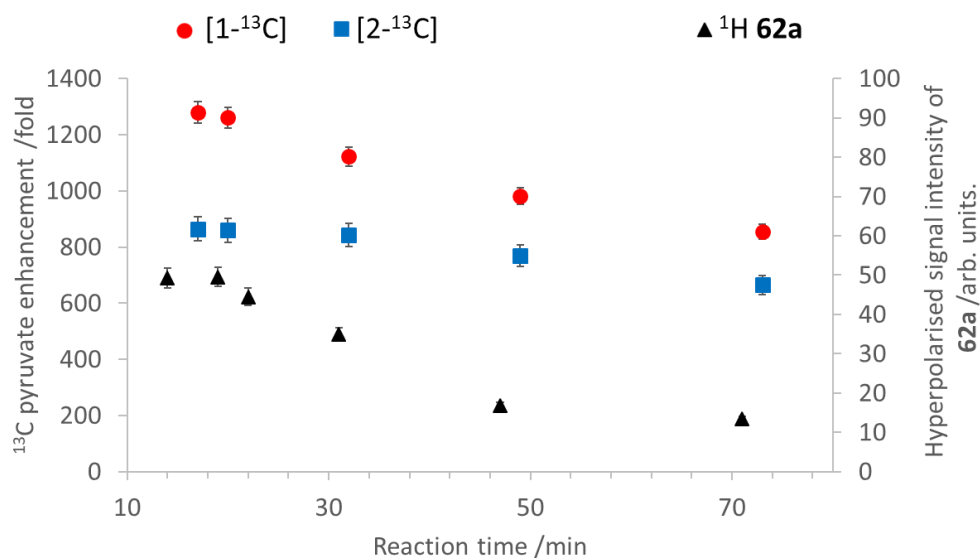
Figure 5.15: The pyruvate ^{13}C NMR signal enhancement for the [1-^{13}C] and [2-^{13}C] sites (left axis) and the signal intensity of the hyperpolarised ^{1}H hydride signals of 62a (right axis) can be monitored as a function of reaction time when a sample containing 2 (5 mM), 22-1,2-[^{13}C$_2$] (6 eq.) and 46 (4 eq.) in methanol-d_4 (0.6 mL) is reacted and shaken with 3 bar p-H$_2$ for 10 seconds in a mu-metal shield at 298 K. Each data point is a measurement with fresh p-H$_2$ shaking. Error bars are based on an average of three measurements for a sample containing 69 where ε_{max} is constant therefore allowing repeat measurements with consistent NMR signal enhancements.

When comparing the performance of the sulfoxides tested in this work, **46**, **69**, **70**, and **75** delivered the highest levels of pyruvate ^{13}C NMR signal enhancement (ε_{max} >1000-fold) while **71-74** produced hyperpolarised pyruvate ^{13} NMR signals of lower intensity (100-550-fold) (see Table 5.6). The trends in the size of hydride hyperpolarisation for the active magnetisation transfer catalysts are closely linked to the size of the pyruvate ^{13}C NMR signal enhancement. Sulfoxides **73** and **74** produce lower proportions of **62a** (R_{62a} of 70% and 45% respectively) which may be responsible for the lower ε_{max} values obtained. In contrast, sulfoxides **69**, **70**, **72**, and **75** result in higher proportions of **62a** ($R_{62a} > 90\%$) and any differences in the pyruvate ^{13}C NMR signal enhancement achieved using these sulfoxides must be linked to other factors such as the efficiency of polarisation transfer within the active catalyst, rather than its concentration. For example, **46** achieves a similar ε_{max} to **70**, **72**, and **75** despite the much lower ratio (60%) of **62a** present in solution. Therefore, polarisation transfer within the active catalyst formed from **46** is more efficient than those formed from **70**, **72**, and **75**. In contrast, **72** contains a similar R_{62a} value to **70** and **75** (90%) yet it yields a much lower pyruvate NMR signal enhancement (ε_{max} <550-fold compared to >1000-fold). This indicates that polarisation transfer within the active catalyst formed from **72** is much less efficient than those formed using **70** or **75**.

The identity of the sulfoxide coligand plays a significant role in influencing the formation and concentration of the active SABRE catalyst and thus the polarisation transfer efficiency. Increasing the proportion of **62a** is clearly an advantage, although ligand exchange processes must also be optimised to achieve optimal pyruvate hyperpolarisation. Of the sulfoxides tested

here, methylphenylsulfoxide, **69**, was the best performing as the active magnetisation transfer complex gave some of the highest ε_{max} and $S_{\textbf{62a}}$ values ($\varepsilon_{max} > 1000$-fold). Of the sulfoxides with $\varepsilon_{max} > 1000$-fold, **69** appeared to be the most stable to catalyst deactivation displaying only a 6% decrease in ε_{max} after 1 hour compared to 23, 32 and 60% for **46, 70** and **75** respectively. Therefore the reaction time can be an important parameter that is rarely optimised or considered in SABRE when hyperpolarising *N*-donor substrates with active polarisation transfer catalysts of the form [Ir(H)$_2$(IMes)(Nsub)$_3$]Cl, which are usually significantly more stable.[77, 102, 155, 200]

5.6.3 Effect of sulfoxide concentration on pyruvate ^{13}C$_2$ NMR signal enhancement

Substrate concentration is often a factor altered to optimise signal gains using SABRE.[92, 102, 117, 155] It is expected that varying the sulfoxide or pyruvate concentration may influence ligand exchange processes within **61** or **62** and the equilibrium position between them. Therefore, altering the sulfoxide or pyruvate concentration may provide a route to optimising the pyruvate ^{13}C NMR signal enhancement. The concentration of **69** was varied to determine the effect of sulfoxide concentration on ε_{max}. A sample containing **2** (5 mM), **22-1,2-[^{13}C$_2$]** (6 eq.) and **69** (2 eq.) in methanol-d_4 (0.6 mL) was shaken with 3 bar *p*-H$_2$ for 10 seconds in a mu-metal shield. Further additions of **69** were made and the pyruvate ^{13}C NMR signal enhancement (ε_{max}) was measured. These values are presented in Figure 5.16a. The highest pyruvate ^{13}C NMR signal gain (1100-fold) was achieved using 10 equivalents of **69** relative to **2**.

Changing the concentration of pyruvate reveals similar effects: samples containing **2** (5 mM), **66** (10 eq.) and 3, 6 or 8.5 equivalents of **22-1,2-[^{13}C$_2$]** were shaken with 3 bar *p*-H$_2$ in methanol-d_4 (0.6 mL). Decreasing the pyruvate concentration from 6 equivalents to 3 equivalents resulted in a decrease of ε_{max} from 1085-fold and 515-fold for free and bound pyruvate respectively to just 770-fold and 365-fold respectively. ε_{max} also dropped to 630-fold and 180-fold for free and bound NMR signal enhancements respectively when the pyruvate concentration was increased from 6 to 8.5 equivalents. It is likely that these concentration effects are linked to optimal ligand exchange processes which differ depending on pyruvate concentration.
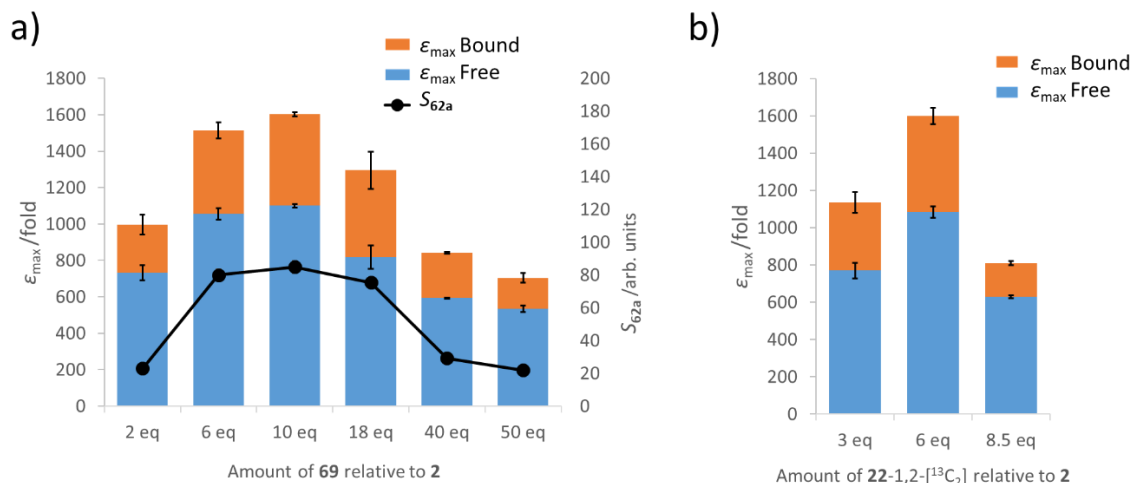
Figure 5.16: Hyperpolarised pyruvate ^{13}C NMR signal enhancements (ε_{max}) (left axis, bars) and ^{1}H hydride NMR signal intensity of the 62a derivative (S_{62a}) (right axis, line) as a function of a) sulfoxide concentration and b) pyruvate concentration.

5.6.4 Decomposition of the active polarisation transfer catalyst

It is important that SABRE catalytic efficiency of the active magnetisation transfer catalyst remains high for as long as possible to allow the refreshable hyperpolarisation of pyruvate. In these cases, while complexes of the form **62a** are able to catalytically transfer polarisation from p-H$_2$ derived hydride ligands to ligated ^{13}C pyruvate, the efficiency of this process appears to decrease at longer reaction times. This is likely related to decomposition of the active catalyst and this is investigated further.

Interestingly, the low pyruvate ^{13}C NMR signal enhancements achieved using sulfoxide **71** is related to its unintended hydrogenation by the iridium catalyst. This was confirmed by studying the behaviour of a solution containing **2** (5 mM) and **71** (4 eq.) in methanol-d_4 (0.6 mL) (in the absence of pyruvate). When 3 bar H$_2$ is added to this solution, hydride containing complexes yielding resonances at $\delta -13.32$, -18.48 and $\delta -15.75$, -21.99 rapidly form, even at 245 K. The hydride resonances at $\delta -13.32$, -18.48 are consistent with formation of [IrCl(H)$_2$(COD)(IMes)], (**68**) which has been observed previously (see Figure 5.10). Over time, the ^{1}H NMR resonances of **71** decrease and are replaced by signals of phenylethylsulfoxide, **78**, as shown in Figure 5.17. NMR spectroscopy at 245 K alongside mass spectrometry were used to confirm identification of **78**. In the case of ^{1}H NMR, this is obvious from a large chemical shift difference between the alkene protons of **71**, at δ 5.97, 6.18 and 6.79 (which decrease in intensity) and those of **78** at δ 1.19, 2.89 and 3.09 (which grow in intensity). The formation of **78** is unsurprising as hydrogenation of **71**, often using rhodium catalysts, has been reported in the literature.[264, 265] Here, an iridium-based catalyst is used to convert 70% of **71** after 13 hours reaction at 298 K. Hydrogenation of **71** with 3 bar H$_2$ at a 0.04 mol% loading of **2** yields a turnover number of 48 at 298 K which is comparable to those reported using Rh systems (turnovers of between 30-70).[265] The initial hydrogenation of **71** is rapid (30% conversion in the

first 15 minutes), as shown in Figure 5.17. This suggests the catalytic system is deactivating and becomes less efficient at longer reaction times.
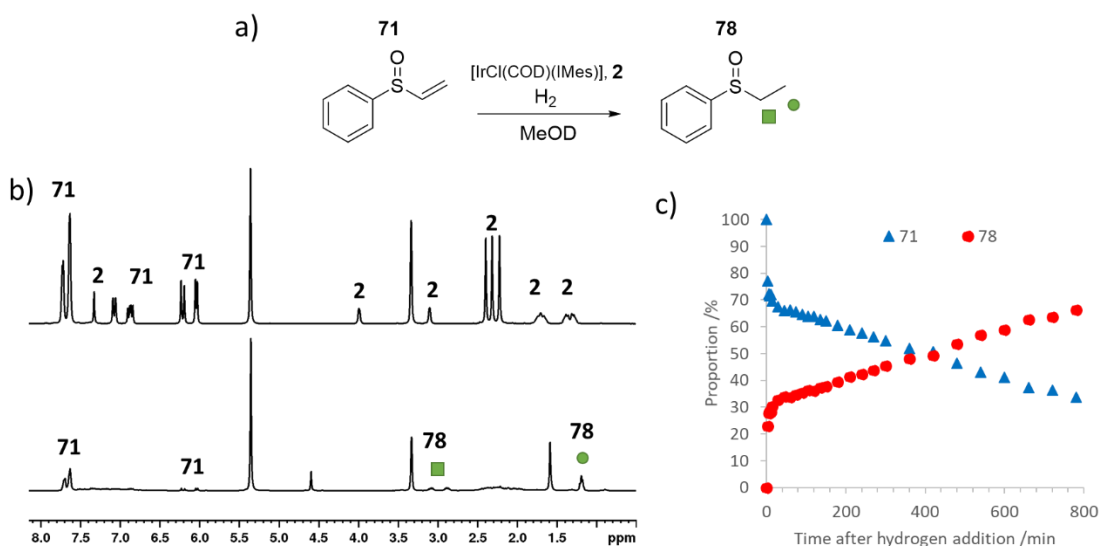
Figure 5.17: a) The hydrogenation of 71 to 78 is catalysed by 2 b) ^{1}H NMR spectrum of 2 and 71 at 245 K prior to H$_2$ addition (above) and the analogous spectrum after the solution has been left under 3 bar H$_2$ at 245 K for 1 hour before increasing to 298 K (below). c) This hydrogenation reaction can be monitored at 298 K by recording a series of ^{1}H NMR spectra.

Since the 1990s, p-H$_2$ has been used to study the mechanism of hydrogenation reactions which typically involve alkenes or alkynes.[61, 266, 267] The hydrogenation of **71** by **2** presents an excellent opportunity for study using p-H$_2$. Indeed, p-H$_2$ can be used to make low concentration intermediates in this process visible to NMR. For example, when a separate sample of **2** (5 mM) and **71** (4 eq.) in methanol-d_4 (0.6 mL) is shaken with 3 bar p-H$_2$ and placed into a 9.4 T NMR spectrometer at 263 K, hyperpolarised hydride signals are observed for **68**. These are accompanied by additional pairs of hydride resonances at (i) δ −15.83, −21.94, (ii) δ −15.93, −22.10 and (iii) δ −29.22, −29.58. As this sample is shaken several times with fresh p-H$_2$ these resonances are found to decrease in intensity and are replaced by new species at (iv) δ −16.20, −22.37 and (v) δ −26.87, −31.28, as shown in Figure 5.17. The hydride resonances for (i), (ii) and (iv) compare well to those of **61** (given in Table 5.2) which suggests these species are of the form [IrCl(H)$_2$(sulfoxide)$_2$(IMes)] which in this case are likely to be [IrCl(H)$_2$(phenylvinylsulfoxide)$_2$(IMes)] (**79**),

[IrCl(H)$_2$(phenylvinylsulfoxide)(phenylethylsulfoxide)(IMes) (**80**) and [IrCl(H)$_2$(phenylethylsulfoxide)$_2$(IMes)] (**81**). Resonances of (ii) and (v) are consistent with the formation of methanol or aqua containing species.[168] A mechanism for iridium catalysed hydrogenation of **71** is proposed in Figure 5.18. In this novel iridium catalysed system, sulfoxide coordination occurs *via* the sulfur lone pair which is in contrast to mechanistic studies of Rh-catalysed hydrogenation of vinyl sulfoxides which propose intermediates involving *O*-donor coordination.[264, 265]
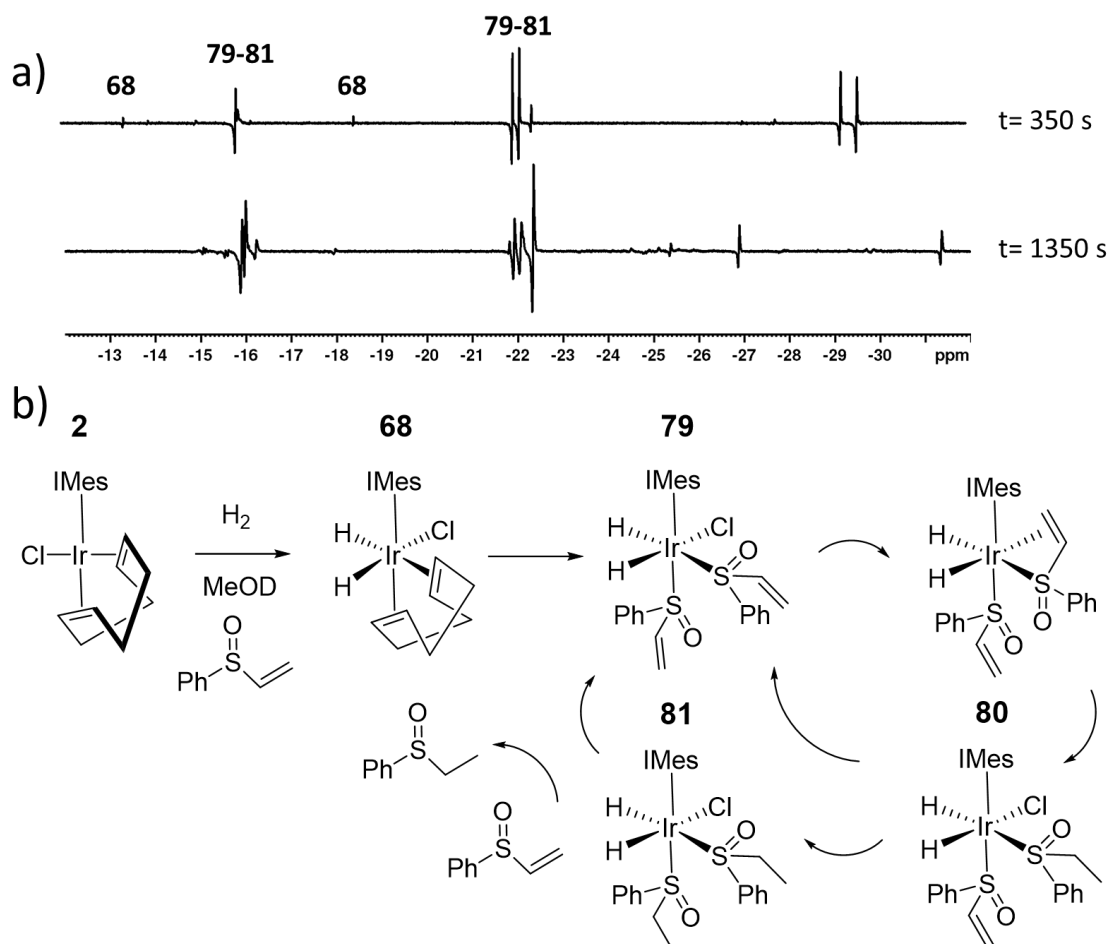
Figure 5.18: a) Partial hyperpolarised ^1H NMR spectra recorded using 45° pulses at 263 K of a solution of 2 (5 mM) and 71 (4 eq.) in methanol-d_4 (0.6 mL) shaken for 10 seconds at 6.5 mT at the specified time intervals after initial p-H_2 addition. b) A proposed catalytic system for the hydrogenation of 71 to form 78.

The reactivity of **71** prevents long term stability of the active polarisation transfer catalyst (**62a**) and results in low ε_{max} and τ_{60} values for this sulfoxide. For example, despite a high ε_{max} when using sulfoxide **75**, the high τ_{60} value (60%, Table 5.6) suggests that catalyst deactivation is extremely rapid. It is expected that reactivity of sulfoxide coligands may account for the eventual decomposition of the active magnetisation transfer catalyst regardless of the sulfoxide used. For example, when solutions that contain **2** (5 mM), **22-1,2-[$^{13}C_2$]** (6 eq.), and **69**, **71**, or **73** (4 eq.) in methanol-d_4 (0.6 mL) are left for several months under 3 bar H_2 at 278 K the growth of single crystals was observed. Single crystal X ray diffraction by Dr. Rachel R. Parker revealed the presence of [Ir(H)$_4$(μ-H)$_2$(IMes)$_2$(methylphenylsulfoxide)$_2$] (**82**), [Ir$_2$(H)$_3$(μ-H)(μ-SPh)$_2$(IMes)$_2$(phenylethylsulfoxide))] (**83**) or [Ir$_2$(H)$_4$(μ-S)(IMes)$_2$(dibenzylsulfoxide)$_2$] (**84**) in the case of sulfoxides **69**, **71** or **73** respectively.[268] The structure of these iridium (III) dimers are shown in Figure 5.19 and selected crystallographic data is given in Table 5.7. These structures represent decomposition products that crystallize out of solution and are expected to be only some of the multiple species present in this complex system thereby making analysis by solution state NMR challenging. **82-84** contain distorted octahedral iridium geometries with Ir-Ir bond distances comparing well to literature values of 2.826 Å,[249] 2.823 Å,[250] 2.734 Å,[251] 2.642 Å,[252] and 2.607 Å;[252] suggesting the presence of metal-metal single bonds. These structures provide

further confirmation of *S*-donor sulfoxide coordination in accordance with the shorter Ir-S bond distance compared to Ir-O distances (see Table 5.7). The presence of **78** bound within **83** confirms that hydrogenation of **71** has occurred. Interestingly, the observation of bridging thiolate ligands shows that reduction and S-C$_a$ bond breaking has occurred within the sulfoxide. The activation of S-C bonds[269-271] and the formation of *S*-bridged iridium dimers in hydrodesulfurisation has been reported previously.[271] Formation of iridium dimers and related sulfoxide reactivity (such as hydrogenation in the case of **71**, or C-S activation in the case of **69, 71**, and **73**) is expected to account for deactivation of the active magnetisation transfer catalyst used to hyperpolarise pyruvate at longer reaction times. It is expected that related products are formed in solution regardless of the sulfoxide used.
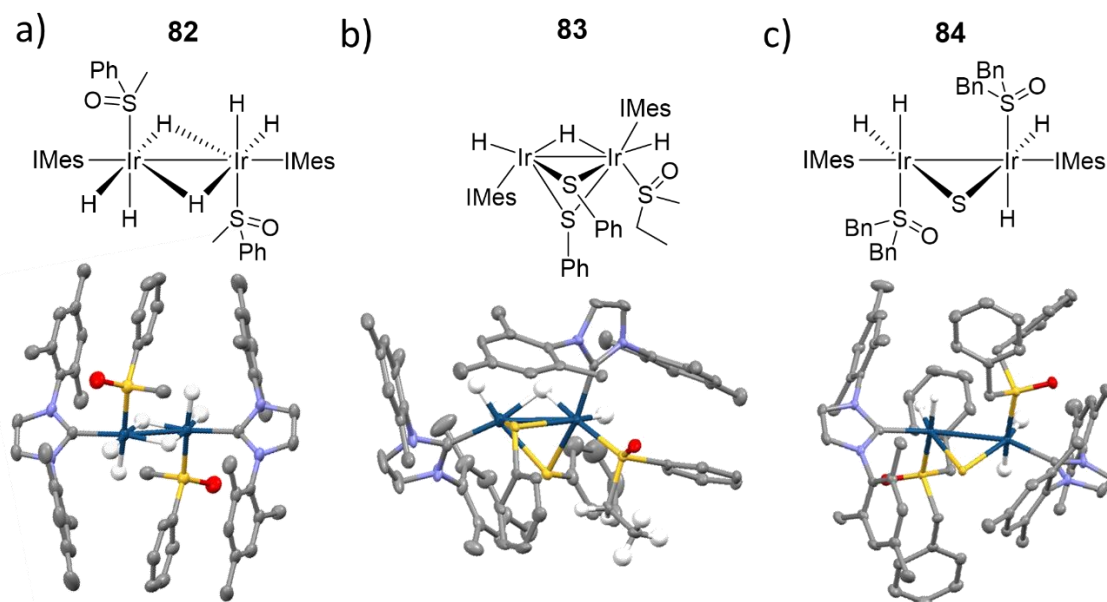
Figure 5.19: Structures of a) 82 b) 83 and c) 84 determined from X ray crystallography. Solvents of crystallisation and selected hydrogen atoms have been omitted for clarity. See the experimental section 7.4.12-14 for refinement details. X ray diffraction data were collected and solved by Dr. Rachel R. Parker.[268]

Table 5.7: Selected X ray crystallography data for 82-84. X ray diffraction data were collected and solved by Dr. Rachel R. Parker.[268] These values are presented to three decimal places and the estimated standard deviation is smaller than 1×10^{-3} Å.

Bond Length /Å	82	83	84
Ir-Ir	2.729	2.798	2.902
Ir-S(sulfoxide)	2.282, 2.282	2.262	2.298, 2.296
Ir-O(sulfoxide)	3.239, 3.239	3.248	3.280, 3.264

5.6.5 Effect of catalyst on pyruvate $^{13}C_2$ NMR signal enhancement

The efficiency of traditional [Ir(H)$_2$(NHC)(*N*sub)$_3$]Cl-based SABRE catalysts (where *N*sub is an *N*-donor substrate) is often influenced by the identity of the NHC ligand.[102] These ligands can effectively tune the lifetime of the active magnetisation transfer catalyst as their steric bulk or electronic properties can influence substrate exchange rates.[102, 158, 159] They can also play a role in

mediating relaxation within the active catalyst.[96, 102] The use of a variety of different [IrCl(COD)(NHC)] precatalysts containing NHC ligands with a range of steric and electronic properties has been used to optimise NMR signal gains for a particular substrate of interest.[96, 97, 159, 200] Variation of these ligands has been used to synthesise water soluble SABRE catalysts.[100, 121, 272] The effect of NHC ligand on ε_{max} was therefore investigated by using the iridium precatalysts shown in Figure 5.20, which were synthesised by Dr. Victoria Annis and Dr. Peter J. Rayner. These include symmetric *N*-heterocyclic carbenes with a variety of % buried volumes and Tolman electronic parameters.[200] Phosphine containing precatalysts[76, 96] and asymmetric *N*-heterocyclic carbenes[245] were included which have both been used previously as SABRE polarisation transfer catalysts.
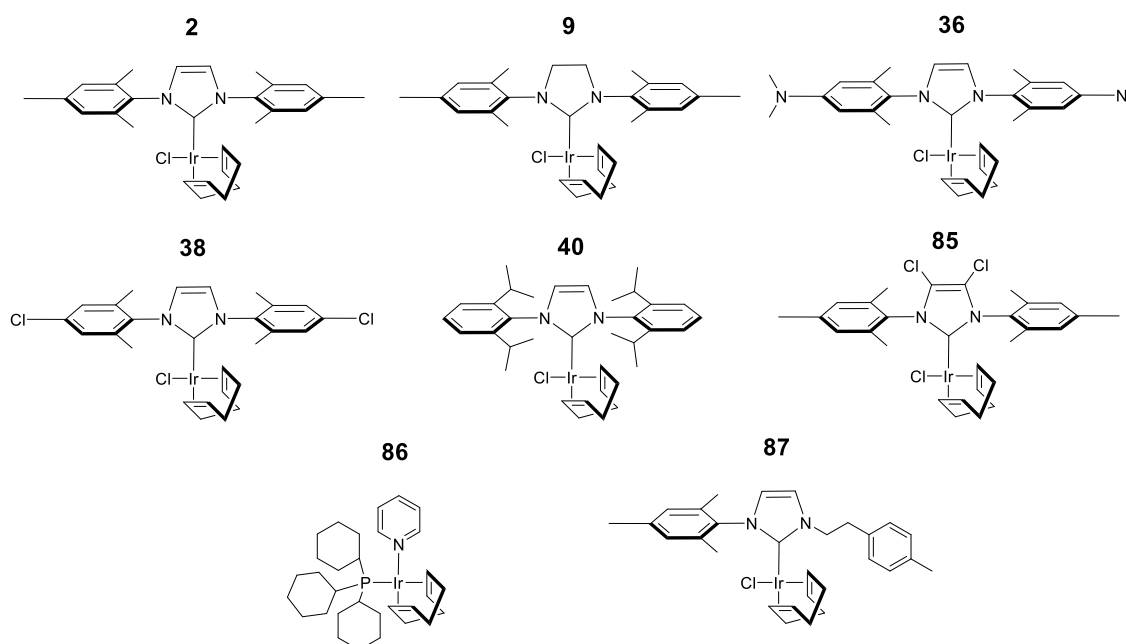
Figure 5.20: Structures of different precatalysts used in this work synthesised by Dr. Victoria Annis and Dr. Peter J. Rayner.

Samples containing one of the precatalysts shown in Figure 5.20 (5 mM), **22-1,2-[^{13}C$_2$]** (6 eq.) and sulfoxide **69** (10 eq.) with 3 bar *p*-H$_2$ in methanol-*d$_4$* (0.6 mL) were shaken with *p*-H$_2$ at different reaction times. The pyruvate ^{13}C NMR signal enhancements for the [1-^{13}C] and [2-^{13}C] sites (ε_{max}) in addition to the hyperpolarised ^{1}H hydride NMR signals for the **62a** type product (S_{62a}) and its relative proportion (R_{62a}) in solution were monitored for the first 90 minutes of reaction. These values for each of the precatalysts tested are given in Table 5.8.

Table 5.8: Comparison of ε_{max}, τ_{60}, and R_{62a} values measured after shaking a solution of the specified precatalyst (5 mM), 22-1,2-[$^{13}C_2$] (6 eq.) and 69 (10 eq.) in methanol-d_4 (0.6 mL) with 3 bar p-H$_2$ for 10 seconds in a mu-metal shield.

Precatalyst	$^{13}C_1$ ε_{max}/fold*	$^{13}C_2$ ε_{max}/fold*	R_{62a} /%
2	1085 ± 35	1085 ± 35	98
9	870 ± 25	860 ± 25	95
36	980 ± 30	980 ± 30	90
38	915 ± 25	905 ± 25	95
40	905 ± 30	885 ± 25	95
85	650 ± 20	660 ± 20	98
86	35 ± 2	25 ± 2	50
87	60 ± 3	55 ± 3	N/A [&]

*These values are single shot measurements as ε_{max} changes over time. Errors are calculated based on a sample containing **2** for which ε_{max} is constant in the time taken to collect repeat measurements.

[&] No signals for **62a** were discerned

For most of these precatalysts there appeared to be little change in the proportion of the **62a** type product in solution ($R_{62a} > 90\%$), although there was a large effect on pyruvate ^{13}C NMR signal enhancement. For example, precatalysts **2** and **85** both gave R_{62a} values of 98% yet yielded very different pyruvate ^{13}C NMR signal enhancements (ε_{max} of 1085-fold and 660-fold for **2** and **85** respectively). This suggests that while maximising the concentration of the active catalyst in solution is important, the efficiency of magnetisation transfer from p-H$_2$ derived hydride ligands to ligated ^{13}C pyruvate sites within the catalyst is different for each system and must also be optimised. In this example, it is more efficient in the system derived from precatalyst **2** than from **85**. The phosphine-based precatalyst **86** yields a S_{62a} value of just 50% and consequently the resulting pyruvate NMR signal enhancement is just 30-fold. In contrast, when precatalyst **87** containing an asymmetric N-heterocyclic carbene ligand is used an isomer of type **62b** forms in greater proportion. This is likely the result of reduced steric crowding when smaller carbene ligands are used. In the case of **87**, the ε_{max} of 60-fold is an order of magnitude lower than those produced using the symmetric carbene **2**. This confirms that the presence of isomer **62a** in solution is essential for achieving high pyruvate NMR signal gains. Interestingly, when **62b** is the major species, the hyperpolarised $^{13}C_2$ pyruvate profile no longer appears in the pattern diagnostic of $^{13}C_2$ singlet order, as shown in Figure 5.21. This suggests that active catalysts of the form **62a** contain the necessary spin topology for efficient polarisation transfer to ligated $^{13}C_2$ pyruvate sites.
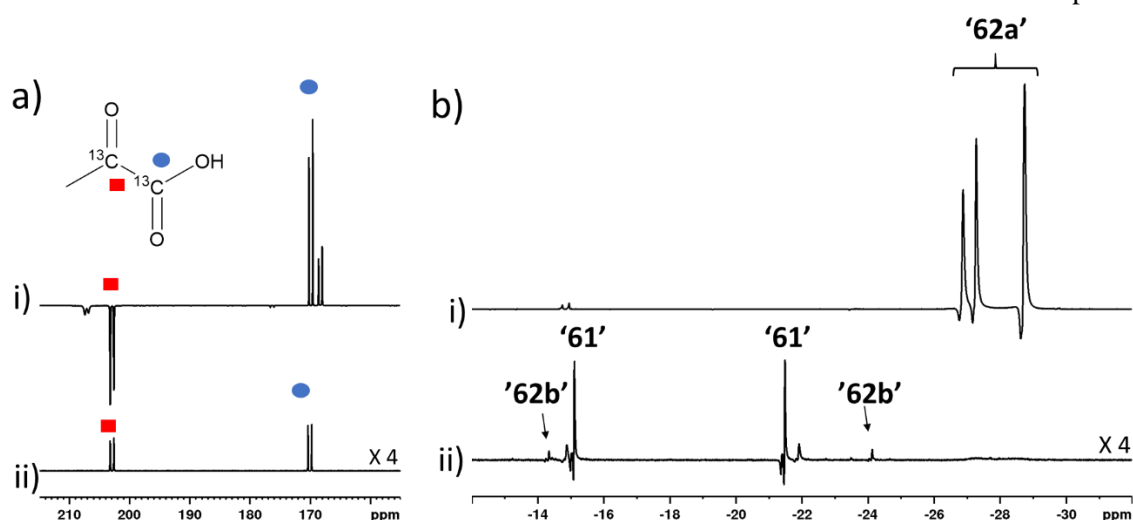
Figure 5.21: Partial hyperpolarised a) ^{13}C and b) ^{1}H NMR spectra after samples of i) 2 (5 mM) or ii) 87 (5 mM) are shaken with 22-1,2-[^{13}C$_2$] (6 eq.), 69 (10 eq.) and 3 bar p-H$_2$ in methanol-d_4 (0.6 mL) for 10 seconds in a mu-metal shield.

For each of these precatalysts, ε_{max} occurs at a different reaction time. This indicates that the time taken to form the active complex is different for each precatalyst and as a result, its maximum concentration, and ε_{max}, are maximised at different time points. For example, **2** activates rapidly and the proportion of its **62a** derivative (and the pyruvate ^{13}C NMR signal gain) is maximised soon after H$_2$ addition. In contrast, **40** has a slower rate of **62a** derivative formation and therefore ε_{max} increases after H$_2$ addition as the concentration of **62a** increases. In all cases, the catalytic efficiency of the system decreases at longer reaction times due to the decomposition processes discussed in section 5.6.4. Therefore, ε_{max} can be used to effectively track the concentration of the active magnetisation transfer catalyst in solution.

These results show that variation of the carbene can have an effect on the pyruvate ^{13}C NMR signal enhancements achieved. Rationalisation of these effects is challenging as both steric and electronic effects of the carbene are likely to be important.[159, 200] It is clear that sterically large carbene ligands are important as they favour formation of the active polarisation transfer catalyst, **62a**. However, in this system ligand effects are likely to be more complex as they can influence multiple processes including the rate of pyruvate exchange within **62**, the rate of H$_2$ exchange in **61**, and the rate of interconversion between **61** and **62**.

5.6.6 Effect of temperature on pyruvate ^{13}C$_2$ NMR signal enhancement

Variation of temperature can be used to alter the rate of ligand exchange processes. Many studies have altered temperature to achieve optimal substrate exchange rates for polarisation transfer using SABRE.[102, 108, 157] Therefore, solutions of **2** (5 mM), **22-1,2-[^{13}C$_2$]** (6 eq.) and one of the sulfoxides shown in Figure 5.14 (4 eq.) were shaken with 3 bar p-H$_2$ in methanol-d_4 (0.6 mL) at three different temperatures (278 K, 293 K, and 323 K). Sulfoxides **46**, **69**-**70**, or **72**-**74** were used as these all give high values of ε_{max} and low values of τ_{60} suggesting that the active catalysts

formed in these mixtures are stable over the time period required to record these measurements. These temperatures were achieved by placing the NMR tube in a temperature controlled water bath for 1 minute before 10 second p-H$_2$ shaking at room temperature. The pyruvate ^{13}C NMR signal enhancement, ε_{max}, was measured for these samples at similar reaction times to ensure that any differences are due to temperature effects and not differing reaction times. The effect of temperature upon the pyruvate ^{13}C NMR signal enhancement is shown in Figure 5.22a. These results show that for sulfoxides **46**, **66**, and **73**, ε_{max} is highest at 293 K while sulfoxides **70** and **72** perform better at 323 K (**74** gives similar ε_{max} values at 293 K and 323 K).

The effect of temperature was also studied using solutions containing one of the precatalysts **2**, **8**, **36**, **38**, **40**, or **85** (5 mM), **22-1,2-[^{13}C$_2$]** (6 eq.) and **66** (10 eq.) in methanol-d_4 (0.6 mL). When these samples are shaken for 10 seconds with 3 bar p-H$_2$ in a mu-metal shield at 278 K, 293 K, or 323 K, ε_{max} also showed a temperature dependency, as shown in Figure 5.22b. For precatalyst **2**, ε_{max} was highest at 293 K with other temperatures likely providing non-optimum exchange rates. It is expected that there must be an optimal pyruvate exchange rate within the active magnetisation transfer complex formed from each sulfoxide, as reported for N-heterocyclic reagents.[157] These rates are likely to be optimal at different temperatures for each catalytic system.[157] Unfortunately, sulfoxide and pyruvate exchange within these complexes could not be quantified using EXSY. Pyruvate exchange is not observed on the EXSY timescale as detailed previously and peak overlap of sulfoxide ^{1}H NMR resonances bound within **61** and **62** prevent reliable selective excitation of these resonances.

Interestingly, each catalytic system gives a different proportion of bound pyruvate polarisation relative to that of the free ligand. This is likely related to a combination of differences in ligand exchange rates and relaxation times within the active magnetisation transfer catalyst. For example, **38**, **40**, and **85** generally give higher proportions of bound pyruvate ^{13}C NMR signal enhancement relative to that free in solution when compared to other precatalysts. This may indicate that pyruvate exchange within systems derived from these precatalysts is slower: this is expected for **38** as it contains an electron withdrawing chloride substituent and is likely to result in stronger pyruvate coordination and slower exchange.[159, 200] Of the precatalysts tested, **85** is the most electron deficient. Therefore, pyruvate exchange in this system is expected to be slower. This is consistent with the high proportions of bound pyruvate NMR signal enhancement and low ε_{max} value which increase at higher temperatures. In contrast, **36** is electron rich which likely leads to faster pyruvate exchange. This is consistent with the lower proportion of bound pyruvate NMR signal enhancement.

Steric effects of the carbene ligand are also important with large carbenes favouring formation of the active isomer of the polarisation transfer catalyst (**62a**), as discussed in section 5.6.5. It might also be expected that sterically demanding carbenes can promote pyruvate exchange. However, in the case of sterically demanding **40**, ε_{max} is comparable to those achieved with the other

precatalysts, and this does not significantly increase at higher temperatures. Therefore, while steric factors are important in favouring the formation of the active magnetisation transfer catalyst, electronic effects can further influence pyruvate NMR signal enhancements which is likely linked to different ligand exchange processes.
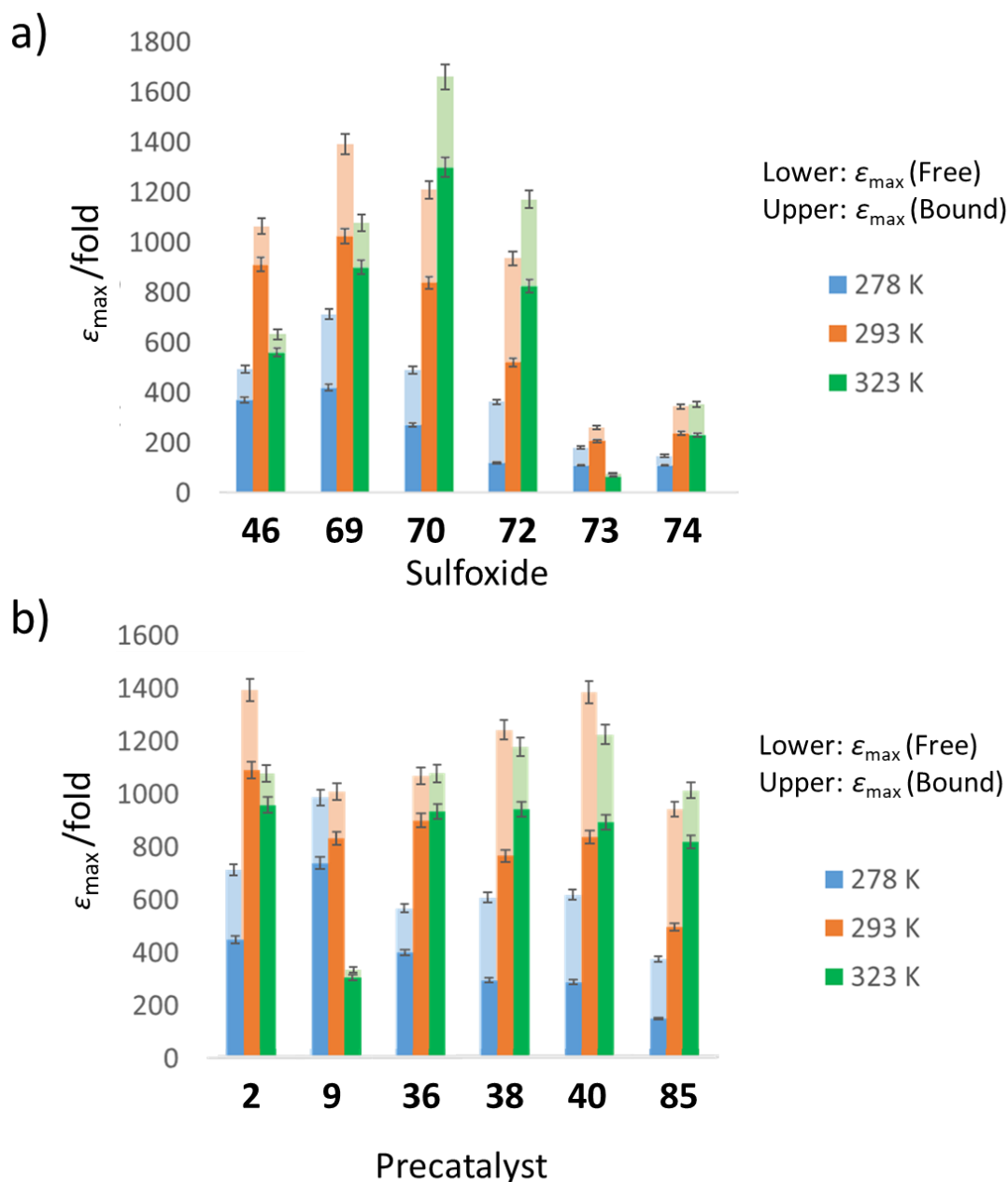
Figure 5.22: Hyperpolarised free (lower, darker) and bound (above, lighter) pyruvate ^{13}C NMR signal enhancements after shaking a) 2 (5 mM), 22-1,2-[^{13}C$_2$] (6 eq.) and the indicated sulfoxide (4 eq.) or b) the indicated precatalyst (5 mM), 22-1,2-[^{13}C$_2$] (6 eq.) and 66 (4 eq.) in methanol-d_4 (0.6 mL) with 3 bar p-H$_2$ in a mu-metal shield for 10 seconds at the indicated temperature.

5.6.7 Effect of chloride on pyruvate $^{13}C_2$ NMR signal enhancement

The active magnetisation transfer catalyst of the form **62a** does not contain a chloride ligand, although species analogous to **61** do. As **61** provides a route to refreshing p-H$_2$ within **62a**, it is expected that exchange between **61** and **62** may play a key role in determining pyruvate ^{13}C NMR signal enhancements. The identity of the chloride ligand in **61** may be very important as it must be displaced by pyruvate to form **62**. Similarly, this ligand must have a comparable binding strength to pyruvate such that pyruvate dissociation can occur to reform **62**. These effects were explored further by changing the identity of the chloride ligand in **61**. This was achieved by activating solutions of [IrBr(COD)(IMes)] (**64**) or [Ir(CH$_3$CN)(COD)(IMes)]PF$_6$ (**66**) precursors (5 mM), **22-1,2-[$^{13}C_2$]** (6 eq.) and **46** (10 eq.) in methanol-d_4 (0.6 mL) with 3 bar H$_2$ to form equilibrium mixtures of [IrBr(H)$_2$(**46**)$_2$(IMes)] (**65**) and [Ir(H)$_2$(CH$_3$CN)(dimethylsulfoxide)$_2$(IMes)]PF$_6$ (**67**) in which the chloride ligand of **61** is replaced with bromide or acetonitrile respectively. When equilibrium mixtures of **62** and **65**, or **62** and **67**, are shaken with 3 bar p-H$_2$ for 10 seconds at 6.5 mT the hyperpolarised hydride resonances of **62a** appear with significantly lower intensity than those achieved using an equilibrium mixture of **61** and **62** (35% and 31% of this signal intensity respectively). When p-H$_2$ shaking is repeated in a mu-metal shield, the hyperpolarised pyruvate ^{13}C NMR signals are now enhanced by just 580-fold and 120-fold for the **64** and **66** derived systems respectively which are lower than those achieved using the analogous **2** system (where ε_{max} = 1070-fold). This reduction in ε_{max} is unlikely related to different hydrogen exchange rates within **61** or **62a** as the linewidths of the hydride resonances of **61**, **65** and **67** are similar (43-45 Hz at 245 K) as are those of **62** in each mixtures (3-5 Hz at 245 K). It is more likely that differences in the catalytic efficiency of these systems is due to the different binding strengths of the ligand (Cl, Br or CH$_3$CN) that must be displaced by pyruvate to form **62** from **61**. When **64** and **66** are used as precatalysts, the amount of **62a** present at equilibrium is lower (S_{62a} values of 22% and 23% respectively compared to 92% achieved using **2**). This suggests that differing binding affinities of Br or NCCH$_3$ alter the position of equilibrium between **61/65/67** and **62** to disfavour formation of **62a**.

5.6.8 Effect of selective deuteration on pyruvate $^{13}C_2$ NMR signal enhancement

Relaxation of active spins within the substrate when ligated to iridium can limit its hyperpolarisation using SABRE. Deuterium labelling of the active polarisation transfer catalyst reduces this and limits unwanted polarisation leakage into ^1H sites of the catalyst.[76, 98, 102, 111] Therefore, the effect of deuterating the sulfoxide and the NHC ligand was examined. A control sample containing **2** (5 mM), **22-1,2-[$^{13}C_2$]** (6 eq.) and **46** (4 eq.) yielded ε_{max} values of 1070-fold and 200-fold for free and ligated pyruvate respectively when shaken with 3 bar p-H$_2$ in methanol-d_4 (0.6 mL) for 10 seconds in a mu-metal shield. When this was repeated using the deuterium labelled sulfoxide **46-d_6** at the same time point after H$_2$ addition, ε_{max} remained comparable at

1070-fold and 220-fold. This suggests that relaxation of hyperpolarised magnetisation *via* ^{1}H sites of the sulfoxide ligand within the active magnetisation transfer catalyst does not limit SABRE efficiency.

In contrast, when an analogous measurement is recorded using a solution of **2-d_{22}** (5 mM), **22-1,2-[^{13}C$_2$]** (6 eq.) and **69** (10 eq.), a fall in ε_{max} from 1085-fold using **2** to 875-fold using **2-d_{22}** is observed, although the bound pyruvate NMR signal enhancements remain comparable at 515-fold and 535-fold respectively. ε_{max} decreases further to 675-fold and 465-fold for free and bound pyruvate respectively when this is repeated using **2-d_{24}** (5 mM). This suggests that deuterium labelling of the carbene ligand is detrimental to SABRE in this case. This is in contrast to many reported examples in which deuteration of [Ir(H)$_2$(NHC)(NSub)$_3$]Cl polarisation transfer catalysts leads to an increase in SABRE efficiency.[76, 98, 102, 111] This discrepancy could be due to the effect of quadrupolar relaxation at the μT magnetic fields used for SABRE caused by the introduction of deuterium.[273]

5.6.9 Further optimisation by varying shaking time and hydrogen pressure

The effect of *p*-H$_2$ shaking time and hydrogen pressure on the pyruvate ^{13}C NMR signal enhancement was also investigated. This involved using a sample of **2** (5 mM), **69** (2 eq.) and **22-1,2-[^{13}C$_2$]** in methanol-d_4 (0.6 mL) at 1, 2 and 3 bar *p*-H$_2$. The resultant ε_{max} values increased from 510-fold to 730-fold when the *p*-H$_2$ pressure was raised from 1 bar to 3 bar. This increase in ε_{max} at these *p*-H$_2$ pressures is linked to increased *p*-H$_2$ refreshment in the **61/62** system. No further increases in ε_{max} were observed at *p*-H$_2$ pressures greater than 3 bar. This suggests that, for this sample, hydrogen exchange is rate limiting at pressures lower than 3 bar but this may not become more efficient at pressures greater than 3 bar and consequently, other ligand exchange or relaxation processes become limiting once this pressure is exceeded (see Appendix 5).

Higher ε_{max} values are achieved when the shaking time is extended from 5 to 30 seconds (1050-fold compared to 425-fold). Increased shaking time allows polarisation to build up more effectively on both bound and free pyruvate. The effect of longer shaking times on the hyperpolarised hydride resonances of **62a** is the opposite. This implies more magnetisation is transferred to the ^{13}C centres of the pyruvate ligand at greater shaking times. This trend is also observed for a sample of **2-d_{24}** with ten equivalents of **69** (data presented in Appendix 7).

Combining all of these optimum conditions simultaneously results in an ε_{max} of 2135-fold (1.7% ^{13}C polarisation) which was achieved using a sample containing **2** (5 mM), **69** (10 eq.) and **22-1,2-[^{13}C$_2$]** (6 eq.) in methanol-d_4 (0.6 mL) shaken with 3 bar *p*-H$_2$ for 30 seconds in a mu-metal shield. Free pyruvate NMR signal gains can be increased from ~30-fold (catalyst **83**, Table 5.8) to 2135-fold by optimisation of factors including sulfoxide, catalyst, temperature, and shaking time. A summary of the effect of these optimisation steps is shown in Figure 5.23.
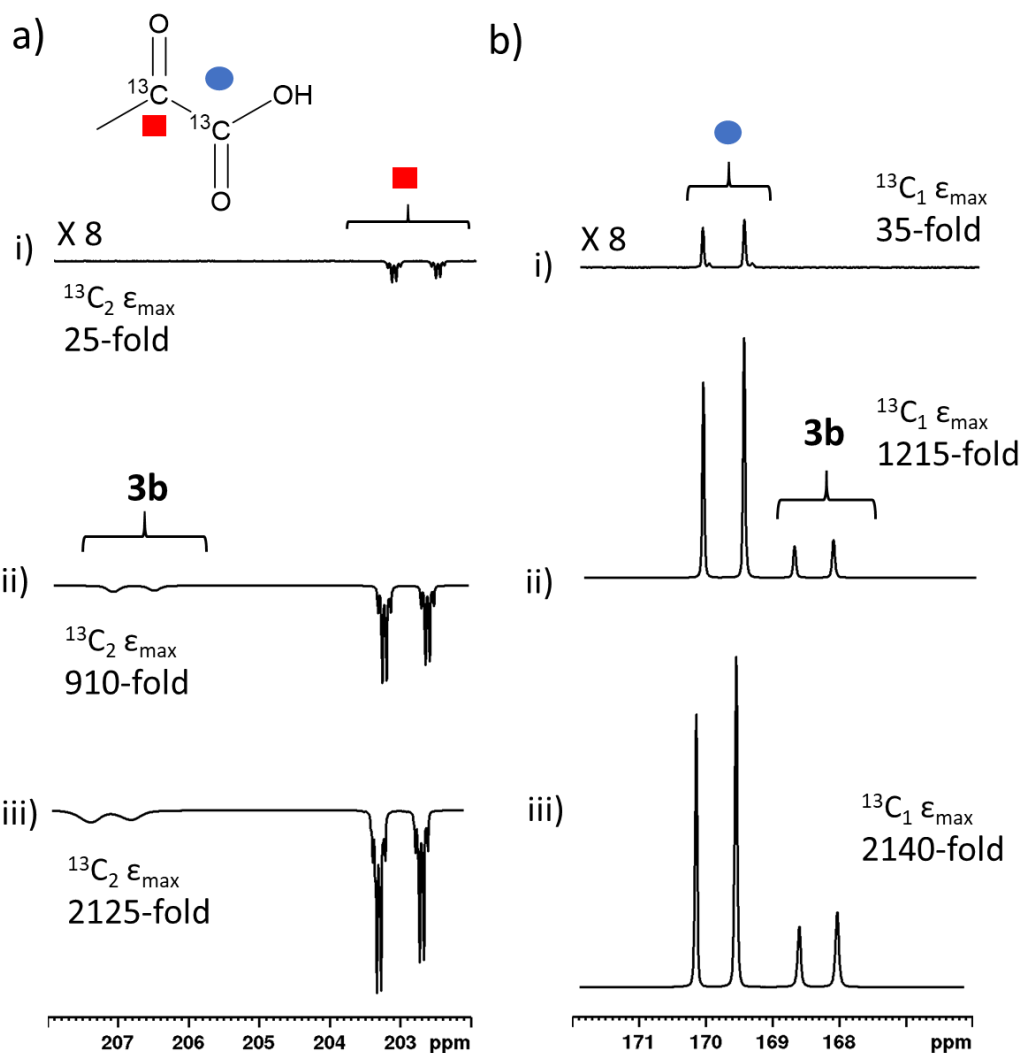
Figure 5.23: Partial hyperpolarised ^{13}C NMR spectra recorded after samples of i) 86 (5 mM), 69 (4 eq.) and 22-1,2-[^{13}C$_2$] (6 eq.) ii) 2 (5 mM), 46 (4 eq.) and 22-1,2-[^{13}C$_2$] (6 eq.) iii) 2 (5 mM), 69 (10 eq.) and 22-1,2-[^{13}C$_2$] (6 eq.) are shaken in methanol-d_4 (0.6 mL) with 3 bar p-H$_2$ for i)-ii) 10 or iii) 30 seconds in a mu-metal shield.

5.7 Conclusions

SABRE can hyperpolarise pyruvate in a cheap, rapid, and reversible method that does not involve the technologically demanding equipment of DNP,[132-137, 139-141, 144] or the multiple chemical alteration steps of PHIP-SAH.[70, 72-75, 127, 263] This is possible due to formation of [Ir(H)$_2$(κ^2-pyruvate)(dimethylsulfoxide)(IMes)] (**62**) polarisation transfer catalysts when solutions of **2** (5 mM), **46** (2-50 eq.) and **22-1,2-[^{13}C$_2$]** (2-10 eq.) in methanol-d_4 (0.6 mL) are activated with 3 bar H$_2$. Sulfoxide coligands are essential for the formation of such active polarisation transfer catalysts. In these cases, **62** forms as two isomers differentiated by the geometry of κ^2-pyruvate coordination. The regioisomer where pyruvate coordinates in the same plane as the hydride ligands (**62a**) is the active polarisation transfer catalyst that can deliver high pyruvate ^{13}C NMR signal enhancements. Interestingly, hyperpolarised ^{13}C$_2$ singlet order within **22-1,2-[^{13}C$_2$]** can be created spontaneously. In contrast to traditional SABRE magnetisation transfer catalysts of the form [Ir(H)$_2$(IMes)(Sub)$_3$]Cl, **62a** undergoes slow ligand exchange and

[IrCl(H)$_2$(dimethylsulfoxide)$_2$(IMes)] (**61**) is highly important in mediating the necessary *p*-H$_2$ exchange processes.

Sterically large carbenes are necessary for the formation of the active isomer, **62a**, although electronic effects are expected to be important in fine tuning ligand exchange processes. Hyperpolarised pyruvate ^{13}C NMR signals are related to the amount of active catalyst, **62a**, in solution, although systems containing similar amounts but different ligands can result in very different pyruvate NMR signal enhancements. These results highlight the tension between many different factors that influence polarisation transfer efficiency within this complex. In all cases a decrease in SABRE catalytic efficiency is observed at longer reaction times which is associated with dimer formation and catalyst deactivation.

While SABRE provides a cheap and reversible approach to hyperpolarise pyruvate with time and cost advantages over DNP and PHIP-SAH, the NMR signal enhancements SABRE can achieve are significantly lower (^{13}C polarisation of 1.7% compared to ~5% for PHIP-SAH[73] or up to 70% for DNP[38]). Nevertheless, the use of these SABRE enhanced NMR signals for applications such as biomedical imaging or reaction monitoring is explored further in Chapter 6. The system presented here has been optimised in methanol-*d*$_4$. For applications such as biomedical imaging, achieving high NMR signal enhancements in aqueous, rather than methanol-*d*$_4$, is more important and this is explored in more detail in Chapter 6. It is anticipated that this approach may be applicable to the hyperpolarisation of a wider range of *α*-keto acids that do not undergo hyperpolarisation using PHIP, traditional SABRE, or SABRE-Relay. Other research groups are now using this approach of using coligands to create novel polarisation transfer catalysts that allow coordination and hyperpolarisation of weakly coordinating *O*-donor ligands using SABRE. For example, Gemeinhardt *et* al have used pyridine as a coligand to hyperpolarise acetate (^{13}C $\varepsilon = 100$-fold).[233] This was speculated to occur *via* formation of [Ir(acetate)(H)$_2$(IMes)(pyridine)$_2$)], although no characterisation data for this species was presented.

The formation and behaviour of these novel sulfoxide containing polarisation transfer catalysts and their applications to hyperpolarise pyruvate are an important step forward as they allow the SABRE hyperpolarisation of molecules previously incompatible with this technique.

Chapter 6. Applications of SABRE hyperpolarised pyruvate

6.1 Introduction

Since the advent of hyperpolarisation techniques, many researches have used enhanced MR signals for a range of new and exciting applications.[7] One of these applications involves monitoring chemical transformations or detecting short lived intermediates using hyperpolarised NMR. While many spectroscopic techniques such as *in situ* IR, UV, and EPR have been developed to monitor chemical change,[274] Magnetic Resonance (MR) remains one of the most widely used as it can study the identity of molecules *in situ* in a non-destructive manner. Differences in chemical shift (δ) can be used as a reporter of changes in nuclear magnetic environment. Despite these advantages, MR signal strength is derived from small perturbations of closely spaced nuclear spin energy levels.[1] Therefore, highly concentrated materials (>mM) and/or long experiment time with significant signal averaging are often required to generate a detectable MR signal. This limits the ability to detect low concentration species (<μM) and reduces the time over which chemical change can be tracked. Hyperpolarisation is able to overcome these limitations by creating signals enhanced by up to 5 orders of magnitude.[7]

In the case of dissolution Dynamic Nuclear Polarisation (d-DNP), one of its most significant applications is the production of hyperpolarised contrast agents suitable for *in vivo* metabolic tracking.[241] These studies are able to monitor chemical transformations of hyperpolarised biomolecules into downstream metabolites. This allows for differences in metabolic pathways to be interrogated and enables diagnosis of certain diseases through metabolic irregularities.[241] The agents used in such studies are typically those involved in the major metabolic pathways in the body. [^{13}C]-Pyruvate is the most investigated hyperpolarised contrast agent to date,[132-137, 139-141, 275] although the hyperpolarisation of a range of other metabolic tracers using d-DNP has also been reported.[41] Studies have already been performed using hyperpolarised pyruvate to successfully localise areas of prostate cancer in the first in human study in 2013.[132] Since then, further studies have used pyruvate hyperpolarised using d-DNP to track metabolism in the human heart[275] and brain.[137] The enhanced MR signals achieved using hyperpolarisation techniques have also been used to interrogate other non-biological chemical transformations in real time. For example, the signal gains provided by d-DNP have been used to monitor Diels-Alder cycloadditions[276] or ligand complexation.[277]

Over the last 35 years, *para*hydrogen (p-H$_2$) has been used to create non-Boltzmann polarization within molecules when its magnetism is unlocked by a chemical reaction.[31, 32, 46] Since then, PHIP has been used to monitor many hydrogenation reactions *in situ* with examples originating in

homogeneously catalysed hydrogenations of alkenes and alkynes[60, 268] and more recently extending to hydrogenation catalysed by solid surfaces[62, 63, 67, 278] or frustrated Lewis pairs.[64, 65] Typically, the magnetism of p-H$_2$ can only be incorporated into a target molecule *via* pairwise addition of both hydrogen nuclei. However, new methods of introducing p-H$_2$ spin order into molecules are being developed. One of these, termed oneH-PHIP, involves incorporation of only a single p-H$_2$ derived proton into an aldehyde which has allowed the study of hydroformylation reactions using PHIP.[279] The enhanced signals PHIP provides can often make low concentration intermediates visible to MR which gives insight into reaction mechanisms.[46, 60, 280, 281] The hyperpolarisation of molecules such as succinate[68, 69, 71] and pyruvate[72, 74, 75] using *Para*-Hydrogen Induced Polarisation (PHIP) and its derivatives has also been used to create agents suitable for *in vivo* metabolic studies, although this technology has not yet progressed to the same stage of clinical trials as d-DNP.[282]

In 2009, Signal Amplification By Reversible Exchange (SABRE) was developed which uses p-H$_2$ to hyperpolarise molecules without chemical incorporation of p-H$_2$ into the analyte.[78] Instead, the symmetry of p-H$_2$ is broken by an oxidative addition reaction with an iridium catalyst. Magnetisation is then transferred from p-H$_2$ derived hydride ligands to ligated substrates through a temporary J-coupled network.[78] This transfer usually occurs at magnetic fields of 6.5 mT for transfer from p-H$_2$ to ^{1}H sites,[78, 102] although direct transfer to ^{15}N and ^{13}C sites can be achieved at μT fields.[171] Dissociation of the hyperpolarised ligand generates a pool of hyperpolarised spins of the ligand free in solution. This substrate polarization is built up in a catalytic process due to the reversible exchange of both p-H$_2$ and the substrate. SABRE and its derivatives have allowed *in situ* monitoring of a wider range of chemical transformations beyond typical hydrogenation or hydroformylation reactions. These include monitoring the incorporation of deuterium labels into *ortho* pyridine sites at 1 T, which is a commonly observed side reaction when pyridine is polarised in methanol-d_4 using SABRE.[150] Other examples have determined the rate of substitution of *tris*(*tert*-butoxy)silanol by triflic anhydride using hyperpolarised ^{29}Si NMR.[109] Some examples of reactions monitored using hyperpolarised MR are presented in Figure 6.1
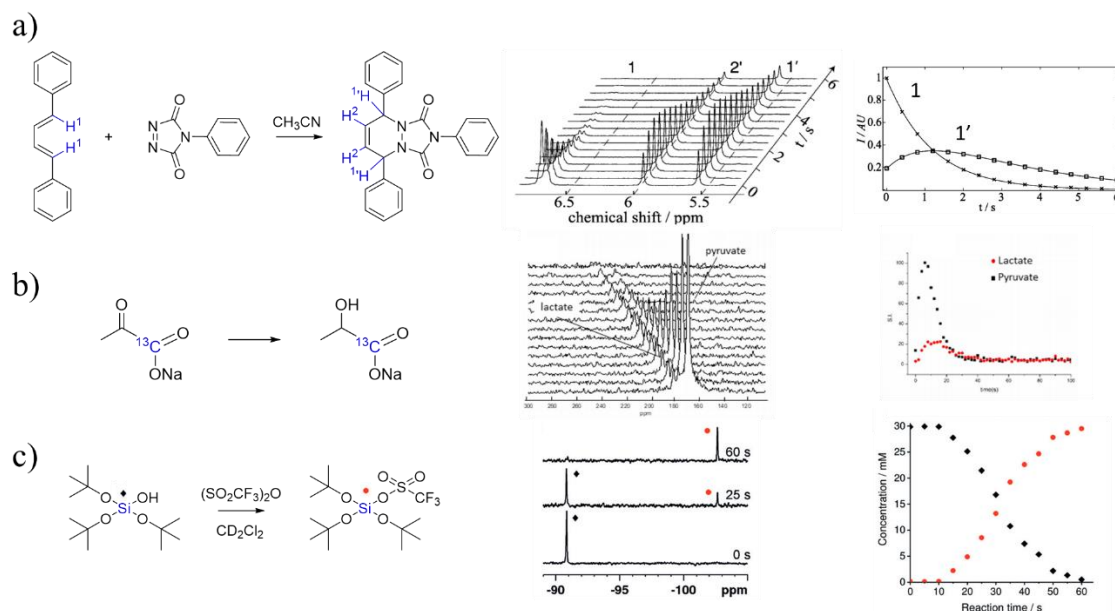
Figure 6.1: Examples of reactions monitored using hyperpolarised NMR. a) Diels-Alder cycloaddition of d-DNP hyperpolarised 1,4-dipheneylbutadiene with 4-phenyl-1,2,4-triazole-3,5-dione. Reprinted (adapted) with permission from H. Zeng, Y. Lee and C. Hilty, *Anal. Chem.*, 2010, 82, 8897-8902 Copyright (2010) American Chemical Society.[276] b) Metabolism of PHIP-SAH hyperpolarised pyruvate to lactate in the heart of a mouse taken from Cavallari et al.[72] c) Reaction between SABRE-Relay hyperpoalrised *tris*(*tert*-butoxy)silanol and triflic anhydride taken from Rayner et al.[109] Note that reactions were monitored using hyperpolarsed NMR signals for the sites shown in blue.

The hyperpolarised magnetisation created by techniques such as SABRE relax back to their Boltzmann derived states according to the time constant, T_1. In order to monitor chemical change of hyperpolarised molecules, it is essential that the rate of transformation is faster than the rate of relaxation to allow for product to be created with retained non-Boltzmann magnetisation. Therefore, hyperpolarised reagents should contain sufficiently enhanced signals with long lifetimes such that chemical change can be monitored over a longer time period. The creation of long lived hyperpolarised singlet magnetisation which decay according to the time constant T_{LLS}, which can be longer than T_1,[50] could allow extension of these time windows. Hyperpolarised reaction monitoring is typically achieved by recording a series of single scan NMR spectra with low flip angle.[276] The succession of pulses effectively uses up the hyperpolarised magnetisation and therefore low flip angles (5-15°) are necessary to allow detection of product before the starting magnetisation is lost due to pulsing and relaxation. However, the detection of small amounts of product is favored by using a large (90°) flip angle, although this depletes more of the initial reagent's enhanced magnetisation. Therefore, the choice of flip angle and time spacing between successive pulses are important factors in hyperpolarised reaction monitoring experiments.

The hyperpolarisation of sodium pyruvate-1,2-[$^{13}C_2$] (**22-1,2-[$^{13}C_2$]**) using SABRE has been presented in Chapter 5. This can be achieved by reacting [IrCl(COD)(IMes)], **2** (5 mM), and **22-**

1,2-[$^{13}C_2$]) (6 eq.) and a sulfoxide with 3 bar H_2 in methanol-d_4 (0.6 mL). When the sulfoxide is dimethylsulfoxide (**46**), the polarization transfer catalyst [Ir(H)$_2$(κ^2-pyruvate)(IMes)(*S*-dimethylsulfoxide)] (**62**) is formed, as summarised in Figure 6.2.[260, 263] These solutions are then shaken with 3 bar *p*-H_2 at μT fields to transfer magnetisation directly from *p*-H_2 derived hydride ligands to ligated ^{13}C pyruvate sites to yield NMR signal enhancements of ~1000-fold in methanol-d_4. Magnetisation transfer catalysts of the form **62** can be used to prepare hyperpolarised **22-1,2-[$^{13}C_2$]** in a long lived nuclear spin state with a T_{LLS} of ~43 s at high field (11.7 T) which exceeds its T_1 times (~34 s and ~21 s for its $^{13}C_1$ and $^{13}C_2$ sites respectively).[263] This may have exciting applications in monitoring chemical transformations over longer time periods.
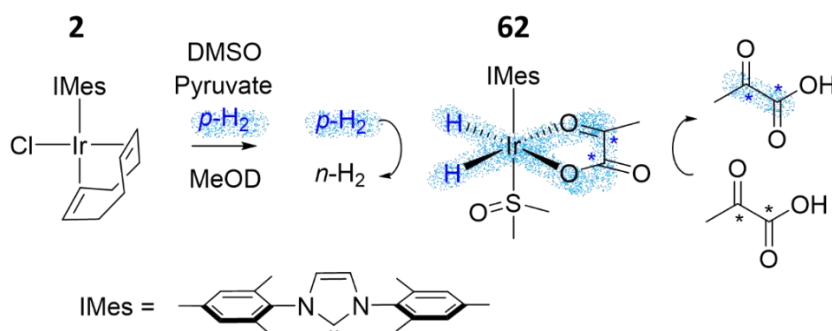
Figure 6.2: Hyperpolarised pyruvate can be produced by SABRE. Upon reaction of [IrCl(COD)(IMes)] with *p*-H_2, sodium pyruvate-1,2-[$^{13}C_2$], and dimethylsulfoxide, [Ir(H)$_2$(κ^2-pyruvate)(IMes)(dimethylsulfoxide)] forms which can yield pyruvate ^{13}C NMR signal enhancements of *c.a.* 1000-fold.

In this chapter, potential applications of SABRE hyperpolarised pyruvate are explored. This includes recording pyruvate ^{13}C NMR signal gains in non-methanolic solvents including 70:30 D_2O:ethanol-d_6 which may be a solvent more appropriate for *in vivo* MR studies.[283] MR images of SABRE hyperpolarised pyruvate are collected *in vitro* and *in vivo* to determine if SABRE can produce hyperpolarised pyruvate suitable for *in vivo* biomedical studies. The NMR signal gains SABRE can achieve are then used for applications such as monitoring organic transformation of pyruvate before the scope of the technique is extended to other substrates with similar structures.

6.2 Hyperpolarisation of pyruvate in more biocompatible solvents

In Chapter 5, the formation of active polarisation transfer catalysts of the form **62** and their role in transferring polarisation from *p*-H_2 derived hydride ligands to ligated ^{13}C sites of pyruvate was discussed. Optimisation in methanol-d_4 has yielded pyruvate ^{13}C NMR signals of 2135-fold (1.7% polarisation). For potential applications in biomedical imaging studies these NMR signal enhancements should be optimised in more biologically relevant D_2O or 70:30 D_2O:ethanol-d_6 mixtures.[283] Therefore, SABRE hyperpolarisation of **22-1,2-[$^{13}C_2$]** was compared in a range of solvents.

Solutions of **2** (5 mM), phenylmethylsulfoxide (**69**) (10 eq.) and sodium pyruvate-1,2-[$^{13}C_2$] (**22-1,2-[$^{13}C_2$]**) (6 eq.) were therefore activated with 3 bar H_2 at 298 K in various different solvents

(0.6 mL) to yield the formation of **62**. The solution was then shaken with 3 bar p-H$_2$ for 10 seconds in a mu-metal shield at 298 K. These conditions were selected as they yielded the highest pyruvate ^{13}C NMR signal gains in methanol-d_4 (as detailed in Chapter 5). The maximum pyruvate ^{13}C NMR signal gains (ε_{max}), relative absolute integrals of the enhanced hydride ^{1}H NMR signals of **62a** (S_{62a}), and the ratio of the **62a** type product at ε_{max} relative to the sum of all hydride containing species (R_{62a}), are given in Table 6.1 for each of the solvents tested.

Table 6.1: Comparison of ε_{max}, S_{62a}, and R_{62a} for solutions of 2 (5 mM), 69 (10 eq.) and 22-1,2-[^{13}C$_2$] (6 eq.) in the indicated solvent (0.6 mL) shaken with 3 bar p-H$_2$ for 10 seconds in a mu-metal shield.

Solvent	Free Pyruvate ε_{max}		Pyruvate bound in 62a ε_{max}		S_{62a}	R_{62a}
	^{13}C$_1$/fold	^{13}C$_2$/fold	^{13}C$_1$/fold	^{13}C$_2$/fold	/arb. units	/%
Methanol-d_4	1090 ± 35	1035 ± 30	420 ± 15	510 ± 15	85	90
Methanol-d_4/D$_2$O 75:25	470 ± 40	375 ± 30	100 ± 10	85 ± 5	36	87
Methanol-d_4/D$_2$O 50:50	130 ± 20	110 ± 15	20 ± 5	20 ± 5	12	100
Methanol-d_4/D$_2$O 25:75	5 ± 1	5 ± 1	0	0	0.5	N/A[%]
Ethanol-d_6	130 ± 5	110 ± 5	165 ± 10	150 ± 10	30	96
Ethanol-d_6/D$_2$O 30:70	160 ± 10	120 ± 5	10 ± 5	15 ± 5	10	99
Nitromethane-d_2	0	0	20 ± 5	15 ± 5	N/A[%]	N/A[%]
Dichloromethane-d_2/D$_2$O 94:6	5 ± 1	5 ± 1	130 ± 10	110 ± 10	N/A[%]	N/A[%]
Ethyl lactate/Methanol-d_4 (98:2)	0	0	0	0	N/A[%]	N/A[%]

[%]No hydride signals for a complex of type **62a** were discerned.

Pyruvate ^{13}C NMR signal gains were found to decrease as the D$_2$O content of methanol-d_4/D$_2$O mixtures is increased. For example, ε_{max} of free pyruvate roughly halves from 1065-fold to 425-fold when a sample of methanol-d_4/D$_2$O 75:25 is compared to pure methanol-d_4. ε_{max} decreases further to 120-fold when the D$_2$O content is increased from 25% to 50%. These effects are related to a lower solubility of p-H$_2$ in D$_2$O which likely reduces the efficiency of hydrogen exchange within the active catalyst.[151] It is also possible that at high D$_2$O concentrations solvent coordination to the iridium catalyst can occur which can change the identity of the active polarisation transfer catalyst.[121, 168, 284] As the D$_2$O content is increased to 75% almost no ^{13}C NMR signal enhancement is observed (5-fold). Under these conditions solubility of the iridium catalyst becomes an issue and methanol-d_4/D$_2$O mixtures with D$_2$O content higher than this cannot be used due to the insolubility of **2** in these mixtures. SABRE catalysts soluble in D$_2$O have been synthesised by functionalising the carbene backbone with PEGylated groups[100] or other water solubilising groups.[121] The use of catalysts such as these could be used to yield SABRE hyperpolarised pyruvate in aqueous solutions, although these catalysts typically yield NMR signal gains lower than those achieved in methanol.

Pyruvate ^{13}C NMR signal gains in ethanol-d_6 are an order of magnitude lower than those recorded in methanol-d_4 (Table 6.1). Interestingly, in ethanol-d_6 the bound pyruvate signal gains are larger than those of the free ligand which may suggest a slower rate of pyruvate dissociation in this

solvent. When the p-H$_2$ shaking time of this sample is increased from 10 to 20 seconds the average ε_{max} for free pyruvate across both [1-^{13}C] and [2-^{13}C] sites increases from 120-fold to 140-fold. The signal gain remains comparable when shaken for 30 seconds (140-fold). These trends are also prevalent in nitromethane-d_2 and dichloromethane-d_2/D$_2$O (94:6) solvents. For example, in both nitromethane-d_2 and dichloromethane-d_2/D$_2$O (94:6) mixtures the ^{13}C NMR signal gains for ligated pyruvate are higher than those for the free ligand. Additionally, the site averaged ε_{max} in dichloromethane-d_2/D$_2$O (94:6) increases from 5-fold to 20-fold when the shaking time is extended from 10 to 30 seconds. Interestingly, when this sample is shaken for 10 seconds after being stored at 323 K for 60 seconds prior to p-H$_2$ shaking, the site averaged ε_{max} increases from 5-fold to 15-fold which supports that ligand exchange processes within the active catalyst are slower in this solvent. In solvents other than methanol-d_4, hydride hyperpolarisation of the active catalyst is much lower (in some cases signals for this species are not discernible, see Table 6.1) which indicates that polarisation transfer is much less efficient. This is likely related to a combination of effects that include slower ligand exchange and lower p-H$_2$ solubility[151] when SABRE is performed in these solvents.

Only a 4-fold free pyruvate ^{13}C NMR signal enhancement is observed when a 70/30 ethanol-d_6/D$_2$O mixture, which might be a system suitable for *in vivo* studies,[283] is tested. However, this can be dramatically increased to 120-fold when **2** (17 mM) and **69** (10 eq.) are activated with 3 bar H$_2$ in ethanol-d_6 (0.18 mL) for 1 hour at 298 K to form **61** before the addition of **22-1,2-[^{13}C$_2$]** in D$_2$O (0.42 mL) is added to form **62** in a second step. This is likely related to more efficient formation of the active catalyst in ethanol-d_6 compared to ethanol-d_6/D$_2$O mixture due to effects including reduced H$_2$ and catalyst solubility in D$_2$O. It is expected that similar optimisation approaches discussed in Chapter 5 can be used to increase the efficiency of SABRE catalysis in ethanol-d_6 or water/alcohol mixtures. For example, selection of catalysts that yield faster exchange kinetics, water soluble catalysts, or an increase of p-H$_2$ pressure may yield an increase in pyruvate NMR signal gains in water containing solvents. Nevertheless, it is clear that SABRE performance is most optimal in methanol-d_4 and the reduced performance in the aqueous containing solvents necessary for biomedical translation are likely to be a serious limitation to use in this application.

6.3 Applications of SABRE hyperpolarised pyruvate for biomolecular imaging

Hyperpolarised pyruvate-[1-^{13}C] has found much success as a hyperpolarised reporter of metabolism *in vivo*.[72, 75, 132-137, 139-141] For these applications d-DNP is most commonly used to achieve the necessary MR signal gains. Here, phantom MR images of SABRE hyperpolarised pyruvate are collected to investigate further if the MR signal gains SABRE can achieve in methanol-d_4 (discussed in Chapter 5) or ethanol-d_6/D$_2$O mixtures (discussed in Section 6.2) are

sufficient to allow detection *in vitro*. Two samples of **2** (5 mM), **46** (10 eq.), and **22-1,2-[¹³C₂]** (6 eq.) in methanol-d_4 (3 mL) were activated with 3 bar H_2 for 1 hour at room temperature to allow the formation of the active polarisation transfer catalyst, **62a**. The formation of **62** is evident from a colour change (orange to colourless). One of these samples was shaken with 3 bar *p*-H_2 for 30 seconds before being rapidly inserted into the 9.4 T imaging coil and the acquisition sequence started. The second sample was also placed inside the coil to compare responses for pyruvate samples recorded under hyperpolarised conditions to their Boltzmann derived counterparts. A more concentrated sample of ethanoic acid (17.4 M) was also used as a reference to illustrate the signal increase achieved using SABRE. The apparatus used to hold these three NMR tubes is shown in Figure 6.3a. A single scan, FID-based, centric encoded ¹³C Chemical Shift Image (CSI) was recorded which splits the 30 mm by 30 mm field of view into a 16 by 16 grid and records a ¹³C NMR spectrum at each point in the grid. A ¹H Fast Low Angle Shot (FLASH) image is also collected to enable spatial localisation of the sample. These two images can be overlaid to identify the regions giving rise to hyperpolarised ¹³C NMR signal. The CSI image overlay alongside the resultant ¹³C NMR spectra from regions of interest within the hyperpolarised and thermal samples are shown in Figure 6.3b, c and d respectively.
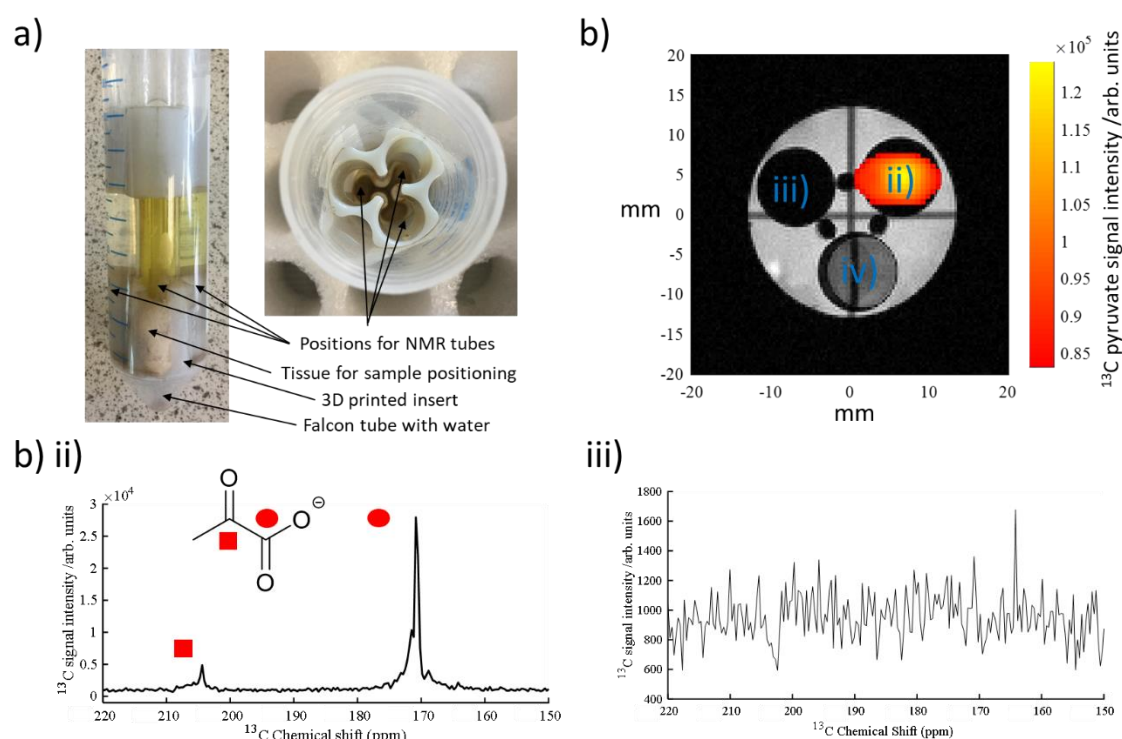
Figure 6.3: a) Photograph of the apparatus used to insert three NMR tubes into the imaging coil of the 9.4 T magnet. This consists of three 10 mm NMR tubes inside a larger 50 mL Falcon tube filled with water. A 3D printed holder was inserted into the Falcon tube to hold the three NMR tubes in place. Paper tissue was used to adjust the NMR tubes to the appropriate height b) i) Overlaid ¹H FLASH (greyscale) and ¹³C CSI image (coloured scale) of SABRE hyperpolarised 22-1,2-[¹³C₂] with regions ii), iii) and iv) corresponding to hyperpolarised pyruvate, thermally polarised pyruvate and glacial ethanoic acid reference respectively. The ¹³C CSI image (16 × 16) was recorded using 5° flip angles and a 20 mm slice thickness. TE = 1.2ms, TR = 100ms, 1200 spectral points, 20 kHz sweep width, 17.4 kHz offset. The coloured scale denotes the area of the hyperpolarised [1-¹³C] pyruvate signal in arbitrary units. b) ii) and iii) are ¹³C NMR spectra from regions containing hyperpolarised pyruvate and thermally polarised pyruvate respectively.

In the regions of interest containing hyperpolarised pyruvate, ^{13}C MR spectra show peaks of hyperpolarised pyruvate at δ 170 and 205. Conversely, signals for the thermally polarised pyruvate and ethanoic acid reference (data not shown) cannot be observed emphasizing the scale of these NMR signal enhancements. The images shown in Figure 6.3b demonstrate that the pyruvate ^{13}C NMR signal gain achieved by SABRE can be detected in an *in vitro* MR image. ^{13}C MR signals are observed for hyperpolarised pyruvate at a concentration of 30 mM while no ^{13}C MR signals for thermally polarised ethanoic acid (17.4 M) are visible. This highlights that SABRE can be used to make low concentration biomolecules visible to MRI.

The methanol-d_4-based system used to collect the images shown in Figure 6.3 is not suitable for *in vivo* biomedical imaging studies as this solvent, and the iridium catalyst (which has not been removed), are toxic.[285] Therefore, MR images of SABRE hyperpolarised pyruvate were also collected on a sample prepared using the same reagent quantities in a D$_2$O/ethanol-d_6 (70:30) mixture, and are shown in Figure 6.4. While the pyruvate signal gains in D$_2$O/ethanol-d_6 (70:30) are lower than those achieved in methanol-d_4 (see section 6.2), they are sufficient to allow *in vitro* ^{13}C MRI detection of SABRE hyperpolarised pyruvate in D$_2$O/ethanol-d_6 (70:30).
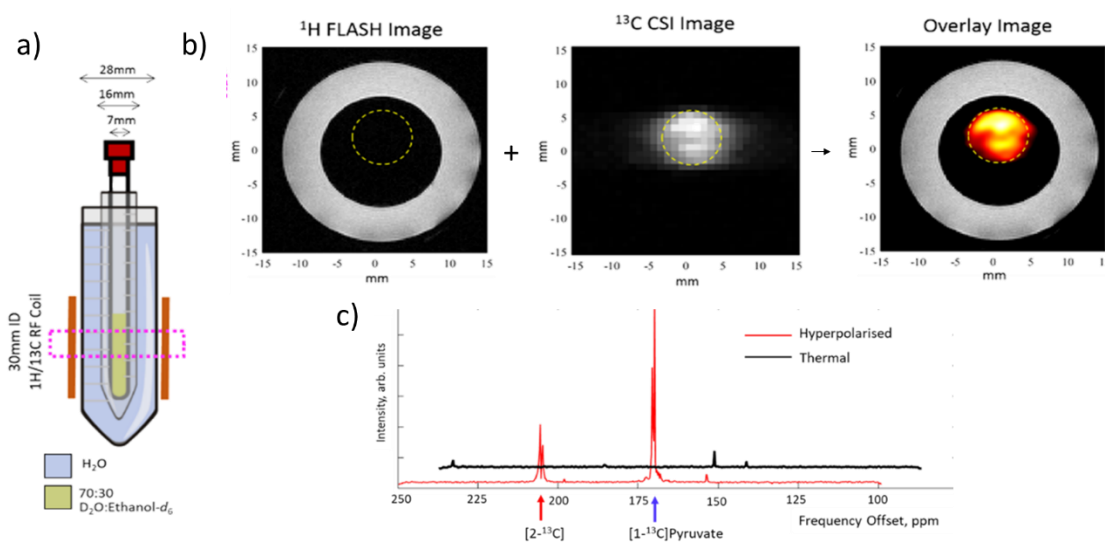
Figure 6.4: a) Diagram of 10 mm NMR tube inside a larger water filled 50 mL Falcon tube inserted into the bore of the 9.4 T magnet b) ^{1}H FLASH, ^{13}C CSI, and overlay images of SABRE hyperpolarised 22-1,2-[^{13}C$_2$] in 70:30 D$_2$O/ethanol-d_6. Note that these are not to the same scale as those presented in Figure 6.3. The ^{13}C CSI image (32 × 32) was recorded using 5° flip angles and a 20 mm slice thickness. TE = 1.2ms, TR = 100ms, 1200 spectral points, 20 kHz sweep width, 17.4 kHz offset. The coloured scale denotes the area of the hyperpolarised [1-^{13}C] pyruvate signal in arbitrary units. c) ^{13}C NMR spectra from a region of interest containing the tube of hyperpolarised 22-1,2-[^{13}C$_2$].

Detecting hyperpolarised pyruvate *in vivo* by MR presents a much greater challenge due to longer transfer times between initial hyperpolarisation and injection into a subject (~30 seconds). This is a limitation of all hyperpolarisation techniques and can be reduced by performing the hyperpolarisation step as close to the site of imaging as possible,[131] or by storing hyperpolarised agents at magnetic fields at which relaxation is slower to allow transportation.[112, 286] Imaging experiments were performed following subcutaneous injection of hyperpolarised **22-1,2-[^{13}C$_2$]** in

methanol-d_4 (1.5 mL) into a sacrificed rat. Injection was made *via* a cannula (750 mm length and 0.4 mm internal diameter) and detected using a Fast Imaging with Steady state Precession (FISP)-based sequence at 7 T.[287] In these images, presented in Figure 6.5, a hyperpolarised ^{13}C MR response was localised in the lower subcutaneous space which is attributed to the hyperpolarised pyruvate signal.
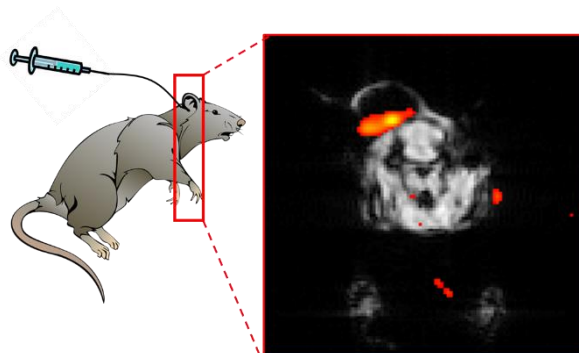
Figure 6.5: FISP-based image of SABRE hyperpolarised pyruvate in methanol-d_4 (1.5 mL) at 7 T injected into the subcutaneous space of a deceased rat. The image has been recorded with 40×40 voxels over a 80 mm^2 FOV with a flip angle of 30° and repetition and echo times of 6.8 ms and 2 ms respectively and a slice thickness of 30 mm.

This result suggests that in principle, SABRE might hyperpolarise pyruvate with ^{13}C MR signal enhancements that are high enough to allow detection *in vivo*. However, aside from the obvious limitations of bio-incompatibility, there are additional challenges faced by the need to remove the iridium SABRE catalyst. This has been reported to be toxic to various cell lines[285] and while methods for its removal have been developed,[116] these create additional steps which increase the transfer time between polarisation and detection. The need to remove additives such as organic radical or hydrogenation catalyst is also required in other hyperpolarisation techniques such as DNP and PHIP respectively. However, as these techniques can achieve higher starting pyruvate ^{13}C polarisation (70%[38] and 5%[73] in aqueous solvents respectively compared to 1.7 % in methanol-d_4 using SABRE) a longer time window for these steps can be afforded. The inability to produce significant MR signal gains in the aqueous solvents necessary for *in vivo* study will provide a significant barrier for biomedical imaging applications of SABRE.

6.4 Applications of SABRE hyperpolarised pyruvate for reaction monitoring

SABRE hyperpolarisation has been used for applications such as chemosensing,[149] detection of low concentration species[107, 124, 288] and reaction monitoring.[109, 150] These applications do not necessitate high NMR signal gains in aqueous solvents and are able to utilise the advantages of SABRE compared to other hyperpolarisation techniques including its simple and reversible nature. Therefore, the use of SABRE hyperpolarised NMR to monitor organic transformations of pyruvate is explored further. The decarboxylation of pyruvate by reaction with hydrogen peroxide (H_2O_2) was studied as it has been reported to be rapid and on a timescale shorter than the lifetime of the hyperpolarised signals.[188, 289-291] The mechanism of this reaction is suggested to occur *via*

a tetrahedral 2-hydroperoxy-2-hydroxypropanoate intermediate, as shown in Figure 6.6.[188, 291, 292] The rate of this reaction is dependent on solution pH with carbon isotope effects suggesting that the rate determining step changes from formation of the intermediate to its decarboxylation as the pH is increased.[292] 2-hydroperoxy-2-hydroxypropanoate is unstable and is typically too short lived to be observed by usual spectroscopic analyses (IR, UV, MS, NMR) at room temperature.[188] However, its observation by ^{13}C NMR at low temperature (238-259 K) has been reported.[188] Monitoring this reaction using SABRE hyperpolarised pyruvate could provide advantages such as allowing detection of intermediates of this type by NMR.
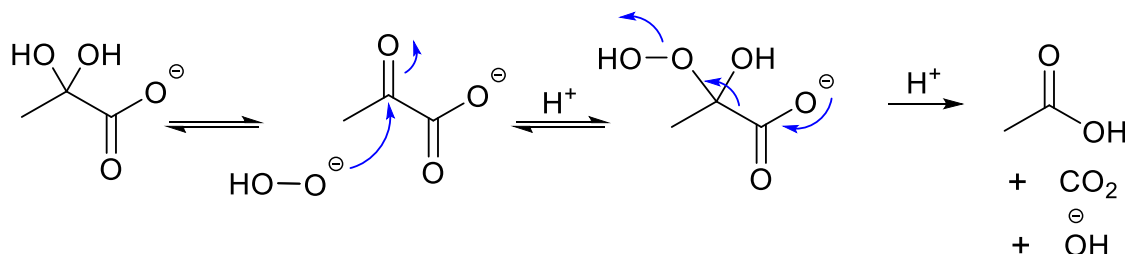
Figure 6.6: Mechanism of the decarboxylation of pyruvate by H_2O_2 involves reversible attack of pyruvate by H_2O_2, or the peroxide anion, to form a tetrahedral 2-hydroperoxy-2-hydroxypropanoate intermediate which decarboxylates to form carbon dioxide and ethanoic acid.

For this work, sodium pyruvate with ^{13}C labels in both the carbonyl and keto positions (**22-1,2-[^{13}C$_2$]**) is used. A comparison of the hyperpolarised lifetimes of **22-1-[1-^{13}C]**, **22-2-[2-^{13}C]** and **22-1,2-[^{13}C$_2$]** is given in Iali *et* al and shows that the hyperpolarised lifetime of ^{13}C sites in **22-1,2-[^{13}C$_2$]** (up to 85 s at low field) is much greater than those of **22-1-[1-^{13}C]** (33 s) and **22-2-[2-^{13}C]** (18 s) (see Appendix 4).[263] These effects result from the creation of singlet order within the coupled spin-½ ^{13}C pair of **22-1,2-[^{13}C$_2$]** which cannot be created within **22-1-[1-^{13}C]** or **22-2-[2-^{13}C]**. Therefore, **22-1,2-[^{13}C$_2$]** is used as a substrate as its longer hyperpolarised lifetime may allow monitoring chemical change over a longer time period in addition to the easier observation of chemical changes occurring at both labelled sites.

6.4.1 Detecting chemical change when SABRE hyperpolarised pyruvate is reacted with H_2O_2

SABRE hyperpolarised NMR was used to detect products of chemical change following the reaction between **22-1,2-[^{13}C$_2$]** and H_2O_2. To do this, solutions of **2** (5 mM), **46** (4 eq.) and **22-1,2-[^{13}C$_2$]** (6 eq.) in ethanol-d_6 (0.18 mL) were activated with 3 bar H_2 for 1 hour at room temperature to form the active polarization transfer catalyst, **62a**. The formation of **62** is obvious from a colour change (orange to colourless). These solutions were then shaken with 3 bar p-H_2 in a mu-metal shield for 30 seconds before the addition of the H_2O_2 reagent (30 % w/w H_2O_2 in H_2O diluted to a total volume of 0.42 mL D_2O). This yielded a final H_2O_2 concentration of 50, 100 or 150 mM in 70:30 D_2O/ethanol-d_6 (0.6 mL). The sample was left inside the mu-metal shield while H_2O_2 was added at room temperature and shaken for 1 second at Earth's magnetic field to ensure

the solution was well mixed. A series of single scan ^{13}C NMR spectra were recorded with 90° flip angles immediately after insertion into a 9.4 T spectrometer at 298 K.

In these measurements, hyperpolarised ^{13}C NMR signals for **22-1,2-[$^{13}C_2$]** (at δ 170 and 202) and **22-1,2-[$^{13}C_2$]** bound within **62a** (at δ 169 and 205) are observed in the first ^{13}C NMR spectrum. In addition, hyperpolarised resonances are also observed for the reaction products ethanoic acid and CO_2 at δ 182 and 122 respectively, an example ^{13}C NMR spectrum is given in Figure 6.7a. Signals for **22-1,2-[$^{13}C_2$]** decrease in intensity over time (due to relaxation and chemical change) while those of the reaction products increase initially as they form before ultimately decaying due to relaxation. When the sample was removed from the spectrometer and shaken again with fresh p-H_2, no hyperpolarised ^{13}C NMR signals for **22-1,2-[$^{13}C_2$]** or reaction products were visible. These experiments were repeated with final H_2O_2 concentrations of 50, 100 and 150 mM and the signal profiles of these samples are presented in Figure 6.7b. They reveal that as the H_2O_2 concentration is increased, a much larger hyperpolarised ^{13}C NMR signal for the CO_2 reaction product is observed (Figure 6.7c). It is therefore clear that SABRE hyperpolarised NMR is able to detect the products of chemical change with retained non-Boltzmann population distributions across their nuclear spin energy levels. This suggests that SABRE hyperpolarised molecules could be used to indirectly detect H_2O_2 concentrations and monitor such chemical changes in real time.
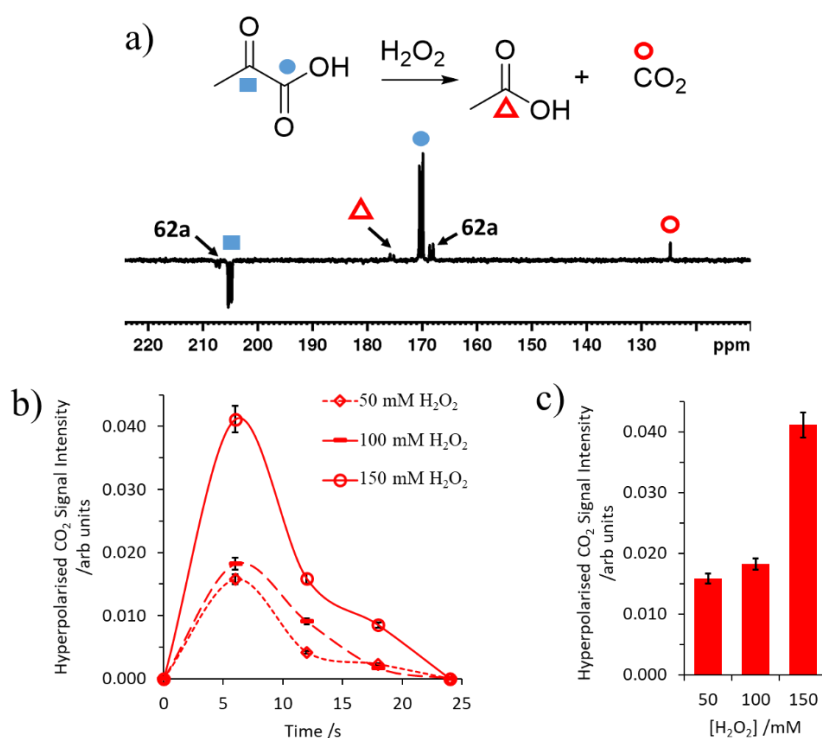
Figure 6.7: a) A partial single scan 90° ^{13}C NMR spectrum recorded 6 seconds after H_2O_2 is added to a solution of SABRE hyperpolarised 22-1,2-[$^{13}C_2$] (final mixture of 150 mM H_2O_2 in D_2O/ethanol-d_6 70:30 (0.6 mL)) b) A plot of the ^{13}C NMR signal intensity of hyperpolarised CO_2 formed during the reaction. Each data point is a successive single scan 90° ^{13}C NMR spectrum. The lines are for visual aid only. c) A plot of hyperpolarised CO_2 signal intensity in the first single scan 90° ^{13}C NMR spectrum for each H_2O_2 concentration. Note that in b) and c) The CO_2 signal intensity at each H_2O_2 concentration is normalised to the hyperpolarised signal for 22-1,2-[$^{13}C_2$] in the first scan. These are single shot measurements with error bars derived from typical values (discussed in Chapter 5).

6.4.2 Using SABRE hyperpolarised NMR to extract a rate of pyruvate reaction with H₂O₂

These experiments in D_2O and ethanol-d_6 mixtures recorded using 90° flip angles allow hyperpolarised ^{13}C NMR signals for **22-1,2-[$^{13}C_2$]** and the hyperpolarised reaction products ethanoic acid and CO_2 to be monitored for ~20 seconds after the first ^{13}C NMR spectrum is collected. This provides a limited time window for monitoring this chemical transformation. Therefore, these experiments were repeated in methanol-d_4/D_2O mixtures using a series of 10° pulses. Under these conditions (which are similar to those used to study this reaction by low temperature ^{13}C NMR in a literature example[188]) the initial hyperpolarised ^{13}C NMR signals for **22-1,2-[$^{13}C_2$]** are expected to be higher (see section 6.2). The use of a lower flip angle will allow reaction monitoring over a longer time window as less hyperpolarised magnetisation is destroyed by the pulse.

For these measurements, solutions of hyperpolarised **22-1,2-[$^{13}C_2$]** are produced by preparing samples containing **2** (3 mM), **46** (8 eq.), and **22-1,2-[$^{13}C_2$]** (6 eq.) in methanol-d_4 (288 μL) and methanol (12 μL). After these solutions are activated with 3 bar H_2 and left at room temperature for 30 minutes to allow the formation of **62a**, they are shaken with fresh p-H_2 (3 bar) for 30 seconds in a mu-metal shield (~ 1 μT) at room temperature. Immediately after p-H_2 shaking the J. Young's tap was removed from the NMR tube whilst leaving the sample in the mu-metal shield. A solution of 9.6 μL H_2O_2 (30% w/w solution in H_2O) and phenanthroline (5 eq. relative to **2**) in 290.4 μL D_2O was added (final H_2O_2 concentration of 150 mM). Phenanthroline has been reported to deactivate the SABRE catalyst[293] and was added to prevent pyruvate re-polarisation during the reaction monitoring step and to limit relaxation of hyperpolarised signals by the metal catalyst (this is discussed in more detail in section 6.4.2). The tap was replaced and the sample was shaken in the shield for 1 second to enable efficient mixing before being rapidly inserted into the 9.4 T spectrometer for detection with a succession of single scan 10° ^{13}C NMR spectra with at 6 second time intervals at 298 K. These measurements show signals of hyperpolarised **22-1,2-[$^{13}C_2$]** which decrease in intensity as reaction time is increased, as shown in Figure 6.8. Similarly, hyperpolarised ^{13}C NMR resonances are also observed for the reaction products ethanoic acid and CO_2. In this case, signals for HCO_3^-,[294] which can exist in equilibrium with CO_2, are also visible. Now, chemical change can be monitored over a much longer time period (up to ~90 and ~40 seconds for the 1-[^{13}C] and 2-[^{13}C] sites respectively).
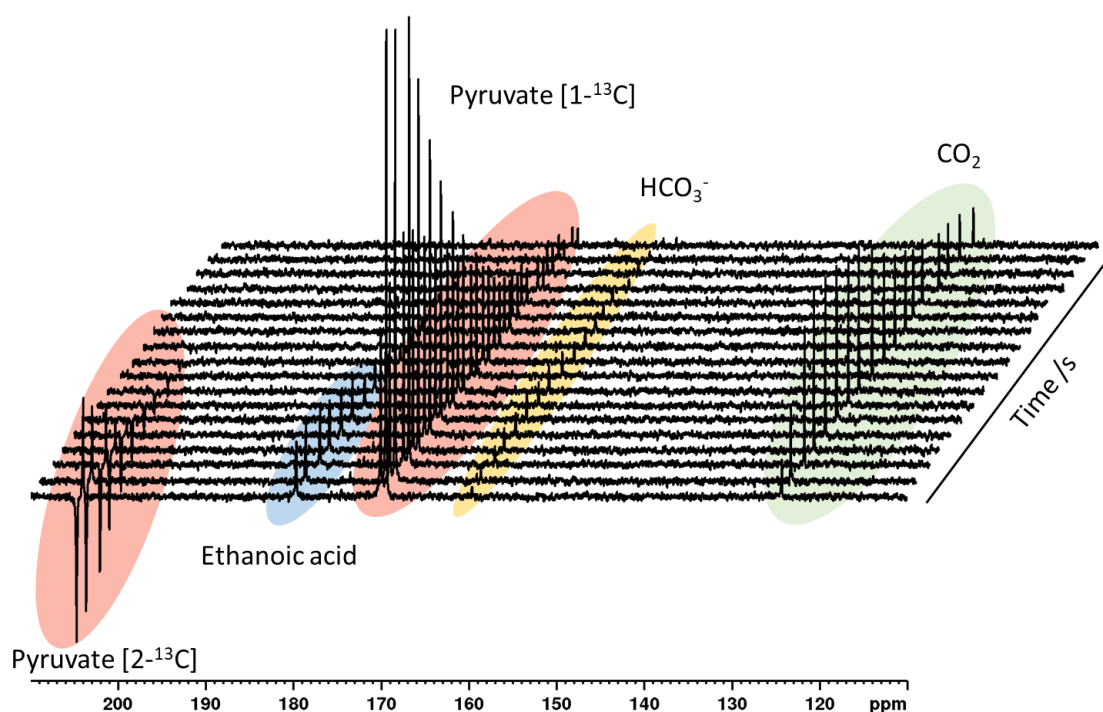
Figure 6.8: A series of partial 10° single scan ¹³C NMR spectra recorded after the addition H₂O₂ (final concentration of 150 mM) and phenanthroline (5 eq. relative to 2) to a solution of SABRE hyperpolarised 22-1,2-[¹³C₂] (15 mM) in methanol-d_4 (0.6 mL) at 298 K.

It is clear that SABRE can detect products of chemical change, and these transformations can be monitored over time. However, extracting a rate of reaction can be challenging considering that hyperpolarised signal intensities are changing due to reactivity, relaxation, and pulse interrogation. Therefore, any kinetic modelling of the data shown in Figure 6.8 must account for all three of these factors. This can be achieved by fitting hyperpolarised signal intensities of either the [1-¹³C] resonance of pyruvate and CO_2, or the pyruvate [2-¹³C] site and ethanoic acid to the following kinetic model. In this model the hyperpolarised signals of species X, S_X, detected by the 10° pulse at time t is calculated using Equation 6.1 where M_X is the magnetisation of species X and θ is the flip angle. The magnetisation of species X remaining after the pulse is given by Equation 6.2.

$$(S_X)_t = (M_X)_{t-\delta t} \sin \theta \qquad (6.1)$$

$$(M_X)_t = (M_X)_{t-\delta t} \cos \theta \qquad (6.2)$$

The magnetisation of pyruvate (M_{Py}), CO_2 (M_{CO2}), and ethanoic acid (M_{Et}), change during the time interval between pulses due to chemical reaction and relaxation according to equations 6.3-6.5 where T_1 is the relaxation time and k is a pseudo first order rate constant described in Equation 6.6. In this model, pyruvate bound within **62a**, pyruvate hydrate, 2-oxy-2-methoxypropanoate, and HCO_3^- were excluded as signals for these species were either not observed, or were only present at $< \sim 3$ % relative to the total hyperpolarised ¹³C NMR signal intensity for all species. A pathway that allows for reaction of pyruvate hydrate or 2-oxy-2-

methoxypropanoate with H_2O_2 was not included as it has been previously reported that this reaction is extremely slow.[188]

$$\left(M_{Py}\right)_{t+\delta t} = \left(M_{Py}\right)_t + \left(-k\left(M_{Py}\right)_t - \frac{\left(M_{Py}\right)_t}{T_1}\right)\delta t \qquad (6.3)$$

$$\left(M_{CO2}\right)_{t+\delta t} = \left(M_{CO2}\right)_t + \left(k\left(M_{CO2}\right)_t - \frac{\left(M_{CO2}\right)_t}{T_1}\right)\delta t \qquad (6.4)$$

$$\left(M_{Et}\right)_{t+\delta t} = \left(M_{Et}\right)_t + \left(k\left(M_{Et}\right)_t - \frac{\left(M_{Et}\right)_t}{T_1}\right)\delta t \qquad (6.5)$$

$$k_{H2O2} = k[H_2O_2] \qquad (6.6)$$

Experimental data shown in Figure 6.8 were normalized to the hyperpolarised pyruvate signal intensity in the first scan (for either the [1-^{13}C] or the [2-^{13}C] site). The initial values of S_X were fixed to those measured in the first scan. Rate constants and relaxation times were found by minimizing the differences between experimentally determined concentrations and calculated values. Similar approaches based on integrated rate equations that account for relaxation and low flip angle have been reported.[276, 295] The spectral patterns shown in Figure 6.8 are caused by both longitudinal single spin and two spin terms which both contribute to the signal intensity. Both of these components will decay at different rates, with the single spin order terms decaying due to T_1. The contribution of only the single spin order terms to the ^{13}C NMR signal intensity can be obtained by summing the integral intensities of the doublets formed at each ^{13}C site for either the [1-^{13}C] or [2-^{13}C] site and therefore only the single relaxation term, T_1 is required in this model. This fitting is shown by the solid lines in Figure 6.9, with the experimental data points (from Figure 6.8) shown by marker points.
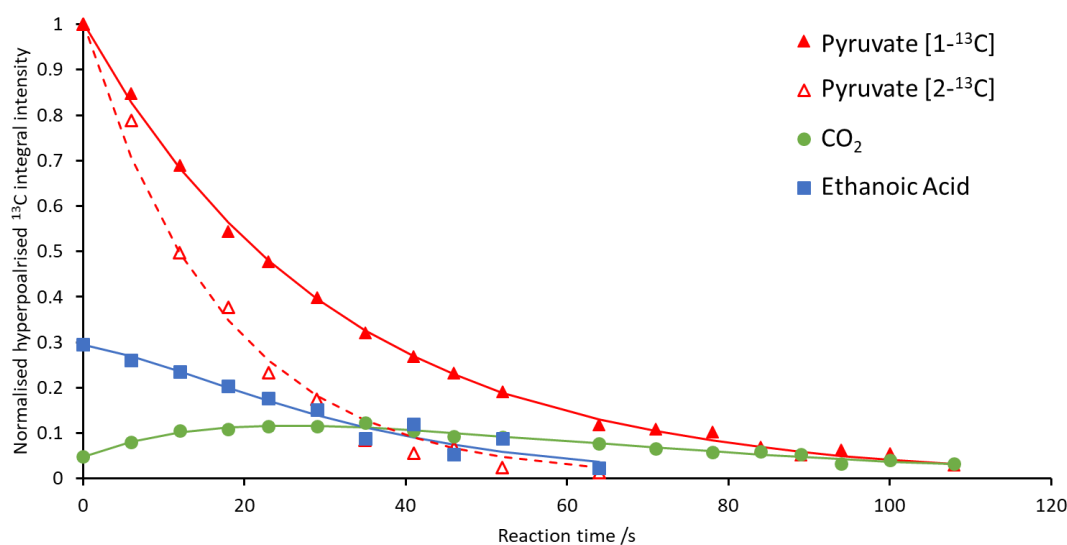
Figure 6.9: Changes in hyperpolarised signal intensity over reaction time can be plotted (marker points, spectra are shown in Figure 6.8) and fitted to the kinetic model described by equations 6.1-6.6 (solid lines). Transformations of the [1-^{13}C] and [2-^{13}C] sites have been fitted separately and are shown here on the same graph.

When the model described by equations 6.1-6.6 is fitted to the experimental data shown in Figure 6.8, relaxation time constants for the [1-^{13}C] and [2-^{13}C] pyruvate sites are found to be 47.3 ± 1.2 s and 20.7 ± 2.9 s respectively. These values are comparable to hyperpolarised T_1 values for these sites of 33.6 ± 0.5 s and 21.2 ± 0.4 s recorded under similar conditions.[263] The model fits T_1 values for ethanoic acid and CO_2 of 34.4 ± 2.0 s and 25.4 ± 9.6 s respectively and a k_{H2O2} of 0.056 ± 0.003 dm^3 mol^{-1} s^{-1} is obtained from modelling the transformation of the [1-^{13}C] site. When this rate is determined from analysis of the [2-^{13}C] pyruvate site and ethanoic acid signals a similar k_{H2O2} of 0.055 ± 0.040 dm^3 mol^{-1} s^{-1} was obtained which is consistent with that determined from analysis of the [1-^{13}C] pyruvate site. There is higher uncertainty in the value determined from transformation of the [2-^{13}C] site which is related to its shorter T_1, compared to the [1-^{13}C] site, which prevents monitoring of chemical changes at this site for longer reaction times ($\sim$40 s compared to $\sim$90 s for the [1-^{13}C] site under these conditions).

6.4.3 Using thermal ^{1}H NMR spectroscopy to measure the rate of pyruvate reaction with H₂O₂

The reaction between pyruvate and H_2O_2 under these conditions cannot be monitored by thermal ^{13}C NMR spectroscopy at room temperature as the signal strengths are not sufficient to observe a response in a single scan. This necessitates signal averaging which limits the ability to monitor changes over a short timescale. However, ^{1}H NMR is able to monitor these changes due to the higher MR receptivity of the ^{1}H nucleus compared to ^{13}C[1] which enables recording sufficient signal with a single scan. A solution of 300 mM H_2O_2 in D_2O (300 μL) (9.4 μL of a 30% w/w H_2O_2 in H_2O solution in 290.4 μL D_2O) was added to sodium pyruvate (30 mM) in 4:96 methanol:methanol-d_4 (300 μL). A series of 90° single scan ^{1}H NMR spectra at 25 second time intervals were recorded immediately after the sample was shaken for $\sim$1 second in the Earth's field to aid mixing. These spectra were recorded with time spacings of 30 seconds to allow for full sample relaxation between each measurement as ^{1}H T_1 measurements of separate 15 mM solutions of sodium pyruvate and ethanoic acid in the same 48:2:48:2 D_2O:H_2O:CD_3OD:CH_3OH solvent mixture yielded T_1 values of 5.7 s and 4.0 s for their CH_3 protons.

When the first spectra of this series is examined, ^{1}H NMR signals for the CH_3 groups of pyruvate and its hydrate are observed at δ 2.35 and 1.45 respectively, as shown in Figure 6.10a. This species is identified as pyruvate hydrate rather than the hemiacetal 2-oxy-2-methoxypropanoate as its ^{1}H NMR chemical shifts compare more closely to those reported for the hydrate in similar solvents.[188] In this first measurement, signals for the methyl and carboxylate protons of ethanoic acid at δ 1.94 and 10.99 respectively are also observed. Resonances of pyruvate and its hydrate decrease as the reaction time is increased while those of ethanoic acid increase. These integral intensities of the ^{1}H CH_3 resonances of pyruvate (A), pyruvate hydrate (B) and ethanoic acid (C) are converted to concentration and fit to a kinetic model to allow the reaction rate (k_{H2O2}) to be calculated. This model is described by equations 6.7-6.10 where δt is an incremental time

difference and k_{H2O2}, k_{Hy} and k_{-Hy} are the rates of reaction between pyruvate and H_2O_2 (D), formation of pyruvate hydrate from pyruvate, and formation of pyruvate from its hydrate respectively. Species such as H_2O, pyruvate dimers, or enol pyruvate were omitted as these species were either in excess or not observed in these measurements.

$$[A]_{t+\delta t} = [A]_t + \left(-k_{H2O2}[A]_t[D]_t - k_{Hy}[A]_t + k_{-Hy}[B]_t\right)\partial t \qquad (6.7)$$

$$[B]_{t+\delta t} = [B]_t + \left(k_{Hy}[A]_t - k_{-Hy}[B]_t\right)\partial t \qquad (6.8)$$

$$[C]_{t+\delta t} = [C]_t + \left(k_{H2O2}[A]_t[D]_t\right)\partial t \qquad (6.9)$$

$$[D]_{t+\delta t} = [D]_t - \left(k_{H2O2}[A]_t[D]_t\right)\partial t \qquad (6.10)$$

Rate constants were found by minimizing the differences between experimentally determined concentrations and calculated values. The model was constrained to set the predicted initial concentrations of each reagent to within 10% of those experimentally determined from the first ^{1}H NMR measurement. Figure 6.10b shows the kinetic fit (solid lines) compared to experimental data (marker points). This model yields a k_{H2O2} of 0.050 ± 0.003 dm^3 mol^{-1} s^{-1}, which is comparable to the value fitted from SABRE hyperpolarised NMR (0.056 ± 0.003 dm^3 mol^{-1} s^{-1}).
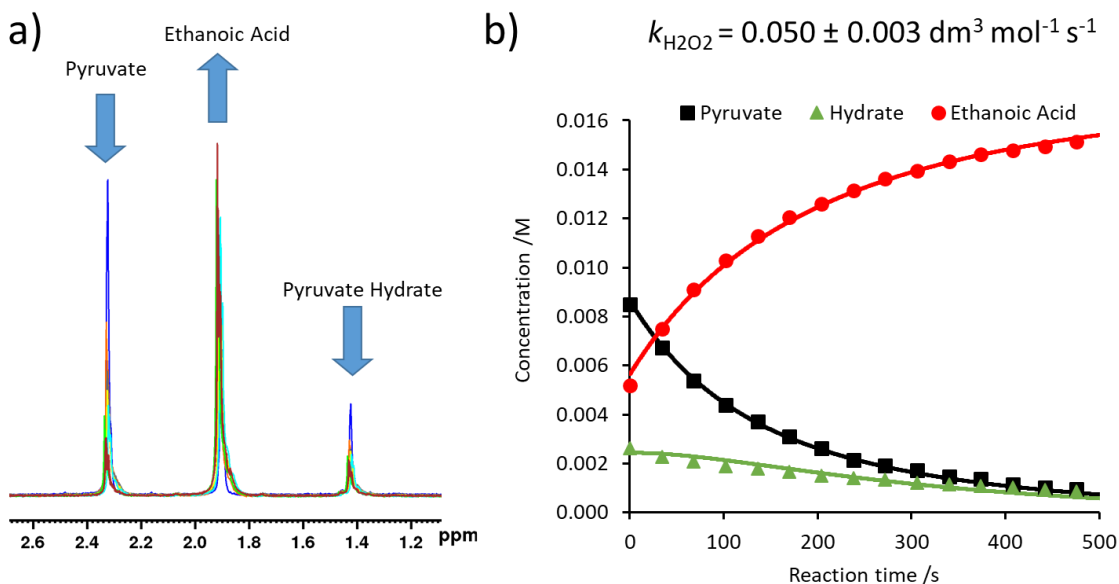
Figure 6.10: a) A series of partial 90° ^{1}H NMR spectra of sodium pyruvate (30 mM) in 4%:96% methanol:methanol-d_4 (300 μL) at 25 second time intervals after the addition of 300 mM H_2O_2 in D_2O (300 μL) b) Kinetic fitting of this NMR data to the model described by equations 6.7-6.10.

These measurements were repeated in the presence of the SABRE catalyst **62a** (3 mM) to determine if the metal has an effect on the rate of reaction between pyruvate and H_2O_2. The kinetic time course collected from ^{1}H NMR spectra in the presence of **62a** no longer fit the model described by equations 6.7-6.10, as shown in Figure 6.11a. This is unsurprising considering that there are now additional reaction pathways such as the binding and rebinding of pyruvate to the

metal that are not accounted for by the model. Additionally, the concentration of pyruvate in solution is expected to be lower as a proportion remains bound within **62a** rather than reacting with H_2O_2. While the chemical shift of pyruvate CH_3 protons bound in **62a** have been presented in Chapter 5 (Table 5.2), in 1D ^1H NMR spectra they overlap with IMes resonances of **62**. This makes accounting for this reactivity in the kinetic model challenging. The influence of the metal can be negated by adding phenanthroline to deactivate **62a** before addition of H_2O_2.[293] ^1H NMR measurements collected following the addition of H_2O_2 to a solution of **62a** which had been deactivated with phenanthroline (5 eq.) fitted the kinetic model (as shown in Figure 6.11b) and yielded k_{H2O2} of 0.051 ± 0.003 dm^3 mol^{-1} s^{-1} which is consistent with k_{H2O2} determined from thermal ^1H NMR measurements without metal (0.050 ± 0.003 dm^3 mol^{-1} s^{-1}) and hyperpolarised ^{13}C SABRE-NMR (0.056 ± 0.003 dm^3 mol^{-1} s^{-1}). This result confirms that the metal catalyst can have an effect on k_{H2O2} and hyperpolarised reaction monitoring using SABRE-NMR should deactivate the metal catalyst to determine a quantitative reaction rate. This is not typically necessary for monitoring reactions that are catalysed by the metal[150] or monitoring reactions of substrates polarised using SABRE-Relay which do not interact with the iridium catalyst.[109]
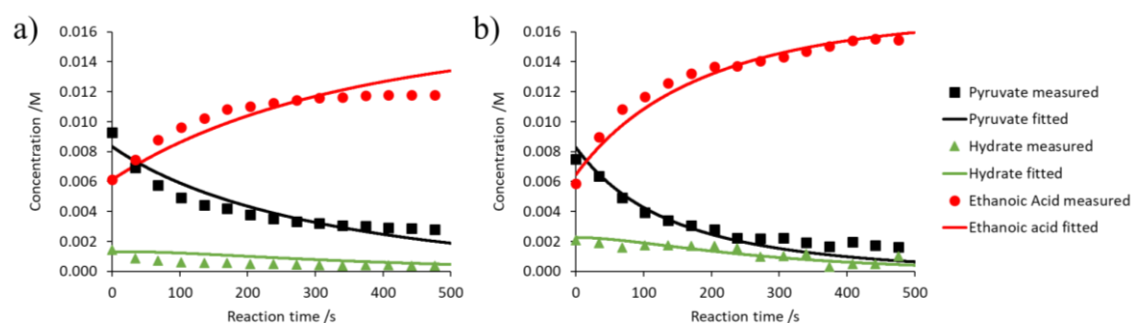
Figure 6.11: Kinetic modelling showing experimental data (markers) and predicted data (solid lines) after a solution of 300 mM H_2O_2 in D_2O (300 μL) (9.4 μL of a 30% w/w H_2O_2 in H_2O solution in 290.4 μL D_2O) is added to a solution containing 62a prepared by preactivating a solution of 2 (5 mM), 46 (8 eq.) and 22 (30 mM) in 4%:96% methanol:methanol-d_4 (300 μL) with 3 bar H_2 for 30 minutes at 298 K. Upon mixing the two solutions the NMR tube was shaken for ~1 second in the Earth's field to aid mixing. In b), phenanthroline (1.5 mg in 100 μL methanol-d_4) was added to 62a and shaken for ~2 seconds in the Earth's field before H_2O_2 was added and the shaking step repeated to aid mixing.

The reaction between pyruvate and H_2O_2 was also determined at a lower H_2O_2 concentration (100 mM compared to 150 mM) using both thermal ^1H NMR and hyperpolarised ^{13}C SABRE-NMR measurements. Kinetic fitting of these data yields k_{H2O2} values of 0.045 ± 0.001 dm^3 mol^{-1} s^{-1} and 0.051 ± 0.003 dm^3 mol^{-1} s^{-1} respectively (data not shown) which are consistent with those values recorded at 150 mM H_2O_2 concentrations. This confirms that SABRE hyperpolarised NMR can be used not only for qualitative monitoring of chemical transformations, but for quantitative determination of reaction rates.

6.4.4 Using UV spectroscopy to measure the rate of pyruvate reaction with H$_2$O$_2$

Ultra-violet (UV) spectroscopy was also used to confirm the rate constant for the reaction between pyruvate and H$_2$O$_2$. A UV spectrum of sodium pyruvate (15 mM) in 51:49 methanol:H$_2$O (1.968 mL) was recorded with a λ_{max} of 316 nm comparing well to previously reported values of 316 nm,[296] 325 nm[187] and 326 nm.[297] A series of UV spectra were then recorded at 5 second time intervals after the addition of H$_2$O$_2$ (150 mM), examples are shown in Figure 6.12a. The decrease in absorption at 316 nm was baseline corrected and fitted to the kinetic model described by equations 6.7-6.10, as shown in Figure 6.12b. The photolysis of pyruvate caused by UV induced $\pi \rightarrow \pi^*$ transitions of the pyruvate keto group has been reported to form a range of products including lactic acid, dimethyltartaric acid and acetoin.[297] A control experiment showed no significant change in the absorption at λ_{max} in the absence of H$_2$O$_2$ and no photolysis products were detected by NMR or MS. This confirms that the absorption decrease at λ_{max} is due to reaction with H$_2$O$_2$ and not photolysis which is consistent with the shorter UV irradiation times used in these experiments (< 5 minutes) compared to those reported for photolysis (~1 hour).[297]
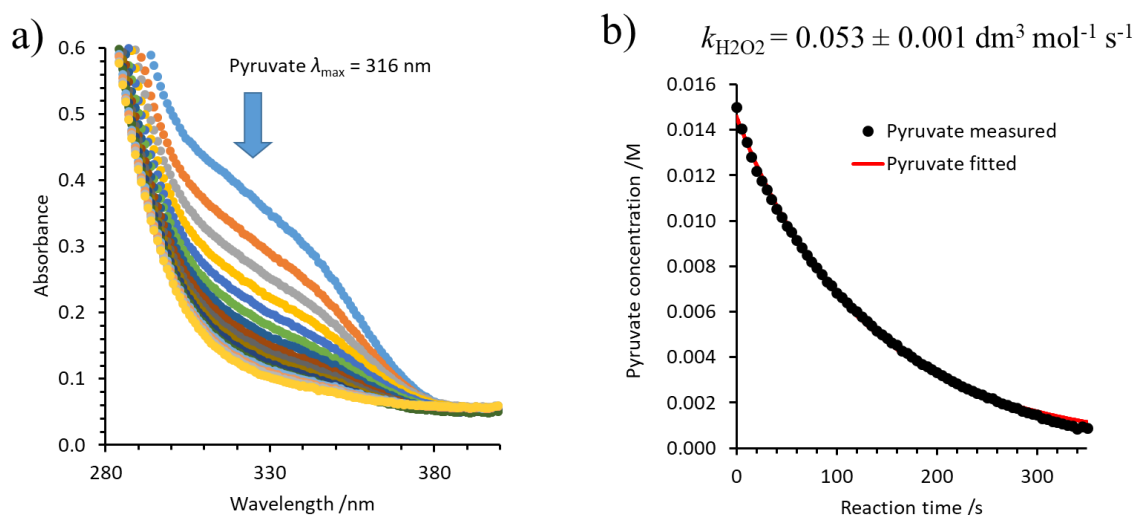
Figure 6.12: a) Partial UV absorption spectra of sodium pyruvate (15 mM) in 51%:49% methanol:H$_2$O (1.968 mL) (upper, blue) with example UV spectra every 30 seconds after the addition of 32 μL H$_2$O$_2$ (30% w/w H$_2$O$_2$ in H$_2$O solution, final H$_2$O$_2$ concentration of 150 mM) b) Kinetic fitting of this UV data according to equations 6.7-6.10.

The value of k_{H2O2} from this UV data was found to be 0.053 ± 0.001 dm^3 mol^{-1} s^{-1} which is consistent with those determined from thermal ^{1}H NMR measurements (k_{H2O2} of 0.050 ± 0.003 dm^3 mol^{-1} s^{-1}). k_{H2O2} from UV measurements has been reported to vary between 0.1 and 1 dm^3 mol^{-1} s^{-1} depending on the pH of the reaction mixture.[291] However, these values are for buffered solutions under more dilute reagent concentrations (1.5 mM pyruvate and 5-30 mM H$_2$O$_2$) which may account for the difference in reaction rate. k_{H2O2} has also been determined using ^{13}C NMR spectroscopy at much lower temperatures (238-259 K).[188] From these data k_{H2O2} is predicted to be ~0.16 dm^3 mol^{-1} s^{-1} at 298 K which is a factor of *c.a* three times faster than values

determined from the data shown in Figures 6.8, 6.10, and 6.12. This is likely related to inefficient sample mixing or slight differences in solvent composition compared to the reported examples.

6.4.5 Advantages of SABRE HP reaction monitoring: Detection of short lived intermediates

The reaction between sodium pyruvate and H_2O_2 has been reported to occur *via* a short lived 2-hydroxperoxy-2-hydroxypropanoate intermediate, as shown in Figure 6.6[292] [188, 291] NMR signals for this intermediate have been reported with ^{13}C chemical shift values of δ 102.9 and 178.3 at low temperature (238-259 K).[188] The closely related ethyl 2-hydroxperoxy-2-hydroxypropanoate, which is formed from reaction of ethyl pyruvate with H_2O_2, has been observed by ^{13}C and ^{1}H NMR spectroscopy at 298 K and is therefore presumably more stable.[291] In the NMR measurements described thus far, no ^{1}H or ^{13}C NMR signals for 2-hydroxperoxy-2-hydroxypropanoate could be observed at 298 K, even under hyperpolarised conditions. This is likely a result of the reaction being too rapid at this temperature to allow detection of this intermediate by NMR. However, signals for this species at δ 101.7 and 175.8 ($^{1}J_{CC}$ = 65 Hz), which compare well to previously reported values,[188, 291] can be observed when these experiments are repeated at reduced temperature. This is achieved by adding H_2O_2 to a solution of SABRE hyperpolarised **22-1,2-[$^{13}C_2$]** frozen at Earth's field inside a dry ice-acetone bath (~195 K) after *p*-H_2 shaking at room temperature. After H_2O_2 addition at ~195 K the sample was shaken for ~1 second at Earth's field to ensure mixing before being inserted into the 9.4 T spectrometer at 260 K for collection of a single scan 90° ^{13}C NMR spectrum. Here, a larger flip angle was used to facilitate detection of the 2-hydroperoxy-2-hydroxypropanoate intermediate. Signals for this intermediate can also be observed in a single scan ^{13}C NMR spectrum when the spectrometer is set to 273 K, although the temperature of the sample is likely to be lower (and undefined) due to previous storage at ~195 K. Nevertheless, the MR sensitivity gains provided by SABRE are able to make this short lived intermediate visible to ^{13}C NMR in just a single scan.
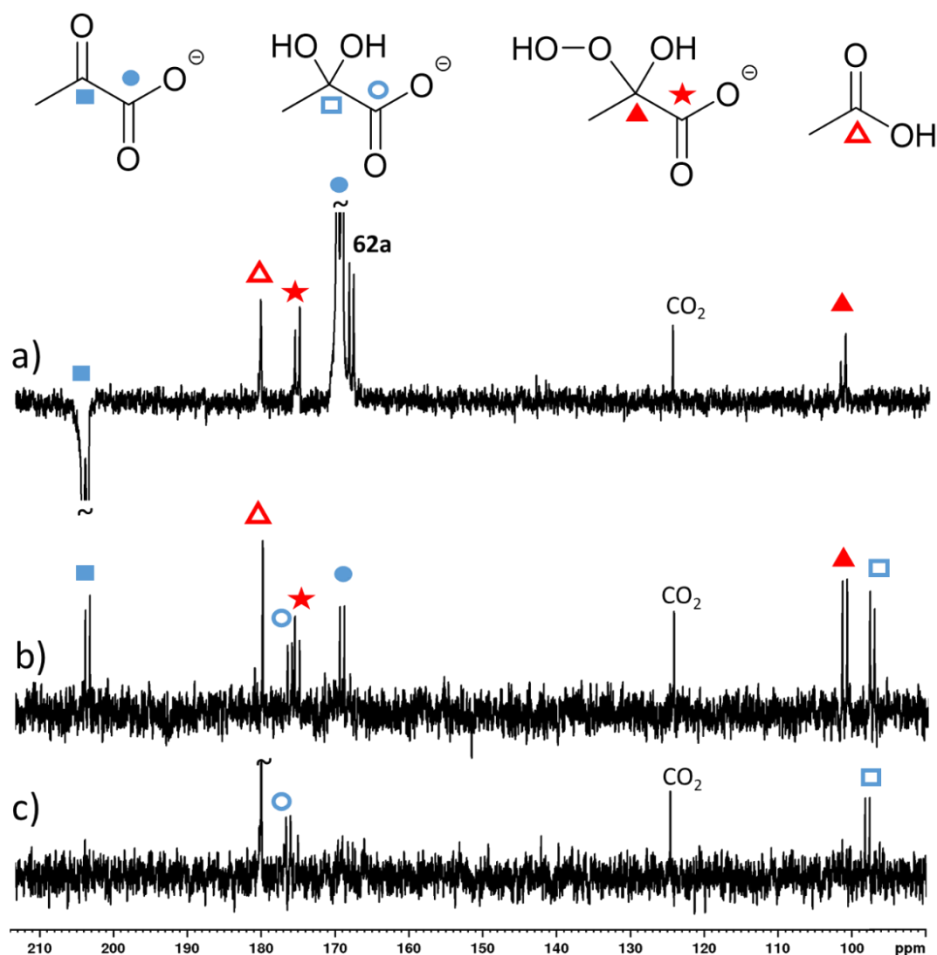
Figure 6.13: a) A single scan 90° hyperpolarised ^{13}C NMR spectrum recorded at 260 K immediately after addition of H$_2$O$_2$ (final H$_2$O$_2$ concentration of 150 mM) at ~ 195 K to a solution containing hyperpolarised sodium pyruvate-1,2-[^{13}C$_2$] b) and c) 128 scan thermal ^{13}C NMR spectrum recorded at 260 K roughly b) 4 minutes and c) 10 minutes after initial H$_2$O$_2$ addition. Note that a) has been expanded vertically by a factor of 4 relative to b) and c).

6.4.6 Limitations of SABRE HP reaction monitoring: Relaxation and catalyst deactivation

Pyruvate has diverse chemical reactivity and has long been reported to undergo transamination reactions to form imines.[298] This transformation is usually mediated by an enzyme and a pyridoxal cofactor, although it can also be facilitated by a transition metal complex.[191] SABRE could provide a route to studying the formation of imines from the reaction of SABRE hyperpolarised pyruvate with an amine. Therefore, a succession of single scan 10° ^{13}C NMR spectra were recorded after the addition of phenylethylamine (26.5 mM) to a solution of SABRE hyperpolarised **22-1,2-[^{13}C$_2$]** (30 mM) in methanol-d_4 (0.6 mL). Enhanced ^{13}C NMR signals for free pyruvate at δ 170 and 203 are visible in addition to those bound within **62a** (5 mM) at δ 169 and 205 and an additional species at δ 176 and 97. This species is present prior to amine addition and is either pyruvate hydrate or 2-oxy-2-methoxypropanoate. There is ambiguity in which species is giving rise to these signals as while these ^{13}C chemical shifts more closely resemble those previously reported for 2-oxy-2-methoxypropanoate,[188] no ^{1}H NMR signals for this species are observed (see section 6.4.3). The hyperpolarised ^{13}C NMR signals of these species are found

to decrease in intensity as the reaction time is increased (due to relaxation of hyperpolarised signals), as shown in Figure 6.14b. No additional ^{13}C NMR signals of the hemiaminal intermediate or imine product are observed over the timescale of this measurement (60 seconds). No chemical changes are evident from single scan ^{13}C NMR measurements when the sample is shaken again with fresh p-H$_2$ and by the third p-H$_2$ shake a signal for hyperpolarised pyruvate is no longer observed.

When this experiment is repeated and a series of 64 scan thermally polarised ^{1}H NMR measurements are recorded they show that signals of **62a** at δ –27.08 and –29.01 are immediately replaced by those of two new complexes at δ –22.44 and –22.48. The species giving rise to these signals are expected to be [Ir(H)$_2$(IMes)(phenethylamine)$_3$]Cl, **27** and [Ir(H)$_2$(IMes)(dimethylsulfoxide)(phenethylamine)$_2$]Cl, **88** and their chemical shifts are consistent with those previously reported for **27**.[104, 106] **27** and **88** form rapidly upon displacement of pyruvate and chloride ligands from **62** by the added amine which is related to the stronger metal binding affinity of the amine ligand.[224, 253] As the reaction time is increased, two new sets of hydride signals at δ –21.52 and –28.50 and δ –21.00 and –26.20 are observed. These chemical shifts are consistent with those of [Ir(H)$_2$(κ^2-α-carboxyimine)(phenethylamine)(IMes)], **29** and [Ir(H)$_2$(κ^2-α-carboxyimine)(dimethylsulfoxide)(IMes)], **47** which have been previously presented in Chapter 4 (albeit in dichloromethane-d_2).[195, 224] These products contain coordinated imine which has formed from the *in situ* condensation reaction between pyruvate and amine which displaces amine ligands from **27** and **88** over a longer timescale, as shown in Figure 6.14. Eventually, signals of **47** dominate and 2D NMR characterisation of this complex at 245 K (which are given in the experimental section 7.4.6) confirm it to be **47**. These chemical changes are summarised in Figure 6.14.

The inability to monitor chemical change of SABRE hyperpolarised pyruvate upon reaction with phenethylamine is due to the slower rate of condensation reaction relative to the rate of hyperpolarised signal decay. No chemical change was observed in these hyperpolarised measurements when the excess of amine was increased (150 mM phenethylamine and 15 mM **22-1,2-[^{13}C$_2$]**). The rate constant of this reaction was monitored thermally using ^{1}H NMR spectroscopy and was estimated as $k = 0.017 \pm 0.001$ dm^3 mol^{-1} s^{-1} which is *c.a.* a factor of three slower than the rate of reaction with H$_2$O$_2$ under analogous experimental conditions ($k = 0.050 \pm 0.003$ dm^3 mol^{-1} s^{-1}). As SABRE can hyperpolarise molecules in a refreshable manner (unlike DNP and PHIP in which hyperpolarisation is created in a batch process) there is potential to monitor concentration changes over longer timescales by simply refreshing p-H$_2$ and repeating the measurement. Therefore, the usual limitation of monitoring reactions that occur faster than the lifetime of the hyperpolarised signals could be circumvented. However, this is not possible in this system due to deactivation of **62a** which prevents refreshable hyperpolarisation of pyruvate. It is clear that using SABRE to monitor reactions in which both secondary reagents or products are able to coordinate to the magnetisation transfer catalyst can provide a challenge to monitoring

such reactions using SABRE. While SABRE could provide a route to monitoring chemical changes on a timescale longer than hyperpolarised lifetimes, this can only occur provided that the lifetime of catalyst deactivation is longer than the reaction timescale.
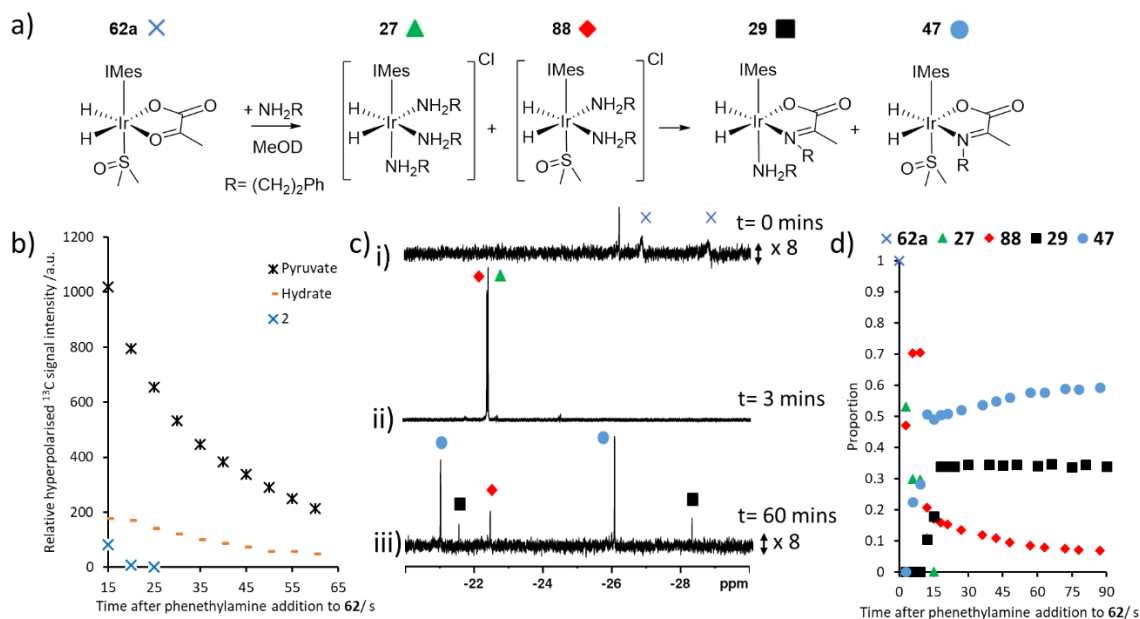
Figure 6.14: a) Summary of chemical changes upon addition of phenethylamine to 62a b) Change in relative hyperpolarised ^{13}C NMR signal intensity of pyruvate, bound pyruvate and the additional species which is likely pyruvate hydrate recorded with a series of 10° ^{13}C NMR spectra c) Representative partial ^{1}H NMR spectra of the hydride region and d) time course determined from a series of 32 scan ^{1}H NMR spectra when phenethylamine (5 eq.) is added to 62a in methanol-d_4 (0.6 mL) at 298 K.

6.5 Using SABRE to create reporters suitable for detection of H$_2$O$_2$

Hydrogen peroxide can be formed in mammalian cells from several biochemical processes. It can be indicative of oxidative stress and is therefore a hallmark of diseases such as lung and pulmonary diseases.[290] The ability to determine H$_2$O$_2$ concentration *in vivo* may therefore provide a route to disease diagnosis. This can be achieved using fluorescent probes[289] although hyperpolarised reporters have also been used.[290, 299] The synthesis and hyperpolarisation (using d-DNP) of molecules with α-keto acid motifs similar to pyruvate that react with H$_2$O$_2$ has been reported.[290] This was achieved using molecules that, unlike pyruvate, cannot be metabolized in other cellular processes *in vivo*. This ensures that any chemical changes are due to reaction with H$_2$O$_2$.

The NMR signal gains SABRE can deliver could allow for imaging the reaction between pyruvate and H$_2$O$_2$. Proof of principle MR images were therefore collected using a sample containing **2** (5 mM), **69** (10 eq.) and **22-1,2-[^{13}C$_2$]** (6 eq.) in methanol-d_4 (3 mL). Upon the formation of **62a**, the sample was shaken with 3 bar p-H$_2$ for 30 seconds in a mu-metal shield before the tube was opened to the atmosphere and H$_2$O$_2$ was added (final H$_2$O$_2$ concentration of 200 mM) before being placed into the bore of a 9.4 T NMR spectrometer. Reference tubes containing ethanoic acid (3 mL) and methanol-d_4 (3 mL) were also placed into the bore of the magnet. A 16 $\times$ 16

FID-based centric encoded ^{13}C CSI was collected in addition to a ^{1}H FLASH image to localize the position of the NMR tubes inside the bore. An overlay of these images is shown in Figure 6.15a. The presence of hyperpolarised pyruvate and the reaction products ethanoic acid and CO_2 highlight that SABRE can provide the ^{13}C NMR sensitivity gains necessary to indirectly detect 200 mM concentrations of H_2O_2 *in vitro*. This experiment highlights that SABRE may provide a route to producing hyperpolarised ^{13}C reporters suitable for H_2O_2 sensing. For biologically relevant applications, a response to much lower concentrations of H_2O_2 (μM) is necessary, and this response should be dependent on H_2O_2 concentration. While typical H_2O_2 concentrations inside cells are difficult to determine, they are typically in the μM concentration range[300] which is significantly lower than those used in these studies (mM).
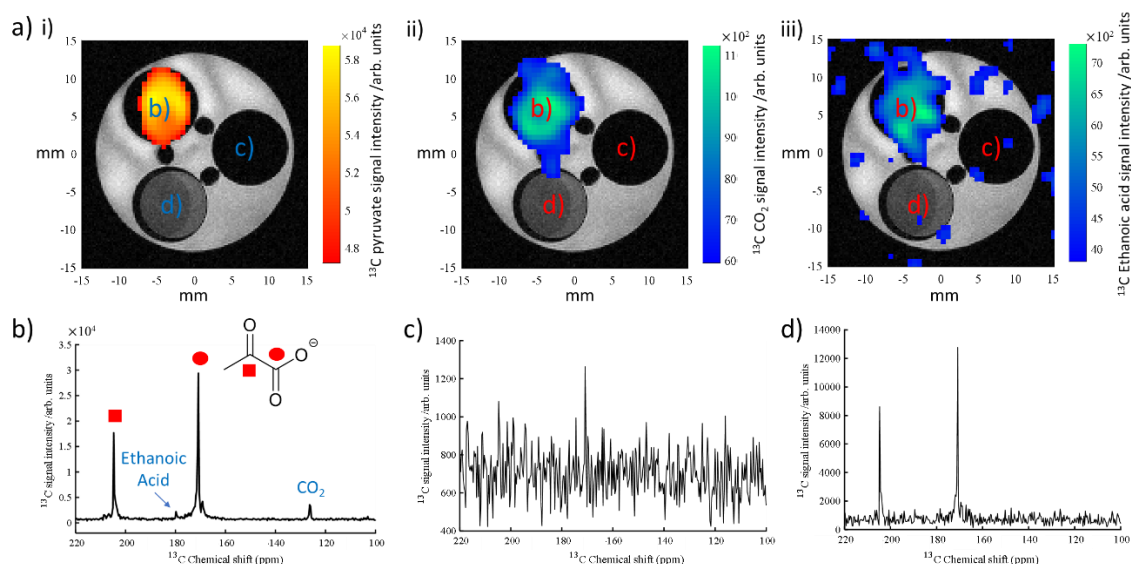
Figure 6.15: a) Overlaid ^{1}H FLASH (greyscale) and ^{13}C CSI image (coloured scale) of i) hyperpolarised pyruvate-1-[^{13}C] (δ 170), ii) CO_2 (δ 122) and iii) ethanoic acid (δ 177) ^{13}C NMR signals following the addition of H_2O_2 (final concentration of 200 mM) to SABRE hyperpolarised 22-1,2-[$^{13}C_2$]. The ^{13}C CSI image (16 $\times$ 16) was recorded using 5° flip angles and a 20 mm slice thickness. TE = 1.2ms, TR = 100ms, 1200 spectral points, 20 kHz sweep width, 17.4 kHz offset. b)-d) ^{13}C NMR spectra from the regions of interest containing b) NMR tube of SABRE hyperpolarised pyruvate, H_2O_2, and the reaction products CO_2 and ethanoic acid c) reference sample of methanol-d_4 (3 mL) and d) reference sample of glacial ethanoic acid (3 mL). d) shows weak signals from hyperpolarised pyruvate in the adjacent tube due to imaging artefacts. The apparatus used in this experiment is shown in Figure 6.3a.

6.6 Extension of sulfoxide-based polarisation transfer catalysts to hyperpolarise molecules with similar structures to pyruvate

For applications in H_2O_2 sensing, it is important that metabolically inactive reporters with related α-keto acid motifs can be hyperpolarised using SABRE. Therefore, the ability of SABRE polarisation transfer catalysts of the form **62** to hyperpolarise a wider range of molecules is examined. These systems have already been applied to the hyperpolarisation of the related sodium oxalate-[$^{13}C_2$].[260] In contrast to pyruvate, oxalate has been reported to bridge iridium dimers upon reaction with **61** which prevents formation of the active catalyst **62** and consequently, no hyperpolarisation of the free ligand is observed using SABRE.[260] However, molecules with

similar α-keto acid functionality were also examined to demonstrate the applicability of the novel polarisation transfer catalysts presented in Chapter 5 to a wider range of substrates. A wide range of molecules with structures similar to that of pyruvate were tested to examine if they could become hyperpolarised using SABRE *via* formation of polarisation transfer catalysts of type **62a**. The structures of these molecules are given in Figure 6.16.
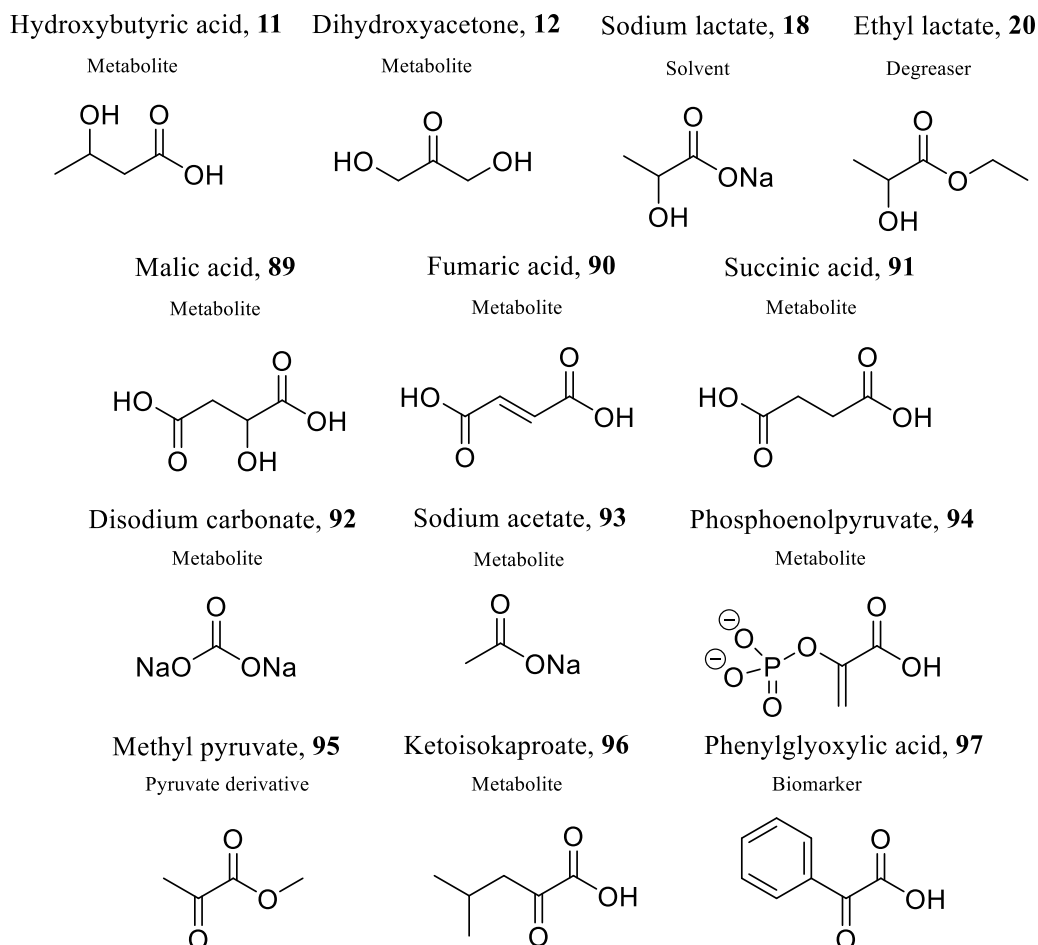
Figure 6.16: Structures of the molecules tested in this work.

Each of these molecules shown in Figure 6.16 (6 eq.) were activated with **2** (5 mM) and either **46** (4 eq.) or **69** (10 eq.) and 3 bar H_2 in methanol-d_4 (0.6 mL). Thermal ^{1}H NMR measurements were recorded to examine whether any hydride containing complexes were formed. In all cases, several hydride resonances were visible. Example ^{1}H NMR spectra of these mixtures are given in Appendix 9. In the case of **12**, **90**, **91**, and **95**, resonances for complexes analogous to **61** are observed. However, **96** was the only substrate that produced hydride resonances indicative of an active magnetisation transfer catalyst of the type **62a**. These samples were also shaken with 3 bar p-H_2 for 10 seconds in a mu-metal shield to identify if the hydride resonances of these complexes were enhanced by PHIP. Hyperpolarised ^{1}H NMR spectra of the hydride region for each of these substrates are also shown in Appendix 9. In most cases, hyperpolarised hydride signals were observed, with a common species visible with ALTADENA appearance at δ -23.43 and -29.79 present in solutions formed from **12**, **18**, **20**, **92**, **93**, **94**, and **97**. No NOE connections

from these hydride resonances to other ^{1}H sites were discerned and therefore the identity of this species could not be confirmed from 2D NMR spectroscopy at 245 K. However, the resonances at δ −23.43 and −29.79 are indicative of chemical environments *trans* to chloride and oxygen respectively. As this species is present in mixtures containing different target substrates, it is unlikely to contain ligated substrate. This species is more likely of the form [IrCl(H)$_2$(IMes)(*O*-L$_1$)(L$_2$)] where L is dimethylsulfoxide, H$_2$O or CD$_3$OD.

The only substrate of those in Figure 6.16 to yield hyperpolarised hydride NMR signals for a complex analogous to **62a** is **96**. These results suggest that substrates containing potential *O*-donor sites on the same carbon atom (**92**, **93**) or at distances greater than two carbon atoms (**11**, **90**, **91**, **94**) cannot form polarisation transfer catalysts analogous to **62a**. This could be related to steric factors such as non-optimal bite angles of these ligands. Substrates that contain potential COOH and OH donor sites on adjacent carbon atoms (**12**, **18**, **20**, **89**) or adjacent CO groups (**95**) also appear unable to form complexes analogous to **62a**. Therefore, the presence of an α-keto acid motif in the substrate is clearly important for SABRE efficiency. Substrate **96**, like pyruvate, is an α-keto acid with COOH and CO groups on adjacent carbon atoms and as a result can form complexes analogous to **62a**. When hyperpolarised ^{13}C NMR spectra are recorded for these substrates, only **96** gave enhanced ^{13}C NMR signals visible in a single scan. This suggests that changing the pyruvate CH$_3$ group in **62a** to a CH$_2$(CH$_3$)$_2$ group does not restrict the ability to form a SABRE active polarisation transfer catalyst. However, no evidence for the formation of **62a** is observed using **97** despite these structural criteria being met. This could be related to steric effects that arise from having a large inflexible phenyl group close to the coordinating *O*-donor sites. In the future, hyperpolarisation of the other molecules presented in Figure 6.16 may be possible using other polarisation transfer catalysts which are not analogous to **62a**. For example, others have reported SABRE hyperpolarisation of **93-1-[^{13}C]** using [Ir(H)$_2$(IMes)(pyridine)$_2$(η^1-*O*-acetate)], although only 100-fold ^{13}C NMR signal enhancements could be obtained and the identity of the polarisation transfer catalyst was not confirmed by structural characterisation.[233]

As **96** was able to form an active polarisation transfer catalyst that delivered enhanced ^{13}C NMR signals *via* SABRE, the ^{13}C labelled analogue, **96-1-[^{13}C]**, was examined further. Two samples were prepared based on the optimised conditions required to hyperpolarise pyruvate (discussed in Chapter 5). These contained either **2** (5 mM), **96-1-[^{13}C]** (6 eq.) and either **46** or **69** (10 eq.) in methanol-d_4 (0.6 mL). Figure 6.17 shows example hyperpolarised ^{1}H NMR spectra of **96** and **96-1-[^{13}C]**. These spectra show evidence for the formation of complexes analogous to **61**, **62a** and **62b**. The magnitude of hyperpolarised hydride NMR signals of the active polarisation transfer catalyst are larger when **96** is used compared to **96-1-[^{13}C]**, this is likely to be indicative of more efficient polarisation transfer from *p*-H$_2$ derived hydride ligands to ^{13}C sites in **96** when isotopically labelled **96-1-[^{13}C]** is used.
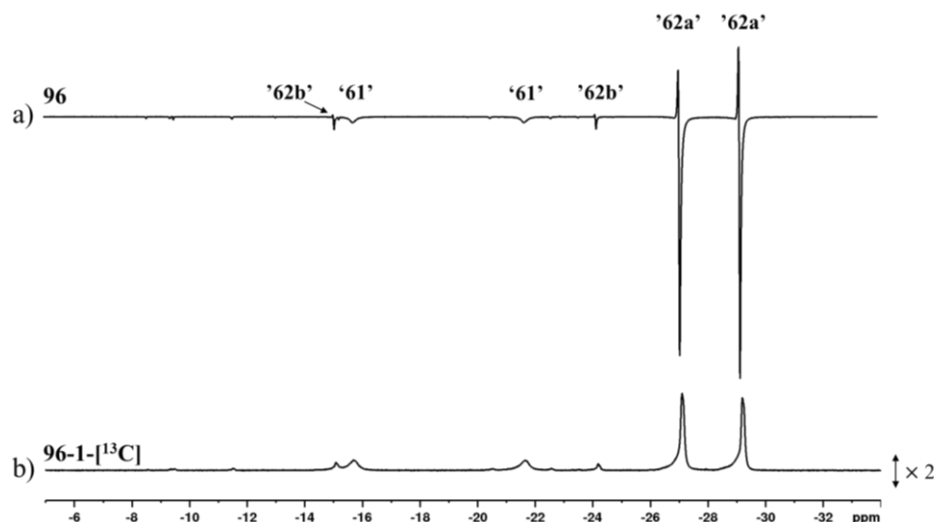
Figure 6.17: Partial hyperpolarised ^{1}H NMR spectra of the hydride region when samples containing 2 (5 mM) and a) 46 (4 eq.) and 96 (6 eq.) or b) 46 (10 eq.) and 96-1-[^{13}C] (6 eq.) in methanol-d_4 (0.6 mL) are shaken for 10 seconds with 3 bar p-H$_2$ at 6.5 mT.

As **96-1-[^{13}C]** (unlike **22-1,2-[^{13}C$_2$]**) does not contain two coupled ^{13}C sites, only hyperpolarised Zeeman magnetisation can be created (and not singlet order). As the formation of Zeeman magnetisation is dependent on magnetic field, the polarisation transfer field is expected to play a larger role in determining SABRE efficiency. Therefore, these samples were shaken for 20 seconds in a mu-metal shield, in addition to a mu-metal shielded solenoid, at various different magnetic fields between 0.1 and 1 μT. These samples were stable over the time period required to record these magnetic field profiles. Figure 6.18 shows the effect of magnetic field on the SABRE efficiency of **96-1-[^{13}C]**. The highest ^{13}C NMR signal gains are achieved at polarisation transfer fields of 0.7 μT and 0.5 μT when sulfoxides **46** and **69** are used respectively. In each case the SABRE ^{13}C NMR signal gains are higher than shaking in the mu-metal shield (955-fold compared to 155-fold and 985-fold compared to 150-fold when **46** and **69** are used respectively). This is consistent with reported SABRE-SHEATH matching conditions required to transfer polarisation from p-H$_2$ derived hydride ligands to directly ligated ^{13}C sites.[233, 263]
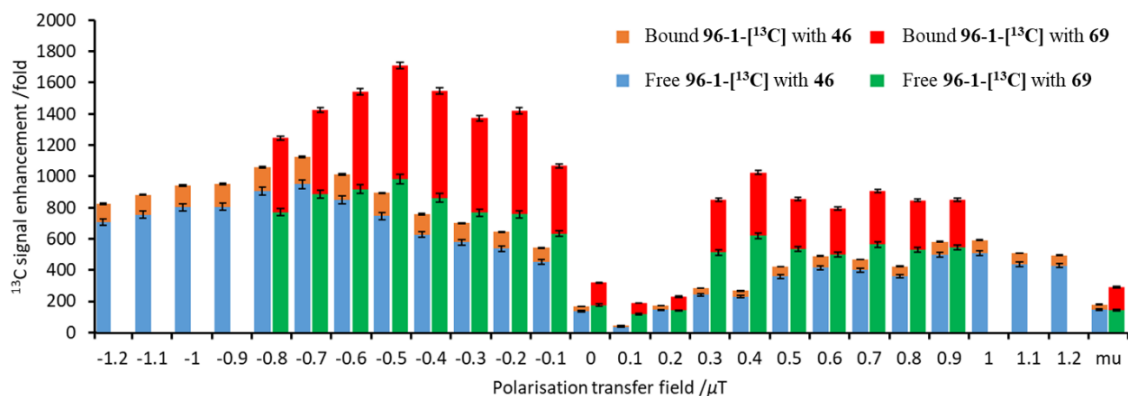
Figure 6.18: Dependence of ^{13}C NMR signal enhancement of free (lower) and bound (upper) 96-1-[^{13}C] (6 eq.) on the polarisation transfer field using samples containing 2 (5 mM) and either 46 (blue and orange) or 69 (green and red) (10 eq.) in methanol-d_4 shaken with p-H$_2$ for 20 seconds. These magnetic fields were achieved using a mu-metal shielded solenoid or a mu-metal shield ($\sim 1\,\mu$T) (final data point, far right). Magnetic fields marked with a negative value denotes that the direction of the field in the solenoid is aligned with that of the 9.4 T magnet. These are single shot measurements with error bars calculated from typical values, as discussed in Chapter 5.

The maximum ^{13}C NMR signal enhancement of free 96-1-[^{13}C] achieved using 46 or 69 at their optimal polarisation transfer fields are comparable (955-fold compared to 985-fold when 46 and 69 are used respectively). However, the ^{13}C NMR signal enhancement for 96-1-[^{13}C] bound within the active polarisation transfer catalyst is significantly higher when 69 is used (730-fold compared to 175-fold). This suggests that polarisation transfer from p-H$_2$ within the active magnetisation transfer catalyst formed using 69 may be more efficient yielding higher total (free and bound) ^{13}C NMR signal enhancements, but slower exchange of 96-1-[^{13}C] or relaxation effects are less optimal compared to the 46 derived system. Example hyperpolarised ^{13}C NMR spectra of 96 and 96-1-[^{13}C] are shown in Figure 6.19. These spectra show enhanced Zeeman magnetisation for ^{13}C NMR resonances of 96 and 96-1-[^{13}C], in addition to singlet magnetisation which is created in the 1.1% of molecules that naturally exist as 96-1,2-[$^{13}C_2$]. These results suggest that polarisation transfer complexes of the form 62a can transfer singlet order from p-H$_2$ derived hydrides to molecules other than pyruvate.
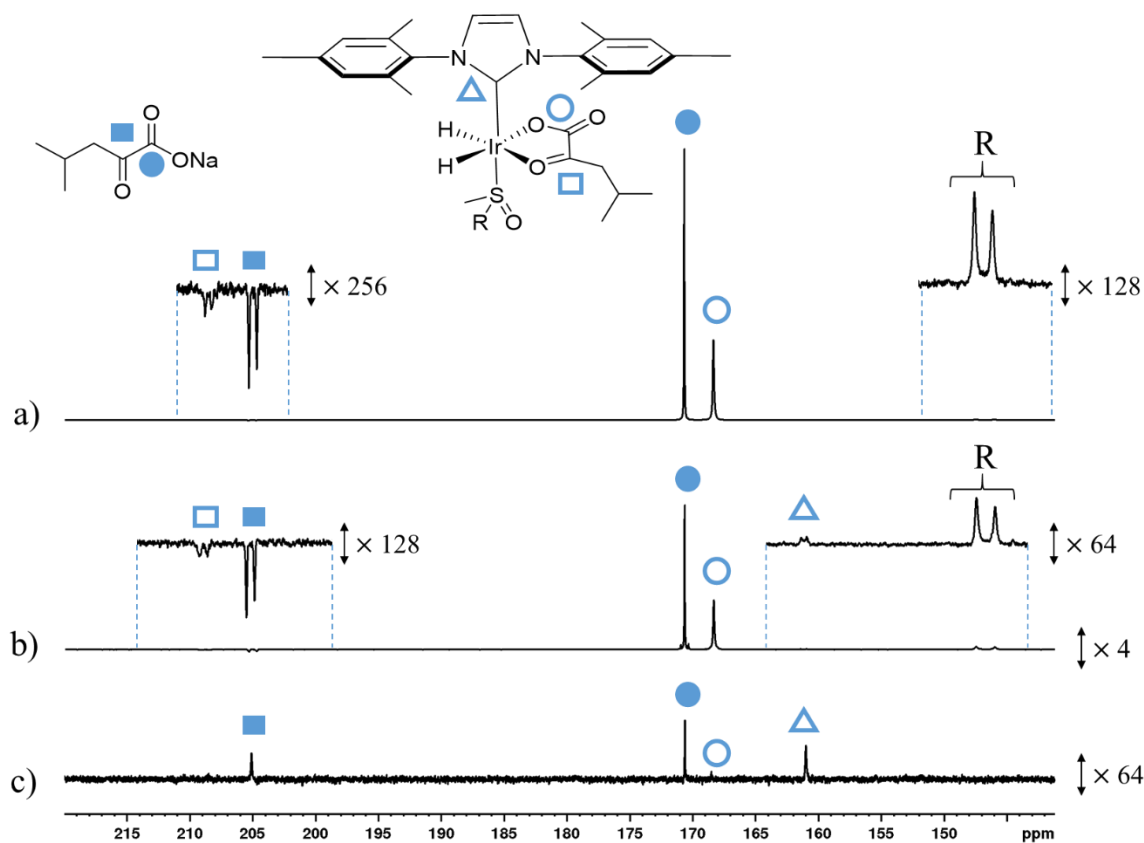
Figure 6.19: Partial hyperpolarised ^{13}C NMR spectra when samples containing a) and b) 2 (5 mM), 69 (10 eq.) and 96-1-[^{13}C] (6 eq.) or c) 2 (5 mM), 46 (4 eq.) and 96 (6 eq.) in methanol-d_4 (0.6 mL) are shaken for 20 seconds with 3 bar p-H$_2$ in a) a mu-metal shielded solenoid at −0.7 μT or b) and c) a mu-metal shield at c.a. 1 μT.

The largest ^{13}C NMR signal gains achieved for **96-1-[^{13}C]** are 985-fold, although it is expected that this value could increase by further optimisation of factors such as temperature, as discussed in Chapter 5. This shows that SABRE can be used to polarise molecules with similar α-keto acid motifs and could lead to a larger range of potential applications in monitoring chemical transformations. For example, **96** is a metabolic precursor to amino acids such as leucine[290] and could be used as a hyperpolarised reporter to study this transformation *in vitro*.

6.7 Conclusions

Using SABRE to hyperpolarise pyruvate can provide some advantages compared to alternative techniques such as DNP and PHIP-SAH as it is faster (30 seconds for SABRE compared to >20 minutes for DNP), cheaper, (SABRE only required a p-H$_2$ generator which is c.a. two orders of magnitude cheaper than a DNP polariser), refreshable (DNP and PHIP-SAH are both batch processes), and does not require chemical alteration of the target (as does PHIP-SAH). Despite this, ^{13}C polarisation levels of pyruvate achieved using SABRE (1.7%) are significantly lower than those achieved using DNP (70%)[137] or PHIP-SAH (5%).[73] While optimal SABRE polarisation values of 1.7% are readily quoted, these values are achieved in methanol-d_4 which is not suitable for *in vivo* biomedical imaging studies. These SABRE-derived NMR signal enhancements decrease dramatically as the D$_2$O content of methanol or ethanol solvents is

increased, as shown in section 6.2. While these NMR signal gains are large enough to allow detection of 0.4 mM pyruvate in a 70:30 D_2O/ethanol-d_6 mixture *in vitro*, as shown in section 6.3, their magnitude will seriously limit any applications of this technique for *in vivo* study.

It is difficult to envision a situation in which SABRE is used for biomedical imaging applications. This is because the NMR signal gains it can achieve are typically not as high as those that are produced using alternative techniques.[301] Therefore, *in vivo* biomedical imaging is unlikely to be a significant application of SABRE hyperpolarised pyruvate. Despite limitations in the biomedical applications of SABRE hyperpolarised pyruvate, potential applications in the area of reaction monitoring are expected to be much more fruitful. For example, pyruvate ^{13}C NMR signal gains achieved in biologically incompatible solvents using SABRE are sufficient in both magnitude and lifetime to allow the monitoring of rapid chemical transformations. For example, in section 6.4, SABRE hyperpolarised ^{13}C NMR was used to monitor the reaction between hyperpolarised sodium pyruvate-1,2-[$^{13}C_2$] and hydrogen peroxide (H_2O_2). A rate constant of reaction between pyruvate (15 mM) and H_2O_2 (150 mM) was determined from hyperpolarised SABRE-NMR which is comparable to values extracted from thermal ^{1}H NMR and UV spectroscopy, as summarised in Table 6.2. The iridium catalyst can influence this transformation, although its effect can be removed by deactivation with phenanthroline. In this case, the studied reaction was also be monitored by thermal ^{1}H NMR and UV spectroscopy to validate the method. In the future it could be extended to monitor more rapid reactions that are too fast to follow using traditional spectroscopic approaches.

Table 6.2: Comparison of the rate constant (k) of reaction between sodium pyruvate (15 mM) and H_2O_2 (150 mM) determined from different spectroscopic techniques.

Method	H_2O_2 concentration /M	Iridium present?	Phenanthroline added?	k / dm^3 mol^{-1} s^{-1}
SABRE hyperpolarised ^{13}C NMR	150	Yes	Yes	0.056 ± 0.003[%]
Thermal ^{1}H NMR	150	Yes	Yes	0.050 ± 0.003
Thermal ^{1}H NMR	150	Yes	No	N/A[&]
Thermal ^{1}H NMR	150	No	N/A[*]	0.051 ± 0.003
UV Spectroscopy	150	No	N/A[*]	0.050 ± 0.003
UV Spectroscopy	N/A[$]	Yes	N/A[$]	N/A[$]
SABRE hyperpolarised ^{13}C NMR	100	Yes	Yes	0.051 ± 0.003[%]
Thermal ^{1}H NMR	100	Yes	Yes	0.045 ± 0.001

[*]Phenanthroline is not required when the iridium catalyst is not present

[%]Values taken from signals for the pyruvate [1-^{13}C] and CO_2 site

[&]Presence of the metal prevented a good fit of experimental data to the model described using equations 6.7-6.10

[$]Presence of the metal masks the λ_{max} peak of pyruvate

The ^{13}C NMR signal gains SABRE provides are sufficient to make a short lived 2-hydroxperoxy-2-hydroxypropanoate intermediate visible in just a single scan ^{13}C NMR spectrum at reduced temperature. Therefore, SABRE could be a useful tool for the detection of short lived reaction

intermediates and reaction monitoring using NMR. As SABRE hyperpolarisation is refreshable it could be used to study transformations that occur on timescales longer than relaxation, although when applied to the condensation reaction between pyruvate and phenethylamine there are additional complications related to catalyst deactivation. However, it is clear that SABRE is able to monitor rapid chemical change which could be extended to reactions that cannot be monitored under Boltzmann derived conditions due to the long measurement time required for sufficient signal averaging.

The hyperpolarised reaction products that form from reaction of SABRE hyperpolarised pyruvate with H_2O_2 can be imaged *in vitro* by MRI, as shown in section 6.5, which may have future applications in determination of H_2O_2 concentrations *in vitro*. The substrate scope of the novel polarization transfer catalysts developed in Chapter 5 is explored in section 6.6 and can be extended to molecules such as ketoisokaproate, **96**, that contain similar α-keto acid functionality to pyruvate. The synthesis of metabolically inactive reporters with related α-keto acid motifs could yield molecules compatible with SABRE hyperpolarisation and may provide a route to H_2O_2 sensing using a cheap and easy to implement method. Extension to a wider range of molecules may also be possible by developments of novel polarisation transfer catalysts which may extend applications of SABRE to monitoring a wider range of chemical transformation.

Chapter 7. Experimental

7.1 Equipment and materials

All NMR measurements were carried out on a 400 MHz Bruker Avance III spectrometer. Hyperpolarised measurements, and 2D NMR characterisation are usually performed at 298 K and 245 K respectively unless otherwise stated. ^{1}H (400 MHz) and ^{13}C (100.6 MHz) NMR spectra were recorded with an internal deuterium lock. Single scan hyperpolarised ^{13}C NMR spectra were recorded without broadband ^{1}H decoupling. Multi-scan ^{13}C NMR measurements recorded under Boltzmann conditions and single scan hyperpolarised ^{1}H-^{13}C INEPT NMR spectra were recorded with broadband ^{1}H decoupling unless otherwise stated. Coupling constants (J) are quoted as an absolute magnitude in Hertz. Chemical shifts are quoted as parts per million and referenced to the solvent peak which in most cases was either methanol-d_4 or dichloromethane-d_2. For SABRE-Relay experiments (chapters 2 and 3) anhydrous dichloromethane-d_2 was used. This was produced by drying dichloromethane-d_2 using activated molecular sieves (3 Å). Electrospray high and low resolution mass spectra were recorded on a Bruker Daltronics microOTOF spectrometer. UV spectra were collected using a Thermoscientific evolution array UV-vis spectrophotometer.

Para-hydrogen (*p*-H$_2$) was produced by passing hydrogen gas over a spin-exchange catalyst (Fe$_2$O$_3$) at 28 K and used for all hyperpolarisation experiments. This method produces constant *p*-H$_2$ with *c.a.* 99% purity.[48] All starting materials (**1**, **3**-**8**, **10**-**22**, **31**-**34**, **41**-**43**, **46**, **48**, **52**, **55**, **57**-**58**, **69**-**75**, **78**, **86**, and **89**-**97**) and any isotopically labelled variants were all purchased from Sigma Aldrich, Fluorochem or Alfa-Aesar and used as purchased without additional purification. Samples of **76** and **77** were provided by Dr. Robin Brabham and Dr. Mark Dowsett. The iridium precatalysts **2** and **9** were synthesised by Dr. Victoria Annis according to a literature procedure.[302] Precatalysts **35**, **36**, **38**, **39**, **85**;[200] **37**[108]; **40**[302] and **87**[245] were synthesised according to similar methods by Dr. Peter J. Rayner. **64** and **66** were synthesised according to a literature procedure[303] by Hannah Kettle. A full list of complex names and numbering is given on Page 245.

^{1}H T_1 relaxation measurements were recorded using an inversion recovery pulse sequence. ^{1}H-^{13}C INEPT pulse sequences were used in some cases to transfer ^{1}H-based magnetisation onto ^{13}C sites. These sequences are described by Keeler[1] and Haake et al.[185] respectively.

7.2 Synthesis of SABRE active magnetisation transfer catalysts

Samples for SABRE hyperpolarisation were prepared in a 5 mM NMR tube that was fitted with a J. Young's tap. Details of the contents of these samples are given in subsequent sections. NMR samples (0.6 mL) were degassed by two freeze-pump-thaw cycles using liquid N$_2$ before filling the tube with H$_2$ at 3 bar pressure to form a SABRE active catalyst.

7.2.1 Formation of [Ir(H)$_2$(NHC)(carrier)$_3$]Cl (26 and 27)

Samples were prepared containing an iridium precatalyst (5 mM) with a carrier molecule (5-20 equivalents relative to iridium) in dichloromethane-d_2 (0.6 mL). All amines used to form catalysts of type [Ir(H)$_2$(NHC)(carrier)$_3$]Cl were liquids and added using a micropipette. However, NH$_3$ was added as a gas using a canister attached to a Schlenk line. Quantification of the amount of NH$_3$ added was achieved using ^{1}H NMR spectroscopy. The integrals of the ^{1}H NMR resonances of NH$_3$ (δ 0.5) and the COD ligand of [IrCl(COD)(NHC)] (δ 3, 4) were used to determine the ratio of NH$_3$ relative to iridium. Additional NH$_3$ was added to the NMR tube using the Schlenk line; excess NH$_3$ was removed by blowing N$_2$ gently through the solution for a few seconds. Degassed solutions (0.6 mL) were then left overnight (∼17 hours) following addition of H$_2$ (3 bar) to allow the formation of polarisation transfer catalysts of the form [Ir(H)$_2$(NHC)(carrier)$_3$]Cl which is accompanied by a colour change from orange to colourless and is confirmed by the presence of a single ^{1}H NMR resonance in the hydride region between δ −22 and −25.[106] At this point no ^{1}H NMR signals for the COD ligand of the precatalyst at δ 3 and 4 are visible and a signal of cyclooctane (δ 1.5) is visible. At this point, p-H$_2$ shaking yield hyperpolarised signals for the carrier.

In cases where these catalysts were then used to relay hyperpolarisation to target molecules the substrate of interest (5 eq.) is then added as a naturally occurring liquid, or solubilised in H$_2$O or dimethylformamide, by removing the J. Young's tap and pipetting the liquid into the NMR tube under a flow of N$_2$ gas to exclude oxygen. The tube was replaced, the N$_2$ atmosphere removed using a vacuum and p-H$_2$ (3 bar) was added.

7.2.2 Formation of [Ir(H)$_2$(κ^2-OOCC(CH$_3$)NCH$_2$Ph)(1,3-bis(2,4,6-trimethyl-phenyl)imidazole-2-ylidene)(NH$_2$CH$_2$Ph)] (28) and [Ir(H)$_2$(κ^2-OOCC(CH$_3$)NCH$_2$CH$_2$Ph)(1,3-bis(2,4,6-trimethyl-phenyl)imidazole-2-ylidene)(NH$_2$CH$_2$CH$_2$Ph)] (29)

Samples containing [Ir(H)$_2$(1,3-bis(2,4,6-trimethyl-phenyl)imidazole-2-ylidene)(NH$_2$CH$_2$Ph)$_3$]Cl (26) or [Ir(H)$_2$(1,3-bis(2,4,6-trimethyl-phenyl)imidazole-2-ylidene)(NH$_2$CH$_2$CH$_2$Ph)$_3$]Cl (27) in dichloromethane-d_2 (0.6 mL) were synthesised according to section 7.2.1. At this point sodium pyruvate-1-[^{13}C] or sodium pyruvate-1,2-[^{13}C$_2$] (1.8 mg, 0.015 mM, 5 equivalents relative to iridium) was dissolved in H$_2$O (40 μL) and added to the NMR tube by removing the J. Young's tap and pipetting the liquid into the NMR tube under a flow of N$_2$ gas to exclude oxygen. The N$_2$ atmosphere was removed using a vacuum and the tube was pressurised with 3 bar p-H$_2$ and left overnight to allow the formation of an equilibrium mixture of 28 or 29 from 26 or 27 respectively.

7.2.3 Formation of [Ir(H)$_2$(κ^2-*O*OCC(CH$_3$)*N*CH$_2$CH$_2$Ph)(1,3-*bis*(2,4,6-trimethyl-phenyl)imidazole-2-ylidene)(L)] (44, 45, 47, 49 and 53)

Equilibrium mixtures of **29** in dichloromethane-d_2 (0.6 mL) were synthesised as described in section 7.2.2. 1 μL (~5 equivalents relative to iridium) of pyridine, dimethylsulfoxide, benzylisocyanide, or ethylisothiocyanate were added to **29** under a flow of N$_2$ gas before the NMR tube was pressurised with 3-bar hydrogen gas to form **44**, **47**, **49**, or **53** respectively. **45** was formed from the addition of imidazole (2 mg) in dichloromethane-d_2 (40 μL) to **29** using the same method. This method also yielded the formation of [Ir(H)$_2$(CNCH$_2$Ph)$_3$(1,3-*bis*(2,4,6-trimethyl-phenyl)imidazole-2-ylidene)]Cl (**50**), [Ir(H)$_2$(CNCH$_2$Ph)$_2$(1,3-*bis*(2,4,6-trimethyl-phenyl)imidazole-2-ylidene)(NH$_2$(CH$_2$)$_2$Ph)]Cl (**51**), [Ir(H)$_2$(1,3-*bis*(2,4,6-trimethyl-phenyl)imidazole-2-ylidene)(SCNEt)$_2$(NH$_2$(CH$_2$)$_2$Ph)]Cl (**54**), and [Ir(H)(κ^2-*O*OCC(CH$_3$)*N*R)(*S*CH$_2$PhCl)(1,3-*bis*(2,4,6-trimethyl-phenyl)imidazole-2-ylidene)] (**56**) following addition of benzylisocyanide, ethylisothiocyanate, or 4-chlorobenzenemethanethiol (2 μL, 5 eq.) to **29** respectively.

7.2.4 Formation of [Ir(Cl)(H)$_2$(sulfoxide)$_2$(NHC)] and [Ir(H)$_2$(κ^2-pyruvate)(sulfoxide)(NHC)] (61 and 62)

Samples were prepared containing iridium precatalyst (5 mM) with sulfoxide (2-50 eq.) and sodium pyruvate-1,2-[^{13}C$_2$] (4-10 eq.) in methanol-d_4 (0.6 mL). After degassing, H$_2$ (3 bar) was added and left at room temperature for 30-45 minutes to allow the formation of equilibrium mixtures of **61** and **62**. This is indicated by the presence of indicative ^{1}H NMR resonances[253, 260, 263] (shown in Table 5.2) and is accompanied by a colour change from orange to colourless. Complexes analogous to **61** can be prepared by repeating this process without the addition of sodium pyruvate-1,2-[^{13}C$_2$]. [IrBr(H)$_2$(dimethylsulfoxide)$_2$(1,3-*bis*(2,4,6-trimethyl-phenyl)imidazole-2-ylidene)] (**65**) and [Ir(acetonitrile)(H)$_2$(dimethylsulfoxide)$_2$(1,3-*bis*(2,4,6-trimethyl-phenyl)imidazole-2-ylidene)] (**67**) were made in this way from the iridium precatalysts **64** and **66** respectively.

7.3 Procedure for recording hyperpolarised NMR measurements

7.3.1 'Shake and drop' method

Once a suitable polarisation transfer catalyst was synthesized, according to section 7.2, the shake & drop method was used for recording SABRE hyperpolarised NMR spectra.[76] Once filled with *p*-H$_2$, the NMR tubes were shaken vigorously for a specified time interval at the appropriate polarisation transfer field. Immediately after shaking, the NMR tubes were put inside the spectrometer for NMR detection. For hyperpolarised ^{1}H NMR spectra, samples were typically shaken for 10 seconds at 6.5 mT. This field was achieved by shaking in the fringe field of the

9.4 T spectrometer, as determined by a Gaussmeter. Upon rapid insertion into the spectrometer single scan ^{1}H NMR spectra were recorded with either 45° or 90° pulse angles. For SABRE-Relay transfer to ^{13}C sites, p-H$_2$ shaking was also performed under these conditions. For polarisation transfer, catalysts of the form **44**, **45**, **47**, **49**, or **53**, ^{13}C NMR signal gains were typically achieved by shaking for 10 seconds in a mu-metal shielded solenoid ($\sim$1 μT). In the case of polarisation transfer catalysts **61** and **62**, ^{13}C NMR signal gains were typically achieved by shaking for 30 seconds in a mu-metal shield ($\sim$1 μT). Some experiments were performed in which the effects of polarisation transfer field on ^{1}H or ^{13}C NMR signal enhancement was varied (sections 2.6 and 5.6.1, 6.6 respectively). For these experiments on ^{1}H nuclei (section 2.6), handheld shakers that provide magnetic fields of between 3 mT and 12 mT as described in Richardson et al.[80] were used. Those experiments involving ^{13}C (section 5.6.1 and 6.6) were performed using a mu-metal shielded solenoid that can produce fields of between 0.1 μT and 3 μT and is described in Iali et al.[263]

7.3.2 Calculating NMR signal enhancements

^{1}H NMR signal enhancements were calculated by dividing the hyperpolarised integral intensity by the analogous intensity from a single scan thermal spectrum recorded and processed under the same conditions (described by equation 1.10). Both hyperpolarised and thermally polarised NMR spectra were recorded on the same sample using the same spectrometer settings. For all ^{1}H and ^{13}C NMR spectra, line broadening filters of 3 Hz and 1 Hz respectively were applied. For hyperpolarised signals that contained antiphase character, integral intensities were calculated as a sum of the modulus of absorption and emissive components. All NMR signal enhancements were recorded at 9.4 T and their absolute magnitudes are quoted.

^{13}C NMR signal enhancements could not be calculated using equation 1.10 as ^{13}C NMR signals recorded under Boltzmann derived conditions were not visible in a single scan. Therefore, they were calculated by reference to either the more concentrated thermal signal, or a more concentrated reference sample according to equation 1.11. ^{13}C NMR signal enhancements for **1**, **6**, **7**, **10**-**28**, **43**, and **89**-**97** were calculated by reference to the ^{13}C NMR signal for the dichloromethane-d_2 solvent (0.6 mL) using equation 1.11. ^{13}C NMR signal enhancements for **22-1,2-[^{13}C$_2$]** and **96-1-[^{13}C]** were calculated by reference to a more concentrated sample of **22-1,2-[^{13}C$_2$]** (1.6 M) in methanol-d_4 (0.6 mL). ^{13}C NMR signal enhancements for **19**-**21** were calculated by reference to a more concentrated sample of **19**-**21** respectively (1.5 M) in dichloromethane-d_2 (0.6 mL).

All NMR signal enhancements are the average of three measurements, unless otherwise stated. For example, ^{13}C NMR signal enhancements of **22-1,2-[^{13}C$_2$]** recorded using polarisation transfer catalysts of the form [Ir(H)$_2$(κ^2-pyruvate)(sulfoxide)(NHC)] are typically one shot measurements. This is related to rapid deactivation of the catalyst which renders consistent NMR signal enhancements using these catalysts challenging. Therefore, errors quoted for these values are

calculated from typical percentage errors for similar measurements for which signal gains were consistent.

All NMR signal enhancements given in fold (^{1}H and ^{13}C) and their errors are rounded to the nearest five, unless smaller than 30-fold.

7.4 Characterisation of products

Compounds were characterised using a combination of 2D NMR spectroscopy, Mass spectrometry, and X ray diffraction. For X ray diffraction a suitable crystal was selected and mounted on an Oxford Diffraction SuperNova- X ray diffractometer. The crystal was kept at 110 K during data collection. Diffractometer control, data collection, initial unit cell determination, frame integration and unit-cell refinement was carried out with the CrystAlis Pro computer programme (from Oxford Diffraction Ltd, Version 1.171.34.41). Face-indexed absorption corrections were applied using spherical harmonics, implemented in SCALE3 ABSPACK scaling algorithm. Using Olex2,[304] the structure was solved with the ShelXT[305] structure solution program using Intrinsic Phasing and refined with the ShelXL[305] refinement package using Least Squares minimisation. All single crystal X ray diffraction structures in this thesis are shown with thermal ellipsoids at 50% probability.

7.4.1 2D NMR characterisation of [Ir(H)$_2$(κ^2-*O*OCC(CH$_3$)*N*CH$_2$Ph)(1,3-*bis*(2,4,6-trimethyl-phenyl)imidazole-2-ylidene)(NH$_2$CH$_2$Ph)] (28)

28 was synthesized according to section 7.2.2 and an aliquot was submitted for MS analysis. HR-ESI$^+$/MS (m/z): for [C$_{38}$H$_{45}$IrN$_4$O$_2$ − H]$^+$, calcd 781.3094, found 781.3064

For NMR characterisation, two samples were used to aid in the data collection and interpretation: These samples contained **2** (10 mM), **4** (10 eq.) and **22-1,2-[^{13}C$_2$]** (10 eq.) in dichloromethane-d_2 (0.6 mL) and H$_2$O (40 μL) and were prepared as described in section 7.2.2. An analogous sample containing ^{15}N labelled benzylamine precursor was also used. The structures of **28A** and **28B** are shown in Figure 7.1 and 7.2. respectively. The NMR resonances for these complexes are given in Table 7.1 and 7.2 respectively.
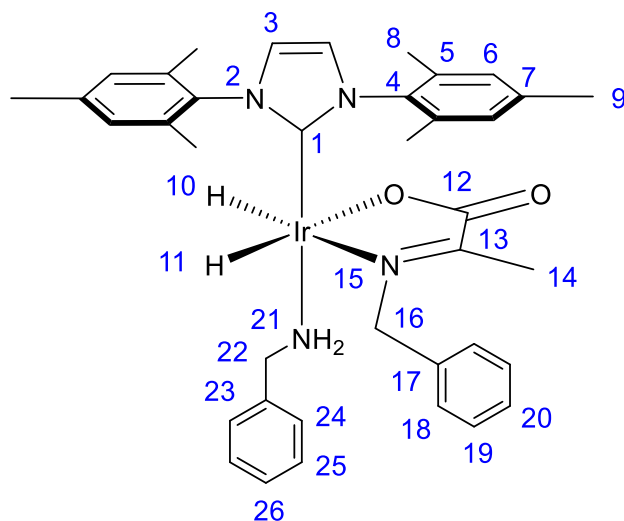
Figure 7.1: Structure of 28A determined from the NMR data given in Table 7.1.

Table 7.1: NMR data collected in dichloromethane-d_2 at 245 K used to determine the structure of 28A shown in Figure 7.1. Resonances are labelled according to Figure 7.1.

Resonance	^{1}H	^{13}C	^{15}N
1	-	141.20	-
2	-	-	-
3	6.76	121.49	-
4	-	138.17	-
5	-	136.37, 136.19	-
6	7.02, 7.07	128.74, 128.68	-
7	-	138.26	-
8	2.20, 2.06	18.16, 18.27	-
9	2.35	21.08	-
10	−21.9 (dd) ($^2J_{HH}$= 9.5 Hz) ($^2J_{NH}$ = 20.7 Hz)	-	-
11	−27.6 (d) ($^2J_{HH}$ = 9.5 Hz)	-	-
12	-	174.83 ($^1J_{CC}$ = 65 Hz) (J = 6.2 Hz)	-
13	-	168.48 ($^1J_{CC}$ = 65 Hz) (J = 10 Hz)	-
14	2.14	10.31	-
15	-	-	276.9 (dd) (J = 10 Hz) (J = 6.5 Hz)
16	3.62, 4.85	62.3	-
17	-	~130 overlap	-
18	7.15, 7.17	128.32, 128.88	-
19	~7.2 overlap	~128 overlap	-
20	~7.2 overlap	~128 overlap	-
21	1.52, 1.81	-	−2.70
22	2.97, 3.25	55.18	-
23	-	~130 overlap	-
24	6.58, 6.60	127.04	-
25	7.13	127.08, 128.19	-
26	~7.2 overlap	~128 overlap	-
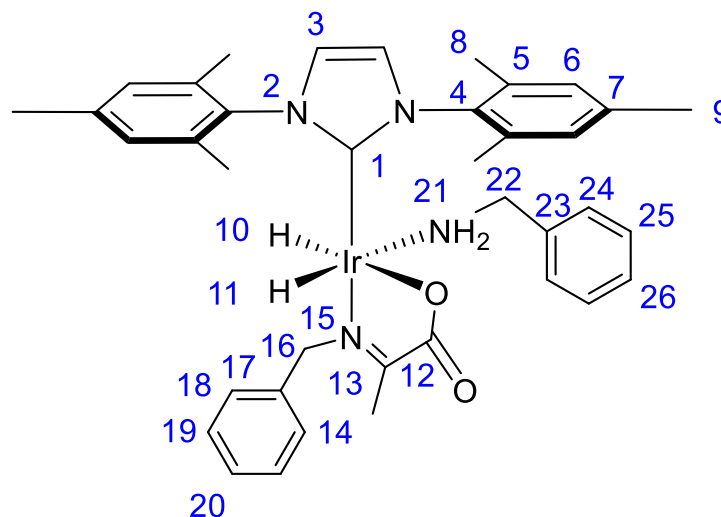
Figure 7.2: Structure of 28B determined from the NMR data given in Table 7.2.

Table 7.2: NMR data collected in dichloromethane-d_2 at 245 K used to determine the structure of 28B shown in Figure 7.2. Resonances are labelled according to Figure 7.2.

Resonance	^{1}H	^{13}C	^{15}N
1	-	141.10	-
2	-	-	-
3	6.86	121.30	-
4	-	137.97	-
5	-	136.21, 135.84	-
6	6.91, 6.85	128.76, 128.72	-
7	-	138.25	-
8	2.16, 2.10	18.14, 18.11	-
9	2.20	20.97	-
10	−24.0 (dd) ($^2J_{HN}$= 17.5 Hz) ($^2J_{HH}$ = 8.2 Hz)	-	-
11	−27.4 (d) ($^2J_{HH}$ = 8.2 Hz)	-	-
12	-	174.35	-
13	-	169.17	-
14	2.06	9.25	-
15	-	-	260.7
16	4.84, 5.31	65.90	-
17	-	~130 overlap	-
18	7.40, 7.41	127.74, 129.95	-
19	7.15, 7.18	129.64, 128.90	-
20	7.20	~128 overlap	-
21	1.41, 1.49	-	−2.47
22	2.90, 2.75	48.14	-
23	-	~130 overlap	-
24	6.63, 6.65	126.64	-
25	7.24, 7.26	~128 overlap	-
26	~7.2 overlap	~128 overlap	-

7.4.2 2D NMR characterisation of [Ir(H)$_2$(κ^2-*O*OCC(CH$_3$)*N*CH$_2$CH$_2$Ph)(1,3-*bis*(2,4,6-trimethyl-phenyl)imidazole-2-ylidene)(NH$_2$CH$_2$CH$_2$Ph)] (29)

29 was synthesized according to section 7.2.2 and an aliquot was submitted for MS analysis. HR-ESI$^+$/MS (m/z): for [C$_{39}$^{13}C$_1$H$_{49}$IrN$_4$O$_2$ + H]$^+$, calcd 812.3597, found 812.3591; for [C$_{39}$^{13}C$_1$H$_{49}$IrN$_4$O$_2$ –H$_6$]$^+$, calcd 806.3127, found 806.3152. For NMR characterisation, a concentrated sample was used containing **2** (10 mM), **5** (10 eq.) and **22-1,2-[^{13}C$_2$]** (10 eq.) in dichloromethane-d_2 (0.6 mL) and H$_2$O (40 μL) prepared as described in section 7.2.2. The structures of **29A** and **29B** are shown in Figure 7.3 and 7.4. respectively. The NMR resonances for these complexes are given in Table 7.3 and 7.4 respectively.
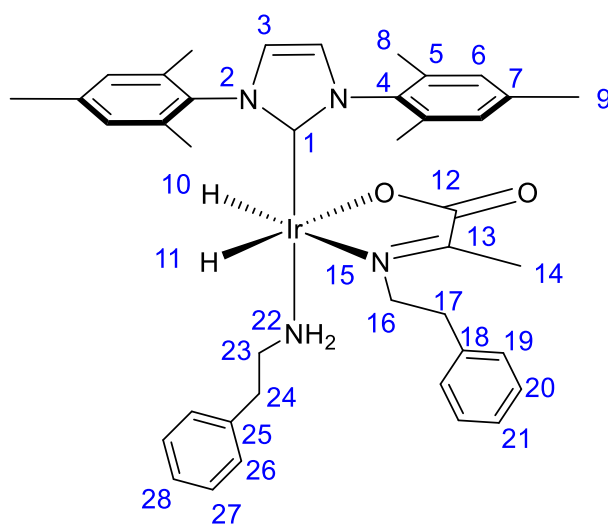
Figure 7.3: Structure of 29A determined from the NMR data given in Table 7.3.

Table 7.3: NMR data collected in dichloromethane-d_2 at 245 K used to determine the structure of 29A shown in Figure 7.3. Resonances are labelled according to Figure 7.3.

Resonance	^{1}H	^{13}C
1	-	141.31
2	-	-
3	6.72	121.26
4	-	136.23
5	-	137.97
6	6.94, 6.98	128.30, 128.71
7	-	135.58
8	2.08	18.07, 18.18
9	2.30	20.89
10	−21.60	-
11	−27.96	-
12	-	174.51 (^{1}J$_{CC}$ = 66 Hz)
13	-	168.02 (^{1}J$_{CC}$ = 66 Hz)
14	1.43	16.60
15	-	-
16	3.67, 3.98	24.51
17	2.09, 2.81	18.02
18	-	~130 overlap
22	1.46, 1.53	-
23	2.12, 2.18	37.95
24	2.06, 2.28	28.44
25	-	~130 overlap
26	6.95	~128 overlap
19-21, 27, 28	~7.2 overlap	~128 overlap
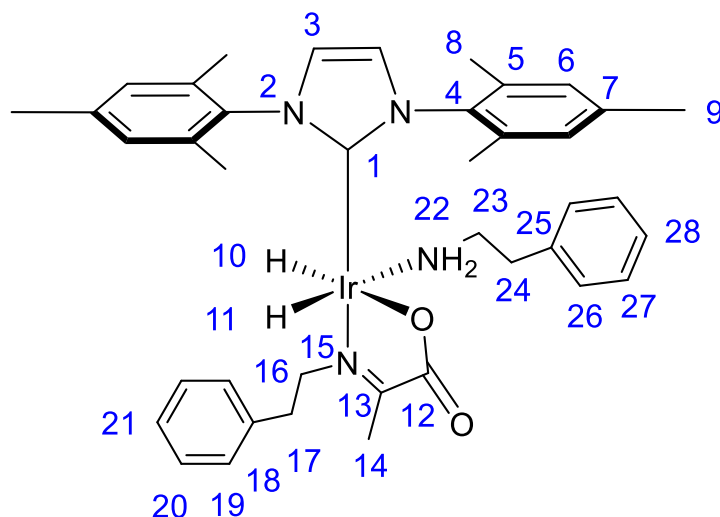
Figure 7.4: Structure of 29B determined from the NMR data given in Table 7.4.

Table 7.4: NMR data collected in dichloromethane-d_2 at 245 K used to determine the structure of 29B shown in Figure 7.4. Resonances are labelled according to Figure 7.4.

Resonance	^{1}H	^{13}C
1	-	141.15
2	-	-
3	6.89	121.14
4	-	138.18
5	-	138.36
6	7.05	128.27
7	-	136.28
8	2.16, 2.18	17.96, 18.09
9	2.35	20.99
10	−23.93	-
11	−27.84	-
12	-	174.39 (^{1}J$_{CC}$ = 66 Hz)
13	-	169.51 (^{1}J$_{CC}$ = 66 Hz)
14	1.81	16.60
15	-	-
16	3.25, 3.69	24.33
17	1.99, 2.84	19.43
18	-	~130 overlap
19	~7.2 overlap	~128 overlap
20	~7.2 overlap	~128 overlap
21	~7.2 overlap	~128 overlap
22	1.60, 1.74	-
23	~2.2 overlap	38.28
24	2.17, 2.34	28.68
25	7.05	~130 overlap
26	~7.2 overlap	~128 overlap
27	~7.2 overlap	~128 overlap
28	~7.2 overlap	~128 overlap

7.4.3 X ray diffraction of [Ir(η^2-CO$_3$)(κ^2-OOCC(CH$_3$)NCH$_2$Ph)(1,3-bis(2,4,6-trimethyl-phenyl)imidazole-2-ylidene)(NH$_2$CH$_2$Ph)] (30)

Crystals of **30** were prepared by removing the H$_2$ atmosphere of solutions of **28** (synthesised according to section 7.2.2), concentrating the sample to ~0.2 mL using a stream of N$_2$ gas, then layering ~3 mL degassed hexane slowly to the top of the NMR tube and leaving under N$_2$ or air for period of several weeks. Crystals of **30** contained several waters of crystallization. Within the asymmetric unit, one of the waters was partially occupied with a refined occupancy of 0.232(5). One of the adjacent waters was modelled in two positions with refined occupancies of 0.66:0.34(3). All hydrogen atoms, including those of the water, were placed using a riding model. Single crystal X ray diffraction data were collected and solved by Dr. Adrian C. Whitwood.[195] The structure was deposited with the Cambridge Crystallographic Database (no. 1881601). The structure of **30** is shown in Figure 3.9; selected crystal data and structure refinement is shown in Table 7.5.

Table 7.5: Selected crystal data and structural refinement details for 30.

Parameter	Value
Empirical formula	C$_{39}$H$_{49.47}$IrN$_4$O$_{8.23}$
Formula weight	898.25
Temperature/K	110.00(10)
Crystal system	triclinic
Space group	P-1
a /Å	11.2957(3)
b /Å	13.4528(3)
c /Å	13.9660(2)
α /°	74.494(2)
β /°	69.969(2)
γ /°	86.356(2)
Volume /Å^3	1920.38(8)
Z	2
ρ_{calc} g/cm^3	1.553
μ/ mm^{-1}	3.533
F(000)	909.0
Crystal size /mm^3	0.294 × 0.229 × 0.174
Radiation	MoK$_\alpha$ (λ = 0.71073)
2Θ range for data collection /°	6.87 to 64.396
Index ranges	$-16 \leq h \leq 16$, $-19 \leq k \leq 19$, $-20 \leq l \leq 20$
Reflections collected	58761
Independent reflections	12678 [R_{int} = 0.0262, R_{sigma} = 0.0199]
Data/restraints /parameters	12678/0/511
Goodness-of-fit on F^2	1.067
Final R indexes [I>=2σ (I)]	R_1 = 0.0170, wR_2 = 0.0391
Final R indexes [all data]	R_1 = 0.0199, wR_2 = 0.0407
Largest diff. peak/hole /e Å^{-3}	1.08/−0.81

7.4.4 X ray diffraction of [Ir(η^2-CO$_3$)(κ^2-OOCC(CH$_3$)NCH$_2$CH$_2$Ph)(1,3-*bis*(2,4,6-trimethyl-phenyl)imidazole-2-ylidene)(NH$_2$CH$_2$CH$_2$Ph)] (31)

Crystals of **31** were prepared by removing the H$_2$ atmosphere of solutions of **29** (synthesised according to section 7.2.2), concentrating the sample to ~0.2 mL using a stream of N$_2$ gas, then layering ~3 mL degassed hexane slowly to the top of the NMR tube and leaving under N$_2$ or air for period of several weeks. Two different asymmetric units of **31** were observed.[195, 224] One of these contained a disordered mixture of water and phenethylamine in a refined ratio of 0.730:0.270(6) centred about a point of inversion. The C-N bond length of phenethylamine was restrained to be 1.45 angstroms, the ADP of all heavy atoms were restrained to be isotropic and the ADP of opposite carbons in the ring were constrained to be equal. The ADP of the phenethylamine nitrogen and the oxygen of the water were constrained to be equal. The second unit cell contained a dichloromethane solvent of crystallization. Single crystal X ray diffraction data were collected and solved by Dr. Adrian C. Whitwood[195] or Dr. Sam J. Hart.[224] The structures were deposited with the Cambridge Crystallographic Database (no. 1893624). The structure of **31** is shown in Figure 3.9; selected crystal data and structure refinement is shown in Table 7.6.

Table 7.6: Selected crystal data and structural refinement details for 31.

Parameter	Value	
Empirical formula	C$_{43.16}$H$_{51.43}$IrN$_{4.27}$O$_{5.73}$	C$_{42}$H$_{49}$Cl$_2$IrN$_4$O$_5$
Solvent of crystallisation	Water and phenethylamine	dichloromethane
Formula weight	913.93	952.95
Temperature/K	110.05(10)	110.05(10)
Crystal system	monoclinic	monoclinic
Space group	P2$_1$/n	P2$_1$/n
a /Å	14.7471(6)	14.08570(10)
b /Å	11.5666(8)	11.99650(10)
c /Å	24.2996(11)	24.9643(2)
α /°	90	90
β /°	94.887(4)	97.6750(10)
γ /°	90	90
Volume /Å^3	4129.8(4)	4180.65(6)
Z	4	4
ρ_{calc} g/cm^3	1.470	1.514
μ/ mm^{-1}	6.663	3.369
F(000)	1853.0	1920.0
Crystal size /mm^3	0.167 × 0.061 × 0.018	0.151 × 0.139 × 0.09
Radiation	CuK$_\alpha$ (λ = 1.54184)	MoK$_\alpha$ (λ = 0.71073)
2Θ range for data collection /°	6.766 to 134.126	6.588 to 63.576
Index ranges	$-16 \leq h \leq 17, -13 \leq k \leq 13,$ $-19 \leq l \leq 29$	$-20 \leq h \leq 20, -17 \leq k \leq 17,$ $-36 \leq l \leq 36$
Reflections collected	14866	63675
Independent reflections	7359 [R_{int} = 0.0298, R_{sigma} = 0.0406]	13379 [R_{int} = 0.0359, R_{sigma} = 0.0291]
Data/restraints /parameters	7359/59/537	13379/0/502
Goodness-of-fit on F^2	1.190	1.043
Final R indexes [I>=2σ (I)]	R_1 = 0.0515, wR_2 = 0.1049	R_1 = 0.0219, wR_2 = 0.0437
Final R indexes [all data]	R_1 = 0.0641, wR_2 = 0.1102	R_1 = 0.0289, wR_2 = 0.0465
Largest diff. peak/hole /e Å^{-3}	1.49/−2.01	0.93/−0.64

7.4.5 Characterisation of [Ir(H)$_2$(κ^2-OOCC(CH$_3$)NCH$_2$CH$_2$Ph)(1,3-*bis*(2,4,6-trimethyl-phenyl)imidazole-2-ylidene)(imidazole)] (45)

An equilibrium mixture of **29** and **45** was synthesised according to section 7.2.3. **45A** was precipitated as a bright orange solid by addition of ~3 mL degassed hexane under N$_2$. **45A** was isolated by filtration and drying under vacuum. The sample was redissolved for NMR characterisation at 245 K. The structure of **45A** is shown in Figure 7.5. and the NMR resonances for these complexes are given in Table 7.7. A sample of the deuterated analogue, **45-d_{24}** was synthesised in the same way using **2-d_{24}** and was analysed by MS. HR-ESI$^+$/MS (m/z): [C$_{38}$^{13}C$_2$H$_{15}$D$_{24}$IrN$_5$O$_2$ − H$_3$]$^+$, calcd 780.4301, found 780.4338; [C$_{38}$^{13}C$_2$H$_{25}$D$_{24}$IrN$_4$O$_2$]$^+$, calcd 836.5058, found 836.4362; [C$_{30}$^{13}C$_2$H$_{12}$D$_{24}$IrN$_3$O$_2$]$^+$, calcd 713.4010, found 713.4030.
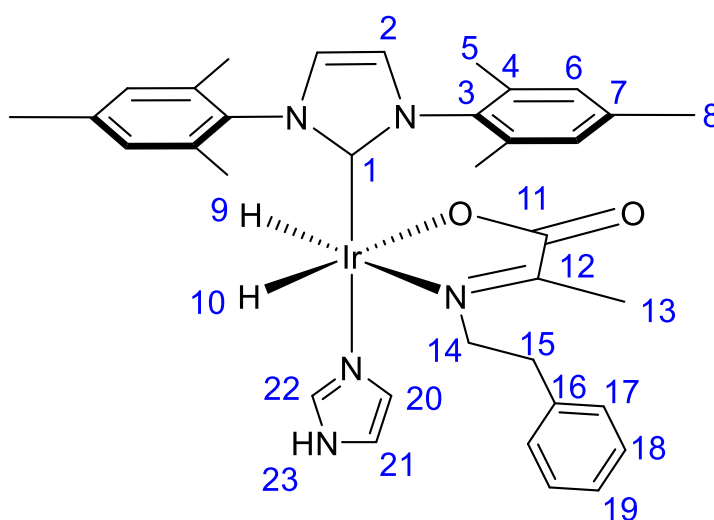
Figure 7.5: Structure of 45A determined from the NMR data given in Table 7.7.

Table 7.7: NMR data collected in dichloromethane-d_2 at 245 K used to determine the structure of 45A shown in Figure 7.5. Resonances are labelled according to Figure 7.5.

Resonance	^{1}H	^{13}C
1	-	N/A (~ 141)
2	6.84, 6.86	128.06, 128.17
3	-	138.10
4	-	N/A (~ 137)
5	2.19	~ 18.6 (overlap)
6	7.02	128.87
7	-	N/A (~ 137)
8	~ 2.2 (overlap)	~ 22.5 (overlap)
9	−21.63 (d, $^2J_{HH}$ = 8 Hz)	-
10	−28.25 (dd, $^2J_{HH}$ = 8 Hz, J = 5 Hz)	-
11	-	175.86 (d, $^1J_{CH}$ = 67 Hz)
12	-	166.28 (d, $^1J_{CH}$ = 67 Hz)
13	1.62	16.32
14	3.75, 3.90	43.72
15	2.78, 2.92	40.13
16	-	139.50
17	7.25	128.32
18	7.23	128.95
19	7.18	126.15
20/21	6.49, 6.69	132.68, 135.84
22	6.78	115.99
23	8.33	-

7.4.6 Characterisation of [Ir(H)₂(κ²-*OO*CC(CH₃)*N*CH₂CH₂Ph)(1,3-*bis*(2,4,6-trimethyl-phenyl)imidazole-2-ylidene)(dimethylsulfoxide)] (47)

An equilibrium mixture of **29** and **47** was synthesised (section 7.2.3). NMR characterisation was not performed due to the presence of multiple species in solution. An aliquot was used for MS analysis. HR-ESI⁺/MS (m/z): $[C_{34}H_{45}IrN_3O_3S + H]^+$, calcd 768.2811, found 768.2815; $[C_{34}H_{45}IrN_3O_3S + Na]^+$, calcd 790.2630, found 790.2635; $[C_{34}H_{45}IrN_3O_3S - C_2H_7OS]^+$, calcd 688.2515, found 688.2528; $[C_{34}H_{45}IrN_3O_3S - C_2H_6OS + Na]^+$, calcd 712.2491, found 712.2483. **47A** could be synthesised by addition of **4** (26.5 mM) to a solution containing **2** (3 mM), **22-1,2-[¹³C₂]** (30 mM) and **46** (8 eq.) in methanol-d_4 (0.6 mL) preactivated with H_2 (3 bar) for 45 min at room temperature to form **61** and **62** (as described in section 7.2.4.). The structure of **47A** is shown in Figure 7.6 and its NMR resonances are given in Table 7.8.
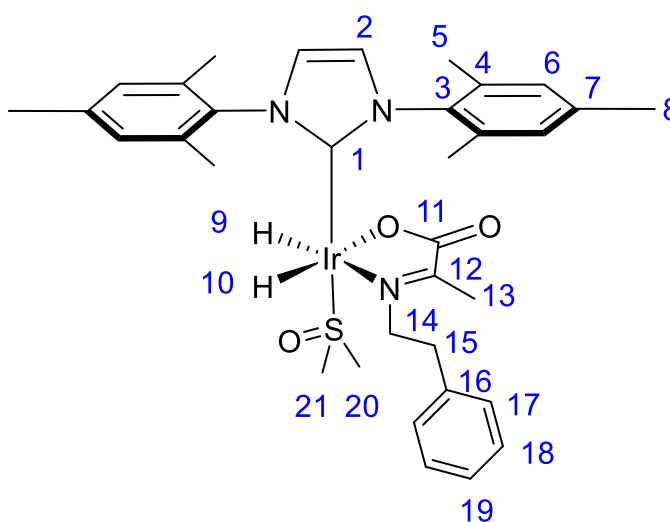
Figure 7.6: Structure of 47A determined from the NMR data given in Table 7.8.

Table 7.8: NMR data collected in methanol-d_4 at 245 K used to determine the structure of 47A shown in Figure 7.6. Resonances are labelled according to Figure 7.6.

Resonance	¹H	¹³C
1	-	N/A
2	7.23	122.90
3	-	136.82
4	-	135.21/135.71
5	2.08, 2.10	17.25
6	7.00, 7.03	128.59
7	-	138.63
8	2.32	19.92
9	−20.79 ($^2J_{HH}$ = 8 Hz)	-
10	−26.18 ($^2J_{HH}$ = 8 Hz)	-
11	-	169.57 ($^1J_{CC}$ = 66 Hz)
12	-	175.22 ($^1J_{CC}$ = 66 Hz)
13	1.90	~17 overlap
14	3.42, 3.87	61.7
15	2.58, 3.11	N/A
16	-	N/A (~130 overlap)
17	7.21	N/A (~128 overlap)
18, 19	N/A (~7.2 overlap)	N/A (~128 overlap)
20, 21	3.02/3.17	46.28/54.89

7.4.7 Characterisation of [Ir(H)₂(κ²-*O*OCC(CH₃)*N*CH₂CH₂Ph)(1,3-*bis*(2,4,6-trimethyl-phenyl)imidazole-2-ylidene)(benzylisocyanide)] (49), [Ir(H)₂(CNCH₂Ph)₃(1,3-*bis*(2,4,6-trimethyl-phenyl)imidazole-2-ylidene)]Cl (50) and [Ir(H)₂(CNCH₂Ph)₂(1,3-*bis*(2,4,6-trimethyl-phenyl)imidazole-2-ylidene)(NH₂(CH₂)₂Ph)]Cl (51)

An equilibrium mixture of **29** and **49**-**51** was synthesised (section 7.2.3) and analysed using 2D NMR spectroscopy at 245 K and MS. The structures of **49B** and **50** are shown in Figures 7.7-7.8 and their NMR resonances are given in Tables 7.9-7.10 respectively. HR-ESI⁺/MS (m/z): **49** [C₄₀H₄₅IrN₄O₂ +H]⁺, calcd 807.3250, found 807.3240; [C₄₀H₄₅IrN₄O₂+Na]⁺, calcd 829.3069, found 829.3057; **50** [Ir(H)₂(IMes)(benzylisocyanate)₃] [C₄₅H₄₆IrN₅]⁺, calcd 850.3461, found 850.3452; **51** [Ir(H)₂(IMes)(phenethylamine)(benzylisocyanate)] [C₄₅H₅₁IrN₅]⁺, calcd 854.3714, found 854.3765.
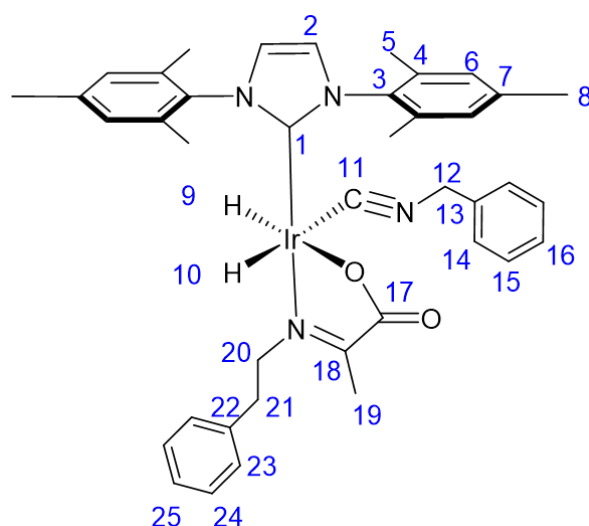
Figure 7.7: Structure of 49B determined from the NMR data given in Table 7.9.

Table 7.9: NMR data collected in dichloromethane-*d*₂ at 245 K used to determine the structure of 49B shown in Figure 7.7. Resonances are labelled according to Figure 7.7.

Resonance	¹H	¹³C
1	-	140.27
2	7.33	128.39
3	-	138.62
4	-	136.43/136.46
5	2.10/2.17	18.13/18.18
6	6.94/7.01	128.44/128.50
7	-	138.09
8	2.29	21.09
9	−8.57	-
10	−24.63	-
11	-	153.6
12	2.13	121.4
14	6.96	128.93
15	7.18	128.29
17	173.7	-
18	169.22	-
19	1.67	16.56
20	3.72, 3.87	63.69
21	2.52	35.39
23	6.98	126.41
13, 16, 22, 24, 25	N/A (~7.2 overlap)	N/A (~128 overlap)
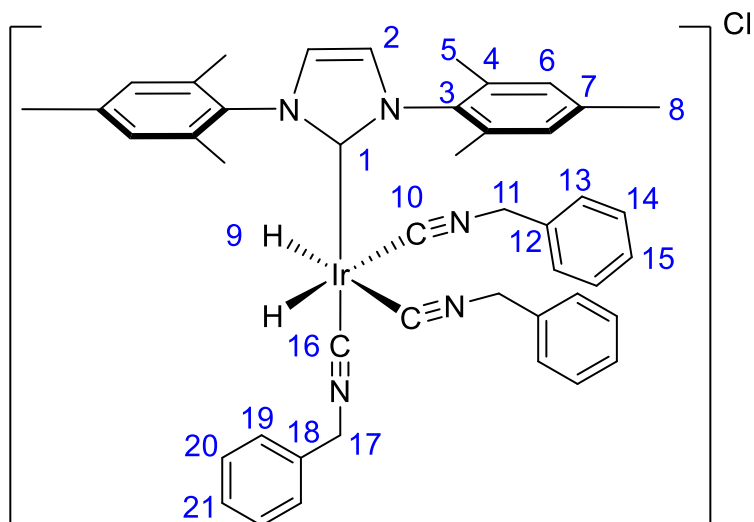
Figure 7.8: Structure of 50 determined from the NMR data given in Table 7.10.

Table 7.10: NMR data collected in dichloromethane-d_2 at 245 K used to determine the structure of 50 shown in Figure 7.8. Resonances are labelled according to Figure 7.8.

Resonance	^{1}H	^{13}C
1	-	N/A ~140
2	7.08	123.02
3	-	135.57
4	-	137.24
5	2.00	18.40
6	6.98	129.06
7	-	139.42
8	2.28	20.9
9	−12.34	-
10	-	156.90
11	4.73	117.93
12	-	N/A (~130 overlap)
13	7.17	N/A (~128 overlap)
14	N/A (~7.2 overlap)	N/A (~128 overlap)
15	N/A (~7.2 overlap)	N/A (~128 overlap)
16	-	150.78
17	4.82	113.95
18	-	N/A (~130 overlap)
19	7.12	N/A (~128 overlap)
20	7.23	N/A (~128 overlap)
21	N/A (~7.2 overlap)	N/A (~128 overlap)

7.4.8 Characterisation of [Ir(H)$_2$(1,3-*bis*(2,4,6-trimethyl-phenyl)imidazole-2-ylidene)(SCNEt)$_2$(NH$_2$(CH$_2$)$_2$Ph)]Cl (54)

Solutions containing **53** in dichloromethane-d_2 (0.6 mL) were formed as described in section 7.2.3. **54** was formed when this solution was left for longer time periods at 298 K (>hours) and characterised using 2D NMR spectroscopy at 245 K and MS. The structure of **54** is shown in Figure 7.9 and the NMR resonances for this complex are given in Table 7.11. HR-ESI$^+$/MS (m/z): [C$_{36}$H$_{51}$IrN$_5$S$_2$ – C$_3$H$_8$NS + Na]$^+$, calcd 743.2735, found 743.2923.
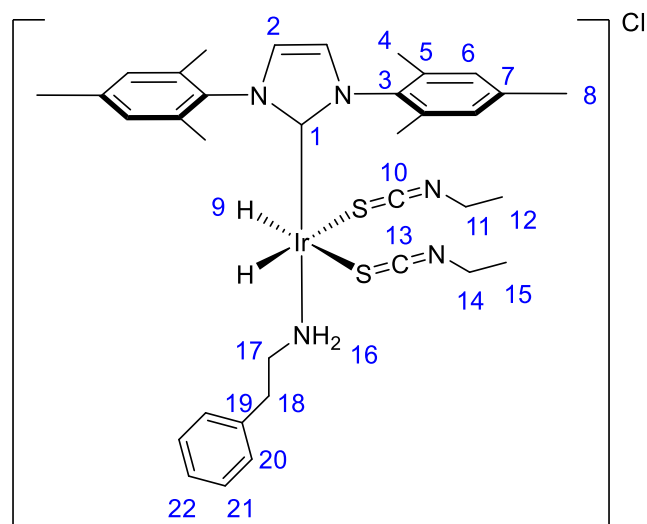
Figure 7.9: Structure of 54 determined from the NMR data given in Table 7.11.

Table 7.11: NMR data collected in dichloromethane-d_2 at 245 K used to determine the structure of 54 shown in Figure 7.9. Resonances are labelled according to Figure 7.9.

Resonance	^{1}H	^{13}C
1	-	140.38
2	~ 7.2 (overlap)	N/A (~126)
3	-	138.23
4	2.13/2.16	17.64/17.67
5	-	135.53
6	7.12/7.19	128.58/129.61
7	-	137.77
8	2.40	21.21
9	−16.05	-
10/13	-	119.99/120.28
11/14	3.57/3.59	39.94/40.27
12/15	1.20/1.35	15.25/15.46
16	1.80	-
17	3.85	35.05
18	2.04, 2.31	28.98
19	-	~130 (overlap)
20	6.96	128.72
21	7.23	~128-130 (overlap)
22	~7.2 (overlap)	~128-130 (overlap)

7.4.9 Characterisation of [Ir(H)(κ^2-OOCC(CH$_3$)NR)(SCH$_2$PhCl)(1,3-bis(2,4,6-trimethyl-phenyl)imidazole-2-ylidene)] (56)

56 was synthesised as described in section 7.2.3 and characterised using 2D NMR spectroscopy at 245 K and MS. The structure of **56** is shown in Figure 7.10 and its NMR resonances are given in Table 7.12. HR-ESI$^+$/MS (m/z): [C$_{45}$^{13}C$_2$H$_{54}$ClIrN$_4$O$_2$S + H]$^+$, calcd 969.3431, found 969.3385; [C$_{45}$^{13}C$_2$H$_{54}$ClIrN$_4$O$_2$S $-$H$_6$ + Na]$^+$, calcd 985.2781, found 985.3394; [C$_{45}$^{13}C$_2$H$_{54}$ClIrN$_4$O$_2$S $-$C$_7$H$_{11}$ClS]$^+$, calcd 806.3082, found 806.2784.
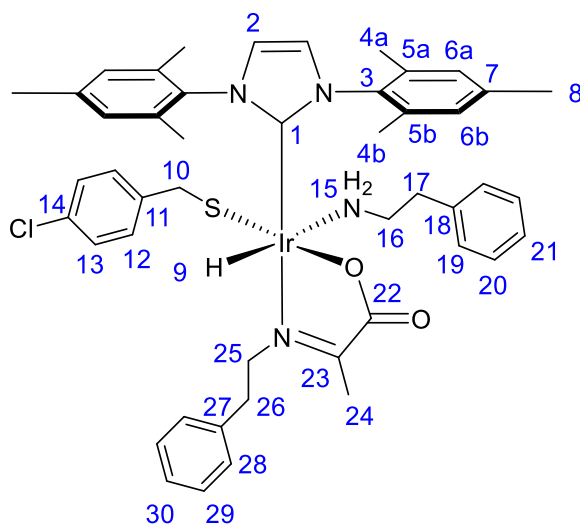
Figure 7.10: Structure of 56 determined from the NMR data given in Table 7.12.

Table 7.12: NMR data collected in dichloromethane-d_2 at 245 K used to determine the structure of 56 shown in Figure 7.10. Resonances are labelled according to Figure 7.10.

Resonance	^{1}H	^{13}C
1	-	140.48
2	6.76	121.67
3	-	~133 (overlap)
4a/4b	2.18/2.13	18.42/17.65
5a/5b	-	128.08/128.63
6a/6b	7.12/7.04	133.72/133.61
7	-	136.88
8	2.37	21.18
9	−21.58	-
10	3.18	47.88
11	-	130.63
12	7.17	128.02
14	-	146.86
15	1.88, 2.08	-
16	2.22, 2.25	30.58
17	3.13, 3.16	35.23
18	-	138.02
19	6.86	130.52
20	7.22	128.83
21	7.20	126.52
22	-	175.51
23	-	167.86
24	1.56	16.20
25	3.49, 3.53	25.54
26	2.91, 2.96	17.83
27	-	135.50
28	7.21	127.73
13, 29, 30	~7.2 (overlap)	~128 (overlap)

7.4.10 X ray diffraction of [Ir₂(H)₄(μ-SCH₂PhCl)2(1,3-*bis*(2,4,6-trimethyl-phenyl)imidazole-2-ylidene)₂] (59)

Crystals of **59** were grown by leaving a sample containing **2** (5 mM), **22-1,2-[¹³C₂]** (6 eq.) and **55** (4 eq.) in methanol-d_4 (0.6 mL) with 3 bar H₂ at 278 K for several months. The selected crystal of **59** showed evidence of minor twinning with two residual density peaks close to the iridium atoms. This could not be resolved using either merohedral or non-merohedral twinning methods. One of the 4-chlorobenzyl groups was disordered and modelled in two positions with refined occupancies of 0.803:0.197(10). Pairs of disordered carbons were constrained to have the same ADP. The S-CH₂ bond-lengths were restrained to be equal as were the CH₂-C(ipso) bond-lengths and the C-Cl bond-lengths. The phenyl ring of the minor form was constrained to be a regular hexagon with a C-C bond length of 1.39 angstroms. For the minor form the CH₂-C(ortho) distances were restrained to be equal as were the C(meta)-Cl distances. The hydrides were initially located by difference map, the Ir-H bond-length was then adjusted to be 1.65 angstroms and then the location fixed to ride on the iridium. Single crystal X ray diffraction data were collected and solved by Dr. Adrian C. Whitwood.[253] The structure was deposited with the Cambridge Crystallographic Database (no. 1957543). The structure of **59** is shown in Figure 5.2; selected crystal data and structural refinement details are shown in Table 7.13.

Table 7.13: Selected crystal data and structural refinement details for 59.

Parameter	Value
Empirical formula	$C_{57}H_{68}Cl_2Ir_2N_4OS_2$
Formula weight	1344.57
Temperature/K	110.00(10)
Crystal system	monoclinic
Space group	P21/c
a /Å	12.9317(2)
b /Å	16.6000(3)
c /Å	25.5365(4)
α /°	90
β /°	90.2757(13)
γ /°	90
Volume /Å³	5481.76(15)
Z	4
ρ_{calc} g/cm³	1.629
μ/ mm⁻¹	11.192
$F(000)$	2664.0
Crystal size /mm³	$0.149 \times 0.09 \times 0.078$
Radiation	CuK$_\alpha$ ($\lambda = 1.54184$)
2Θ range for data collection /°	6.924 to 134.152
Index ranges	$-15 \leq h \leq 14, -19 \leq k \leq 18, -29 \leq l \leq 30$
Reflections collected	20688
Independent reflections	9782 [$R_{int} = 0.0256$, $R_{sigma} = 0.0331$]
Data/restraints /parameters	9782/4/650
Goodness-of-fit on F^2	1.036
Final R indexes [$I \geq 2\sigma (I)$]	$R_1 = 0.0299$, w$R_2 = 0.0678$
Final R indexes [all data]	$R_1 = 0.0357$, w$R_2 = 0.0712$
Largest diff. peak/hole /e Å⁻³	1.92/−1.36

7.4.11 X ray diffraction of *fac*-[Ir(H)$_3$(PPh$_3$)$_3$] (60)

Crystals of **60** were grown by leaving a sample containing **2** (5 mM), **22-1,2-[^{13}C$_2$]** (6 eq.) and **58** (4 eq.) in methanol-d_4 (0.6 mL) with 3 bar H$_2$ at 278 K for several months. The asymmetric unit contained a partial methanol whose occupancy refined to 0.283(5). Single crystal X ray diffraction data were collected and solved by Dr. Adrian C. Whitwood.[253] The structure was deposited with the Cambridge Crystallographic Database (no. 1957542). The structure of **60** is shown in Figure 5.2; selected crystal data and structural refinement details are shown in Table 7.14.

Table 7.14: Selected crystal data and structural refinement details for 60.

Parameter	Value
Empirical formula	C$_{54.28}$H$_{49.13}$IrO$_{0.28}$P$_3$
Formula weight	991.09
Temperature/K	110.00(10)
Crystal system	monoclinic
Space group	P21/c
a /Å	17.31801(12)
b /Å	12.99024(10)
c /Å	19.71788(16)
α /°	90
β /°	94.4442(7)
γ /°	90
Volume /Å^3	4422.50(6)
Z	4
ρ_{calc} g/cm^3	1.489
μ/ mm^{-1}	7.149
F(000)	1996.4
Crystal size /mm^3	0.197 × 0.099 × 0.037
Radiation	CuK$_\alpha$ (λ = 1.54184)
2Θ range for data collection /°	8.158 to 134.152
Index ranges	$-15 \leq h \leq 20, -15 \leq k \leq 15, -23 \leq l \leq 21$
Reflections collected	17542
Independent reflections	7896 [R_{int} = 0.0226, R_{sigma} = 0.0296]
Data/restraints /parameters	7896/0/557
Goodness-of-fit on F^2	1.047
Final R indexes [I>=2σ (I)]	R_1 = 0.0199, wR_2 = 0.0458
Final R indexes [all data]	R_1 = 0.0237, wR_2 = 0.0480
Largest diff. peak/hole /e Å^{-3}	0.71/$-$0.53

7.4.12 X ray diffraction of [Ir(H)$_4$(μ-H)$_2$(1,3-*bis*(2,4,6-trimethyl-phenyl)imidazole-2-ylidene)$_2$(methylphenylsulfoxide)$_2$] (82)

Crystals of **82** were grown by leaving a sample containing **2** (5 mM), **22-1,2-[^{13}C$_2$]** (6 eq.) and **69** (4 eq.) in methanol-d_4 (0.6 mL) with 3 bar H$_2$ at 278 K for several weeks. The hydrides was initially located by difference map and then the Ir-H bond length fixed at 1.65 angstroms. Single crystal X ray diffraction data were collected and solved by Dr. Adrian C. Whitwood. The structure of **82** is shown in Figure 5.19; selected crystal data and structural refinement details are shown in Table 7.15.

Table 7.15: Selected crystal data and structural refinement details for 82.

Parameter	Value
Empirical formula	C$_{46}$H$_{64}$Ir$_2$N$_4$O$_2$S$_3$
Formula weight	1185.59
Temperature/K	110.00(10)
Crystal system	orthorhombic
Space group	Pna21
a /Å	16.5217(3)
b /Å	11.6762(2)
c /Å	24.9575(5)
α /°	90
β /°	90
γ /°	90
Volume /Å^3	4814.60(15)
Z	4
ρ_{calc} g/cm^3	1.636
μ/ mm^{-1}	12.062
$F(000)$	2344.0
Crystal size /mm^3	$0.142 \times 0.098 \times 0.077$
Radiation	CuK$_\alpha$ (λ = 1.54184)
2Θ range for data collection /°	7.084 to 134.15
Index ranges	$-14 \le h \le 19, -10 \le k \le 13, -29 \le l \le 28$
Reflections collected	10987
Independent reflections	6963 [R_{int} = 0.0204, R_{sigma} = 0.0318]
Data/restraints /parameters	6963/1/531
Goodness-of-fit on F^2	1.044
Final R indexes [I>=2σ (I)]	R_1 = 0.0247, wR_2 = 0.0556
Final R indexes [all data]	R_1 = 0.0309, wR_2 = 0.0594
Largest diff. peak/hole /e Å^{-3}	0.94/−0.67

7.4.13 X ray diffraction of [Ir$_2$(H)$_3$(μ-H)(μ-SPh)$_2$(1,3-*bis*(2,4,6-trimethyl-phenyl)imidazole-2-ylidene)$_2$(S(O)(Et)(Ph))] (83)

Crystals of **83** were grown by leaving a sample containing **2** (5 mM), **22-1,2-[^{13}C$_2$]** (6 eq.) and **71** (4 eq.) in methanol-d_4 (0.6 mL) with 3 bar H$_2$ at 278 K for several weeks. Single crystal X ray diffraction data were collected and solved by Dr. Rachel R. Parker.[268] The structure was deposited with the Cambridge Crystallographic Database (no. 1949693). The structure of **83** is shown in Figure 5.19; selected crystal data and structural refinement details are shown in Table 7.16.

For analysis by high resolution mass spectrometry, a solid sample containing **83** was prepared by adding 3 bar H$_2$ to a solution of **2** (5 mM) and **71** (4 eq.) in methanol (0.6 mL) and leaving for several days before removing the solvent.

HR-ESI$^+$/MS (m/z): [C$_{62}$H$_{72}$Ir$_2$N$_4$OS$_3$ − C$_{27}$H$_{35}$IrN$_2$S + Na]$^+$ calc. 781.1874 found 781.1898 (**71** fragment); [C$_8$H$_{10}$NaOS + Na]$^+$ calc. 177.0350 found 177.0343 (**78**)

Table 7.16: Selected crystal data and structural refinement details for 83.

Parameter	Value
Empirical formula	C$_{63}$H$_{76}$Ir$_2$N$_4$O$_2$S$_3$
Formula weight	1401.85
Temperature/K	110.05(10)
Crystal system	triclinic
Space group	P-1
a /Å	11.9397(4)
b /Å	12.7147(4)
c /Å	20.2094(6)
α /°	91.573(3)
β /°	92.120(3)
γ /°	101.839(3)
Volume /Å^3	2998.74(16)
Z	2
ρ_{calc} g/cm^3	1.553
μ/ mm^{-1}	4.583
F(000)	1400.0
Crystal size /mm^3	0.147 × 0.125 × 0.067
Radiation	MoK$_\alpha$ (λ = 0.71073)
2Θ range for data collection /°	6.758 to 56.55
Index ranges	$-15 \leq h \leq 14, -16 \leq k \leq 16, -26 \leq l \leq 26$
Reflections collected	24647
Independent reflections	13472 [R_{int} = 0.0297, R_{sigma} = 0.0517]
Data/restraints /parameters	13472/7/719
Goodness-of-fit on F^2	1.102
Final R indexes [I>=2σ (I)]	R_1 = 0.0368, wR_2 = 0.0786
Final R indexes [all data]	R_1 = 0.0512, wR_2 = 0.0861
Largest diff. peak/hole /e Å^{-3}	2.44/−1.41

7.4.14 X ray diffraction of [Ir$_2$(H)$_4$(μ-S)(1,3-*bis*(2,4,6-trimethyl-phenyl)imidazole-2-ylidene)$_2$(dibenzylsulfoxide)$_2$] (84)

Crystals of **84** were grown by leaving a sample containing **2** (5 mM), **22-1,2-[^{13}C$_2$]** (6 eq.) and **73** (4 eq.) in methanol-d_4 (0.6 mL) with 3 bar H$_2$ at 278 K for several weeks. Single crystal X ray diffraction data were collected and solved by Dr. Rachel R. Parker.[268] The structure was deposited with the Cambridge Crystallographic Database (no. 1949692). The structure of **84** is shown in Figure 5.19; selected crystal data and structural refinement details are shown in Table 7.17.

For analysis by high resolution mass spectrometry, a solid sample containing **84** was prepared by adding 3 bar H$_2$ to a solution of **2** (5 mM) and **73** (4 eq.) in methanol (0.6 mL) and leaving for several days before removing the solvent.

HR-ESI$^+$/MS (m/z): [C$_{70}$H$_{80}$Ir$_2$N$_4$O$_2$S$_3$ $-$ C$_{21}$H$_{27}$N$_2$S]$^+$ calc. 1151.2807 found 1151.2761 (**84** fragment)

Table 7.17: Selected crystal data and structural refinement details for 84.

Parameter	Value
Empirical formula	C$_{70}$H$_{80}$Ir$_2$N$_4$O$_2$S$_3$
Formula weight	1489.96
Temperature/K	110.10(14)
Crystal system	monoclinic
Space group	P2$_1$/c
a /Å	19.8526(2)
b /Å	15.10020(10)
c /Å	21.9966(2)
α /°	90
β /°	105.3940(10)
γ /°	90
Volume /Å^3	6357.53(10)
Z	4
ρ_{calc} g/cm^3	1.557
μ/ mm^{-1}	4.328
F(000)	2984.0
Crystal size /mm^3	$0.199 \times 0.165 \times 0.121$
Radiation	MoK$_\alpha$ (λ = 0.71073)
2Θ range for data collection /°	6.64 to 52.744
Index ranges	$-14 \leq h \leq 24$, $-17 \leq k \leq 18$, $-27 \leq l \leq 21$
Reflections collected	26164
Independent reflections	12962 [R_{int} = 0.0259, R_{sigma} = 0.0408]
Data/restraints /parameters	12962/0/758
Goodness-of-fit on F^2	1.059
Final R indexes [I>=2σ (I)]	R_1 = 0.0260, wR_2 = 0.0535
Final R indexes [all data]	R_1 = 0.0353, wR_2 = 0.0576
Largest diff. peak/hole /e Å^{-3}	1.15/-0.94

7.5. Density Functional Theory (DFT)

All DFT calculations were performed on the full molecule (without simplification) by Dr. Richard O. John using the Gaussian 09 software package. All structures were optimized in combination with solvent effects modelled with the integral equation formalism variant of the Polarisable Continuum Model (IEFPCM).[306-308] All calculations had the solvent specified as either dichloromethane or methanol as appropriate. All calculations used the PBE0 DFT functional[309] and the basis set family defined as def2-SVP from Ahlrichs[310, 311] for all atoms (taken from the EMSL website[312, 313]) except hydride atoms and iridium. The hydride atoms were assigned the larger def2-TZVPP basis set[310, 311] and iridium was assigned the LANL08(f) basis set with the associated effective core potential (ECP).[314] Frequency calculations were used to confirm that the structures obtained were local minima along with zero-point energies and thermal corrections to the energy at 298.15 K. Single point calculations (again with solvation) were then undertaken with all atoms apart from iridium assigned the larger basis sets from the def2-TZVPP family (the LANL08(f) basis set was maintained for iridium). These calculations also included the GD3BJ empirical dispersion correction from Grimme which includes Beck-Johnson damping.[315] The thermal energy corrections were then applied to obtain chemical enthalpies and free energies.[316] This approach has previously been used to model the reactions of similar systems.[221] The calculations were checked for Basis Set Superposition Errors (BSSE). The resulting counterpoise calculation[317] revealed that errors of around 5 kJ mol^{-1} were present in all systems and so corrections were applied appropriately.

7.6. Kinetic Modelling and determination of rate constants

7.6.1 General procedure for kinetic fitting

Kinetic rate equations for a process of interest are generated and given in the main text. Rate constants are found using Microsoft Excel Solver function that give the lowest sum of the least squared fit between calculated percentage abundances using this model, and experimentally determined percentage abundances from experimental measurements. Errors in these rate constants are calculated according to established procedures.[222]

7.6.2 Transmission rates from 29 to 44, 45 and 47

A series of ^{1}H NMR spectra were recorded after the addition of either pyridine, imidazole or dimethylsulfoxide (5 eq.) to **29**. The proportion of each complex was determined on the basis of the integral intensities of the hydride NMR resonance *trans* to nitrogen which are free from spectral overlap. This time course data were fit to the kinetic model as described by equations 4.7-4.12, an example is presented in Figure 4.13b. Selected transmission rates are presented in Table 4.4, all transmission rates are given in Table 7.18.

Table 7.18: Transmission rate constants describing interconversion between 29 and 44, 45 or 47 calculated by fitting the EXSY data (examples shown in Figures 4.13b and 7.11) to the model in Figure 4.13a described by Equations 4.7-4.12. Note that the model sets values smaller than $1 \times 10^{-6}\,\text{s}^{-1}$ to zero.

Rate constant	29 and 44 /10^{-5} s^{-1}	29 and 45 /10^{-5} s^{-1}	29 and 47 /10^{-5} s^{-1}
k_1	0.0 ± 0.3	0.0 ± 0.0	0.0 ± 0.0
k_2	0.9 ± 0.2	0.3 ± 0.0	0.6 ± 0.1
k_3	0.0 ± 0.0	5.1 ± 2.3	0.0 ± 0.0
k_4	0.7 ± 0.3	0.2 ± 0.0	0.0 ± 0.0
k_5	0.0 ± 0.0	0.2 ± 0.3	1.7 ± 0.1
k_6	0.2 ± 0.6	0.0 ± 0.0	0.0 ± 0.0
k_{-1}	2.9 ± 2.5	1.7 ± 0.7	10.6 ± 1.2
k_{-2}	0.2 ± 0.0	0.4 ± 0.0	1.3 ± 0.1
k_{-3}	2.7 ± 0.3	1.6 ± 2.3	9.9 ± 1.0
k_{-4}	4.9 ± 1.6	0.0 ± 0.0	0.0 ± 0.0
k_{-5}	0.0 ± 0.0	0.0 ± 0.0	0.0 ± 0.0
k_{-6}	2.0 ± 0.1	0.0 ± 0.0	0.6 ± 0.1

7.6.3 Transmission rates from 29 to 44 and 45

A series of ^{1}H NMR spectra were recorded after the addition of an equimolar solution of pyridine and imidazole (5 eq.) in dichloromethane-d_2 (20 μL) to an equilibrium mixture of **29**. The proportions of **29**, **44** and **45** were determined from the integral intensities of the hydride resonance *trans* to nitrogen which are free from spectral overlap. This time course data were fit to a kinetic model allowing for the exchange of all six observed species. This model is summarised in Figure 7.11 and Equations 7.1-7.9 where $[X]_{\text{t}-\delta\text{t}}$ and $[X]_t$ are the concentration or proportion of species X in solution at t= t $-$ δt and t=t where ∂t is the incremental time difference. Rate constants were found by minimizing the sum of the squared differences between experimental and predicted values. Initial concentration values of the metal complexes at $t = 0$ were taken from ^{1}H NMR integral intensities whereas $[\mathbf{5}]_0$, $[\mathbf{8}]_0$ and $[\mathbf{43}]_0$ were allowed to change. Some initial data points immediately after coligand addition were omitted due to non equilibrium behaviour including large initial fluctuations in $[\mathbf{5}]_0$ having an effect on the equilibrium between amine and imine in solution.
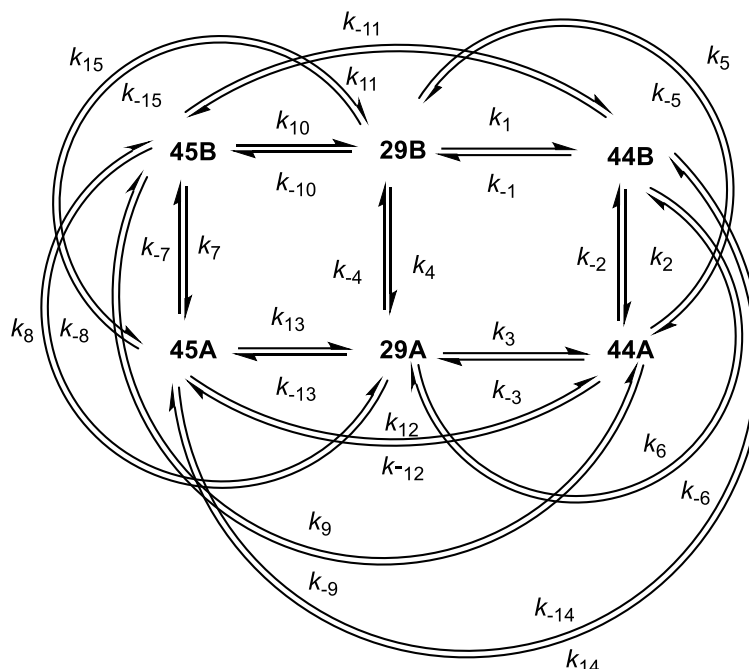
Figure 7.11: Exchange model used for kinetic modelling.

$$[\text{29A}]_t = [\text{29A}]_{t-\delta t} + (k_1[\text{29B}] - k_{-1}[\text{29A}] - k_2[\text{43}][\text{29A}] + k_{-2}[\text{44A}][\text{5}] - k_{-6}[\text{29A}][\text{43}] + k_6[\text{44B}][\text{5}]$$
$$+ k_{-11}[\text{45B}][\text{5}] - k_{11}[\text{29A}][\text{8}] - k_{14}[\text{29A}][\text{8}] + k_{-14}[\text{45A}][\text{5}])\partial t \qquad (7.1)$$

$$[\text{29B}]_t = [\text{29B}]_{t-\delta t} + (-k_1[\text{29B}] + k_{-1}[\text{29A}] - k_5[\text{43}][\text{29B}] + k_{-5}[\text{44A}][\text{5}] - k_4[\text{29B}][\text{43}] + k_{-4}[\text{44B}][\text{5}]$$
$$+ k_{15}[\text{45A}][\text{5}] - k_{-15}[\text{29B}][\text{8}] + k_{10}[\text{45B}][\text{5}] - k_{-10}[\text{29B}][\text{8}])\partial t \qquad (7.2)$$

$$[\text{44A}]_t = [\text{44A}]_{t-\delta t} + (k_2[\text{29A}][\text{43}] - k_{-2}[\text{44A}][\text{5}] - k_{-5}[\text{44A}][\text{5}] + k_5[\text{29B}][\text{43}] - k_{-3}[\text{44A}] + k_3[\text{44B}]$$
$$- k_{-9}[\text{44A}][\text{8}] + k_9[\text{45B}][\text{43}] - k_{-12}[\text{44A}][\text{8}] + k_{12}[\text{45A}][\text{43}])\partial t \qquad (7.3)$$

$$[\text{44B}]_t = [\text{44B}]_{t-\delta t} + (-k_{-4}[\text{44B}][\text{5}] + k_4[\text{29B}][\text{43}] - k_3[\text{44B}] + k_{-3}[\text{44A}] - k_6[\text{44B}][\text{5}] + k_{-6}[\text{29A}][\text{43}]$$
$$+ k_8[\text{44B}][\text{8}] + k_{-8}[\text{45B}][\text{43}] - k_{13}[\text{44B}][\text{8}] + k_{13}[\text{45A}][\text{5}])\partial t \qquad (7.4)$$

$$[\text{45A}]_t = [\text{45A}]_{t-\delta t} + (-k_{12}[\text{45A}][\text{43}] + k_{-12}[\text{44A}][\text{8}] + k_{-13}[\text{44B}][\text{8}] - k_{13}[\text{45A}][\text{43}] - k_{-7}[\text{45A}]$$
$$+ k_7[\text{45B}] - k_{15}[\text{45A}][\text{5}] + k_{-15}[\text{29B}][\text{8}] - k_{-14}[\text{45A}][\text{5}]$$
$$+ k_{14}[\text{29A}][\text{8}])\partial t \qquad (7.5)$$

$$[\text{45B}]_t = [\text{45B}]_{t-\delta t} + (k_8[\text{44B}][\text{8}] - k_{-8}[\text{45B}][\text{43}] - k_9[\text{45B}][\text{43}] + k_{-9}[\text{44A}][\text{8}] - k_7[\text{45B}] + k_{-7}[\text{45A}]$$
$$- k_{-11}[\text{45B}][\text{5}] + k_{11}[\text{29A}][\text{8}] - k_{10}[\text{45B}][\text{5}] + k_{-10}[\text{29B}][\text{8}])\partial t \qquad (7.6)$$

$$[\text{5}]_t = [\text{5}]_{t-\delta t} + (k_4[\text{29B}][\text{43}] - k_{-4}[\text{44B}][\text{5}] + k_2[\text{29A}][\text{43}] - k_{-2}[\text{44A}][\text{5}] - k_6[\text{44B}][\text{5}]$$
$$+ k_{-6}[\text{29A}][\text{43}] - k_{-5}[\text{44A}][\text{5}] + k_5[\text{29B}][\text{43}] - k_{10}[\text{45B}][\text{5}] + k_{-10}[\text{29B}][\text{8}] + k_{-15}[\text{29B}][\text{8}]$$
$$- k_{15}[\text{45A}][\text{5}] - k_{14}[\text{29A}][\text{5}] + k_{-14}[\text{45A}][\text{5}] + k_{11}[\text{29A}][\text{8}]$$
$$- k_{-11}[\text{45B}][\text{5}])\partial t \qquad (7.7)$$

$$[\text{43}]_t = [\text{43}]_{t-\delta t} + (-k_4[\text{29B}][\text{43}] + k_{-4}[\text{44B}][\text{5}] - k_2[\text{29A}][\text{43}] + k_{-2}[\text{44A}][\text{5}] + k_6[\text{44B}][\text{5}]$$
$$- k_{-6}[\text{29A}][\text{43}] + k_{-5}[\text{44A}][\text{5}] - k_5[\text{29B}][\text{43}] + k_8[\text{44B}][\text{8}] - k_{-8}[\text{45B}][\text{43}] + k_{13}[\text{44B}][\text{8}]$$
$$- k_{13}[\text{45A}][\text{43}] - k_9[\text{45B}][\text{43}] + k_{-9}[\text{44A}][\text{8}] - k_{12}[\text{45A}][\text{43}]$$
$$+ k_{-12}[\text{44A}][\text{8}])\partial t \qquad (7.8)$$

$$[\text{8}]_t = [\text{8}]_{t-\delta t} + (-k_8[\text{44B}][\text{8}] + k_{-8}[\text{45B}][\text{43}] - k_9[\text{44A}][\text{8}] + k_9[\text{45B}][\text{43}] - k_{12}[\text{44A}][\text{8}]$$
$$+ k_{-12}[\text{45A}][\text{43}] - k_{-13}[\text{44B}][\text{8}] + k_{13}[\text{45A}][\text{43}] + k_{10}[\text{45B}][\text{5}] - k_{-10}[\text{29B}][\text{8}]$$
$$- k_{-15}[\text{29B}][\text{8}] + k_{15}[\text{45A}][\text{5}] + k_{14}[\text{29A}][\text{8}] - k_{-14}[\text{45A}][\text{5}] - k_{11}[\text{29A}][\text{8}]$$
$$+ k_{-11}[\text{45B}][\text{5}])\partial t \qquad (7.9)$$

The kinetic time course of these data is shown in Figure 7.12 and the transmission rates are given in Table 7.19.
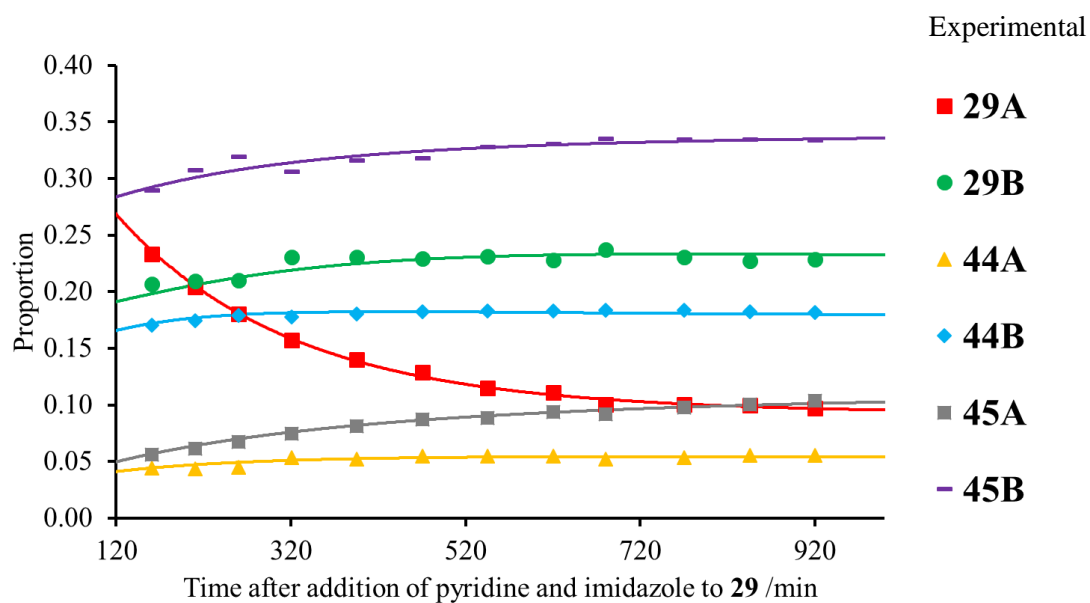
Figure 7.12: Kinetic modelling showing experimental data (markers) and predicted data (solid lines) after the addition of an equimolar solution of pyridine and imidazole to 29. The rate constants used to fit these data are shown in Table 7.19.

Table 7.19: Transmission rates used to fit kinetic data shown in Figure 7.12 according to the model shown in Figure 7.11 and Equations 7.1-7.9. All errors are less than 1×10^{-6} s^{-1}.

Rate constant	/10^{-5} s^{-1}	Rate constant	/10^{-5} s^{-1}
k_1	0.22	k_{-1}	0.07
k_2	0.06	k_{-2}	0.22
k_3	0.15	k_{-3}	0.001
k_4	0.48	k_{-4}	0.23
k_5	0.18	k_{-5}	0.11
k_6	0.13	k_{-6}	0.002
k_7	0.83	k_{-7}	0.16
k_8	0.26	k_{-8}	0.001
k_9	0.18	k_{-9}	0.22
k_{10}	0.78	k_{-10}	0.10
k_{11}	0.22	k_{-11}	0.09
k_{12}	0.30	k_{-12}	0.23
k_{13}	0.13	k_{-13}	0.002
k_{14}	0.001	k_{-14}	0.002
k_{15}	0.002	k_{-15}	0.002

Conclusions and future work

Polarisation transfer catalysts of the form $[Ir(H)_2(NHC)(amine)_3]Cl$ are able to hyperpolarise carrier amines with significant signal gains, with subsequent proton exchange effects allowing relayed transfer of hyperpolarisation to target molecules, as discussed in Chapters 2 and 3. This approach, SABRE-Relay, can deliver ^1H and ^{13}C NMR signal enhancements of 700-fold and 1400-fold respectively for the simple alcohol 3-methyl-1-butanol. This can be extended to more complex OH-containing molecules such as the natural products nerol, geraniol, and linalool (^1H and ^{13}C NMR signal enhancements of up to 355-fold and 500-fold respectively) and lactate esters such as methyl lactate (^1H and ^{13}C NMR signal gains as high as 110-fold and 1015-fold respectively). These accomplishments are significant as hyperpolarisation of these unsaturated, non-ligating, molecules cannot be achieved using techniques such as PHIP or SABRE and uses much simpler technology than d-DNP.

The mechanism of relayed polarisation transfer has been investigated using the simple alcohol 3-methyl-1-butanol as an example substrate. SABRE-Relay efficiency is dependent on three key factors: i) polarisation transfer from $p\text{-}H_2$ to carrier in the active $[Ir(H)_2(NHC)(carrier)_3]Cl$ catalyst ii) relay of polarisation from carrier to substrate *via* proton exchange and iii) propagation of polarisation within the substrate CH framework. All of these factors play an important role in determining SABRE-Relay efficiency. The finite carrier polarisation can be optimised by variation of the carrier identity and the carrier to catalyst ratio. NH_3 generally relays the highest alcohol polarisation compared to use of aliphatic amines benzylamine or phenethylamine. Further optimisation of alcohol NMR signal enhancements can result from variation of the carrier to alcohol ratio which effectively tunes OH ↔ NH exchange. Aliphatic branching can influence polarisation propagation from the exchanging OH into the substrate aliphatic framework. This highlights the tension between the multiple factors that determine SABRE-Relay performance.

There are exciting applications of SABRE-Relay that can be extended in the future. For example, related alcohols such as deuterated tertiary butanol has been hyperpolarised using d-DNP and used as perfusion imaging agents.[318] There are also exciting analytical applications as alcohol concentrations as low as $28\,\mu M$ can be detected in a single SABRE-Relay hyperpolarised ^{13}C NMR spectrum. This detection limit could be reduced through further optimisation of the carrier molecule, catalyst or coligand. Interestingly, a linear relationship between hyperpolarised signal intensity and concentration is achieved for dilute alcohols under anhydrous conditions. This suggests that SABRE-Relay could have uses in the low concentration detection of alcohols in mixtures. However, polarisation levels are affected by the presence of other molecules with exchangeable protons which can prevent the detection of small quantities of alcohol when other molecules containing exchangeable protons are present at higher concentrations. Further work on this topic is needed to apply these findings appropriately to a useful real world application.

SABRE-Relay has not expanded the substrate scope of SABRE to all molecules containing exchangeable protons tested in this thesis. This is related to the limited solubility of some target molecules in SABRE-Relay compatible solvents and the presence of destructive proton exchange pathways due to the presence of large amounts of water which may be required to aid substrate solubilisation. In the case of pyruvate, ^{13}C NMR signal enhancements of just 65-fold are achieved and there are serious limitations of this approach including rapid deactivation of [Ir(H)$_2$(NHC)(amine)$_3$]Cl due to *in situ* condensation between pyruvate and amine. Currently, SABRE Relay is only applicable to selected examples and cannot deliver NMR signal enhancements as high as d-DNP. This may limit widespread use of the technique in hyperpolarised MR, particularly for applications in which hyperpolarisation in aqueous solvents is essential. The substrate scope of SABRE-Relay could be expanded by solvent optimisation or inclusion of solubilising molecular tags which can be rapidly cleaved. This approach could be applied to the production of hyperpolarised lactate from lactate esters. Future improvements in catalyst design, carrier hyperpolarisation levels, and methodologies to transfer ^{1}H derived magnetisation to ^{13}C sites may allow such applications in the future.

Polarisation transfer catalysts of the form [Ir(H)$_2$(κ^2-OOCC(CH$_3$)NR)(NH$_2$R)(IMes)] can be synthesised from the *in situ* condensation reaction between amine and pyruvate and display strongly hyperpolarised hydride ^{1}H and ^{13}C NMR resonances for the non-exchanging imine, as explored in Chapter 4. Interestingly, ^{13}C$_2$ singlet order within the coordinated imine could be created spontaneously at low field. This provides a rare example of a naturally occurring heteronuclear singlet state within a transition metal complex. These ^{13}C NMR signal enhancements and singlet state lifetimes can be extended to 750-fold and 20 s respectively when isotopic labelling techniques are used. The amine ligand of these complexes can be replaced by pyridine, imidazole, dimethylsulfoxide, and many others to yield a suite of iridium carboxyimine complexes with hydride chemical shifts sensitive to the identity of bound ligand. ∼15.5 ppmin a typically uncrowded region of ^{1}complexes could therefore act as unique sensors with changes in ^{1}H hydride chemical shift and hydride hyperpolarisation levels used to give information about the identity and binding strengths of coligands in solutionFuture work should focus on developing these complexes for quantitative coligand sensing applications.

Related magnetisation transfer catalysts of the form [Ir(H)$_2$(κ^2-ketoacid)(sulfoxide)(NHC)] can be used to hyperpolarise α-keto acids such as sodium pyruvate and sodium ketoisokaproate in a cheap, rapid, and reversible method, as shown in Chapter 5. Hyperpolarised ^{13}C$_2$ singlet order within sodium pyruvate-1,2-[^{13}C$_2$] enhanced by up to 2135-fold in methanol-d_4 can be created spontaneously. In contrast to traditional SABRE magnetisation transfer catalysts, [IrCl(H)$_2$(sulfoxide)$_2$(NHC)] mediates p-H$_2$ exchange. Hyperpolarised pyruvate ^{13}C NMR signals are related to the amount of active catalyst in solution, although systems containing similar amounts but different ligands can result in very different pyruvate NMR signal enhancements. These results highlight the tension between different factors that influence polarisation transfer

efficiency of this catalyst. In all cases, a decrease in SABRE catalytic efficiency is observed at longer reaction times which is linked to the formation of dimers and catalyst deactivation.

The formation of these novel sulfoxide containing polarisation transfer catalysts and their applications to hyperpolarise pyruvate are an important step forward in SABRE hyperpolarisation as they facilitate the hyperpolarisation of molecules previously incompatible with this technique. While SABRE provides a cheap and reversible approach to hyperpolarise pyruvate with time and cost advantages over DNP and PHIP-SAH, the NMR signal enhancements SABRE can achieve are significantly lower (^{13}C polarisation of 1.7% compared to ∼5% for PHIP-SAH[73] or 70% for DNP[38]). While these signal gains are large enough to allow detection of 0.4 mM pyruvate in a 70:30 D_2O/ethanol-d_6 mixture *in vitro*, low NMR signal enhancements and low biocompatibility will limit applications of this technique for *in vivo* biomedical imaging studies, as discussed in Chapter 6. Future studies should further optimize ligand exchange processes within the polarization transfer catalyst with a focus on synthesis of catalysts efficient in aqueous solvents. Synthesis of a new generation of polarisation transfer catalysts that are not based on typical NHC ligands, or on iridium, are likely necessary for significant increases in the pyruvate ^{13}C NMR signal gains that can be achieved using SABRE.

Nevertheless, [Ir(H)$_2$(κ^2-ketoacid)(sulfoxide)(NHC)] catalysts can be used to produce hyperpolarised pyruvate suitable for reaction monitoring. For example, SABRE hyperpolarised ^{13}C NMR can be used to monitor the reaction between hyperpolarised sodium pyruvate-1,2-[^{13}C$_2$] and hydrogen peroxide (H_2O_2). A rate constant of reaction between pyruvate (15 mM) and H_2O_2 (150 mM) can be extracted from hyperpolarised SABRE-NMR (k = 0.056 ± 0.003 dm^3 mol^{-1} s^{-1}) and is consistent with those determined from thermal ^{1}H NMR (k = 0.050 ± 0.003 dm^3 mol^{-1} s^{-1}) and UV (0.050 ± 0.003 dm^3 mol^{-1} s^{-1}). The ^{13}C NMR signal gains SABRE provides can make a short lived 2-hydroxperoxy-2-hydroxypropanoate intermediate visible in just a single scan ^{13}C NMR spectrum at reduced temperature. This shows that SABRE can have exciting applications for hyperpolarised reaction monitoring, and intermediate detection. Structural modification of [Ir(H)$_2$(κ^2-ketoacid)(sulfoxide)(NHC)] polarisation transfer catalysts may also extend SABRE hyperpolarisation to a wider range of molecules. The synthesis of metabolically inactive reporters with α-keto acid motifs could yield molecules compatible with SABRE hyperpolarisation that are responsive to H_2O_2 in a cheap and easy to implement method.

In conclusion, the polarisation transfer catalysts developed in this thesis have allowed the catalytic transfer of magnetism from p-H$_2$ to a wider range of target substrates than ever before. These catalysts have expanded the substrate scope of the SABRE technique and have allowed novel applications in NMR such as chemosensing, low concentration detection, reaction monitoring and intermediate detection.

Abbreviations

ABV: Alcohol By Volume

ADP: Adenosine DiPhosphate

ALTADENA: Adiabatic Longitudinal Transport After Dissociation Engenders Net Alignment

ATP: Adenosine TriPhosphate

Bn: Benzyl (CH_2Ph)

BOLD: Blood Oxygen Level Dependant

calc.: calculated

CEST: Chemical Exchange Saturation Transfer

CoA: Co-enzyme A

COD: *cis*,*cis*-1,5-cyclooctadiene

COSY: homonuclear COrrelation SpectroscopY

CSI: Chemical Shift Imaging

CT: Computed Tomography

d: doublet

dd: doublet of doublets

d-DNP: dissolution Dynamic Nuclear Polarisation

DFT: Density Functional Theory

DNP: Dynamic Nuclear Polarisation

dppe: 1,2-bis(diphenylphosphino)ethane

EDTA: EthyleneDiamineTetraAcetic acid

EPR: Electron Paramagnetic Resonance

eq.: equivalents

ESSI: Electron Spin Interaction

Et: Ethyl

EXSY: Exchange SpectroscopY

EZI: Electron Zeeman Interaction

FAD: Flavin Adenine Dinucleotide

FISP: Fast Imaging with Steady-state free Precession

FLASH: Fast Low Angle Shot

f-MRI: functional Magnetic Resonance Imaging

FOV: Field Of View

GC: Gas Chromatography

GDP: Guanosine DiPhosphate

GTP: Guanosine-5'-TriPhosphate

HMQC: Heteronuclear Multiple Quantum Coherence

HP: HyperPolarised

INEPT: Insensitive Nuclei Enhanced by Polarisation Transfer

IMes: 1,3-*bis*(2,4,6-trimethyl-phenyl)imidazole-2-ylidene

IR: InfraRed

L: Ligand

LAC: Level Anti-Crossing

LDH: Lactate DeHydrogenase

M: Molar

MR: Magnetic Resonance

MRI: Magnetic Resonance Imaging

MS: Mass Spectrometry

N/A: Not Applicable

NAD: Nicotinamide Adenine Dinucleotide

NHC: *N*-heterocyclic carbene

NMR: Nuclear Magnetic Resonance

NOE: Nuclear Overhauser Effect

NOESY: Nuclear Overhauser Effect SpectroscopY

NS: Number of Scans

NSF: Nephrogenic System Fibrosis

Nsub: *N*-donor substrate

NZI: Nuclear Zeeman Interaction

o-H$_2$: *ortho*hydrogen

paraCEST: paramagnetic Chemical Exchange Saturation Transfer

PASADENA: *Para*-hydrogen And Synthesis Allow Dynamic Nuclear Alignment

PEG: PolyEthylene Glycol

PET: Positron Emission Tomography

p-H$_2$: *para*hydrogen

Ph: Phenyl

PHIP: *Para*Hydrogen Induced Polarisation

PHIP-SAH: *Para*Hydrogen Induced Polarisation Side Arm Hydrogenation

PTF: Polarisation Transfer Field

RENCA: RENal cell Carcinoma

r.f.: radiofrequency

s: seconds

SABRE: Signal Amplification By Reversible Exchange

SABRE-SHEATH: SABRE SHield Enabled Alignment Through Heteronuclei

SEOP: Spin Exchange Optical Pumping

SINO: Signal to Noise ratio

T: Tesla

TE: Echo Time

TFPA: 2,2,3,3-*Tetra*FluoroPropyl-[1-^{13}C]-Acrylate-*d*(2,3,3)

TFPP: 2,2,3,3-*Tetra*FluoroPropyl-[1-^{13}C]-Propionate-*d*(2,3,3)

TR: Repetition Time

UV: UltraViolet

w/w: weight per weight

1D: 1 Dimensional

2D: 2 Dimensional

3D: 3 Dimensional

List of Compounds

1. 3-Methyl-1-butanol

2. [IrCl(*cis*,*cis*-1,5-cyclooctadiene)(1,3-*bis*(2,4,6-trimethyl-phenyl)imidazole-2-ylidene)]

3. NH_3

4. Benzylamine

5. Phenethylamine

6. 3-Pentanol

7. 2-Methyl-2-butanol

8. Imidazole

9. [IrCl(*cis*,*cis*-1,5-cyclooctadiene)(1,3-*bis*(2,4,6-trimethyl-phenyl)dihydroimidazol-2-ylidene)]

10. Choline chloride

11. *β*-Hydroxybutyric acid

12. Dihydroxyacetone

13. Norepinephrine

14. Ascorbic acid

15. Nerol

16. Geraniol

17. Linalool

18. Sodium lactate

19. Methyl lactate

20. Ethyl lactate

21. Butyl lactate

22. Sodium pyruvate

23. Pyruvate hydrate

24. $CH_3C(NHR)(OH)COONa$

25. $CH_3C(NHR)COONa$

26. [Ir(H)$_2$(1,3-*bis*(2,4,6-trimethyl-phenyl)imidazole-2-ylidene)(benzylamine)$_3$]Cl

27. [Ir(H)$_2$(1,3-*bis*(2,4,6-trimethyl-phenyl)imidazole-2-ylidene)(phenethylamine)$_3$]Cl

28. [Ir(H)$_2$(κ^2-*O*OCC(CH$_3$)*N*CH$_2$Ph)(1,3-*bis*(2,4,6-trimethyl-phenyl)imidazole-2-ylidene)(NH$_2$CH$_2$Ph)]

29. [Ir(H)$_2$(κ^2-*O*OCC(CH$_3$)*N*CH$_2$CH$_2$Ph)(1,3-*bis*(2,4,6-trimethyl-phenyl)imidazole-2-ylidene)(NH$_2$CH$_2$CH$_2$Ph)]

30. [Ir(η^2-CO$_3$)(κ^2-OOCC(CH$_3$)NCH$_2$Ph)(1,3-*bis*(2,4,6-trimethyl-phenyl)imidazole-2-ylidene)(NH$_2$CH$_2$Ph)]

31. [Ir(η^2-CO$_3$)(κ^2-OOCC(CH$_3$)NCH$_2$CH$_2$Ph)(1,3-*bis*(2,4,6-trimethyl-phenyl)imidazole-2-ylidene)(NH$_2$CH$_2$CH$_2$Ph)]

32. Phenylpropylamine

33. Phenoxyethylamine

34. Aniline

35. [IrCl(*cis,cis*-1,5-cyclooctadiene)(1,3-*bis*(2,4,6-trimethylphenyl)-4,5-dimethylimidazol-2-ylidine)]

36. [IrCl(*cis,cis*-1,5-cyclooctadiene)(1,3-*bis*(4-(dimethylamino)-2,6-dimethylphenyl)imidazol-2-ylidine)]

37. [IrCl(*cis,cis*-1,5-cyclooctadiene)(1,3-*bis*(2,4,6-trimethylphenyl)-4-(dimethylamino)imidazol-2-ylidine)]

38. [IrCl(*cis,cis*-1,5-cyclooctadiene)(1,3-*bis*(4-chloro-2,6-dimethylphenyl)imidazol-2-ylidine)]

39. [IrCl(*cis,cis*-1,5-cyclooctadiene)(1,3-*bis*(4-*tert*-butyl-2,6-dimethylphenyl)imidazole-2-ylidine)]

40. [IrCl(*cis,cis*-1,5-cyclooctadiene)(1,3-*bis*(2,6-diisopropylphenyl)imidazole-2-ylidene)]

41. Acetonitrile

42. Thiophene

43. Pyridine

44. [Ir(H)$_2$(κ^2-OOCC(CH$_3$)NCH$_2$CH$_2$Ph)(1,3-*bis*(2,4,6-trimethyl-phenyl)imidazole-2-ylidene)(pyridine)]

45. [Ir(H)$_2$(κ^2-OOCC(CH$_3$)NCH$_2$CH$_2$Ph)(1,3-*bis*(2,4,6-trimethyl-phenyl)imidazole-2-ylidene)(imidazole)]

46. Dimethylsulfoxide

47. [Ir(H)$_2$(κ^2-OOCC(CH$_3$)NCH$_2$CH$_2$Ph)(1,3-*bis*(2,4,6-trimethyl-phenyl)imidazole-2-ylidene)(dimethylsulfoxide)]

48. Benzylisocyanide

49. [Ir(H)$_2$(κ^2-OOCC(CH$_3$)NCH$_2$CH$_2$Ph)(1,3-*bis*(2,4,6-trimethyl-phenyl)imidazole-2-ylidene)(CNCH$_2$Ph)]

50. [Ir(H)$_2$(CNCH$_2$Ph)$_3$(1,3-*bis*(2,4,6-trimethyl-phenyl)imidazole-2-ylidene)]Cl

51. [Ir(H)$_2$(CNCH$_2$Ph)$_2$(1,3-*bis*(2,4,6-trimethyl-phenyl)imidazole-2-ylidene)(NH$_2$(CH$_2$)$_2$Ph)]Cl

52. Ethylisothiocyanate

53. [Ir(H)$_2$(κ^2-OOCC(CH$_3$)NCH$_2$CH$_2$Ph)(1,3-*bis*(2,4,6-trimethyl-phenyl)imidazole-2-ylidene)(SCNEt)]

54. [Ir(H)$_2$(1,3-*bis*(2,4,6-trimethyl-phenyl)imidazole-2-ylidene)(SCNEt)$_2$(NH$_2$(CH$_2$)$_2$Ph)]Cl

55. 4-chlorobenzenemethanethiol

56. [Ir(H)(κ^2-OOCC(CH$_3$)NR)(SCH$_2$PhCl)(1,3-*bis*(2,4,6-trimethyl-phenyl)imidazole-2-ylidene)]

57. Benzyaldehyde

58. Triphenylphosphine

59. [Ir$_2$(H)$_4$(μ-SCH$_2$PhCl)$_2$(1,3-*bis*(2,4,6-trimethyl-phenyl)imidazole-2-ylidene)$_2$]

60. [Ir(H)$_3$(PPh$_3$)$_3$]

61. [Ir(Cl)(H)$_2$(dimethylsulfoxide)$_2$(1,3-*bis*(2,4,6-trimethyl-phenyl)imidazole-2-ylidene)]

62. [Ir(H)$_2$(κ^2-pyruvate)(dimethylsulfoxide)(1,3-*bis*(2,4,6-trimethyl-phenyl)imidazole-2-ylidene)]

63. [Ir(*cis*,*cis*-1,5-cyclooctadiene)(1,3-*bis*(2,4,6-trimethyl-phenyl)imidazole-2-ylidene)(OH$_2$)]Cl.

64. [IrBr(*cis*,*cis*-1,5-cyclooctadiene)(1,3-*bis*(2,4,6-trimethyl-phenyl)imidazole-2-ylidene)]

65. [IrBr(H)$_2$(dimethylsulfoxide)$_2$(1,3-*bis*(2,4,6-trimethyl-phenyl)imidazole-2-ylidene)]

66. [Ir(CH$_3$CN)(*cis*,*cis*-1,5-cyclooctadiene)(1,3-*bis*(2,4,6-trimethyl-phenyl)imidazole-2-ylidene)]PF$_6$

67. [Ir(acetonitrile)(H)$_2$(dimethylsulfoxide)$_2$(1,3-*bis*(2,4,6-trimethyl-phenyl)imidazole-2-ylidene)]

68. [IrCl(H)$_2$(*cis*,*cis*-1,5-cyclooctadiene)(1,3-*bis*(2,4,6-trimethyl-phenyl)imidazole-2-ylidene)]

69. Methylphenylsulfoxide

70. Chloromethylphenylsulfoxide

71. Vinylsulfoxide

72. Diphenylsulfoxide

73. Dibenzylsulfoixde

74. Butylsulfoxide

75. Methylenesulfoxide

76. L-Methionine sulfoxide

77. FMoc-L-methionine sulfoxide

78. Phenylethylsulfoxide

79. [IrCl(H)$_2$(phenylvinylsulfoxide)$_2$(1,3-*bis*(2,4,6-trimethyl-phenyl)imidazole-2-ylidene)],

80. [IrCl(H)$_2$(phenylvinylsulfoxide)(phenylethylsulfoxide)(1,3-*bis*(2,4,6-trimethyl-phenyl)imidazole-2-ylidene)]

81. IrCl(H)$_2$(phenylethylsulfoxide)$_2$(1,3-*bis*(2,4,6-trimethyl-phenyl)imidazole-2-ylidene)]

82. [Ir(H)$_4$(μ-H)$_2$(1,3-*bis*(2,4,6-trimethyl-phenyl)imidazole-2-ylidene)$_2$(methylphenylsulfoxide)$_2$]

83. [Ir$_2$(H)$_3$(μ-H)(μ-SPh)$_2$(1,3-*bis*(2,4,6-trimethyl-phenyl)imidazole-2-ylidene)$_2$(S(O)(Et)(Ph))]

84. [Ir$_2$(H)$_4$(μ-S)(1,3-*bis*(2,4,6-trimethyl-phenyl)imidazole-2-ylidene)$_2$(dibenzylsulfoxide)$_2$]

85. [IrCl(COD)(1,3-bis(2,4,6-trimethylphenyl)-4,5-dichloroimidazol-2-ylidine)]

86. [Ir(COD)(PCy$_3$)(pyridine)]

87. [IrCl(*cis*,*cis*-1,5-cyclooctadiene)(1-(2,4,6-trimethyl-phenyl)-3-ethylphenylimidazole-2-ylidene)]

88. [Ir(H)$_2$(1,3-*bis*(2,4,6-trimethyl-phenyl)imidazole-2-ylidene)(dimethylsulfoxide)(phenethylamine)$_2$]Cl

89. Malic acid

90. Fumaric acid

91. Succinic acid

92. Disodium carbonate

93. Sodium acetate

94. Phosphoenolpyruvate

95. Methyl pyruvate

96. Ketoisokaproate

97. Phenylglyoxylic acid

Appendix

Chemical Science

EDGE ARTICLE

View Article Online
View Journal | View Issue

Relayed hyperpolarization from *para*-hydrogen improves the NMR detectability of alcohols†

Peter J. Rayner, [ID] Ben. J. Tickner, [ID] Wissam Iali, [ID] Marianna Fekete, [ID] Alastair D. Robinson [ID] and Simon B. Duckett [ID] *

The detection of alcohols by magnetic resonance techniques is important for their characterization and the monitoring of chemical change. Hyperpolarization processes can make previously inpractical measurements, such as the determination of low concentration intermediates, possible. Here, we investigate the SABRE-Relay method in order to define its key characteristics and improve the resulting ^{1}H NMR signal gains which subsequently approach 10^3 per proton. We identify optimal amine proton transfer agents for SABRE-Relay and show how catalyst structure influences the outcome. The breadth of the method is revealed by expansion to more complex alcohols and the polarization of heteronuclei.

Molecules that contain an alcohol functional group are present widely in materials used in industrial, biochemical and medical applications. Their complexity can vary from simple structures such as ethanol to polyfunctional macromolecules such as DNA and carbohydrates. The solution state characterization and quantification of these materials commonly involves Nuclear Magnetic Resonance (NMR) spectroscopy and, to a lesser extent, Magnetic Resonance Imaging (MRI). MR techniques have the benefit of being non-invasive and do not require ionizing radiation thereby securing their clinical importance. However, both NMR and MRI suffer from low sensitivity as their underlying signal strength is derived from the population difference that exists between two distinct nuclear spin orientations that are close in energy.

The perturbation of the spin state populations of these energy levels away from the Boltzmann distribution can be achieved using methods that are collectively known as hyperpolarization. Dynamic Nuclear Polarization (DNP) is one of the most well-developed of these techniques and has been applied to the study of disease through the *in vivo* monitoring of biomolecule metabolism.[1–7] Additionally, Spin Exchange Optical Pumping of noble gas nuclei has proven successful in producing diagnostic high resolution images of lung pathologies.[8,9]

A related technique, termed *Para*-Hydrogen Induced Polarization (PHIP), which has provoked a significant amount of attention, derives its non-Boltzmann spin distribution from *para*-hydrogen (p-H$_2$) gas. Its two nuclear spins are aligned antiparallel in a singlet state and were predicted to deliver strong ^{1}H NMR signals when added to an unsaturated material.[10,11]

Centre for Hyperpolarisation in Magnetic Resonance, Department of Chemistry, University of York, Heslington, YO10 5DD, UK. E-mail: simon.duckett@york.ac.uk

† Electronic supplementary information (ESI) available: Experimental methods, NMR spectra. See DOI: 10.15124/db5b8475-8c71-4714-95f7-eb5e2a49632c

Experimentally, this hypothesis has since been validated many times and the resulting enhanced signals have been used for the examination of numerous reaction mechanisms[12–18] and for the determination of low concentration intermediates.[19–21] A major barrier to the widespread application of this approach is the requirement that an unsaturated p-H$_2$ acceptor is needed to create a magnetic environment where the singlet symmetry of p-H$_2$ is broken and hence allows the products of chemical change to be detected.[22–25] One route to overcome this challenge has involved the application of cleavable unsaturated molecular tags which has ultimately allowed the hyperpolarization of pyruvate, acetate and lactate and the subsequent monitoring of metabolism.[26–28]

Alternatively, it is possible to hyperpolarize a range of molecules using p-H$_2$ without chemical modification through the Signal Amplification By Reversible Exchange process (SABRE).[29,30] This requires the simultaneous and reversible binding of the substrate and p-H$_2$ derived hydrogen atoms to a suitable reaction center. The spin–spin couplings[31] that result between their NMR active nuclei allows spontaneous hyperpolarization transfer to occur at low-field.[32–35] Upon substrate dissociation, the NMR resonances of these chemically unchanged materials become strongly enhanced. A growing range of substrates have proven to be amenable to the SABRE polarization method that typically contain a nitrogen heterocycle,[29] nitrile,[36] diazirine[37,38] or amine[39] functionality with their ^{1}H and X-nuclei being sensitized.[30,40]

More recently, the SABRE substrate scope has been extended to include poorly ligating molecules that contain a labile proton.[41] In this development, termed SABRE-Relay (Scheme 1), the initial SABRE polarization of an amine enables a hyperpolarized proton to be transferred into the target analyte *via* proton exchange. Subsequently, the resulting enhanced nuclear spin population difference can be seen in the analyte's NMR
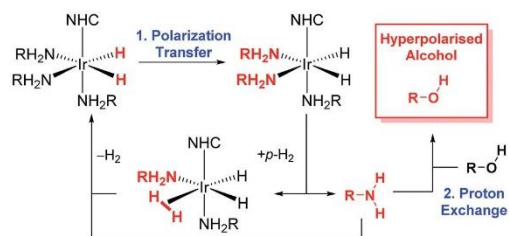
Scheme 1 The SABRE-Relay catalytic cycle for hyperpolarization for alcohols. Polarization is initially transferred from the p-H_2 derived hydride ligands to a carrier amine (RNH$_2$) which subsequently transfer polarization to the alcohol via proton exchange. NHC is N-heterocyclic carbene.

Fig. 1 (Top) Structures of carrier agents **A–X** screened for SABRE-Relay polarization of 1-propanol and the resulting ^{1}H NMR signal enhancements within the spin system per proton at 9.4 T they achieve (Bottom). Enhancements for each proton environment are characterized by the height of each individual colour bar.

active nuclei. When this process is conducted in the presence of just 1 μL of an alcohol, ^{1}H and ^{13}C NMR signal gains of up to 650-fold and 600-fold respectively have been reported in the single scan NMR spectra of the straight chain alcohols methanol through octanol at 9.4 T.[41] Hence, the analytical potential of this method for the detection of alcohols at low concentrations is clear.

We seek here to probe the underlying processes that govern SABRE-Relay and control them for the optimal ^{1}H and heteronuclear NMR detection of alcohols. We begin by using 1-propanol as a test analyte prior to increasing substrate complexity by introducing secondary and tertiary alcohols and other functional groups. A number of kinetic factors are observed to be central to the multi-step SABRE-Relay technique. First, it is well established that the lifetime of active catalyst is instrumental in controlling SABRE polarization transfer efficiency.[35] There are a number of methods for controlling this parameter including ligand design[42,43] and temperature variation. The optimal catalyst lifetime is related to the size of its hydride–hydride and hydride–substrate scalar coupling constants.[32,35,44] The second consideration for SABRE-Relay is the rate of proton transfer between the SABRE hyperpolarized amine and the target alcohol. It might be expected that their relative pK_a values should be important and thus the identity of the amine could be critical for achieving large NMR signal gains. It has been previously shown that primary amines themselves achieve good levels of SABRE polarization, with up to 1000-fold enhancement in the NH proton responses of d_7-BnNH$_2$ being quantified at 9.4 T.[39] Additionally, aromatic amines, such as imidazole, also undergo efficient SABRE transfer and could therefore be potential hyperpolarization carriers.[45] We now set out to examine these effects.

Role of carrier amine

Our study begins with an examination of the 24 hyperpolarization carriers shown in Fig. 1. Multiple samples containing [IrCl(COD)(IMes)] (5 mM), the amine (**A–X**, 10 eq.), 1-propanol (1 μL) and dichloromethane-d_2 (0.6 mL) were prepared and then exposed to 3 bar H$_2$ for 16 h at room temperature to form the active SABRE catalyst [Ir(H)$_2$(IMes)(**A–X**)$_3$]Cl. These samples were then shaken with 3 bar p-H$_2$ for 10 seconds at 70 G prior to
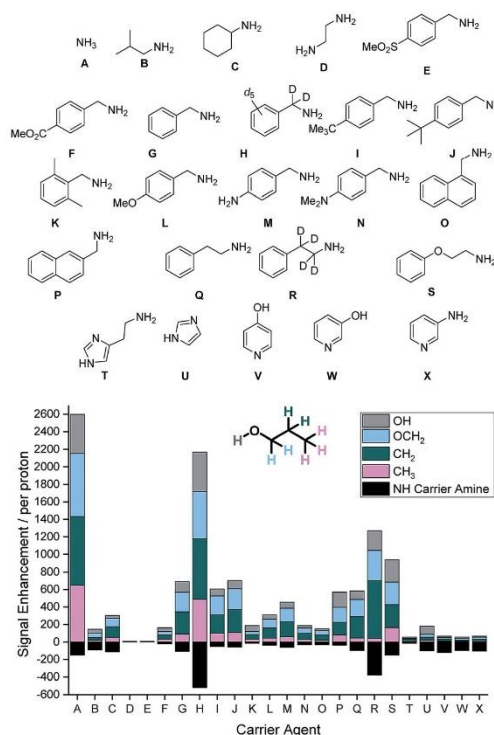
rapid transfer into a 9.4 T field for interrogation by NMR spectroscopy. The resulting ^{1}H NMR signal enhancements for each proton environment in 1-propanol were then calculated. These values are presented per proton graphically in Fig. 1 alongside the NH enhancement levels for the carrier amines in the absence of 1-propanol.

SABRE-Relay conditions that use ammonia (**A**) as the carrier gave the largest signal enhancements for 1-propanol. We quantified enhancements of 441, 723, 783 and 648-fold per proton in the OH, OCH_2, CH_2 and CH_3 positions respectively. In contrast, isobutylamine (**B**) gave comparably poor signal enhancements of less than 50-fold per proton environment. When cyclohexylamine (**C**) was employed the signal gains were slightly improved relative to **B** (*ca.* 50–120-fold), however, ethylenediamine (**D**) resulted in no polarization transfer to 1-propanol. This is due to the formation of a stable complex as the result of bidentate binding of the diamine which prevents ligand exchange. Such methods have previously been used to deactivate the SABRE catalyst and return substrate T_1 values to their usual value in the absence of the SABRE catalyst.[46]

248

The carrier amines **E–P** all contain the benzylamine motif, however the substituents on the aromatic ring differ. Firstly, 4-methylsulfonylbenzyl amine (**E**) does not exhibit polarization transfer to 1-propanol due an active SABRE catalyst not being formed. The methyl ester derivative (**F**) does facilitate SABRE-Relay polarization transfer, however the signal gains now reach a maximum of 48-fold for the OCH_2 resonance. Benzylamine (**G**) performs better with signal enhancements of 225-fold for the OCH_2. This result can be significantly improved upon through the use of the deuterated isotopologue, d_7-benzylamine (**H**) which now gives enhancements of 452, 537, 690 and 489-fold for the OH, OCH_2, CH_2 and CH_3 positions respectively. Introduction of either a methyl (**I**) or *tert*-butyl (**J**) group on the aromatic ring gave comparable results to that of benzylamine and we would therefore expect a similar increase in SABRE-Relay performance on deuteration. The introduction of the electron donating groups methoxy (**L**), amino (**M**) and dimethylamino (**N**) all reduced the efficacy of polarization transfer to 1-propanol despite exhibiting consistent NH signal gains.

Regioisomeric naphthyl derivatives, 1-napthylmethyl amine (**O**) and 2-napthylmethyl amine (**P**), also facilitate SABRE-Relay polarization of 1-propanol. **P** though gives significantly improved performance when compared to **O**. We attribute this to the improved polarization of the NH proton in the carrier amine whose enhancements are now *ca.* 3-fold greater for **P**, an effect which is likely to be due to steric differences in the regioisomers. For the case of phenylethylamine (**Q**), where a CH_2 spacer is added into the aliphatic chain, the signal gains of 1-propanol are slightly below those of benzylamine. Deuteration of the aliphatic portion of this carrier amine (**R**) again improves the polarization levels in the alcohol and highlights the importance that isotopic labelling has on the SABRE-Relay outcome. This increase is attributed to a corresponding increase in the NH signal gain of the free amine (108 compared to 391-fold per proton for **Q** and **R** respectively). Introducing an ether linkage to give phenoxyethylamine (**S**) also improves the signal gains seen in 1-propanol above those with benzylamine. Now the signal enhancements were quantified to be 255, 258, 261 and 165-fold for the OH, OCH_2, CH_2 and CH_3 resonances respectively. This is the best performing of the organic amines tested that does not contain deuterium; we would expect its SABRE-Relay enhancement to further improve if it were ^{2}H-labelled. However, despite a number of synthetic methods being employed to yield the deuterated variant, we were unable to isolate the desired product with high isotopic enrichment.

Finally, a number of aromatic amines were screened for SABRE-Relay transfer, however, they all showed disappointing signal gains for 1-propanol. Interestingly, all of these carrier amines showed good signal gains for their NH resonances. Consequently, we propose that the necessary NH ↔ OH proton transfer step no longer occurs on an appropriate timescale to efficiently mediate the transfer of polarization into 1-propanol.

The optimum amine SABRE-Relay transfer agents for the polarization of propanol in this series were therefore NH$_3$ (**A**) and d_7-BnNH$_2$ (**F**). This is despite the fact that the raw SABRE signal enhancement seen per NH proton in NH$_3$ is worse (*ca.* 150-fold) than that of d_7-BnNH$_2$ (*ca.* 570-fold). Furthermore, the NH protons of NH$_3$ exhibit a T_1 relaxation time of just 5.5 s in dichloromethane-d_2 at 9.4 T while those of d_7-BnNH$_2$ are 10.1 s.[39] Hence, it is postulated that NH ↔ OH proton exchange between NH$_3$ and 1-propanol must proceed on a more favorable timescale for polarization transfer than the analogous process between d_7-BnNH$_2$ and 1-propanol. We note that for both carrier agents, this exchange rate is too rapid for measurement by EXSY, even at reduced temperatures, and that the conjugate acids of NH$_3$ and BnNH$_2$ have very close pK_a values of 9.21 and 9.34 respectively in H$_2$O.[47] However, d_7-BnNH$_2$ does have one significant advantage over the use of NH$_3$ as the SABRE-Relay carrier amine because it is a liquid at room temperature. Therefore, it can be accurately measured into these samples whereas the handling of gaseous NH$_3$ is more challenging.

Effect of contaminant H$_2$O

During the course of these hyperpolarization measurements, it was noted that the presence of residual H$_2$O in the sample, originating from the solvent, alcohol or amine, dramatically affects the resulting signal gains. To quantify this effect, a sample containing [IrCl(COD)(IMes)], d_7-BnNH$_2$ (10 eq.) and 1-propanol (1 μL) in dichloromethane-d_2 was doped with 1 and 5 μL of H$_2$O. This resulted in the observed NMR signal enhancements falling dramatically from 537-fold for the OCH_2 resonance to 48 and 11-fold respectively. In addition, an NMR signal of growing strength is seen for hyperpolarized H$_2$O in these samples. This change is due to a combination of increased spin-dilution, as the finite p-H$_2$ polarization reservoir is shared with an increased number of spins and a reduced efficacy in polarization transfer between the amine and the alcohol. For this reason, we conclude that carrying out SABRE-Relay under anhydrous conditions, a process that can be readily achieved by distillation of the solvent from CaH$_2$, is beneficial.[48]

Effect of amine and alcohol concentration

SABRE derived signal enhancements are known to be highly dependent on the ratio of catalyst to substrate with lower concentrations typically yielding higher signal gains.[49,50] It is accepted that this is a consequence of the available p-H$_2$ derived polarization pool being shared across a finite number of spins. Co-ligands have therefore been employed to reduce spin-dilution and often provide improved signal gains.[43,51] For SABRE-Relay, we propose that it is not only the total signal enhancement of the carrier amine but the efficiency of constructive proton exchange between the amine and the alcohol that is important. To probe these two effects a number of dry samples were prepared that contained increasing concentrations of d_7-BnNH$_2$ and alcohol relative to the [IrCl(COD)(IMes)] pre-catalyst. We chose to focus our attention on the amine d_7-BnNH$_2$ due to the ability to accurately vary the amount of amine added.

First, the effect of the amine concentration was determined by increasing the number of d_7-BnNH$_2$ equivalents relative to iridium from 5 to 25 in the presence of 1 μL of 1-propanol. This study showed that the highest signal gains seen for the OCH_2 resonance of 1-propanol were observed when between 5–8 equivalents d_7-BnNH$_2$ was employed and this corresponds to an amine concentration of 25–40 mM (see ESI†). For example, at 5 equivalents of d_7-BnNH$_2$ a 718-fold signal gain for the OCH_2 was recorded whereas at 8 equivalents a comparable signal gain of 695-fold was quantified. The OCH_2 signal gain decreases to *ca.* 58-fold with the highest amine concentration of 125 mM.

Second, the effect of alcohol concentration was determined in a similar fashion by varying the volume of 1-propanol between 0.1–7.0 μL (0.4–30 eq. based on iridium) whilst maintaining a fixed 5 eq. of d_7-BnNH$_2$ and a 5 mM concentration of [IrCl(COD)(IMes)]. At low relative concentrations of alcohol, the OCH_2 signal gain was reduced. For example, when just 0.4 eq. (2 mM) of 1-propanol was present in the SABRE-Relay catalysis, a signal gain of 128-fold was quantified. As the relative amount of alcohol is increased to 5 equivalents, the OCH_2 signal gain increases to reach a maximum of 723-fold per proton. Increasing the alcohol concentration further then leads to a decrease in signal gain.

These observations confirm that the relative rate of NH ↔ OH exchange is important. Based on the literature, it is likely to be bimolecular in nature, proceeding through an [R-NH$_3^+$][$^-$O-R′] type intermediate.[52,53] When the alcohol is present at low concentration, NH ↔ NH exchange between the carrier amine dominates. This reduces the proliferation of polarization to 1-propanol and lower signal gains result. At the higher loadings of 1-propanol, either NH ↔ OH and OH ↔ OH exchange is too rapid for efficient low field polarization or there is a reduction based on the increasing number of protons relative to those in p-H$_2$ which are limited in accordance with the volume of gas in the NMR tube. Therefore, working with higher pressures of p-H$_2$ could be expected to further increase the size of the hyperpolarized signals. It is possible to conclude here that for 1-propanol, the largest relayed NMR signal enhancements are achieved when using equimolar amounts of alcohol and carrier amine.

Influence of polarization transfer field

For SABRE, the most efficient polarization transfer is observed at the magnetic level anti-crossing point[54] where the size of the hydride–hydride coupling matches optimally with the difference between precession frequencies of hydride and substrate nuclei.[32,44] However, for SABRE-Relay, whilst the hydride–hydride coupling in the *tris*-amine complex of the type [Ir(H)$_2$(IMes)(amine)$_3$]Cl will determine the optimal polarization field for the carrier amine polarization while transfer within the alcohol will be governed by spin–spin couplings between the OH and the aliphatic chain. Therefore, the field dependence on the observed polarization levels was probed over the range 20 to 140 G using an automated NMR flow system.[55] Due to the volatility of NH$_3$ and dichloromethane-d_2, we carried out these experiments using BnNH$_2$ with CDCl$_3$ as solvent. The

relative signal enhancements from these measurements are shown in Fig. 2. The most efficient polarization transfer was observed at 70 G which is optimal for polarization transfer utilizing the hydride–NH ^3J coupling within the active SABRE catalyst. Hence, it would seem that the initial SABRE polarization transfer step is critical to this process. Interestingly, as the transfer field increases above 130 G a growth in NMR signal enhancement is observed which reflects the limit of our equipment.

Catalyst identity

We have previously shown that the rate of NH$_3$ ligand loss from [Ir(H)$_2$(IMes)(NH$_3$)$_3$]Cl is just 1.64 s^{-1} at 298 K (ref. 39) and therefore lower than that predicted[34] to be optimal. One option to increase this dissociation rate is to warm the samples and thus, at 308 K the resulting SABRE induced signal gain of NH$_3$ increases from 154-fold to 251-fold. However, an alternative method to modulate the rate of substrate dissociation is *via* changes to the catalysts' N-heterocyclic carbene ligand.[43] As such we chose to compare the IMes derived catalyst to one with *tert*-butyl substituents on the aryl arms of the NHC and one with methyl groups on the imidazole ring (catalysts **2** and **3** of Fig. 3). Additionally, we prepared a further electron rich NHC that bears an NMe$_2$ group on the imidazole ring (catalyst **4**), which has previously been shown to increase the efficacy of palladium catalyzed Buchwald–Hartwig aminations.[56] To the best of our knowledge this highly electron rich catalyst has not been used for SABRE polarization transfer before. Samples containing [IrCl(COD)(NHC)] (**1–4**, 5 mM), NH$_3$ (6–8 eq.) and propanol (1 μL) in anhydrous dichloromethane-d_2 (0.6 mL) were exposed to 3 bar p-H$_2$ and shaken in a 70 G field. Signal enhancements per proton were then quantified for each catalyst system as detailed in Fig. 3.

It is apparent that catalyst **2** improves the observed NMR signal enhancements for 1-propanol when compared to those achieved with the IMes derived catalyst, **1**. Consequently, an increase in NMR signal gain for each aliphatic site is observed;
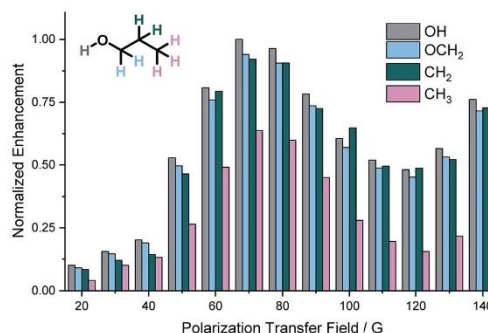
Fig. 2 Normalized ^{1}H NMR signal enhancements in propanol achieved using BnNH$_2$ as the SABRE-Relay agent as a function of the size of the polarization transfer field.

250
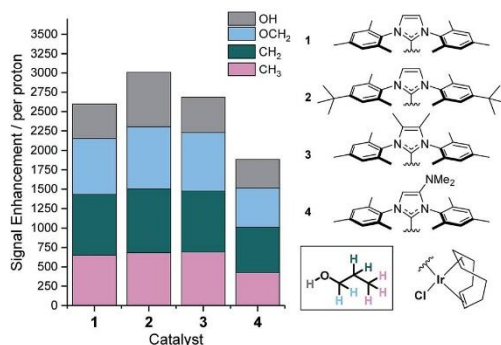
Fig. 3 Structures of catalysts **1–4** and the resulting ^{1}H NMR signal enhancements per proton they deliver to 1-propanol at 9.4 T after SABRE-Relay transfer from NH$_3$. Enhancements for each proton environment are characterized by the height of each individual colour bar.

Fig. 4 Effective rates of ligand dissociation (s^{-1}) from the corresponding SABRE catalyst at 298 K as measured by EXSY spectroscopy.

for example the OCH_2 signal gain improves from 783-fold with **1** to 821-fold with **2** at 9.4 T. However, the OH polarization level actually increases far more dramatically from 442 to 701-fold which reflects a *ca.* 70% increase. These signal gain increases are attributed to the resulting increase in rate of NH$_3$ dissociation from the active catalyst which is now 3.20 s^{-1} at 298 K and approximately double that seen for **1**. Further, small improvements in these signal enhancement levels were observed when using the deuterated isotopologue of **2**, d_{34}-**2**.[43] In this case, the signal gains per proton are now 721, 843, 820, 691-fold for the OH, OCH_2, CH_2 and CH_3 positions respectively. Intriguingly, these relayed changes are less significant than for substrates that undergo direct SABRE polarization, where increases of up to 150% have been seen when using a deuterated NHC instead of its protio counterpart.[51] To investigate this behavior, we measured the T_1 relaxation times of the NH resonance in NH$_3$ whilst in the presence of the active catalysts formed from **2** and d_{34}-**2** under 3 bar H$_2$. The T_1 relaxation time is slightly extended from 5.31 to 5.64 s when the deuterated isotopologue is used. This extension is just 6% and significantly smaller than that typically observed for substrates which participate in direct SABRE transfer and may account for the corresponding reduced polarization increases seen during SABRE-Relay.[43,51]

Catalyst **3** also gave modest improvements in NMR signal gain when compared to **1** but less than those of **2**. For this ligand scaffold, the rate of NH$_3$ dissociation from the active catalyst is 2.99 s^{-1} at 298 K and therefore comparable to **2** (Fig. 4). However, now the rate of hydride ligand loss to form H$_2$ is more than doubled from 0.32 s^{-1} for **1** to 0.75 s^{-1} for **3**. This increase will cause more rapid *p*-H$_2$ consumption and could result in less efficient SABRE as the amount of *p*-H$_2$ present within the experiment is finite. In contrast, the rate of hydride loss from the catalyst derived from **2** is lower at 0.17 s^{-1}. Lower signal enhancements are observed with **4** when compared to **1**–**3**. For this system, the rate of dissociation of NH$_3$ and the hydride ligands from the active catalyst is significantly higher with values of 6.29 s^{-1} and 0.86 s^{-1} recorded respectively at 298
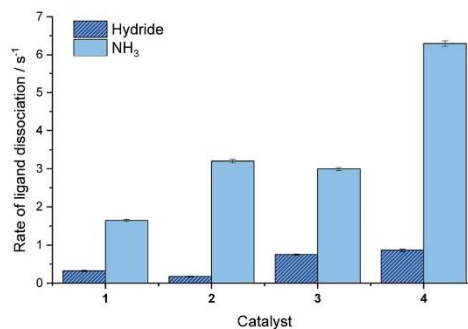
K. This suggests that the new catalyst lifetime is less than optimal for efficient SABRE transfer.[34,43]

Introducing structural complexity

^{1}H-signal gains under SABRE-Relay

To further understand the SABRE-Relay method, structurally complex alcohols were examined, including secondary and tertiary alcohols alongside other OH containing materials, as shown in Fig. 5. First, the regioisomeric alcohols 3-methyl-1-butanol, 3-pentanol and 2-methyl-2-butanol were polarized using the optimized SABRE-Relay conditions for propanol (5 mM of **1**, 7 equivalents of ammonia and 5 equivalents of alcohol in dry dichloromethane-d_2). 3-Methyl-1-butanol gave good ^{1}H signal gains with the OCH_2 signal now being 455-fold larger than the signal produced under Boltzmann conditions which is comparable to that of 1-propanol. Polarization is also
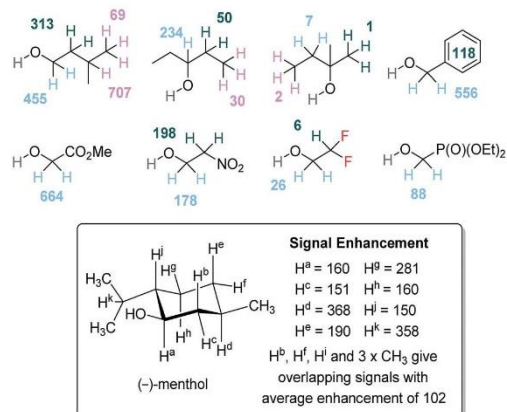
Fig. 5 ^{1}H NMR per proton signal gains for structurally diverse alcohols at 9.4 T. NMR assignments of (−)-menthol were made by comparison to literature data.[57]

proliferated throughout the aliphatic chain, with signal gains of 313, 707 and 69-fold being quantified for the CH_2, CH and CH_3 groups respectively.

When the secondary alcohol 3-pentanol was investigated under the same conditions, the ^1H NMR resonance for OCH showed a 234-fold signal gain. However, SABRE-Relay enhancements of 50 and 30-fold were seen for the β and γ-positions. Poor SABRE-Relay performance is observed for the tertiary alcohol 2-methyl-2-butanol, for which ^1H signal gains of just 1–7-fold could be quantified. Interestingly, the OH NMR signal enhancements were comparable for both of these materials (between 200 and 300-fold). Therefore, we conclude that a limiting factor in SABRE-Relay polarization transfer is propagation through the alcohol's scalar coupling network from the OH group. The tension between optimal SABRE polarization of the carrier amine and subsequent proliferation of polarization after proton exchange is thus highlighted.

Benzyl alcohol gave good ^1H NMR signal enhancements for the OCH_2 site, giving a 556-fold per proton gain while those protons of the phenyl ring achieved an average signal gain of 118-fold per proton. Other structurally diverse alcohols such as methyl glycolate and 2-nitroethanol also give good ^1H signal enhancement for their aliphatic OCH_2 resonance of 664-fold and 178-fold respectively. Finally, we investigated the natural product (−)-menthol which contains three stereogenic centers and fourteen distinct proton environments. After SABRE-Relay polarization transfer using NH_3 as the carrier amine we were able to detect ^1H signal enhancements in each of the protons with up to 368-fold signal gain being quantified.

^{13}C-signal gains under SABRE-Relay

SABRE-Relay derived polarization can also be transferred to the ^{13}C nuclei within the target molecule.[41] For our test substrate, 1-propanol, we are able to achieve signal gains of 281, 342 and 128-fold for the OCH_2, CH_2 and CH_3 positions respectively when using the previously optimised conditions for ^1H polarisation (5 mM of d_{34}-2, 5 equivalents of NH_3 and 5 equivalents of 1-propanol). These signal gains are sufficient to obtain a fully diagnostic ^{13}C NMR spectrum in a single scan after spontaneous polarisation transfer at 70 G to the carbon nuclei that are present at their natural isotopic abundance for a sample containing 25 mM of 1-propanol.

The effect of SABRE-Relay polarization into the ^{13}C nuclei in more structurally complex alcohols was also investigated. For 3-methyl-1-butanol, the signals for all its ^{13}C sites are also readily observed in the corresponding NMR spectrum after spontaneous polarization transfer at 70 G (Fig. 6a). Now the signal gains were quantified to be 1404 and 1090-fold for the OCH_2 and CH_2 resonances respectively and an average of 403-fold being seen across the overlapping CH and CH_3 signals. The signal to noise ratio in this NMR spectrum that was collected at 9.4 T on a 5 mm inverse probe was 18 for the OCH_2 resonance. We note that the conditions required to achieve the highest ^1H signal gains for 3-methyl-1-butanol discussed earlier also result in the highest ^{13}C signal gains. When the concentration of alcohol or carrier is varied from these optimal conditions, the
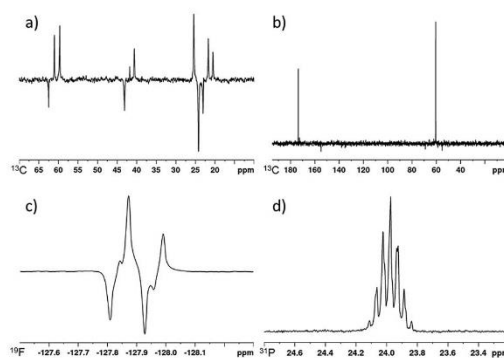
Fig. 6 (a) SABRE-Relay hyperpolarized ^{13}C spectrum of 3-methyl-1-butanol, (b) SABRE-Relay hyperpolarized ^1H–^{13}C spectrum of methyl glycolate, (c) SABRE-Relay hyperpolarized ^1H–^{19}F INEPT spectrum of 2,2-difluoroethanol, (d) SABRE-Relay hyperpolarized ^{31}P spectrum of diethyl (hydroxymethyl) phosphonate. Corresponding thermally polarised spectra are available in the ESI.†

corresponding ^{13}C signal gains decrease in the same fashion as the ^1H signal enhancements (see ESI†). We also note that for 3-methyl-1-butanol, the use of NH_3 (A) as a carrier is necessary to observe SABRE-Relay hyperpolarization in the ^{13}C responses in a single scan. When d_7-BnNH$_2$ (H) is utilized for this alcohol, no hyperpolarised ^{13}C resonances are detectable in a single scan. We attribute this to significantly reduced polarization transfer to 3-methyl-1-butanol which is also reflected in weak ^1H polarisation levels observed under the same conditions (96, 77, 187 and 56-fold for the OCH_2, CH_2, CH and CH_3 respectively). These values are significantly lower than those achieved using A.

When the ^{13}C SABRE-Relay polarization of 3-pentanol was investigated using A as the carrier, significantly lower signal gains were recorded when compared to 3-methyl-1-butanol (67, 0 and 38-fold for CH, CH_2 and CH_3 positions respectively). We hypothesize that this is likely to be due to inefficient proliferation of the polarization through the alcohol's scalar coupling network at the polarization transfer field. However, by using a ^1H–^{13}C INEPT sequence at high field the signal to noise ratio of the alcohol's ^{13}C response can be improved from 3 to 8. Contrastingly, no ^{13}C signals are visible for the tertiary alcohol 2-methyl-2-butanol after either spontaneous polarization transfer or using a ^1H–^{13}C INEPT sequence which is consistent with its limited ^1H performance.

^{19}F and ^{31}P signal gains under SABRE-Relay

The SABRE-Relay polarization of other heteronuclei in molecules that contain an alcohol functional group was also explored. When 2,2-difluoroethanol was used as the target alcohol, SABRE-Relay transfer could be observed into both the ^1H and ^{19}F spins. The OCH_2 ^1H-signal gains were just 26-fold and an 11-fold signal gain in the ^{19}F spectrum was observed after spontaneous transfer at 70 G during the SABRE-Relay process. The observed ^{19}F signal could be improved by using a ^1H–^{19}F INEPT sequence and now a 63-fold enhancement was

252

quantified (Fig. 6c). This improvement is likely to be a combination of inefficient transfer into the ^{19}F nuclei at the polarization transfer field and a reflection of the longer ^{1}H T_1 values (18.9 and 24.6 s for the OCH_2 and CHF$_2$ resonance respectively at 11.7 T) when compared to ^{19}F (7.2 s at 11.7 T). This acts to limit visible ^{19}F magnetisation after direct transfer in the polarization transfer field.

Interestingly, the signal gains seen for this fluorinated alcohol were substantially lower than those of the fully protio counterpart for which ^{1}H signal gains of *ca.* 500-fold have been previously reported.[41] We attribute this change in part to modulation in the pK_a of the alcohol caused by introduction of the electronegative fluorine atoms. This is supported by the fact that very limited OH polarization is observed in the ^{1}H NMR spectrum after SABRE-Relay. Use of even more acidic fluorinated alcohols such as hexafluoroisopropanol (pK_a = 9.3 (ref. 58)) result in no SABRE-Relay polarization being observed.

Similarly, the SABRE-Relay polarization of ^{31}P nuclei is also achievable. When diethyl (hydroxymethyl) phosphonate was exposed to 3 bar *p*-H$_2$ in the presence of d_{34}-2 and NH$_3$, a 30-fold signal enhancement is observed for the ^{31}P resonance after spontaneous polarization transfer at 70 G. Additionally, an 88-fold ^{1}H signal gain for the OCH_2 resonance was quantified. These signal gains are significantly reduced when compared to 1-propanol or 3-methyl-1-butanol and may be indicative of the alcohol being too acidic for SABRE-Relay with NH$_3$. A further screen of less basic carrier amines may thus yield improved results.

Conclusions

In summary, we have shown that the SABRE-Relay method can be used to transfer polarization from *p*-H$_2$ to an alcohol *via* a polarization carrier amine. These results demonstrate how it is possible to broaden the scope of this hyperpolarization method to allow the rapid and cost effective detection of molecules present at low concentrations by magnetic resonance techniques. The SABRE-Relay effect is successfully mediated by the formation of an active polarisation transfer catalyst of the type [Ir(H)$_2$(-NHC)(amine)$_3$]Cl and subsequent proton exchange between the hyperpolarised amine's NH and the target alcohol OH.

The amine plays a prominent role in this process and determines the size of the resulting signal gains seen in the nuclear spin orientation enhancement of the alcohol after SABRE-Relay transfer. Of the 24 amines investigated, NH$_3$ performed best, yielding over 700-fold gains per proton in the OCH_2 resonance of propanol. We conclude that in this case, the rate of proton exchange between NH$_3$ and the alcohol most closely matches that needed for optimal NMR signal enhancement. The next best performing amine was d_7-BnNH$_2$ which, whilst exhibiting higher NH polarisation levels and longer relaxation times than NH$_3$, led to alcohol NMR signal gains that were *ca.* 10% lower. Based on these data a match between carrier amine and target agent will be needed to deliver optimal SABRE-Relay performance. However, a role for isotopic labelling in the amine was exemplified with deuterated isotopologues yielding SABRE-Relay enhancements that were *ca.* 3 times higher than those of their protio counterparts. We attribute this

to a reduction in the effects of polarisation transfer into the amine which leads to higher NH polarisation levels, alongside an increase in the NH relaxation time.

The effect of the magnetic field experienced by the sample during the SABRE-Relay transfer step was also examined over the range 0.5 to 140 G. It was shown that the largest signal gains were observed when this was set to *ca.* 70 G which corresponds to the point where the scalar couplings within the active SABRE catalyst must match optimally with PTF requirements for successful NH polarisation.[32,54] This effect dominates even though a different field might be expected for subsequent spontaneous polarization transfer within the amine after proton exchange. This limitation is particularly evident when polarization is transferred from the OH into ^{1}H, ^{13}C, ^{19}F or ^{31}P nuclei in functionalised alcohols but could be circumvented in the future through the use of radio frequency driven transfer.[59,60] Alternatively, this may open the door to the use of in-high-field methods such as LIGHT-SABRE.[61–63]

We were able to further improve on the initial polarisation levels by modulating the rate of ligand exchange during the SABRE process. Thus, by using a *tert*-butyl derived NHC ligand, the rate of amine dissociation from the active complex of type [Ir(H)$_2$(NHC)(amine)$_3$]Cl increased to 3.20 s^{-1} which results in improved NH signal gains and is followed through by improved NMR signal enhancements in the alcohol when compared to the [IrCl(COD)(IMes)] derived catalyst where the rate of loss is 1.64 s^{-1}. When the amine dissociation rate is increased further by increasing the level of electron donation by ligands on the catalyst, the observed alcohol signal gains decrease. This supports previous evidence[34,43] that the lifetime of the active SABRE complex governs the observed polarisation level and is shown here to be conveyed into the SABRE-Relay mechanism.

The results presented here have demonstrated that alcohols can be readily detected at concentrations as low as 2 mM using our SABRE-Relay conditions. However, at low relative equivalents of the target alcohol to the carrier amine the observed signal gains are reduced due to less efficient proton transfer. To overcome this and to further reduce the detection limit we propose that using a suitable co-ligand[64,65] would enable the use of a substoichiometric amount of carrier amine. Thus, this would allow for a more efficacious ratio of amine to alcohol. For ^{13}C detection the use of NH$_3$ as a carrier is necessary and we have detected 3-methyl-1-butanol at a concentration of 14 mM in a single scan on a 9.4 T NMR system using an inverse probe. We expect this ^{13}C detection limit can be improved upon by use and optimisation of ^{1}H–^{13}C INEPT pulse sequences. Low concentration detection of alcohols such as 3-methyl-1-butanol, which is present as an additive in many foods and drinks,[66,67] demonstrates a potential role for SABRE-Relay in the detection of important low concentration analytes.

Given the ubiquitous nature of alcohols throughout chemical and biochemical literature, the results reported here could lead to the ability to gain further mechanistic insight into their reactivity by allowing the detection of low concentration species, whether as contaminants or intermediates. Finally, as the SABRE-Relay process expands the number of substrates

amenable to p-H$_2$ based polarisation this study may be useful in identifying a pathway to determine optimal conditions for the polarization of other functional groups.

Conflicts of interest

There are no conflicts to declare.

Acknowledgements

Notes and references

1 T. H. Witney, M. I. Kettunen and K. M. Brindle, *J. Biol. Chem.*, 2011, **286**, 24572–24580.

2 H. Gutte, A. E. Hansen, H. H. Johannesen, A. E. Clemmensen, J. H. Ardenkjar-Larsen, C. H. Nielsen and A. Kjar, *Am. J. Nucl. Med. Mol. Imaging*, 2015, **5**, 548–560.

3 W. C. Chen, X. Q. Teo, M. Y. Lee, G. K. Radda and P. Lee, *NMR Biomed.*, 2015, **28**, 1021–1030.

4 T. B. Rodrigues, E. M. Serrao, B. W. C. Kennedy, D.-E. Hu, M. I. Kettunen and K. M. Brindle, *Nat. Med.*, 2013, **20**, 93.

5 T. Harris, H. Degani and L. Frydman, *NMR Biomed.*, 2013, **26**, 1831–1843.

6 C. von Morze, P. E. Z. Peder, S. Hu, K. Keshari, D. M. Wilson, J. H. Ardenkjaer-Larsen, A. Goga, R. Bok, J. Kurhanewicz and D. B. Vigneron, *Magn. Reson. Imaging*, 2011, **33**, 692–697.

7 M. Fuetterer, J. Busch, S. M. Peereboom, C. von Deuster, L. Wissmann, M. Lipiski, T. Fleischmann, N. Cesarovic, C. T. Stoeck and S. Kozerke, *J. Cardiovasc. Magn. Reson.*, 2017, **19**, 46.

8 P. Nikolaou, A. M. Coffey, L. L. Walkup, B. M. Gust, N. Whiting, H. Newton, S. Barcus, I. Muradyan, M. Dabaghyan, G. D. Moroz, M. S. Rosen, S. Patz, M. J. Barlow, E. Y. Chekmenev and B. M. Goodson, *Proc. Natl. Acad. Sci. U. S. A.*, 2013, **110**, 14150–14155.

9 P. Nikolaou, A. M. Coffey, L. L. Walkup, B. M. Gust, N. Whiting, H. Newton, I. Muradyan, M. Dabaghyan, K. Ranta, G. D. Moroz, M. S. Rosen, S. Patz, M. J. Barlow, E. Y. Chekmenev and B. M. Goodson, *Magn. Reson. Imaging*, 2014, **32**, 541–550.

10 C. R. Bowers and D. P. Weitekamp, *Phys. Rev. Lett.*, 1986, **57**, 2645–2648.

11 C. R. Bowers and D. P. Weitekamp, *J. Am. Chem. Soc.*, 1987, **109**, 5541–5542.

12 J. López-Serrano, S. B. Duckett and A. Lledós, *J. Am. Chem. Soc.*, 2006, **128**, 9596–9597.

13 I. V. Koptyug, K. V. Kovtunov, S. R. Burt, M. S. Anwar, C. Hilty, S.-I. Han, A. Pines and R. Z. Sagdeev, *J. Am. Chem. Soc.*, 2007, **129**, 5580–5586.

14 S. B. Duckett and N. J. Wood, *Coord. Chem. Rev.*, 2008, **252**, 2278–2291.

15 C. Godard, J. Lopez-Serrano, M. D. Galvez-Lopez, M. Rosello-Merino, S. B. Duckett, I. Khazal, A. Lledos and A. C. Whitwood, *Magn. Reson. Chem.*, 2008, **46**, S107–S114.

16 C. Godard, S. B. Duckett, S. Polas, R. Tooze and A. C. Whitwood, *Dalton Trans.*, 2009, 2496–2509.

17 O. Torres, B. Procacci, M. E. Halse, R. W. Adams, D. Blazina, S. B. Duckett, B. Eguillor, R. A. Green, R. N. Perutz and D. C. Williamson, *J. Am. Chem. Soc.*, 2014, **136**, 10124–10131.

18 F. Dalitz, M. Cudaj, M. Maiwald and G. Guthausen, *Prog. Nucl. Magn. Reson. Spectrosc.*, 2012, **60**, 52–70.

19 S. A. Colebrooke, S. B. Duckett, J. A. B. Lohman and R. Eisenberg, *Chem.–Eur. J.*, 2004, **10**, 2459–2474.

20 L. S. Lloyd, R. W. Adams, M. Bernstein, S. Coombes, S. B. Duckett, G. G. R. Green, R. J. Lewis, R. E. Mewis and C. J. Sleigh, *J. Am. Chem. Soc.*, 2012, **134**, 12904–12907.

21 N. Eshuis, N. Hermkens, B. J. A. van Weerdenburg, M. C. Feiters, F. P. J. T. Rutjes, S. S. Wijmenga and M. Tessari, *J. Am. Chem. Soc.*, 2014, **136**, 2695–2698.

22 K. V. Kovtunov, E. V. Pokochueva, O. G. Salnikov, S. F. Cousin, D. Kurzbach, B. Vuichoud, S. Jannin, E. Y. Chekmenev, B. M. Goodson, D. A. Barskiy and I. V. Koptyug, *Chem.–Asian J.*, 2018, **13**, 1857–1871.

23 T. C. Eisenschmid, R. U. Kirss, P. P. Deutsch, S. I. Hommeltoft, R. Eisenberg, J. Bargon, R. G. Lawler and A. L. Balch, *J. Am. Chem. Soc.*, 1987, **109**, 8089–8091.

24 J. Colell, P. Türschmann, S. Glöggler, P. Schleker, T. Theis, M. Ledbetter, D. Budker, A. Pines, B. Blümich and S. Appelt, *Phys. Rev. Lett.*, 2013, **110**, 137602.

25 M. G. Pravica and D. P. Weitekamp, *Chem. Phys. Lett.*, 1988, **145**, 255–258.

26 F. Reineri, T. Boi and S. Aime, *Nat. Commun.*, 2015, **6**, 5858.

27 E. Cavallari, C. Carrera, S. Aime and F. Reineri, *Chem. - Eur. J.*, 2017, **23**, 1200–1204.

28 E. Cavallari, C. Carrera, M. Sorge, G. Bonne, A. Muchir, S. Aime and F. Reineri, *Sci. Rep.*, 2018, **8**, 8366.

29 R. W. Adams, J. A. Aguilar, K. D. Atkinson, M. J. Cowley, P. I. P. Elliott, S. B. Duckett, G. G. R. Green, I. G. Khazal, J. López-Serrano and D. C. Williamson, *Science*, 2009, **323**, 1708–1711.

30 P. J. Rayner and S. Duckett, *Angew. Chem., Int. Ed.*, 2018, **57**, 6742–6753.

31 N. Eshuis, R. L. E. G. Aspers, B. J. A. van Weerdenburg, M. C. Feiters, F. P. J. T. Rutjes, S. S. Wijmenga and M. Tessari, *J. Magn. Reson.*, 2016, **265**, 59–66.

32 R. W. Adams, S. B. Duckett, R. A. Green, D. C. Williamson and G. G. R. Green, *J. Chem. Phys.*, 2009, **131**, 194505.

33 R. A. Green, R. W. Adams, S. B. Duckett, R. E. Mewis, D. C. Williamson and G. G. R. Green, *Prog. Nucl. Magn. Reson. Spectrosc.*, 2012, **67**, 1–48.

34 D. A. Barskiy, A. N. Pravdivtsev, K. L. Ivanov, K. V. Kovtunov and I. V. Koptyug, *Phys. Chem. Chem. Phys.*, 2016, **18**, 89–93.

35 S. Knecht, A. N. Pravdivtsev, J.-B. Hovener, A. V. Yurkovskaya and K. L. Ivanov, *RSC Adv.*, 2016, **6**, 24470–24477.

36 R. E. Mewis, R. A. Green, M. C. R. Cockett, M. J. Cowley, S. B. Duckett, G. G. R. Green, R. O. John, P. J. Rayner and D. C. Williamson, *J. Phys. Chem. B*, 2015, **119**, 1416–1424.

254

37 T. Theis, G. X. Ortiz, A. W. J. Logan, K. E. Claytor, Y. Feng, W. P. Huhn, V. Blum, S. J. Malcolmson, E. Y. Chekmenev, Q. Wang and W. S. Warren, *Sci. Adv.*, 2016, **2**, e1501438.

38 K. Shen, A. W. J. Logan, J. F. P. Colell, J. Bae, G. X. Ortiz Jr, T. Theis, W. S. Warren, S. J. Malcolmson and Q. Wang, *Angew. Chem.*, 2017, **129**, 12280–12284.

39 W. Iali, P. J. Rayner, A. Alshehri, A. J. Holmes, A. J. Ruddlesden and S. B. Duckett, *Chem. Sci.*, 2018, **9**, 3677–3684.

40 J.-B. Hövener, A. N. Pravdivtsev, B. Kidd, C. R. Bowers, S. Glöggler, K. V. Kovtunov, M. Plaumann, R. Katz-Brull, K. Buckenmaier, A. Jerschow, F. Reineri, T. Theis, R. V. Shchepin, S. Wagner, P. Bhattacharya, N. M. Zacharias and E. Y. Chekmenev, *Angew. Chem., Int. Ed.*, 2018, **57**, 11140–11162.

41 W. Iali, P. J. Rayner and S. B. Duckett, *Sci. Adv.*, 2018, **4**, eaao6250.

42 M. J. Cowley, R. W. Adams, K. D. Atkinson, M. C. R. Cockett, S. B. Duckett, G. G. R. Green, J. A. B. Lohman, R. Kerssebaum, D. Kilgour and R. E. Mewis, *J. Am. Chem. Soc.*, 2011, **133**, 6134–6137.

43 P. J. Rayner, P. Norcott, K. M. Appleby, W. Iali, R. O. John, S. J. Hart, A. C. Whitwood and S. B. Duckett, *Nat. Commun.*, 2018, **9**, 4251.

44 D. A. Barskiy, S. Knecht, A. V. Yurkovskaya and K. L. Ivanov, *Prog. Nucl. Magn. Reson. Spectrosc.*, 2019, **114–115**, 33–70.

45 M. Fekete, P. J. Rayner, G. G. R. Green and S. B. Duckett, *Magn. Reson. Chem.*, 2017, **55**, 944–957.

46 R. E. Mewis, M. Fekete, G. G. R. Green, A. C. Whitwood and S. B. Duckett, *Chem. Commun.*, 2015, **51**, 9857–9859.

47 H. K. Hall, *J. Am. Chem. Soc.*, 1957, **79**, 5441–5444.

48 L. Kinard, K. Kasper and A. Mikos, *Protoc. Exch.*, 2012, DOI: 10.1038/protex.2012.1026.

49 L. S. Lloyd, A. Asghar, M. J. Burns, A. Charlton, S. Coombes, M. J. Cowley, G. J. Dear, S. B. Duckett, G. R. Genov, G. G. R. Green, L. A. R. Highton, A. J. J. Hooper, M. Khan, I. G. Khazal, R. J. Lewis, R. E. Mewis, A. D. Roberts and A. J. Ruddlesden, *Catal. Sci. Technol.*, 2014, **4**, 3544–3554.

50 R. V. Shchepin, D. A. Barskiy, D. M. Mikhaylov and E. Y. Chekmenev, *Bioconjugate Chem.*, 2016, **27**, 878–882.

51 P. J. Rayner, M. J. Burns, A. M. Olaru, P. Norcott, M. Fekete, G. G. R. Green, L. A. R. Highton, R. E. Mewis and S. B. Duckett, *Proc. Natl. Acad. Sci. U. S. A.*, 2017, **114**, E3188–E3194.

52 T. B. McMahon and J. L. Beauchamp, *J. Phys. Chem.*, 1977, **81**, 593–598.

53 G. S. Denisov and N. S. Golubev, *J. Mol. Struct.*, 1981, **75**, 311–326.

54 A. N. Pravdivtsev, A. V. Yurkovskaya, H.-M. Vieth, K. L. Ivanov and R. Kaptein, *ChemPhysChem*, 2013, **14**, 3327–3331.

55 R. E. Mewis, K. D. Atkinson, M. J. Cowley, S. B. Duckett, G. G. R. Green, R. A. Green, L. A. R. Highton, D. Kilgour, L. S. Lloyd, J. A. B. Lohman and D. C. Williamson, *Magn. Reson. Chem.*, 2014, **52**, 358–369.

56 Y. Zhang, V. César, G. Storch, N. Lugan and G. Lavigne, *Angew. Chem., Int. Ed.*, 2014, **53**, 6482–6486.

57 C. J. Turner, *Org. Magn. Reson.*, 1984, **22**, 531–534.

58 T. Kida, S.-i. Sato, H. Yoshida, A. Teragaki and M. Akashi, *Chem. Commun.*, 2014, **50**, 14245–14248.

59 K. D. Atkinson, M. J. Cowley, S. B. Duckett, P. I. P. Elliott, G. G. R. Green, J. López-Serrano, I. G. Khazal and A. C. Whitwood, *Inorg. Chem.*, 2009, **48**, 663–670.

60 A. N. Pravdivtsev, A. V. Yurkovskaya, H.-M. Vieth and K. L. Ivanov, *J. Phys. Chem. B*, 2015, **119**, 13619–13629.

61 T. Theis, M. Truong, A. M. Coffey, E. Y. Chekmenev and W. S. Warren, *J. Magn. Reson.*, 2014, **248**, 23–26.

62 D. A. Barskiy, K. V. Kovtunov, I. V. Koptyug, P. He, K. A. Groome, Q. A. Best, F. Shi, B. M. Goodson, R. V. Shchepin, A. M. Coffey, K. W. Waddell and E. Y. Chekmenev, *J. Am. Chem. Soc.*, 2014, **136**, 3322–3325.

63 S. S. Roy, G. Stevanato, P. J. Rayner and S. B. Duckett, *J. Magn. Reson.*, 2017, **285**, 55–60.

64 N. Eshuis, B. J. A. van Weerdenburg, M. C. Feiters, F. P. J. T. Rutjes, S. S. Wijmenga and M. Tessari, *Angew. Chem., Int. Ed.*, 2015, **54**, 1481–1484.

65 I. Reile, N. Eshuis, N. K. J. Hermkens, B. J. A. van Weerdenburg, M. C. Feiters, F. P. J. T. Rutjes and M. Tessari, *Analyst*, 2016, **141**, 4001–4005.

66 D. González-Arjona, V. González-Gallero, F. Pablos and A. G. González, *Anal. Chim. Acta*, 1999, **381**, 257–264.

67 D. W. Lachenmeier, E.-M. Sohnius, R. Attig and M. G. López, *J. Agric. Food Chem.*, 2006, **54**, 3911–3915.

Appendix 2

Special Issue

Iridium α-Carboxyimine Complexes Hyperpolarized with *para*-Hydrogen Exist in Nuclear Singlet States before Conversion into Iridium Carbonates

Ben. J. Tickner,[a] Wissam Iali,[a] Soumya S. Roy,[a] Adrian C. Whitwood,[b] and Simon B. Duckett*[a]

Dedicated to the memory of Robin Virgo

The formation and hyperpolarization of an [Ir(H)₂(amine)(I-Mes)(η^2-imine)]Cl complex that can be created in a hyperpolarized nuclear singlet state is reported. These complexes are formed when an equilibrium mixture of pyruvate, amine (benzylamine or phenylethylamine), and the corresponding imine condensation product, react with preformed [Ir(H)₂(amine)₃(IMes)]Cl. These iridium α-carboxyimine complexes exist as two regioisomers differentiated by the position of amine. When examined with *para*-hydrogen the hydride resonances of the isomer with amine trans to hydride become strongly hyperpolarized. The initial hydride singlet states readily transfer to the corresponding $^{13}C_2$ state in the labelled imine and exhibit magnetic state lifetimes of up to 11 seconds. Their ^{13}C signals have been detected with up to 420 fold signal gains at 9.4 T. On a longer timescale, and in the absence of H₂, further reaction leads to the formation of neutral carbonate containing [Ir(amine)(η^2-CO₃)(IMes)(η^2-imine)]. Complexes are characterized by, IR, MS, NMR and X-ray diffraction.

Nuclear magnetic resonance (NMR) is one of the most versatile analytical tools available to physical science. Despite this success, it suffers greatly from low sensitivity due to the weak interaction between nuclear spins and an external magnetic field. As the magnitude of this interaction depends on the nucleus, the effects of insensitivity are more severe for low γ nuclei such as ^{13}C, when compared to ^{1}H, with only 1 in nearly every 800,000 ^{13}C nuclei contributing positively to a signal detected in the 1.5 T field of a routine MRI scanner. Over the last decade hyperpolarization has begun to challenge the insensitivity of magnetic resonance by producing signals many orders of magnitude stronger than those seen under Boltzmann populated conditions.[1] Recently, Dynamic Nuclear Polarization

(DNP) has successfully utilized this effect for human disease diagnosis.[2,3]

A readily accessible hyperpolarization method employs *para*-hydrogen (*p*-H₂) as the source of its signal gain.[4,5] This *para*-hydrogen induced polarization (PHIP) approach was pioneered by Weitekamp, Eisenberg, and Bargon in the 1990s and has provided many significant observations in the field of catalysis.[4–7] The related hydrogenation of unsaturated substrates has led to their successful *in vivo* detection.[8–10] A similar approach, called signal amplification by reversible exchange (SABRE), was first described in 2009.[11,12] SABRE takes *p*-H₂, a readily formed spin-zero isomer of H₂, and binds it to a metal complex in a way that allows the rapid transfer of latent hyperpolarization into suitable receptor nuclei without chemical alteration, as shown conceptually in Scheme 1.
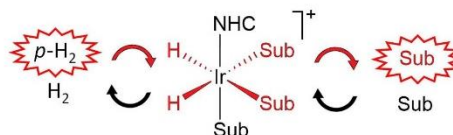
Scheme 1. Hyperpolarization is readily created catalytically in a substrate (Sub) *via* *p*-H₂ derived hydride ligands and a suitable hyperpolarization transfer catalyst (where NHC is an N-heterocyclic carbene).

Suitable ^{1}H receptor nuclei feature in an array of SABRE amenable nitrogen and sulfur containing heterocycles,[13–16] amines[17,18] and nitriles.[19] The catalyst plays an essential role in this process by controlling the ultimate level of hyperpolarization,[13,20,21] with a combination of selective deuteration of both the catalyst and substrate allowing ^{1}H polarization levels of over 50% to be attained.[22] SABRE is truly heteronuclear in scope and very significant improvements in ^{15}N response levels have been realized. These optimally involve low-field SABRE-SHEATH methods, as exemplified for *N*-heterocycles,[23,24] nitriles,[24] Schiff bases,[25] and diazirines.[26] Others have targeted responses in less well studied nuclei such as ^{13}C,[27,28] ^{19}F,[29,30] ^{31}P,[31] ^{119}Sn and ^{31}Si.[32] Furthermore, while the required polarization transfer conditions are readily met at low field, high-field transfer through radio frequency excitation is also feasible.[33] Hence, *p*-H₂ now reflects a truly versatile hyperpolarization

[a] B. J. Tickner, Dr. W. Iali, Dr. S. S. Roy, Prof. S. B. Duckett
Centre for Hyperpolarisation in Magnetic Resonance
University of York, Heslington, U.K. YO10 5NY
E-mail: simon.duckett@york.ac.uk
[b] Dr. A. C. Whitwood
Department of Chemistry, University of York, Heslington, U.K. Kingdom YO10 5DD

platform and it is not surprising that high sensitivity analytical approaches have been demonstrated.[34,35] The necessary progress into aqueous media has also been significant and is expected to lead to successful *in vivo* study in the future.[15,36–38]

In this paper, p-H$_2$ is used to hyperpolarize a α-carboxyimine complex that is initially created in a singlet state. This achievement stems from the fact that α-carboxyimines are readily formed when pyruvate and an amine combine in a condensation reaction.[39] Here, the imine proves to bind in a bidentate fashion to form an iridium dihydride complex that shows high levels of PHIP. This study starts by exploring the behavior of 0.14 M solutions of sodium pyruvate-1,2-[^{13}C$_2$] in dichloromethane-d_2 that contain 40 µl of H$_2$O and an equimolar amount of either benzylamine (BnNH$_2$) or phenylethylamine (PEA). Monitoring by ^{13}C NMR spectroscopy (see supporting information) reveals the formation of an equilibrium mixture which includes the corresponding imine products **A** and **B** of Scheme 2 and their hydrated counterparts.[40,41] In a second

A R= CH$_2$Ph
B R= CH$_2$CH$_2$Ph
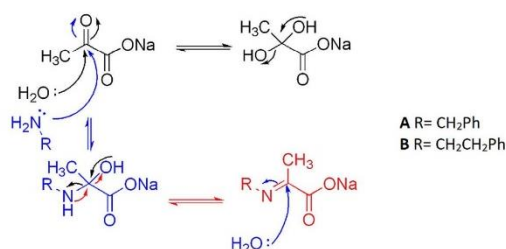
Scheme 2. Pyruvate and amine react together to form an equilibrium mixture of the imine (**A** or **B**), the hydrated imine, and the starting materials.[42]

stage, samples of [IrCl(COD)(IMes)], **1**, were first reacted with 5 equivalents of BnNH$_2$ or PEA under 3-bar of hydrogen gas to preform [Ir(H$_2$)(amine)$_3$(IMes)]Cl, **2** or **3**. These known products yield hydride resonances at δ−24.0 (**2**) and δ−23.7 (**3**) respectively.[18] Furthermore, when these reactions are completed with p-H$_2$, the free amine's NMR signals become strongly enhanced as a consequence of SABRE.[17,18]

When such imine mixtures are added to preformed **2** and **3** and the resulting samples placed under 3-bar of H$_2$ gas the single hydride resonances of **2** and **3** are replaced in both cases by two pairs of hydrides. When samples of pyruvate are added to **2** or **3** in the presence of p-H$_2$ a hyperpolarized response for pyruvate is observed, as previously reported, until the conversion to **4** or **5** is complete.[18] For BnNH$_2$, two dominant hydride resonances appear at δ−21.9 and δ−27.6 which share a common splitting of 9.5 Hz that are assigned to complex **4$_{major}$** of Scheme 3. These hydride resonances sharpen at 245 K where multinuclear NMR measurements using labelled ^{13}C$_2$ pyruvate and ^{15}N amine precursors were undertaken. In the corresponding ^{15}N data a connection between the δ −21.9 hydride signal and a ^{15}N signal at δ 276.9 was observed due to a shared *trans* ^{1}H-^{15}N coupling of 20.7 Hz. A further bound amine ^{15}N signal was seen at δ −2.7 which is located *trans* to

2, 4 R= CH$_2$Ph
3, 5 R= CH$_2$CH$_2$Ph
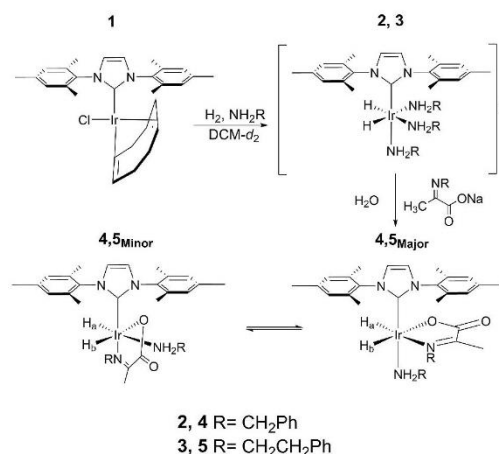
Scheme 3. [IrCl(COD)(IMes)], **1**, reacts with the amines BnNH$_2$ or PEA and H$_2$ in dichloromethane-d_2 to produce **2** or **3**. Further reaction with an equilibrium mixture of pyruvate and imine yield the Iridium α-carboxyimine complexes **4** and **5**.

the carbene according to nOe measurements. Identification of the ligand *trans* to the hydride yielding the δ −27.6 resonance was secured by the nOe interactions to CH$_3$ groups of the imine and carbene. Kinetic product **4$_{major}$** therefore is [Ir(-H$_2$)(amine)(IMes)(η^2-**A**)]Cl with the ligand arrangement shown in Scheme 3 and logically arises due to the high lability of the amine when located *trans* to hydride.[17,18] Similar α-ketoimine chelates with late transition metal centers have been reported for ruthenium, cobalt, nickel, copper and zinc.[43–45] The remaining minor product, **4$_{minor}$** is a regioisomer of **4$_{major}$** which yields hydride resonances at δ −24.0 and δ −27.4, of which the former is *trans* to BnNH$_2$ as indicated by the 17.5 Hz coupling to a ^{15}N signal at δ −2.47. After imine addition to **2**, **4$_{major}$** appears to form exclusively, but after 1 hour at 298 K these two species exist in an approximate 1:30 ratio. An equilibrium 1:2 ratio is established after 7 hours with **4$_{major}$** confirmed as the kinetic and thermodynamic product.

When exchange spectroscopy is used on a slower timescale to probe their dynamic behavior, exchange of the hydride ligands of **4$_{minor}$** alongside the formation of free H$_2$ was observed, as illustrated by Figure 1a. The rate of production of free H$_2$ was estimated to be 15.5 s^{-1} ($\pm$0.6) at 283 K. The associated transition state barriers were determined by probing these changes as a function of temperature over the range 253–283 K. The resulting $\Delta H^{\neq}$ value for free H$_2$ production is 103.7 $\pm$ 1.6 kJ mol^{-1} while $\Delta S^{\neq}$ is $+145 \pm 6$ J K^{-1} mol^{-1} as detailed in the supporting information. Increasing amine concentrations suppress the H$_2$ production pathway in accordance with a process that is preceded by dissociative amine loss. This type of behavior is typical for systems of this type.[46] Furthermore, **4$_{major}$** appears to be inert on this timescale.

As a consequence of this visible dihydrogen exchange pathway, we reexamined this process with p-H$_2$. Now, the hydride resonances of **4$_{minor}$** become strongly enhanced while
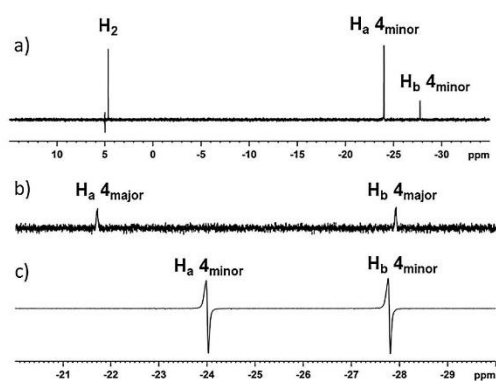
Figure 1. (a) ^{1}H-EXSY NMR spectrum recorded at 283 K 0.05 s after selective excitation of the H_a resonance $\delta-24.0$ of 4_{minor} showing exchange peaks with free hydrogen at $\delta-4.6$ and H_b; (b) Reference ^{1}H NMR spectrum with the corresponding p-H_2-hyperpolarized NMR spectrum (c). The relative vertical expansion of (b):(c) is 32:1.

Figure 2. Thermal (top) and hyperpolarized (bottom) ^{13}C spectra of 4_{minor} after shaking with 3 bar p-H_2 for 10 seconds at 65 G. Note that the thermal NMR spectrum has been expanded vertically by a factor of 4 relative to the hyperpolarized response.

those of 4_{major} remain unaffected (Figure 1c). The PEA system proved to behave in a similar way, forming the corresponding complexes 5_{minor} and 5_{major} in a 1:11 ratio at 298 K 1 hour after imine addition to **3**. However, after 7 hours, 5_{minor} dominates as their ratio becomes 2:1. This suggests that while 5_{major} is still the kinetic product, 5_{minor} is now the thermodynamic product. The rate of H_2 appearance from 5_{minor} proved to be slower than that of 4_{minor} at 4.11 s^{-1} (± 0.06) at 283 K. The corresponding value for $\Delta H^{\neq}$ of H_2 loss is 81.0 ± 2.2 kJ mol^{-1} whilst $\Delta S^{\neq}$ is $+53 \pm 5$ J K^{-1} mol^{-1}. Rates of hydrogen elimination for similar octahedral iridium carbene complexes are slower and range between 0.56 and 5.11 s^{-1} at the higher temperature of 295 K.[32] The hydrogen exchange process for 4_{minor} and 5_{minor} is therefore very rapid. Similarly to **4**, 5_{major} proved to be inert to H_2 loss on this timescale and 5_{minor} is observed to react reversibly with p-H_2 and its hydride resonances exhibit a similar antiphase profile.

When samples of **4** or **5** containing the corresponding 1,2 ^{13}C$_2$ labelled imine were shaken with fresh p-H_2 at a field of 65 G prior to observation, both of their bound 1,2 ^{13}C$_2$ resonances proved to be strongly polarized. However, for a 90° excitation pulse, the two corresponding ^{13}C signals strangely appear in absorption and emission respectively as shown in Figure 2. The average ^{13}C enhancement levels proved to be 420-fold for 4_{minor} and 280-fold for 5_{minor}. These ^{13}C spins exhibit chemical shift differences of 4.8 and 6.1 ppm for 4_{minor} and 5_{minor} respectively at 9.4 T whilst their mutual J-coupling constants are equal at 66 Hz. Hence, they are weakly coupled in this observation field but in the fringe field of the magnet ($\sim$6 mT) where polarization transfer takes place they are strongly coupled.

In order to account for this strange signal phase behavior the initial singlet state of the dihydride must first evolve on the metal complex under chemical shift and coupling propagators into new singlet order on the bound imine. Adiabatic sample transfer from low to high field then causes the initial $|S_0\rangle$ term
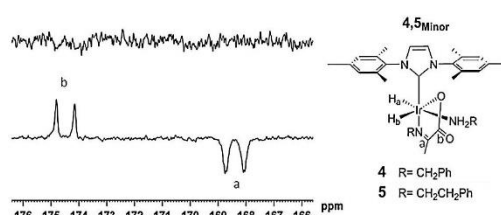
to populate just the $|\alpha\beta\rangle$ level, which when probed by a 90° pulse leads to two resonance pairs with opposite phase. This behavior would suggest that a long-lived magnetic state could therefore exist between these ^{13}C spins in the strongly coupled low field regime. We, and others, have previously established routes to create and assess the lifetimes of such states in pairs of coupled spins.[25,26,47,48] When such methods are applied here, the lifetime of the corresponding hyperpolarized magnetic states in low field show a dependence on p-H_2 pressure, see supporting information for more detail. It is clear that rapid H_2 exchange continually repolarizes the relaxing sample and therefore these data are reflective of both the p-H_2 decay rate and the low-field singlet state lifetime. This was confirmed by repeating the decay profile measurement with interleaved sample shaking to dissolve fresh p-H_2. Now, a saw-tooth decay was observed in agreement with competing continuous repolarization. Hence, the signal decay profile is not a mono-exponential process, but instead exhibits bi-exponential behavior with contributions from both the singlet state lifetime and p-H_2 repolarizing. These two effects can be deconvoluted by recording measurements at different p-H_2 pressures which decay with a variable p-H_2 replenishment term, but a fixed low field singlet lifetime. Bi-exponential fitting yields a singlet state lifetime of 10.9 ± 1.1 s and 8.8 ± 1.4 s for 4_{minor} and 5_{minor} respectively.

When the hydrogen atmosphere of solutions containing **4** and **5** are replaced by N_2 or air, the slow precipitation of single crystals of products **6** and **7** occurs. Subsequent X-ray diffraction studies reveal that they are the carbonate containing [Ir(IMes)(η^2-CO$_3$)(η^2-imine)(amine)] complexes, for example as shown in Figure 3. While **4** and **5** exist as two regioisomers depending on the geometry of amine, only one isomer of **6** and **7** is observed in the crystalline state. Iridium complexes containing η^2-bound carbonate ligands have been reported.[49] In fact, infrared spectroscopy of the crystals of **6** reveal the presence of vibrational bands for ν(OCO) at 1584.18 and 1485.84 cm^{-1} which are characteristic of those of metal carbonates and compare well to those of other iridium and osmium η^2-CO$_3^{2-}$ complexes at 1580, 1482 cm^{-1} and 1575 and 1496 cm^{-1} respectively.[50,51] Solutions of **4** and **5** are stable under H_2 over a time period of many weeks, and the addition of NaHCO$_3$ and removal of H_2 failed to speed up the conversion to **6** or **7**. When sodium pyruvate-1-[^{13}C] is used as a starting
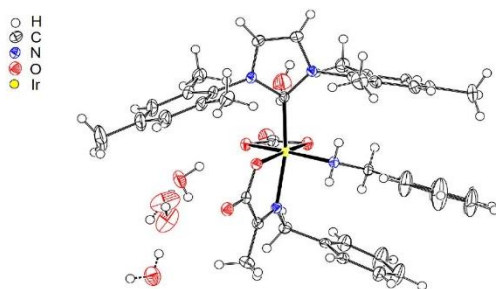
Figure 3. Structure of **6** determined from X-ray crystallography; the anisotropic displacement parameters and waters of crystallization should be noted.

material for the synthesis of **4**, a $^{13}CO_3^{2-}$ signal of **6** at δ 172 was observed. This indicates that the η^2-bound carbonate ligands of **6** are derived from pyruvate.

It is known that under physiological conditions pyruvate can be metabolized to carbondioxide[52] and some metal pyruvate complexes have been reported to thermally degrade at high temperatures to give metal carbonates.[53] Therefore, the conversion of pyruvate into carbonate in a process facilitated by a transition metal complex is not totally unexpected. It is therefore suggested that upon removing the H_2 atmosphere from **4** or **5**, its hydride ligands become replaced by η^1-pyruvate which subsequently rearrange to **6** and **7**. To our knowledge **6** and **7** are the first examples of metal carbonate complexes formed from the metal catalyzed decomposition of pyruvate.

In conclusion, we have shown here that **2** and **3** react rapidly with an α-carboxyimine to form **4** and **5** according to Scheme 2. The hydride ligands of the minor isomers of **4** and **5** undergo rapid exchange with p-H_2 such that its hydride resonances become very strongly enhanced. Furthermore, we establish that when the imine is 1,2-$[^{13}C]_2$ labelled, polarization flows readily from these hydride sites to dramatically improve the detectability of the imine ^{13}C response. The visible ^{13}C signal intensities at 9.4 T were quantified as exhibiting 420-fold and 280-fold enhancements for **4**$_{minor}$ and **5**$_{minor}$ respectively. Unusually though, the low-field nature of this process creates a long-lived 1,2-$[^{13}C]_2$ state in the first instance, the lifetimes of which approach 11 s. This low field approach[54] has been used previously to access such states in small molecule ^1H,[55,56] ^{15}N[57,58] and ^{13}C[59,60] spin systems where the longer magnetic state lifetimes are hoped to be useful for the *in vivo* probing of metabolism. Here though we have demonstrated a route to create a continually refreshable heteronuclear singlet state in a metal complex *via* reversible p-H_2 addition. Such states may now prove highly beneficial when looking for intermediates in chemical reactions, one of the main early benefits of PHIP. This development will augment continuous hyperpolarization by SABRE approaches[61] that have already seen it used to create the Z-magnetization needed to achieve sub-millihertz resolution[62] and Zero-Field NMR.[63]

Furthermore, upon the removal of the H_2 atmosphere from **4** and **5** a carbonate containing complex is formed which is characterized by IR, NMR, and X-ray diffraction. When pyruvate-$^{13}C_1$ is used, the presence of $^{13}CO_3^{2-}$ in **6** suggests that this product results from decomposition of pyruvate. While both metal carbonates and the transformation of pyruvate into carbonate are known, further work is being directed at elucidating the mechanism of this unusual observation.

Acknowledgements

Conflict of Interest

The authors declare no conflict of interest.

[1] J. H. Ardenkjær-Larsen, B. Fridlund, A. Gram, G. Hansson, L. Hansson, M. H. Lerche, R. Servin, M. Thaning, K. Golman, *Proc. Natl. Acad. Sci.* **2003**, *100*, 10158–10163.
[2] K. M. Brindle, *J. Am. Chem. Soc.* **2015**, *137*, 6418–6427.
[3] K. M. Brindle, S. E. Bohndiek, F. A. Gallagher, M. I. Kettunen, *Magn. Reson. Med.* **2011**, *66*, 505–519.
[4] C. R. Bowers, D. P. Weitekamp, *J. Am. Chem. Soc.* **1987**, *109*, 5541–5542.
[5] T. C. Eisenschmid, R. U. Kirss, P. P. Deutsch, S. I. Hommeltoft, R. Eisenberg, J. Bargon, R. G. Lawler, A. L. Balch, *J. Am. Chem. Soc.* **1987**, *109*, 8089–8091.
[6] S. B. Duckett, C. L. Newell, R. Eisenberg, *J. Am. Chem. Soc.* **1994**, *116*, 10548–10556.
[7] K. V. Kovtunov, I. E. Beck, V. I. Bukhtiyarov, I. V. Koptyug, *Angew. Chem. Int. Ed.* **2008**, *47*, 1492–1495; *Angew. Chem.* **2008**, *120*, 1514–1517.
[8] P. Bhattacharya, E. Y. Chekmenev, W. H. Perman, K. C. Harris, A. P. Lin, V. A. Norton, C. T. Tan, B. D. Ross, D. P. Weitekamp, *J. Magn. Reson.* **2007**, *186*, 150–155.
[9] N. M. Zacharias, H. R. Chan, N. Sailasuta, B. D. Ross, P. Bhattacharya, *J. Am. Chem. Soc.* **2011**, *134*, 934–943.
[10] F. Reineri, T. Boi, S. Aime, *Nat. Commun.* **2015**, *6*, 5858.
[11] R. W. Adams, J. A. Aguilar, K. D. Atkinson, M. J. Cowley, P. I. Elliott, S. B. Duckett, G. G. Green, I. G. Khazal, J. López-Serrano, D. C. Williamson, *Science.* **2009**, *323*, 1708–1711.
[12] P. J. Rayner, S. Duckett, *Angew. Chem. Int. Ed.* **2018**.
[13] M. J. Cowley, R. W. Adams, K. D. Atkinson, M. C. Cockett, S. B. Duckett, G. G. Green, J. A. Lohman, R. Kerssebaum, D. Kilgour, R. E. Mewis, *J. Am. Chem. Soc.* **2011**, *133*, 6134–6137.
[14] E. B. Dücker, L. T. Kuhn, K. Münnemann, C. Griesinger, *J. Magn. Reson.* **2012**, *214*, 159–165.
[15] P. Spannring, I. Reile, M. Emondts, P. P. Schleker, N. K. Hermkens, N. G. van der Zwaluw, B. J. van Weerdenburg, P. Tinnemans, M. Tessari, B. Blümich, *Chem. Eur. J.* **2016**, *22*, 9277–9282.
[16] H. Zeng, J. Xu, J. Gillen, M. T. McMahon, D. Artemov, J.-M. Tyburn, J. A. Lohman, R. E. Mewis, K. D. Atkinson, G. G. Green, *J. Magn. Reson.* **2013**, *237*, 73–78.
[17] W. Iali, P. J. Rayner, A. Alshehri, A. J. Holmes, A. J. Ruddlesden, S. B. Duckett, *Chem. Sci.* **2018**.
[18] W. Iali, P. J. Rayner, S. B. Duckett, *Sci. Adv.* **2018**, *4*, eaao6250.
[19] R. E. Mewis, R. A. Green, M. C. Cockett, M. J. Cowley, S. B. Duckett, G. G. Green, R. O. John, P. J. Rayner, D. C. Williamson, *J. Phys. Chem. B.* **2015**, *119*, 1416–1424.

Appendix 3

Check for updates

Using coligands to gain mechanistic insight into iridium complexes hyperpolarized with *para*-hydrogen†

Ben. J. Tickner, [a] Richard O. John, [a] Soumya S. Roy, [a] Sam J. Hart,[b] Adrian C. Whitwood [b] and Simon B. Duckett [*a]

We report the formation of a series of novel [Ir(H)$_2$(IMes)(α-^{13}C$_2$-carboxyimine)L] complexes in which the identity of the coligand L is varied. When examined with *para*-hydrogen, complexes in which L is benzylamine or phenethylamine show significant ^{1}H hydride and ^{13}C$_2$ imine enhancements and may exist in ^{13}C$_2$ singlet spin order. Isotopic labeling techniques are used to double ^{13}C$_2$ enhancements (up to 750-fold) and singlet state lifetimes (up to 20 seconds) compared to those previously reported. Exchange spectroscopy and Density Functional Theory are used to investigate the stability and mechanism of rapid hydrogen exchange in these complexes, a process driven by dissociative coligand loss to form a key five coordinate intermediate. When L is pyridine or imidazole, competitive binding to such intermediates leads to novel complexes whose formation, kinetics, behaviour, structure, and hyperpolarization is investigated. The ratio of the observed PHIP enhancements were found to be affected not only by the hydrogen exchange rates but the identity of the coligands. This ligand reactivity is accompanied by decoherence of any ^{13}C$_2$ singlet order which can be preserved by isotopic labeling. Addition of a thiol coligand proved to yield a thiol oxidative addition product which is characterized by NMR and MS techniques. Significant 870-fold ^{13}C enhancements of pyridine can be achieved using the Signal Amplification By Reversible Exchange (SABRE) process when α-carboxyimines are used to block active coordination sites. [Ir(H)$_2$(IMes)(α-^{13}C$_2$-carboxyimine)L] therefore acts as unique sensors whose ^{1}H hydride chemical shifts and corresponding hyperpolarization levels are indicative of the identity of a coligand and its binding strength.

Introduction

Nuclear Magnetic Resonance (NMR) is one of the most widely used techniques in the structural and behavioural characterization of molecules and materials. Despite its widespread use it remains fundamentally insensitive as its signal intensity is derived from very small population differences across closely spaced nuclear spin energy levels. While only 1 in 32 000 ^{1}H nuclei are visible to NMR at 9.4 T, this problem becomes more pronounced for low γ nuclei such as ^{13}C as only 1 in 800 000 nuclear spins contribute efficiently to the NMR response at the 1.5 T field used by a common clinical scanner. Hyperpolarization techniques have developed over the last few decades to address this insensitivity issue by premagnetising samples and

*a*Center for Hyperpolarization in Magnetic Resonance (CHyM), University of York, Heslington, York, YO10 5NY, UK. E-mail: simon.duckett@york.ac.uk

*b*Department of Chemistry, University of York, Heslington, York, YO10 5DD, UK

hence creating non-Boltzmann population differences across their NMR addressable energy levels.[1-7] Techniques such as Dynamic Nuclear Polarization (DNP),[1,2] *para*-Hydrogen Induced Polarization (PHIP)[3-6] and Spin Exchange Optical Pumping (SEOP)[7] are used in this regard to produce hyperpolarized molecules with growing success.

The technique of DNP has already found applications in a clinical context as it can deliver ^{1}H and ^{13}C nuclei with polarization levels of 92% and 70% respectively after preparation times of 150 seconds and 20 minutes respectively.[2] It exploits the transfer of polarization from an electron in a stable radical at cryogenic temperatures of between 1 and 2 K that is located in a magnetic field of between 1 and 7 T to achieve this.[1,2] The successful hyperpolarization of biochemically relevant agents such as pyruvate,[8-14] succinate,[15,16] and fumarate[17,18] and their subsequent *in vivo* detection when thawed reflects a significant advance in diagnostic magnetic resonance imaging (MRI). In addition, SEOP delivers hyperpolarized samples of the gases ^{3}He and ^{129}Xe which have been used for human lung imaging.[19,20]

The PHIP technique utilizes easy to access *p*-H$_2$, the singlet nuclear spin isomer of hydrogen, to achieve hyperpolarization.

This is readily realized when it is incorporated into a molecule by a hydrogenation reaction and has enabled the *in vivo* detection of MRI sensitised reaction products.[15,21–23] Recently, a variant of PHIP, termed PHIP-SAH, employed the hydrogenation of a readily cleaved and unsaturated side arm that is attached to pyruvate or acetate to ultimately hyperpolarize them.[24,25]

In contrast, the PHIP method, Signal Amplification By Reversible Exchange (SABRE) rapidly hyperpolarizes substrates in a cost-efficient and reproducible fashion without the chemical alteration of the substrate.[26–28] Substrate polarization is now facilitated by the temporary association of the target agent within an organometallic complex at low (0–100 G) magnetic field, although polarization transfer can be driven at high field by radio frequency excitation.[28–31] The most commonly used substrates for SABRE contain N-heterocyclic motifs such as those found in pyridines,[26,32–34] nicotinamides,[26,35,36] and pyrazines.[32,33] The metal binding restriction has been lifted by the SABRE-Relay approach which involves the chemical exchange of hyperpolarized nuclei.[37–39]

In fact, SABRE has achieved 63% ^{1}H polarization in methyl-4,6-d_2-nicotinate in just a few seconds and can therefore deliver a similar output to DNP.[40] A SABRE-SHEATH variation, demonstrated for N-heterocycles,[35,41] nitriles,[41] Schiff bases,[42] and diazirines,[43,44] has targeted ^{15}N nuclei through transfer in milli-Gauss fields. SABRE has also hyperpolarized ^{13}C,[45,46] ^{19}F,[47,48] ^{31}P,[49] ^{119}Sn and ^{31}Si[50] nuclei and is therefore truly multinuclear in scope. Hence, PHIP and SABRE now find uses in a wide range of situations including reaction monitoring and the detection of low concentration analytes in mixtures or short lived intermediates in the field of catalysis.[3,4] There are also an array of high sensitivity analytical applications[51,52] alongside reports to produce biocompatible mixtures suitable for *in vivo* injection.[53–55]

Normally in NMR, relaxation can be counted as a friend because it allows the user to signal average. However, for hyperpolarization relaxation is widely thought of as a foe because the non-equilibrium state it utilises must be encoded for measurement before it vanishes. Consequently, a number of methods have been developed to extend the detectible lifetimes of hyperpolarized signals through deuterium labeling[26,40,56,57] and/or storage as singlet spin order.[58–60] We communicated previously the formation and behaviour of two labelled iridium α-carboxyimine complexes that are hyperpolarized by PHIP and exist initially as ^{13}C$_2$ nuclear singlet states.[37] These products result from binding of the imine formed by the *in situ* condensation reaction of amine and pyruvate. In solution, these [Ir(H)$_2$(IMes)(η^2-α-carboxyimine)(amine)] complexes (where IMes = 1,3-bis(2,4,6-trimethyl-phenyl)imidazole-2-ylidene) exist as two isomers, denoted **A** or **B** of Chart 1, that are differentiated according to the coordination geometry of the imine. Isomer, **C**, was not detected in this study.

Only those isomers denoted as **A** exhibited rapid hydrogen exchange and hence produced high levels of hydride and ^{13}C$_2$ signal enhancements under PHIP conditions. When comparing these complexes, **1A** was reported to undergo
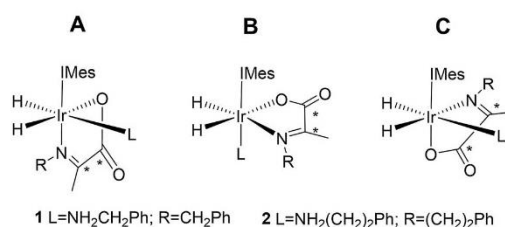
Chart 1 Structural isomers of the iridium α-carboxyimine complexes seen in this work. An asterisk (*) denotes a ^{13}C labeled position. IMes = 1,3-bis(2,4,6-trimethyl-phenyl)imidazole-2-ylidene.

a faster rate of H$_2$ loss (15.5 ± 0.6 s^{-1}) when compared to **2A** (4.11 ± 0.06 s^{-1}) at 283 K. This was suggested to account for the higher ^{13}C signal enhancements it exhibits (420-fold for **1A** *versus* 280-fold for **2A**). Its ^{13}C$_2$ singlet state also exhibited an increased lifetime (10.9 ± 1.1 s in **1A** compared to 8.8 ± 1.4 s for **2A**). Given the potential importance of hyperpolarised NMR for the rationalisation of reaction mechanisms and the characterisation of materials in low concentration, alongside their use in MRI as clinical diagnostics, we set out here to study these complexes in more detail. Specifically, we expected that these hyperpolarization levels and their visible lifetimes could be improved through optimization of the hydrogen loss rate and selective deuteration.[40] We explore the hydrogen exchange pathway of these iridium carboxyimine complexes by studying them as a function of amine ligand concentration and hydrogen pressure through NMR spectroscopy methods. Results are then linked to a mechanism which is supported by Density Functional Theory (DFT) calculations. By studying the reactivity of these complexes towards the eight ligands of Chart 1 we form a series of novel complexes that allow us to further rationalise this behaviour. Subsequently their hyperpolarisation with *p*-H$_2$ is examined and we establish a route to produce strong ^{13}C signal gains. By expanding this work to include the effects of ^{15}N and ^{2}H isotopic labelling we develop further insight into the important SABRE mechanism.

Results and discussion

This work starts with the formation of neutral [Ir(H)$_2$(IMes)(η^2-α-carboxyimine)(amine)] (**1** and **2**) which exist as two regioisomers that are differentiated according to whether the amine is *trans* to hydride (**A**) or the N-heterocyclic carbene ligand (**B**) as shown in Chart 1. These complexes are prepared *in situ* by taking dichloromethane-d_2 solutions of a [Ir(IMes)(COD)Cl] precursor and reacting it with 5 equivalents of both pyruvate and the amine (see Experimental) in the presence of a 3 bar H$_2$ atmosphere.[37] The initial products of this process are iridium(III) dihydride complexes of the type [Ir(H)$_2$(IMes)(amine)$_3$]Cl which have been reported to undergo both H$_2$ loss and amine loss *via* the formation of a common 16 electron intermediate [Ir(H)$_2$(IMes)(amine)$_2$]Cl. These species go on to form **1** and **2** in the presence of pyruvate.

261

Edge Article

Hydrogen loss mechanism for the iridium dihydride α carboxyimine complex 2A

Upon the selective radio frequency (r.f.) excitation of a hydride resonance of the related phenylethylamine product **2A**, exchange of this hydride into both free H_2 and the inequivalent hydride site is observed. This suggests the presence of a reaction pathway that allows for both H_2 exchange and interchange of the hydride ligand sites. Modelling this exchange spectroscopy (EXSY) data allowed the experimentally observed rates of hydrogen production ($k_{(obs)H_2}$) and hydride site interchange ($k_{(obs)Hi}$) to be determined from the corresponding signal integrals as a function of reaction time. The results of this process are shown in Tables 1 and 2.

On the basis of similar Ir(III) reactions, it might be expected that hydrogen exchange is again preceded by dissociative amine loss from 18 electron **2A** to form a 16 electron five coordinate intermediate.[33] The $k_{(obs)H_2}$ rate constants of Table 1 fall as the amine concentration increases. This change is consistent with the fact that the five coordinate intermediate $[Ir(H)_2(IMes)(\eta^2-\alpha-carboxyimine)]$ of Fig. 1 is more likely to reform **2A** at higher amine concentrations than react with H_2 thereby reducing $k_{(obs)H_2}$ and consequently increasing the value of $k_{(obs)Hi}$. Subsequent rebinding of the amine reforms the starting complex **2A**, with or without hydride ligand interchange depending on the face of amine attack on the 16 electron intermediate. This subtle effect is a consequence of the fact the hydride ligands of the 16-electron intermediate are made chemically inequivalent by virtue of the imine asymmetry. In contrast, when the H_2 pressure is increased the five coordinate intermediate is more likely to react with H_2 than amine leading to more efficient H_2 loss via $[Ir(H)_2(\eta^2-H_2)(IMes)(\eta^2-\alpha-carboxyimine)(amine)]$ which is reflected in an increase in $k_{(obs)H_2}$ and a decrease in $k_{(obs)Hi}$.

In order to provide further evidence for these deductions, Density Functional Theory (DFT) calculations were used to predict the relative energies of closely related **1A–1C** as detailed in Fig. 1. Their relative stability is $1A \geq 1B \gg 1C$ which matches the solution based NMR observations. The energy changes associated with direct H_2 loss to form the corresponding four coordinate Ir(I) 16-electron product are also shown in Fig. 1. The enthalpy and free energy changes of direct H_2 loss are both in excess of 100 kJ mol^{-1} at 298 K making such a process energetically unfavourable. In contrast, amine loss to form the corresponding trigonal bipyramidal 16-electron Ir(III) intermediate of Fig. 1 predicted earlier is more favourable by over 60 kJ mol^{-1} there-by supporting a route to H_2 loss in a constant iridium

Table 1 Rate constants for H_2 production ($k_{(obs)H_2}$) and hydride interchange ($k_{(obs)Hi}$) of **2A** determined by EXSY at 273 K as a function of amine concentration[a] when H_2 pressure was fixed at 3 bar

[Amine]	$k_{(obs)H_2}/s^{-1}$	$k_{(obs)Hi}/s^{-1}$
5 eq.	1.85 ± 0.05	0.40 ± 0.02
10 eq.	1.47 ± 0.03	0.70 ± 0.01
15 eq.	1.13 ± 0.01	0.88 ± 0.01

[a] Amine concentration is relative to the iridium precatalyst.

Table 2 Rate constants for H_2 production ($k_{(obs)H_2}$) and hydride interchange ($k_{(obs)Hi}$) of **2A** determined by EXSY at 273 K as a function of H_2 pressure when amine concentration was fixed at 15 eq. relative to iridium precatalyst

H_2 pressure	$k_{(obs)H_2}/s^{-1}$	$k_{(obs)Hi}/s^{-1}$
1 bar	0.60 ± 0.01	1.05 ± 0.01
2 bar	0.95 ± 0.01	0.92 ± 0.01
3 bar	1.13 ± 0.01	0.88 ± 0.01

oxidation state cycle involving $[Ir(H)_2(H_2)(IMes)(\eta^2-\alpha-carboxyimine)]$ as shown in Fig. 1. The hydride ligands in the optimized geometry of these intermediates are inequivalent in agreement with the observed kinetic effects described earlier (Fig. S8 of ESI†). Additionally, the energy changes for amine loss are larger for isomer **B** in accordance with its experimentally observed reduced reactivity.

Formation of analogous iridium α-carboxyimine complexes 3–5 from 2 by reaction with pyridine, imidazole and dimethylsulfoxide

As amine loss from **2A** mediates p-H_2 exchange we mixed solutions of it with several neutral two electron donors to probe this process. These materials, hence forth referred to as co-ligands, are illustrated in Scheme 1 alongside the corresponding reaction products. It might reasonably be expected that trapping of the resulting 16-electron intermediate $[Ir(H)_2(IMes)(\eta^2-\alpha-carboxyimine)]$ would result in a number of new PHIP enhanced reaction products which could themselves have implications for SABRE.
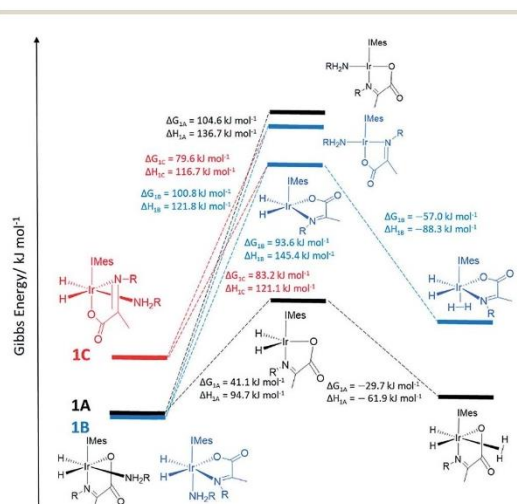
Fig. 1 DFT energy level diagram supporting a hydrogen exchange pathway that is preceded by dissociative amine loss to form the indicated five coordinate intermediates. These are intermediate energies and do not reflect transition state barriers.
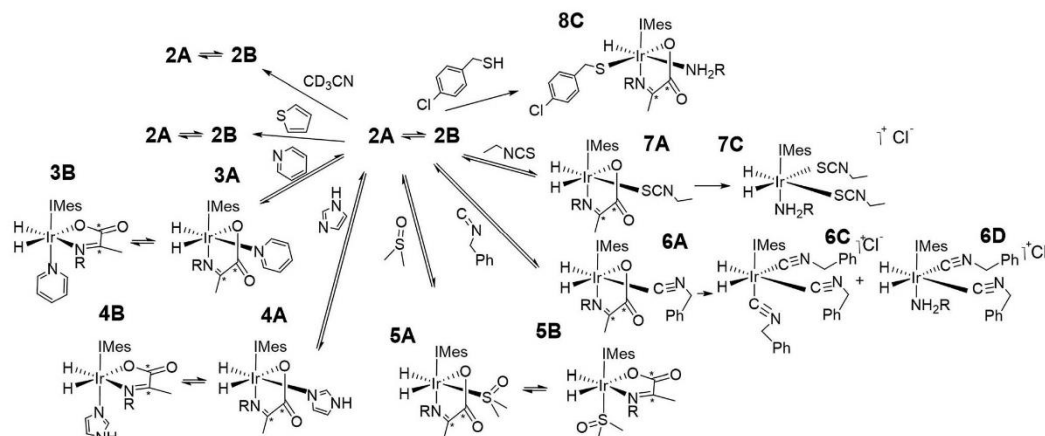
Scheme 1 Complexes synthesised in this work.

Upon adding an ~5-fold excess relative to iridium of one of the weak donors acetonitrile-d_3 or thiophene to a sample of **2** no changes in the corresponding ^{1}H NMR spectra are observed. Hence the predicted ligand exchange products must be unstable with respect to **2** and consequently the Ir–amine bond energy must exceed that of both Ir–acetonitrile and Ir–thiophene. This agrees with the corresponding DFT calculations (Fig. S8 of ESI†) which suggest these substitution products are at least 20 kJ mol^{-1} less stable than **2**.

However, when a 4-fold excess of pyridine is added to **2** in DCM-d_2 two new hydride resonances immediately appear at δ −23.47 and δ −27.37 in the corresponding ^{1}H NMR spectrum. These resonances exhibit a mutual J_{HH} coupling of 7.5 Hz and are therefore due to a *cis*-dihydride complex, the amine replacement product **3A**. Upon leaving this solution overnight at 278 K two further hydride resonances appear at δ −20.96 and δ −26.99, this time sharing a mutual coupling of 9 Hz, due to isomer **3B** of Scheme 1. Hence pyridine and phenylethylamine bind competitively to [Ir(H)$_2$(IMes)(η^2-α-carboxyimine)]. At this point in the reaction, hydride ligand ^{1}H NMR signals are visible for all four of the associated complexes. A fresh sample was prepared to track these speciation changes at 298 K over a 17 hour time period by ^{1}H NMR spectroscopy. Examination of these data revealed that the signals for **2A**, and then **2B**, decrease upon pyridine addition leading first to the detection of **3A** and then **3B**. The signals for **3B** are most readily seen in the later stages of reaction due to its low proportion in the final equilibrium mixture of all four species. These observations fit to a kinetic model (see ESI†) from which pseudo rate constants for their relative rates of transmission can be determined. The model does not involve the common 16-electron intermediate that forms regardless of the identity of the ligand that is lost. Collectively, these observations alongside the DFT predictions of Fig. 2 are consistent with faster amine loss from **2A** (transmission rate $k_{trans2A3A}$ of $9.2 \pm 1.8 \times 10^{-6}$ s^{-1}) than from **2B** ($k_{trans2B3B}$ is $7.1 \pm 2.9 \times 10^{-6}$ s^{-1}). According to the kinetic

model $k_{trans2A3A}$ is always greater than $k_{trans2B3B}$. While these rates of transmission are similar, **3A** dominates over **3B** at equilibrium because it is more stable to pyridine loss (supported by DFT as shown in Fig. 2). The ratio of **3A** to **2** is, however, influenced by the associated equilibria which are complicated by the *in situ* pyruvate reaction to form the imine, alongside the fact DFT predicts them all to be close in energy.

Similar changes in the hydride region of analogous NMR spectra were seen when a solution of **2** is mixed with imidazole
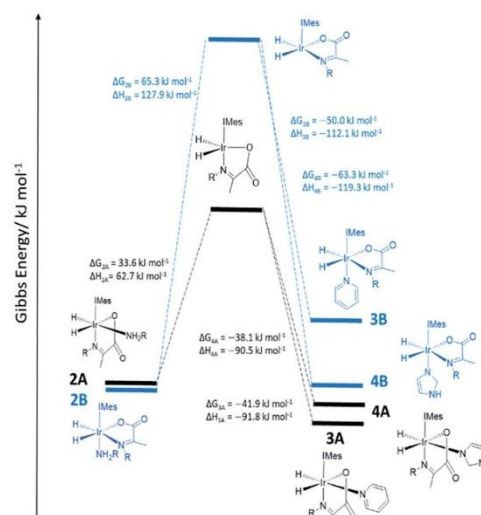
Fig. 2 DFT energy level diagram for amine loss from **2** and subsequent binding of pyridine or imidazole coligands to the five coordinate intermediates indicated. Energies do not reflect transition state barriers.

263

rather than pyridine. This is reflected in the appearance of two new mutually coupled hydride resonances at δ −21.96 and δ −28.14 (J_{HH} = 8 Hz) due to imidazole containing **4A** of Scheme 1. Isomer **4B** yields resonances at δ −21.41 and δ −27.59 (J = 9 Hz) and again becomes visible most readily at longer reaction times. Fitted transmission rate constants suggest again that there is a faster effective rate of amine replacement from **2A** to form **4A** ($k_{trans2A4A}$ = 3.1 ± 0.4 × 10^{-6} s^{-1}) when compared to **2B** ($k_{trans2B4B}$ = 1.9 ± 0.4 × 10^{-6} s^{-1}), although these changes proceed slower than those for pyridine. Hence the rate of imidazole binding to [Ir(H)$_2$(IMes)(η^2-α-carboxyimine)] must be slower than pyridine even though **4B** ultimately exists in higher proportion than **3B** at equilibrium. DFT now confirms that **2** and **4** are close in energy.

To further confirm this observation, an equimolar amount of pyridine and imidazole were simultaneously added to **2** to produce the corresponding equilibrium mixture of **2**, **3** and **4**. The resulting transmission constants agree with faster amine replacement in **2A** when compared to **2B** and faster rates of pyridine binding when compared to imidazole.

For dimethylsulfoxide, the corresponding complexes **5A** and **5B** result which now yield broad hydride resonances at δ −13.37 and δ −25.77 alongside sharp mutually coupled resonances at δ −21.14 and δ −25.89 (J = 9 Hz) respectively. The former hydride resonances of **5A** being broadened by rapid H$_2$ loss. **5B** proved to exist in high proportion and fitted transmission rate constants confirm faster rates of amine replacement in **2A** ($k_{trans2A5A}$ = 6 ± 1 × 10^{-6} s^{-1}) when compared to **2B** and now a fast rate of isomerization of **5A** into **5B** ($k_{trans5A5B}$ = 1 ± 0.1 × 10^{-4} s^{-1}).

Upon removal of the H$_2$ atmosphere and addition of ∼3 mL of degassed hexane to the equilibrium mixtures of **2** with **3**, **4**, or **5**, slow precipitation of a series of single crystals was observed. Subsequent X-ray diffraction studies revealed the common presence of known [Ir(amine)(η^2-CO$_3$)(IMes)(η^2-imine)] as detailed in the ESI.† These are formed as the metal mediates the conversion of pyruvate into carbonate.[8,37] It is the reversible binding of the amine, pyridine, imidazole, or DMSO that allows this conversion to occur.[37]

Formation of novel iridium α-carboxyimine complexes 6–8 from 2 by variation of the coligand L

In contrast, while the addition of benzyl isocyanide does indeed result in the formation of **6A**, as reflected in the observation of hydride resonances at δ −8.49 and δ −24.69 (J = 5.5 Hz), this product is not stable over long time periods. The ratio of **2A** : **6A** changes from 1 : 2 to 1 : 6 after 5 min and 1 hour respectively. After this time products associated with the loss of imine are clearly detected. They yield two singlets in the hydride region at δ −10.22 and δ −12.34 in a 1.5 : 1 ratio which indicates the corresponding hydride ligands are *trans* to soft donors. According to accurate mass spectrometry analysis they reflect tris isocyanide and bis isocyanide-amine complexes. These products form in a 1 : 12 ratio when H$_2$ is added to a solution of [IrCl(COD)(IMes)] with 5 equivalents PEA, and benzyl isocyanide. NMR characterization of this mixture confirms the

singlet at δ −12.34 is due to tris isocyanide **6C** while the complex yielding the resonance at δ −10.22 could not be characterized due to its low concentration, but most likely corresponds to bis isocyanide-amine **6D**. As iridium(III) isocyanide complexes have been previously reported the stability of these products is not surprising.[61,62]

The addition of a 4-fold excess of ethyl isothiocyanate to **2A** proceeds more rapidly to the related imine loss product [Ir(H)$_2$(IMes)(phenethylamine)(SCNEt)$_2$], **7C** than benzyl isocyanide yielding a single hydride signal at δ −16.05. At short reaction times resonances for **7A** at δ −17.87 and δ −28.27 (J = 9 Hz) are seen, although the ratio of **2A**, **2B**, **7A** and **7C** is 0 : 7.3 : 1 : 2.8 after just 30 min. There are also a wide range of reported stable isothiocyanate complexes.[63,64] We note that **7C** is not formed when [IrCl(COD)(IMes)], PEA, and ethyl isothiocyanate react with H$_2$. Full characterization data for **7C** is detailed in the ESI.† Hence the binding of ethyl isothiocyanate and benzyl isocyanide is sufficiently strong as to displace the chelated imine.

When the coligand is 4-chlorobenzenemethanethiol, the major product is **8C**. It yields a single hydride signal at δ −21.56 and reflects a species which is stable at 278 K for weeks. Structural characterization of this product by NMR spectroscopy confirmed it to be a monohydride with retained amine and carboxyimine ligands. It actually corresponds to the H$_2$ replacement product that is formed by S–H bond oxidative addition. Such reactivity is well known for metal surfaces[65] and bimetallic complexes.[66,67] Similar iridium N-heterocyclic carbene complexes containing bound thiolates have been prepared from the displacement of Ir–Cl under basic conditions.[68] Hence there is a clear rational for this behaviour and related products are expected to account for the catalyst deactivation seen in SABRE catalysis upon scavenging with a supported thiol.[55,69]

Effect of coligand, L, on H$_2$ exchange and hydride ligand NMR signal enhancements in 2–7

When an equilibrium mixture of **2** and **3** are shaken with p-H$_2$ for 10 seconds at 65 G and then placed into the NMR spectrometer for detection with a 45° pulse, PHIP hyperpolarized hydride resonances are observed for both **2A** and **3A** as shown in Fig. 3. The hyperpolarized response of **3A** is ∼100 times more intense than that of **2A** which is now just 2% of the size that was observed before pyridine addition. These hydride signal enhancements are difficult to precisely quantify due to rapid dynamic exchange and peak overlap effects. Nonetheless, the selective radio frequency excitation of the hydride resonances of **3A** does reveal slow conversion to free H$_2$ at a rate of 0.17 ± 0.01 s^{-1} at 273 K. This compares to the corresponding rate of H$_2$ loss from **2A** of 1.14 ± 0.03 s^{-1} at 273 K and is consistent with the now proven higher thermodynamic stability of **3A**. The striking difference in hyperpolarization levels for **3A** might initially be thought to imply the opposite because they normally relate to the flux of p-H$_2$ through a species. However, this behaviour can be rationalized by simply examining an equilibrium mixture of **2** and **4** with p-H$_2$. As expected, hyperpolarized hydride resonances are observed for both **2A** and **4A**. The signal for **4A** is
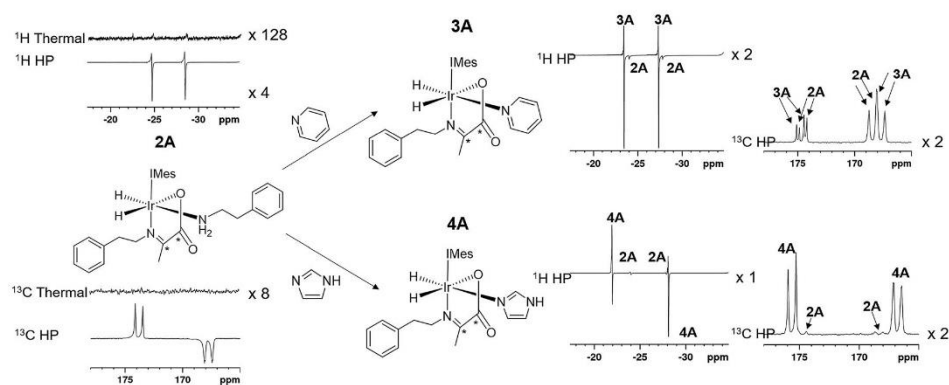
Fig. 3 The structure and partial thermal and hyperpolarized ^{1}H and ^{13}C spectra for the amine complex **2A** are shown. Upon addition of the coligands pyridine or imidazole the complexes **3A** and **4A** form, the ^{1}H and ^{13}C resonances of which hyperpolarize in addition to those of the starting **2A** as shown. All ^{1}H or ^{13}C spectra are shown on the same vertical scale.

though just 16 times more intense than that of **2A** which has now dropped to 20% of its intensity prior to imidazole addition (Fig. 3). Significantly though, the corresponding EXSY measurements fail to detect any H$_2$ loss for **4A** on this short relaxation controlled timescale. It is therefore clear that the high signal enhancements seen for **3A** and **4A** are not just due to H$_2$ exchange within them without other ligand scrambling, termed direct-PHIP, but must also include a contribution from coligand addition to the common 5 coordinate reaction intermediate that results from amine loss from **2A**, a process that we now term indirect PHIP. The higher overall PHIP enhancements visible in equilibrium mixtures of **2** and **4** when compared to **2** and **3** are therefore due to proportionally more **2A** being present and hence greater turnover of the linked intermediate [Ir(H)$_2$(-IMes)(η^2-α-carboxyimine)] which is trapped at steady state.

To further prove this hypothesis an equimolar addition of pyridine and imidazole was simultaneously made to a solution of **2**, forming an equilibrium mixture of **2**, **3** and **4** with amine, pyridine and imidazole coligands respectively. It might be expected from the faster rate of pyridine binding that the hyperpolarised response of **3A** would be greater than that of **4A**, but upon shaking with p-H$_2$ the hydride resonances of these complexes hyperpolarise with a 1 : 2.8 : 4.8 intensity ratio of **2A**, **3A** and **4A** respectively. This discrepancy is simply due to the different extents to which polarization flows into the other NMR active sites in these metal complexes under SABRE. Polarization proves to be localised much more effectively on the hydride ligands of **4A** whereas in **3A** it readily spreads into the ^{1}H sites of the pyridine coligand. This confirms that while these complexes form from the same common reaction intermediate, the relative rate constants for the formation of each cannot be measured directly from these intensity data as has been common for many other PHIP studies.

This deduction is confirmed by examining a solution of **2** containing equimolar amounts of pyridine-d_5 and imidazole. The hyperpolarised hydride signals observed due to **2A**, **3A**-d_5

and **4A** now appear in a 1 : 6.4 : 4.6 ratio respectively. Hence **3A**-d_5 now exhibits a hydride signal of higher intensity than that of **4A** as the leakage of hyperpolarisation into the ^{1}H resonances of the pyridine is quenched by deuteration. While these relative hyperpolarisation levels are now consistent with a faster rate of pyridine binding compared to imidazole, they still fail though to reflect the factor of 4 difference in observed transmission rates predicted earlier. One contribution to this difference will be the difference in average T_1 values of the hydride ligands which are 3.5 s, 7.7 s, and 7.0 s for the hydride ligands of **2A**, **3A** and **4A** respectively at 9.4 T and will act to reduce the visible signal strengths seen for **2A** and **4A** relative to **3A**. However, the biggest challenge here arises from differing contributions from direct-PHIP and indirect-PHIP (coligand addition to the common 5 coordinate reaction intermediate) and what is known as internal resonance cancellation which reduces the measured intensity of antiphase peaks as a consequence of line-broadening effects. The width at half height for these three signals are 14, 11 and 10 Hz for **2A**, **3A**-d_5 and **4A** respectively which means this contribution will vary depending on the species.

When an equilibrium mixture of **2** and **5** is examined in a similar way, hyperpolarized responses are again seen for **2A** and **5A**, albeit this time the signal intensity of the **2A** response is half that which is seen prior to DMSO addition and the signals which corresponded to **5A** are actually incredibly weak. This is reflective of proportionally lower amounts of **2A** present at equilibrium, alongside a much greater proportion of PHIP inactive **5B**.

For similar reasons, equilibrium mixtures of **2** and **6** do not give any hyperpolarized ^{1}H or ^{13}C responses for any species. However, upon shaking mixtures of **2** and **7** with p-H$_2$, weak hyperpolarized hydride resonances are seen for both **2A** and **7A**, although only at 9% and 3% of the initial signal intensity of **2A**. One further consequence of this dramatic reduction in p-H$_2$ cycling is that no hyperpolarized ^{13}C responses are observed.

Isotopic labelling to improve $^{13}C_2$ enhancements and singlet lifetimes of iridium α-carboxyimine complex 1

Under SABRE the PHIP enhancement seen for the hydride ligands can transfer to coupled heteronuclear spins in a process that is magnetic field dependant.[26] Furthermore, as $^{13}C_2$ labelled pyruvate is used as a precursor, this transfer process could generate a singlet state in the product which is interesting because of its potentially long lifetime.[59] Here we aim to probe these effects further and detail how coupled spins in L may influence this outcome. In fact, it has already been reported that the p-H_2 derived singlet order in 1A and 2A can transfer into the $^{13}C_2$ spins of the carboxyimine core.[37] For SABRE, relaxation of a substrate when it is bound to the catalyst limits the degree of hyperpolarisation that can be created in the free ligand. This effect can be reduced by the inclusion of deuterium labels with the NHC ligand as this acts to increase bound substrate relaxation times and the visible lifetime of hyperpolarized signals.[26,40,56,57] Hence we link these approaches here to create the ^{2}H labelled analogues 1A-d_{14} and 1A-d_{38} of Chart 2 and test their hyperpolarisation properties. As expected, these complexes react with p-H_2 to yield good $^{13}C_2$ signal enhancements in the corresponding ^{13}C NMR experiments (Table 3). Furthermore, a singlet state lifetime of 19.9 ± 1.0 s (compared to 10.9 ± 1.1 s in the ^{1}H form) for 1A-d_{38} was determined. In contrast 1A-d_{14}, where the starting amine is deuterated, exhibits a similar lifetime to that of 1A (7.9 ± 0.9 s). Hence we can conclude interactions with the carbene ligand are critical to the resulting spin state lifetime.

It has previously been suggested that ^{13}C hyperpolarization levels can be increased by removing the effect of quadrupolar ^{14}N nuclei in related systems.[46] Therefore, a 1A-^{15}N-d_{24} isotopologue in which ^{15}N-labeled benzylamine and IMes-d_{24} were used as precursors was also prepared. The resulting $^{13}C_2$ NMR signal enhancements and magnetic state lifetime for this complex are now 750 fold and 17.5 ± 3.9 s respectively. This suggests that while the presence of ^{15}N does indeed enhance the level of ^{13}C polarization, it does not have a large effect on singlet state lifetime here. For this complex, a SABRE-SHEATH measurement was also undertaken to hyperpolarize the ^{15}N responses, this revealed strong signals for the bound imine and free amine, as detailed in the ESI.†
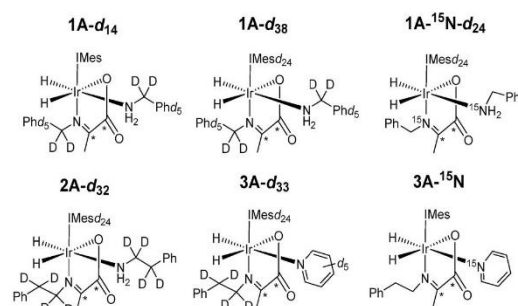
Effect of coligand, L, on $^{13}C_2$ enhancement levels and singlet spin order lifetime

In the corresponding ^{13}C experiments with added coligand, hyperpolarized responses for the $^{13}C_2$ labelled imine cores of 3A and 4A are readily visible at δ 174.79 and δ 167.71 ($J = 66.5$ Hz) and δ 175.63 and δ 166.76 ($J = 66.5$ Hz) respectively. These resonances partially overlap with those of 2A and appear with similar intensity in the case of 3A but are 17 times stronger in the case of 4A as shown in Fig. 4. The hyperpolarized $^{13}C_2$ resonances of 3A and 4A though no longer exhibit the original 'up–up–down–down' pattern typical of the singlet state.[37] This suggests that Zeeman magnetization is now dominant and that rapid singlet state decoherence occurs. In fact, shaking samples of 4A with p-H_2 at different polarization transfer fields yield a hyperpolarized $^{13}C_2$ response between 1 mG and 100 G, although the maximum signal intensity is seen at 65 G as shown in Fig. 4e. The spin states detected in these complexes can be the result of p-H_2 derived transfer within 3A or 4A, or from p-H_2 transfer within 2A and subsequent ligand loss and binding of the co-ligand.

There are three hyperpolarization p-H_2 derived proton transfer mechanisms that might operate in these complexes to enhance the signals of these ^{13}C nuclei and their efficiencies must be linked to the ligand exchange dynamics. The first of these transfer processes, R_1, is singlet magnetization transfer from p-H_2, and its efficiency should be independent of magnetic field.[59] The second, R_2 is direct polarization transfer to create ^{13}C Zeeman magnetization in a process known as SABRE-SHEATH that occurs at a mG field. Finally, Zeeman magnetization can also be relayed indirectly from the hydride ligands to ^{13}C via hyperpolarized ^{1}H sites in process, R_3, whose first step will be optimal at around 65 G.[26,39,56]

Previous work has shown that when mixtures containing solely 1 or 2 are shaken at 65 G, the resonance condition for R_1 is met alongside R_3 and long lived singlet state profiles dominate as previously reported.[37] The maintenance of this singlet in 1A and 2A is augmented during this process by on-going p-H_2 exchange, this effect is expected to be minimal in 3A and 4A due to their much slower H_2 loss rates.

When mixtures of 2 and 3 or 2 and 4 are shaken with p-H_2 at 65 G the ^{13}C response of 2A is dramatically reduced in the same way as their ^{1}H hydride signals. The corresponding ^{13}C signals for 3A and 4A appear as a mixture of both singlet and Zeeman magnetization as shown in Fig. 4a. The role played by 2A in the formation of 3A and 4A therefore results in singlet decoherence.

As deuterium labelling can enhance singlet state lifetimes and perhaps suppress singlet decoherence, we tested the effect of its incorporation on the spin-state lifetime of 3A by using phenethylamine-d_4, IMes-d_{24}, and pyridine-d_5 to create an equilibrium mixture of 2A-d_{32} and 3A-d_{33}. The resulting $^{13}C_2$ signals of both 2A-d_{32} and 3A-d_{33} after transfer at 65 G proved to be much stronger than their protio-analogues, as shown in Fig. 4b. Now, the balance in Zeeman and singlet magnetization (R_3 and R_1 processes) does indeed favour the latter and unusual ^{13}C signal behaviour is discerned. This is in part a consequence of the fact polarization no longer spreads into the coligand/

1A-d_{14} 1A-d_{38} 1A-^{15}N-d_{24}

2A-d_{32} 3A-d_{33} 3A-^{15}N

Chart 2 Structures of isotopologues used in this work.

Table 3 ^{1}H and ^{13}C signal enhancements (ε) and ^{13}C$_2$ singlet lifetimes of deuterated analogues

Complex	ε ^{1}H hydride/fold	ε ^{13}C$_2$ imine/fold	^{13}C$_2$ singlet lifetime/s
1A-d_{14}	110	510	7.9 ± 0.9
1A-d_{38}	300	560	19.9 ± 1.0
1A-^{15}N-d_{24}	480	750	17.5 ± 3.9
2A-d_{32}	740	340	N/A
2A/3A	N/A	**2A**, 220	N/A
		3A, 190	
2A-d_{32}/3A-d_{33}	**2A-d_{32}**, 720	**2A-d_{32}**, 330	N/A
	3A-d_{33}, 380	**3A-d_{33}**, 260	
		Pyridine, 0	
2A/3A-^{15}N	**2A**, 230	**2A**, 230	N/A
	3A-^{15}N, 390	**3A-^{15}N**, 260	
		Pyridine, 190	
1A-^{15}N-d_{24}/3A-^{15}N$_2$-d_{24}	**1A-^{15}N-d_{24}**, 1620	**2A** N/A^a	N/A
	3A-^{15}N$_2$-d_{24}, 590	**3A-^{15}N**, N/A^a	
		Pyridine, 870	

^{a} Spectral overlap prevents signal enhancements being calculated for each complex. Note pyridine enhancements include bound and free signals.

catalyst. However, ^{2}H labelling suppresses the indirect polarization transfer route R_3 which is *via* ^{1}H and must occur though the CH$_3$ group of the imine or the NH$_2$ group of the amine. Consequently, the singlet spin order of **3A-d_{33}** does not decohere rapidly. We repeated this process at 65 G before introducing a 5 second storage period in a mu metal shield before observation. The resulting signals for **3A-d_{33}** then lose much of their singlet character due to decoherence effects.

Synthesizing **3A** with ^{15}N-labeled pyridine to create **3A-^{15}N** results in a ^{13}C$_2$ profile that is more typical of a singlet state, as

shown in Fig. 4c. We demonstrated previously that while the introduction of this ^{15}N label in **1A-^{15}N-d_{24}** did increase signal strength, it did not significantly enhance the singlet state lifetime of **1A**. Now though, it significantly increases the singlet state retention in **3A-^{15}N** and confirms quadrupolar ^{14}N plays a major role in its relaxation.

When **3A-^{15}N$_2$-d_{24}** was studied, in which both pyridine and benzylamine precursors were ^{15}N labelled and the IMes catalyst was deuterated, the hyperpolarized profile after 10 second shaking at 65 G shown in Fig. 4d was obtained. However,
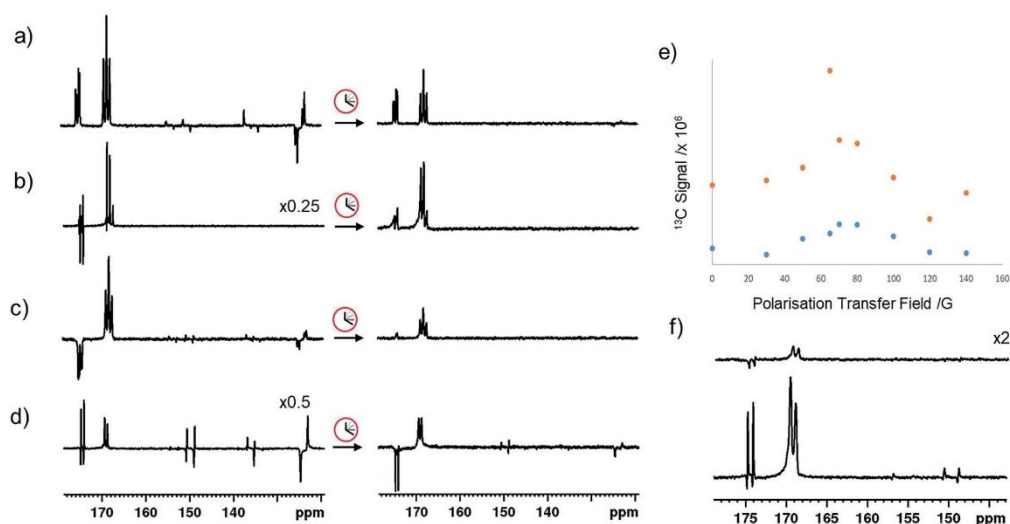
Fig. 4 Partial hyperpolarized ^{13}C spectra for equilibrium mixture of (a) **2A** and **3A**, (b) **2A-d_{32}** and **3A-d_{33}**, (c) **3A** and **3A-^{15}N** and (d) **1A-^{15}N-d_{24}** and **3A-^{15}N$_2$-d_{24}** shaken for 10 seconds at 65 G (left) and after storing in a mu metal shield for 5 seconds after 65 G shaking (right) (e) integrated hyperpolarized resonances for **4A** and **2A** as a function of polarization transfer field (f) hyperpolarized ^{13}C responses for an equilibrium mixture of **1A-^{15}N-d_{24}** and **3A-^{15}N$_2$-d_{24}** shaken for 10 seconds at 65 G and then stored in a mu metal shield for 30 seconds (top) and shaking in the shield for 5 seconds after 30 seconds storage time.

267

storage at this point in a mu metal shield for 10 seconds instead of proceeding directly to data collection now allows the singlet state product profile to be readily distinguished. Consequently, full ^{15}N labelling clearly extends the lifetime over which this product remains visible. However, when $3A$-$^{15}N_2$-d_{24} is first polarised for 10 seconds at 65 G before being left for 30 seconds in a mu metal shield before again shaking it for 5 seconds now in the shield (Fig. 4f) the measured signals are due predominantly to low field direct SABRE-SHEATH transfer (R_2) and outweigh any singlet state that remains.

Heteronuclear coligand enhancements of iridium α-carboxyimine complexes

The hyperpolarized ^{13}C resonances of bound and free pyridine that are also observed in $3A$, as shown in Fig. 4, are also worthy of comment. The significant 866-fold total ^{13}C enhancement of pyridine suggests that the incorporation of a chelating carboxyimine may reflect a positive route to increasing substrate polarization. In contrast no ^{13}C signals of the amine of $2A$ or the imidazole of $4A$ are visible. This suggests that the lifetime of pyridine in $3A$ is suitable for it to receive polarization from its hydride ligands whereas that of the amine is too short. For ^{15}N pyridine, the corresponding ^{1}H NMR total signal gains seen under these conditions are 1600-fold while for imidazole they are just 31-fold.

Interestingly, the hyperpolarized ^{13}C response for pyridine vanishes for $3A$-d_{33}, as shown in Fig. 4c. This confirms that under 65 G transfer the main route to ^{13}C signal gain is *via* the pyridine proton sites and any direct transfer, or indeed transfer *via* nitrogen is less important. $3A$-^{15}N does yield hyperpolarized ^{13}C pyridine responses but they are of lower intensity than those in $3A$, as shown in Fig. 4d. Hence, at this polarization transfer field there is no significant polarization relay *via* ^{15}N.[70]

Experimental

All NMR measurements were carried out on a 400 MHz Bruker Avance III spectrometer at 298 K unless otherwise stated. *para*-Hydrogen (p-H_2) was produced by passing hydrogen gas over a spin-exchange catalyst (Fe_2O_3) at 28 K and used for all hyperpolarization experiments. This method produces constant p-H_2 with *ca.* 93% purity. ^{1}H (400 MHz) and ^{13}C (100.6 MHz) NMR spectra were recorded with an internal deuterium lock. Chemical shifts are quoted as parts per million and referenced to CD_2Cl_2. ^{13}C NMR spectra were recorded with broadband proton decoupling. Coupling constants (J) are quoted in hertz. Electrospray high and low resolution mass spectra were recorded on a Bruker Daltronics microOTOF spectrometer. The coligands pyridine, imidazole, thiophene, acetonitrile, DMSO, benzyl isocyanide, ethylisothiocyanate and 4-chlorobenzenemethanethiol were all purchased from Sigma Aldrich, Fluorochem or Alfa-Aesar and used as supplied without further purification.

The shake & drop method was employed for recording hyperpolarized SABRE NMR spectra.[26] Samples were prepared in a 5 mm NMR tube that was fitted with a J. Young's tap. The

iridium precatalyst used was [IrCl(COD)(IMes)] (where IMes = 1,3-bis(2,4,6-trimethyl-phenyl)imidazole-2-ylidene and COD = *cis,cis*-1,5-cyclooctadiene) and was synthesized in our laboratory according to a literature procedure.[71] The NMR samples were subsequently degassed by two freeze–pump–thaw cycles before filling the tube with p-H_2 at 3 bar pressure. Once filled with p-H_2, the tubes were shaken vigorously for 10 seconds in the 65 Gauss fringe field of a 9.4 T Bruker spectrometer. Immediately after that, the NMR tubes were put inside the spectrometer for NMR detection. ^{1}H shake and drop measurements were recorded with a 45° pulse unless otherwise stated.

Hydride signal enhancements were calculated by dividing the hyperpolarized integral intensity by the corresponding intensity from a 1 scan thermal recorded and processed under the same conditions. Thermal 1,2-$^{13}C_2$ coordinated imine resonances were not visible in 1 thermal scan, so ^{13}C enhancements were calculated as shown in the ESI.† Hydrogen exchange rates and singlet state lifetimes were recorded as previously reported.[37] All characterisation data, kinetic modelling and DFT calculations are shown in the ESI.†

Formation of 1 and 2

3 bar hydrogen gas was added to a degassed solution of [IrCl(COD)(IMes)] (2 mg, 0.003 mmol; 1 equivalent) and $BnNH_2$ or phenethylamine (PEA) (1.8 μL or 2.0 μL, 0.015 mmol, 5 equivalents) (for 1 and 2 respectively) dissolved in 0.6 mL DCM-d_2. Upon the formation of [Ir(H)$_2$(IMes)(NH$_2$Bn)$_3$] the solution goes from yellow to colourless.[39] At this point sodium pyruvate-1,2-[$^{13}C_2$] (1.8 mg, 0.015 mmol, 5 equivalents) was dissolved in 40 μL H_2O and added to the NMR tube under a flow of N_2. The tube was repressurized with 3 bar p-H_2 and left overnight to allow the formation of an equilibrium mixture of 1 or 2 as previously reported.[37]

Formation of 3–8

1 μL (~5 equivalents relative to precatalyst) of the corresponding coligand (pyridine for 3, DMSO for 5, benzylisocyanide for 6, ethylisothiocyanate for 7 and 4-chlorobenzenemethanethiol for 8) was added to 2 under a flow of N_2 gas before the NMR tube was repressurised with 3 bar hydrogen gas. 4 was formed from the addition of 2 mg imidazole in 40 μL DCM-d_2 to 2 in the same manner.

Conclusions

In conclusion, we have synthesised a range of novel [Ir(H)$_2$(IMes)(α-$^{13}C_2$-carboxyimine)L] complexes in which the identity of the coligand L can be amine, pyridine, DMSO, benzyl isothiocyanide or ethyl isothiocyanate. In the latter two cases further reaction and sample degradation occurs to yield new products that include [Ir(H)$_2$(IMes)(EtSCN)$_2$(amine)]. Upon the addition of a thiol we observe and characterise the novel SH bond activated [Ir(H)(IMes)(α-$^{13}C_2$-carboxyimine)(S-thiolate)] product. When examined with *para*-hydrogen, complexes in which L is amine, pyridine or imidazole show significant ^{1}H hydride and $^{13}C_2$ imine signal enhancements. We have shown

268

that dissociative amine loss is a key step in the p-H_2 exchange process that leads to these signal enhancements. The coligands effectively trap the associated hyperpolarised intermediate $[Ir(H)_2(IMes)(\alpha\text{-}^{13}C_2\text{-carboxyimine})]$ to achieve this result. Despite this mechanism, the hyperpolarised hydride signal intensities are not always reflective of the rates of coligand binding to this intermediate. This is because hydride based hyperpolarisation flows into the ligands attached to the complex and therefore great care must be taken when attempting to interpret such signal intensity data in a quantitative fashion.

This study has also demonstrated how isotopic labelling techniques can be used to achieve $^{13}C_2$ signal enhancement levels of 750-fold whilst accessing singlet state lifetimes of up to 20 seconds. Coligand addition can though cause rapid decoherence of any resulting $^{13}C_2$ singlet order in these products, but it can be preserved to some extent by prudent isotopic labelling. Furthermore, the α-carboxyimine ligand acts to block exchangeable coordination sites with the result that significant ^{13}C enhancement can be seen in pyridine as p-H_2 hyperpolarisation is now directed efficiently into the co-ligand.

The strongly enhanced hydride resonances of the array of $[Ir(H)_2(IMes)(\alpha\text{-}^{13}C_2\text{-carboxyimine})L]$ complexes provide a unique response which means they can act as efficient sensors of the identity of L. Given this spectral region is normally transparent to ^1H NMR background signals the detection of trace compounds through these responses might subsequently reflect a key application of this work.

Conflicts of interest

There are no conflicts to declare.

Acknowledgements

References

1 J. H. Ardenkjær-Larsen, B. Fridlund, A. Gram, G. Hansson, L. Hansson, M. H. Lerche, R. Servin, M. Thaning and K. Golman, *Proc. Natl. Acad. Sci.*, 2003, **100**, 10158–10163.

2 S. Jannin, A. Bornet, R. Melzi and G. Bodenhausen, *Chem. Phys. Lett.*, 2012, **549**, 99–102.

3 C. R. Bowers and D. P. Weitekamp, *J. Am. Chem. Soc.*, 1987, **109**, 5541–5542.

4 T. C. Eisenschmid, R. U. Kirss, P. P. Deutsch, S. I. Hommeltoft, R. Eisenberg, J. Bargon, R. G. Lawler and A. L. Balch, *J. Am. Chem. Soc.*, 1987, **109**, 8089–8091.

5 R. Eisenberg, *Acc. Chem. Res.*, 1991, **24**, 110–116.

6 J. Hovener, A. N. Pravdivtsev, B. Kidd, C. R. Bowers, S. Glöggler, K. V. Kovtunov, M. Plaumann, R. Katz-Brull, K. Buckenmaier and A. Jerschow, *Angew. Chem.*, 2018, **57**, 11140–11162.

7 T. G. Walker and W. Happer, *Rev. Mod. Phys.*, 1997, **69**, 629.

8 A. Z. Lau, A. P. Chen, N. R. Ghugre, V. Ramanan, W. W. Lam, K. A. Connelly, G. A. Wright and C. H. Cunningham, *Magn. Reson. Med.*, 2010, **64**, 1323–1331.

9 S. J. DeVience, X. Lu, J. Proctor, P. Rangghran, E. R. Melhem, R. Gullapalli, G. M. Fiskum and D. Mayer, *Sci. Rep.*, 2017, **7**, 1907.

10 A. Esposito, A. Lukas, J. Meany and Y. Pocker, *Can. J. Chem.*, 1999, **77**, 1108–1117.

11 J. D. MacKenzie, Y.-F. Yen, D. Mayer, J. S. Tropp, R. E. Hurd and D. M. Spielman, *Radiology*, 2011, **259**, 414–420.

12 M. Marjańska, I. Iltis, A. A. Shestov, D. K. Deelchand, C. Nelson, K. Uğurbil and P.-G. Henry, *J. Magn. Reson.*, 2010, **206**, 210–218.

13 S. J. Nelson, J. Kurhanewicz, D. B. Vigneron, P. E. Larson, A. L. Harzstark, M. Ferrone, M. van Criekinge, J. W. Chang, R. Bok and I. Park, *Sci. Transl. Med.*, 2013, **5**, 198ra108.

14 M. Pourfathi, Y. Xin, S. J. Kadlecek, M. F. Cereda, H. Profka, H. Hamedani, S. M. Siddiqui, K. Ruppert, N. A. Drachman and J. N. Rajaei, *Magn. Reson. Med.*, 2017, **78**, 2106–2115.

15 P. Bhattacharya, E. Y. Chekmenev, W. H. Perman, K. C. Harris, A. P. Lin, V. A. Norton, C. T. Tan, B. D. Ross and D. P. Weitekamp, *J. Magn. Reson.*, 2007, **186**, 150–155.

16 N. M. Zacharias, H. R. Chan, N. Sailasuta, B. D. Ross and P. Bhattacharya, *J. Am. Chem. Soc.*, 2011, **134**, 934–943.

17 M. R. Clatworthy, M. I. Kettunen, D.-E. Hu, R. J. Mathews, T. H. Witney, B. W. Kennedy, S. E. Bohndiek, F. A. Gallagher, L. B. Jarvis and K. G. Smith, *Proc. Natl. Acad. Sci.*, 2012, **109**, 13374–13379.

18 T. Witney, M. Kettunen, D. Hu, F. Gallagher, S. Bohndiek, R. Napolitano and K. Brindle, *Br. J. Cancer*, 2010, **103**, 1400.

19 S. Fain, M. L. Schiebler, D. G. McCormack and G. Parraga, *J. Magn. Reson. Imaging*, 2010, **32**, 1398–1408.

20 Z. I. Cleveland, G. P. Cofer, G. Metz, D. Beaver, J. Nouls, S. S. Kaushik, M. Kraft, J. Wolber, K. T. Kelly and H. P. McAdams, *PLoS One*, 2010, **5**, e12192.

21 R. V. Shchepin, A. M. Coffey, K. W. Waddell and E. Y. Chekmenev, *J. Am. Chem. Soc.*, 2012, **134**, 3957–3960.

22 E. Y. Chekmenev, J. Hövener, V. A. Norton, K. Harris, L. S. Batchelder, P. Bhattacharya, B. D. Ross and D. P. Weitekamp, *J. Am. Chem. Soc.*, 2008, **130**, 4212–4213.

23 A. B. Schmidt, S. Berner, M. Braig, M. Zimmermann, J. Hennig, D. von Elverfeldt and J.-B. Hövener, *PLoS One*, 2018, **13**, e0200141.

24 F. Reineri, T. Boi and S. Aime, *Nat. Commun.*, 2015, **6**, 5858.

25 E. Cavallari, C. Carrera, S. Aime and F. Reineri, *J. Magn. Reson.*, 2018, **289**, 12–17.

26 R. W. Adams, J. A. Aguilar, K. D. Atkinson, M. J. Cowley, P. I. Elliott, S. B. Duckett, G. G. Green, I. G. Khazal, J. López-Serrano and D. C. Williamson, *Science*, 2009, **323**, 1708–1711.

27 P. J. Rayner and S. Duckett, *Angew. Chem.*, 2018, **57**, 6742–6753.

28 K. D. Atkinson, M. J. Cowley, S. B. Duckett, P. I. P. Elliott, G. G. R. Green, J. López-Serrano, I. G. Khazal and A. C. Whitwood, *Inorg. Chem.*, 2009, **48**, 663–670.

29 A. N. Pravdivtsev, A. V. Yurkovskaya, H.-M. Vieth and K. L. Ivanov, *Phys. Chem. Chem. Phys.*, 2014, **16**, 24672–24675.

269

30 S. S. Roy, G. Stevanato, P. J. Rayner and S. B. Duckett, *J. Magn. Reson.*, 2017, **285**, 55–60.

31 T. Theis, M. Truong, A. M. Coffey, E. Y. Chekmenev and W. S. Warren, *J. Magn. Reson.*, 2014, **248**, 23–26.

32 M. Fekete, O. Bayfield, S. B. Duckett, S. Hart, R. E. Mewis, N. Pridmore, P. J. Rayner and A. Whitwood, *Inorg. Chem.*, 2013, **52**, 13453–13461.

33 M. J. Cowley, R. W. Adams, K. D. Atkinson, M. C. Cockett, S. B. Duckett, G. G. Green, J. A. Lohman, R. Kerssebaum, D. Kilgour and R. E. Mewis, *J. Am. Chem. Soc.*, 2011, **133**, 6134–6137.

34 E. B. Dücker, L. T. Kuhn, K. Münnemann and C. Griesinger, *J. Magn. Reson.*, 2012, **214**, 159–165.

35 M. L. Truong, T. Theis, A. M. Coffey, R. V. Shchepin, K. W. Waddell, F. Shi, B. M. Goodson, W. S. Warren and E. Y. Chekmenev, *J. Phys. Chem. C*, 2015, **119**, 8786–8797.

36 P. Spannring, I. Reile, M. Emondts, P. P. Schleker, N. K. Hermkens, N. G. van der Zwaluw, B. J. van Weerdenburg, P. Tinnemans, M. Tessari and B. Blümich, *Chem.–Eur. J.*, 2016, **22**, 9277–9282.

37 B. J. Tickner, W. Iali, S. S. Roy, A. C. Whitwood and S. B. Duckett, *ChemPhysChem*, 2019, **20**, 241–245.

38 S. S. Roy, K. M. Appleby, E. J. Fear and S. B. Duckett, *J. Phys. Chem. Lett.*, 2018, **9**, 1112–1117.

39 W. Iali, P. J. Rayner, A. Alshehri, A. J. Holmes, A. J. Ruddlesden and S. B. Duckett, *Chem. Sci.*, 2018, **9**, 3677–3684.

40 P. J. Rayner, M. J. Burns, A. M. Olaru, P. Norcott, M. Fekete, G. G. Green, L. A. Highton, R. E. Mewis and S. B. Duckett, *Proc. Natl. Acad. Sci.*, 2017, 201620457.

41 J. F. Colell, A. W. Logan, Z. Zhou, R. V. Shchepin, D. A. Barskiy, G. X. Ortiz Jr, Q. Wang, S. J. Malcolmson, E. Y. Chekmenev and W. S. Warren, *J. Phys. Chem. C*, 2017, **121**, 6626–6634.

42 A. W. Logan, T. Theis, J. F. Colell, W. S. Warren and S. J. Malcolmson, *Chem.–Eur. J.*, 2016, **22**, 10777–10781.

43 K. Shen, A. W. Logan, J. F. Colell, J. Bae, G. X. Ortiz Jr, T. Theis, W. S. Warren, S. J. Malcolmson and Q. Wang, *Angew. Chem.*, 2017, **129**, 12280–12284.

44 T. Theis, G. X. Ortiz, A. W. Logan, K. E. Claytor, Y. Feng, W. P. Huhn, V. Blum, S. J. Malcolmson, E. Y. Chekmenev and Q. Wang, *Sci. Adv.*, 2016, **2**, e1501438.

45 S. Duckett, S. Roy, P. Norcott, P. J. Rayner and G. G. Green, *Chem.–Eur. J.*, 2017, **23**, 10496–10500.

46 D. A. Barskiy, R. V. Shchepin, C. P. Tanner, J. F. Colell, B. M. Goodson, T. Theis, W. S. Warren and E. Y. Chekmenev, *ChemPhysChem*, 2017, **18**, 1493–1498.

47 A. M. Olaru, T. B. Robertson, J. S. Lewis, A. Antony, W. Iali, R. E. Mewis and S. B. Duckett, *ChemistryOpen*, 2018, **7**, 97–105.

48 R. V. Shchepin, B. M. Goodson, T. Theis, W. S. Warren and E. Y. Chekmenev, *ChemPhysChem*, 2017, **18**(2), 1493–1498.

49 M. J. Burns, P. J. Rayner, G. G. Green, L. A. Highton, R. E. Mewis and S. B. Duckett, *J. Phys. Chem. B*, 2015, **119**, 5020–5027.

50 A. M. Olaru, A. Burt, P. J. Rayner, S. J. Hart, A. C. Whitwood, G. G. Green and S. B. Duckett, *Chem. Commun.*, 2016, **52**, 14482–14485.

51 N. Eshuis, N. Hermkens, B. J. van Weerdenburg, M. C. Feiters, F. P. Rutjes, S. S. Wijmenga and M. Tessari, *J. Am. Chem. Soc.*, 2014, **136**, 2695–2698.

52 N. Eshuis, B. J. van Weerdenburg, M. C. Feiters, F. P. Rutjes, S. S. Wijmenga and M. Tessari, *Angew. Chem.*, 2015, **54**, 1481–1484.

53 W. Iali, A. M. Olaru, G. G. R. Green and S. B. Duckett, *Chem.–Eur. J.*, 2017, **23**, 10491–10495.

54 A. Manoharan, P. J. Rayner, W. Iali, M. J. Burns, V. H. Perry and S. B. Duckett, *ChemMedChem*, 2018, **13**, 352–359.

55 D. A. Barskiy, L. A. Ke, X. Li, V. Stevenson, N. Widarman, H. Zhang, A. Truxal and A. Pines, *J. Phys. Chem. Lett.*, 2018, **9**, 2721–2724.

56 H. Zeng, J. Xu, J. Gillen, M. T. McMahon, D. Artemov, J.-M. Tyburn, J. A. Lohman, R. E. Mewis, K. D. Atkinson and G. G. Green, *J. Magn. Reson.*, 2013, **237**, 73–78.

57 A. J. Holmes, P. J. Rayner, M. J. Cowley, G. G. Green, A. C. Whitwood and S. B. Duckett, *Dalton Trans.*, 2015, **44**, 1077–1083.

58 S. S. Roy, P. J. Rayner, P. Norcott, G. G. Green and S. B. Duckett, *Phys. Chem. Chem. Phys.*, 2016, **18**, 24905–24911.

59 G. Pileio, M. Carravetta and M. H. Levitt, *Proc. Natl. Acad. Sci.*, 2010, **107**, 17135–17139.

60 E. Y. Chekmenev, V. A. Norton, D. P. Weitekamp and P. Bhattacharya, *J. Am. Chem. Soc.*, 2009, **131**, 3164–3165.

61 N. M. Shavaleev, F. Monti, R. D. Costa, R. Scopelliti, H. J. Bolink, E. Ortí, G. Accorsi, N. Armaroli, E. Baranoff, M. Grätzel and M. K. Nazeeruddin, *Inorg. Chem.*, 2012, **51**, 2263–2271.

62 N. M. Shavaleev, F. Monti, R. Scopelliti, A. Baschieri, L. Sambri, N. Armaroli, M. Grätzel and M. K. Nazeeruddin, *Organometallics*, 2013, **32**, 460–467.

63 G. R. Clark and G. J. Palenik, *Inorg. Chem.*, 1970, **9**, 2754–2760.

64 N. F. A. Cotton, W. R. Robinson, R. A. Walton and R. Whyman, *Inorg. Chem.*, 1967, **6**, 929–935.

65 C. M. Friend and D. A. Chen, *Polyhedron*, 1997, **16**, 3165–3175.

66 D. M. Antonelli and M. Cowie, *Inorg. Chem.*, 1990, **29**, 3339–3345.

67 L.-S. Wang, R. McDonald and M. Cowie, *Inorg. Chem.*, 1994, **33**, 3735–3744.

68 O. Halter, I. Fernández and H. Plenio, *Chem.–Eur. J.*, 2017, **23**, 711–719.

69 B. E. Kidd, J. L. Gesiorski, M. E. Gemeinhardt, R. V. Shchepin, K. V. Kovtunov, I. V. Koptyug, E. Y. Chekmenev and B. M. Goodson, *J. Phys. Chem. C*, 2018, **122**, 16848–16852.

70 N. V. Chukanov, O. G. Salnikov, R. V. Shchepin, A. Svyatova, K. V. Kovtunov, I. V. Koptyug and E. Y. Chekmenev, *J. Phys. Chem. C*, 2018, **122**, 23002–23010.

71 L. D. Vazquez-Serrano, B. T. Owens and J. M. Buriak, *Inorg. Chim. Acta*, 2006, **359**, 2786–2797.

270

Appendix 4

Hyperpolarising Pyruvate through Signal Amplification by Reversible Exchange (SABRE)

Wissam Iali[+], Soumya S. Roy[+], Ben J. Tickner, Fadi Ahwal, Aneurin J. Kennerley, and Simon B. Duckett*

Abstract: Hyperpolarisation methods that premagnetise agents such as pyruvate are currently receiving significant attention because they produce sensitivity gains that allow disease tracking and interrogation of cellular metabolism by magnetic resonance. Here, we communicate how signal amplification by reversible exchange (SABRE) can provide strong ^{13}C pyruvate signal enhancements in seconds through the formation of the novel polarisation transfer catalyst $[Ir(H)_2(\eta^2$-pyruvate)-(DMSO)(IMes)]$. By harnessing SABRE, strong signals for $[1$-$^{13}C]$- and $[2$-$^{13}C]pyruvate$ in addition to a long-lived singlet state in the $[1,2$-$^{13}C_2]$ form are readily created; the latter can be observed five minutes after the initial hyperpolarisation step. We also demonstrate how this development may help with future studies of chemical reactivity.

Pyruvate lies at the junction of many metabolic processes in living cells, being produced from glucose before it enters cellular energy production pathways.[1] Pyruvate is converted into lactate under the anaerobic conditions associated with cancer, offering a route to diagnose cellular abnormalities.[2] Clinical trials are progressing that harness this approach for the diagnosis of cancer by magnetic resonance imaging (MRI).[3] These developments build from decades of research into hyperpolarisation techniques such as dynamic nuclear polarisation (DNP),[4] the method that has allowed the hyperpolarisation and subsequent in vivo detection of such biomolecules by MRI.[3b,c,5]

Hyperpolarisation can also be created by parahydrogen (*p*-H₂) induced polarisation (PHIP). This approach utilises the reactivity and nuclear spin orientations of *p*-H₂ to create highly visible hydrogenation products.[6] Molecules hyper-

polarised using PHIP have been widely used in NMR spectroscopy, and there are examples that feature in vivo imaging.[5,6c,7] While pyruvate has no readily accessible unsaturated precursor suitable for hydrogenation using PHIP, Aime and co-workers have developed an elegant route to form aqueous solutions of hyperpolarised pyruvate by incorporation of a rapidly hydrogenated and subsequently hydrolysed side arm.[8]

Here though, we hyperpolarise pyruvate based on the non-hydrogenative PHIP derived signal amplification by reversible exchange (SABRE) process, which is shown in Figure 1.[9] The chemical identity of pyruvate is unaffected by this process, which has already achieved substantial levels of polarisation (63% in ¹H,[10] 25% in ¹³C,[11] and 43% in ¹⁵N[12]) in a range of materials that predominantly bind to a metal polarisation transfer catalyst through nitrogen centres.[13]
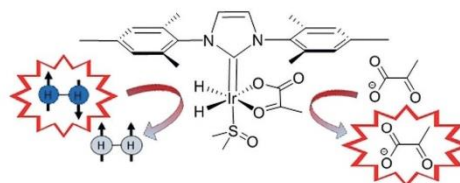
Figure 1. Schematic depiction of the SABRE hyperpolarisation process in which parahydrogen is used to hyperpolarise pyruvate via the polarisation transfer catalyst [Ir(H)₂(η²-pyruvate)(DMSO)(IMes)].

SABRE harnesses *p*-H₂, which is one of a growing range of molecules that exists as a nuclear spin singlet. When this molecule binds to a transition-metal centre to form a dihydride complex, it is possible to transfer polarisation from *p*-H₂ into a ligand if there are different hydrides coupling to the nucleus that receive it. The potentially long lifetime of such states makes them ideal fuels for polarisation transfer[14] or indeed later detection.[13a,c,15] *p*-H₂ can be formed in >95% purity by simply cooling H₂ gas to <40 K in the presence of a suitable conversion catalyst.[16]

In a remarkable development, Levitt and co-workers created a molecular spin singlet state by radiofrequency excitation in 2004,[17] and more recently demonstrated the existence of a coupled spin-1/2 nuclear ¹³C pair with a singlet-state lifetime that exceeds one hour.[18] Levitt created a 1,2-¹³C₂ singlet state in pyruvate using DNP[15b,19] that had a reported lifetime of 70 s. Here, we use SABRE to create pyruvate hyperpolarisation, including the singlet form of the

[*] Dr. W. Iali,[+] Dr. S. S. Roy,[+] B. J. Tickner, Dr. F. Ahwal,
Dr. A. J. Kennerley, Prof. Dr. S. B. Duckett
Centre for Hyperpolarisation in Magnetic Resonance (CHyM)
Department of Chemistry, University of York
Heslington, York, YO10 5NY (UK)
E-mail: simon.duckett@york.ac.uk
Dr. S. S. Roy[+]
Present address: Department of Inorganic and Physical Chemistry
Indian Institute of Science, Bangalore 560012 (India)

[+] These authors contributed equally to this work.

Supporting information and the ORCID identification number(s) for the author(s) of this article can be found under:
https://doi.org/10.1002/anie.201905483.

1,2-$^{13}C_2$ isotopologue in a process that proceeds spontaneously without the need for complex instrumentation or pulse sequences.

In order to achieve this goal, we first had to overcome the challenge of weak iridium pyruvate binding, which prevents typical hyperpolarisation of pyruvate using SABRE. The presence of an appropriate dimethyl sulfoxide (DMSO) co-ligand allows for the assembly of a highly reactive polarisation transfer catalyst that overcomes poor pyruvate ligation. This is achieved by the reaction of [Ir(Cl)(COD)(IMes)] (IMes = 1,3-bis(2,4,6-trimethylphenyl)imidazol-2-ylidene, COD = *cis,cis*-1,5-cyclooctadiene), the well-known SABRE catalyst precursor,[20] with DMSO, H_2, and sodium pyruvate to form [Ir(H)$_2$(η^2-pyruvate)(DMSO)(IMes)]. The resulting high-field NMR spectra and characterisation data that confirm this product formation are detailed in the Supporting Information, and its structure is represented in Figure 1. The [1-^{13}C]- (**1**), [2-^{13}C]- (**2**), and [1,2-$^{13}C_2$]-pyruvate (**3**) isotopologues of sodium pyruvate (**4**) are used in this work.

Because of the low symmetry of pyruvate, [Ir(H)$_2$(η^2-pyruvate)(DMSO)(IMes)] yields two inequivalent hydride ligands such that at low magnetic fields, an [AA′B] spin system is formed. Modelling the propagation of hyperpolarisation from the *p*-H_2-derived hydride ligands of this product into the bound pyruvate ^{13}C nuclei predicts optimum polarisation transfer at a magnetic field strength of $\pm(-J_{HH} + J_{HC^*})/\Delta\gamma$[13a,21] (see the Supporting Information). Here, J_{HH} corresponds to the J coupling between the hydride ligands, J_{HC^*} is $(J_{HC} + J_{H'C})/2$, the combined hydride–carbon cross-coupling in the complex, and $\Delta\gamma$ is the difference in magnetogyric ratios ($\gamma_H - \gamma_C$) of proton and carbon nuclei. The predicted field strengths are about 100 times lower than the Earth's natural magnetic field and were achieved experimentally by housing the sample in a mu-metal shield in conjunction with a field top-up solenoid as detailed in the Supporting Information.[22] This approach reflects a variant of SABRE that has been called SABRE-SHEATH.[22,23]

A sample of **1**, [IrCl(COD)(IMes)] precatalyst, and DMSO with 3 bar *p*-H_2 was therefore prepared. This was shaken in the mu-metal-shielded solenoid for 20 s at 9 mG. Upon transfer into a 9.4 T magnet, strongly hyperpolarised ^{13}C resonances corresponding to free pyruvate were observed. Subsequently, polarisation transfer between +20 to −21 mG confirmed that ±9 mG reflects the maximum signal intensity as portrayed by both Figure 2a and the model. An overall ^{13}C polarisation level of about 1% results for a sample containing [Ir(Cl)(COD)(IMes)] (5 mM), DMSO, and the corresponding pyruvate isotopologue in a 1:8:5 ratio after shaking with 3 bar of *p*-H_2 for 20 s. When a similar sample containing **2** was examined, the corresponding maximum polarisation level proved to be 0.6% when transfer took place at ±3 mG. This reduction in efficiency is due to a smaller $J_{^1H-^{13}C}$ transfer coupling and shorter spin-state lifetime (see Table 1), which results in more efficient signal decay during the slow polarisation transfer step.[24] Close examination of the hyperpolarised ^{13}C NMR spectra of **1** and **2** revealed peaks for catalyst-bound pyruvate in [Ir(H)$_2$(η^2-pyruvate)(DMSO)-(IMes)] and [1,2-$^{13}C_2$]pyruvate (**3**) as illustrated in Figure 2b. The detection of **3**, present at 1.1% natural abundance,
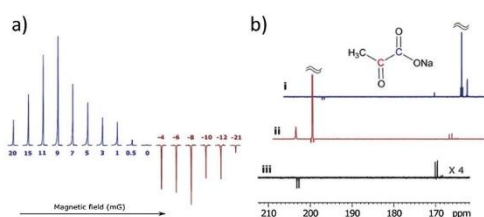
Figure 2. SABRE-hyperpolarised NMR spectra of pyruvate. A) Plot showing how the intensity of the ^{13}C NMR response of **1** varies with the magnetic field that the sample experiences during polarisation transfer; maximum polarisation transfer efficiency (signal intensity) is achieved with a ca. 9 mG field. B) SABRE-hyperpolarised ^{13}C NMR spectra of i) **1** and ii) **2** after transfer in a 5 mG mixing field, which show strongly enhanced signals from the labelled carbon atoms. These spectra also reveal a singlet response originating from the 1.1% of **3** present; iii) corresponding spectrum of **1** after hyperpolarisation transfer in the Earth's field (ca. 500 mG), which selects signals from **3**.

Table 1: Hyperpolarisation levels and lifetimes for isotopologues **1–4**.

Substrate	Net ^{13}C polarisation [%]	Thermally polarised lifetimes T_1 [s]	Hyperpolarised lifetimes T_1 and T_{LLS} [s]
1	C_1: 0.96	C_1: 35.4 ± 0.5	C_1 T_1: 32.5 ± 4.7
2	C_2: 0.60	C_2: 20.1 ± 0.5	C_2 T_1: 18.2 ± 3.0
3	C_1: 1.85	C_1: 33.6 ± 0.5	T_{LLS} (HF): 43.5 ± 0.8
	C_2: 1.65	C_2: 21.2 ± 0.4	T_{LLS} (LF): 85.4 ± 8.5
4	C_1: 0.55	C_1: 31.4 ± 1.2	C_1 T_1: 28.5 ± 5.5
	C_2: 0.35	C_2: 8.6 ± 1.5	C_2 T_1: 15.7 ± 1.9
	C_3: 0.22	C_3: 3.3 ± 0.7	C_3 T_1: 3.0 ± 2.5

confirms the impressive nature of the signal amplification that is achieved. The ^{13}C relaxation times and polarisation levels of these species are detailed in Table 1.[15b,19] Values of 32.5 ± 4.7 s and 18.2 ± 3.0 s were obtained, respectively, for the in high-field relaxation times of the ^{13}C signals of **1** and **2**, which are close to the normal values of 35.4 ± 0.5 s and 20.1 ± 0.5 s, respectively. Hence, the presence of the SABRE catalyst in these solutions does not significantly change their value. This reflects the fact that magnetisation build up by this catalyst is slow due to slow ligand exchange and small propagating J_{HC} values, which differs from the typical response achieved when nitrogen-containing heterocycles are examined.[10,25]

In contrast to the situation with **1** and **2**, isotopomer **3** is predicted to give a singlet-based response after polarisation transfer between 0 G and 1 kG (Figure 3 a,b).[13a] This reflects the fact that the metal dihydride complex that results is now of the [AA′BB′] type at low field.[22] This prediction was confirmed experimentally by monitoring the effect of excitation angle on the resulting signal profile as shown in Figure 3c,d. A close fit between the experimental and predicted data is observed. Furthermore, the singlet state forms with an amplitude that is 1740 times larger than the normal Zeeman polarisation observed in this sample when detected at 11.75 T, which reflects a purity of 1.75% relative to it; the sample contained [Ir(Cl)(COD)(IMes)] (5 mM), DMSO, and **3** in a ratio of 1:8:5. The lifetime of this
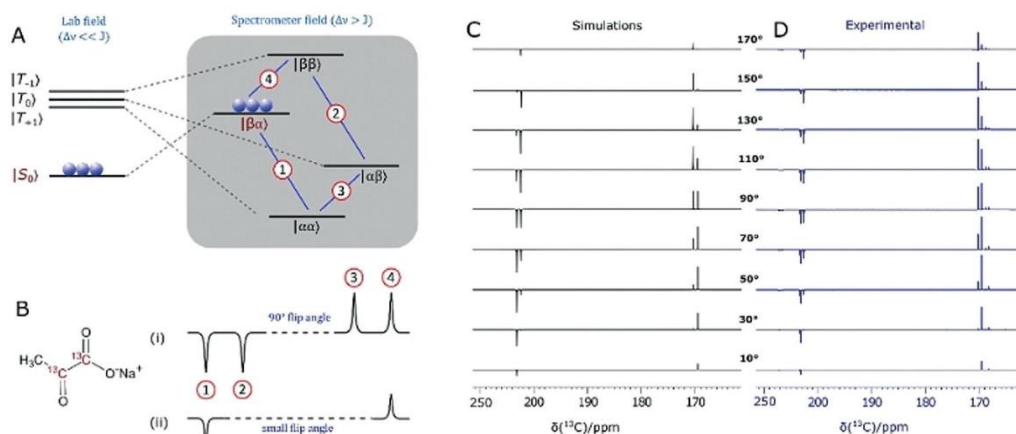
Figure 3. Demonstrating singlet character. A) Energy level diagram for the evolution of the two spin-1/2 1,2-$^{13}C_2$ coupled spin system of **3** after hyperpolarisation and sample movement from low (left) to high field (right). B) Simulated NMR spectra resulting from i) 90° and ii) low flip angle excitations. C) Simulated and D) experimentally observed ^{13}C NMR signal patterns for **3** after transfer in the Earth's field (ca. 500 mG) as a function of flip angle pulse duration (10° to 170° in steps of 20°) to confirm singlet state formation.
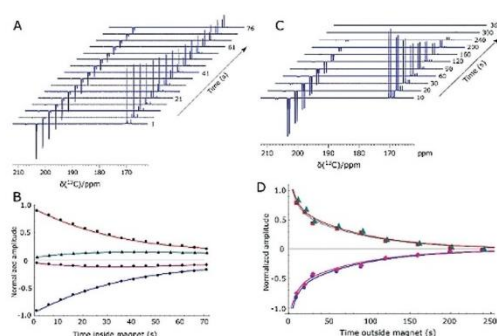
Figure 4. Determination of singlet lifetime. A) Series of hyperpolarised ^{13}C NMR spectra of **3** acquired 1 s to 76 s after sample insertion into the spectrometer with a 9° flip angle pulse. B) The corresponding signal intensity plot whose fitting (solid lines) yields a high-field (HF) lifetime, T_{LLS}, of 43.5 ± 0.8 s. Similar data is shown in (C) and (D) after sample storage at 0.5 G (LF) time. These points yield a T_{LLS} (LF) value of 85.4 ± 8.5 s.

magnetisation was assessed after sample storage at both low and high field as a function of catalyst loading (see typical plots in Figure 4). These high-field observations (Figure 4a) indicate that cross-relaxation-induced polarisation transfer occurs within the spin system during this period that makes the originally weaker resonance components increase in intensity (Figure 4b). The corresponding magnetic state lifetime is 85.4 ± 8.5 s with low-field storage (0.5 G) but at 11.7 T it is reduced to 43.5 ± 0.8 s as a consequence of the change in characteristics of the underlying spin states. Consequently, harnessing states that start out as a singlet, rather than the quicker relaxing Zeeman terms, may improve the duration of signal visibility. This may provide interesting

applications for SABRE hyperpolarised pyruvate. While the polarisation levels that we demonstrate here are not as high as those that have been reported using PHIP-SAH[8] and DNP,[1,3b,c,19,26] this route can create singlet hyperpolarisation in a refreshable, lower-cost alternative technique that may provide significant advantages in the future.

We demonstrate in Figure 5 that in vitro MRI detection of a 0.4 mM sample of **3** in a 70:30 $D_2O/[D_6]$ethanol mixture is possible. We also show a future potential use in hyperpolarised reaction monitoring in Figure 6. Here, hydrogen peroxide is added to a solution of SABRE-hyperpolarised **3** in 70:30 $D_2O/[D_6]$ethanol, and signals for hyperpolarised etha-
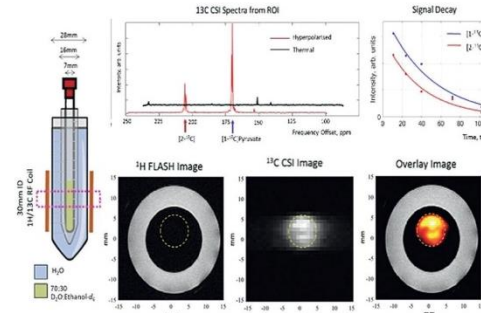
Figure 5. Hyperpolarised image detection. Hyperpolarised ^{13}C FLASH image (orange) overlaid onto a ^1H FLASH image of water (white outer ring) originating from the sample (left). The ^{13}C CSI image reflects a 32×32 mm region of this hyperpolarised solution at 1 mm resolution. The data was collected at 9.4 T using single-shot FLASH and EPI measurements and confirms that MRI detection is possible with these enhancement levels.
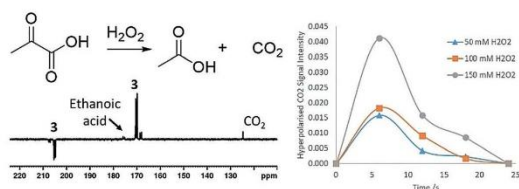
Figure 6. Hyperpolarised reaction monitoring. Resonances corresponding to ethanoic acid and CO_2 appear after the addition of H_2O_2 to solutions of SABRE-hyperpolarised pyruvate. This reaction was monitored by recording a series of hyperpolarised ^{13}C NMR spectra.

noic acid and carbon dioxide are seen, which encode concentration changes that take place over 25 s.

In conclusion, we have presented an approach to hyperpolarise pyruvate directly by SABRE in just a few seconds. This simple process harnesses a solenoid housed within a mu-metal shield to optimise the polarisation transfer pathway within a novel $[Ir(H)_2(\eta^2\text{-pyruvate})(IMes)(DMSO)]$ catalyst. The hyperpolarised ^{13}C signals appear with intensities that are three orders of magnitude above their thermal values. Furthermore, when $[1,2\text{-}^{13}C_2]$pyruvate is employed, the ready formation of a long-lived singlet state with a low field lifetime of 85.4 ± 8.5 s is achieved. We demonstrate that these polarisation levels allow in vitro images to be collected of a 70:30 $D_2O/[D_6]$ethanol mixture and a simple organic transformation to be viewed. We expect that the signal gain can be improved by optimisation of the ligand exchange processes within the polarisation transfer catalyst and by using higher pressures of $p\text{-}H_2$ with continuous bubbling.[22,27] Furthermore, it is clear that the ligand sphere of the metal catalyst controls substrate binding. We therefore expect further refinements of this "co-ligand" approach to extend SABRE to a much wider range of substrates that bind through oxygen or nitrogen. Hence this work reflects an important step in the future development of SABRE.

Acknowledgements

Conflict of interest

W.I., S.S.R., B.J.T., and S.B.D. are inventors on a University of York patent application on this work (Patent No. GB1818171.9, filed 7 November 2018).

How to cite: *Angew. Chem. Int. Ed.* **2019**, *58*, 10271–10275
Angew. Chem. **2019**, *131*, 10377–10381

[1] L. R. Gray, S. C. Tompkins, E. B. Taylor, *Cell. Mol. Life Sci.* **2014**, *71*, 2577–2604.

[2] F. Hirschhaeuser, U. G. A. Sattler, W. Mueller-Klieser, *Cancer Res.* **2011**, *71*, 6921–6925.

[3] a) D. Saslow, C. Boetes, W. Burke, S. Harms, M. O. Leach, C. D. Lehman, E. Morris, E. Pisano, M. Schnall, S. Sener, *Ca-Cancer J. Clin.* **2007**, *57*, 75–89; b) S. J. Nelson, J. Kurhanewicz, D. B. Vigneron, P. E. Z. Larson, A. L. Harzstark, M. Ferrone, M. van Criekinge, J. W. Chang, R. Bok, I. Park, G. Reed, L. Carvajal, E. J. Small, P. Munster, V. K. Weinberg, J. H. Ardenkjaer-Larsen, A. P. Chen, R. E. Hurd, L.-I. Odegardstuen, F. J. Robb, J. Tropp, J. A. Murray, *Sci. Transl. Med.* **2013**, *5*, 198ra108; c) J. T. Grist, M. A. McLean, F. Riemer, R. F. Schulte, S. S. Deen, F. Zaccagna, R. Woitek, C. J. Daniels, J. D. Kaggie, T. Matys, *NeuroImage* **2019**, *189*, 171–179.

[4] J. H. Ardenkjaer-Larsen, B. Fridlund, A. Gram, G. Hansson, L. Hansson, M. H. Lerche, R. Servin, M. Thaning, K. Golman, *Proc. Natl. Acad. Sci. USA* **2003**, *100*, 10158–10163.

[5] K. Golman, R. in't Zandt, M. Lerche, R. Pehrson, J. H. Ardenkjaer-Larsen, *Cancer Res.* **2006**, *66*, 10855–10860.

[6] a) C. R. Bowers, D. P. Weitekamp, *J. Am. Chem. Soc.* **1987**, *109*, 5541–5542; b) T. C. Eisenschmid, R. U. Kirss, P. P. Deutsch, S. I. Hommeltoft, R. Eisenberg, J. Bargon, R. G. Lawler, A. L. Balch, *J. Am. Chem. Soc.* **1987**, *109*, 8089–8091; c) E. Y. Chekmenev, J. Hovener, V. A. Norton, K. Harris, L. S. Batchelder, P. Bhattacharya, B. D. Ross, D. P. Weitekamp, *J. Am. Chem. Soc.* **2008**, *130*, 4212–4213.

[7] P. Bhattacharya, E. Y. Chekmenev, W. H. Perman, K. C. Harris, A. P. Lin, V. A. Norton, C. T. Tan, B. D. Ross, D. P. Weitekamp, *J. Magn. Reson.* **2007**, *186*, 150–155.

[8] E. Cavallari, C. Carrera, M. Sorge, G. Bonne, A. Muchir, S. Aime, F. Reineri, *Sci. Rep.* **2018**, *8*, 8366.

[9] R. W. Adams, J. A. Aguilar, K. D. Atkinson, M. J. Cowley, P. I. P. Elliott, S. B. Duckett, G. G. R. Green, I. G. Khazal, J. Lopez-Serrano, D. C. Williamson, *Science* **2009**, *323*, 1708–1711.

[10] P. J. Rayner, M. J. Burns, A. M. Olaru, P. Norcott, M. Fekete, G. G. R. Green, L. A. R. Highton, R. E. Mewis, S. B. Duckett, *Proc. Natl. Acad. Sci. USA* **2017**, *114*, E3188–E3194.

[11] D. A. Barskiy, R. V. Shchepin, C. P. N. Tanner, J. F. P. Colell, B. M. Goodson, T. Theis, W. S. Warren, E. Y. Chekmenev, *ChemPhysChem* **2017**, *18*, 1493–1498.

[12] B. E. Kidd, J. L. Gesiorski, M. E. Gemeinhardt, R. V. Shchepin, K. V. Kovtunov, I. V. Koptyug, E. Y. Chekmenev, B. M. Goodson, *J. Phys. Chem. C* **2018**, *122*, 16848–16852.

[13] a) T. Theis, G. X. Ortiz, A. W. Logan, K. E. Claytor, Y. Feng, W. P. Huhn, V. Blum, S. J. Malcolmson, E. Y. Chekmenev, Q. Wang, W. Warren, *Sci. Adv.* **2016**, *2*, e1501438; b) W. Iali, P. J. Rayner, S. B. Duckett, *Sci. Adv.* **2018**, *4*, eaao6250; c) D. A. Barskiy, R. V. Shchepin, A. M. Coffey, T. Theis, W. S. Warren, B. M. Goodson, E. Y. Chekmenev, *J. Am. Chem. Soc.* **2016**, *138*, 8080–8083; d) J. F. P. Colell, A. W. J. Logan, Z. J. Zhou, R. V. Shchepin, D. A. Barskiy, G. X. Ortiz, Q. Wang, S. J. Malcolmson, E. Y. Chekmenev, W. S. Warren, T. Theis, *J. Phys. Chem. C* **2017**, *121*, 6626–6634; e) Z. Zhou, J. Yu, J. F. P. Colell, R. Laasner, A. W. Logan, D. A. Barskiy, R. V. Shchepin, E. Y. Chekmenev, V. Blum, W. S. Warren, *J. Phys. Chem. Lett.* **2017**, *8*, 3008–3014; f) N. Eshuis, R. L. E. G. Aspers, B. J. A. van Weerdenburg, M. C. Feiters, F. P. J. T. Rutjes, S. S. Wijmenga, M. Tessari, *Angew. Chem. Int. Ed.* **2015**, *54*, 14527–14530; *Angew. Chem.* **2015**, *127*, 14735–14738; g) S. Knecht, A. S. Kiryutin, A. V. Yurkovskaya, K. L. Ivanov, *J. Magn. Reson.* **2018**, *287*, 10–14; h) P. Spannring, I. Reile, M. Emondts, P. P. M. Schleker, N. K. J. Hermkens, N. G. J. van der Zwaluw, B. J. A. van Weerdenburg, P. Tinnemans, M. Tessari, B. Blumich, F. Rutjes, M. C. Feiters, *Chem.*

Eur. J. **2016**, *22*, 9277–9282; i) S. S. Roy, K. M. Appleby, E. J. Fear, S. B. Duckett, *J. Phys. Chem. Lett.* **2018**, *9*, 1112–1117.

[14] R. Eisenberg, *Acc. Chem. Res.* **1991**, *24*, 110–116.

[15] a) P. R. Vasos, A. Comment, R. Sarkar, P. Ahuja, S. Jannin, J. P. Ansermet, J. A. Konter, P. Hautle, B. van den Brandt, G. Bodenhausen, *Proc. Natl. Acad. Sci. USA* **2009**, *106*, 18469–18473; b) M. C. D. Tayler, I. Marco-Rius, M. I. Kettunen, K. M. Brindle, M. H. Levitt, G. Pileio, *J. Am. Chem. Soc.* **2012**, *134*, 7668–7671; c) S. S. Roy, P. J. Rayner, P. Norcott, G. G. R. Green, S. B. Duckett, *Phys. Chem. Chem. Phys.* **2016**, *18*, 24905–24911; d) S. S. Roy, P. Norcott, P. J. Rayner, G. G. R. Green, S. B. Duckett, *Chem. Eur. J.* **2017**, *23*, 10496–10500; e) K. Shen, A. W. J. Logan, J. F. P. Colell, J. Bae, G. X. Ortiz, Jr., T. Theis, W. S. Warren, S. J. Malcolmson, Q. Wang, *Angew. Chem. Int. Ed.* **2017**, *56*, 12112–12116; *Angew. Chem.* **2017**, *129*, 12280–12284; *Angew. Chem.* **2017**, *129*, 12280–12284.

[16] a) S. Wagner, *Magn. Reson. Mater. Phys. Biol. Med.* **2014**, *27*, 195–199; b) D. Canet, C. Aroulanda, P. Mutzenhardt, S. Aime, R. Gobetto, F. Reineri, *Concepts Magn. Reson. Part A* **2006**, *28*, 321–330; c) P. M. Richardson, R. O. John, A. J. Parrott, P. J. Rayner, W. Iali, A. Nordon, M. E. Halse, S. B. Duckett, *Phys. Chem. Chem. Phys.* **2018**, *20*, 26362–26371.

[17] M. Carravetta, O. G. Johannessen, M. H. Levitt, *Phys. Rev. Lett.* **2004**, *92*, 153003.

[18] G. Stevanato, J. T. Hill-Cousins, P. Hakansson, S. S. Roy, L. J. Brown, R. C. D. Brown, G. Pileio, M. H. Levitt, *Angew. Chem. Int. Ed.* **2015**, *54*, 3740–3743; *Angew. Chem.* **2015**, *127*, 3811–3814.

[19] I. Marco-Rius, M. C. D. Tayler, M. I. Kettunen, T. J. Larkin, K. N. Timm, E. M. Serrao, T. B. Rodrigues, G. Pileio, J. H. Ardenkjaer-Larsen, M. H. Levitt, K. M. Brindle, *NMR Biomed.* **2013**, *26*, 1696–1704.

[20] M. J. Cowley, R. W. Adams, K. D. Atkinson, M. C. R. Cockett, S. B. Duckett, G. G. R. Green, J. A. B. Lohman, R. Kerssebaum,

D. Kilgour, R. E. Mewis, *J. Am. Chem. Soc.* **2011**, *133*, 6134–6137.

[21] R. V. Shchepin, M. L. Truong, T. Theis, A. M. Coffey, F. Shi, K. W. Waddell, W. S. Warren, B. M. Goodson, E. Y. Chekmenev, *J. Phys. Chem. Lett.* **2015**, *6*, 1961–1967.

[22] M. L. Truong, T. Theis, A. M. Coffey, R. V. Shchepin, K. W. Waddell, F. Shi, B. M. Goodson, W. S. Warren, E. Y. Chekmenev, *J. Phys. Chem. C* **2015**, *119*, 8786–8797.

[23] a) R. V. Shchepin, D. A. Barskiy, A. M. Coffey, T. Theis, F. Shi, W. S. Warren, B. M. Goodson, E. Y. Chekmenev, *ACS Sens.* **2016**, *1*, 640–644; b) T. Theis, M. L. Truong, A. M. Coffey, R. V. Shchepin, K. W. Waddell, F. Shi, B. M. Goodson, W. S. Warren, E. Y. Chekmenev, *J. Am. Chem. Soc.* **2015**, *137*, 1404–1407.

[24] R. V. Shchepin, L. Jaigirdar, E. Y. Chekmenev, *J. Phys. Chem. C* **2018**, *122*, 4984–4996.

[25] a) P. Norcott, M. J. Burns, P. J. Rayner, R. E. Mewis, S. B. Duckett, *Magn. Reson. Chem.* **2018**, *56*, 663–671; b) R. W. Adams, S. B. Duckett, R. A. Green, D. C. Williamson, G. G. R. Green, *J. Chem. Phys.* **2009**, *131*, 194505.

[26] a) M. J. Albers, R. Bok, A. P. Chen, C. H. Cunningham, M. L. Zierhut, V. Y. Zhang, S. J. Kohler, J. Tropp, R. E. Hurd, Y.-F. Yen, S. J. Nelson, D. B. Vigneron, J. Kurhanewicz, *Cancer Res.* **2008**, *68*, 8607–8615; b) J. H. Ardenkjær-Larsen, S. Bowen, J. R. Petersen, O. Rybalko, M. S. Vinding, M. Ullisch, N. C. Nielsen, *Magn. Reson. Med.* **2019**, *81*, 2184–2194.

[27] a) R. E. Mewis, K. D. Atkinson, M. J. Cowley, S. B. Duckett, G. G. R. Green, R. A. Green, L. A. R. Highton, D. Kilgour, L. S. Lloyd, J. A. B. Lohman, *Magn. Reson. Chem.* **2014**, *52*, 358–369; b) S. Lehmkuhl, M. Wiese, L. Schubert, M. Held, M. Küppers, M. Wessling, B. Blümich, *J. Magn. Reson.* **2018**, *291*, 8–13.

Appendix 5

Check for updates

Mechanistic insight into novel sulfoxide containing SABRE polarisation transfer catalysts†‡

Ben. J. Tickner, [ID] [a] Jennifer S. Lewis, [ID] [a] Richard O. John, [ID] [a] Adrian C. Whitwood [ID] [b] and Simon B. Duckett [ID] *[a]

Signal Amplification By Reversible Exchange (SABRE) is a hyperpolarisation technique that commonly uses [Ir(H)$_2$(carbene)(substrate)$_3$]Cl complexes to catalytically transfer magnetisation from *para*-hydrogen derived hydride ligands to coordinated substrates. Here, we explore the reactivity of a novel class of such catalysts based on sulfoxide containing [IrCl(H)$_2$(carbene)(DMSO)$_2$], which are involved in the hyperpolarisation of pyruvate using SABRE. We probe the reactivity of this species by NMR and DFT and upon reaction with sodium pyruvate establish the formation of two isomers of [Ir(H)$_2$(η^2-pyruvate)(DMSO)(IMes)]. Studies with related disodium oxalate yield [Ir$_2$(H)$_4$(IMes)$_2$(DMSO)$_2$(η^2-κ^2-Oxalate)] that is characterised by NMR and X-ray diffraction.

Introduction

Small molecule bond activation is an important area of inorganic chemistry that finds a central role in a range of applications in biochemistry,[1] recycling,[2] and organic synthesis.[3] In fact, many rather inert reagents such as CO$_2$[4] and R$_3$CH[5] can be activated by light[6] or transition metal systems.[7,8] The activation of small homonuclear diatomic molecules such as H$_2$ and O$_2$ by oxidative addition to metal centres has been known for many years.[9,10] It typically occurs *via* a concerted mechanism wherein the newly introduced groups are located in a *cis* relationship.[11] Activation of more polar molecules such as CH$_3$I is, however, more often complex and this difference is revealed in the *trans* relationship between the two newly introduced groups.[9] Orbital overlap effects during H$_2$ addition, as revealed through density function theory (DFT), are also complex with repulsive interactions between filled orbitals on the metal and H$_2$ yielding a barrier to the oxidative addition process that must be overcome.[12]

Many catalytic processes exploit the oxidative addition of H$_2$ to a transition metal centre by enabling the subsequent transfer of the two hydrogen atoms into an unsaturated centre[13,14] However, recent examples in main group chemistry involving frustrated Lewis pairs mean that direct addition is

also possible.[15] Understanding of these reactions can be improved by exploiting a technique known as *para*-Hydrogen Induced Polarisation (PHIP) to detect reaction intermediates.[16,17] This process incorporates the two protons of a single *para*-hydrogen (*p*-H$_2$) molecule into a substrate *via* a hydrogenation reaction to see the PHIP effect. *p*-H$_2$ is a spin isomer of H$_2$ and exists as a singlet state with a nuclear spin order of zero. H$_2$ gas can be enriched (>98%) in its *para* state by simply cooling it in the presence of a paramagnetic catalyst such as Fe$_2$O$_3$ or activated charcoal.[18-20] If the spin orientation of *p*-H$_2$ survives the ensuing hydrogenation reaction the NMR properties of the product can be harvested to increase product detectability. This effect was exemplified in 1986 by Bowers and Weitekamp[21,22] with Eisenberg and Bargon[23,24] producing similar independent observations around the same time. As the net nuclear spin of *p*-H$_2$ is zero it is invisible to an NMR experiment but once the symmetry of its two protons is broken the resulting spin order can be detected. In fact, the NMR signal intensity of the now NMR visible, and hyperpolarised, product is derived from the resulting large non-Boltzmann populations that lie across its nuclear spin energy levels. Since its introduction PHIP has been used to detect low concentration analytes and true intermediates in the field of catalysis.[22,25-27] Excitement has resulted from the hydrogenation of some unsaturated clinical agents which has led to their *in vivo* MRI detection.[28-30]

Since 2009, the *p*-H$_2$ based method Signal Amplification By Reversible Exchange (SABRE) has been used to harness signal gains from *p*-H$_2$ without the need for the direct hydrogenation of a substrate (sub).[31] It achieves the catalytic transfer of magnetisation into a substrate through the formation of a *J*-coupled network within the associated catalyst.[32] The first

Dalton Transactions

step in SABRE typically involves the conversion of a stable 16 electron precursor such as [IrCl(COD)(IMes)] (**1**) (where IMes = 1,3-bis(2,4,6-trimethylphenyl)imidazol-2-ylidene and COD = *cis,cis*-1,5-cyclooctadiene) into an intermediate [Ir(COD)(IMes)(sub)]Cl which then undergoes hydrogen addition to form highly reactive [Ir(H)$_2$(COD)(IMes)(sub)]Cl.[33–35] Subsequent hydrogenation of the COD ligand then leads to a SABRE catalyst such as [Ir(H)$_2$(IMes)(sub)$_3$]Cl which importantly reversibly binds both H$_2$ and sub. In SABRE, H$_2$ addition to square planar [Ir(COD)(IMes)(Sub)]Cl typically occurs over the COD-Ir-Sub axis rather than the COD-Ir-IMes axis.[36] This observation has been explained in terms of both reduced steric interactions with the bulky carbene ligand and electronic effects in terms of orbital interactions.[36] It has been suggested that H$_2$ addition is favoured over axis containing ligands with π acceptor orbitals which provide additional stabilising interactions as the geometry of the complex changes during the addition step.[37]

The most common substrate molecules used in SABRE have proven to feature *N*-donor sites that readily coordinate to iridium. *N*-Heterocycles such as pyridine,[31,38–41] nicotinamides,[31,42,43] pyrazines,[39,40] and pyrazoles[41] reflect common examples although other *N*-functionalities found in nitriles[44] and amines[45] have been used. It has recently been reported that in the presence of a stabilising sulfoxide coligand, the reversible coordination and subsequent hyperpolarisation of oxygen ligating pyruvate can occur.[46]

The direct hyperpolarisation of pyruvate was made possible in this case by the formation of the novel polarization transfer catalyst [Ir(H)$_2$(η^2-pyruvate)(DMSO)(IMes)]. In addition to this active catalyst, [IrCl(H)$_2$(DMSO)$_2$(IMes)], is also present in solution and is expected to be critical in improving the efficiency of this important hyperpolarisation transfer process. In this work we investigate the formation, behaviour, and ligand exchange processes exhibited by this sulfoxide containing polarisation transfer catalyst. We do this in solvents that were purchased from Sigma and used without further purification as our aim is to study reactivity without taking any special precautions. This is reflective of the most likely scenario when used by the non-specialist. We extend this method to include an examination of the behaviour of oxalate with the aim of developing the range of materials that can be hyperpolarised with sulfoxide containing SABRE polarisation transfer catalysts.

Results and discussion

Formation of [Ir(COD)(IMes)(OH$_2$)]Cl (2) from [IrCl(COD)(IMes)] (1)

When the SABRE precatalyst [IrCl(COD)(IMes)] (**1**) is dissolved in 0.6 mL of methanol-d_4 at 298 K, ^{1}H NMR resonances can be observed for **1** in addition to a minor product, **2** which forms at the ~2% level. The ratio of this product increases to 13% after the addition of 50 μL H$_2$O, as shown in Fig. 1 thereby confirming a role of the original H$_2$O contaminant in metha-
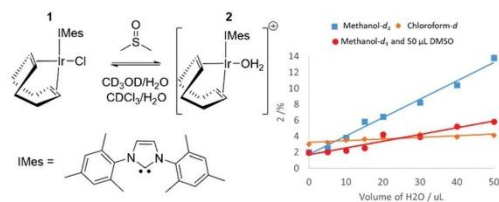
Fig. 1 Demonstrating the proportion of **2** in solution increases with the level of added water in the solvents methanol and chloroform in addition to a methanol–DMSO mixture thereby confirming its identity as [Ir(COD)(IMes)(OH$_2$)]Cl as shown.

nol-d_4. When this experiment was repeated in a solution of 0.6 mL methanol-d_4 doped with 5 μL DMSO, the ratio of **2** formed after the addition of 50 μL of H$_2$O proved to be just 6%. It is noteworthy that no evidence for [IrCl(COD)(DMSO)(IMes)] was apparent. A similar ^{1}H NMR measurement of **1** in a solution of CDCl$_3$ revealed the presence of **2** at the 3% level. Subsequent addition of H$_2$O increases this to 5% but the immiscibility of CDCl$_3$ and H$_2$O prevents the use of high water concentrations. Hence, the equilibrium position between **1** and **2** is dependent on solvent choice and water concentration. **2** is assigned as [Ir(COD)(IMes)(OH$_2$)]Cl which is further confirmed by 2D NMR characterisation data (see ESI‡) at 245 K which shows a NOE between the bound aqua ligand at δ 8.15 and the IMes backbone at δ 2.16. ^{1}H NMR resonances for hexa-aqua species are often found between δ 8 and δ 11.[47] The formation of **2** is not unexpected as iridium aqua complexes are known and the reactions performed throughout this work are not completed under anhydrous conditions because our aim is to achieve SABRE catalysis using an air stable precursor with minimum end-user challenge.[48–50]

DFT calculations have been used to further confirm these product assignments, with their predicted relative energies detailed in Table 1 (see ESI‡ for details). These calculations used full models of the complexes, [Ir(COD)(IMes)(X)], and are relative to a zero point which includes all species (indicated complex, DMSO, H$_2$O and CH$_3$OH) in an equimolar amount. They do not reflect transition state barriers and excess reagents are not accounted for. These calculations confirm that **1**, where X = Cl, is most stable in agreement with experiment. [Ir(COD)(IMes)(OH$_2$)]Cl, **2** is predicted to be more stable than the corresponding methanol or sulfoxide adducts, again supporting our NMR observations.

Table 1 Relative enthalpy (*H*) and Gibbs free energies (*G*) of a series of [Ir(COD)(IMes)(X)] complexes according to DFT calculations

X	*H*/kJ mol^{-1}	*G*/kJ mol^{-1}
Cl	0	0
OH$_2$	52.8	57.0
S-DMSO	42.3	68.9
HOCH$_3$	56.1	69.4

277

Formation of [IrCl(H)₂(DMSO)₂(IMes)] (3)

When H₂ is added to an equilibrium mixture of **1** and **2** containing 4 equivalents of DMSO in methanol-d_4 at 245 K the initial ¹H NMR spectra reveal two hydride resonances at δ −15.49 and δ −21.51 which share a mutual J coupling of 5.5 Hz. Low temperature NMR characterisation of the complex yielding these signals confirms it to be of the form [Ir(H)₂(IMes)(DMSO)₂(L)], **3**.[46] The formation of iridium(III) sulfoxide complexes bound through sulphur for use in SABRE hyperpolarisation studies has been reported previously.[51] When this hydrogenation reaction is examined at 245 K in CDCl₃ or dichloromethane-d_2 (DCM-d_2) hydride resonances appear at δ −15.50, δ −21.12 and δ −15.67, δ −21.36, respectively. The similarity in these signals suggests the common presence of **3** in both cases. This chemistry is complicated, however, by the fact **3** is unstable in solution over long timescales, as detailed in the ESI.‡

The identity of **3** was further confirmed by repeating this experiment using [IrBr(COD)(IMes)], as the corresponding reaction product [IrBr(H)₂(DMSO)₂(IMes)] yields hydride signals at δ −15.67 and δ −20.45 in methanol-d_4 which are clearly different to those of **3**. Furthermore, when [Ir(CH₃CN)(COD)(IMes)]PF₆ is used instead, [Ir(H)₂(CH₃CN)(DMSO)₂(IMes)]PF₆ forms which yields signals at δ −15.76 and δ −19.83 at 255 K; we note there was no evidence for the displacement of CH₃CN by DMSO in the associated NMR spectra. Hence, the hydride resonance in these complexes shift according to the identity of the ligand that is *trans* to it thereby confirming the indicated product identities. The identity of **3** was also studied by DFT as detailed in the results shown in Table 2. [IrCl(H)₂(DMSO)₂(IMes)] was found to be lower in energy than the corresponding species where chloride is replaced by water, methanol or sulfoxide.

When the reaction of H₂ with an equilibrium mixture of **1** and **2** in methanol-d_4 containing DMSO was monitored at 245 K (Fig. 2) no evidence for the formation of any H₂ addition products except **3** is observed. This suggests that H₂ addition is slow, and subsequent COD hydrogenation in intermediate **1-H₂** of Fig. 2 is fast. Interestingly, the proportion of **2** remains roughly constant as this conversion proceeds thereby suggesting any equilibrations involving it are also slow. The route to **3** is therefore most likely to involve direct H₂ addition to **1** rather than **2**. DFT confirms that H₂ addition to **1** proceeds over its COD-Ir–Cl axis rather than the COD-Ir-IMes axis according to the relative energies of the corresponding products (see ESI‡). This is supported by the fact that when this H₂ addition

Table 2 Relative enthalpy (H) and Gibbs free energies (G) of a series of [IrX(H)₂(DMSO)₂(IMes)] complexes according to DFT calculations

X	H/kJ mol⁻¹	G/kJ mol⁻¹
Cl	0	0
OH₂	24.4	34.3
S-DMSO	39.1	70.8
ODCH₃	29.3	45.4
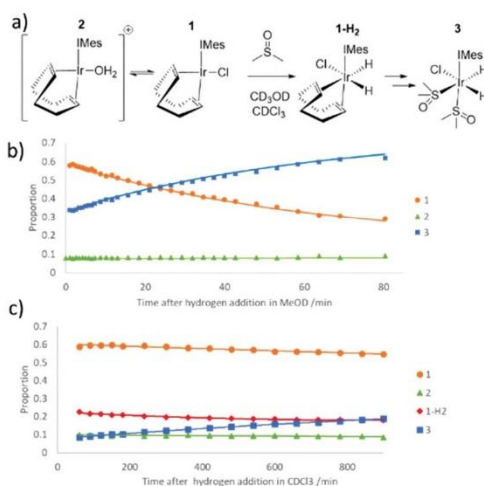
Fig. 2 (a) Reaction steps involved in the conversion of **1** to **3** in the presence of DMSO and H₂, (b) time course for the reaction, as determined in methanol-d_4 solution when the starting concentrations are 5 mM [IrCl(COD)(IMes)], 1 μL DMSO and 3 bar hydrogen pressure and (c) analogous reaction time course data in CDCl₃ at 245 K.

reaction is monitored in CDCl₃ at 245 K, resonances corresponding to **1-H₂**, at δ −13.39 and δ −18.42, are detected in addition to those of **3**. The resonances for **1-H₂** rapidly disappear upon warming this solution to 298 K where **3** then forms.

Ligand exchange processes of [IrCl(H)₂(DMSO)₂(IMes)] (3)

When **3** is formed from a methanol-d_4 solution containing 2 mg of **1**, 1 μL of DMSO and 3-bar H₂, its hydride resonances appear very broad at 298 K (line width of ~120 Hz) which is consistent with rapid hydrogen loss. This deduction is confirmed upon shaking methanol-d_4 solutions of **3** with 3-bar p-H₂ for 10 seconds at 65 G at 298 K. Its hydride resonances exhibit PHIP signal enhancement alongside a free DMSO signal that yields a weak SABRE ¹H NMR signal enhancement of 7-fold (see ESI‡). This is consistent with the reversible pairwise addition of H₂ to **3** and loss of DMSO. Product **3** actually yields four distinct ¹H NMR signals for the methyl groups of its two DMSO ligands. The DMSO ligand *cis* to carbene yields a pair of inequivalent CH₃ signals at δ 2.83 and 3.12 while DMSO *trans* to carbene resonates at δ 3.19 and 3.27. Upon selective excitation of bound DMSO resonances *cis* to carbene in **3**, evidence for chemical exchange into free DMSO is observed. In contrast, we observe no exchange of the DMSO ligand that lies *trans* to carbene on this timescale although we do observe interchange of the inequivalent CH₃ groups. This suggests that loss of the DMSO ligand *cis* to IMes accounts for this scrambling of the inequivalent CH₃ resonances of the DMSO *trans* to IMes.

Measuring the change in these resonance's signal intensities as a function of time after the initial *r.f.* excitation step

allowed the associated ligand loss rates to be calculated. The rate of reversible hydrogen loss, k_{H_2}, was found to be 3.31 ± 0.25 s^{-1} at 263 K and is faster than that seen in many related systems.[52] Loss, and hence exchange of the DMSO ligand *cis* to IMes, was found to occur on a similar timescale with k_{DMSO} 3.35 ± 0.01 s^{-1} at 263 K. Repeating these measurements at different temperatures allowed the transition state barriers for these two processes to be determined as $\Delta H^{\ddagger}_{(H_2)}$ 78 ± 6 kJ mol^{-1}, $\Delta S^{\ddagger}_{(H_2)}$ 60 ± 25 J K^{-1} mol^{-1} and $\Delta H^{\ddagger}_{(DMSO)}$ 79 ± 6 kJ mol^{-1}, $\Delta S^{\ddagger}_{(DMSO)}$ 66 ± 8 J K^{-1} mol^{-1} respectively. This enthalpic barrier to hydrogen loss is comparable to those for similar complexes, overall the entropy change suggests that a dissociative pathway is adopted.[53]

The effects of H_2 pressure and DMSO concentration on these exchange processes were also studied in methanol-d_4 at 243 K for differing reagent concentrations. k_{H_2} proved to increase at higher H_2 concentrations before reaching a plateau as detailed in the ESI.‡ The rate of DMSO exchange is unaffected by increasing DMSO or H_2 concentration. We therefore propose that DMSO and H_2 loss proceed *via* formation of the common 16-electron intermediate [IrCl(H)$_2$(DMSO)(IMes)] in what is a dissociative first step. H_2 exchange then proceeds *via* the formation of [IrCl(H)$_2$(H$_2$)(DMSO)(IMes)]; such indirect H_2 exchange, rather than direct H_2 loss, has been reported for several similar systems.[51,54] When similar EXSY data were collected in CD$_2$Cl$_2$, the rate of hydrogen and DMSO loss proved to be slower than those in methanol-d_4, as summarised in Table 3.

These deductions were confirmed through further DFT calculations that revealed the products of direct H_2 loss to form a 16 electron product as being highly energetically unfavourable, as shown in Table 4. The five coordinate product formed by loss of DMSO *trans* to carbene proved highly unstable, undergoing spontaneous rearrangement to form an intermediate with a vacancy in the equatorial plane; this is consistent with the EXSY data. In contrast, the predicted ligand dissociation pathway involves the formation of five-coordinate [IrCl(H)$_2$(DMSO)(IMes)] *via* loss of the DMSO ligand that lies *cis* to carbene.

Even at low temperature (245–265 K), H/D exchange leading to [IrCl(D)(H)(DMSO)$_2$(IMes)] (**3-*d***) and [IrCl(D)$_2$(DMSO)$_2$(IMes)] was evident. Binding of solvent methanol to [IrCl(H)$_2$(DMSO)(IMes)] is an obvious route to deuterium exchange and the formation of these species alongside HD and D$_2$ gas. While we do not directly observe methanol bound adducts, they are suggested to form in similar systems and indeed proposed to account for the hydrogen isotope exchange

Table 4 Relative enthalpy (*H*) and Gibbs free energies (*G*) of products arising from ligand loss of **3** according to DFT calculations. These energies are relative to those of **3** and do not reflect transition state barriers

Loss of	H/kJ mol^{-1}	G/kJ mol^{-1}
H$_2$	89.0	58.5
Cl	39.6	3.9
DMSO *cis* carbene	32.7	−10.1

reaction that is often observed to run in parallel to SABRE.[50,55] Experimentally, at low temperature it proved possible to reliably and selectively excite the hydride resonance of **3** or **3-*d***. The selective excitation of the hydride resonances for these two species revealed their selective chemical exchange into H$_2$ and HD, from **3** and **3-*d*** respectively. Therefore, k_{H_2} and k_{HD} can be determined as previously described. These values proved to be the same within error and hence, there is little or no kinetic isotope effect which is consistent with other reports.[56,57] We note that exchange between **3** and **3-*d*** is not observed in the associated EXSY data which provides confirmation that the underlying deuterium exchange processes involving methanol-d_4 are slow.

Formation of [Ir(H)$_2$(η^2-pyruvate)(DMSO)(IMes)], (4)

When sodium pyruvate (5 equivalents relative to iridium) is added to a solution of preformed **3** in methanol-d_4 at 245 K, two new hydride ligand containing products form, which correspond to isomers **4a** and **4b** of [Ir(H)$_2$(η^2-pyruvate)(DMSO)(IMes)] as detailed in Fig. 3a. Logically, a further isomer of **4a** is possible, **4c**, in which the orientation of the pyruvate is rotated but this is not observed in solution. These products are differentiated from each other by the geometry of the co-ordinated pyruvate ligand and their proportion is both reaction time and temperature dependent (Fig. 3b). DFT (Table 5) is used to confirm that **4a** exhibits the ligand geometry shown in Fig. 3a and that **4b** is the most stable species. Despite observation of a 10 Hz coupling between the pyruvate COOH group and the hydride *trans* to oxygen, according to DFT the pyruvate CH$_3$ and DMSO groups of **4a** are arranged in a *cis* fashion as shown in Fig. 3a. This deduction was further confirmed by the observation of an NOE peak between the pyruvate CH$_3$ group and the phenyl protons on the mesityl group of the carbene ligand.

When this solution was examined with a 32 scan ^{1}H NMR measurement at 298 K, unlike the 245 K data of Fig. 3b, the main hydride containing complex observed is **4b** and reso-

Table 3 Rate and thermodynamic parameters for hydrogen and DMSO exchange of **3**

Solvent	Process	$k_{(263\ K)}$/s^{-1}	$\Delta H^{\ddagger}$/kJ mol^{-1}	$\Delta S^{\ddagger}$/J K^{-1} mol^{-1}
Methanol-d_4	Hydrogen exchange (k_{H_2})	3.31 ± 0.25	78 ± 6	60 ± 25
	DMSO exchange (k_{DMSO})	3.35 ± 0.04	79 ± 6	66 ± 8
Dichloromethane-d_2	Hydrogen exchange (k_{H_2})	1.16 ± 0.04	83 ± 8	73 ± 29
	DMSO exchange (k_{DMSO})	1.56 ± 0.01	84 ± 2	78 ± 8
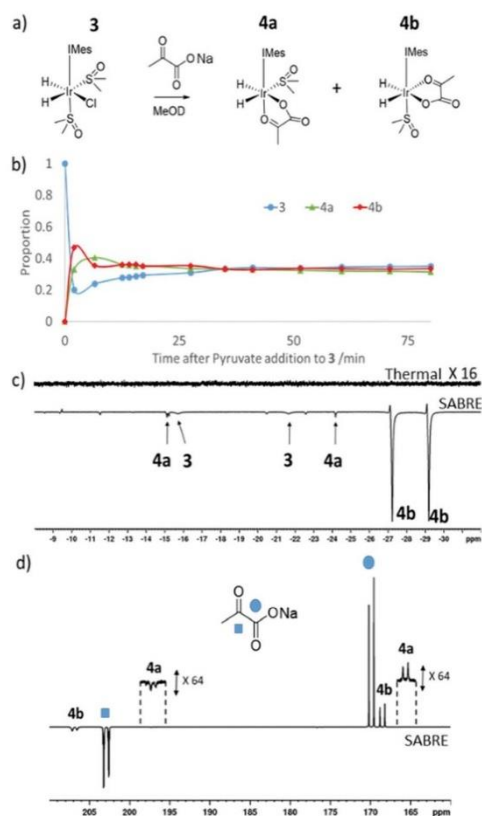
Fig. 3 (a) Reaction of **3** and pyruvate to form **4** (b) monitoring pyruvate addition to **3** using ¹H NMR spectroscopy. Pyruvate addition was made at room temperature to a solution of preformed **3** at 245 K before it was introduced into the spectrometer whose probe was at 245 K. There is therefore a rapid temperature change at the start of this data series. Upon shaking a solution of **3** and **4** with 3-bar *p*-H₂ for 10 seconds at (c) 65 G or (d) in a mu metal shield strongly hyperpolarised ¹H (c) or ¹³C (d) resonances of **4b** are observed compared to the thermal trace.

Table 5 Relative enthalpy (*H*) and Gibbs free energies (*G*) of **4** according to DFT calculation

Complex	$H/kJ\ mol^{-1}$	$G/kJ\ mol^{-1}$
4a	8.5	14.8
4b	0	0
4c	22.6	28.1

nances for **3** and **4a** cannot be discerned. **4a** and **4b** have previously been implicated in pyruvate polarisation using SABRE and their NMR characterisation data has been reported.[46] **4** is also detected immediately after H₂ addition to a solution of **1** containing pyruvate (5 equivalents relative to iridium) and DMSO (10 equivalents) at 298 K. When an equilibrium mixture

of **3** and **4** is shaken with 3 bar *p*-H₂ at 65 G enhanced hydride resonances are observed in the ¹H NMR spectrum as shown in Fig. 3c, which are strongest for **4b**.

If sodium-1,2-pyruvate-[¹³C₂] is used as the substrate and the *p*-H₂ shaking process is performed under SABRE-SHEATH conditions in a mu metal shield (see Experimental) an enhanced ¹³C response for the free material at δ 169 and δ 203 can also be readily detected.[46] Two enhanced signals can be also seen for the bound pyruvate ligand in **4b** at δ 168 and δ 207 in these NMR spectra. It is also possible to observe extremely weak hyperpolarised signals for the bound pyruvate ligand in **4a** at δ 161 and δ 198, as shown in Fig. 4d. Interestingly, when EXSY measurements are used to probe these signals, the selective excitation of the hydride resonances of **4b** reveals no exchange into H₂ on the NMR timescale. Furthermore, when ¹³C-EXSY is used to probe the bound signals of **4b**, no exchange is seen into free pyruvate on this timescale. Hence **4b** appears to be relatively stable in agreement with the DFT study, but this is not consistent with the strong hydride polarisation that is evident for **4b** in Fig. 3. Consequently, a role for **3** which is present and undergoes rapid H₂ exchange as discussed earlier in its formation is indicated. It is by this route that the delivery of fresh *p*-H₂ into **4** and the resulting enhancement of hydride and pyruvate ligand signals is achieved. As the NMR relaxation times of the ¹³C resonances in pyruvate are much longer than those of ¹H, slow exchange is still commensurate with the build-up of pyruvate polarisation in solution. Related relayed *p*-H₂ enhancement effects have been described recently.[58,59]

An equilibrium mixture containing **4** can also be formed if sodium-1,2-pyruvate-[¹³C₂] is added to a preformed methanol-*d*₄ solution of [IrBr(H)₂(DMSO)₂(IMes)] (**3-Br**) or [Ir(H)₂(CH₃CN)(DMSO)₂(IMes)]PF₆ (**3-Acn**). When these samples are shaken with *p*-H₂ for 10 seconds at 65 G strongly hyperpolarised hydride resonances can again be observed for **4b** in the corresponding high field NMR measurement. These resonances appear with significantly lower intensity than those achieved with **3** derived systems (35% and 31% of this signal
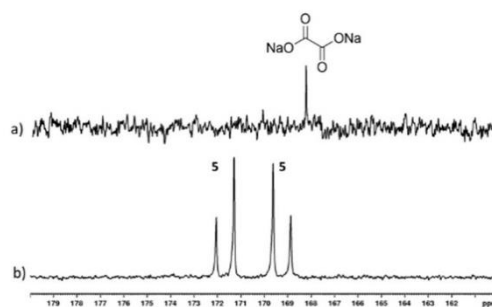
Fig. 4 (a) 128 scan ¹³C spectrum of a solution of **1**, DMSO and sodium-1,2-oxalate-[¹³C₂] (1:5:5) in methanol-*d*₄ (b) ¹³C NMR signals seen after shaking an NMR tube with 3-bar *p*-H₂ in a mu metal shield for 30 seconds.

280

intensity respectively). Furthermore, when the p-H$_2$ shaking step is repeated in a mu metal shield, hyperpolarised resonances for ^{13}C-pyruvate are again visible. The corresponding ^{13}C-pyruvate signal enhancements are typically 580-fold and 120-fold for the **3-Br** and **3-Acn** derived systems respectively. These are lower than those achieved for the analogous **3** system (1070-fold) which is consistent with the reduced amount of **4b** which is present at equilibrium when these precursors are used (22 and 23% respectively when compared to 92% with **3**).

We note that the linewidths of the hydride resonances of **4b** at 298 K are similar in each of these samples (43–45 Hz). Similarly, the linewidths of **3**, **3-Br** and **3-Acn** are comparable at 245 K (3–5 Hz). Therefore, we do not expect that differences in hydride polarisation levels seen for **4b** in these solutions are due to different hydrogen exchange rates in **3**, but rather the different binding strengths of the coligands that must be displaced by pyruvate to form **4** from **3**. Hence, whilst there appears to be a link between pyruvate polarisation level and **4b** concentration, the identity of L in [Ir(H)$_2$(DMSO)$_2$(IMes)L] must play a large effect on the level of pyruvate signal enhancement. These data further confirm that **3** is important in mediating efficient H$_2$ exchange within the **3**/**4** hyperpolarisation mixture.

Using [IrCl(H)$_2$(DMSO)$_2$(IMes)] (3) to hyperpolarise sodium-1,2-oxalate-[^{13}C$_2$]

We have shown how **3** can be formed *in situ* and subsequently used as a precursor to form [Ir(H)$_2$(η^2-pyruvate)(DMSO)(IMes)], (**4**) which delivers SABRE enhancement to pyruvate. This α-keto acid motif also features in oxalate, a metabolic product that binds mineral ions in the body and is found in many foods.[60] Indeed, Levitt and coworkers have reported the creation of a long lived hyperpolarised ^{13}C$_2$ singlet spin pair for a deuterated ester derivative of oxalate using DNP.[61] Consequently, we now describe tests on sodium-1,2-oxalate-[^{13}C$_2$]. This involved shaking a mixture of **1**, DMSO, and sodium-1,2-oxalate-[^{13}C$_2$] (1 : 5 : 5) with 3-bar p-H$_2$ in 0.6 mL methanol-d_4 for 30 seconds in a mu metal shield. Hyperpolarised ^{13}C resonances were observed at δ 169.20 and δ 171.66 that share a J_{CC} coupling of 76 Hz, as shown in Fig. 4. These signals cannot be due to free sodium-1,2-oxalate-[^{13}C$_2$] as a single resonance is expected.

While the complexation dynamics of oxalate are complex,[62–64] based on the pyruvate observations described earlier it should be possible to form a species such as [Ir(H)$_2$(η^2-oxalate)(DMSO)(IMes)], **5** which would account for this observation. In fact, the ^{13}C$_2$ NMR signal profile shown in Fig. 4 is indicative of Zeeman magnetisation in such a product rather than singlet spin order. This indicates that while ^{13}C polarisation transfer from a set of p-H$_2$ derived hydride ligands initially results this must be associated with a [AA′BB′] spin system, which converts to the [AMSX] type with inequivalent hydride ligands in high field. A product with ligand arrangement analogous to **4a** would match with this hypothesis.[46] Unfortunately, examination of the hydride region of the result-

ing ^{1}H NMR spectra reveal signals for **3** at δ −15.45 and δ −21.53 alongside over seven minor hydride containing complexes. None of the hydride resonances of these species correlated to these two ^{13}C signals in an overnight 2D measurement at 243 K. Studying this reaction again at 315 K, proved to be of no benefit as conversion of **3** into the same range of hydride containing species results.

In contrast, when this experiment was repeated in DCM-d_2 the hydride resonances of **3** are again observed at δ −15.71 and δ −21.27 but no ^{13}C oxalate derived polarisation is seen. There is very low solubility of sodium oxalate in this medium. As a consequence, samples of **3** in CD$_2$Cl$_2$ or CH$_3$OD were prepared and reacted with 50 μL D$_2$O solutions of sodium-1,2-oxalate-[^{13}C$_2$]. Now a new product forms cleanly, that yields a hydride signal at δ −27.1 alongside diagnostic resonances for the IMes at δ 2.10, δ 2.34, δ 6.99, δ 7.15 and DMSO at δ 2.92 whose relative signal intensities suggest the presence of a [Ir(H)$_2$(IMes)(DMSO)(L)$_n$]$_x$ species, **6**. Upon shaking with p-H$_2$ the hydride resonances for **6** do not enhance, however, the addition of 3 mL of degassed hexane results in the growth of single crystals. Subsequent X-ray diffraction studies confirmed that the product **6** corresponds to the dimer [Ir$_2$(H)$_4$(IMes)$_2$(DMSO)$_2$(η^2-κ^2-Oxalate)] with structure shown in Fig. 5 (full X-ray and NMR characterisation data are given in the in the ESI‡). The ability of oxalate to form such dimers restricts its dissociation and thereby limits its use in these hyperpolarisation studies. Nonetheless, the structure of **6** reflects a common binding mode of oxalate with transition metals.[63,65,66]

Experimental

All NMR measurements were carried out on a 400 MHz Bruker Avance III spectrometer using solutions at room temperature (298 K) unless otherwise stated. *Para*-hydrogen (p-H$_2$) was produced by passing hydrogen gas over a spin-exchange catalyst (Fe$_2$O$_3$) and used for all hyperpolarisation experiments. This method produces constant p-H$_2$ with *ca.* 93% purity. ^{1}H (400 MHz) and ^{13}C (100.6 MHz) NMR spectra were recorded
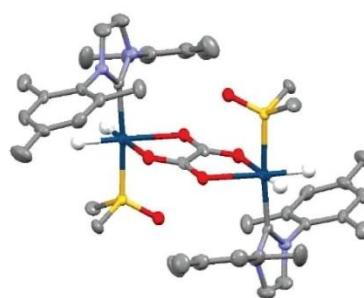
Fig. 5 Structure of [Ir$_2$(H)$_4$(IMes)$_2$(DMSO)$_2$(η^2-κ^2-Oxalate)], **6**, determined by X-ray crystallography. All non-hydride hydrogen atoms and solvent of crystallisation have been omitted for clarity.

with an internal deuterium lock. Chemical shifts are quoted as parts per million and referenced to the solvent. ^{13}C NMR spectra were recorded with broadband proton decoupling. Coupling constants (J) are quoted in Hertz.

Samples were prepared containing 2 mg [IrCl(COD)(IMes)] precatalyst (where IMes = 1,3-bis(2,4,6-trimethyl-phenyl)imidazole-2-ylidene and COD = *cis,cis*-1,5-cyclooctadiene) in 0.6 mL of deuterated methanol-d_4 unless otherwise stated in a 5 mm NMR tube that was fitted with a J. Young's tap. All commercial compounds were purchased from Sigma-Aldrich, Fluorochem, or Alfa-Aesar and used as supplied. [IrCl(COD)(IMes)] was synthesized according to a literature procedure.[67] The resulting solutions were degassed by two freeze–pump–thaw cycles before the addition of 3-bar H_2.

The shake and drop method was employed for recording hyperpolarised NMR spectra. This involves filling NMR tubes with *p*-H_2 at 3 bar pressure and shaking them vigorously for 10 seconds in a 65 G magnetic field if ^{1}H NMR spectra are to be recorded at 9.4 T. A mu metal shield is used if ^{13}C NMR spectra are to be recorded. Unless otherwise stated multiple shake and drop measurements are undertaken and average signal enhancement values quoted. Signal enhancements and exchanges rates were calculated according to literature procedures.[68]

Conclusions

In conclusion, we have confirmed that the complex [IrCl(H)$_2$(DMSO)$_2$(IMes)] can be used as a polarisation transfer catalyst for hyperpolarising pyruvate. Complexes of this type undergo rapid hydrogen exchange which through a mechanistic investigation involving EXSY and DFT is expected to proceed dissociatively *via* five coordinate [IrCl(H)$_2$(DMSO)(IMes)]. When this process is completed in the presence of an α-ketoacid, such as pyruvate, reaction to form [Ir(H)$_2$(η^2-pyruvate)(DMSO)(IMes)], which exists in two coordination isomers, occurs readily. Isomer **4b**, in which the hydride ligands lie *trans* to pyruvate, is implicated in strong SABRE hyperpolarisation despite it undergoing slow ligand exchange. Consequently, a role for [IrCl(H)$_2$(DMSO)$_2$(IMes)], which undergoes rapid H_2 and DMSO loss, is indicated in this process. When pyruvate is replaced by oxalate, stronger and more complex ligand binding is evident. The trapping of oxalate within the dimer **6** is expected to explain its much less efficient hyperpolarisation. Nonetheless, we predict that variations of the sulfoxide and NHC will enable future hyperpolarisation of oxalate and those of a wider range of other α-keto acids.

Conflicts of interest

B. J. T. and S. B. D. (and others) are inventors on a patent application filed by the University of York related to this work (patent no. GB1818171.9, filed 7 November 2018).

References

1 T. S. Leyh, *Crit. Rev. Biochem. Mol. Biol.*, 1993, **28**, 515–542.
2 X. Liu, L. He, Y.-M. Liu and Y. Cao, *Acc. Chem. Res.*, 2013, **47**, 793–804.
3 H. Amii and K. Uneyama, *Chem. Rev.*, 2009, **109**, 2119–2183.
4 D. M. Ermert and L. J. Murray, *Dalton Trans.*, 2016, **45**, 14499–14507.
5 R. Pretorius, M. R. Fructos, H. Müller-Bunz, R. A. Gossage, P. J. Pérez and M. Albrecht, *Dalton Trans.*, 2016, **45**, 14591–14602.
6 H. Huo, X. Shen, C. Wang, L. Zhang, P. Röse, L.-A. Chen, K. Harms, M. Marsch, G. Hilt and E. Meggers, *Nature*, 2014, **515**, 100.
7 L.-S. Wang, R. McDonald and M. Cowie, *Inorg. Chem.*, 1994, **33**, 3735–3744.
8 M. Álvarez, E. Álvarez, M. R. Fructos, J. Urbano and P. J. Pérez, *Dalton Trans.*, 2016, **45**, 14628–14633.
9 P. B. Chock and J. Halpern, *J. Am. Chem. Soc.*, 1966, **88**, 3511–3514.
10 W. H. Thompson and C. T. Sears, *Inorg. Chem.*, 1977, **16**, 769–774.
11 K. Searles, M. Pink, K. G. Caulton and D. J. Mindiola, *Dalton Trans.*, 2012, **41**, 9619–9622.
12 C. E. Johnson and R. Eisenberg, *J. Am. Chem. Soc.*, 1985, **107**, 3148–3160.
13 N. Wang, M. Wang, Y. Wang, D. Zheng, H. Han, M. r. S. G. Ahlquist and L. Sun, *J. Am. Chem. Soc.*, 2013, **135**, 13688–13691.
14 C. R. Landis and T. W. Brauch, *Inorg. Chim. Acta*, 1998, **270**, 285–297.
15 S. Grimme, H. Kruse, L. Goerigk and G. Erker, *Angew. Chem., Int. Ed.*, 2010, **49**, 1402–1405.
16 K. Sorochkina, V. V. Zhivonitko, K. Chernichenko, V.-V. Telkki, T. Repo and I. V. Koptyug, *J. Phys. Chem. Lett.*, 2018, **9**, 903–907.
17 V. V. Zhivonitko, K. Sorochkina, K. Chernichenko, B. Kótai, T. Földes, I. Pápai, V.-V. Telkki, T. Repo and I. Koptyug, *Phys. Chem. Chem. Phys.*, 2016, **18**, 27784–27795.
18 S. Wagner, *Magn. Reson. Mater. Phys., Biol. Med.*, 2014, **27**, 195–199.

282

19 D. Canet, C. Aroulanda, P. Mutzenhardt, S. Aime, R. Gobetto and F. Reineri, *Concepts Magn. Reson., Part A*, 2006, **28**, 321–330.

20 P. M. Richardson, R. O. John, A. J. Parrott, P. J. Rayner, W. Iali, A. Nordon, M. E. Halse and S. B. Duckett, *Phys. Chem. Chem. Phys.*, 2018, **20**, 26362–26371.

21 C. R. Bowers and D. P. Weitekamp, *Phys. Rev. Lett.*, 1986, **57**, 2645.

22 C. R. Bowers and D. P. Weitekamp, *J. Am. Chem. Soc.*, 1987, **109**, 5541–5542.

23 T. C. Eisenschmid, R. U. Kirss, P. P. Deutsch, S. I. Hommeltoft, R. Eisenberg, J. Bargon, R. G. Lawler and A. L. Balch, *J. Am. Chem. Soc.*, 1987, **109**, 8089–8091.

24 R. Eisenberg, *Acc. Chem. Res.*, 1991, **24**, 110–116.

25 T. C. Eisenschmid, R. U. Kirss, P. P. Deutsch, S. I. Hommeltoft, R. Eisenberg, J. Bargon, R. G. Lawler and A. L. Balch, *J. Am. Chem. Soc.*, 1987, **109**, 8089–8091.

26 S. B. Duckett, C. L. Newell and R. Eisenberg, *J. Am. Chem. Soc.*, 1994, **116**, 10548–10556.

27 K. V. Kovtunov, I. E. Beck, V. I. Bukhtiyarov and I. V. Koptyug, *Angew. Chem., Int. Ed.*, 2008, **47**, 1492–1495.

28 P. Bhattacharya, E. Y. Chekmenev, W. H. Perman, K. C. Harris, A. P. Lin, V. A. Norton, C. T. Tan, B. D. Ross and D. P. Weitekamp, *J. Magn. Reson.*, 2007, **186**, 150–155.

29 N. M. Zacharias, H. R. Chan, N. Sailasuta, B. D. Ross and P. Bhattacharya, *J. Am. Chem. Soc.*, 2011, **134**, 934–943.

30 F. Reineri, T. Boi and S. Aime, *Nat. Commun.*, 2015, **6**, 5858.

31 R. W. Adams, J. A. Aguilar, K. D. Atkinson, M. J. Cowley, P. I. Elliott, S. B. Duckett, G. G. Green, I. G. Khazal, J. López-Serrano and D. C. Williamson, *Science*, 2009, **323**, 1708–1711.

32 R. W. Adams, S. B. Duckett, R. A. Green, D. C. Williamson and G. G. Green, *J. Chem. Phys.*, 2009, **131**, 194505.

33 A. J. Ruddlesden, R. E. Mewis, G. G. Green, A. C. Whitwood and S. B. Duckett, *Organometallics*, 2015, **34**, 2997–3006.

34 A. J. Ruddlesden and S. B. Duckett, *Chem. Commun.*, 2016, **52**, 8467–8470.

35 L. S. Lloyd, A. Asghar, M. J. Burns, A. Charlton, S. Coombes, M. J. Cowley, G. J. Dear, S. B. Duckett, G. R. Genov and G. G. R. Green, *Catal. Sci. Technol.*, 2014, **4**, 3544–3554.

36 K. M. Appleby, R. E. Mewis, A. M. Olaru, G. G. R. Green, I. J. S. Fairlamb and S. B. Duckett, *Chem. Sci.*, 2015, **6**, 3981–3993.

37 A. L. Sargent and M. B. Hall, *Inorg. Chem.*, 1992, **31**, 317–321.

38 M. Fekete, O. Bayfield, S. B. Duckett, S. Hart, R. E. Mewis, N. Pridmore, P. J. Rayner and A. Whitwood, *Inorg. Chem.*, 2013, **52**, 13453–13461.

39 M. J. Cowley, R. W. Adams, K. D. Atkinson, M. C. Cockett, S. B. Duckett, G. G. Green, J. A. Lohman, R. Kerssebaum, D. Kilgour and R. E. Mewis, *J. Am. Chem. Soc.*, 2011, **133**, 6134–6137.

40 H. Zeng, J. Xu, J. Gillen, M. T. McMahon, D. Artemov, J.-M. Tyburn, J. A. Lohman, R. E. Mewis, K. D. Atkinson and G. G. Green, *J. Magn. Reson.*, 2013, **237**, 73–78.

41 E. B. Dücker, L. T. Kuhn, K. Münnemann and C. Griesinger, *J. Magn. Reson.*, 2012, **214**, 159–165.

42 M. L. Truong, T. Theis, A. M. Coffey, R. V. Shchepin, K. W. Waddell, F. Shi, B. M. Goodson, W. S. Warren and E. Y. Chekmenev, *J. Phys. Chem. C*, 2015, **119**, 8786–8797.

43 P. Spannring, I. Reile, M. Emondts, P. P. Schleker, N. K. Hermkens, N. G. van der Zwaluw, B. J. van Weerdenburg, P. Tinnemans, M. Tessari and B. Blümich, *Chem. – Eur. J.*, 2016, **22**, 9277–9282.

44 R. E. Mewis, R. A. Green, M. C. Cockett, M. J. Cowley, S. B. Duckett, G. G. Green, R. O. John, P. J. Rayner and D. C. Williamson, *J. Phys. Chem. B*, 2015, **119**, 1416–1424.

45 W. Iali, P. J. Rayner, A. Alshehri, A. J. Holmes, A. J. Ruddlesden and S. B. Duckett, *Chem. Sci.*, 2018, **9**, 3677–3684.

46 W. Iali, S. S. Roy, B. J. Tickner, F. Ahwal, A. J. Kennerley and S. B. Duckett, *Angew. Chem.*, 2019, **131**, 10377–10381.

47 A. F. Oliveri, L. A. Wills, C. R. Hazlett, M. E. Carnes, I.-Y. Chang, P. H.-Y. Cheong and D. W. Johnson, *Chem. Sci.*, 2015, **6**, 4071–4085.

48 L. Dadci, H. Elias, U. Frey, A. Hoernig, U. Koelle, A. E. Merbach, H. Paulus and J. S. Schneider, *Inorg. Chem.*, 1995, **34**, 306–315.

49 S. Ogo, N. Makihara, Y. Kaneko and Y. Watanabe, *Organometallics*, 2001, **20**, 4903–4910.

50 S. Knecht, S. Hadjiali, D. A. Barskiy, A. Pines, G. Sauer, A. S. Kiryutin, K. L. Ivanov, A. V. Yurkovskaya and G. Buntkowsky, *J. Phys. Chem. C*, 2019, **123**, 16288–16293.

51 B. J. Tickner, R. O. John, S. S. Roy, S. J. Hart, A. C. Whitwood and S. B. Duckett, *Chem. Sci.*, 2019, **10**, 5235–5245.

52 A. M. Olaru, A. Burt, P. J. Rayner, S. J. Hart, A. C. Whitwood, G. G. Green and S. B. Duckett, *Chem. Commun.*, 2016, **52**, 14482–14485.

53 B. J. Tickner, W. Iali, S. S. Roy, A. C. Whitwood and S. B. Duckett, *ChemPhysChem*, 2019, **20**, 241–245.

54 B. E. Hauger, D. Gusev and K. G. Caulton, *J. Am. Chem. Soc.*, 1994, **116**, 208–214.

55 O. Semenova, P. M. Richardson, A. J. Parrott, A. Nordon, M. E. Halse and S. B. Duckett, *Anal. Chem.*, 2019, **91**, 6695–6701.

56 P. Zhou, A. A. Vitale, J. San Filippo Jr. and W. H. Saunders Jr., *J. Am. Chem. Soc.*, 1985, **107**, 8049–8054.

57 F. Abu-Hasanayn, A. S. Goldman and K. Krogh-Jespersen, *J. Phys. Chem.*, 1993, **97**, 5890–5896.

58 B. J. Tickner, R. O. John, S. S. Roy, S. Hart, A. C. Whitwood and S. B. Duckett, *Chem. Sci.*, 2019, **10**, 5235–5245.

59 S. S. Roy, K. M. Appleby, E. J. Fear and S. B. Duckett, *J. Phys. Chem. Lett.*, 2018, **9**, 1112–1117.

60 H. Sidhu, R. Gupta, S. K. Thind and R. Nath, *Ann. Nutr. Metab.*, 1987, **31**, 354–361.

61 C. Laustsen, G. Pileio, M. C. D. Tayler, L. J. Brown, R. C. D. Brown, M. H. Levitt and J. H. Ardenkjaer-Larsen, *Magn. Reson. Med.*, 2012, **68**, 1262–1265.

62 N. Hao, E. Shen, Y. G. Li, E. B. Wang, C. W. Hu and L. Xu, *Eur. J. Inorg. Chem.*, 2004, **2004**, 4102–4107.

283

Appendices

Paper

Dalton Transactions

63 B. Modec, J. V. Brenčič and J. Koller, *Eur. J. Inorg. Chem.*, 2004, **2004**, 1611–1620.

64 M. Gruselle, C. Train, K. Boubekeur, P. Gredin and N. Ovanesyan, *Coord. Chem. Rev.*, 2006, **250**, 2491–2500.

65 B. Modec, J. V. Brenčič, D. Dolenc and J. Zubieta, *Dalton Trans.*, 2002, 4582–4586.

66 M. E. Robinson, J. E. Mizzi, R. J. Staples and R. L. LaDuca, *Cryst. Growth Des.*, 2015, **15**, 2260–2271.

67 L. D. Vazquez-Serrano, B. T. Owens and J. M. Buriak, *Inorg. Chim. Acta*, 2006, **359**, 2786–2797.

68 B. J. Tickner, W. Iali, S. S. Roy, A. C. Whitwood and S. B. Duckett, *ChemPhysChem*, 2019, **20**, 241–245.

284

Appendix 6

Probing the Hydrogenation of Vinyl Sulfoxides Using *para*-Hydrogen

Ben J. Tickner,[†] Rachel R. Parker,[‡] Adrian C. Whitwood,[‡] and Simon B. Duckett*,[†]

[†]Center for Hyperpolarisation in Magnetic Resonance (CHyM), University of York, Heslington, York YO10 5NY, United Kingdom
[‡]Department of Chemistry, University of York, Heslington, York YO10 5DD, United Kingdom

S *Supporting Information*

ABSTRACT: Vinyl sulfoxides are an important functional group used in a wide range of organic transformations. Here, we use $[IrCl(COD)(IMes)]$ where IMes = 1,3-bis(2,4,6-trimethyl-phenyl)imidazole-2-ylidene and COD = *cis,cis*-1,5-cyclooctadiene to rapidly hydrogenate phenylvinylsulfoxide. We use *para*-hydrogen-induced hyperpolarization (PHIP) to follow this reaction with $[IrCl(H)_2(IMes)(S(O)(Ph)(Et))_2]$ dominating in the later stages. Decomposition to form the reduced C−S bond cleavage product $[Ir_2(H)_3(\kappa^2\text{-H})(\kappa^2\text{-SPh})_2(IMes)_2(S(Et)(Ph)O)]$ limits turnover. The related product $[Ir_2(H)_4(\kappa^2\text{-S})(IMes)_2(S(O)(CH_2Ph)_2)_2]$ is formed from dibenzylsulfoxide, demonstrating the wider utility of this transformation.
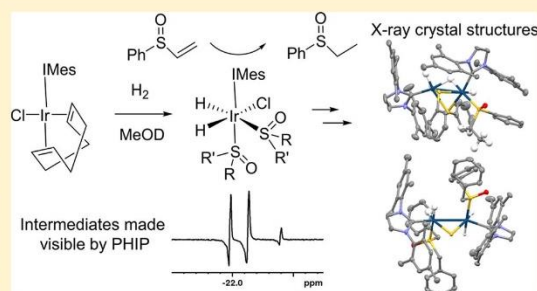
Sulfoxides are present in many organic compounds that find uses as laboratory solvents, pharmaceutical drugs,[1] synthetic agents,[2] and ligands for metal binding.[3] This key functional group is of great interest in asymmetric synthesis due to the chirality of the central sulfur atom.[4] The preparation of chiral sulfoxides in an enantiomerically pure form is possible due to the large barrier to inversion of the tetrahedral sulfur atom.[5] Vinyl sulfoxides contain conjugated S=O and alkene groups, which can be used in a wide range of organic transformations. Examples include uses as acetylene equivalents in cycloaddition reactions and as Michael acceptors.[6] The hydrogenation of vinylsulfoxides, either by transition metal catalysts or free radicals, has also been reported.[7,8] Indeed, when chiral hydrogenation catalysts are used, hydrogenated sulfoxides can be prepared in enantiomeric excess.[8] These metal-mediated hydrogenations are often facilitated by initial sulfoxide coordination to an active catalyst that in many cases involves rhodium. The mechanisms of these Rh-catalyzed hydrogenation processes have been investigated using NMR spectroscopy and/or high level density functional theory calculations.[7−9]

Reaction mechanism and low concentration intermediates can also be powerfully studied using a technique called *para*-hydrogen-induced polarization (PHIP).[10,11] Short lived or low concentration species cannot routinely be observed by NMR spectroscopy due to its inherent low sensitivity. However, the PHIP approach creates the necessary non-Boltzmann population distributions within a target molecule by employing *para*-hydrogen (*p*-H₂), a singlet spin isomer of dihydrogen. The NMR signals derived from these *p*-H₂ hydrogenated products can be up to 3 orders of magnitude larger than those

when recorded under Boltzmann conditions.[10,11] PHIP belongs to a larger family of hyperpolarization techniques that include dynamic nuclear polarization (DNP) and spin exchange optical pumping (SEOP), which have now produced hyperpolarized molecules suitable for detection in vivo.[12,13] Although PHIP has also produced hyperpolarized biomolecules for in vivo detection[14,15] it is more commonly used to probe reaction mechanisms, with the sensitivity gains it provides having allowed low concentration catalytic intermediates in Rh-catalyzed alkene hydrogenation reactions to be detected.[16−19] H₂ activation by frustrated Lewis pairs reflects another area of successful study using PHIP.[20,21]

Signal amplification by reversible exchange (SABRE) is a *p*-H₂-based hyperpolarization method that does not involve the direct hydrogenation of a target molecule.[22] Instead, it uses an oxidative addition reaction to break the symmetry of *p*-H₂. Magnetization can then be catalytically transferred from *p*-H₂-derived hydride ligands to a ligated target molecule at low (∼mT) field through the formation of a temporary *J*-coupled network.[23] This approach and its derivatives, SABRE-SHEATH and SABRE-relay, have led to the polarization of a wide range of molecules and functional groups.[24,25] SABRE has been used to make low concentration species visible either in mixtures[26] or in chemical reactions.[27] Hence, SABRE has been used to track and gain mechanistic insight into chemical reactivity.[28]

In this communication, we use the typical SABRE precatalyst $[IrCl(COD)(IMes)]$ (where IMes = 1,3-bis(2,4,6-

trimethylphenyl)imidazole-2-ylidene and COD = *cis,cis*-1,5-cyclooctadiene), which has been used to derive high signal gains for N-donor atoms[22,29] to hydrogenate phenylvinylsulfoxide. We then use p-H_2 to study this hydrogenation reaction and find that $[IrCl(H)_2(IMes)(sulfoxide)_2]$-type intermediates can be made visible to NMR. We use 2D NMR techniques to study and characterize the detected complexes and those created when closely related dibenzylsulfoxide is studied. Notably, X-ray diffraction is used to identify two iridium dimers that are formed by C−S bond activation and account for the catalyst deactivations that are associated with these reactions.

Examination of a methanol-d_4 solution containing [IrCl-(COD)(IMes)] (**1**) and phenylvinylsulfoxide (**A**) (4 equiv) at 245 K yields in the first instance ^1H NMR resonances corresponding to the two starting materials. There is no visible evidence to suggest that sulfoxide **A** can displace the chloride ligand of **1** to form $[Ir(COD)(IMes)(A)]Cl$ as is typically seen with many N-donor reagents.[22,30] Upon addition of 3 bar H_2 to this solution, hydride-containing complexes yielding resonances at δ −13.32, −18.48, and δ −15.75, −21.99 rapidly form, even at 245 K. These low intensity hydride-containing products are unstable, and their proportion decreases when the reaction time is increased. Notably, the hydride resonances at δ −13.32, −18.48 are consistent with the formation of a species of the type $[IrCl(H)_2(COD)(IMes)]$, **2**, which results from direct hydrogen addition to **1**, and their appearance is independent of sulfoxide ligand. Over time, the resonances corresponding to **A** decrease and are eventually replaced by those of phenylethylsulfoxide, **B**, as shown in Figure 1. NMR spectroscopy at 245 K alongside mass spectrometry was used to confirm its identity (see the Supporting Information). The formation of **B** is readily evident from the large chemical shift difference that exists between the associated alkene protons of

A at δ 5.97, 6.18, and 6.79, which decrease in intensity, and those of the hydrogenated product **B** at δ 1.19, 2.89, and 3.09, which grow in intensity. We note that the two CH_2 protons in phenylethylsulfoxide, as denoted by the green square in Figure 1, are diastereotopic. Under these conditions, the slow hydrogenation of **A** is indicated (Figure 1a) such that after 50 min a turnover frequency of 1.01×10^{-4} s^{-1} can be estimated. Slow hydrogenation is a consequence of the low reaction temperature (245 K). The formation of **B** is unsurprising as the hydrogenation of this vinylsulfoxide has been reported in the literature.[7,8] However, many reported procedures use rhodium catalysts.[7,8] Here, we use cheaper iridium-based catalysts to achieve the hydrogenation of a vinylsulfoxide. As a control, we note that a methanol-d_4 solution of **A** is stable under 3 bar H_2 at room temperature overnight.

We use the PHIP approach to study the hydrogenation of **A** by **1** in more detail. A similar methanol-d_4 solution of **1** containing 4 equiv of **A** was therefore exposed to 3 bar p-H_2 and immediately shaken for 10 s at 65 G before being placed into a 9.4 T spectrometer. Upon ^1H NMR detection at 298 K, hyperpolarized resonances for the CH_2 and CH_3 groups of **B** were observed with an ALTADENA-type appearance,[31] as shown in Figure 2a. Upon ejecting this sample, immediately adding fresh p-H_2, and shaking it for 10 s at 65 G before re-examination, the intensity of these hyperpolarized responses is seen to dramatically decrease. These effects were, however, no

Figure 1. (a) Hydrogenation of **A** to **B** catalyzed by **1** can be monitored at 245 K using ^1H NMR spectroscopy. (b) ^1H NMR spectrum of **A** and **1** at 245 K prior to H_2 addition (top) and the corresponding spectrum after the solution has been left under 3 bar H_2 at 245 K for 1 h before increasing to 298 K.
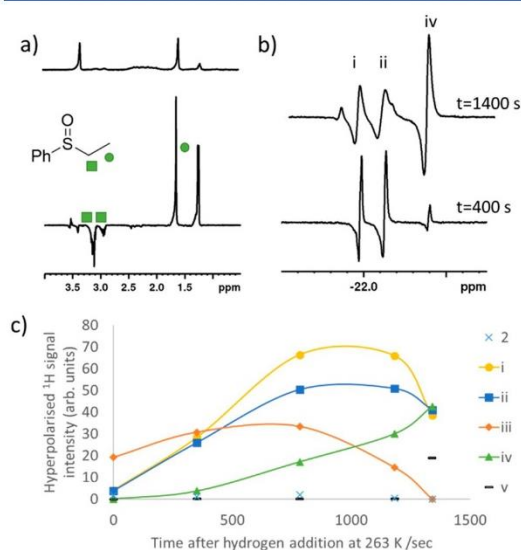
Figure 2. (a) Thermal (top) and hyperpolarized (bottom) ^1H spectra recorded using 45° pulses of a solution of **1** and **A** shaken for 10 s at 65 G immediately after the addition of 3 bar p-H_2 at 298 K. (b) Partial hyperpolarized ^1H spectra recorded using 45° pulses of a solution of **1** and **A** shaken for 10 s at 65 G ∼400 and ∼1400 s after initial p-H_2 addition at 263 K. Full spectra are given in the Supporting Information. (c) Change in hyperpolarized signals of these hydride-containing species with successive fresh p-H_2 shaking can be monitored at 263 K; even though the presented experimental data represent a single sample and, therefore, a series of single-point measurements, we expect them to exhibit a 5% error based on other studies and note the same trends were reproduced by other samples.
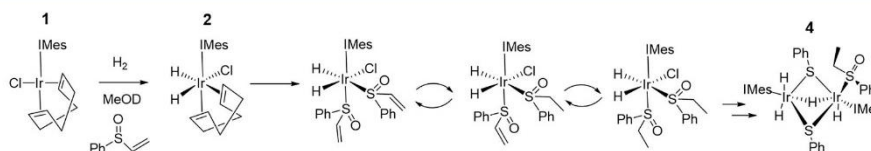
Figure 3. Proposed reaction scheme that allows the hydrogenation of vinylsulfoxide **A**. **4** is a decomposition product observed by X-ray diffraction.

longer visible when this sequence of steps is repeated again. This is reflective of the speed of initial hydrogenation, which rapidly consumes both H_2 and **A**; it is so fast that a PHIP response is not seen in a multiple scan measurement. When the hydride region of these single-scan ^1H NMR spectra are examined more closely, a pair of strongly hyperpolarized hydride resonances are observed at δ −16.09 and −22.44, which increase in intensity when fresh p-H_2 is shaken (see Supporting Information). The species giving rise to these resonances is not visible in the corresponding ^1H NMR spectrum recorded when signal strengths are derived from Boltzmann conditions. The complexity of the hydride region of these NMR spectra also increases when monitored after subsequent additions of fresh p-H_2.

We can gain a clearer view of these changes when a fresh solution is monitored in a series of single-scan hyperpolarized ^1H NMR spectra at 263 K. The associated measurements start by observing a pair of hydride signals corresponding to **2**, which are accompanied by additional sets at δ −15.83, −21.94 (i), δ −15.93, −22.10 (ii), and δ −29.22, −29.58 (iii). After repeating the fresh p-H_2 shaking and observation process several times, these resonances are found to decrease in intensity and are replaced by others at δ −16.20, −22.37 (iv) and δ −26.87, −31.28 (v), as shown in Figure 2b,c. The hydride resonances for (iii) and (v) compare well with those previously reported for methanol or water-containing species,[32] whereas those of (i), (ii), and (iv) correlate with the chemical shifts previously reported for $[IrCl(H)_2(DMSO)_2(IMes)]$.[33] We therefore expect that these signals arise from similar complexes, which in this case are likely to be of the form $[IrCl(H)_2(A)_2(IMes)]$ (i) $[IrCl(H)_2(A)(B)(IMes)]$ (ii), and $[IrCl(H)_2(B)_2(IMes)]$ (iv). Based on these observations, we suggest a mechanism for the iridium-catalyzed hydrogenation of **A** as detailed in Figure 3. It starts with the formation of $[IrCl(H)_2(IMes)(S(O)(CH=CH_2)(Ph))_2]$, which is followed by $[IrCl(H)_2(IMes)(S(O)(CH=CH_2)(Ph))(S(O)(Et)-(Ph))]$ on the basis of rapid ligand exchange *trans* to hydride prior to $[IrCl(H)_2(IMes)(S(O)(Et)(Ph))_2]$.

To confirm this behavior, we also investigated dibenzylsulfoxide, **C**, as a control that does not contain an unsaturated vinyl group. When 3 bar H_2 was added to a methanol-d_4 solution of **1** and **C** (4 equiv relative to iridium), the associated reaction proceeds to form a major product that yields ^1H NMR signals for two coupled hydride ligands at δ −15.78 and −20.89 ($^2J_{HH} = 6$ Hz). The formation of this species at 245 K was monitored by recording a series of ^1H NMR spectra, and the reaction time course is shown in the Supporting Information. NMR characterization of this complex at 245 K reveals it to be $[IrCl(H)_2(C)_2(IMes)]$, **3**. It yields four pairs of diastereotopic CH_2 protons due to bound **C**, as detailed in the Supporting Information. These groups show both COSY and NOESY connections to resonances within the phenyl group of the sulfoxide. NOESY measurements confirmed which resonances arise from the sulfoxide ligand that lies *trans* to

the hydride on the basis of a connection to a carbene ligand CH_3 resonance. Full NMR characterization data for **3** are given in the Supporting Information. Its hydride chemical shifts at δ −15.78 and −20.89 are indicative of chemical environments *trans* to chloride and S-donor ligands, respectively, and correlate well with those of similar complexes.[33] We note that addition of **A** (4 equiv) to a solution of preformed **3** also results in the formation of **B**, which confirms the lability of the sulfoxide ligands in these complexes necessary for catalysis.

Many of the mechanistic studies that focus on Rh-catalyzed hydrogenation propose intermediates that involve sulfoxide coordination through oxygen rather than sulfur.[7,8] In this novel iridium-based system, we suggest that the primary mode of sulfoxide coordination is through the sulfur lone pair. The S-donor binding modes of these sulfoxides in similar iridium(III) complexes have been determined based on the characteristic sulfoxide S−C chemical shift change upon binding.[33]

When solutions that contain **1** and **A** in methanol-d_4 are left under 3 bar H_2 at 278 K, the growth of single crystals was observed. Unfortunately, subsequent X-ray diffraction revealed they contain $[Ir_2(H)_3(\kappa^2\text{-}H)(\kappa^2\text{-}SPh)_2(IMes)_2(S(O)(Et)-(Ph))]$ (**4**), the structure of which is shown in Figure 4 rather than the mononuclear species shown in Figure 3 This iridium(III)-based dimer contains a phenylethylsulfoxide ligand on one center that supports the hydrogenation of **A**. This ligand is coordinated through a sulfur lone pair rather than oxygen in accordance with the shorter Ir−S bond distance (2.262 Å compared to a 3.248 Å Ir−O distance). Both iridium centers exhibit distorted octahedral geometries, with an Ir−Ir bond distance of 2.798 Å, comparing well to literature values of 2.826,[34] 2.823,[35] 2.734,[36] 2.642,[37] and 2.607 Å,[37] which suggests there is a metal−metal single bond. Interestingly, the observation of two bridging thiolate ligands confirms that S−C_α bond breaking occurs within the hydrogenated product. The activation of S−C bonds[38−40] and subsequent formation of S-bridged iridium dimers in hydrodesulfurization processes has been reported previously.[40] In this case, mass spectrometry and NMR confirmed that S−C bond cleavage is limited to the metal products, and there is no evidence for thiol buildup in solution. Hence, **4** is a minor decomposition product that forms slowly.

A related S−C bond cleavage step occurs over long reaction times when solutions of **1** and **C** in methanol-d_4 are left under 3 bar H_2 at 278 K. In this case, the associated reaction results in the growth of $[Ir_2(H)_4(\kappa^2\text{-}S)(IMes)_2(S(O)(CH_2Ph)_2)_2]$ (**5**) crystals, the structure of which is also shown in Figure 4. Shorter Ir−S bond distances (2.298 and 2.296 Å) compared to Ir−O distances (3.280 and 3.264 Å) are again seen that indicate sulfur binding. The slightly longer Ir−Ir bond distance of 2.902 Å suggests a weaker metal−metal interaction.

These sulfoxide C−S bond activations are expected to account for catalyst deactivation and the reducing turnover with time. We note that only trace amounts of **4** and **5**
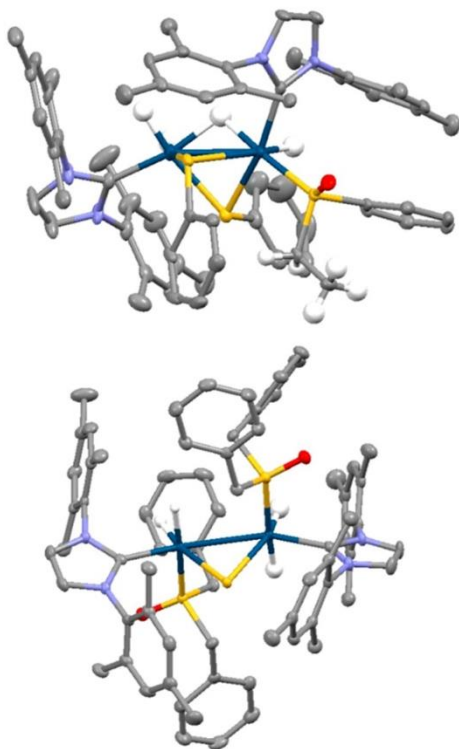
Figure 4. Structures of single crystals of (a) $[Ir_2(H)_3(\kappa^2\text{-}H)(\kappa^2\text{-}SPh)_2(IMes)_2(S(O)(Et)(Ph))]$, **4**, and (b) $[Ir_2(H)_4(\kappa^2\text{-}S)(IMes)_2(S(O)(CH_2Ph)_2)_2]$, **5**, determined from X-ray crystallography. Solvents of crystallization and selected hydrogen atoms have been omitted for clarity.

crystallized, and that these reflect only some of the many species present in the system at this stage of reaction.

When 4 equiv of **A** is used relative to **1**, 70% of **A** is hydrogenated after 12 h under 3 bar H_2 at 298 K. However, a significant amount of vinylsulfoxide is hydrogenated in the initial stages of the reaction: 30% is converted in the first 15 min, which corresponds to a turnover of 1.2×10^{-3} s^{-1} in this time period. This suggests that catalyst deactivation caused by S−C bond activation and subsequent dimer formation in these systems is rapid. The initial turnover frequency is comparable to those reported for the hydrogenation of vinylsulfoxide using other Rh-based systems (between 1.4×10^{-3} and 2.2×10^{-2} s^{-1} in MeOD using 5 bar H_2).[8] Although these turnovers are not improved by increasing the ratio of **A** to catalyst (see Supporting Information), in related Rh-based systems, they can be improved by up to 2 orders of magnitude by variation of solvent and the catalyst's ligands. When hydrogenating a sample of **A** with a 0.04 mol % catalyst loading relative to substrate at 298 K with 3 bar H_2, we calculate a turnover number of 48, which is comparable to those reported with Rh systems (30−70).[8] We expect that similar variations in this iridium-based system, including working at higher H_2 pressures, higher temperatures, and variation of solvent, could increase these turnovers and turnover numbers.

In conclusion, we have demonstrated that precatalyst $[IrCl(COD)(IMes)]$ is active for the hydrogenation of phenylvinylsulfoxide. This ligand hydrogenation reaction leads to the conversion of initially formed $[IrCl(H)_2(\mathbf{A})_2(IMes)]$ into $[IrCl(H)_2(\mathbf{A})(\mathbf{B})(IMes)]$ and $[IrCl(H)_2(\mathbf{B})_2(IMes)]$. We expect that such products are important species in the catalytic hydrogenation of vinylsulfoxides and have observed some of these intermediates using PHIP. However, none of these complexes exhibit long-term stability, with S−C bond cleavage leading to the iridium dimer $[Ir_2(H)_3(\kappa^2\text{-}H)(\kappa^2\text{-}SPh)_2(IMes)_2(S(O)(Et)(Ph))]$. This lack of S−C bond stability is also evident in the chemistry of dibenzylsulfoxide, which leads first to $[IrCl(H)_2(sulfoxide)_2(IMes)]$ and then slowly the iridium dimer, $[Ir_2(H)_4(\kappa^2\text{-}S)(IMes)_2(S(O)(CH_2Ph)_2)_2]$. Interestingly, our catalytic system involves S-donor sulfoxide coordination rather than an O-donor. The N-heterocyclic (NHC) ligands used in our catalytic system reflect a structurally diverse range of ligands that are commonly used in SABRE[41,42] and other organocatalysis reactions.[43] Chiral NHCs can be prepared,[44] and the use of such ligands for the enantioselective hydrogenation of sulfoxides may reflect an exciting future application of this work.[8]

■ ASSOCIATED CONTENT

ⓢ Supporting Information

The Supporting Information is available free of charge on the ACS Publications website at DOI: 10.1021/acs.organomet.9b00610. NMR data for this paper can be found at DOI 10.15124/b11b7146-b95d-4aca-bf39-f6fcc9421035.

Experimental details, NMR characterization data, crystallographic data and reaction monitoring (PDF)

Accession Codes

CCDC 1949692−1949693 contain the supplementary crystallographic data for this paper. These data can be obtained free of charge via www.ccdc.cam.ac.uk/data_request/cif, or by emailing data_request@ccdc.cam.ac.uk, or by contacting The Cambridge Crystallographic Data Centre, 12 Union Road, Cambridge CB2 1EZ, UK; fax: +44 1223 336033.

■ AUTHOR INFORMATION

Corresponding Author
*E-mail: simon.duckett@york.ac.uk.

ORCID 🄾
Ben J. Tickner: 0000-0002-8144-5655
Adrian C. Whitwood: 0000-0002-5132-5468
Simon B. Duckett: 0000-0002-9788-6615

Notes
The authors declare no competing financial interest.

■ REFERENCES

(1) Cotton, H.; Elebring, T.; Larsson, M.; Li, L.; Sörensen, H.; von Unge, S. Asymmetric synthesis of esomeprazole. *Tetrahedron: Asymmetry* **2000**, *11* (18), 3819−3825.

(2) Carreño, M. C. Applications of sulfoxides to asymmetric synthesis of biologically active compounds. *Chem. Rev.* **1995**, *95* (6), 1717−1760.

(3) Cotton, F.; Francis, R. Sulfoxides as ligands. I. A preliminary survey of methyl sulfoxide complexes. *J. Am. Chem. Soc.* **1960**, *82* (12), 2986−2991.

(4) Trost, B. M.; Rao, M. Development of chiral sulfoxide ligands for asymmetric catalysis. *Angew. Chem., Int. Ed.* **2015**, *54* (17), 5026−5043.

(5) Fernandez, I.; Khiar, N. Recent developments in the synthesis and utilization of chiral sulfoxides. *Chem. Rev.* **2003**, *103* (9), 3651−3706.

(6) Sipos, G.; Drinkel, E. E.; Dorta, R. The emergence of sulfoxides as efficient ligands in transition metal catalysis. *Chem. Soc. Rev.* **2015**, *44* (11), 3834−3860.

(7) Ando, D.; Bevan, C.; Brown, J. M.; Price, D. W. Contrasting pathways for the directed homogeneous hydrogenation of vinyl sulfoxides and vinyl sulfones. *J. Chem. Soc., Chem. Commun.* **1992**, *8*, 592−594.

(8) Lao, J. R.; Fernández-Pérez, H.; Vidal-Ferran, A. Hydrogenative Kinetic Resolution of Vinyl Sulfoxides. *Org. Lett.* **2015**, *17* (16), 4114−4117.

(9) Dornan, P. K.; Kou, K. G.; Houk, K.; Dong, V. M. Dynamic Kinetic Resolution of Allylic Sulfoxides by Rh-Catalyzed Hydrogenation: A Combined Theoretical and Experimental Mechanistic Study. *J. Am. Chem. Soc.* **2014**, *136* (1), 291−298.

(10) Eisenschmid, T. C.; Kirss, R. U.; Deutsch, P. P.; Hommeltoft, S. I.; Eisenberg, R.; Bargon, J.; Lawler, R. G.; Balch, A. L. Para hydrogen induced polarization in hydrogenation reactions. *J. Am. Chem. Soc.* **1987**, *109* (26), 8089−8091.

(11) Bowers, C. R.; Weitekamp, D. P. Parahydrogen and synthesis allow dramatically enhanced nuclear alignment. *J. Am. Chem. Soc.* **1987**, *109* (18), 5541−5542.

(12) Patz, S.; Hersman, F. W.; Muradian, I.; Hrovat, M. I.; Ruset, I. C.; Ketel, S.; Jacobson, F.; Topulos, G. P.; Hatabu, H.; Butler, J. P. Hyperpolarized 129Xe MRI: a viable functional lung imaging modality? *Eur. J. Radiol.* **2007**, *64* (3), 335−344.

(13) Nelson, S. J.; Kurhanewicz, J.; Vigneron, D. B.; Larson, P. E. Z.; Harzstark, A. L.; Ferrone, M.; van Criekinge, M.; Chang, J. W.; Bok, R.; Park, I.; et al. Metabolic imaging of patients with prostate cancer using hyperpolarized [1−13C] pyruvate. *Sci. Transl. Med.* **2013**, *5* (198), 198ra108.

(14) Zacharias, N. M.; Chan, H. R.; Sailasuta, N.; Ross, B. D.; Bhattacharya, P. Real-time molecular imaging of tricarboxylic acid cycle metabolism in vivo by hyperpolarized 1−13C diethyl succinate. *J. Am. Chem. Soc.* **2012**, *134* (2), 934−943.

(15) Bhattacharya, P.; Chekmenev, E. Y.; Perman, W. H.; Harris, K. C.; Lin, A. P.; Norton, V. A.; Tan, C. T.; Ross, B. D.; Weitekamp, D. P. Towards hyperpolarized 13C-succinate imaging of brain cancer. *J. Magn. Reson.* **2007**, *186* (1), 150−155.

(16) Hübler, P.; Giernoth, R.; Kümmerle, G.; Bargon, J. Investigating the kinetics of homogeneous hydrogenation reactions using PHIP NMR spectroscopy. *J. Am. Chem. Soc.* **1999**, *121* (22), 5311−5318.

(17) Giernoth, R.; Heinrich, H.; Adams, N. J.; Deeth, R. J.; Bargon, J.; Brown, J. M. PHIP detection of a transient rhodium dihydride intermediate in the homogeneous hydrogenation of dehydroamino acids. *J. Am. Chem. Soc.* **2000**, *122* (49), 12381−12382.

(18) Ahlqvist, M.; Gustafsson, M.; Karlsson, M.; Thaning, M.; Axelsson, O.; Wendt, O. F. Rhodium (I) hydrogenation in water: Kinetic studies and the detection of an intermediate using 13C {1H} PHIP NMR spectroscopy. *Inorg. Chim. Acta* **2007**, *360* (5), 1621−1627.

(19) Duckett, S. B.; Newell, C. L.; Eisenberg, R. Observation of new intermediates in hydrogenation catalyzed by wilkinson's catalyst, RhCl (PPh3) 3, using parahydrogen-induced polarization. *J. Am. Chem. Soc.* **1994**, *116* (23), 10548−10556.

(20) Sorochkina, K.; Zhivonitko, V. V.; Chernichenko, K.; Telkki, V.-V.; Repo, T.; Koptyug, I. V. Spontaneous 15N Nuclear Spin Hyperpolarization in Metal-Free Activation of Parahydrogen by Molecular Tweezers. *J. Phys. Chem. Lett.* **2018**, *9* (4), 903−907.

(21) Zhivonitko, V. V.; Sorochkina, K.; Chernichenko, K.; Kótai, B.; Földes, T.; Pápai, I.; Telkki, V.-V.; Repo, T.; Koptyug, I. Nuclear spin hyperpolarization with ansa-aminoboranes: a metal-free perspective for parahydrogen-induced polarization. *Phys. Chem. Chem. Phys.* **2016**, *18* (40), 27784−27795.

(22) Adams, R. W.; Aguilar, J. A.; Atkinson, K. D.; Cowley, M. J.; Elliott, P. I.; Duckett, S. B.; Green, G. G.; Khazal, I. G.; López-Serrano, J.; Williamson, D. C. Reversible interactions with para-hydrogen enhance NMR sensitivity by polarization transfer. *Science* **2009**, *323* (5922), 1708−1711.

(23) Adams, R. W.; Duckett, S. B.; Green, R. A.; Williamson, D. C.; Green, G. G. R. A theoretical basis for spontaneous polarization transfer in non-hydrogenative para hydrogen-induced polarization. *J. Chem. Phys.* **2009**, *131* (19), 194505.

(24) Iali, W.; Rayner, P. J.; Duckett, S. B. Using parahydrogen to hyperpolarize amines, amides, carboxylic acids, alcohols, phosphates, and carbonates. *Sci. Adv.* **2018**, *4* (1), No. eaao6250.

(25) Truong, M. L.; Theis, T.; Coffey, A. M.; Shchepin, R. V.; Waddell, K. W.; Shi, F.; Goodson, B. M.; Warren, W. S.; Chekmenev, E. Y. 15N hyperpolarization by reversible exchange using SABRE-SHEATH. *J. Phys. Chem. C* **2015**, *119* (16), 8786−8797.

(26) Eshuis, N.; van Weerdenburg, B. J. A.; Feiters, M. C.; Rutjes, F. P. J. T.; Wijmenga, S. S.; Tessari, M. Quantitative trace analysis of complex mixtures using SABRE hyperpolarization. *Angew. Chem., Int. Ed.* **2015**, *54* (5), 1481−1484.

(27) Procacci, B.; Aguiar, P. M.; Halse, M. E.; Perutz, R. N.; Duckett, S. B. Photochemical pump and NMR probe to monitor the formation and kinetics of hyperpolarized metal dihydrides. *Chem. Sci.* **2016**, *7* (12), 7087−7093.

(28) Semenova, O.; Richardson, P. M.; Parrott, A. J.; Nordon, A.; Halse, M. E.; Duckett, S. B. Reaction monitoring using SABRE-hyperpolarized benchtop (1 T) NMR spectroscopy. *Anal. Chem.* **2019**, *91* (10), 6695−6701.

(29) Truong, M. L.; Theis, T.; Coffey, A. M.; Shchepin, R. V.; Waddell, K. W.; Shi, F.; Goodson, B. M.; Warren, W. S.; Chekmenev, E. Y. N-15 Hyperpolarization by Reversible Exchange Using SABRE-SHEATH. *J. Phys. Chem. C* **2015**, *119* (16), 8786−8797.

(30) Appleby, K. M.; Mewis, R. E.; Olaru, A. M.; Green, G. G. R.; Fairlamb, I. J. S.; Duckett, S. B. Investigating pyridazine and phthalazine exchange in a series of iridium complexes in order to define their role in the catalytic transfer of magnetisation from para-hydrogen. *Chem. Sci.* **2015**, *6* (7), 3981−3993.

(31) Pravica, M. G.; Weitekamp, D. P. Net NMR alignment by adiabatic transport of parahydrogen addition products to high magnetic field. *Chem. Phys. Lett.* **1988**, *145* (4), 255−258.

(32) Knecht, S.; Hadjiali, S.; Barskiy, D. A.; Pines, A.; Sauer, G.; Kiryutin, A. S.; Ivanov, K. L.; Yurkovskaya, A. V.; Buntkowsky, G. Indirect Detection of Short-lived Hydride Intermediates of Iridium N-Heterocyclic Carbene Complexes via Chemical Exchange Saturation Transfer (CEST) Spectroscopy. *J. Phys. Chem. C* **2019**, *123* (26), 16288−16293.

(33) Iali, W.; Roy, S. S.; Tickner, B. J.; Ahwal, F.; Kennerley, A. J.; Duckett, S. B. Hyperpolarizing Pyruvate through Signal Amplification By Reversible Exchange (SABRE). *Angew. Chem.* **2019**, *131* (130), 10377−10381.

(34) Rasmussen, P. G.; Anderson, J. E.; Bailey, O. H.; Tamres, M.; Bayón, J. C. A novel metal-metal bonded iridium (II) dimer. *J. Am. Chem. Soc.* **1985**, *107* (1), 279−281.

(35) Gilbert, T. M.; Hollander, F. J.; Bergman, R. G. (Pentamethylcyclopentadienyl) iridium polyhydride complexes: synthesis of intermediates in the mechanism of formation of (pentamethylcyclopentadienyl) iridium tetrahydride and the preparation of several

iridium (V) compounds. *J. Am. Chem. Soc.* **1985**, *107* (12), 3508–3516.

(36) Jones, W. D.; Chin, R. M. Hydrodesulfurization of thiophene to butadiene and butane by a homogeneous iridium complex. *J. Am. Chem. Soc.* **1994**, *116* (1), 198–203.

(37) Li, M.-L.; Yang, S.; Su, X.-C.; Wu, H.-L.; Yang, L.-L.; Zhu, S.-F.; Zhou, Q.-L. Mechanism Studies of Ir-Catalyzed Asymmetric Hydrogenation of Unsaturated Carboxylic Acids. *J. Am. Chem. Soc.* **2017**, *139* (1), 541–547.

(38) Wang, L.; He, W.; Yu, Z. Transition-metal mediated carbon–sulfur bond activation and transformations. *Chem. Soc. Rev.* **2013**, *42* (2), 599–621.

(39) Luh, T.-Y.; Ni, Z.-J. Transition-metal-mediated CS bond cleavage reactions. *Synthesis* **1990**, *1990* (02), 89–103.

(40) O'Connor, J. M.; Bunker, K. D.; Rheingold, A. L.; Zakharov, L. Sulfoxide Carbon– Sulfur Bond Activation. *J. Am. Chem. Soc.* **2005**, *127* (12), 4180–4181.

(41) Fekete, M.; Bayfield, O.; Duckett, S. B.; Hart, S.; Mewis, R. E.; Pridmore, N.; Rayner, P. J.; Whitwood, A. Iridium (III) Hydrido N-heterocyclic carbene–phosphine complexes as catalysts in magnetization transfer reactions. *Inorg. Chem.* **2013**, *52* (23), 13453–13461.

(42) van Weerdenburg, B. J.; Eshuis, N.; Tessari, M.; Rutjes, F. P.; Feiters, M. C. Application of the π-accepting ability parameter of N-heterocyclic carbene ligands in iridium complexes for signal amplification by reversible exchange (SABRE). *Dalton Trans* **2015**, *44* (35), 15387–15390.

(43) Marion, N.; Díez-González, S.; Nolan, S. P. N-heterocyclic carbenes as organocatalysts. *Angew. Chem., Int. Ed.* **2007**, *46* (17), 2988–3000.

(44) Gade, L. H.; Bellemin-Laponnaz, S. Chiral N-heterocyclic carbenes as stereodirecting ligands in asymmetric catalysis. *N-Heterocyclic Carbenes in Transition Metal Catalysis*; Springer, 2006; pp 117–157.

Appendix 7

PAPER

Check for updates

Optimisation of pyruvate hyperpolarisation using SABRE by tuning the active magnetisation transfer catalyst†

Ben. J. Tickner, [ID][a] Olga Semenova, [ID]‡[a] Wissam Iali, [ID]§[a] Peter J. Rayner, [ID][a] Adrian C. Whitwood [ID][b] and Simon B. Duckett [ID]*[a]

Hyperpolarisation techniques such as signal amplification by reversible exchange (SABRE) can deliver NMR signals several orders of magnitude larger than those derived under Boltzmann conditions. SABRE is able to catalytically transfer latent magnetisation from *para*-hydrogen to a substrate in reversible exchange *via* temporary associations with an iridium complex. SABRE has recently been applied to the hyperpolarisation of pyruvate, a substrate often used in many *in vivo* MRI studies. In this work, we seek to optimise the pyruvate-$^{13}C_2$ signal gains delivered through SABRE by fine tuning the properties of the active polarisation transfer catalyst. We present a detailed study of the effects of varying the carbene and sulfoxide ligands on the formation and behaviour of the active $[Ir(H)_2(\eta^2\text{-pyruvate})(\text{sulfoxide})(\text{NHC})]$ catalyst to produce a rationale for achieving high pyruvate signal gains in a cheap and refreshable manner. This optimisation approach allows us to achieve signal enhancements of 2140 and 2125-fold for the 1-^{13}C and 2-^{13}C sites respectively of sodium pyruvate-1,2-$[^{13}C_2]$.

Introduction

Nuclear magnetic resonance (NMR) and magnetic resonance imaging (MRI) are some of the most widely used tools for the characterisation of molecules and the clinical diagnosis of disease. While these techniques are used widely in their fields, they remain insensitive as their signal strengths are derived from small Boltzmann population differences across the nuclear spin energy levels they probe. Recently, a growing number of researchers are turning their attention to hyperpolarisation to help address this problem.[1–3] For example, dynamic nuclear polarisation (DNP) can achieve polarisation levels of 92% and 70% for ^{1}H and ^{13}C signals in times as short as 150 seconds and 20 minutes respectively.[4,5] DNP transfers the inherent polarisation of an electron into target nuclei when both are located in a frozen glass matrix and subject to microwave irradiation at or near the resonance frequency of the electron at very low temperatures (1–2 K).[4–6] Rapid heating of such solids then generates materials that yield MR signal enhancements in solution of up to 5 orders of magnitude.[5,6] This approach has been applied to the production of hyperpolarised biomolecules such as pyruvate,[7–14] succinate,[15,16] and fumarate[17,18] which are then injected and detected *in vivo* alongside their metabolic by-products. Imaging the formation of such metabolites provides a route to studying biochemical tissue function in real time with obvious benefits for disease diagnosis.[7–17]

Para-Hydrogen induced polarisation (PHIP) methods are potentially a faster and cheaper alternative to DNP.[19–21] The feedstock of PHIP is *para*-hydrogen (*p*-H_2), which is the isomer of dihydrogen that exists as a nuclear spin singlet. In the first generation of PHIP studies, *p*-H_2 was typically incorporated into a substrate *via* a hydrogenation reaction.[22,23] The resulting product detection by NMR has since provided many significant observations in the field of catalysis wherein reaction intermediates are detected.[24–26] The catalytic production of hyperpolarised probes suitable for *in vivo* study using this version of PHIP was therefore limited to biomolecules that have facile access to their dehydro-precursor.[15,27,28] This limitation has been elegantly alleviated using a variant of PHIP, termed *para*-hydrogen induced polarisation by side arm hydrogenation (PHIP-SAH), which can produce aqueous solutions of hyperpolarised pyruvate and acetate.[29] In the precursor, pyruvate is functionalised as an ester with an unsaturated side arm which, after

[a] *Centre for Hyperpolarization in Magnetic Resonance (CHyM), University of York, Heslington, YO10 5NY, UK. E-mail: simon.ducket@york.ac.uk*
[b] *Department of Chemistry, University of York, Heslington, YO10 5DD, UK*

† Electronic supplementary information (ESI) available. CCDC 1957542–1957543. For ESI and crystallographic data in CIF or other electronic format see DOI: 10.1039/c9cy02498k

‡ Present Address: Dr. O. Semenova, Drug Discovery Unit, School of Life Sciences, University of Dundee, Dundee, DD1 5EH, United Kingdom.
§ Present Address: Dr. W. Iali, Department of Chemistry, King Fahd University of Petroleum and Minerals (KFUPM), Dhahran, 31261, Saudi Arabia.

This journal is © The Royal Society of Chemistry 2020

Catal. Sci. Technol., 2020, **10**, 1343–1355 | **1343**

hydrogenation by p-H$_2$ and a magnetic field cycling step to transfer polarisation into the modified pyruvate, can be rapidly released through simultaneous hydrolysis and phase separation.[29,30] The resulting pyruvate can then be detected by MRI through a much stronger, hyperpolarised, response. Hyperpolarised pyruvate prepared in this way is the result of a one-shot, irreversible batch synthesis.

In contrast, signal amplification by reversible exchange (SABRE) is an alternative non-hydrogenative PHIP based method that involves the transfer of spin polarisation from p-H$_2$ to a substrate when both are concurrently bound to an iridium catalyst, as depicted in Fig. 1.[31] As the ligands are in reversible exchange, a pool of hyperpolarised substrate is readily created in solution. Hence, the magnetisation transfer step is catalytic in nature, occurring via the temporary J-coupled network within the organometallic complex. Consequently, the process is completed without chemical change and is continuous and refreshable in nature.[32] The identity of the ligands used in such SABRE magnetisation transfer catalysts are important in delivering high MR signal gains and controlling the type of substrates that can be hyperpolarised.[33–35] SABRE has had the greatest success to date in polarising structures with N-heterocyclic motifs which have a simple and readily understandable binding mode.[34,36–38] In these cases, polarisation transfer catalysts of the form [Ir(H)$_2$(NHC)(Sub)$_3$]Cl provide suitable substrate (Sub) and H$_2$ exchange rates for significant polarisation build up in solution.

Until recently α-keto acids, such as pyruvate, were incompatible with SABRE because they were unable to form stable complexes due to their weak ligation to iridium.[39] A related technique, SABRE-Relay, has allowed the hyperpolarisation of a wide range of non-ligating substrates that contain functional groups which can receive hyperpolarised protons through exchange from a suitable carrier.[40,41] When applied to sodium pyruvate-1-[^{13}C] this

approach readily delivers 50-fold ^{13}C enhancements.[40] However, rapid $in\ situ$ condensation of pyruvate with the amine carrier forms products of the type [Ir(H)$_2$(η^2-α-carboxyimine)(amine)(NHC)] which deactivate the system to further pyruvate polarisation.[42]

It has since been reported that by using appropriate stabilising ligands, SABRE can hyperpolarise pyruvate in a low cost, fast, and reversible fashion that does not involve the technologically demanding equipment of DNP, or the multiple steps of PHIP-SAH.[39] This is possible due to the formation of the polarisation transfer catalyst [Ir(H)$_2$(η^2-pyruvate)(DMSO)(IMes)] (where IMes = 1,3-bis(2,4,6-trimethyl-phenyl)imidazol-2-ylidene) when solutions of [IrCl(COD)-(IMes)] (**1a**) (where COD = cis,cis-1,5-cyclooctadiene), DMSO and sodium pyruvate in methanol-d_4 or 70 : 30 mixtures of D$_2$O and ethanol-d_6 are activated with 3 bar of H$_2$. These sulfoxide based complexes exhibit significantly more elaborate catalysis than more commonly observed in SABRE with N-donor substrates as the Sub and H$_2$ exchange pathways are no longer localised within a single inorganic species.[43] This is because while [Ir(H)$_2$(η^2-pyruvate)(DMSO)-(IMes)] reflects the active polarisation transfer catalyst for ^{13}C pyruvate enhancement, it is [IrCl(H)$_2$(DMSO)$_2$(IMes)] (**2**) that mediates the necessary H$_2$ exchange processes.[43] This situation is complicated yet further by the fact [Ir(H)$_2$(η^2-pyruvate)(DMSO)(IMes)] (**3**) exists as two regioisomers that are differentiated by the geometry of η^2-pyruvate coordination, as depicted in Fig. 1b. We have previously shown that the regioisomer where pyruvate binds in the same plane as the hydride ligands (**3b**) contains a spin topology that allows active polarisation transfer of singlet order from p-H$_2$ derived hydride ligands to coordinated ^{13}C pyruvate sites in the catalyst.[39,43]

SABRE is dependent on the magnetic field experienced by the sample during polarisation transfer because a suitable matching condition for optimal polarisation transfer between p-H$_2$ derived hydride ligands and the ligated target substrate must be achieved. For ^{13}C-SABRE by complexes of this type, optimal transfer typically occurs at mG fields if direct transfer from the p-H$_2$ derived hydride ligands into bound ^{13}C sites is involved.[39,43,44] For sodium pyruvate-1-[^{13}C] and sodium pyruvate-2-[^{13}C] this necessitates fields of ±9 and ±3 mG respectively.[39] Interestingly, when sodium pyruvate-1,2-[^{13}C$_2$] is used, the resulting process leads to the spontaneous creation of long lived ^{13}C$_2$ singlet order in the product being detected whose decoherence lifetime exceeds that of T_1.[39] In such states, the underlying magnetisation involves two coupled spins and, in this case, its formation is independent of magnetic field. In the context of this paper, it is important to appreciate that p-H$_2$ reflects another example of such a singlet state which is now not only very long lived, but NMR invisible. This singlet order becomes visible to NMR by a symmetry breaking reaction, such as the oxidative addition of p-H$_2$ to the iridium centre.[45] In contrast to p-H$_2$, the two coupled ^{13}C spins of sodium pyruvate-1,2-[^{13}C$_2$] are already magnetically distinct and consequently its singlet state is
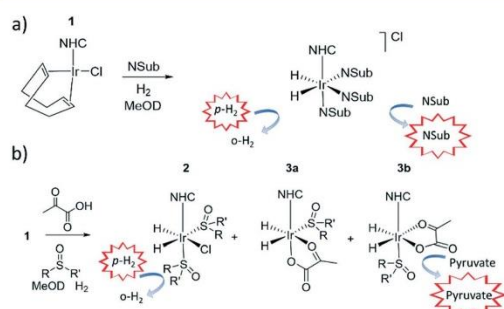
Fig. 1 a) Traditionally, SABRE catalytically transfers magnetisation from p-H$_2$ to an N-donor substrate (NSub) through a temporary J-coupled network when both p-H$_2$ and NSub are in reversible exchange with a complex such as [Ir(H)$_2$(IMes)(NSub)Cl b) pyruvate hyperpolarisation using SABRE can be achieved via [Ir(H)$_2$(η^2-pyruvate)(DMSO)(IMes)] where p-H$_2$ exchange is now predominantly mediated by [IrCl(H)$_2$(DMSO)$_2$(IMes)].

immediately accessible by NMR and evolves more quickly that than of p-H$_2$.

In this paper we report on a series of rigorous catalytic studies that investigate the role that the [Ir(H)$_2$(IMes)(η^2-pyruvate)(sulfoxide)] and [IrCl(H)$_2$(DMSO)$_2$(IMes)] type species play in the ^{13}C hyperpolarisation of pyruvate. Throughout this work we use sodium pyruvate-1,2-[^{13}C$_2$] as the target substrate because the longer lifetime of its hyperpolarised singlet state may have future benefits in reaction monitoring or medical imaging. It must be remembered that as we create the hyperpolarised molecule remote to the final point of observation there is a time delay between preparation and detection. Thus increased magnetic state lifetimes extend the timescale over which signal detection is possible and offer significant potential benefits for tracer analysis. We show here that optimisation of the hyperpolarisation level delivered by the catalyst is complex, with factors such as catalyst identity, concentration and temperature exhibiting non-trivial behaviour due to the complex interplay that exists between the roles of the different species present in solution. Consequently, we explore the properties of the active catalyst by varying the identity of both sulfoxide and NHC ligand to produce a rationale for achieving high ^{13}C pyruvate NMR signal enhancements using SABRE.

Results and discussion

Formation of an active sulfoxide containing magnetisation transfer catalyst, [Ir(H)$_2$(IMes)(η^2-pyruvate)(DMSO)]

When sodium pyruvate-1-2-[^{13}C$_2$] (6 equivalents relative to iridium) is used as the substrate and added to **1** in the presence of dimethyl sulfoxide (DMSO) (4 equivalents) and 3 bar H$_2$ in methanol-d_4, an equilibrium mixture of [IrCl(H)$_2$(sulfoxide)$_2$(NHC)] (**2**) and [Ir(H)$_2$(η^2-pyruvate)-(sulfoxide)(NHC)] (**3**) is formed (Fig. 1b).[39,43] The regioisomer containing ligated pyruvate which lies *trans* to both hydride, and the NHC, is labelled **3a** whereas the regioisomer where pyruvate lies in the same plane as the two hydride ligands is labelled **3b**. Both of these structures are illustrated in Fig. 1b.

When examining these solutions with a signal averaged 32 scan ^{1}H NMR measurement at 298 K, the main hydride containing complex present is **3b**. Resonances for **2** and **3a** could not be discerned under these conditions, although, upon shaking this solution with 3 bar of p-H$_2$ for 10 seconds at 65 G, hyperpolarised hydride responses for **2**, **3a** and **3b** are immediately detected, as shown in Fig. 2a.[39,43] Furthermore, upon shaking this sample for 10 seconds in a mu metal shield (*ca.* 300-fold shielding), hyperpolarised ^{13}C resonances are observed, as shown in Fig. 2b. These correspond to those of free pyruvate at δ 169 and δ 203 (J_{CC} = 62 Hz) and pyruvate bound in **3b** at δ 168 and δ 207 (J_{CC} = 60 Hz) and we quantify the ^{13}C signal gains as 1215-fold and 910-fold for the [1-^{13}C] and [2-^{13}C] sites respectively in the free material. Additional resonances corresponding to pyruvate hydrate at δ 97 and δ 177 (J_{CC} = 62 Hz) and pyruvate bound within **3a** at δ 166 and δ 196 (J_{CC} = 63 Hz) are also visible. A
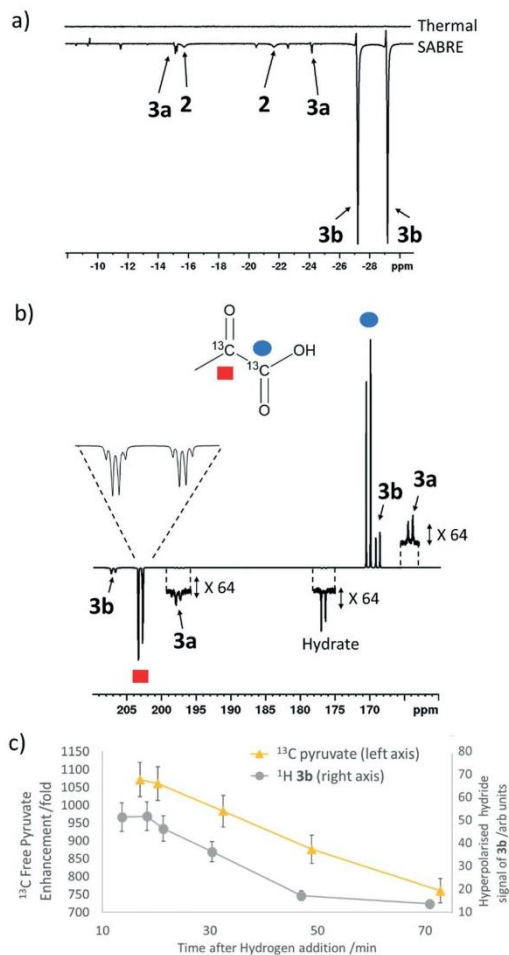
Fig. 2 NMR spectra of a) ^{1}H hydride region and b) ^{13}C carbonyl region after shaking a solution of **1a**, 6 equivalents sodium pyruvate-1,2-[^{13}C$_2$] and 4 equivalents of DMSO with 3 bar p-H$_2$ for 10 seconds a) at 65 G or b) in a mu metal shield c) the averaged ^{13}C signal gain across the [1-^{13}C] and [2-^{13}C] sites and hyperpolarised hydride signal intensity of **3b** can be monitored over time with fresh p-H$_2$ shaking. Note that one anomalous data point was omitted.

multi-scan thermally polarised ^{13}C{^{1}H} NMR measurement confirms these assignments for ligated pyruvate in both **3a** and **3b** in addition to those of the free material and its hydrate. 2D NMR characterisation data for these complexes has been previously reported.[39] When we examine the signals of the [1-^{13}C] and [2-^{13}C] sites more closely we observe ~2 Hz and ~20 Hz resonance broadening upon pyruvate coordination respectively. We note that the [2-^{13}C] resonance of the free material appears as a doublet of quartets with a $^1J_{CC}$ value of 62 Hz and a smaller $^2J_{HC}$ coupling between the adjacent methyl group protons of 6 Hz. This smaller $^2J_{HC}$ is

not visible for pyruvate bound in **3b** due to broadening effects. In order to explore how the efficiency of polarisation transfer changes with reaction time, this sample was shaken with fresh p-H_2 at various time intervals after initial p-H_2 addition. The hyperpolarised ^{13}C and ^1H signals that could be detected for pyruvate and **3b** respectively were found to decrease with time, as shown in Fig. 2c, which is consistent with catalyst decomposition.

Variation of the $[Ir(H)_2(IMes)(\eta^2\text{-pyruvate})(L)]$ co-ligand, L

Polarisation transfer catalysts of the form $[Ir(H)_2(IMes)(\eta^2\text{-pyruvate})(L)]$ containing η^2-ligated pyruvate and p-H_2 derived hydride ligands are essential for catalytic polarisation transfer into bound pyruvate ^{13}C sites and ultimately free pyruvate after ligand dissociation. A range of different co-ligands, L, (5 equivalents relative to iridium) were screened with $[IrCl(COD)(IMes)]$ (**1a**) (5 mM), and sodium pyruvate-1,2-$[^{13}C_2]$ (6 equivalents), and 3 bar p-H_2 in methanol-d_4 to identify if any other classes of co-ligands besides DMSO could form analogous complexes to **2** and **3**.

The use of 4-chlorobenzenemethanethiol as a co-ligand did not initially yield any hydride containing species. However, upon leaving the solution for a period of several months at 278 K, the growth of single crystals was observed. Upon examination by X-ray diffraction they were found to correspond to $[Ir_2(H)_4(\kappa^2\text{-SCH}_2C_6H_4Cl)(IMes)_2]$ as detailed in the ESI.† We, and others, have reported structures of similar sulphur bridged iridium dimers[26,46] and other products resulting from SH bond functionalisation.[47] The other tested co-ligands, formaldehyde, triphenylphosphine (PPh$_3$), ethylisothiocyanate and thiophene, all resulted in the formation of hydride complexes within 1 hour of H_2 addition, but the corresponding solutions did not display any PHIP enhanced hydride signals upon shaking with p-H_2. When a solution of **1a**, PPh$_3$ and sodium pyruvate-1,2-$[^{13}C_2]$ with 3 bar H_2 in methanol-d_4 is left at 278 K for several months, the growth of single crystals was again observed. X-ray diffraction studies identified the product as $[Ir(H)_3(PPh_3)_3]$, as detailed in the ESI.† In contrast, the use of imidazole as a co-ligand did result in a hydride complex at δ −22.3 that exhibited PHIP, as detailed in the ESI.†[48,49] However, in each of these cases no additional ^{13}C pyruvate resonances were observed by NMR spectroscopy thereby suggesting that pyruvate coordination to iridium in these systems does not occur.

Of the co-ligands tested here, only sulfoxides supported pyruvate ligation to iridium. We expect this to be related to the optimum binding strength of the co-ligand which must be similar to that of pyruvate if its binding is not to be inhibited. For example, when the nitrogen based donor imidazole is used it seems to out compete pyruvate binding.[31,34,50–52] In these cases $[Ir(H)_2(IMes)(NSub)_3]Cl$ type complexes form as revealed by a single hydride signal around δ −22.3.[47,48] The use of a sulfoxide based co-ligand is therefore a suitable compromise that leads to pyruvate

binding and subsequent ^{13}C signal gains and for this reason we explore how its identity affects this process.

Effect of sulfoxide identity on pyruvate $^{13}C_2$ signal enhancement

Studies on the effect of sulfoxide identity on the formation of $[IrCl(H)_2(\text{sulfoxide})_2(NHC)]$ (**2**) and $[Ir(H)_2(\eta^2\text{-pyruvate})(\text{sulfoxide})(NHC)]$ (**3**) and the subsequent ^{13}C pyruvate enhancement proved to be complex. For this work $[IrCl(COD)(IMes)]$ (**1a**) was activated in methanol-d_4 with 3 bar H_2 in the presence of 6 equivalents of sodium pyruvate-1,2-$[^{13}C_2]$ and 4 equivalents of one of the ten sulfoxides (**I–X**) of Fig. 3. The pyruvate ^{13}C signal enhancement was then quantified after shaking the sample with fresh p-H_2 several times over a 90 minute time period following H_2 addition. In order to compare the performance efficiency as a function of sulfoxide identity we define several parameters. The first, ε_{max}, describes the highest attained free ^{13}C pyruvate signal enhancement for either the 1-$[^{13}C]$ or 2-$[^{13}C]$ site relative to the Boltzmann derived response. We observe that in most cases the signal gain on the 1-$[^{13}C]$ and 2-$[^{13}C]$ sites are the same within error, and we also quote averaged signal enhancements across the two sites. This is due to creation of $^{13}C_2$ singlet order which must be shared equally amongst the two ^{13}C sites. The second parameter, τ_{60}, describes the percentage decrease in ^{13}C pyruvate signal enhancement at the 60 minute reaction point when compared to the first measurement. R_{3b} is the ratio of the **3b** type product at the ε_{max} point relative to the sum of all the hydride containing species and this should illustrate the stability of the sulfoxide–catalyst combination. The relative absolute integrals of the enhanced hydride ^1H NMR signals of **3b** after shaking at 65 G, S_{3b}, was also determined during the reaction period and was found to exhibit similar behaviour. These values are presented for each of the sulfoxides **I–X** in Table 1.

For sulfoxides **I–VIII**, hyperpolarised ^{13}C pyruvate responses are observed immediately upon shaking the sample with 3 bar p-H_2 in a mu metal shield. Over the next
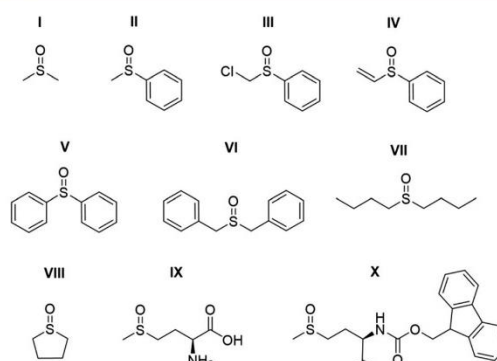
Fig. 3 Structures of the sulfoxides I–X used in this work.

Table 1 Comparison of ε_{max}, τ_{60}, S_{3b} and R_{3b} values (see text for definition) for methanol-d_4 solutions of **1a**, 6 equivalents of sodium pyruvate-1,2-[$^{13}C_2$] and 4 equivalents of the specified sulfoxide I–X of Fig. 3 after shaking with 3 bar p-H$_2$ for 10 seconds in a mu metal shield.

Sulfoxide	$^{13}C_1$ ε_{max}/fold^a	$^{13}C_2$ ε_{max}/fold^a	τ_{60}/%	S_{3b}/arb. units	R_{3b}/%
I	1215 ± 40	910 ± 30	23	50	60
II	1090 ± 35	1035 ± 30	6	85	90
III	1090 ± 35	1040 ± 30	32	20	93
IV	115 ± 5	105 ± 5	92	5	N/A^b
V	555 ± 15	545 ± 15	3	60	90
VI	195 ± 5	180 ± 5	3	5	70
VII	400 ± 10	385 ± 10	9	25	45
VIII	1150 ± 35	1040 ± 30	60	70	95
IX	0	0	N/A	N/A	0
X	130 ± 5	115 ± 5	17	N/A^c	N/A^c

^{a} These reflect one shot measurements due to the change in signal over time. Errors are based on an average of three measurements for a sample containing **II** where the observed enhancement is relatively constant thereby allowing repeat measurement. ^{b} Rapid sample degradation prevented recording R_{3b} at a similar time point to ε_{max}. ^{c} No signals for a species analogous to **3b** were evident.

90 minute time period, the resulting ^{13}C pyruvate signal enhancements all gradually decrease (see ESI†). In all cases, the major dihydride complex present in solution proved to be of type **3b**. Similarly, the hydride signals corresponding to **3b** type products dominate the associated hyperpolarised hydride region of these ^1H NMR spectra, and the intensity of their signals also decrease with increasing reaction time. Increasing the structural complexity of the co-ligand through the use of amino acid derived sulfoxide, **IX**, resulted in no ^{13}C pyruvate signal enhancement, or detection of signals for species of type **3**. While a hydride containing complex forms, which yields resonances at δ −12.3 and δ −27.3 that exhibit weak PHIP enhancement upon shaking with p-H$_2$ (see ESI†), no evidence of pyruvate coordination was found. The poor performance of this sulfoxide could relate to the ready formation of an insoluble white precipitate, likely to be the corresponding [pyruvate-COO$^-$ + $^+$NH$_3$-**IX**] salt. When the protected co-ligand analogue, **X**, is used instead, pyruvate coordination and subsequent enhancement is again observed, but the resulting signal gains are just ~120 fold. This is consistent with the lack of visible hydride signals for species of type **3**. Hence, we link these low pyruvate enhancements to a low concentration of what we prove later to be the active magnetisation transfer catalyst.

Sulfoxides **I–III** and **VIII** delivered the highest levels of ^{13}C signal enhancement for pyruvate across this series (ε_{max} > 1000 fold) while **IV–VII** produced hyperpolarised ^{13}C pyruvate signals of lower intensity (100–550 fold). These trends broadly matched those seen for the levels of hydride hyperpolarisation of the corresponding **3b** derivatives. In the case of **IV**, the ^{13}C pyruvate response rapidly decayed to zero as a consequence of hydrogenation of the original sulfoxide ligand and subsequent catalyst decomposition which has been observed in closely related systems.[26] We have reported that C–S bond activation products result from this process which logically accounts for the low R_{3b} and ε_{max} values achieved by **IV**.[26] In fact, we suggest that similar sulfoxide reactivity accounts for the loss of the **3b** derivatives in all samples. We highlight that despite a high ε_{max} being

quantified for **VIII**, catalyst deactivation is extremely rapid. Hence, it is clear that SABRE efficiency is linked to the concentration of the **3b** derivative in solution, which falls as the reaction time increases.

Sulfoxides **VI** and **VII** result in lower proportions of **3b** (R_{3b} of 70% and 45% in solution respectively) being present in these mixtures which will contribute to the lower pyruvate signal enhancements that are observed. In contrast, sulfoxides **II–V** commonly result in high proportions of **3b** (R_{3b} > 90%) and any differences in pyruvate ^{13}C signal enhancement between these sulfoxides must now relate more closely to the efficiency of the polarisation transfer catalysis rather than catalyst concentration. For example, we note that **I** achieves a similar level of pyruvate enhancement to **II**, **III** and **VIII** despite the much lower ratio (60%) of **3b** present in solution. In contrast, **IV** and **V** contain similar R_{3b} values to **II** and **III** (90%) yet yield much lower pyruvate enhancements (<550-fold as compared to >1000 fold). This suggests that when sulfoxide **I** is utilized, a more effective catalytic system is created when compared to those derived from co-ligands **IV** and **V**.

We conclude from these data that the sulfoxide co-ligand identity plays a significant role in determining the concentration of the active SABRE catalyst in solution and the efficiency of the polarisation transfer process. Thus increasing the proportion of **3b** present in solution is clearly one requirement for optimal SABRE. Of the four sulfoxides that gave pyruvate ^{13}C NMR signal enhancements greater than 1000-fold, **II** appeared to be most stable to catalyst decomposition exhibiting only a 6% drop in signal intensity after 1 hour compared to 23, 32 and 60% for **I**, **III** and **VIII** respectively. These results show that H$_2$ reaction time is also an important parameter that must be considered when optimising these pyruvate ^{13}C NMR signal gains. This is often neglected when polarising N-donor substrates using SABRE as the associated magnetisation transfer catalysts are often more stable over longer reaction times.

Methylphenylsulfoxide, **II**, was identified as the best performing sulfoxide of this series as the associated complex gave some of the highest ^{13}C pyruvate signal enhancements whilst also

This journal is © The Royal Society of Chemistry 2020

Catal. Sci. Technol., 2020, **10**, 1343–1355 | **1347**

resulting in the highest hyperpolarised hydride ligand signal intensities for the isomer of type **3b**. The concentration of methylphenylsulfoxide **II** was then varied to determine its effect on pyruvate enhancement. Similar behaviour is seen for both the ^{1}H and ^{13}C NMR signal enhancements of **3b** when compared to those seen for free pyruvate. We find that using 10 equivalents of sulfoxide **II** relative to **1a** provides the highest ^{13}C pyruvate response, as shown in the ESI.† We expect that this is related to optimal ligand exchange processes at these effective reagent concentrations.

We have previously reported that complexes of the type [IrCl(H)$_2$(NHC)(sulfoxide)$_2$] (**2**) exchange hydrogen rapidly and are important in refreshing the p-H$_2$ derived hydride ligands within the catalytic system.[43] It is therefore likely that the rate of this process depends on sulfoxide identity and is reflected in the differing hydride signal intensities for the **3b** isomer. The rate of H$_2$ exchange within **2** was found to be independent of sulfoxide concentration when the sulfoxide is in excess (6–14 equivalents relative to iridium)[43] in accordance with the first step of this process being the dissociative loss of sulfoxide. Therefore, we expect that changing sulfoxide concentration must have a greater effect on exchange between **2** and **3**, however this process could not be quantified using EXSY methods. It is clear that the sulfoxide identity plays a role in p-H$_2$ refreshment within **2** and likely the exchange between **2** and **3**.

Effect of chloride ions on pyruvate ^{13}C$_2$ signal enhancement

The rapid rate of H$_2$ exchange in **2** in comparison to **3** indicates that **2** provides a clear route to refresh the p-H$_2$ derived hydride ligands in **3**. It is for this reason that the rate of exchange between **2** and **3** is proposed to play a significant role in determining the observed ^{13}C pyruvate signal enhancement. As **2** contains a chloride ligand that is released into solution when **3** is formed, the concentration of available chloride might also be important in the formation of **3**. We have already reported that there is a large decrease in the resulting pyruvate signal enhancement when chloride is replaced by bromide or acetonitrile.[43] Here, we investigate the effect of changing the chloride concentration. To do this, solutions of **1a** (5 mM), 10 equivalents of sulfoxide **I** and 5 equivalents of sodium pyruvate-1,2-[^{13}C$_2$] in 0.6 mL methanol-d_4 containing 0–5 equivalents of NaCl in 5 μL of D$_2$O were prepared. The resulting SABRE solutions were then activated with 3 bar H$_2$ and their ^{13}C NMR pyruvate signal enhancements monitored as a function of time. The associated signal intensity *versus* reaction time profiles are given in the ESI† and they all show an initial increase in ^{13}C pyruvate signal enhancement over the first ~30 minute period followed by a subsequent decrease as the reaction time increases. This change mirrors the associated change in concentration of **3b** based on changes in hyperpolarised hydride resonance intensity. Upon increasing the chloride concentration from 0 to 1 equivalents, we observe a decrease in the average pyruvate enhancement across the two sites

from 1000-fold to 920-fold. Further decreases to 715-fold and 570-fold are observed as the amount of NaCl is increased to 3 and 5 equivalents respectively. We note that greater chloride concentrations also result in higher proportions of free pyruvate signal relative to that seen for the associated bound resonances within **3b**. These changes are accompanied by an increase in the size of the hydride signals seen for **2** relative to those of **3b**, as shown in Fig. 4. These changes are therefore consistent with a shift in the equilibrium position towards **2** and the resulting fall in pyruvate signal gain is linked to a reduction in the amount of the active polarisation transfer catalyst, **3b** present in these solutions.

The effect of the reduction in active catalyst concentration was tested explicitly by increasing the initial amount of **1a** and **II** so that a greater amount of **3b** was present in solution. The resulting mixture with **1a** (10 mM), **II** (100 mM) and sodium pyruvate-1,2-[^{13}C$_2$] in a 1:10:6 ratio yielded averaged ^{13}C NMR signal enhancements of 705 and 255-fold for free and bound pyruvate respectively. The corresponding enhancements for the same solution containing 5 equivalents NaCl in 5 μL D$_2$O were now much closer for the free pyruvate signal at 690-fold but the bound signal fell to 140 fold. These results confirm that the elevated chloride concentrations increase the proportion of free pyruvate enhancement relative to its bound counterpart. In addition they show that at the 10 mM catalyst concentration the free pyruvate signal enhancement remains comparable to that with the higher NaCl concentration. When the metal concentration was 5 mM, a reduction of pyruvate signal gain upon salt addition takes the averaged signal gain down from 1000-fold to 570-fold. As expected, this difference suggests the greater flux associated with improved efficiency in what would be a bimolecular H$_2$ addition step can help offset the effect of increased chloride concentration.

The equilibrium between **2** and **3** is also expected to be influenced by the concentration of pyruvate in solution. Therefore, samples containing **1a**, 10 equivalents of **II** and 3, 6 or 8.5 equivalents of sodium pyruvate-1,2-[^{13}C$_2$] were shaken with 3 bar p-H$_2$ in methanol-d_4. Lowering the pyruvate concentration from 6 equivalents to 3 equivalents resulted in the averaged pyruvate signal enhancement reducing from 1085-fold and 515-fold for the free and bound pyruvate respectively to just 770-fold and 365-fold respectively. An increase in pyruvate concentration from 6 to 8.5 equivalents was accompanied by a similar drop in averaged signal gain to 630-fold and 180-fold respectively for the free and bound signals in comparative runs. Interestingly, as the ratio of pyruvate to iridium increases, the proportion of free pyruvate enhancement relative to the bound counterpart in **3b** also increases. This is consistent with an increased likelihood of binding unpolarised pyruvate during SABRE as its concentration increases.

Effect of catalyst identity on pyruvate ^{13}C$_2$ signal enhancement

The efficiency of traditional [Ir(H)$_2$(NHC)(Sub)$_3$]Cl based SABRE catalysts is also influenced by the identity of the NHC
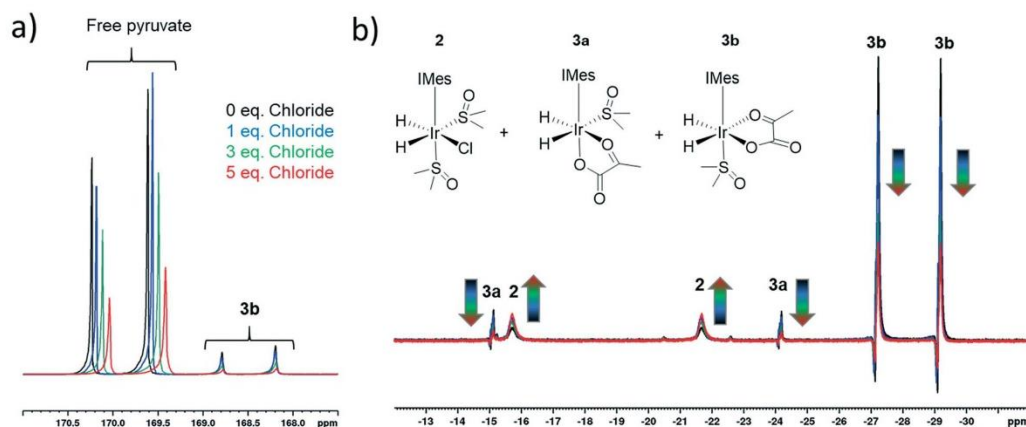
Fig. 4 Partial a) ^{13}C and b) ^{1}H hyperpolarised NMR spectra resulting from shaking a sample of [IrCl(COD)(IMes)], 5 equivalents of sodium pyruvate-1,2-[^{13}C$_2$], and 10 equivalents of DMSO with varying amounts of NaCl in 0.6 mL methanol-d_4 with 3 bar p-H$_2$ for 10 seconds, a) in a mu metal shield 35 minutes following the initial H$_2$ addition step and b) at 65 G, 10 minutes following the initial H$_2$ addition step.

ligand in the [IrCl(COD)(NHC)] precatalyst.[34] Variation of this ligand has been used as a route to optimise signal enhancements by tuning substrate exchange rates.[35,53–55] Changes to these ligands has also been used to synthesise water soluble SABRE catalysts.[56–58] The effect of catalyst identity on the pyruvate signal enhancement was therefore probed by investigating the behaviour of the iridium precatalysts, 1a–h, of Fig. 5. These complexes were chosen to

include symmetric N-heterocyclic carbenes with a range of Tolman electronic parameters and % buried volumes.[55] Additionally, asymmetric N-heterocyclic carbenes[59] and phosphine containing precatalysts,[31,35] which have both been used previously for SABRE, were also included. Samples were prepared containing 6 equivalents of pyruvate and 10 equivalents of methylphenylsulfoxide (II) with 3 bar p-H$_2$ in 0.6 mL methanol-d_4. The ^{13}C pyruvate signal enhancement, ^{1}H hydride signal enhancement for the 3b type product, and its relative proportion in solution as measured in a 32 scan thermal ^{1}H NMR spectrum, were monitored periodically over the first 90 minutes of reaction. These values are shown in Table 2 and are displayed graphically in the ESI.†

The identity of the precatalyst 1a–1f proved to have little effect on the proportion of the 3b type product in solution although there was an effect on ^{13}C pyruvate signal
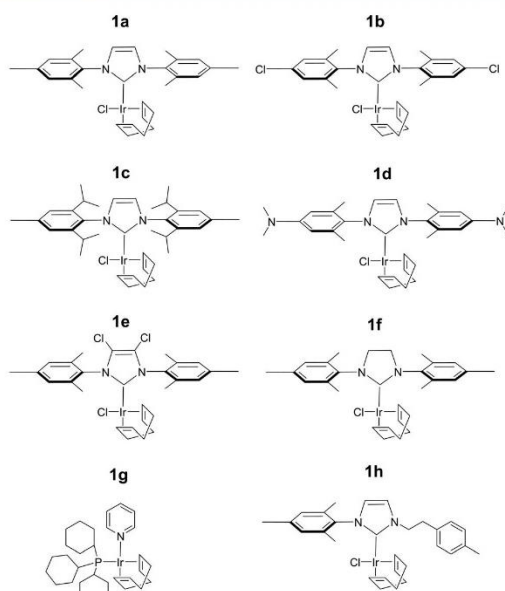
Fig. 5 Structures of the eight precatalysts used in this work.

Table 2 Comparison of ε_{max}, τ_{60}, and R_{3b} values (see text for definition) measured after shaking a solution of 6 equivalents sodium-1,2-pyruvate-[^{13}C$_2$] and 10 equivalents II with the specified iridium precatalyst 1a–h of Fig. 5 in methanol-d_4 with 3 bar p-H$_2$ for 10 seconds in a mu metal shield

Precatalyst	^{13}C$_1$ ε_{max}/fold^a	^{13}C$_2$ ε_{max}/fold^a	R_{3b}/%
1a	1085 ± 35	1085 ± 35	98
1b	905 ± 25	905 ± 25	95
1c	905 ± 30	885 ± 25	95
1d	980 ± 30	980 ± 30	90
1e	650 ± 20	660 ± 20	98
1f	870 ± 25	860 ± 25	95
1g	35 ± 2	25 ± 2	50
1h	60 ± 3	55 ± 3	N/A^b

^{a} These data reflect one shot measurements due to the change in signal over time. Errors are calculated based on an average of three measurements for a sample containing 1a where the observed enhancement is relatively constant thereby allowing repeat measurements. ^{b} No signals for the form corresponding to 3b were discerned.

enhancement. In all cases, a hyperpolarised ^{13}C pyruvate response was observed after shaking with 3 bar p-H$_2$. In contrast to **1a**, precatalysts **1b**–**1h** result in lower ^{13}C pyruvate signal enhancements immediately after H$_2$ addition. For some of these precatalysts, ε_{max}, occurs at much longer reaction times. Hence the differing precatalysts exhibit different activation periods and subsequently, different time points where the maximum concentration of **3b** is reached. This demonstrates how reaction time can be an important parameter that plays a large effect on the observed signal gain. For example, **1a** activates very rapidly and the proportion of its **3b** derivative is at a maximum shortly after the initial H$_2$ addition step. The corresponding ^{13}C pyruvate signal enhancement is also maximised at this time point. In contrast, **1c** has one of the slowest rates of **3b** derivative formation and hence the corresponding hyperpolarised pyruvate signal increases after the initial H$_2$ addition step as a function of the growth in **3b** concentration (see ESI†). Other precatalysts, such as **1b** and **1d**, also form **3b** derivatives which is reflected in an initial increase in pyruvate enhancement followed by a slow decrease as the concentration of **3** falls over a longer timescale. The resulting ^{13}C pyruvate signal enhancements can therefore be used as a route to effectively track the concentrations of **3b** type products in solution and hence monitor the conversion of **1** to **3**.

The phosphine based precatalyst **1g** yields just 50% of the **3b** type product in solution and the resulting pyruvate signal enhancements are now just ~30-fold. In contrast, when precatalyst **1h**, containing an asymmetric N-heterocyclic carbene ligand is used an isomer of type **3b** no longer forms. Here, we form larger amounts of **3a** which we expect to be due to reduced steric crowding associated with the smaller carbene ligand. Now, the hyperpolarised pyruvate signal shows a ~60-fold enhancement which is an order of magnitude lower than that provided by the symmetric carbene **1a**. This is consistent with the fact isomer **3b** is essential for attaining high levels of pyruvate polarisation. Interestingly, when **3a** is the more dominant species, the hyperpolarised ^{13}C$_2$ pyruvate profile no longer appears in the typical pattern diagnostic of ^{13}C$_2$ singlet order as created with catalysts **1a**–**1g**. This is also consistent with previous theoretical modelling studies which suggest that the spin topology of **3a** is incompatible with the easy retention of p-H$_2$ derived singlet spin order in the product.[39] It is clear that **3b**, which is formed when the precatalysts **1a**–**f** are used, reflects an active polarisation transfer catalysts with the necessary spin topology to mediate efficient polarisation transfer into bound ^{13}C$_2$ pyruvate. Some examples of representative NMR spectra are shown in Fig. 6.

Effect of temperature on pyruvate ^{13}C$_2$ signal enhancement

Many studies have varied the temperature to achieve a substrate exchange rate optimum for SABRE magnetisation transfer.[34,41,60] To this end, solutions of **1a**, 6 equivalents of sodium pyruvate-1,2-[^{13}C$_2$], and 4 equivalents of the sulfoxides **I–III**, **IV–VII**, shown in Fig. 3, were shaken with 3 bar p-H$_2$ in
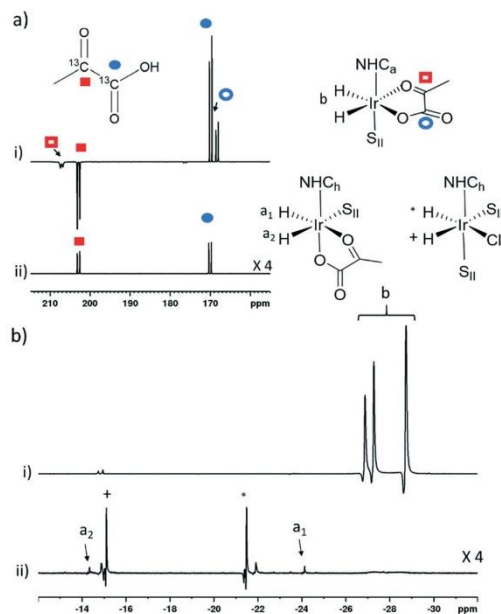
Fig. 6 Partial hyperpolarised a) ^{13}C and b) ^{1}H NMR responses after samples of i) **1a** and ii) **1h** containing 6 equivalents of sodium pyruvate-1,2-[^{13}C$_2$], and 10 equivalents of II are shaken in methanol-d_4 with 3 bar p-H$_2$ for 10 seconds in a mu metal shield. S_{II} and h in the structures refers to II and ligand h as shown in Fig. 3 and 5 respectively.

methanol-d_4 at three different temperatures. These temperatures (278 K, 293 K and 323 K) were achieved by placing the NMR tube in a thermostatically controlled water bath for 60 seconds prior to shaking for 10 seconds under p-H$_2$ at room temperature. Care was taken to record the NMR measurements at similar reaction times in order to compare these data. The effect of temperature upon the observed pyruvate ^{13}C signal enhancement is shown in Fig. 7a. For **I**, **II**, **VI**, and **VII** the resulting free pyruvate ^{13}C signal enhancement is maximised at room temperature while sulfoxides **III** and **V** perform better at the elevated temperature. Hence, whilst ligand exchange is slow and not detectable on the EXSY timescale, there must be an optimum rate for each complex as reported for other N-heterocyclic substrates.[60]

When this study was expanded to include solutions of the iridium precatalysts **1a**–**f** of Fig. 5, 6 equivalents of sodium pyruvate-1,2-[^{13}C$_2$], and 10 equivalents of methylphenylsulfoxide (**II**), similar temperature effects were seen as shown in Fig. 7b. For **1a**, 293 K proved optimal with warming clearly moving away from the required exchange rate. For **1b** and **1c**, the proportion of bound substrate polarisation is much higher relative to the free material when compared to the other precatalysts which may suggest slower exchange. This is expected for **1b** on account of the chloride substituent which decreases electron density on the metal

1350 | *Catal. Sci. Technol.*, 2020, **10**, 1343–1355

This journal is © The Royal Society of Chemistry 2020
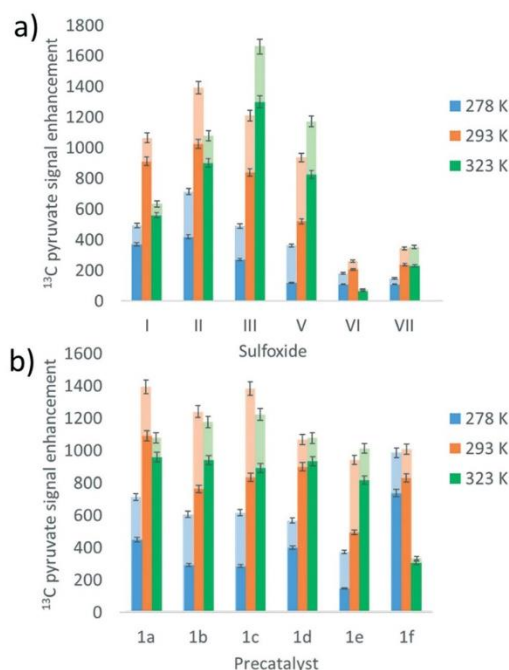
Fig. 7 Averaged hyperpolarised free (lower, darker colour) and bound (upper, lighter colour) ^{13}C pyruvate NMR signal enhancement values following shaking of methanol-d_4 solutions under SABRE containing a) 4 equivalents of sulfoxide I–III, V–VII with **1a** and b) the iridium precatalysts **1a**–**1f** with 6 equivalents of sodium pyruvate-1,2-[^{13}C$_2$] and 10 equivalents of II at 3 bar p-H$_2$ in a mu metal shield after 10 seconds exposure at the specified temperatures.

relative to **1a** and is therefore likely to result in stronger pyruvate binding and slower ligand exchange. **1c** contains a sterically demanding NHC which might be expected to promote exchange, although this is clearly not the case. In contrast, the metal centre in **1d** is electron rich thereby increasing exchange which agrees with the lower retained bound pyruvate polarisation level. Of the series, **1e** is the most electron deficient with high proportions of bound pyruvate signal and low levels of pyruvate enhancement which increase at higher temperatures. This is consistent with slower pyruvate exchange in the **1e** system.

We conclude that variation of the NHC ligand can have a large effect on the attained pyruvate enhancements. Understanding these effects is challenging and we expect that both steric and electronic effects associated with the ligands are important, as previously suggested for SABRE with N-heterocyclic substrates.[53,55] Here though, the ligand effects are likely to be more complex as they will not only influence the rate of pyruvate exchange within **3**, but also the rate of interconversion between **2** and **3** and the rate of H$_2$ exchange in **2**. Steric effects are important in determining the concentration of the active polarisation transfer catalyst, **3b**,

that forms in solution. Further optimisation of pyruvate signal gain is possible by subtle variation of the electronic effects of the active catalyst.

Effect of selective deuteration on pyruvate ^{13}C$_2$ signal enhancement

Relaxation within the substrate when bound to the catalyst has been shown to limit its degree of ^{1}H hyperpolarisation using SABRE. This effect has been reduced by the inclusion of deuterium labels within the active polarisation transfer catalyst whilst simultaneously reducing any polarisation leakage into the catalyst.[31,34,61,62] Therefore, we examined the effect of deuterating the sulfoxide ligand and the IMes backbone of the precatalyst.

Shaking a solution of **1a** with 6 equivalents of sodium pyruvate-1,2-[^{13}C$_2$], 4 equivalents of **I** and 3 bar p-H$_2$ in methanol-d_4 for 10 seconds in a mu metal shield yielded averaged free and bound pyruvate ^{13}C signal enhancements of 1070 and 200-fold respectively. When this process was repeated using the corresponding deuterium labelled sulfoxide **I**-d_6 at the same time point after H$_2$ addition these enhancements remained comparable at 1070 and 220-fold. This suggests that there is little polarisation leakage into this sulfoxide and that relaxation of hyperpolarised magnetisation via ^{1}H sites in its **3b** derivative does not limit the efficiency of SABRE.

In contrast, when the results from shaking a solution of **1a** with 6 equivalents of sodium pyruvate-1,2-[^{13}C$_2$], and 10 equivalents of **II** under 3 bar p-H$_2$ in methanol-d_4 are compared to those achieved with **1a**-d_{22} an effect is seen; in this case all the protons in the NHC except the two in the imidazole ring are labelled with ^{2}H. This is reflected in a fall in the averaged free ^{13}C$_2$ signal enhancement from 1085 to 875-fold although the bound pyruvate signals remain comparable at 515-fold and 535-fold respectively. When this measurement is repeated using **1a**-d_{24} these signal gains further decrease to 675 and 465-fold for free and bound pyruvate respectively. This suggests that ^{2}H labelling of the NHC is now detrimental to SABRE: a finding which is in direct contrast to commonly observed effects when [Ir(H)$_2$(NHC)(NSub)$_3$]Cl polarisation transfer catalysts are deuterated.[31,34,61,62] We suggest this could be due to the effects of quadrupolar relaxation at the mG polarisation transfer field caused by the introduction of deuterium, whereas previous studies have typically employed G polarisation transfer fields.

Further optimisation of pyruvate ^{13}C$_2$ signal enhancement by varying shaking time and hydrogen pressure

The effects of the p-H$_2$ shaking time and hydrogen pressure on the ^{13}C pyruvate signal enhancements were also investigated. This involved using a sample of **1a** with two equivalents of **II** at 1, 2 and 3 bar of p-H$_2$. The results revealed that there was a growth in averaged hyperpolarisation level for free pyruvate from 510 to 730-fold upon increasing the pressure from 1 bar to 3 bar, after which point the signal gain plateaus (see ESI†). This suggests that,

This journal is © The Royal Society of Chemistry 2020

Catal. Sci. Technol., 2020, **10**, 1343–1355 | **1351**

in this case, hydrogen exchange is rate limiting at pressures lower than 3 bar but once this pressure is exceeded it is ligand exchange and the associated relaxation processes within the catalyst that become limiting. We have already investigated how hydrogen exchange within $[IrCl(H)_2(IMes)(DMSO)_2]$ increases as H_2 pressure is increased from 0.5–2 bar.[43] We expect that the increase in pyruvate signal at these H_2 pressures is related to increased p-H_2 refreshment in the 2/3 system which does not become more efficient at pressures higher than 3 bar.

Higher averaged $^{13}C_2$ pyruvate signal enhancements result (1050 compared to 425-fold) when the shaking time in the mu metal shield is extended from 5 to 30 seconds in 5 second intervals, as detailed in the ESI.† This change allows polarisation to build up more effectively on both the bound and free ^{13}C sites. The observed effect on the ^1H signals of the hydride resonances in 3b is the opposite, with the visible signal gains decreasing. This implies more signal is transferred to the ^{13}C centres at longer shaking times. We confirmed that these trends are also observed for a sample of 1a-d_{24} with ten equivalents of II.

Combining optimisation steps to achieve improved pyruvate $^{13}C_2$ signal enhancement

We were able to achieve a maximum averaged pyruvate ^{13}C signal enhancement of 2135-fold (1.7% polarisation) for the free material alongside a 585-fold bound pyruvate signal

Fig. 8 Partial hyperpolarised ^{13}C NMR spectra for a) keto region and b) carbonyl region recorded after samples of i) 1g (5 mM), 10 eq. II and 6 equivalents of sodium pyruvate-1,2-[$^{13}C_2$] ii) 1a (5 mM), 4 eq. I and 6 equivalents of sodium pyruvate-1,2-[$^{13}C_2$] and iii) 1a (5 mM), 10 eq. II and 6 equivalents of sodium pyruvate-1,2-[$^{13}C_2$] are shaken in methanol-d_4 with 3 bar p-H_2 for i) and ii) 10 or iii) 30 seconds in a mu metal shield.

gain. This averaged gain corresponds to signal enhancements of 2140 and 2125-fold for the 1-^{13}C and 2-^{13}C sites respectively. We can therefore increase pyruvate signal gains by two orders of magnitude (from 30-fold for catalyst 1g, Table 2, to 2135-fold) by careful optimisation of factors including temperature, shaking time, catalyst, sulfoxide and their concentrations. These optimum enhancements involved a sample containing 1a (5 mM), 10 equivalents II and 6 equivalents sodium pyruvate-1,2-[$^{13}C_2$] in 0.6 mL methanol-d_4 that was shaken with 3 bar p-H_2 for 30 seconds in a mu metal shield. The effect of these optimisation steps on improving the signal gain is depicted in Fig. 8. We failed to see further increases with deuterium labelling of the sulfoxide or the NHC ligands or by shaking with 4.5 bar p-H_2. When all ^{13}C species in this sample, including bound pyruvate and its hydrated form, are included a net ^{13}C polarisation of 2845-fold (2.3% polarisation) is achieved which exceeds those previously reported.[39] We also note that the preparations used here are stable for a greater time period after hydrogen addition, thereby allowing for more repeat measurements and improved sample examination.

Conclusions

Optimising pyruvate signal gains is important for a range of applications that may include hyperpolarised reaction monitoring. For example, we have already demonstrated how the reaction of sodium pyruvate with hydrogen peroxide can be monitored using hyperpolarised ^{13}C NMR spectroscopy.[39] We have presented a detailed study that optimises the pyruvate signal gain by variation of sulfoxide and carbene ligand within $[Ir(H)_2(\eta^2$-pyruvate)(DMSO)(NHC)]$ polarisation transfer catalysts. We have shown that sulfoxide co-ligands are essential for the formation of these active species and the highest pyruvate signals can be achieved using a $[IrCl(COD)(IMes)]$ precatalyst in conjunction with 10 equivalents of phenylmethylsulfoxide. Sterically large carbenes are required if the formation of the active isomer 3b is to be favoured, although electronic effects are important in fine tuning the ligand exchange processes. Hyperpolarised $^{13}C_2$ pyruvate signal intensities are shown to be closely linked to the amount of the 3b isomer present in solution, although systems containing similar amounts but different ligands can result in very different pyruvate enhancements. These results highlight the tension between many different factors that influence the efficiency of polarisation transfer within this complex. In all cases we observe a decrease in both hyperpolarised $^{13}C_2$ pyruvate level and the ^1H hydride ligand signals of the 3b type isomer at longer reaction times which we associate with catalyst deactivation. By combining these effects we attained an averaged pyruvate ^{13}C signal enhancement level of 2135-fold (1.7% polarisation) for free sodium pyruvate-1,2-[$^{13}C_2$].

For biomedical applications, attaining high signal enhancements in aqueous, rather than methanolic solvents, is of more importance. When a solution of 1a and 10 eq. II

1352 | Catal. Sci. Technol., 2020, 10, 1343–1355

This journal is © The Royal Society of Chemistry 2020

are preactivated with 3 bar H_2 in ethanol-d_6 before adding sodium pyruvate-1,2-[$^{13}C_2$] in D_2O and shaking in a mu metal shield for 30 seconds ^{13}C signal gains are approximately an order of magnitude lower than those achieved in methanol-d_4. In these 70/30 D_2O/ethanol-d_6 mixtures, which might reflect a system suitable for future *in vivo* studies, the proportion of bound pyruvate enhancement is significantly higher than those achieved in methanol-d_4. It is therefore clear that in non-methanolic solvents pyruvate exchange is reduced which limits the attained polarisation levels. It is expected that the application of a similar optimisation approach would lead to improved pyruvate enhancements in this biocompatible solvent mixture *via* catalysts that exhibit faster exchange kinetics.

In summary, while SABRE provides a cheap, simple and reversible route to hyperpolarise pyruvate with time and cost advantages over alternative techniques such as DNP and PHIP-SAH, there is a limitation associated with the lower signal enhancements delivered here. Nevertheless, the formation and behaviour of these novel polarisation transfer catalysts and their applications to hyperpolarise pyruvate reflect an important step forward in *para*-hydrogen based hyperpolarisation. Future work is directed at gaining greater understanding of these catalyst effects, probing the ligand exchange processes that govern the attained polarisation levels and optimising them for use in conjunction with biocompatible solvents.

Experimental

All NMR measurements were carried out on a 400 MHz Bruker Avance III spectrometer using solutions at room temperature (298 K) unless otherwise stated. *Para*-Hydrogen (p-H_2) was produced by passing hydrogen gas over a spin-exchange catalyst (Fe_2O_3) and used for all hyperpolarisation experiments. This method produces constant p-H_2 with *ca.* 99% purity. ^1H (400 MHz) and ^{13}C (100.6 MHz) NMR spectra were recorded with an internal deuterium lock. Chemical shifts are quoted as parts per million and referenced to methanol-d_4. ^{13}C NMR spectra were recorded with broadband proton decoupling. Coupling constants (J) are quoted in Hertz. All commercial compounds listed were purchased from Sigma-Aldrich, Fluorochem, or Alfa-Aesar and used as supplied unless otherwise stated.

Samples were prepared containing 2 mg iridium catalyst with 6 equivalents of sodium pyruvate-1,2-[$^{13}C_2$] and 4 equivalents of sulfoxide unless otherwise stated in 0.6 mL of methanol-d_4 in a 5 mm NMR tube that was fitted with a J. Young's tap. Unless otherwise stated the iridium precatalyst used was [IrCl(COD)(IMes)] (where IMes = 1,3-bis(2,4,6-trimethyl-phenyl)imidazole-2-ylidene and COD = *cis*,*cis*-1,5-cyclooctadiene). Iridium precatalysts used in this work were synthesized in our laboratory according to literature procedures.[63] The solutions were subsequently degassed by two freeze–pump–thaw cycles.

The shake & drop method was employed for recording hyperpolarised NMR spectra. NMR tubes were filled with p-H_2 at 3 bar pressure and shaken vigorously for 10 seconds unless otherwise stated in the 65 G stray field next to a 9.4 T magnet for ^1H polarisation or in a mu metal shield (*ca.* 300-fold shielding) for ^{13}C polarisation and placing inside a 9.4 T spectrometer for NMR detection. Pyruvate ^{13}C enhancements were calculated by reference to a more concentrated thermal sample as outlined in Shchepin *et al.*[64] In cases where averaged ^{13}C enhancements are given across both 1-[^{13}C] and [2-^{13}C] sites the sum of these integrals is referenced to the sum of these integrals in the corresponding thermal measurement. Data points usually reflect an average of three shake and drop measurements while those that monitor signal growth over time are single point measurements with typical errors as determined from averaged data.

Conflicts of interest

B. J. T., W. I., and S. B. D. (and others) are inventors on a patent application filed by the University of York related to this work (patent no. GB1818171.9, filed 7 November 2018).

Notes and references

1 K. Golman, M. Lerche, R. Pehrson and J. H. Ardenkjaer-Larsen, *Cancer Res.*, 2006, **66**, 10855–10860.
2 K. Golman and M. Thaning, *Proc. Natl. Acad. Sci. U. S. A.*, 2006, **103**, 11270–11275.
3 S. E. Day, M. I. Kettunen, F. A. Gallagher, D.-E. Hu, M. Lerche, J. Wolber, K. Golman, J. H. Ardenkjaer-Larsen and K. M. Brindle, *Nat. Med.*, 2007, **13**, 1382.
4 S. Jannin, A. Bornet, R. Melzi and G. Bodenhausen, *Chem. Phys. Lett.*, 2012, **549**, 99–102.
5 J. H. Ardenkjær-Larsen, S. Bowen, J. R. Petersen, O. Rybalko, M. S. Vinding, M. Ullisch and N. C. Nielsen, *Magn. Reson. Med.*, 2019, **81**, 2184–2194.
6 J. H. Ardenkjær-Larsen, B. Fridlund, A. Gram, G. Hansson, L. Hansson, M. H. Lerche, R. Servin, M. Thaning and K. Golman, *Proc. Natl. Acad. Sci. U. S. A.*, 2003, **100**, 10158–10163.
7 A. Z. Lau, A. P. Chen, N. R. Ghugre, V. Ramanan, W. W. Lam, K. A. Connelly, G. A. Wright and C. H. Cunningham, *Magn. Reson. Med.*, 2010, **64**, 1323–1331.
8 J. D. MacKenzie, Y.-F. Yen, D. Mayer, J. S. Tropp, R. E. Hurd and D. M. Spielman, *Radiology*, 2011, **259**, 414–420.
9 M. Pourfathi, Y. Xin, S. J. Kadlecek, M. F. Cereda, H. Profka, H. Hamedani, S. M. Siddiqui, K. Ruppert, N. A. Drachman and J. N. Rajaei, *Magn. Reson. Med.*, 2017, **78**, 2106–2115.

This journal is © The Royal Society of Chemistry 2020

Catal. Sci. Technol., 2020, **10**, 1343–1355 | **1353**

10 E. M. Serrao, M. I. Kettunen, T. B. Rodrigues, P. Dzien, A. J. Wright, A. Gopinathan, F. A. Gallagher, D. Y. Lewis, K. K. Frese and J. Almeida, *Gut*, 2016, **64**, 465–475.

11 M. Marjańska, I. Iltis, A. A. Shestov, D. K. Deelchand, C. Nelson, K. Uğurbil and P.-G. Henry, *J. Magn. Reson.*, 2010, **206**, 210–218.

12 S. J. DeVience, X. Lu, J. Proctor, P. Rangghran, E. R. Melhem, R. Gullapalli, G. M. Fiskum and D. Mayer, *Sci. Rep.*, 2017, **7**, 1907.

13 S. J. Nelson, J. Kurhanewicz, D. B. Vigneron, P. E. Larson, A. L. Harzstark, M. Ferrone, M. van Criekinge, J. W. Chang, R. Bok and I. Park, *Sci. Transl. Med.*, 2013, **5**, 198ra108.

14 T. Witney, M. Kettunen, D. Hu, F. Gallagher, S. Bohndiek, R. Napolitano and K. Brindle, *Br. J. Cancer*, 2010, **103**, 1400.

15 N. M. Zacharias, H. R. Chan, N. Sailasuta, B. D. Ross and P. Bhattacharya, *J. Am. Chem. Soc.*, 2011, **134**, 934–943.

16 P. C. Bhattacharya, E, Y, W. H. Perman, K. C. Harris, A. P. Lin, V. A. Norton, C. T. Tan, B. D. Ross and D. P. Weitekamp, *J. Magn. Reson.*, 2007, **186**, 150–155.

17 M. R. Clatworthy, M. I. Kettunen, D.-E. Hu, R. J. Mathews, T. H. Witney, B. W. Kennedy, S. E. Bohndiek, F. A. Gallagher, L. B. Jarvis and K. G. Smith, *Proc. Natl. Acad. Sci. U. S. A.*, 2012, **109**, 13374–13379.

18 J. Eills, J. Alonso-Valdesueiro, D. E. Salazar Marcano, J. Ferreira da Silva, S. Alom, G. J. Rees, J. V. Hanna, M. Carravetta and M. H. Levitt, *ChemPhysChem*, 2018, **19**, 40–44.

19 T. C. Eisenschmid, R. U. Kirss, P. P. Deutsch, S. I. Hommeltoft, R. Eisenberg, J. Bargon, R. G. Lawler and A. L. Balch, *J. Am. Chem. Soc.*, 1987, **109**, 8089–8091.

20 R. Eisenberg, *Acc. Chem. Res.*, 1991, **24**, 110–116.

21 J. B. Hövener, A. N. Pravdivtsev, B. Kidd, C. R. Bowers, S. Glöggler, K. V. Kovtunov, M. Plaumann, R. Katz-Brull, K. Buckenmaier and A. Jerschow, *Angew. Chem., Int. Ed.*, 2018, **57**, 11140–11162.

22 T. C. Eisenschmid, R. U. Kirss, P. P. Deutsch, S. I. Hommeltoft, R. Eisenberg, J. Bargon, R. G. Lawler and A. L. Balch, *J. Am. Chem. Soc.*, 1987, **109**, 8089–8091.

23 C. R. Bowers and D. P. Weitekamp, *J. Am. Chem. Soc.*, 1987, **109**, 5541–5542.

24 S. B. Duckett, C. L. Newell and R. Eisenberg, *J. Am. Chem. Soc.*, 1994, **116**, 10548–10556.

25 K. V. Kovtunov, I. E. Beck, V. I. Bukhtiyarov and I. V. Koptyug, *Angew. Chem., Int. Ed.*, 2008, **47**, 1492–1495.

26 B. J. Tickner, R. R. Parker, A. C. Whitwood and S. B. Duckett, *Organometallics*, 2019, **38**, 4377–4382.

27 P. Bhattacharya, E. Y. Chekmenev, W. H. Perman, K. C. Harris, A. P. Lin, V. A. Norton, C. T. Tan, B. D. Ross and D. P. Weitekamp, *J. Magn. Reson.*, 2007, **186**, 150–155.

28 A. B. Schmidt, S. Berner, M. Braig, M. Zimmermann, J. Hennig, D. von Elverfeldt and J.-B. Hövener, *PLoS One*, 2018, **13**, e0200141.

29 F. Reineri, T. Boi and S. Aime, *Nat. Commun.*, 2015, **6**, 5858.

30 E. Cavallari, C. Carrera, S. Aime and F. Reineri, *J. Magn. Reson.*, 2018, **289**, 12–17.

31 R. W. Adams, J. A. Aguilar, K. D. Atkinson, M. J. Cowley, P. I. Elliott, S. B. Duckett, G. G. Green, I. G. Khazal, J. López-Serrano and D. C. Williamson, *Science*, 2009, **323**, 1708–1711.

32 J.-B. Hövener, N. Schwaderlapp, T. Lickert, S. B. Duckett, R. E. Mewis, L. A. R. Highton, S. M. Kenny, G. G. R. Green, D. Leibfritz and J. G. Korvink, *Nat. Commun.*, 2013, **4**, 2946.

33 M. J. Burns, P. J. Rayner, G. G. Green, L. A. Highton, R. E. Mewis and S. B. Duckett, *J. Phys. Chem. B*, 2015, **119**, 5020–5027.

34 P. J. Rayner, M. J. Burns, A. M. Olaru, P. Norcott, M. Fekete, G. G. R. Green, L. A. R. Highton, R. E. Mewis and S. B. Duckett, *Proc. Natl. Acad. Sci. U. S. A.*, 2017, **114**, E3188–E3194.

35 M. Fekete, O. Bayfield, S. B. Duckett, S. Hart, R. E. Mewis, N. Pridmore, P. J. Rayner and A. Whitwood, *Inorg. Chem.*, 2013, **52**, 13453–13461.

36 P. Norcott, M. J. Burns, P. J. Rayner, R. E. Mewis and S. B. Duckett, *Magn. Reson. Chem.*, 2018, **56**, 663–671.

37 R. V. Shchepin, D. A. Barskiy, D. M. Mikhaylov and E. Y. Chekmenev, *Bioconjugate Chem.*, 2016, **27**, 878–882.

38 M. L. Truong, T. Theis, A. M. Coffey, R. V. Shchepin, K. W. Waddell, F. Shi, B. M. Goodson, W. S. Warren and E. Y. Chekmenev, *J. Phys. Chem. C*, 2015, **119**, 8786–8797.

39 W. Iali, S. S. Roy, B. J. Tickner, F. Ahwal, A. J. Kennerley and S. B. Duckett, *Angew. Chem.*, 2019, **131**, 10377–10381.

40 W. Iali, P. J. Rayner and S. B. Duckett, *Sci. Adv.*, 2018, **4**, eaao6250.

41 P. J. Rayner, B. J. Tickner, W. Iali, M. Fekete, A. D. Robinson and S. B. Duckett, *Chem. Sci.*, 2019, **10**, 7709–7717.

42 B. J. Tickner, W. Iali, S. S. Roy, A. C. Whitwood and S. B. Duckett, *ChemPhysChem*, 2019, **20**, 241–245.

43 B. J. Tickner, J. S. Lewis, R. O. John, A. C. Whitwood and S. B. Duckett, *Dalton Trans.*, 2019, **48**, 15198–15206.

44 M. Gemeinhardt, M. Limbach, T. Gebhardt, C. Eriksson, S. Eriksson, J. Lindale, E. Goodson, W. Warren, E. Chekmenev and B. Goodson, *Angew. Chem.*, 2020, **132**, 426–431.

45 R. W. Adams, S. B. Duckett, R. A. Green, D. C. Williamson and G. G. R. Green, *J. Chem. Phys.*, 2009, **131**, 194505.

46 W. D. Jones and R. M. Chin, *J. Am. Chem. Soc.*, 1994, **116**, 198–203.

47 B. J. Tickner, R. O. John, S. S. Roy, S. Hart, A. C. Whitwood and S. B. Duckett, *Chem. Sci.*, 2019, **10**, 5235–5245.

48 R. V. Shchepin, D. A. Barskiy, A. M. Coffey, T. Theis, F. Shi, W. S. Warren, B. M. Goodson and E. Y. Chekmenev, *ACS Sens.*, 2016, **1**, 640–644.

49 M. Fekete, P. J. Rayner, G. G. R. Green and S. B. Duckett, *Magn. Reson. Chem.*, 2017, **55**, 944–957.

50 P. J. Rayner and S. Duckett, *Angew. Chem., Int. Ed.*, 2018, **57**, 6742–6753.

51 W. Iali, P. J. Rayner, A. Alshehri, A. J. Holmes, A. J. Ruddlesden and S. B. Duckett, *Chem. Sci.*, 2018, **9**, 3677–3684.

52 M. J. Cowley, R. W. Adams, K. D. Atkinson, M. C. Cockett, S. B. Duckett, G. G. Green, J. A. Lohman, R. Kerssebaum, D.

302

Kilgour and R. E. Mewis, *J. Am. Chem. Soc.*, 2011, **133**, 6134–6137.

53 B. J. A. van Weerdenburg, N. Eshuis, M. Tessari, F. P. J. T. Rutjes and M. C. Feiters, *Dalton Trans.*, 2015, **44**, 15387–15390.

54 M. J. Cowley, R. W. Adams, K. D. Atkinson, M. C. R. Cockett, S. B. Duckett, G. G. R. Green, J. A. B. Lohman, R. Kerssebaum, D. Kilgour and R. E. Mewis, *J. Am. Chem. Soc.*, 2011, **133**, 6134–6137.

55 P. J. Rayner, P. Norcott, K. M. Appleby, W. Iali, R. O. John, S. J. Hart, A. C. Whitwood and S. B. Duckett, *Nat. Commun.*, 2018, **9**, 4251.

56 P. Spannring, I. Reile, M. Emondts, P. P. M. Schleker, N. K. J. Hermkens, N. G. J. van der Zwaluw, B. J. A. van Weerdenburg, P. Tinnemans, M. Tessari, B. Blumich, F. Rutjes and M. C. Feiters, *Chem. - Eur. J.*, 2016, **22**, 9277–9282.

57 M. Fekete, C. Gibard, G. J. Dear, G. G. R. Green, A. J. J. Hooper, A. D. Roberts, F. Cisnetti and S. B. Duckett, *Dalton Trans.*, 2015, **44**, 7870–7880.

58 F. Shi, P. He, Q. A. Best, K. Groome, M. L. Truong, A. M. Coffey, G. Zimay, R. V. Shchepin, K. W. Waddell and E. Y. Chekmenev, *J. Phys. Chem. C*, 2016, **120**, 12149–12156.

59 C. M. Wong, M. Fekete, R. Nelson-Forde, M. R. D. Gatus, P. J. Rayner, A. C. Whitwood, S. B. Duckett and B. A. Messerle, *Catal. Sci. Technol.*, 2018, **8**, 4925–4933.

60 D. A. Barskiy, A. N. Pravdivtsev, K. L. Ivanov, K. V. Kovtunov and I. V. Koptyug, *Phys. Chem. Chem. Phys.*, 2016, **18**, 89–93.

61 H. Zeng, J. Xu, J. Gillen, M. T. McMahon, D. Artemov, J.-M. Tyburn, J. A. Lohman, R. E. Mewis, K. D. Atkinson and G. G. Green, *J. Magn. Reson.*, 2013, **237**, 73–78.

62 A. J. Holmes, P. J. Rayner, M. J. Cowley, G. G. Green, A. C. Whitwood and S. B. Duckett, *Dalton Trans.*, 2015, **44**, 1077–1083.

63 L. D. Vazquez-Serrano, B. T. Owens and J. M. Buriak, *Inorg. Chim. Acta*, 2006, **359**, 2786–2797.

64 R. V. Shchepin, L. Jaigirdar, T. Theis, W. S. Warren, B. M. Goodson and E. Y. Chekmenev, *J. Phys. Chem. C*, 2017, **121**, 28425–28434.

This journal is © The Royal Society of Chemistry 2020

Catal. Sci. Technol., 2020, **10**, 1343–1355 | **1355**

303

Appendix 8

Using SABRE Hyperpolarized ^{13}C NMR Spectroscopy to Interrogate Organic Transformations of Pyruvate

Ben. J. Tickner, Peter J. Rayner, and Simon B. Duckett*

Cite This: https://dx.doi.org/10.1021/acs.analchem.0c01334

Read Online

ACCESS | Metrics & More | Article Recommendations | Supporting Information

ABSTRACT: Signal amplification by reversible exchange (SABRE) is a hyperpolarization technique that uses a metal complex to catalytically transfer magnetization from parahydrogen to molecules of interest. SABRE is used here to monitor the decarboxylation of sodium pyruvate-1,2-$[^{13}C_2]$ at a 15 mM concentration to form ethanoic acid and CO_2 upon reaction with hydrogen peroxide (150 mM). The rate constant of this reaction is determined by hyperpolarized ^{13}C SABRE-NMR spectroscopy as 0.056 ± 0.003 dm^3 mol^{-1} s^{-1} at 298 K and is comparable to that determined from thermal ^{1}H NMR ($k = 0.050 \pm 0.003$ dm^3 mol^{-1} s^{-1}) and UV measurements ($k = 0.053 \pm 0.001$ dm^3 mol^{-1} s^{-1}). The hyperpolarized reaction intermediate 2-hydroperoxy-2-hydroxypropanoate is detected in a single scan hyperpolarized ^{13}C NMR spectrum. This work highlights how SABRE hyperpolarization can be used as a tool for the precise monitoring of chemical transformations by hyperpolarized NMR spectroscopy.
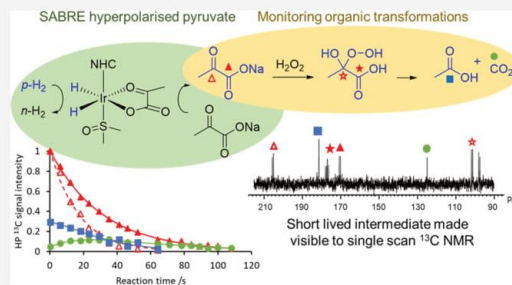
Monitoring chemical change in real time gives insight into reaction mechanisms and subsequent yield optimizations. Many spectroscopic approaches have been developed to achieve this goal, such as IR and UV spectroscopies.[1] Nuclear magnetic resonance (NMR) spectroscopy is an alternative method, which uses non-ionizing radiation to study the magnetic environment of nuclei in a nondestructive manner. Despite this accomplishment, MR methods are relatively insensitive on a molecular level as the detected signal intensities are derived from small population perturbations between closely spaced nuclear spin energy levels. Consequently, at 9.4 T only 1 out of every 128,000 ^{13}C nuclei contribute positively to the MR signal detected for a ^{13}C enriched sample. This challenge often necessitates long experiment durations which limit both the ability of MR to detect species present at concentrations $< \mu$M and the time scales over which chemical change can be accurately monitored.

Various hyperpolarization techniques are emerging which create non-Boltzmann derived population differences across these energy levels to address this sensitivity issue.[2] Of these, dissolution dynamic nuclear polarization (d-DNP) has provided sufficient signal enhancement to enable the monitoring of chemical transformations such as Diels−Alder cycloadditions[3] or ligand complexation.[4] d-DNP also yields hyperpolarized probes suitable for monitoring metabolic transformations *in vivo*.[5] For example, the anaerobic conversion of hyperpolarized sodium pyruvate-1-$[^{13}C]$ into

products such as lactate and alanine can be used to identify cancer.[5,6]

An alternative method based on parahydrogen (p-H$_2$), a singlet spin isomer of dihydrogen, has also been developed. This approach began in the late 1980s with the detection of hydrogenation products[7,8] and has been termed parahydrogen induced polarization (PHIP).[9] The NMR signal gains that PHIP provides have made the detection of low concentration catalytic intermediates[10−12] analytes,[13] and metabolites[9,14,15] by MR methods feasible. PHIP has provided mechanistic insight when p-H$_2$ is used to study hydrogenation reactions catalyzed by solid surfaces[16−18] or frustrated Lewis pairs.[19,20] However, a major limitation of PHIP is that it can only be applied to molecules containing unsaturated functionality. Over the past few decades, researchers have investigated new ways to introduce p-H$_2$ spin order into target molecules. One approach termed oneH-PHIP has been used to incorporate a single p-H$_2$ derived proton into an aldehyde.[21] This has allowed hydroformylation reactions to now be interrogated using p-H$_2$, and consequently, the enhanced NMR sensitivity has allowed detection of many intermediates in this process.[22]

In 2009, a non-hydrogenative variant of PHIP called signal amplification by reversible exchange (SABRE) was developed which does not require direct p-H_2 incorporation into the analyte.[23] Instead, the symmetry of p-H_2 is first broken by its oxidative addition to a metal center. Magnetization can then be transferred from the p-H_2 derived hydride ligands of the product to ligated substrates *via* the coupling network within the complex.[23,24] This process is catalytic in nature as p-H_2 and the substrate are both in reversible exchange. Therefore, the only requirement for hyperpolarization of a substrate using SABRE is the transient existence of a suitable metal catalyst.

This is usually achieved by the reaction of a stable SABRE precatalyst such as $[IrCl(COD)(IMes)]$, (**1**, where IMes = 1,3-bis(2,4,6-trimethylphenyl)imidazole-2-ylidene and COD = *cis*,*cis*-1,5-cyclooctadiene) with a substrate (sub) to form an active polarization transfer catalyst such as $[Ir(H)_2(IMes)(sub)_3]Cl$. Molecules containing N-donor sites that readily ligate to iridium such as N-heterocycles,[23,25,26] diazirines,[27−29] nitriles,[30] and amines[31] are among the most commonly reported examples of substrates that are hyperpolarized using SABRE.[32] Because of the matching conditions associated with the polarization transfer step involved in SABRE, it is usually performed at fields of around 6.5 mT for transfer into ^1H sites in the target,[23,25,26] while transfer to heteronuclei such as ^{15}N and ^{13}C is achieved at μT fields.[33,34]

SABRE has the potential to allow *in situ* monitoring of a wider range of chemical transformations than PHIP. Some early examples include monitoring deuterium incorporation into the ortho sites of pyridine which occurs as a consequence of a hydrogen isotope exchange reaction.[35] Recently, the types of functional groups that SABRE can sensitize have been expanded by relayed proton exchange effects, termed SABRE-Relay. This has allowed the hyperpolarization of nonligating molecules including alcohols, carboxylic acids, carbonates, phosphates, amides, and silanols.[36−38] These effects have then been used to determine the rate of rapid reaction between tris(*tert*-butoxy)silanol and triflic anhydride.[38]

Hyperpolarized magnetization within target substrates decays back to its Boltzmann derived state according to a relaxation time constant, normally called T_1. Consequently, in order to monitor chemical change of hyperpolarized molecules, it is essential that the rate of transformation is faster than the rate of relaxation to allow for product to be created with retained non-Boltzmann magnetization. It is therefore clear that the following requirements must be met when selecting reactions suitable for monitoring using SABRE:

1. A reagent must be hyperpolarized with significant signal gains using SABRE.

2. A SABRE hyperpolarized reagent should contain a long lifetime to maximize the time scale over which chemical change can be monitored.

3. The chemical transformation should occur faster than relaxation to allow for the formation of product with hyperpolarized signal intensities.

SABRE has been used to create long-lived p-H_2 derived singlet order within target substrates[27−29,39−41] (also called long-lived singlet states) that now decay according to the time constant T_{LLS}, which is typically longer than T_1.[42] Consequently, the monitoring of reactions over longer time scales (of many minutes) may be feasible.

The strong substrate MR signals associated with hyperpolarization mean that reactions are often monitored by recording a series of single scan NMR spectra using low flip angle excitation.[3] The choice of flip angle is important as each excitation pulse consumes some of the available magnetization while the detection of small concentrations of product is favored by using a 90° flip angle. Low flip angles between 5° and 15°are often a sensible balance point that allows reaction monitoring, while preventing signal loss before there is sufficient conversion to product. Therefore, the flip angle and time spacing between successive excitation pulses in addition to the nuclear spin relaxation rate and the reaction rate are important factors when deciding how best to examine a chemical transformation using hyperpolarized NMR.

We have recently reported the hyperpolarization of O-donor substrates such as sodium pyruvate-1,2-$[^{13}C_2]$ using SABRE.[40] This was achieved by reacting a solution containing $[IrCl(COD)(IMes)]$ (**1**, 5 mM), DMSO (8 equiv), and sodium pyruvate-1,2-$[^{13}C_2]$ (6 equiv) with 3 bar H_2 in methanol-d_4 (0.6 mL) to form $[Ir(H)_2(\eta^2$-pyruvate$)(IMes)(DMSO)]$ (**2**) as depicted in Figure 1.[40,43] Upon shaking these solutions with
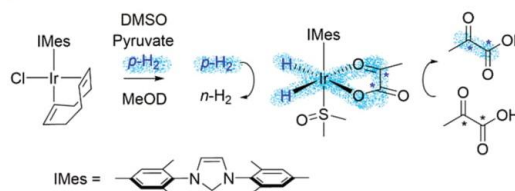
Figure 1. Hyperpolarization of sodium pyruvate-1,2-$[^{13}C_2]$ by SABRE. Reaction of $[IrCl(COD)(IMes)]$ with p-H_2, sodium pyruvate-1,2-$[^{13}C_2]$, and DMSO yields the SABRE catalyst $[Ir(H)_2(\eta^2$-pyruvate$)(IMes)(DMSO)]$. Note that the asterisk (*) denotes a ^{13}C labeled position.

3 bar p-H_2 at the μT fields necessary to transfer magnetization directly from p-H_2 derived hydride ligands to ligated ^{13}C pyruvate sites, ^{13}C NMR signal enhancements of ~1000-fold are readily achieved.[44] Interestingly, SABRE can be used to prepare hyperpolarized pyruvate-$[^{13}C_2]$ in a long-lived nuclear spin state with a T_{LLS} of ~43 s at high field (11.7 T), which exceeds the T_1 times of the individual spins (~34 and ~21 s for its $^{13}C_1$ and $^{13}C_2$ sites, respectively).[40]

In this work we show that the ^{13}C pyruvate signal gains achieved using SABRE are sufficient in both magnitude and lifetime to allow the monitoring of rapid chemical transformations. We do this by using SABRE to monitor the reaction between hyperpolarized sodium pyruvate-1,2-$[^{13}C_2]$ and hydrogen peroxide (H_2O_2) to form ethanoic acid and carbon dioxide. This reaction begins with nucleophilic attack of peroxide on the keto group of pyruvate to give 2-hydroperoxy-2-hydroxypropanoate, which readily decarboxylates under acidic conditions, as shown in Figure 2.[45−47] The rate of this reaction is dependent on pH and carbon kinetic isotope effects, suggesting that as the pH is increased, the rate-determining step changes from formation of the tetrahedral intermediate to its decarboxylation.[47] The associated 2-hydroperoxy-2-hydroxypropanoate intermediate is unstable and too short-lived to be observed by typical spectroscopic analyses at room temperature.[45] Nevertheless, it has been observed by NMR when the reaction between sodium pyruvate-1-$[^{13}C]$ or sodium pyruvate-2-$[^{13}C]$ and H_2O_2 is performed at low temperature (238−259 K).[45] Here, we use

B
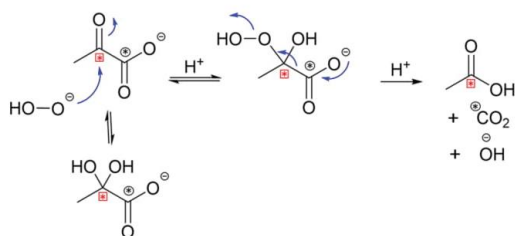
Figure 2. Reaction mechanism for the decarboxylation of pyruvate by hydrogen peroxide. This process involves the reversible attack of pyruvate by hydrogen peroxide, or the peroxide anion, to form a tetrahedral 2-hydroperoxy-2-hydroxypropanoate intermediate which decarboxylates to form ethanoic acid and carbon dioxide. Note that the asterisk (*) denotes a ^{13}C labeled position.

the NMR signal gains SABRE can deliver to make this intermediate visible in a single scan ^{13}C NMR spectrum at 298 K. We also examine the condensation reaction that takes place between sodium pyruvate and an amine that proceeds over a

longer time scale[48] and demonstrate that it is too slow to follow by this approach.[39] In doing so, we produce results that allow us to discuss the feasibility of using SABRE to monitor reactions in which reactants or products coordinate to the SABRE catalyst.

■ EXPERIMENTAL SECTION

Materials. All commercial compounds were purchased from Sigma-Aldrich and used as supplied. The SABRE precatalyst [IrCl(COD)(IMes)] was synthesized according to literature procedures.[49] Parahydrogen (p-H$_2$) with *ca.* 99% purity[50] was produced by passing hydrogen gas over a spin-exchange catalyst (Fe$_2$O$_3$) at 28 K.

Equipment. NMR measurements were carried out on a 400 MHz Bruker Avance III spectrometer using solutions at room temperature unless otherwise stated. ^{1}H (400 MHz) and ^{13}C (100.6 MHz) NMR spectra were recorded with an internal deuterium lock. ^{13}C NMR spectra were recorded with broadband proton decoupling. Chemical shifts (δ) are quoted as parts per million and referenced to methanol-d_4 solvent. UV
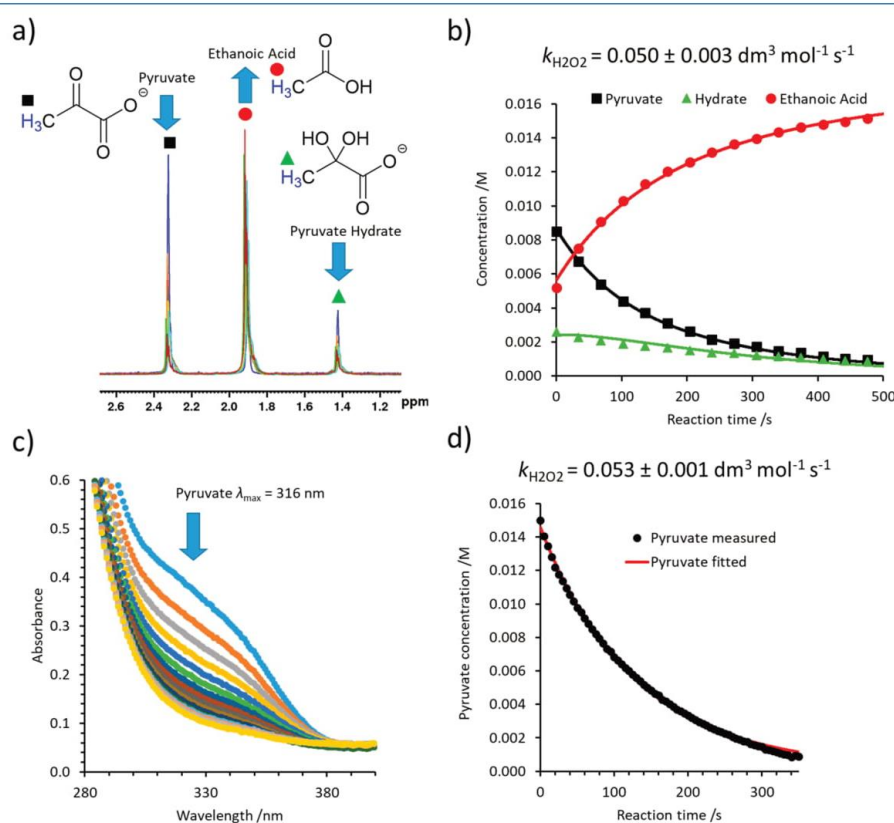
Figure 3. (a) Series of partial 90° ^{1}H NMR spectra of a solution of sodium pyruvate (30 mM) in 4:96 (%) methanol:methanol-d_4 (300 μL) recorded at 25 s time intervals after the addition of 300 mM H$_2$O$_2$ in D$_2$O (300 μL) to illustrate reaction progress. (b) Kinetic fitting of this NMR data. (c) Partial UV absorption spectra of an analogous solution of sodium pyruvate (15 mM) in 51:49 methanol:H$_2$O (1.968 mL) (top, blue) where example UV traces are recorded every 30 s after the addition of 32 μL of H$_2$O$_2$ (30% (w/w) H$_2$O$_2$ in H$_2$O solution; final H$_2$O$_2$ concentration of 150 mM). (d) Associated kinetic fitting of this UV data with extracted rate constant.

spectra were collected using a Thermo Scientific evolution array UV−vis spectrophotometer.

Reaction of Sodium Pyruvate with H_2O_2 by ^1H NMR Spectroscopy. A solution of 300 mM H_2O_2 in D_2O (300 μL) (9.6 μL of a 30% (w/w) H_2O_2 in H_2O solution in 290.4 μL of D_2O) was added to sodium pyruvate (30 mM) in 4:96 methanol:methanol-d_4 (300 μL) in a J. Young's fitted NMR tube at 298 K. A series of 90° single scan ^1H NMR spectra (Figure 3), at 25 s time intervals, were recorded immediately after the sample was shaken for ∼1 s in the Earth's field to aid mixing. The integral intensities of the ^1H CH_3 resonances of pyruvate (A), pyruvate hydrate (B), and ethanoic acid (C) were converted to concentration and then plotted over time. These data were fitted to a kinetic model to extract the rate of reaction between pyruvate and H_2O_2 (D). The model is depicted in Scheme 1 and described by eqs 1−4, where δt is an

Scheme 1. Model Used to Fit the Reaction between Sodium Pyruvate and H_2O_2

$$B \underset{k_{Hy}}{\overset{k_{-Hy}}{\rightleftharpoons}} A \overset{k_{H2O2}}{\underset{+ H_2O_2}{\longrightarrow}} C$$

incremental time difference and $k_{H_2O_2}$, k_{Hy}, and k_{-Hy} are the rates of reaction between pyruvate and H_2O_2, formation of pyruvate hydrate from pyruvate, and formation of pyruvate from its hydrate, respectively. Species such as H_2O, pyruvate dimers, or enol pyruvate were omitted as they were either in excess or not observed in these measurements. A pathway that allows for reaction of pyruvate hydrate with H_2O_2 was not included as it has been previously reported to be slow.[45]

$$[A]_{t+\delta t} = [A]_t + (-k_{H_2O_2}[A]_t[D]_t - k_{Hy}[A]_t + k_{-Hy}[B]_t)\,\partial t \quad (1)$$

$$[B]_{t+\delta t} = [B]_t + (k_{Hy}[A]_t - k_{-Hy}[B]_t)\,\partial t \quad (2)$$

$$[C]_{t+\delta t} = [C]_t + (k_{H_2O_2}[A]_t[D]_t)\,\partial t \quad (3)$$

$$[D]_{t+\delta t} = [D]_t - (k_{H_2O_2}[A]_t[D]_t)\,\partial t \quad (4)$$

Rate constants were found by minimizing the differences between experimentally determined concentrations and calculated values. The model was constrained to set the predicted initial concentrations of each reagent to within 10% of those experimentally determined from the first ^1H NMR spectrum.

Monitoring H_2O_2 Reaction with Pyruvate by UV Spectroscopy. A series of UV spectra, separated by 5 s time intervals, were recorded following the addition of 32 μL of H_2O_2 (30% (w/w) H_2O_2 in H_2O solution, final H_2O_2 concentration of 150 mM) to sodium pyruvate (15 mM) in 51:49 methanol:H_2O (1.97 mL). The resulting absorbances at λ_{max} were baseline corrected and fitted to the kinetic model described by eqs 1−4.

Production of Hyperpolarized Pyruvate Using SABRE. Solutions of hyperpolarized sodium pyruvate-1,2-$[^{13}C_2]$ are produced by preparing samples containing $[IrCl(COD)-(IMes)]$ (3 mM), DMSO (8 equiv), and sodium pyruvate-1,2-$[^{13}C_2]$ (6 equiv) in 288 μL of methanol-d_4 and 12 μL of methanol in a 5 mm NMR tube fitted with a J. Young's tap. The solutions were subsequently degassed by two freeze−pump−thaw cycles and were activated with 3 bar H_2 and left at

room temperature for 30 min to allow the formation of $[Ir(H)_2(\eta^2$-pyruvate)(IMes)(DMSO)]$ as confirmed by ^1H NMR spectroscopy.[40,43] Subsequently, the sample was shaken with fresh p-H_2 (3 bar) for 30 s in a mu metal shield (ca. 300-fold shielding) at room temperature to produce SABRE hyperpolarized pyruvate. This has been described in more detail elsewhere.[40,43,44]

Monitoring H_2O_2 Reaction with Pyruvate Hyperpolarized Using SABRE. Immediately after p-H_2 shaking solutions of 2, the J. Young's valve was removed from the NMR tube while leaving the sample in the mu metal shield. A solution of H_2O_2 (9.6 μL of a 30% (w/w) solution in H_2O) in D_2O (290.4 μL) was added to give a final H_2O_2 concentration of 150 mM. The valve was replaced and the sample shaken for ∼1 s in the shield to mix the solution at room temperature before rapidly inserting into the 9.4 T spectrometer for NMR monitoring. This involved the collection of a succession of single scan 10° ^{13}C NMR spectra at 298 K separated by 6 s time intervals up to a 120 s reaction time. The integral intensities of the $[1$-$^{13}C]$ resonance of pyruvate (A) and CO_2 (E), or the pyruvate $[2$-$^{13}C]$ site (A) and ethanoic acid (C) were analyzed according to a kinetic model. In this model the hyperpolarized signals of species X, S_X detected by the 10° pulse at time t is calculated according to eq 5, where M_X is the magnetization of species X and θ is the flip angle. The magnetization of species X remaining after the pulse is given by eq 6.

$$(S_X)_t = (M_X)_{t-\delta t}\sin\theta \quad (5)$$

$$(M_X)_t = (M_X)_{t-\delta t}\cos\theta \quad (6)$$

The magnetization of pyruvate (A) and CO_2 (E) or ethanoic acid (C) changes during the time interval between pulses due to chemical reaction and relaxation according to eqs 7 and 8, where T_A and $T_{C,E}$ are the relaxation times of the ^{13}C resonances of pyruvate, CO_2, or ethanoic acid, respectively, and k is a pseudo-first-order rate constant described in eq 9.

$$(M_A)_{t+\delta t} = (M_A)_t + \left(-k(M_A)_t - \frac{(M_A)_t}{T_A}\right)\delta t \quad (7)$$

$$(M_{C,E})_{t+\delta t} = (M_{C,E})_t + \left(k(M_{C,E})_t - \frac{(M_{C,E})_t}{T_{C,E}}\right)\delta t \quad (8)$$

$$k_{H_2O_2} = k[D] \quad (9)$$

Bound pyruvate, pyruvate hydrate, and HCO_3^- (which often exists in equilibrium with CO_2,[45] particularly in living systems)[5] were excluded from this model as no hyperpolarized signals for these species were visible, or in the case of HCO_3^-, its hyperpolarized integral intensities were <∼3% of all the hyperpolarized ^{13}C NMR signals. Rate constants were then determined as described previously. Relaxation times of these species were not fixed, and fitted parameters are given in the Supporting Information.

Monitoring the Reaction between Pyruvate and Amine by NMR Spectroscopy. A succession of single scan ^{13}C NMR spectra, acquired with 10° pulses, were recorded after the addition of phenylethylamine (PEA; 26.5 mM) to SABRE hyperpolarized sodium pyruvate-1,2-$[^{13}C_2]$ (30 mM) in methanol-d_4 (0.6 mL). This reaction was also monitored by thermally polarized ^1H NMR measurements at 298 K and a

reaction rate constant extracted using a similar model to that described by eqs 1−4 (see Supporting Information.).

■ RESULTS AND DISCUSSION

Monitoring the Reaction of Sodium Pyruvate with H$_2$O$_2$ by ^{1}H NMR Spectroscopy. A solution of sodium pyruvate (15 mM) and hydrogen peroxide (150 mM) in D$_2$O was monitored using ^{1}H NMR spectroscopy at 9.4 T. This involved recording a series of single scan spectra using a 90° flip angle that were separated by 25 s in order to ensure a quantitative response. This time interval was chosen as ^{1}H T_1 measurements on separate 15 mM solutions of sodium pyruvate and ethanoic acid in the proportion 48:2:48:2 D$_2$O:H$_2$O:CD$_3$OD:CH$_3$OH yielded values of 5.7 and 4.0 s for their CH$_3$ protons at 9.4 T. When the first ^{1}H NMR spectrum of this series is examined, ^{1}H NMR resonances corresponding to the CH$_3$ group of pyruvate at δ 2.35 and its hydrate at δ 1.45 are observed. No signals for pyruvate hemiacetal were observed in these measurements. Weaker signals appear for the methyl and carboxylate protons of ethanoic acid at δ 1.94 and 10.99, respectively. Representative spectra are given in the Supporting Information. As the reaction proceeds, the resonances corresponding to pyruvate and its hydrate decrease in intensity, while those of ethanoic acid increase. These signal intensity changes are proportional to concentration and fit to a kinetic model (described in Experimental Section) in order to obtain the effective reaction rate constant, $k_{H_2O_2}$, of 0.050 ± 0.003 dm^3 mol^{-1} s^{-1} (see the Supporting Information.). $k_{H_2O_2}$ determined by UV measurements has been reported to vary between 0.1 and 1 dm^3 mol^{-1} s^{-1}, depending on the pH of the buffered reaction mixture.[46] However, these rates are from studies with more dilute reagent concentrations (1.5 mM pyruvate and 5−30 mM H$_2$O$_2$). $k_{H_2O_2}$ has also been determined using ^{13}C NMR spectroscopy at much lower temperatures (238−259 K).[45] From these data $k_{H_2O_2}$ at 298 K is predicted to be ~0.16 dm^3 mol^{-1} s^{-1}. Therefore, $k_{H_2O_2}$ calculated from our ^{1}H NMR measurements is slower than that predicted by a factor of 3. Inefficient sample mixing or differences in solvent composition may account for this. Analogous measurements using ^{13}C NMR spectroscopy could not be recorded here as the signal strengths are not sufficient to detect a signal in the necessary time period, even with signal averaging.

These experiments were then repeated in the presence of the SABRE catalyst [Ir(H)$_2$(η^2-pyruvate)(IMes)(DMSO)] (**2**, 3 mM) to determine if the presence of the metal complex influences the rate of reaction between pyruvate and H$_2$O$_2$. In these cases, the kinetic time course from analogous ^{1}H NMR measurements no longer fit the model described in Experimental Section (see the Supporting Information). This is perhaps unsurprising as additional reaction pathways, which include reversible ligation of pyruvate to the metal catalyst, can occur. The chemical shift of the pyruvate CH$_3$ signal when bound in **2** has been reported, although it overlaps with signals of the IMes ligand.[40] The influence of the metal on this reaction can, however, be negated by adding a chelating ligand such as phenanthroline to destroy **2** before the addition of H$_2$O$_2$.[51] When the corresponding kinetic data are collected following the addition of H$_2$O$_2$ to a solution of **2** deactivated with phenanthroline (5 equiv), $k_{H_2O_2}$ was found to be 0.051 ± 0.003 dm^3 mol^{-1} s^{-1}. This value is therefore consistent with that determined from solutions without **2** (0.050 ± 0.003 dm^3

mol^{-1} s^{-1}), thereby establishing that the presence of the metal complex influences the reaction and can be suppressed if it is first deactivated by phenanthroline addition.

Monitoring the Reaction of Sodium Pyruvate with H$_2$O$_2$ by UV Spectroscopy. The rate of reaction between sodium pyruvate and hydrogen peroxide was also determined using ultraviolet (UV) spectroscopy. A UV spectrum of sodium pyruvate (15 mM) in 51:49 methanol:H$_2$O (1.97 mL) revealed a λ_{max} of 316 nm which compares well to previously reported values of 316 nm,[52] 325 nm,[53] and 326 nm.[54] This involved recording a series of UV spectra at 5 s time intervals after the addition of H$_2$O$_2$ (150 mM). The decrease in λ_{max} at 316 nm was fitted to the kinetic model described by eqs 1−4 (see Experimental Section). As a control, no significant change in λ_{max} was observed when solutions were monitored in the absence of H$_2$O$_2$. Furthermore, photolysis of pyruvate is known to cause UV induced $\pi \rightarrow \pi^*$ transitions in the pyruvate keto group, which leads to the formation of a range of products, including lactic acid, dimethyltartaric acid, and acetoin.[54] None of these photolysis products were detected by NMR or MS, which is consistent with the shorter UV irradiation times in these kinetic measurements (<5 min) compared to the photolysis studies (~1 h).[54] $k_{H_2O_2}$ was subsequently determined to be 0.053 ± 0.001 dm^3 mol^{-1} s^{-1} (by UV spectroscopy), which is consistent with the value determined by ^{1}H NMR spectroscopy. The effect the SABRE catalyst has on this reaction could not be investigated by UV spectroscopy as its presence masked UV absorption by pyruvate (see the Supporting Information).

Monitoring the Reaction of Sodium Pyruvate and H$_2$O$_2$ Using SABRE Hyperpolarized NMR Spectroscopy. The rate of reaction between sodium pyruvate and hydrogen peroxide was then measured using SABRE hyperpolarized ^{13}C NMR spectroscopy. Sodium pyruvate, with ^{13}C labels in both the carboxyl and keto positions, was used as the reagent because the presence of these two ^{13}C labels results in the creation of singlet spin order by SABRE which has a longer lifetime than the more usual single spin (Zeeman) order associated with NMR.[40] Consequently, its use should facilitate the observation of chemical change occurring over a longer time window than would otherwise be possible. A further benefit is that the chemical fate of both sites can be followed in a single experiment.

The required SABRE hyperpolarized pyruvate (15 mM) was produced by shaking **2** with 3 bar p-H$_2$ in a mu metal shield for 30 s before H$_2$O$_2$ was added (final concentration of 150 mM) and the sample was inserted into a 9.4 T spectrometer at 298 K. A series of time separated single scan ^{13}C measurements were then recorded with 10° flip angles. Insertion into the magnet will convert the initial ^{13}C$_2$ singlet state created during SABRE into both longitudinal two and single spin order terms which both contribute to the detected signal intensity.[40,43,44] The former does so in the form of an antiphase doublet, while the latter leads to in-phase doublets of opposite relative phase at the two sites.[40]

Hyperpolarized ^{13}C NMR signals for free pyruvate (δ 170 and 202) and pyruvate bound within **2** (δ 169 and 205) are observed with both of these features in the early ^{13}C NMR spectra. Hyperpolarized resonances are also readily observed for the reaction products ethanoic acid and CO$_2$ at δ 182 and 122, respectively, in these NMR spectra (see the Supporting Information). As expected, the two pyruvate ^{13}C NMR signals
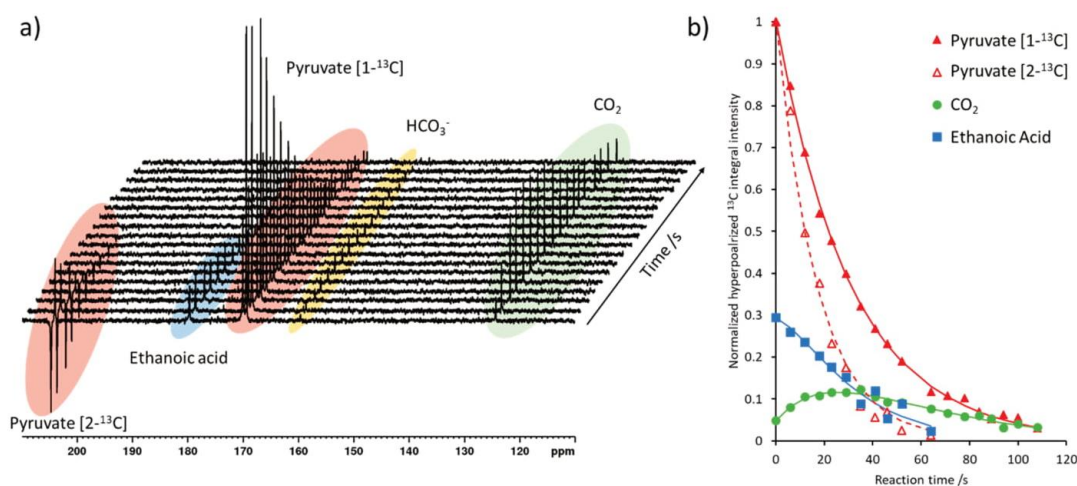
Figure 4. (a) Series of partial 10° single scan ^{13}C NMR spectra recorded after the addition of 150 mM H_2O_2 and phenanthroline (5 equiv relative to **2**) to a solution of SABRE hyperpolarized sodium pyruvate-1,2-[$^{13}C_2$] (15 mM) in methanol-d_4 (0.6 mL) at 298 K. (b) Associated changes in hyperpolarized signal intensity over reaction time can be plotted (marker points) and are fit to the kinetic model described by eqs 5−9 (solid lines). The fitting parameters are given in the Supporting Information.

decrease in intensity over time, while those of the reaction products first increase as they build-up and then fall as the effects of relaxation begin to dominate. When such a sample was removed from the spectrometer and shaken with fresh p-H_2, no hyperpolarized signals were visible; at this time point reaction between pyruvate and H_2O_2 is complete. It is therefore clear that SABRE is able to monitor this change, a feat that is not possible using the usual Boltzmann derived ^{13}C Zeeman polarization due to low sensitivity and the need for signal averaging.

A kinetic rate constant for this chemical change can be derived from these data. However, kinetic modeling must now account for reactivity, signal relaxation, and the magnetization reduction associated with the successive 10° pulses. We have shown earlier how **2** can affect this process, and therefore we negate its effect by addition of phenanthroline (Figure 4). Both pyruvate [1-^{13}C] and [2-^{13}C] sites should receive the same initial hyperpolarization as magnetization is shared equally across the two coupled ^{13}C sites of the singlet state.[40,44] However, the shorter reported T_1 time of the [2-^{13}C] site (~21 s compared to ~34 s for the [1-^{13}C] site[40] results in a lower signal intensity for this site at longer measurement times. This is evident in spectra shown in Figure 4a, which are recorded 10−15 s after initial preparation of the hyperpolarized $^{13}C_2$ state due to the time taken to add phenanthroline and H_2O_2. The contribution from the two spin order terms was removed by taking the sum of the two individual peaks involved in each multiplet for each pyruvate ^{13}C signal. Upon fitting this data using the model described by eqs 5−9 of the experimental to the [1-^{13}C] pyruvate signal, a $k_{H_2O_2}$ value of 0.056 ± 0.003 dm^3 mol^{-1} s^{-1} was obtained, which is consistent with the value obtained from the corresponding thermal ^1H NMR measurements ($k_{H_2O_2}$ = 0.050 ± 0.003 dm^3 mol^{-1} s^{-1}).

When the [2-^{13}C] pyruvate signal and the ethanoic acid signal are analyzed, the corresponding $k_{H_2O_2}$ value proved to be 0.055 ± 0.040 dm^3 mol^{-1} s^{-1}. The higher uncertainty of this

value stems from the shorter T_1 of the [2-^{13}C] pyruvate site (model fitted values of 20.6 ± 3.7 s compared to 47.3 ± 1.2 s for the [1-^{13}C] site) which reduces the time scale over which the reaction can be followed (to ~40 s rather than ~90 s for the [1-^{13}C] site). These thermal and hyperpolarized NMR measurements were repeated at a final H_2O_2 concentration of 100 mM and yielded comparable values of $k_{H_2O_2}$ (0.051 ± 0.003 dm^3 mol^{-1} s^{-1} compared to 0.045 ± 0.001 dm^3 mol^{-1} s^{-1} from thermal NMR; see the Supporting Information).

SABRE Making Visible the Short-Lived 2-Hydro-peroxy-2-hydroxypropanoate Intermediate in Single Scan ^{13}C NMR Spectroscopy. The reaction between sodium pyruvate and H_2O_2 occurs via the tetrahedral 2-hydroxyperoxy-2-hydroxypropanoate intermediate of Figure 2.[47,45,46] ^{13}C NMR signals for this intermediate have previously been reported at δ 102.9 and 178.3 in conjunction with a low temperature (238−259 K) study.[45] Closely related ethyl 2-hydroxperoxy-2-hydroxypropanoate, formed from the analogous reaction with ethyl pyruvate, has also been observed by ^{13}C and ^1H NMR analyses at 298 K.[46] In the SABRE NMR measurements just described, we failed to observe ^1H or ^{13}C NMR signals for this species at 298 K. However, this species was detected in a single scan ^{13}C NMR spectrum at 260 K with a 90° read pulse when this study was repeated by adding H_2O_2 to hyperpolarized sodium pyruvate-1,2-[$^{13}C_2$] at ~195 K. ^{13}C NMR signals for 2-hydroperoxy-2-hydroxypropanoate appear at δ 101.7 and 175.8 ($^1J_{CC}$ = 65 Hz), as shown in Figure 5 and compare well with previously reported values.[45,46] Signals for pyruvate, pyruvate bound in **62a**, ethanoic acid, and CO_2 are also visible in addition to a species at δ 97.94 and 176.68, which we assign as pyruvate hydrate, though they could be consistent with pyruvate hemiacetal.[45] Signals for this intermediate can also be observed in a single scan when the spectrometer is set to 273 K (see the Supporting Information). We conclude the lifetime of this species must be too short to allow detection at 298 K under the conditions reported here.
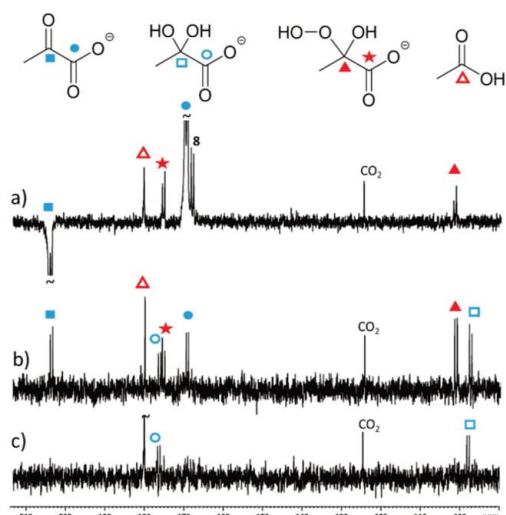
Figure 5. (a) Single scan hyperpolarized ^{13}C NMR spectrum recorded with a 90° flip angle immediately after the addition of H_2O_2 (final H_2O_2 concentration of 150 mM) at ~195 K to a solution containing hyperpolarized sodium pyruvate-1,2-[$^{13}C_2$]. (b, c) 128 scan ^{13}C NMR spectra recorded under Boltzmann conditions at 260 K roughly (b) 4 min and (c) 10 min after initial H_2O_2 addition. Note that panel a has been expanded vertically by a factor of 4 relative to panels b and c. The spectrometer was set to 260 K in these experiments, although in panel a the solution temperature is likely to be lower as the temperature equilibrates.

SABRE Hyperpolarized Sodium Pyruvate to Study Organic Transformations. α-Keto acids such as pyruvate exhibit a diverse range of chemical reactivity being well-known to form imines *via* transamination reactions with amines.[48] This reaction is usually slow and can be facilitated by an enzyme and pyridoxal cofactor, although it can also be promoted by transition metal complexes.[39] SABRE hyperpolarized NMR was therefore used to see if it could provide a way to follow such imine formation. A succession of single scan ^{13}C NMR spectra recorded with 10° pulses were recorded after the addition of phenylethylamine (26.5 mM) to SABRE hyperpolarized sodium pyruvate-1,2-[$^{13}C_2$] (30 mM) in methanol-d_4 (0.6 mL). Unfortunately, while enhanced ^{13}C NMR signals were seen for free pyruvate, pyruvate hydrate, and **2** (see the Supporting Information), these signals decreased in intensity with increase in reaction time and no signals for additional species were observed. Hence, neither the hemiaminal intermediate nor the imine product were observed over the ~60 s observation window afforded by the hyperpolarized response.

When this experiment was repeated using a series of 64 scan thermally polarized ^1H NMR measurements to encode the reaction, signals corresponding to **2** at $\delta - 27.08$ and -29.01 were immediately replaced by those of two new complexes that yield hydride signals at $\delta - 22.44$ and -22.48. The species giving rise to these signals are $[Ir(H)_2(IMes)(PEA)_3]Cl$ (**3**) and $[Ir(H)_2(IMes)(DMSO)(PEA)_2]Cl$ (**4**) as reported previously.[31,37] Unfortunately, these species form rapidly as a result of the reaction of **2** with added amine.[44,55] As the reaction time is extended, additional sets of hydride signals appear at $\delta -21.52$, -28.50 and $\delta -21.00$, -26.20. These
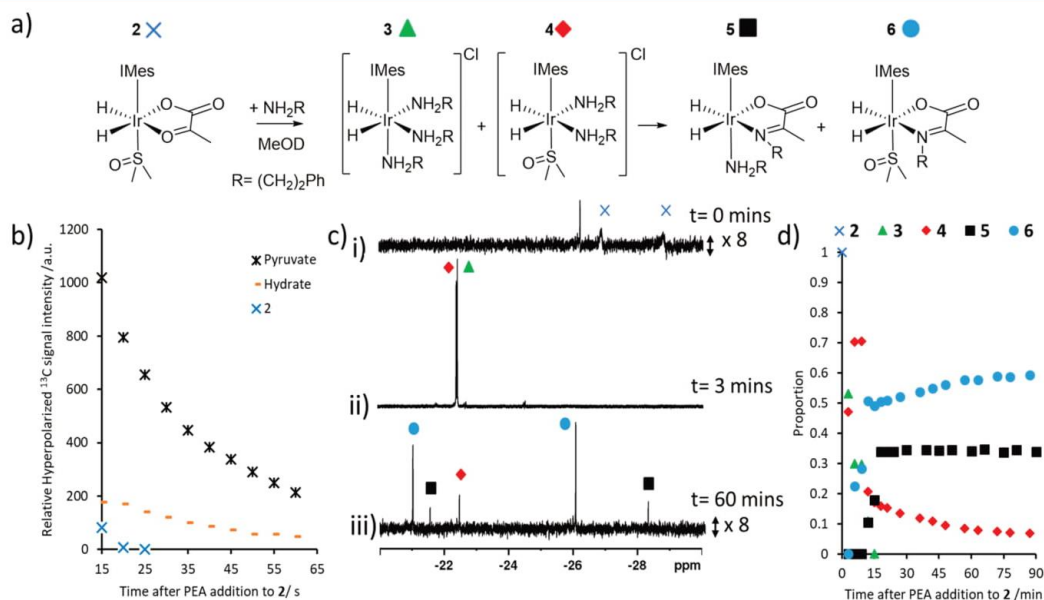
Figure 6. (a) Summary of chemical changes that occur upon addition of phenethylamine to **2**. (b) Change in relative hyperpolarized ^{13}C signal intensity of pyruvate, bound pyruvate, and pyruvate hydrate as determined by recording a series of ^{13}C NMR spectra with 10° flip angles. (c) Representative ^1H NMR spectra of the hydride region and (d) associated time course data as determined from a series of 32 scan ^1H NMR measurements when PEA (5 equiv) is added to **2** in methanol-d_4 (0.6 mL) at 298 K.

products are identified as $[Ir(H)_2(\eta^2\text{-}\alpha\text{-carboxyimine})(PEA)\text{-}(IMes)]$ (**5**) and $[Ir(H)_2(\eta^2\text{-}\alpha\text{-carboxyimine})(DMSO)\text{-}(IMes)]$ (**6**)[39,55] of Figure 6 and result from the expected pyruvate condensation. Eventually, **6** dominates these ^1H NMR spectra and 2D NMR characterization at 245 K confirms this assignment (see the Supporting Information). We associate the inability of hyperpolarized NMR to follow the reaction between pyruvate and amine to be the result of the slow reaction rate when compared to T_1. Tests to increase the reaction rate by increasing the phenethylamine concentration to 150 mM in conjunction with a 15 mM sodium pyruvate-1,2-$[^{13}C_2]$ concentration were also unsuccessful (see the Supporting Information). However, the corresponding thermal ^1H NMR spectroscopy measurements now yielded a reaction rate constant, k, of 0.017 ± 0.001 dm^3 mol^{-1} s^{-1} (see the Supporting Information). This reaction is therefore *ca.* three times slower than that with H_2O_2, which is consistent with the failure to monitor this reaction using SABRE enhanced NMR.

CONCLUSIONS

We show here that SABRE hyperpolarized ^{13}C NMR spectroscopy can be used to monitor the rapid chemical transformation of sodium pyruvate-1,2-$[^{13}C_2]$ into CO_2 and ethanoic acid. Quantification of the SABRE response allowed the successful monitoring of this reaction *via* $[1\text{-}^{13}C]$ and $[2\text{-}^{13}C]$ pyruvate ^{13}C NMR signals, the former having the longest T_1. Analysis of the time dependent intensities of these signals, following removal of the effects of relaxation, led to a rate constant of 0.056 ± 0.003 dm^3 mol^{-1} s^{-1} for this reaction at 298 K. This rate constant is consistent with those determined from analogous ^1H NMR and UV control measurements (0.050 ± 0.003 dm^3 mol^{-1} s^{-1} and 0.053 ± 0.001 dm^3 mol^{-1} s^{-1}, respectively), thereby establishing the validity of the method. The presence of the iridium SABRE catalyst was shown to influence the rate of this transformation, but its effect was removed once it was deactivated by the addition of phenanthroline. This reaction involves the intermediate 2-hydroxperoxy-2-hydroxypropanoate which is too short-lived to be detected by NMR spectroscopy at 298 K; however, the ^{13}C NMR signal gains arising from SABRE enabled its observation in a single scan ^{13}C NMR measurement at reduced temperature.

Attempts were also made to monitor the conversion of pyruvate into an imine by reaction with phenethylamine. Unfortunately, this reaction was too slow to follow by SABRE enhanced NMR analysis, although a rate constant of 0.017 ± 0.001 dm^3 mol^{-1} s^{-1} could be estimated by ^1H NMR spectroscopy. Normally, since SABRE is reversible, it can continually rehyperpolarize molecules (unlike DNP and PHIP in which hyperpolarization is created in a batch process). Hence, there is the potential to monitor concentration changes over longer time scales by simply repeating the SABRE process. Sadly, this option was not possible here because the addition of phenethylamine to the SABRE hyperpolarized pyruvate solution leads to destruction of **2**, which prevents the rehyperpolarization of pyruvate.

In conclusion, we have demonstrated in this work how SABRE enhanced NMR can be used to follow a reaction and produce accurate reaction rate data while detecting a short-lived reaction intermediate. SABRE has been applied to hyperpolarize a growing range of substrates with diverse chemical reactivity;[32] some of these have been created as long-lived $^{15}N_2$ singlet states,[27−29] and others have been prepared

with significant longitudinal magnetic lifetimes.[25,41,56] Therefore, it is likely that the benefits of the simple analytical route presented in this work will be applicable to the study of chemical reactivity and reaction kinetics of a wider range of chemical systems. Recent work showing that low-field NMR measurements are possible in conjunction with hyperpolarization have firmly demonstrated that low MR sensitivity can be addressed.[35,57−59] Both singlet state lifetimes, and indeed relaxation times more generally, may extend dramatically under these conditions. Therefore, the low field monitoring of reactivity on time scales which may approach tens of minutes could become a future reality.

ASSOCIATED CONTENT

Supporting Information

The Supporting Information is available free of charge at https://pubs.acs.org/doi/10.1021/acs.analchem.0c01334.

Kinetic fitting of reaction rates, example UV and NMR spectra, and characterization data for **6** (PDF)

AUTHOR INFORMATION

Corresponding Author

Simon B. Duckett − *Center for Hyperpolarization in Magnetic Resonance (CHyM), Department of Chemistry, University of York, Heslington, York YO10 5NY, United Kingdom;* orcid.org/0000-0002-9788-6615; Email: simon.ducket@york.ac.uk

Authors

Ben. J. Tickner − *Center for Hyperpolarization in Magnetic Resonance (CHyM), Department of Chemistry, University of York, Heslington, York YO10 5NY, United Kingdom;* orcid.org/0000-0002-8144-5655

Peter J. Rayner − *Center for Hyperpolarization in Magnetic Resonance (CHyM), Department of Chemistry, University of York, Heslington, York YO10 5NY, United Kingdom;* orcid.org/0000-0002-6577-4117

Complete contact information is available at: https://pubs.acs.org/10.1021/acs.analchem.0c01334

Notes

The authors declare no competing financial interest.

REFERENCES

(1) Hunger, M.; Weitkamp, J. *Angew. Chem., Int. Ed.* **2001**, *40*, 2954−2971.
(2) Nikolaou, P.; Goodson, B. M.; Chekmenev, E. Y. *Chem. - Eur. J.* **2015**, *21*, 3156−3166.
(3) Zeng, H.; Lee, Y.; Hilty, C. *Anal. Chem.* **2010**, *82*, 8897−8902.
(4) Jannin, S.; Helm, L.; Bodenhausen, G. *J. Am. Chem. Soc.* **2010**, *132*, 5006−5007.
(5) Keshari, K. R.; Wilson, D. M. *Chem. Soc. Rev.* **2014**, *43*, 1627−1659.
(6) Nelson, S. J.; Kurhanewicz, J.; Vigneron, D. B.; Larson, P. E. Z.; Harzstark, A. L.; Ferrone, M.; van Criekinge, M.; Chang, J. W.; Bok, R.; Park, I.; Reed, G.; Carvajal, L.; Small, E. J.; Munster, P.; Weinberg, V. K.; Ardenkjaer-Larsen, J. H.; Chen, A. P.; Hurd, R. E.;

Odegardstuen, L.-I.; Robb, F. J.; et al. *Sci. Transl. Med.* **2013**, *5*, 198ra108.

(7) Eisenschmid, T. C.; Kirss, R. U.; Deutsch, P. P.; Hommeltoft, S. I.; Eisenberg, R.; Bargon, J.; Lawler, R. G.; Balch, A. L. *J. Am. Chem. Soc.* **1987**, *109*, 8089−8091.

(8) Bowers, C. R.; Weitekamp, D. P. *J. Am. Chem. Soc.* **1987**, *109*, 5541−5542.

(9) Hövener, J. B.; Pravdivtsev, A. N.; Kidd, B.; Bowers, C. R.; Glöggler, S.; Kovtunov, K. V.; Plaumann, M.; Katz-Brull, R.; Buckenmaier, K.; Jerschow, A.; et al. *Angew. Chem., Int. Ed.* **2018**, *57*, 11140−11162.

(10) Tickner, B. J.; Parker, R. R.; Whitwood, A. C.; Duckett, S. B. *Organometallics* **2019**, *38*, 4377−4382.

(11) Kiryutin, A. S.; Sauer, G.; Yurkovskaya, A. V.; Limbach, H.-H.; Ivanov, K. L.; Buntkowsky, G. *J. Phys. Chem. C* **2017**, *121*, 9879−9888.

(12) Ahlquist, M.; Gustafsson, M.; Karlsson, M.; Thaning, M.; Axelsson, O.; Wendt, O. F. *Inorg. Chim. Acta* **2007**, *360*, 1621−1627.

(13) Sellies, L.; Reile, I.; Aspers, R.; Feiters, M. C.; Rutjes, F. P. J. T.; Tessari, M. *Chem. Commun.* **2019**, *55*, 7235−7238.

(14) Bhattacharya, P.; Chekmenev, E. Y.; Perman, W. H.; Harris, K. C.; Lin, A. P.; Norton, V. A.; Tan, C. T.; Ross, B. D.; Weitekamp, D. P. *J. Magn. Reson.* **2007**, *186*, 150−155.

(15) Cavallari, E.; Carrera, C.; Di Matteo, G.; Bondar, O.; Aime, S.; Reineri, F. *Front. Oncol.* **2020**, *10*, 497.

(16) Wang, W.; Xu, J.; Zhao, Y.; Qi, G.; Wang, Q.; Wang, C.; Li, J.; Deng, F. *Phys. Chem. Chem. Phys.* **2017**, *19*, 9349−9353.

(17) Kovtunov, K. V.; Zhivonitko, V. V.; Corma, A.; Koptyug, I. V. *J. Phys. Chem. Lett.* **2010**, *1*, 1705−1708.

(18) Svyatova, A.; Kononenko, E. S.; Kovtunov, K. V.; Lebedev, D.; Gerasimov, E. Y.; Bukhtiyarov, A.; Prosvirin, I.; Bukhtiyarov, V.; Müller, C. R.; Fedorov, A.; Koptyug, I. V. *Catal. Sci. Technol.* **2020**, *10*, 99−104.

(19) Zhivonitko, V. V.; Sorochkina, K.; Chernichenko, K.; Kótai, B.; Földes, T.; Pápai, I.; Telkki, V.-V.; Repo, T.; Koptyug, I. *Phys. Chem. Chem. Phys.* **2016**, *18*, 27784−27795.

(20) Sorochkina, K.; Zhivonitko, V. V.; Chernichenko, K.; Telkki, V.-V.; Repo, T.; Koptyug, I. V. *J. Phys. Chem. Lett.* **2018**, *9*, 903−907.

(21) Permin, A. B.; Eisenberg, R. *J. Am. Chem. Soc.* **2002**, *124*, 12406−12407.

(22) Godard, C.; Duckett, S. B.; Polas, S.; Tooze, R.; Whitwood, A. C. *J. Am. Chem. Soc.* **2005**, *127*, 4994−4995.

(23) Adams, R. W.; Aguilar, J. A.; Atkinson, K. D.; Cowley, M. J.; Elliott, P. I. P.; Duckett, S. B.; Green, G. G. R.; Khazal, I. G.; Lopez-Serrano, J.; Williamson, D. C. *Science* **2009**, *323*, 1708−1711.

(24) Ivanov, K. L.; Pravdivtsev, A. N.; Yurkovskaya, A. V.; Vieth, H.-M.; Kaptein, R. *Prog. Nucl. Magn. Reson. Spectrosc.* **2014**, *81*, 1−36.

(25) Rayner, P. J.; Burns, M. J.; Olaru, A. M.; Norcott, P.; Fekete, M.; Green, G. G. R.; Highton, L. A. R.; Mewis, R. E.; Duckett, S. B. *Proc. Natl. Acad. Sci. U. S. A.* **2017**, *114*, E3188−E3194.

(26) Dücker, E. B.; Kuhn, L. T.; Münnemann, K.; Griesinger, C. *J. Magn. Reson.* **2012**, *214*, 159−165.

(27) Theis, T.; Ortiz, G. X.; Logan, A. W.; Claytor, K. E.; Feng, Y.; Huhn, W. P.; Blum, V.; Malcolmson, S. J.; Chekmenev, E. Y.; Wang, Q.; Warren, W. *Sci. Adv.* **2016**, *2*, No. e1501438.

(28) Shen, K.; Logan, A. W. J.; Colell, J. F. P.; Bae, J.; Ortiz, G. X., Jr; Theis, T.; Warren, W. S.; Malcolmson, S. J.; Wang, Q. *Angew. Chem.* **2017**, *129*, 12280−12284.

(29) Zhang, G.; Colell, J. F. P.; Glachet, T.; Lindale, J. R.; Reboul, V.; Theis, T.; Warren, W. S. *Angew. Chem.* **2019**, *131*, 11235−11241.

(30) Mewis, R. E.; Green, R. A.; Cockett, M. C. R.; Cowley, M. J.; Duckett, S. B.; Green, G. G. R.; John, R. O.; Rayner, P. J.; Williamson, D. C. *J. Phys. Chem. B* **2015**, *119*, 1416−1424.

(31) Iali, W.; Rayner, P. J.; Alshehri, A.; Holmes, A. J.; Ruddlesden, A. J.; Duckett, S. B. *Chem. Sci.* **2018**, *9*, 3677−3684.

(32) Barskiy, D. A.; Knecht, S.; Yurkovskaya, A. V.; Ivanov, K. L. *Prog. Nucl. Magn. Reson. Spectrosc.* **2019**, *114-115*, 33−70.

(33) Theis, T.; Truong, M. L.; Coffey, A. M.; Shchepin, R. V.; Waddell, K. W.; Shi, F.; Goodson, B. M.; Warren, W. S.; Chekmenev, E. Y. *J. Am. Chem. Soc.* **2015**, *137*, 1404−1407.

(34) Barskiy, D. A.; Shchepin, R. V.; Tanner, C. P. N.; Colell, J. F. P.; Goodson, B. M.; Theis, T.; Warren, W. S.; Chekmenev, E. Y. *ChemPhysChem* **2017**, *18*, 1493−1498.

(35) Semenova, O.; Richardson, P. M.; Parrott, A. J.; Nordon, A.; Halse, M. E.; Duckett, S. B. *Anal. Chem.* **2019**, *91*, 6695−6701.

(36) Rayner, P. J.; Tickner, B. J.; Iali, W.; Fekete, M.; Robinson, A. D.; Duckett, S. B. *Chem. Sci.* **2019**, *10*, 7709−7717.

(37) Iali, W.; Rayner, P. J.; Duckett, S. B. *Sci. Adv.* **2018**, *4*, No. eaao6250.

(38) Rayner, P. J.; Richardson, P. M.; Duckett, S. B. *Angew. Chem.* **2020**, *132*, 2732−2736.

(39) Tickner, B. J.; Iali, W.; Roy, S. S.; Whitwood, A. C.; Duckett, S. B. *ChemPhysChem* **2019**, *20*, 241−245.

(40) Iali, W.; Roy, S. S.; Tickner, B. J.; Ahwal, F.; Kennerley, A. J.; Duckett, S. B. *Angew. Chem.* **2019**, *131*, 10377−10381.

(41) Zhou, Z.; Yu, J.; Colell, J. F.; Laasner, R.; Logan, A. W.; Barskiy, D. A.; Shchepin, R. V.; Chekmenev, E. Y.; Blum, V.; Warren, W. S.; Theis, T. *J. Phys. Chem. Lett.* **2017**, *8*, 3008−3014.

(42) Carravetta, M.; Johannessen, O. G.; Levitt, M. H. *Phys. Rev. Lett.* **2004**, *92*, 153003.

(43) Tickner, B. J.; Lewis, J. S.; John, R. O.; Whitwood, A. C.; Duckett, S. B. *Dalton Trans.* **2019**, *48*, 15198−15206.

(44) Tickner, B. J.; Semenova, O.; Iali, W.; Rayner, P. J.; Whitwood, A. C.; Duckett, S. B. *Catal. Sci. Technol.* **2020**, *10*, 1343−1355.

(45) Asmus, C.; Mozziconacci, O.; Schöneich, C. *J. Phys. Chem. A* **2015**, *119*, 966−977.

(46) Lopalco, A.; Dalwadi, G.; Niu, S.; Schowen, R. L.; Douglas, J.; Stella, V. J. *J. Pharm. Sci.* **2016**, *105*, 705−713.

(47) Melzer, E.; Schmidt, H.-L. *Biochem. J.* **1988**, *252*, 913−915.

(48) Leussing, D. L.; Hanna, E. M. *J. Am. Chem. Soc.* **1966**, *88*, 693−696.

(49) Vazquez-Serrano, L. D.; Owens, B. T.; Buriak, J. M. *Inorg. Chim. Acta* **2006**, *359*, 2786−2797.

(50) Richardson, P. M.; John, R. O.; Parrott, A. J.; Rayner, P. J.; Iali, W.; Nordon, A.; Halse, M. E.; Duckett, S. B. *Phys. Chem. Chem. Phys.* **2018**, *20*, 26362−26371.

(51) Mewis, R. E.; Fekete, M.; Green, G. R. R.; Whitwood, A. C.; Duckett, S. B. *Chem. Commun.* **2015**, *51*, 9857−9859.

(52) Margolis, S. A.; Coxon, B. *Anal. Chem.* **1986**, *58*, 2504−2510.

(53) Esposito, A.; Lukas, A.; Meany, J. E.; Pocker, Y. *Can. J. Chem.* **1999**, *77*, 1108−1117.

(54) Griffith, E. C.; Carpenter, B. K.; Shoemaker, R. K.; Vaida, V. *Proc. Natl. Acad. Sci. U. S. A.* **2013**, *110*, 11714−11719.

(55) Tickner, B. J.; John, R. O.; Roy, S. S.; Hart, S.; Whitwood, A. C.; Duckett, S. B. *Chem. Sci.* **2019**, *10*, 5235−5245.

(56) Shchepin, R. V.; Birchall, J. R.; Chukanov, N. V.; Kovtunov, K. V.; Koptyug, I. V.; Theis, T.; Warren, W. S.; Gelovani, J. G.; Goodson, B. M.; Shokouhi, S.; et al. *Chem. - Eur. J.* **2019**, *25*, 8829−8836.

(57) Barskiy, D. A.; Kovtunov, K. V.; Koptyug, I. V.; He, P.; Groome, K. A.; Best, Q. A.; Shi, F.; Goodson, B. M.; Shchepin, R. V.; Truong, M. L.; et al. *ChemPhysChem* **2014**, *15*, 4100−4107.

(58) Buckenmaier, K.; Rudolph, M.; Back, C.; Misztal, T.; Bommerich, U.; Fehling, P.; Koelle, D.; Kleiner, R.; Mayer, H. A.; Scheffler, K.; Bernarding, J.; Plaumann, M. *Sci. Rep.* **2017**, *7*, 13431.

(59) Gong, Q.; Gordji-Nejad, A.; Blümich, B.; Appelt, S. *Anal. Chem.* **2010**, *82*, 7078−7082.

Appendix 9
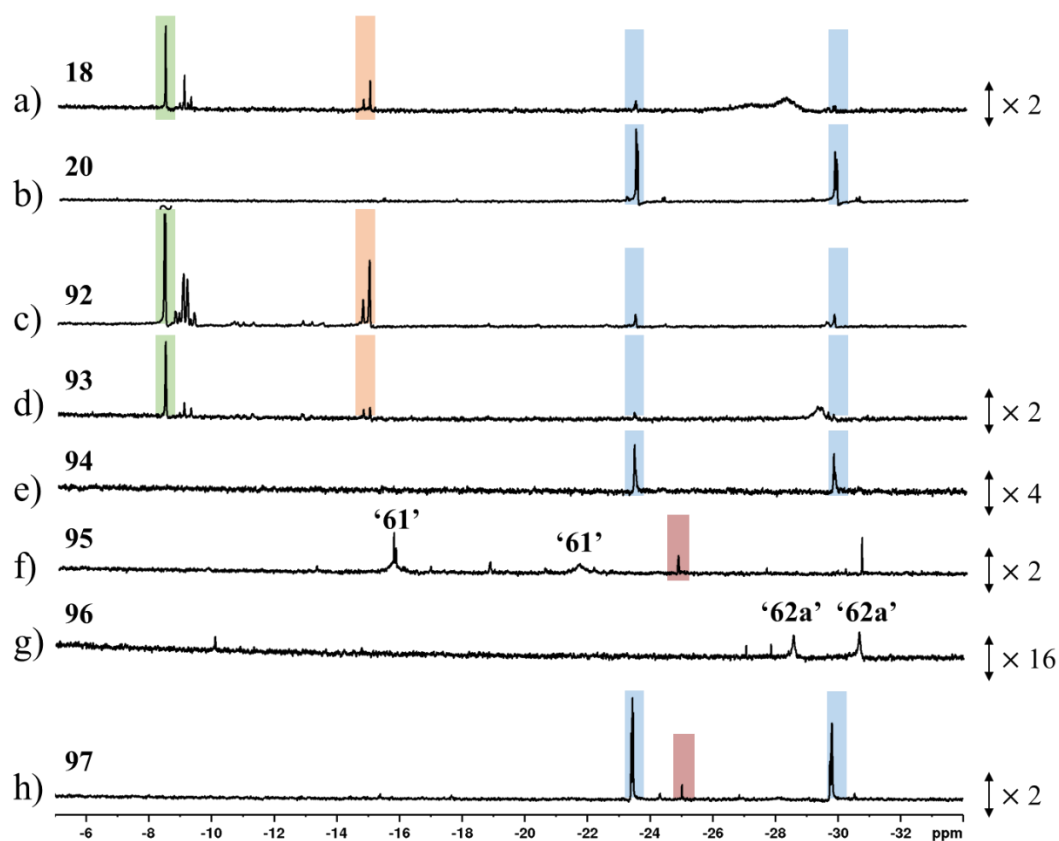
Appendix 9.1: Partial 32 scan ^{1}H NMR spectra of the hydride region when samples containing 2 (5 mM), 69 (10 eq.) and the indicated substrate (4 eq.) in methanol-d_4 (0.6 mL) are activated with 3 bar H$_2$ for 1 hour at room temperature. In the case of 95 and 96 the sulfoxide 46 (10 eq) was used. The structures of the substrates used are given in Figure 6.16. Coloured highlights indicate resonances belonging to the same complex.
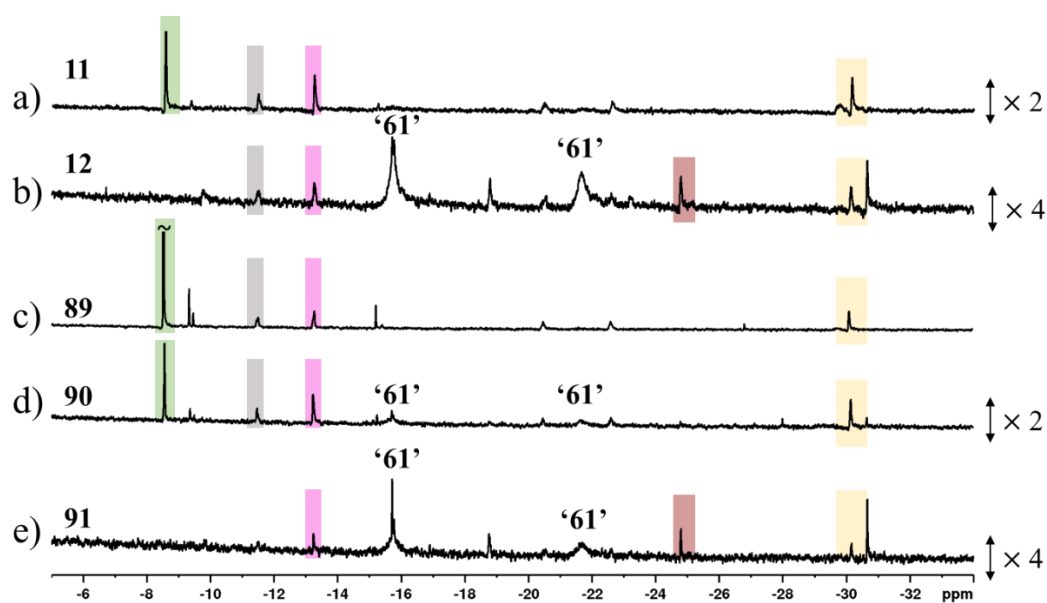
Appendix 9.2: Partial 128 scan ^{1}H NMR spectra of the hydride region when samples containing 2 (5 mM), 46 (10 eq.) and the indicated substrate (4 eq.) in methanol-d_4 (0.6 mL) are activated with 3 bar H$_2$ for 1 hour at room temperature. The structures of the substrates used are given in Figure 6.16. Coloured highlights indicate resonances belonging to the same complex.
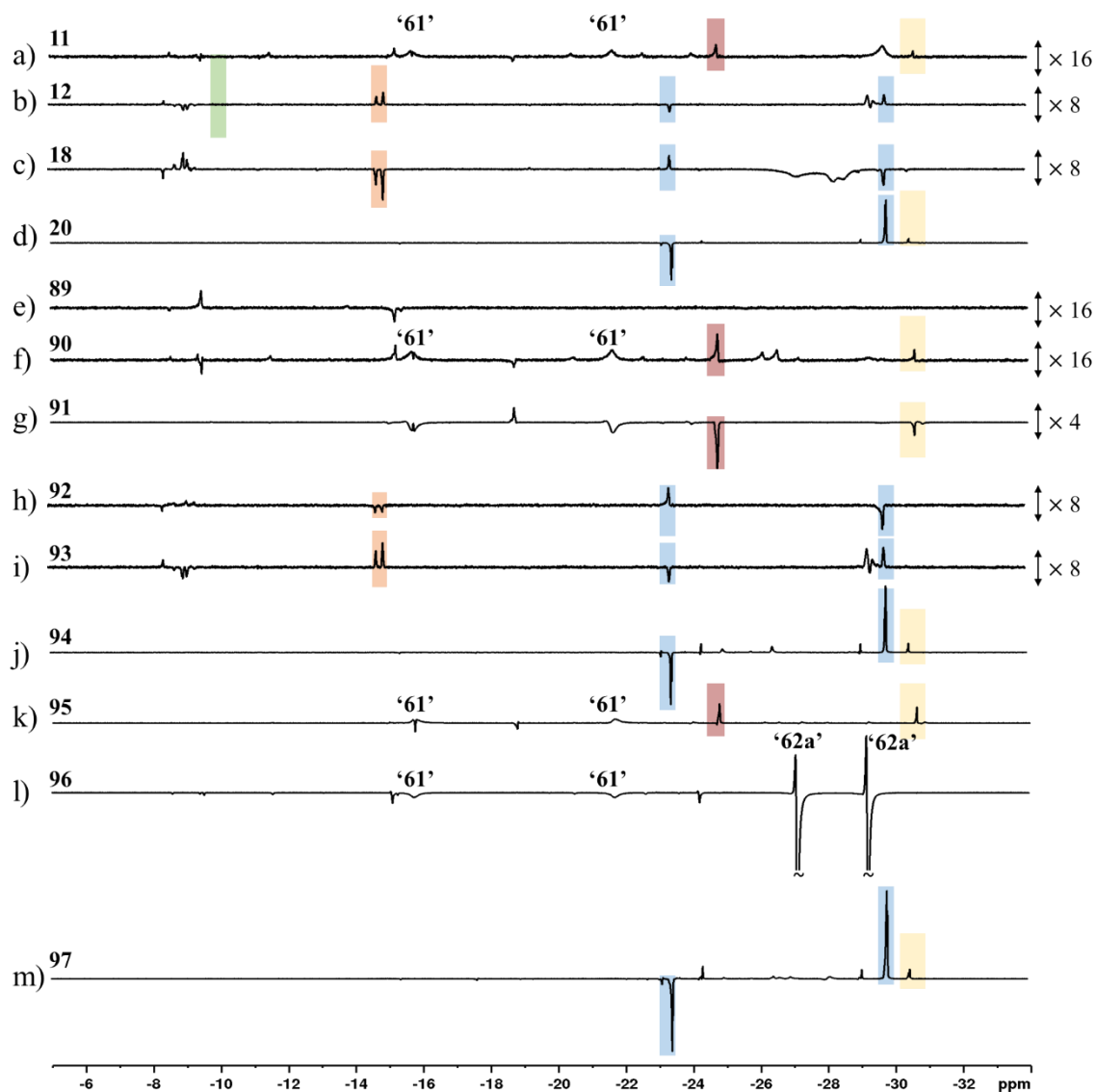
Appendix 9.3: Partial single scan hyperpolarised[1]H NMR spectra of the hydride region when samples containing 2 (5 mM), sulfoxide (10 eq.) and the indicated substrate (4 eq.) in methanol-d_4 (0.6 mL) are shaken with 3 bar *p*-H$_2$ for 10 seconds at 6.5 mT. For 11, 12, 89, 90, 91, 95 and 96 sulfoxide 46 was used. For 18, 20, 92, 93, 94 and 97 sulfoxide 69 was used. The structures of the substrates used are given in Figure 6.16. Coloured highlights indicate resonances belonging to the same complex.

References

1.   J. Keeler, *Understanding NMR spectroscopy*, John Wiley & Sons, 2011.
2.   M. H. Levitt, *Spin Dynamics*, 2001.
3.   P. J. Hore, *Nuclear Magnetic Resonance*, Oxford University Press, USA, 2015.
4.   M. A. Brown and R. C. Semelka, *MRI: Basic Principles and Applications*, John Wiley & Sons, 2011.
5.   P. Nikolaou, B. M. Goodson and E. Y. Chekmenev, *Chem. Eur. J.*, 2015, **21**, 3156-3166.
6.   A. S. Merbach, L. Helm and E. Toth, *The Chemistry of Contrast Agents in Medical Magnetic Resonance Imaging*, John Wiley & Sons, 2013.
7.   L. T. Kuhn and Ü. Akbey, *Hyperpolarization Methods in NMR Spectroscopy*, Springer, 2013.
8.   P. Caravan, J. J. Ellison, T. J. McMurry and R. B. Lauffer, *Chem. Rev.*, 1999, **99**, 2293-2352.
9.   K. Ward, A. Aletras and R. S. Balaban, *J. Magn. Reson.*, 2000, **143**, 79-87.
10. S. Zhang, M. Merritt, D. E. Woessner, R. E. Lenkinski and A. D. Sherry, *Acc. Chem. Res.*, 2003, **36**, 783-790.
11. M. Woods, D. Woessner and A. Sherry, *Chem. Soc. Rev.*, 2006, **35**, 500-551.
12. A. D. Sherry and M. Woods, *Biomed. Eng.* , 2008, **10**, 391-411.
13. B. Zhang, L. Liang, W. Chen, C. Liang and S. Zhang, *PloS one*, 2015, **10**, e0129720.
14. R. McDonald, J. McDonald, D. Kallmes, M. Jentoft, D. Murray, K. Thielen, E. Williamson and L. Eckel, *Radiol.*, 2105, **275**, 772-782.
15. V. Runge, J. Clanton, A. Price, C. Wehr, W. Herzer, C. Partain and A. James, *Magn. Reson. Im.*, 1985, **3**, 43-55.
16. D. Spinosa, A. Matsumoto, K. Hagspiel, J. Angle and G. Hartwell, *Am. J. Roentgenol.*, 1999, **173**, 1403-1409.
17. C.-T. Yang, P. Chandrasekharan, T. He, Z. Poh, A. Raju, K.-H. Chuang and E. Robins, *Biomat.*, 2014, **35**, 327-336.
18. M. Mirzaei, B. Mehravi, M. Ardestani, S. Ziaee and P. Pourghasem, *Mol. Im. Biol.*, 2015, **17**, 770-776.
19. T. Courant, V. Roullin, C. Cadiou, M. Callewaert, M. Andry, C. Portefaix, C. CHoeffel, M. de Goltstein, M. Port, S. Laurent, L. Elst, R. Muller, M. Molinari and F. Chuburu, *Angew. Chem. Int. Ed.*, 2012, **51**, 9119-9122.
20. S. Ogawa, T.-M. Lee, A. R. Kay and D. W. Tank, *Proc. Natl. Acad. Sci.*, 1990, **87**, 9868-9872.
21. N. K. Logothetis, *Nat.*, 2008, **453**, 869-878.
22. E. L. Que and C. J. Chang, *Chem. Soc. Rev.*, 2010, **39**, 51-60.
23. G. Angelovski and É. Tóth, *Chem. Soc. Rev.*, 2017, **46**, 324-336.
24. P. Caravan, *Acc. Chem. Res.*, 2009, **42**, 851-862.
25. B. K. Siesjö and F. Bengtsson, *J. Cerebr. Blood F. Met.*, 1989, **9**, 127-140.
26. G. Angelovski, P. Fouskova, I. Mamedov, S. Canals, E. Toth and N. K. Logothetis, *Chem. Bio. Chem*, 2008, **9**, 1729-1734.
27. S. Fain, M. L. Schiebler, D. G. McCormack and G. Parraga, *J. Magn. Reson. Im.*, 2010, **32**, 1398-1408.
28. Z. I. Cleveland, G. P. Cofer, G. Metz, D. Beaver, J. Nouls, S. S. Kaushik, M. Kraft, J. Wolber, K. T. Kelly and H. P. McAdams, *PloS one*, 2010, **5**, e12192.
29. J. H. Ardenkjær-Larsen, B. Fridlund, A. Gram, G. Hansson, L. Hansson, M. H. Lerche, R. Servin, M. Thaning and K. Golman, *Proc. Natl. Acad. Sci.*, 2003, **100**, 10158-10163.
30. S. Jannin, A. Bornet, R. Melzi and G. Bodenhausen, *Chem. Phys. Lett.*, 2012, **549**, 99-102.
31. C. R. Bowers and D. P. Weitekamp, *J. Am. Chem. Soc.*, 1987, **109**, 5541-5542.
32. T. C. Eisenschmid, R. U. Kirss, P. P. Deutsch, S. I. Hommeltoft, R. Eisenberg, J. Bargon, R. G. Lawler and A. L. Balch, *J. Am. Chem. Soc.*, 1987, **109**, 8089-8091.
33. C. R. Bowers and D. P. Weitekamp, *Phys. Rev. Lett*, 1986, **57**, 2645.
34. R. Eisenberg, *Acc. Chem. Res.*, 1991, **24**, 110-116.

35. A. W. Overhauser, *Phys. Rev.*, 1953, **92**, 411-415.
36. T. R. Carver and C. P. Slichter, *Phys. Rev.* , 1953, **92**, 212-213.
37. T. R. Carver and C. P. Slichter, *Phys. Rev.*, 1956, **102**, 975-980.
38. J. H. Ardenkjær-Larsen, S. Bowen, J. R. Petersen, O. Rybalko, M. S. Vinding, M. Ullisch and N. C. Nielsen, *Magn. Reson. Med.*, 2019, **81**, 2184-2194.
39. A. Abragam and M. Goldman, *Rep. Prog. Phys.*, 1978, **41**, 395.
40. T. Maly, G. Debelouchina, V. Bajaj, K.-N. Hu, C.-G. Joo, M. Mak–Jurkauskas, J. Sirigiri, P. van der Wel, J. Herzfeld, R. J. Temkin and R. Griffin, *J. Chem. Phys.*, 2008, **128**, 2211.
41. K. R. Keshari and D. M. Wilson, *Chem. Soc. Rev.*, 2014, **43**, 1627-1659.
42. M. Goldman and A. Landesman, *Phys. Rev.*, 1963, **132**, 610-620.
43. Y. Hovav, A. Feintuch and S. Vega, *Phys. Chem. Chem. Phys.*, 2013, **15**, 188-203.
44. P. J. M. Van Bentum, G. H. A. van der Heijden, J. A. Villanueva-Garibay and A. P. M. Kentgens, *Phys. Chem. Chem. Phys.*, 2011, **13**, 17831-17840.
45. J. B. Hövener, A. N. Pravdivtsev, B. Kidd, C. R. Bowers, S. Glöggler, K. V. Kovtunov, M. Plaumann, R. Katz-Brull, K. Buckenmaier and A. Jerschow, *Angew. Chem. Int. Ed.*, 2018, **57**, 11140-11162.
46. S. B. Duckett and D. Blazina, *Eur. J. Inorg. Chem*, 2003, **2003**, 2901-2912.
47. R. W. Harkness and W. E. Deming, *J. Am. Chem. Soc.*, 1932, **54**, 2850-2852.
48. P. M. Richardson, R. O. John, A. J. Parrott, P. J. Rayner, W. Iali, A. Nordon, M. E. Halse and S. B. Duckett, *Phys. Chem. Chem. Phys.*, 2018, **20**, 26362-26371.
49. M. Carravetta and M. H. Levitt, *J. Chem Phys.*, 2005, **122**, 214505.
50. M. Carravetta, O. G. Johannessen and M. H. Levitt, *Phys. Rev. Lett.*, 2004, **92**, 153003.
51. R. K. Ghosh, S. J. Kadlecek, J. H. Ardenkjaer-Larsen, B. M. Pullinger, G. Pileio, M. H. Levitt, N. N. Kuzma and R. R. Rizi, *Magn. Reson. Med.*, 2011, **66**, 1177-1180.
52. M. Carravetta and M. H. Levitt, *J. Am. Chem Soc.*, 2004, **126**, 6228-6229.
53. Z. Zhou, J. Yu, J. F. P. Colell, R. Laasner, A. Logan, D. A. Barskiy, R. V. Shchepin, E. Y. Chekmenev, V. Blum and W. S. Warren, *J. Phys. Chem. Lett.*, 2017, **8**, 3008-3014.
54. G. Pileio, J. T. Hill-Cousins, S. Mitchell, I. Kuprov, L. J. Brown, R. C. D. Brown and M. H. Levitt, *J. Am. Chem. Soc.*, 2012, **134**, 17494-17497.
55. T. Theis, G. X. Ortiz, A. W. Logan, K. E. Claytor, Y. Feng, W. P. Huhn, V. Blum, S. J. Malcolmson, E. Y. Chekmenev and Q. Wang, *Sci. Adv.*, 2016, **2**, e1501438.
56. S. S. Roy, P. J. Rayner, M. J. Burns and S. B. Duckett, *J. Chem. Phys.*, 2020, **152**, 014201.
57. G. Stevanato, J. T. Hill-Cousins, P. Håkansson, S. S. Roy, L. J. Brown, R. C. D. Brown, G. Pileio and M. H. Levitt, *Angew. Chem. Int. Ed.*, 2015, **54**, 3740-3743.
58. C. P. N. Tanner, J. R. Lindale, S. L. Eriksson, Z. Zhou, J. F. P. Colell, T. Theis and W. S. Warren, *J. Chem. Phys.*, 2019, **151**, 044201.
59. S. B. Duckett and R. E. Mewis, *Acc. Chem. Res.*, 2012, **45**, 1247-1257.
60. S. B. Duckett and N. J. Wood, *Coord. Chem. Rev.*, 2008, **252**, 2278-2291.
61. S. B. Duckett, C. L. Newell and R. Eisenberg, *J. Am. Chem. Soc.*, 1994, **116**, 10548-10556.
62. D. B. Burueva, K. V. Kovtunov, A. V. Bukhtiyarov, D. A. Barskiy, I. P. Prosvirin, I. S. Mashkovsky, G. N. Baeva, V. I. Bukhtiyarov, A. Y. Stakheev and I. V. Koptyug, *Chem. Eur. J.*, 2018, **24**, 2547-2553.
63. W. Wang, J. Xu, Y. Zhao, G. Qi, Q. Wang, C. Wang, J. Li and F. Deng, *Phys. Chem. Chem. Phys.*, 2017, **19**, 9349-9353.
64. K. Sorochkina, V. V. Zhivonitko, K. Chernichenko, V.-V. Telkki, T. Repo and I. V. Koptyug, *J. Phys. Chem. Lett.*, 2018, **9**, 903-907.
65. V. V. Zhivonitko, K. Sorochkina, K. Chernichenko, B. Kótai, T. Földes, I. Pápai, V.-V. Telkki, T. Repo and I. Koptyug, *Phys. Chem. Chem. Phys.*, 2016, **18**, 27784-27795.
66. K. V. Kovtunov, I. E. Beck, V. I. Bukhtiyarov and I. V. Koptyug, *Angew. Chem. Int. Ed.*, 2008, **47**, 1492-1495.
67. A. Svyatova, E. S. Kononenko, K. V. Kovtunov, D. Lebedev, E. Y. Gerasimov, A. V. Bukhtiyarov, I. P. Prosvirin, V. I. Bukhtiyarov, C. R. Müller and A. Fedorov, *Cat. Sci. Technol.*, 2020, **10**, 99-104.

68.   P. Bhattacharya, E. Y. Chekmenev, W. H. Perman, K. C. Harris, A. P. Lin, V. A. Norton, C. T. Tan, B. D. Ross and D. P. Weitekamp, *J. Magn. Reson.*, 2007, **186**, 150-155.

69.   N. M. Zacharias, H. R. Chan, N. Sailasuta, B. D. Ross and P. Bhattacharya, *J. Am. Chem. Soc.*, 2011, **134**, 934-943.

70.   F. Reineri, T. Boi and S. Aime, *Nat. Commun.*, 2015, **6**, 5858.

71.   N. M. Zacharias, C. R. McCullough, S. Wagner, N. Sailasuta, H. R. Chan, Y. Lee, J. Hu, W. H. Perman, C. Henneberg, B. D. Ross and P. Bhattacharya, *J. Mol. Im. Dyn.*, 2016, **6**, 123.

72.   E. Cavallari, C. Carrera, M. Sorge, G. Bonne, A. Muchir, S. Aime and F. Reineri, *Sci. Rep.*, 2018, **8**, 8366.

73.   E. Cavallari, C. Carrera, S. Aime and F. Reineri, *J. Magn. Reson.*, 2018, **289**, 12-17.

74.   E. Cavallari, C. Carrera, S. Aime and F. Reineri, *Chem. Eur. J.*, 2017, **23**, 1200-1204.

75.   E. Cavallari, C. Carrera, S. Aime and F. Reineri, *ChemPhysChem*, 2019, **20**, 318-325.

76.   R. W. Adams, J. A. Aguilar, K. D. Atkinson, M. J. Cowley, P. I. Elliott, S. B. Duckett, G. G. Green, I. G. Khazal, J. López-Serrano and D. C. Williamson, *Science*, 2009, **323**, 1708-1711.

77.   K. M. Appleby, R. E. Mewis, A. M. Olaru, G. G. R. Green, I. J. S. Fairlamb and S. B. Duckett, *Chem. Sci.*, 2015, **6**, 3981-3993.

78.   R. W. Adams, S. B. Duckett, R. A. Green, D. C. Williamson and G. G. Green, *J. Chem. Phys.*, 2009, **131**, 194505.

79.   D. A. Barskiy, S. Knecht, A. V. Yurkovskaya and K. L. Ivanov, *Prog. Nucl. Magn. Reson. Spec.*, 2019, **114-115**, 33-70.

80.   P. M. Richardson, S. Jackson, A. Parrott, A. Nordon, S. B. Duckett and M. E. Halse, *Magn. Reson. Chem.*, 2017, **56**, 641-650.

81.   R. E. Mewis, K. D. Atkinson, M. J. Cowley, S. B. Duckett, G. G. R. Green, R. A. Green, L. A. R. Highton, D. Kilgour, L. Lloyd, J. A. B. Lohman and D. C. Williamson, *Magn. Reson. Chem.*, 2014, **52**, 358–369.

82.   S. Lehmkuhl, M. Wiese, L. Schubert, M. Held, M. Küppers, M. Wessling and B. B, *J. Magn. Reson.*, 2018, **291**, 8-13.

83.   M. L. Truong, T. Theis, A. M. Coffey, R. V. Shchepin, K. W. Waddell, F. Shi, B. M. Goodson, W. S. Warren and E. Y. Chekmenev, *J. Phys. Chem. C*, 2015, **119**, 8786-8797.

84.   J. F. Colell, A. W. Logan, Z. Zhou, R. V. Shchepin, D. A. Barskiy, G. X. Ortiz Jr, Q. Wang, S. J. Malcolmson, E. Y. Chekmenev and W. S. Warren, *J. Phys. Chem. C*, 2017, **121**, 6626-6634.

85.   A. W. Logan, T. Theis, J. F. Colell, W. S. Warren and S. J. Malcolmson, *Chem. Eur. J.*, 2016, **22**, 10777-10781.

86.   K. Shen, A. W. Logan, J. F. Colell, J. Bae, G. X. Ortiz Jr, T. Theis, W. S. Warren, S. J. Malcolmson and Q. Wang, *Angew. Chem.*, 2017, **129**, 12280-12284.

87.   S. Roy, P. Norcott, P. J. Rayner, G. G. Green and S. Duckett, *Chem. Eur. J.*, 2017, **23**, 10496-10500.

88.   D. A. Barskiy, R. V. Shchepin, C. P. Tanner, J. F. Colell, B. M. Goodson, T. Theis, W. S. Warren and E. Y. Chekmenev, *ChemPhysChem*, 2017, **18**, 1493-1498.

89.   A. M. Olaru, T. B. Robertson, J. S. Lewis, A. Antony, W. Iali, R. E. Mewis and S. B. Duckett, *ChemistryOpen*, 2018, **7**, 97-105.

90.   R. V. Shchepin, B. M. Goodson, T. Theis, W. S. Warren and E. Y. Chekmenev, *ChemPhysChem*, 2017, **18**, 1961-1965.

91.   M. J. Burns, P. J. Rayner, G. G. Green, L. A. Highton, R. E. Mewis and S. B. Duckett, *J. Phys. Chem. B*, 2015, **119**, 5020-5027.

92.   A. M. Olaru, A. Burt, P. J. Rayner, S. J. Hart, A. C. Whitwood, G. G. Green and S. B. Duckett, *Chem. Commun.*, 2016, **52**, 14482-14485.

93.   S. S. Roy, P. Norcott, P. J. Rayner, G. G. R. Green and S. B. Duckett, *Chem. Eur. J.*, 2017, **23**, 10496-10500.

94.   A. N. Pravdivtsev, A. V. Yurkovskaya, H.-M. Vieth and K. L. Ivanov, *Phys. Chem. Chem. Phys.*, 2014, **16**, 24672-24675.

95.   S. S. Roy, G. Stevanato, P. J. Rayner and S. B. Duckett, *J. Magn. Reson.*, 2017, **285**, 55-60.

96. M. Fekete, O. Bayfield, S. B. Duckett, S. Hart, R. E. Mewis, N. Pridmore, P. J. Rayner and A. Whitwood, *Inorg. Chem.*, 2013, **52**, 13453-13461.
97. M. J. Cowley, R. W. Adams, K. D. Atkinson, M. C. Cockett, S. B. Duckett, G. G. Green, J. A. Lohman, R. Kerssebaum, D. Kilgour and R. E. Mewis, *J. Am. Chem. Soc.*, 2011, **133**, 6134-6137.
98. H. Zeng, J. Xu, J. Gillen, M. T. McMahon, D. Artemov, J.-M. Tyburn, J. A. Lohman, R. E. Mewis, K. D. Atkinson and G. G. Green, *J. Magn. Reson. Im.*, 2013, **237**, 73-78.
99. E. B. Dücker, L. T. Kuhn, K. Münnemann and C. Griesinger, *J. Magn. Reson.*, 2012, **214**, 159-165.
100. P. Spannring, I. Reile, M. Emondts, P. P. Schleker, N. K. Hermkens, N. G. van der Zwaluw, B. J. van Weerdenburg, P. Tinnemans, M. Tessari and B. Blümich, *Chem. Eur. J.*, 2016, **22**, 9277-9282.
101. R. E. Mewis, R. A. Green, M. C. Cockett, M. J. Cowley, S. B. Duckett, G. G. Green, R. O. John, P. J. Rayner and D. C. Williamson, *J. Phys. Chem. B*, 2015, **119**, 1416-1424.
102. P. J. Rayner, M. J. Burns, A. M. Olaru, P. Norcott, M. Fekete, G. G. Green, L. A. Highton, R. E. Mewis and S. B. Duckett, *Proc. Natl. Acad. Sci.*, 2017, 201620457.
103. R. E. Mewis, *Magn. Reson. Chem.*, 2015, **53**, 789-800.
104. W. Iali, P. J. Rayner and S. B. Duckett, *Sci. Adv.*, 2018, **4**, eaao6250.
105. K. X. Moreno, K. Nasr, M. Milne, A. D. Sherry and W. J. Goux, *J. Magn. Reson.*, 2015, **257**, 15-23.
106. W. Iali, P. J. Rayner, A. Alshehri, A. J. Holmes, A. J. Ruddlesden and S. B. Duckett, *Chem. Sci.*, 2018, **9**, 3677-3684.
107. P. M. Richardson, W. Iali, S. S. Roy, P. J. Rayner, M. E. Halse and S. B. Duckett, *Chem. Sci.*, 2019, **10**, 10607-10619.
108. P. J. Rayner, B. J. Tickner, W. Iali, M. Fekete, A. D. Robinson and S. B. Duckett, *Chem. Sci.*, 2019, **10**, 7709-7717.
109. P. J. Rayner, P. M. Richardson and S. B. Duckett, *Angew. Chem.*, 2020, **132**, 2732-2736.
110. H. Zeng, J. Xu, M. T. McMahon, J. A. Lohman and P. C. Van Zijl, *J. Magn. Reson.*, 2014, **246**, 119-121.
111. A. J. Holmes, P. J. Rayner, M. J. Cowley, G. G. Green, A. C. Whitwood and S. B. Duckett, *Dalton Trans.*, 2015, **44**, 1077-1083.
112. G. Pileio, M. Carravetta and M. H. Levitt, *Proc. Natl. Acad. Sci.*, 2010, **107**, 17135-17139.
113. J. Eills, J. Alonso-Valdesueiro, D. E. Salazar Marcano, J. Ferreira da Silva, S. Alom, G. J. Rees, J. V. Hanna, M. Carravetta and M. H. Levitt, *ChemPhysChem*, 2018, **19**, 40-44.
114. S. S. Roy, P. J. Rayner, P. Norcott, G. G. Green and S. B. Duckett, *Phys. Chem. Chem. Phys.*, 2016, **18**, 24905-24911.
115. P. Vasos, A. Comment, R. Sarkar, P. Ahuja, S. Jannin, J.-P. Ansermet, J. Konter, P. Hautle, B. Van Den Brandt and G. Bodenhausen, *Proc. Natl. Acad. Sci.*, 2009, **106**, 18469-18473.
116. D. A. Barskiy, L. A. Ke, X. Li, V. Stevenson, N. Widarman, H. Zhang, A. Truxal and A. Pines, *J. Phys. Chem. Lett.*, 2018, **9**, 2721-2724.
117. W. Iali, A. M. Olaru, G. G. Green and S. B. Duckett, *Chem. Eur. J.*, 2017, **23**, 10491-10495.
118. F. Shi, A. M. Coffey, K. W. Waddell, E. Y. Chekmenev and B. M. Goodson, *Angew. Chem. Int. Ed.*, 2014, **126**, 7625-7628.
119. K. V. Kovtunov, L. M. Kovtunova, M. E. Gemeinhardt, A. Bukhtiyarov, J. Gesiorski, V. I. Bukhtiyarov, E. Y. Chekmenev, I. V. Koptyug and B. M. Goodson, *Angew. Chem. Int. Ed.*, 2017, **129**, 10569-10573.
120. M. L. Truong, F. Shi, P. He, B. Yuan, K. N. Plunkett, A. N. Coffey, R. V. Shchepin, D. A. Barskiy, K. V. Kovtunov, I. V. Koptyug, K. W. Waddell, B. M. Goodson and E. Y. Chekmenev, *J. Phys. Chem. B*, 2014, **118**, 13882-13889.
121. M. Fekete, C. Gibard, G. J. Dear, G. G. R. Green, A. J. J. Hooper, D. Roberts, F. Cisnetti and S. B. Duckett, *Dalton Trans.*, 2015, **44**, 7870-7880.
122. N. Eshuis, B. J. van Weerdenburg, M. C. Feiters, F. P. Rutjes, S. S. Wijmenga and M. Tessari, *Angew. Chem. Int. Ed.*, 2015, **54**, 1481-1484.

123. L. S. Lloyd, R. W. Adams, M. Bernstein, S. Coombes, S. B. Duckett, G. G. Green, R. J. Lewis, R. E. Mewis and C. J. Sleigh, *J. Am. Chem. Soc.*, 2012, **134**, 12904-12907.

124. N. Eshuis, N. Hermkens, B. J. van Weerdenburg, M. C. Feiters, F. P. Rutjes, S. S. Wijmenga and M. Tessari, *J. Am. Chem. Soc.*, 2014, **136**, 2695-2698.

125. R. V. Shchepin, L. Jaigirdar, T. Theis, W. S. Warren, B. M. Goodson and E. Y. Chekmenev, *J. Phys. Chem. C*, 2017, **121**, 28425-28434.

126. J.-B. Hövener, E. Y. Chekmenev, K. C. Harris, W. H. Perman, T. T. Tran, B. D. Ross and P. Bhattacharya, *Magn. Reson. Mater. Phys.*, 2009, **22**, 123-134.

127. F. Reineri, A. Viale, S. Ellena, T. Boi, V. Daniele, R. Gobetto and S. Aime, *Angew. Chem. Int. Ed.*, 2011, **50**, 7350-7353.

128. K. Golman, J. H. Ardenkjær-Larsen, J. S. Petersson, S. Månsson and I. Leunbach, *Proc. Natl. Acad. Sci.*, 2003, **100**, 10435-10439.

129. K. Golman, O. Axelsson, H. Johannesson, S. Månsson, C. Olofsson and J. S. Petersson, *Magn. Reson. Im.*, 2001, **46**, 1-5.

130. A. B. Schmidt, S. Berner, W. Schimpf, C. Müller, T. Lickert, N. Schwaderlapp, S. Knecht, J. G. Skinner, A. Dost, P. Rovedo, J. Hennig, D. von Elverfeldt and J.-B. Hövener, *Nat. Commun.*, 2017, **8**, 14535.

131. A. B. Schmidt , S. Berner, M. Braig, M. Zimmermann, J. Hennig, D. von Elverfeldt and J.-B. Hövener, *PloS one*, 2018, **13**, e0200141.

132. S. J. Nelson, J. Kurhanewicz, D. B. Vigneron, P. E. Larson, A. L. Harzstark, M. Ferrone, M. van Criekinge, J. W. Chang, R. Bok and I. Park, *Sci. Trans. Med.*, 2013, **5**, 198ra108-198ra108.

133. M. Marjańska, I. Iltis, A. A. Shestov, D. K. Deelchand, C. Nelson, K. Uğurbil and P.-G. Henry, *J. Magn. Reson.*, 2010, **206**, 210-218.

134. T. Witney, M. Kettunen, D. Hu, F. Gallagher, S. Bohndiek, R. Napolitano and K. Brindle, *Br. J. Cancer.*, 2010, **103**, 1400.

135. E. M. Serrao, M. I. Kettunen, T. B. Rodrigues, P. Dzien, A. J. Wright, A. Gopinathan, F. A. Gallagher, D. Y. Lewis, K. K. Frese and J. Almeida, *Gut*, 2015, gutjnl-2015-310114.

136. J. D. MacKenzie, Y.-F. Yen, D. Mayer, J. S. Tropp, R. E. Hurd and D. M. Spielman, *Radiol.*, 2011, **259**, 414-420.

137. J. T. Grist, M. A. McLean, F. Riemer, R. F. Schulte, S. S. Deen, F. Zaccagna, R. Woitek, C. J. Daniels, J. D. Kaggie and T. Matys, *NeuroIm.*, 2019, **189**, 171-179.

138. H. R. Horton, L. A. Moran, R. S. Ochs, J. D. Rawn and K. G. Scrimgeour, *Principles of Biochemistry*, Prentice Hall Upper Saddle River, NJ, 1996.

139. M. Pourfathi, Y. Xin, S. J. Kadlecek, M. F. Cereda, H. Profka, H. Hamedani, S. M. Siddiqui, K. Ruppert, N. A. Drachman and J. N. Rajaei, *Magn. Reson. Med.*, 2017, **78**, 2106-2115.

140. A. Z. Lau, A. P. Chen, N. R. Ghugre, V. Ramanan, W. W. Lam, K. A. Connelly, G. A. Wright and C. H. Cunningham, *Magn. Reson. Med.*, 2010, **64**, 1323-1331.

141. S. J. DeVience, X. Lu, J. Proctor, P. Rangghran, E. R. Melhem, R. Gullapalli, G. M. Fiskum and D. Mayer, *Sci. Rep.*, 2017, **7**, 1907.

142. O. J. Rider, A. Apps, J. J. Miller, J. Y. C. Lau, A. J. M. Lewis, M. A. Peterzan, M. S. Dodd, A. Z. Lau, C. Trumper and F. Gallagher, *Circ. Res.*, 2020, **126**, 725-736.

143. S. E. Day, M. I. Kettunen, F. A. Gallagher, D.-E. Hu, M. Lerche, J. Wolber, K. Golman, J. H. Ardenkjaer-Larsen and K. M. Brindle, *Nat. Med.*, 2007, **13**, 1382.

144. L. Lumata, M. E. Merritt, C. R. Malloy, A. D. Sherry and Z. Kovacs, *J. Phys. Chem. A*, 2012, **116**, 5129-5138.

145. A. Capozzi, M. Karlsson, J. R. Petersen, M. H. Lerche and J. H. Ardenkjaer-Larsen, *J. Phys. Chem. C*, 2018, **122**, 7432-7443.

146. M. R. Clatworthy, M. I. Kettunen, D.-E. Hu, R. J. Mathews, T. H. Witney, B. W. Kennedy, S. E. Bohndiek, F. A. Gallagher, L. B. Jarvis and K. G. Smith, *Proc. Natl. Acad. Sci.*, 2012, **109**, 13374-13379.

147. N. Eshuis, R. L. E. G. Aspers, B. J. A. van Weerdenburg, M. C. Feiters, F. P. J. T. Rutjes, S. S. Wijmenga and M. Tessari, *Angew. Chem. Int. Ed.*, 2015, **54**, 14527-14530.

148. N. K. J. Hermkens, R. L. E. G. Aspers, M. C. Feiters, F. P. J. T. Rutjes and M. Tessari, *Magn. Reson. Chem.*, 2018, **56**, 633-640.

149. L. Sellies, I. Reile, R. L. E. G. Aspers, M. C. Feiters, F. P. J. T. Rutjes and M. Tessari, *Chem. Commun.*, 2019, **55**, 7235-7238.

150. O. Semenova, P. M. Richardson, A. J. Parrott, A. Nordon, M. E. Halse and S. B. Duckett, *Anal. Chem.*, 2019, **91**, 6695-6701.

151. T. Katayama and T. Nitta, *J. Chem. Eng.*, 1976, **21**, 194-196.

152. P. Bhattacharya, E. Y. Chekmenev, W. F. Reynolds, S. Wagner, N. Zacharias, H. R. Chan, R. Bünger and B. D. Ross, *NMR Biomed.*, 2011, **24**, 1023-1028.

153. T. Harris, O. Szekely and L. Frydman, *J. Phys. Chem. B.*, 2014, **118**, 3281-3290.

154. R. A. Dwek, J. G. Kenworthy and R. E. Richards, *Mol. Phys.*, 1966, **10**, 529-532.

155. P. J. Rayner and S. Duckett, *Angew. Chem. Int. Ed.*, 2018, **57**, 6742-6753.

156. D. A. Barskiy, K. V. Kovtunov, I. V. Koptyug, P. He, K. A. Groome, Q. A. Best, F. Shi, B. M. Goodson, R. V. Shchepin and A. M. Coffey, *J. Am. Chem. Soc.*, 2014, **136**, 3322-3325.

157. D. A. Barskiy, A. N. Pravdivtsev, K. L. Ivanov, K. V. Kovtunov and I. V. Koptyug, *Phys. Chem. Chem. Phys.*, 2016, **18**, 89-93.

158. E. V. Stanbury, P. M. Richardson and S. B. Duckett, *Cat. Sci. Technol.*, 2019, **9**, 3914-3922.

159. B. J. van Weerdenburg, N. Eshuis, M. Tessari, F. P. Rutjes and M. C. Feiters, *Dalton Trans.*, 2015, **44**, 15387-15390.

160. A. N. Pravdivtsev, A. V. Yurkovskaya, H. M. Vieth, K. L. Ivanov and R. Kaptein, *ChemPhysChem*, 2013, **14**, 3327-3331.

161. C. R. Bowers, H. W. Long, T. Pietrass, H. C. Gaede and A. Pines, *Chem. Phys. Lett.*, 1993, **205**, 168-170.

162. D. W. Lachenmeier, E.-M. Sohnius, R. Attig and M. G. López, *J. Agri. Food Chem.*, 2006, **54**, 3911-3915.

163. C. Bauer-Christoph, N. Christoph, B. O. Aguilar-Cisneros, M. G. Lopez, E. Richling, A. Rossmann and P. Schreier, *Eur. Food Res. Technol.*, 2003, **217**, 438-443.

164. D. González-Arjona, V. González-Gallero, F. Pablos and A. G. González, *Anal. Chim. Acta*, 1999, **381**, 257-264.

165. G. S. Denisov and N. S. Golubev, *J. Mol. Struct.*, 1981, **75**, 311-326.

166. T. McMahon and J. Beauchamp, *J. Phys. Chem.*, 1977, **81**, 593-598.

167. H. K. Hall Jr., *J. Am. Chem. Soc.*, 1957, **79**, 5441-5444.

168. S. Knecht, S. Hadjiali, D. A. Barskiy, A. Pines, G. Sauer, A. S. Kiryutin, K. L. Ivanov, A. V. Yurkovskaya and G. Buntkowsky, *J. Phys. Chem. C.*, 2019, **123**, 16288-16293.

169. T. Theis, M. Truong, A. M. Coffey, E. Y. Chekmenev and W. S. Warren, *J. Magn. Reson.*, 2014, **248**, 23-26.

170. A. N. Pravdivtsev, A. V. Yurkovskaya, H.-M. Vieth and K. L. Ivanov, *J. Phys. Chem. B*, 2015, **119**, 13619-13629.

171. T. Theis, M. L. Truong, A. M. Coffey, R. V. Shchepin, K. W. Waddell, F. Shi, B. M. Goodson, W. S. Warren and E. Y. Chekmenev, *J. Am. Chem. Soc.*, 2015, **137**, 1404-1407.

172. I. Reile, R. L. E. G. Aspers, J. M. Tyburn, J. G. Kempf, M. C. Feiters, F. P. J. T. Rutjes and M. Tessari, *Angew. Chem.*, 2017, **129**, 9302-9305.

173. B. T. Chung, H.-Y. Chen, J. Gordon, D. Mammoli, R. Sriram, A. W. Autry, L. M. Le Page, M. Chaumeil, P. Shin and J. Slater, *J. Magn. Reson.*, 2019, **309**, 106617.

174. C. Gabellieri, S. Reynolds, A. Lavie, G. S. Payne, M. O. Leach and T. R. Eykyn, *J. Am. Chem. Soc.*, 2008, **130**, 4598-4599.

175. H. Allouche-Arnon, A. Gamliel, C. M. Barzilay, R. Nalbandian, J. M. Gomori, M. Karlsson, M. H. Lerche and R. Katz-Brull, *Contrast Media Mol. Im.*, 2011, **6**, 139-147.

176. C. von Morze, M. A. Ohliger, I. Marco-Rius, D. M. Wilson, R. R. Flavell, D. Pearce, D. B. Vigneron, J. Kurhanewicz and Z. J. Wang, *Magn. Reson. Med.*, 2018, **79**, 1862-1869.

177. K. X. Moreno, S. Satapati, R. J. DeBerardinis, S. C. Burgess, C. R. Malloy and M. E. Merritt, *J. Bio. Chem.*, 2014, **289**, 35859-35867.

178. O. Szekely, G. L. Olsen, I. C. Felli and L. Frydman, *Anal. Chem.*, 2018, **90**, 6169-6177.

179. B. W. C. Kennedy, M. I. Kettunen, D.-E. Hu and K. M. Brindle, *J. Am. Chem. Soc.*, 2012, **134**, 4969-4977.

180. J. Wang, F. Kreis, A. J. Wright, R. L. Hesketh, M. H. Levitt and K. M. Brindle, *Magn. Reson. Med.*, 2018, **79**, 741-747.
181. A. P. Chen, J. Kurhanewicz, R. Bok, D. Xu, D. Joun, V. Zhang, S. J. Nelson, R. E. Hurd and D. B. Vigneron, *Magn. Reson. Im.*, 2008, **26**, 721-726.
182. C. Prottey, D. George, R. W. Leech, J. G. Black, D. Howes and C. F. H. Vickers, *Br. J. Dermatol.*, 1984, **110**, 475-485.
183. S. Korchak, S. Yang, S. Mamone and S. Glöggler, *ChemistryOpen*, 2018, **7**, 344-348.
184. S. Korchak, S. Mamone and S. Glöggler, *ChemistryOpen*, 2018, **7**, 672-676.
185. M. Haake, J. Natterer and J. Bargon, *J. Am. Chem. Soc.*, 1996, **118**, 8688-8691.
186. J. Damitio, G. Smith, J. Meany and Y. Pocker, *J. Am. Chem. Soc.*, 1992, **114**, 3081-3087.
187. A. Esposito, A. Lukas, J. E. Meany and Y. Pocker, *Canad. J. Chem.*, 1999, **77**, 1108-1117.
188. C. Asmus, O. Mozziconacci and C. Schöneich, *J. Phys. Chem. A.*, 2015, **119**, 966-977.
189. E. Cordes and W. Jencks, *J. Am. Chem. Soc.*, 1962, **84**, 832-837.
190. E. H. Cordes and W. P. Jencks, *J. Am. Chem. Soc.*, 1963, **85**, 2843-2848.
191. J. Harrowfield and A. Sargeson, *J. Am. Chem. Soc.*, 1979, **101**, 1514-1520.
192. N. Dharmaraj, P. Viswanathamurthi and K. Natarajan, *Trans. Met. Chem.*, 2001, **26**, 105-109.
193. Z. H. Chohan, A. Munawar and C. T. Supuran, *Met. Based Drugs*, 2001, **8**, 137-143.
194. R. P. Eckberg, R. A. Henry, L. W. Cary and J. H. Nelson, *Inorg. Chem.*, 1977, **16**, 2977-2979.
195. B. J. Tickner, W. Iali, S. S. Roy, A. C. Whitwood and S. B. Duckett, *ChemPhysChem*, 2019, **20**, 241-245.
196. A. J. Edwards, S. Elipe, M. A. Esteruelas, F. J. Lahoz, L. A. Oro and C. Valero, *Organomet.*, 1997, **16**, 3828-3836.
197. D. W. Lee, C. M. Jensen and D. Morales-Morales, *Organomet.*, 2003, **22**, 4744-4749.
198. B. Raju and B. Sivasankar, *J. Therm. Anal. Calorim.*, 2009, **98**, 371-376.
199. H. J. Lawson and J. D. Atwood, *J. Am. Chem. Soc.*, 1988, **110**, 3680-3682.
200. P. J. Rayner, P. Norcott, K. M. Appleby, W. Iali, R. O. John, S. J. Hart, A. C. Whitwood and S. B. Duckett, *Nat. Commun.*, 2018, **9**, 1-11.
201. B. J. A. van Weerdenburg, S. Glöggler, N. Eshuis, A. H. J. T. Engwerda, J. M. M. Smits, R. de Gelder, S. Appelt, S. S. Wymenga, M. Tessari, M. C. Feiters, B. Blümich and F. P. J. T. Rutjes, *Chem. Commun.*, 2013, **49**, 7388-7390.
202. R. A. Kelly III, H. Clavier, S. Giudice, N. M. Scott, E. D. Stevens, J. Bordner, I. Samardjiev, C. D. Hoff, L. Cavallo and S. P. Nolan, *Organomet.*, 2008, **27**, 202-210.
203. J. H. McNeill, K. H. Thompson, L. R. Kelland, N. Birch, P. Rhodes, R. H. Weiss, S. Spinelli, A. R. Butler, C. F. Shaw and C. Orvig, *Uses of Inorganic Chemistry in Medicine*, Royal Society of Chemistry, 2007.
204. B. Procacci, P. M. Aguiar, M. E. Halse, R. N. Perutz and S. B. Duckett, *Chem. Sci.*, 2016, **7**, 7087-7093.
205. M. E. Merritt, C. Harrison, Z. Kovacs, P. Kshirsagar, C. R. Malloy and A. D. Sherry, *J. Am. Chem Soc.*, 2007, **129**, 12942-12943.
206. Y. Xing, A. K. Jindal, M. Regueiro-Figueroa, M. Le Fur, N. Kervarec, P. Zhao, Z. Kovacs, L. Valencia, P. Pérez-Lourido and R. Tripier, *Chem. Eur. J.*, 2016, **22**, 16657-16667.
207. J. Natterer and J. Bargon, *Prog. Nucl. Magn. Reson.*, 1997, **31**, 293-315.
208. B. Procacci, S. S. Roy, P. Norcott, N. Turner and S. B. Duckett, *J. Am. Chem Soc.*, 2018, **140**, 16855-16864.
209. S. S. Roy, P. J. Rayner, P. Norcott, G. G. R. Green and S. B. Duckett, *Phys. Chem. Chem. Phys.*, 2016, **18**, 24905-24911.
210. A. M. Olaru, S. S. Roy, L. S. Lloyd, S. Coombes, G. G. R. Green and S. B. Duckett, *Chem. Commun.*, 2016, **52**, 7842-7845.
211. I. Marco-Rius, M. C. D. Tayler, M. I. Kettunen, T. J. Larkin, K. N. Timm, E. M. Serrao, T. B. Rodrigues, G. Pileio, J. H. Ardenkjaer-Larsen and M. H. Levitt, *NMR Biomed.*, 2013, **26**, 1696-1704.
212. G. Pileio, M. Carravetta, E. Hughes and M. H. Levitt, *J. Am. Chem Soc.*, 2008, **130**, 12582-12583.

213. M. C. D. Tayler and M. H. Levitt, *Phys. Chem. Chem. Phys.*, 2011, **13**, 9128-9130.
214. G. Pileio, *J. Chem. Phys.*, 2011, **134**, 214505.
215. C. A. Tolman, *Chem. Soc. Rev.*, 1972, **1**, 337-353.
216. J. T. Anhaus, T. P. Kee, M. H. Schofield and R. R. Schrock, *J. Am. Chem Soc.*, 1990, **112**, 1642-1643.
217. K. Searles, M. Pink, K. G. Caulton and D. J. Mindiola, *Dalton Trans.*, 2012, **41**, 9619-9622.
218. B. E. Hauger, D. Gusev and K. G. Caulton, *J. Am. Chem. Soc.*, 1994, **116**, 208-214.
219. C. E. Johnson and R. Eisenberg, *J. Am. Chem. Soc.*, 1985, **107**, 3148-3160.
220. N. K. J. Hermkens, M. C. Feiters, F. P. J. T. Rutjes, S. S. Wijmenga and M. Tessari, *J. Magn. Reson.*, 2017, **276**, 122-127.
221. J. E. Richards, A. J. J. Hooper, O. W. Bayfield, M. C. R. Cockett, G. J. Dear, A. J. Holmes, R. O. John, R. E. Mewis, N. Pridmore and A. D. Roberts, *Chem. Commun.*, 2018, **54**, 10375-10378.
222. D. C. Harris, *J. Chem. Edu.*, 1998, **75**, 119.
223. D. Farcasiu, *J. Chem. Edu.*, 1975, **52**, 76.
224. B. J. Tickner, R. O. John, S. S. Roy, S. J. Hart, A. C. Whitwood and S. B. Duckett, *Chem. Sci.*, 2019, **10**, 5235-5245.
225. N. M. Shavaleev, F. Monti, R. Scopelliti, A. Baschieri, L. Sambri, N. Armaroli, M. Grätzel and M. K. Nazeeruddin, *Organomet.*, 2013, **32**, 460-467.
226. N. M. Shavaleev, F. Monti, R. D. Costa, R. Scopelliti, H. J. Bolink, E. Ortí, G. Accorsi, N. Armaroli, E. Baranoff and M. Grätzel, *Inorg. Chem.*, 2012, **51**, 2263-2271.
227. F. A. Cotton, W. R. Robinson, R. A. Walton and R. Whyman, *Inorg. Chem.*, 1967, **6**, 929-935.
228. G. J. Palenik and G. R. Clark, *Inorg. Chem.*, 1970, **9**, 2754-2760.
229. C. M. Friend and D. A. Chen, *Polyhed.*, 1997, **16**, 3165-3175.
230. D. M. Antonelli and M. Cowie, *Inorg. Chem.*, 1990, **29**, 3339-3345.
231. L.-S. Wang, R. McDonald and M. Cowie, *Inorg. Chem.*, 1994, **33**, 3735-3744.
232. O. Halter, I. Fernández and H. Plenio, *Chem. Eur. J.*, 2017, **23**, 711-719.
233. M. E. Gemeinhardt, M. N. Limbach, T. R. Gebhardt, C. W. Eriksson, S. L. Eriksson, J. R. Lindale, E. A. Goodson, W. S. Warren, E. Y. Chekmenev and B. M. Goodson, *Angew. Chem.*, 2020, **132**, 426-431.
234. K. Golman, M. Lerche, R. Pehrson and J. H. Ardenkjaer-Larsen, *Cancer Res.*, 2006, **66**, 10855-10860.
235. K. Golman and M. Thaning, *Proc. Natl. Acad. Sci.*, 2006, **103**, 11270-11275.
236. C.-H. Fung, A. S. Mildvan and J. S. Leigh Jr, *Biochem.*, 1974, **13**, 1160-1169.
237. C. H. Fung, R. K. Gupta and A. S. Mildvan, *Biochem.*, 1976, **15**, 85-92.
238. M. Gruselle, C. Train, K. Boubekeur, P. Gredin and N. Ovanesyan, *Coord. Chem. Rev.*, 2006, **250**, 2491-2500.
239. D. K. Simanshu, P. S. Satheshkumar, H. S. Savithri and M. R. N. Murthy, *Biochem. Biophys. Res. Commun.*, 2003, **311**, 193-201.
240. A. S. Mildvan and M. C. Scrutton, *Biochem.*, 1967, **6**, 2978-2994.
241. S. J. Nelson, D. Vigneron, J. Kurhanewicz, A. Chen, R. Bok and R. Hurd, *Appl. Mag. Reson.*, 2008, **34**, 533-544.
242. A. J. Ruddlesden, R. E. Mewis, G. G. Green, A. C. Whitwood and S. B. Duckett, *Organomet.*, 2015, **34**, 2997-3006.
243. A. J. Ruddlesden and S. B. Duckett, *Chem. Commun.*, 2016, **52**, 8467-8470.
244. L. S. Lloyd, A. Asghar, M. J. Burns, A. Charlton, S. Coombes, M. J. Cowley, G. J. Dear, S. B. Duckett, G. R. Genov and G. G. R. Green, *Cat. Sci. Technol.*, 2014, **4**, 3544-3554.
245. C. M. Wong, M. Fekete, R. Nelson-Forde, M. R. D. Gatus, P. J. Rayner, A. C. Whitwood, S. B. Duckett and B. A. Messerle, *Cat. Sci. Technol.*, 2018, **8**, 4925-4933.
246. F. F. Diaz-Rullo, F. Zamberlan, R. E. Mewis, M. Fekete, L. Broche, L. A. Cheyne, S. Dall'Angelo, S. B. Duckett, D. Dawson and M. Zanda, *Bioorg. Med. Chem.*, 2017, **25**, 2730-2742.
247. J. Colell, A. W. J. Logan, Z. Zhou, J. R. Lindale, R. Laasner, R. Shchepin, E. Chekmenev, V. Blum, W. S. Warren and S. J. Malcolmson, *Chem. Commun.*, 2020.

248. R. V. Shchepin, D. A. Barskiy, A. M. Coffey, T. Theis, F. Shi, W. S. Warren, B. M. Goodson and E. Y. Chekmenev, *ACS Sensors*, 2016, **1**, 640-644.

249. P. G. Rasmussen, J. E. Anderson, O. H. Bailey, M. Tamres and J. C. Bayón, *J. Am. Chem. Soc.*, 1985, **107**, 279-281.

250. T. M. Gilbert, F. J. Hollander and R. G. Bergman, *J. Am. Chem. Soc.*, 1985, **107**, 3508-3516.

251. W. D. Jones and R. M. Chin, *J. Am. Chem. Soc.*, 1994, **116**, 198-203.

252. M.-L. Li, S. Yang, X.-C. Su, H.-L. Wu, L.-L. Yang, S.-F. Zhu and Q.-L. Zhou, *J. Am. Chem. Soc.*, 2017, **139**, 541-547.

253. B. J. Tickner, O. Semenova, W. Iali, P. J. Rayner, A. C. Whitwood and S. B. Duckett, *Cat. Sci. Technol.*, 2020, **10**, 1343-1355.

254. R. A. T. M. van Benthem, H. Hiemstra, P. W. N. M. van Leeuwen, J. W. Geus and W. N. Speckamp, *Angew. Chem. Intl. Ed.*, 1995, **34**, 457-460.

255. G. Sipos, E. E. Drinkel and R. Dorta, *Chem. Soc. Rev.*, 2015, **44**, 3834-3860.

256. M. Calligaris, *Coord. Chem. Rev.*, 2004, **248**, 351-375.

257. J. A. Davies, in *Advances in Inorganic Chemistry and Radiochemistry*, Elsevier, 1981, vol. 24, pp. 115-187.

258. T. Diao, P. White, I. Guzei and S. S. Stahl, *Inorg. Chem.*, 2012, **51**, 11898-11909.

259. A. F. Oliveri, L. A. Wills, C. R. Hazlett, M. E. Carnes, I. Y. Chang, P. H.-Y. Cheong and D. W. Johnson, *Chem. Sci.*, 2015, **6**, 4071-4085.

260. B. J. Tickner, J. S. Lewis, R. O. John, A. C. Whitwood and S. B. Duckett, *Dalton Trans.*, 2019, **48**, 15198-15206.

261. A. N. Pravdivtsev, K. L. Ivanov, A. V. Yurkovskaya, P. A. Petrov, H.-H. Limbach, R. Kaptein and H.-M. Vieth, *J. Magn. Reson.*, 2015, **261**, 73-82.

262. A. S. Kiryutin, A. V. Yurkovskaya, H. Zimmermann, H. M. Vieth and K. L. Ivanov, *Magn. Reson. Chem.*, 2018, **56**, 651-662.

263. W. Iali, S. S. Roy, B. J. Tickner, F. Ahwal, A. J. Kennerley and S. B. Duckett, *Angew. Chem.*, 2019, **131**, 10377-10381.

264. D. Ando, C. Bevan, J. M. Brown and D. W. Price, *J. Chem. Soc. Chem. Commun.*, 1992, 592-594.

265. J. R. Lao, H. c. Fernández-Pérez and A. Vidal-Ferran, *Org. Lett.*, 2015, **17**, 4114-4117.

266. D. Schleyer, H. G. Niessen and J. Bargon, *New J. Chem.*, 2001, **25**, 423-426.

267. R. Gobetto, L. Milone, F. Reineri, L. Salassa, A. Viale and E. Rosenberg, *Organomet.*, 2002, **21**, 1919-1924.

268. B. J. Tickner, R. R. Parker, A. C. Whitwood and S. B. Duckett, *Organomet.*, 2019, **38**, 4377-4382.

269. L. Wang, W. He and Z. Yu, *Chem. Soc. Rev.*, 2013, **42**, 599-621.

270. T.-Y. Luh and Z.-J. Ni, *Synthesis*, 1990, **1990**, 89-103.

271. J. M. O'Connor, K. D. Bunker, A. L. Rheingold and L. Zakharov, *J. Am. Chem. Soc.*, 2005, **127**, 4180-4181.

272. F. Shi, P. He, Q. A. Best, K. Groome, M. L. Truong, A. M. Coffey, G. Zimay, R. V. Shchepin, K. W. Waddell and E. Y. Chekmenev, *J. Phys. Chem. C.*, 2016, **120**, 12149-12156.

273. J. P. Kintzinger and J. M. Lehn, *Mol. Phys.*, 1971, **22**, 273-287.

274. M. Hunger and J. Weitkamp, *Angew. Chem. Int. Ed.*, 2001, **40**, 2954-2971.

275. C. H. Cunningham, J. Y. C. Lau, A. P. Chen, B. J. Geraghty, W. J. Perks, I. Roifman, G. A. Wright and K. A. Connelly, *Circ. Res.*, 2016, **119**, 1177-1182.

276. H. Zeng, Y. Lee and C. Hilty, *Anal. Chem.*, 2010, **82**, 8897-8902.

277. S. Jannin, L. Helm and G. Bodenhausen, *J. Am. Chem. Soc.*, 2010, **132**, 5006-5007.

278. K. V. Kovtunov, V. V. Zhivonitko, A. Corma and I. V. Koptyug, *J. Phys. Chem. Lett.*, 2010, **1**, 1705-1708.

279. A. B. Permin and R. Eisenberg, *J. Am. Chem. Soc.*, 2002, **124**, 12406-12407.

280. C. Godard, S. B. Duckett, S. Polas, R. Tooze and A. C. Whitwood, *J. Am. Chem. Soc.*, 2005, **127**, 4994-4995.

281. C. Godard, S. B. Duckett, C. Henry, S. Polas, R. Toose and A. C. Whitwood, *Chem. Commun.*, 2004, 1826-1827.

282. N. J. Stewart and S. Matsumoto, *Magn. Reson. Med. Sci.*, 2019, rev-2019.

283. J.-B. Hövener, N. Schwaderlapp, R. Borowiak, T. Lickert, S. B. Duckett, R. E. Mewis, R. W. Adams, M. J. Burns, L. A. Highton and G. G. Green, *Anal. Chem.*, 2014, **86**, 1767-1774.

284. M. Fekete, S. S. Roy and S. B. Duckett, *Phys. Chem. Chem. Phys.*, 2020, **22**, 5033-5037.

285. A. Manoharan, P. J. Rayner, W. Iali, M. J. Burns, V. H. Perry and S. B. Duckett, *ChemMedChem*, 2018, **13**, 352-359.

286. X. Ji, A. Bornet, B. Vuichoud, J. Milani, D. Gajan, A. J. Rossini, L. Emsley, G. Bodenhausen and S. Jannin, *Nat. Commun.*, 2017, **8**, 1-7.

287. G. J. Topping, C. Hundshammer, L. Nagel, M. Grashei, M. Aigner, J. G. Skinner, R. F. Schulte and F. Schilling, *Magn. Reson. Mater. Phy.*, 2019, 1-36.

288. V. Daniele, F. X. Legrand, P. Berthault, J. N. Dumez and G. Huber, *ChemPhysChem*, 2015, **16**, 3413-3417.

289. B. C. Dickinson and C. J. Chang, *J. Am. Chem. Soc.*, 2008, **130**, 9638-9639.

290. A. R. Lippert, K. R. Keshari, J. Kurhanewicz and C. J. Chang, *J. Am. Chem. Soc.*, 2011, **133**, 3776-3779.

291. A. Lopalco, G. Dalwadi, S. Niu, R. L. Schowen, J. Douglas and V. J. Stella, *J. Pharmaceu. Sci.*, 2016, **105**, 705-713.

292. E. Melzer and H.-L. Schmidt, *Biochem. J.*, 1988, **252**, 913-915.

293. R. E. Mewis, M. Fekete, G. R. R. Green, A. C. Whitwood and S. B. Duckett, *Chem. Commun.*, 2015, **51**, 9857-9859.

294. C. Perinu, B. Arstad and K.-J. Jens, *Energy Procedia*, 2013, **37**, 7310-7317.

295. E. Cavallari, C. Carrera, G. Di Matteo, O. Bondar, S. Aime and F. Reineri, *Front. Oncol.*, 2020, **10**, 497.

296. S. A. Margolis and B. Coxon, *Anal. Chem.*, 1986, **58**, 2504-2510.

297. E. C. Griffith, B. K. Carpenter, R. K. Shoemaker and V. Vaida, *Proc. Natl. Acad. Sci.*, 2013, **110**, 11714-11719.

298. D. L. Leussing and E. M. Hanna, *J. Am. Chem. Soc.*, 1966, **88**, 693-696.

299. A. Wibowo, J. M. Park, S.-C. Liu, C. Khosla and D. M. Spielman, *ACS Chem. Biol.*, 2017, **12**, 1737-1742.

300. H. J. Forman, A. Bernardo and K. J. A. Davies, *Arch. Biochem. Biophys.*, 2016, **603**, 48-53.

301. H. Park, G. Zhang, J. Bae, T. Theis, W. S. Warren and Q. Wang, *Bioconjug. Chem.*, 2020.

302. R. Savka and H. Plenio, *Dalton Trans.*, 2015, **44**, 891-893.

303. O. Torres, M. Martín and E. Sola, *Organomet.*, 2009, **28**, 863-870.

304. O. V. Dolomanov, L. J. Bourhis, R. J. Gildea, J. A. Howard and H. Puschmann, *J. Appl. Cryst.*, 2009, **42**, 339-341.

305. G. M. Sheldrick, *Acta Crystallogr. A*, 2015, **71**, 3-8.

306. E. Cances, B. Mennucci and J. Tomasi, *J. Chem. Phys.*, 1997, **107**, 3032-3041.

307. B. Mennucci, E. Cances and J. Tomasi, *J. Phys. Chem. B*, 1997, **101**, 10506-10517.

308. E. Cancès and B. Mennucci, *J. Math. Chem.*, 1998, **23**, 309-326.

309. C. Adamo and V. Barone, *J. Chem. Phys.*, 1999, **110**, 6158-6170.

310. F. Weigend and R. Ahlrichs, *Phys. Chem. Chem. Phys.*, 2005, **7**, 3297-3305.

311. A. Schäfer, H. Horn and R. Ahlrichs, *J. Chem. Phys.*, 1992, **97**, 2571-2577.

312. D. Feller, *J. Comput. Chem.*, 1996, **17**, 1571-1586.

313. K. L. Schuchardt, B. T. Didier, T. Elsethagen, L. Sun, V. Gurumoorthi, J. Chase, J. Li and T. L. Windus, *J. Chem. Inf. Model.*, 2007, **47**, 1045-1052.

314. L. E. Roy, P. J. Hay and R. L. Martin, *J. Chem. Theory Comput.*, 2008, **4**, 1029-1031.

315. S. Grimme, S. Ehrlich and L. Goerigk, *J. Comput. Chem.*, 2011, **32**, 1456-1465.

316. M. Bühl, C. Reimann, D. A. Pantazis, T. Bredow and F. Neese, *J. Chem. Theory Comput.*, 2008, **4**, 1449-1459.

317. S. Simon, M. Duran and J. J. Dannenberg, *J. Chem. Phys.*, 1996, **105**, 11024-11031.

318. C. von Morze, R. A. Bok, G. D. Reed, J. H. Ardenkjaer-Larsen, J. Kurhanewicz and D. B. Vigneron, *Magn. Reson. Med.*, 2014, **72**, 1599-1609.